



HAL
open science

Identification and characterization of mechanical and structural properties against static damage and fatigue of a composite floating wind turbine blade

Owaisur Rahman Shah

► **To cite this version:**

Owaisur Rahman Shah. Identification and characterization of mechanical and structural properties against static damage and fatigue of a composite floating wind turbine blade. Mechanical engineering [physics.class-ph]. Université de Bretagne occidentale - Brest, 2014. English. NNT : 2014BRES0103 . tel-02368497

HAL Id: tel-02368497

<https://theses.hal.science/tel-02368497>

Submitted on 18 Nov 2019

HAL is a multi-disciplinary open access archive for the deposit and dissemination of scientific research documents, whether they are published or not. The documents may come from teaching and research institutions in France or abroad, or from public or private research centers.

L'archive ouverte pluridisciplinaire **HAL**, est destinée au dépôt et à la diffusion de documents scientifiques de niveau recherche, publiés ou non, émanant des établissements d'enseignement et de recherche français ou étrangers, des laboratoires publics ou privés.



université de bretagne
occidentale



THÈSE / UNIVERSITÉ DE BRETAGNE OCCIDENTALE

sous le sceau de l'Université européenne de Bretagne

pour obtenir le titre de

DOCTEUR DE L'UNIVERSITÉ DE BRETAGNE OCCIDENTALE

Génie Mécanique

École Doctorale des Science de la Mer

présentée par

Owaisur Rahman SHAH

Préparée au Laboratoire Brestois de
Mécanique et des Systèmes (EA 4325),
ENSTA Bretagne.

Thèse soutenue le 21 novembre 2014

devant le jury composé de :

Mohamed BENBOUZID

Professeur, Université Européenne de Bretagne / *Examineur*

Malk BENZEGGAGH

Ancien Professeur à l'UTC, Consultant / *Examineur*

Daniel COUTELLIER

Professeur, Univ. de Valenciennes et du Hainaut / *Rapporteur*

Abdellatif IMAD

Professeur, Université de Lille1, Polytech'Lille / *Examineur*

Khalid LAFDI

Professeur, University of Dayton / *Président du Jury*

Abdelouahed LAKSIMI

Professeur, Université de Technologie de Compiègne / *Rapporteur*

Alexis Martin

DCNS / *Invité*

Alain NEME,

Maître de Conférences, ENSTA Bretagne / *Examineur*

Jean Yves PRADILLON

Enseignant Chercheur, ENSTA Bretagne / *Invité*

Mostapha TARFAOUI

Enseignant Chercheur - HDR, ENSTA Bretagne / *Directeur de thèse*

Identification et caractérisation des propriétés mécaniques et structurales en endommagement statique et tenue en fatigue d'une pale composite d'éolienne flottante.

Identification and characterization of mechanical and structural properties against static damage and fatigue of a composite floating wind turbine blade.

Acknowledgements

Table of Contents

| | | |
|------------------|--|-----------|
| Chapter 1 | State of the art | 5 |
| 1.1 | Advances in Blade technology | 8 |
| 1.2 | Methods of fabrication | 10 |
| 1.3 | Resistance of composites to damage | 11 |
| 1.4 | Resistance to delamination and de-bonding | 14 |
| 1.4.1 | Analytical approach | 14 |
| 1.4.2 | Finite Element approach using VCCT. | 16 |
| 1.4.3 | Numerical approach using cohesive zone models. | 17 |
| 1.5 | Fatigue behavior of Materials. | 21 |
| 1.6 | Delamination fatigue. | 24 |
| 1.7 | Wind turbine form design | 25 |
| 1.8 | Fabrication of Blades | 28 |
| 1.9 | Full-scale testing of Wind Turbine Blades | 32 |
| 1.10 | Finite element modeling of Wind Turbine Blades | 33 |
| 1.11 | Conclusion | 35 |
| | | |
| Chapter 2 | Design methodology for Wind turbine Blades | 36 |
| 2.1 | Design Parameters | 38 |
| 2.1.1 | Swept area and Power generated | 38 |
| 2.1.2 | Coefficient of performance | 38 |
| 2.2 | Calculation of the shape of the wind turbine blade | 40 |
| 2.2.1 | Aerodynamic geometry of the wind turbine blade; Blade Element Momentum Theory | 40 |
| 2.2.2 | Optimum design of the blade | 43 |
| 2.3 | Power generated by the rotor | 45 |
| 2.4 | Convergence of the BEM calculation (HELICIEL) | 46 |
| 2.5 | Determination of the structure: | 47 |
| 2.6 | Normal Wind conditions | 52 |
| 2.7 | Extreme wind conditions | 52 |
| 2.8 | Determination of the blade cross section | 54 |
| 2.8.1 | Method of maximum stress | 54 |
| 2.8.2 | Method of maximum deflection | 55 |
| 2.9 | Finite element modeling of the blade | 58 |
| 2.10 | Materials used for the modeling | 58 |
| 2.11 | Modeling of the material | 59 |
| 2.12 | Determination of the initial layup | 61 |
| 2.13 | Convergence of Mesh | 63 |
| 2.14 | Modeling of the structural response of the blade using finite elements | 65 |
| 2.15 | Inertial loading due to blade's weight | 65 |
| 2.16 | Aerodynamic loading due to incident wind | 69 |
| 2.17 | Centrifugal load due to rotation of the blade | 70 |
| 2.18 | Behavior subject to global loading: Aerodynamic, gravitational and centrifugal | 70 |
| 2.19 | Modifications to the initial blade design | 80 |
| 2.20 | Conclusions and Discussion | 85 |

| | | |
|------------------|--|------------|
| Chapter 3 | Experimental characterization of material properties | 86 |
| 3.1 | Fabrication of composite panels | 88 |
| 3.2 | Materials | 91 |
| 3.3 | Equipment used for mechanical testing | 93 |
| 3.4 | Determination of fiber content | 96 |
| 3.5 | Quasi static material properties | 96 |
| 3.5.1 | Tensile tests | 96 |
| 3.5.2 | Flexural tests | 103 |
| 3.6 | Discussion on results | 107 |
| 3.7 | Summary of test results | 109 |
| | | |
| Chapter 4 | Fracture Resistance in Monolithic Interfaces | 110 |
| 4.1 | Mode I opening mode: Experimental setup | 112 |
| 4.2 | Analytical calculation of Strain energy release rate for Mode I (GI) | 114 |
| 4.2.1 | MBT 1 (Modified Beam Theory 1) | 114 |
| 4.2.2 | MBT 2 (Modified Beam Theory 2) | 114 |
| 4.2.3 | CBBM (Compliance Based Beam Method). | 115 |
| 4.2.4 | CC (Compliance Calibration Method). | 115 |
| 4.2.5 | Calculation using J-integral | 116 |
| 4.2.6 | Virtual crack closure technique (VCCT) | 116 |
| 4.3 | Results of Mode I DCB tests | 120 |
| 4.4 | Mode II shearing mode: Experimental setup | 122 |
| 4.5 | Analytical calculation of Strain energy release rate for Mode II (GII) | 124 |
| 4.5.1 | Beam theory (BT) | 124 |
| 4.5.2 | Shearing Height theory (SH) | 125 |
| 4.5.3 | Compliance calibration (CC) | 125 |
| 4.5.4 | Virtual Crack Closure Technique (VCCT) | 125 |
| 4.6 | Conclusions and Discussion | 127 |
| | | |
| Chapter 5 | Fracture Resistance in Bonded Interfaces and Sandwich Structures | 129 |
| 5.1 | Mode I opening mode: Experimental setup | 131 |
| 5.2 | Analytical calculation of Strain energy release rate Mode I (GI) | 133 |
| 5.2.1 | MBT 1 (Modified Beam Theory 1) | 134 |
| 5.2.2 | MBT 2 (Modified Beam Theory 2) | 134 |
| 5.2.3 | CC (Compliance Calibration Method) | 135 |
| 5.2.4 | Virtual crack closure technique (VCCT) | 135 |
| 5.3 | Results of Mode I DCB tests | 137 |
| 5.4 | Mode II shearing mode bonded beams: Experimental setup | 143 |
| 5.5 | Analytical calculation of Strain energy release rate Mode II (GII): Bonded Beams | 145 |
| 5.5.1 | Beam theory (BT) | 148 |
| 5.5.2 | Compliance calibration (CC) | 148 |
| 5.6 | Results of Mode II ENF tests for bonded beams | 148 |
| 5.7 | Mode II shearing mode of sandwich beams: Experimental setup | 149 |
| 5.8 | Analytical calculation of Strain energy release rate Mode II (GII): Sandwich Beams | 151 |

| | | |
|------------------|---|------------|
| 5.9 | Mode II SLB results for Sandwich beams | 152 |
| 5.10 | Observations on Results | 153 |
| Chapter 6 | Experimental study of behavior of materials under cyclic loading | 156 |
| 6.1 | Composite material | 158 |
| 6.1.1 | Test procedure | 159 |
| 6.1.2 | Measurements | 162 |
| 6.1.3 | Self heating and degradation of stiffness | 163 |
| 6.1.4 | Effect of loading rate | 164 |
| 6.1.5 | Endurance limit using self heating | 166 |
| 6.1.6 | Rate of damage progression | 167 |
| 6.2 | Fatigue tests on UD specimens | 168 |
| 6.2.1 | Degradation of stiffness | 169 |
| 6.2.2 | Failure Modes | 170 |
| 6.3 | Discussion | 172 |
| 6.4 | Self heating tests on NORPOL | 175 |
| 6.5 | Conclusions and Discussion | 178 |
| Chapter 7 | Finite element modeling of the wind turbine blade | 180 |
| 7.1 | Characterization of materials | 181 |
| 7.1.1 | Modeling | 183 |
| 7.1.2 | Discussion | 186 |
| 7.2 | Characterization of interfaces | 187 |
| 7.2.1 | Model setups for DCB tests | 189 |
| 7.2.2 | Discussion on Results | 192 |
| 7.2.3 | Model setups for ENF tests | 197 |
| 7.3 | Modeling of single lap joints | 199 |
| 7.3.1 | Modeling strategy | 200 |
| 7.3.2 | Discussion on Results | 202 |
| 7.4 | Modeling of the complete blade | 207 |
| 7.4.1 | Modeling strategy | 207 |
| 7.4.2 | Tier 1: Complete blade model | 208 |
| 7.4.3 | Tier 2: 3D Shell blade section | 211 |
| 7.4.4 | Tier 3: 3D Solid blade section | 215 |
| 7.4.5 | Tier 4: Sub model of the Tier 3 solid model | 220 |
| 7.4.6 | Tier 5: Sub model of Tier 4 including cohesive zones | 223 |
| 7.5 | Conclusions and Discussion | 229 |
| | Conclusions and Perspectives | 230 |
| | Appendix A Detail of composite layup for initial blade design | 241 |
| | Appendix B Layup plans and cross sections: GEV HP SPM184f 30m | 268 |
| | Appendix C GEV HP SPM184f 30m blade Static test results | 289 |

Table of Figures

| | | |
|--------------|--|----|
| Figure 1-1: | Increase in the global installed wind energy production capacity (GW) | 6 |
| Figure 1-2: | Power output versus rotor diameter for typical commercial turbines | 7 |
| Figure 1-3: | Distribution of offshore wind resources of the coasts of France. | 7 |
| Figure 1-4: | Basic schematic of the wind turbine | 8 |
| Figure 1-5: | Typical wind turbine blade box and shear web, structural cross-sections | 9 |
| Figure 1-6: | Five-step bonding process for a wind turbine blade. | 10 |
| Figure 1-7: | Application of the polyurethane adhesive into the first shell | 11 |
| Figure 1-8: | Blade damage types | 12 |
| Figure 1-9: | Solid model of the adhesive joint for wind turbine blade | 12 |
| Figure 1-10: | Determination of crack energy release rates using VCCT | 16 |
| Figure 1-11: | A general traction separation behavior for CZMs | 17 |
| Figure 1-12: | Different one dimensional effective displacement based models. | 18 |
| Figure 1-13: | Normal traction curve | 19 |
| Figure 1-14: | Tangential traction curve | 19 |
| Figure 1-15: | Normal and tangential traction surface | 20 |
| Figure 1-16: | Different paths followed by a crack based on the resistance to crack propagation in each mode | 21 |
| Figure 1-17: | Some failed wind turbine blades during their service. | 24 |
| Figure 1-18: | Rotor tip speed plotted against typical rotor diameters for polymer based composite blades. | 26 |
| Figure 1-19: | Deformation of a fiber bonded to a matrix and of a free fiber. | 29 |
| Figure 1-20: | Bending moment applied due to differential shrinkage of plies. | 30 |
| Figure 1-21: | Distribution of thermal stresses created during the hardening of matrix in a thermoplastic matrix composite. | 31 |
| Figure 1-22: | A typical box section spar blade cross section | 31 |
| Figure 1-23: | A VESTAS® 25m blade loaded till final failure | 33 |
| Figure 1-24: | 3D Shell with classical composite plate theory definition. | 33 |
| Figure 1-25: | A wind turbine deformed under aerodynamic loads showing end deflections. Prediction of buckling strength based on these loads. | 34 |
| Figure 2-1: | Choice of rotor based on tip speed ratios. | 38 |
| Figure 2-2: | Evolution of coefficient of performance as a function of wind speed. | 40 |
| Figure 2-3: | Evolution of the power generated as a function of wind speed. | 40 |
| Figure 2-4: | Principle of airflow around a blade section. | 41 |
| Figure 2-5: | Distribution of real cord and optimal cord. | 44 |
| Figure 2-6: | Distribution of power developed along the length of the blade. | 44 |
| Figure 2-7: | Effect of the twist on the power produced. | 45 |
| Figure 2-8: | Distribution of bending moment along the blade length, 2 cases: 55m/s and 70m/s. | 45 |
| Figure 2-9: | Distribution of induction factors along the length of the blade. | 46 |
| Figure 2-10: | Convergence of BEM based on torque and axial force. | 47 |
| Figure 2-11: | Different blade cross sections considered in the study. | 48 |
| Figure 2-12: | Different blade cross section and material configuration structural performance. | 49 |

| | | |
|--------------|--|----|
| Figure 2-13: | Summary of deflections of different section types of different materials in use. | 50 |
| Figure 2-14: | Aerodynamic loads as experienced by the blade cross section. | 51 |
| Figure 2-15: | Material distribution being put in place by the present design methodology. | 51 |
| Figure 2-16: | Position and orientation of the equivalent load applied on a blade element. | 52 |
| Figure 2-17: | Modeling of the blade as a cantilever beam. | 52 |
| Figure 2-18: | Distribution of bending moment along the length of the blade. | 53 |
| Figure 2-19: | Definition of the section as a primitive | 54 |
| Figure 2-20: | Comparison of the I_o calculated with the help of 2-25 and CATIA V5 | 55 |
| Figure 2-21: | Modeling of the blade and the loads associated with it. | 55 |
| Figure 2-22: | Flow chart of the Blade Model. | 56 |
| Figure 2-23: | Composite plate under flexural loading | 58 |
| Figure 2-24: | Chain of calculations for the design of blade. | 58 |
| Figure 2-25: | A simple composite tube loaded as a cantilever beam. | 60 |
| Figure 2-26: | Problem as modeled in ABAQUS. | 60 |
| Figure 2-27: | Layup models in ABAQUS, thickness of 0.1 to 2mm. | 61 |
| Figure 2-28: | Free end deflection of the beam. | 61 |
| Figure 2-29: | Distribution of the thickness. | 62 |
| Figure 2-30: | Zones of the blade partition. | 63 |
| Figure 2-31: | ABAQUS Blade model for the convergence study. | 64 |
| Figure 2-32: | Mesh size convergence. | 64 |
| Figure 2-33: | Blade Mesh. | 64 |
| Figure 2-34: | Effect of the twist pivot on the form of the spar. | 67 |
| Figure 2-35: | Effect of mesh finesse on the damage sensitivity. | 68 |
| Figure 2-36: | Pressures applied on the wind turbine blade elements | 69 |
| Figure 2-37: | Pressure distribution on the blade. | 70 |
| Figure 2-38: | Blade relevant coordinate system. | 74 |
| Figure 2-39: | Representation of the damage in the Blade 1. | 75 |
| Figure 2-40: | Representation of the damage in the Blade 2. | 76 |
| Figure 2-41: | Damaged Zones. | 77 |
| Figure 2-42: | Distribution of thickness. | 78 |
| Figure 2-43: | Damaged zones after modifications. | 78 |
| Figure 2-44: | Distribution of thickness. | 79 |
| Figure 2-45: | Final damaged zones. | 79 |
| Figure 2-46: | Damaged zone. | 79 |
| Figure 2-47: | Reaction force measured at the root of the blade against the blade tip deflection | 81 |
| Figure 2-48: | Reaction force measured at the root of the blade against the blade tip deflection. | 82 |
| Figure 2-49: | Point of damage in the loads deflection graphs under load case 7. | 83 |
| Figure 2-50: | Onset of damage in Blade 1 -NACA-4424-60m-200MPa- at different stages during the loading until complete failure. | 83 |
| Figure 2-51: | Onset of damage in Blade 2 - NACA-4424-60m-CL-200MPa- at different stages during the loading until complete failure. | 84 |
| Figure 2-52: | Onset of damage in Blade 1 and Blade 2 Spar at different stages during the loading until failure. | 84 |

| | | |
|--------------|---|-----|
| Figure 2-53: | Maximum stress calculated by ABAQUS along the length of the blade. | 85 |
| Figure 3-1: | The general design process shown in hierarchy where the specimen level material testing lies at the fourth tier. | 87 |
| Figure 3-2: | Woven structures for the production and manufacture of specimens. | 87 |
| Figure 3-3: | Different types of layups and composite layup configurations at different locations within a wind turbine blade. | 88 |
| Figure 3-4: | Fabrication of composite panels. | 89 |
| Figure 3-5: | Fabrication of sandwich panels. | 90 |
| Figure 3-6: | A composite specimen loaded into the UTS tensile test machine, instrumented with a biaxial strain gauge for the measurement of longitudinal and transverse strains. | 97 |
| Figure 3-7: | Failed specimens after traction tests used for the characterization of the materials. | 97 |
| Figure 3-8: | NORPOL Adhesive specimen | 98 |
| Figure 3-9: | Longitudinal elastic properties of E-Glass/polyester lamina. | 98 |
| Figure 3-10: | Transverse elastic properties of E-Glass/polyester lamina.. | 99 |
| Figure 3-11: | Shearing properties of E-Glass/polyester lamina. | 99 |
| Figure 3-12: | Tensile properties for NORPOL adhesive | 99 |
| Figure 3-13: | Sandwich specimens used for the characterization of the foam core | 104 |
| Figure 3-14: | Schematic of flexion test specimens. | 104 |
| Figure 3-15: | Force-displacement curves for | 105 |
| Figure 3-16: | Presence of resin in the core of the sandwich. | 107 |
| Figure 3-17: | A comparison of the three sandwich thicknesses under bending. | 108 |
| Figure 4-1: | Kink band formation demonstrated with the help of a stack of paper under in-plane compressive load. | 111 |
| Figure 4-2: | DCB specimen used for Mode I fracture resistance tests. | 112 |
| Figure 4-3: | Experimental setup to calculate/measure the crack growth in DCB tests. | 113 |
| Figure 4-4: | Image used for the identification of crack tip | 114 |
| Figure 4-5: | Schematic for VCCT used in equation 4-10. | 117 |
| Figure 4-6: | Mesh distribution for the DCB specimen: (a) Complete specimen and (b) Zoom on the crack tip. | 118 |
| Figure 4-7: | Mesh sensitivity for the calculation of GI, mesh size as on crack tip. | 119 |
| Figure 4-8: | Nodal variables for calculating GI | 119 |
| Figure 4-9: | Typical image taken by the CCD camera for tracking the crack length. | 120 |
| Figure 4-10: | Included angle of the two half beams at each applied load step. | 120 |
| Figure 4-11: | Evolution of GI against crack propagation | 122 |
| Figure 4-12: | ENF specimen used for Mode II fracture resistance tests. | 122 |
| Figure 4-13: | Force-displacement curves for stable and unstable crack growth. | 123 |
| Figure 4-14: | Mesh sensitivity for calculating GII SERR. | 125 |
| Figure 4-15: | Unbroken fibers connecting the lower and upper half beams well behind the crack tip. | 127 |
| Figure 4-16: | Crack front in DCB specimens. | 128 |
| Figure 5-1: | Example of a bonded joint at the trailing edge of the wind turbine (Nass & Wind, s.d.). | 130 |

| | | |
|--------------|--|-----|
| Figure 5-2: | Sandwich structures used to stiffen the unsupported spans of the wind turbine blade sections. | 130 |
| Figure 5-3: | DCB specimen used for Mode I fracture resistance tests. | 131 |
| Figure 5-4: | DCB specimen used for Mode I fracture resistance tests. | 132 |
| Figure 5-5: | Experimental setup to calculate/measure the crack growth in DCB tests. | 133 |
| Figure 5-6: | Image used for the identification of crack tip. | 133 |
| Figure 5-7: | Schematic for VCCT used in equation 5-7. | 135 |
| Figure 5-8: | Mesh distribution for the DCB specimen.. | 136 |
| Figure 5-9: | Nodal variables for calculating GI | 136 |
| Figure 5-10: | Typical image taken by the CCD camera for tracking the crack length. | 138 |
| Figure 5-11: | Force displacement curves for bonded specimens. | 139 |
| Figure 5-12: | Evolution of GI against crack propagation. | 142 |
| Figure 5-13: | ENF specimen used for Mode II fracture resistance tests. | 143 |
| Figure 5-14: | Force displacement curves for different specimens showing a stable crack growth at a a_0/L ratio of 0.25 | 144 |
| Figure 5-15: | Force displacement curves for the different bonded specimens. | 145 |
| Figure 5-16: | Force-displacement curves for, 3mm adhesive thickness. | 146 |
| Figure 5-17: | Force-displacement curves for bonded specimens, 4mm adhesive thickness. | 147 |
| Figure 5-18: | Foam core being buckled and crushed in ENF tests due to weak compressive properties. | 149 |
| Figure 5-19: | SLB specimen geometry | 150 |
| Figure 5-20: | Force displacement curve for sandwich SLB specimens. | 152 |
| Figure 5-21: | Crack growing within the (a) Adhesive layer, (b) Substrate-Adhesive interface. | 154 |
| Figure 5-22: | Values of Mode II SERR GII calculated using the formulation developed in (Manca, et al., 2012) | 155 |
| | | |
| Figure 6-1: | Types of fatigue loading | 158 |
| Figure 6-2: | Dimensions of the specimens used for fatigue tests | 159 |
| Figure 6-3: | Applied stress steps and the corresponding heat generated. | 161 |
| Figure 6-4: | Test setup for fatigue tests. 1) Instron fatigue test machine, 2) Data acquisition system, 3) Extensometer, 4) T-type thermocouples. | 161 |
| Figure 6-5: | Stress distributions on a rectangular test specimen. | 162 |
| Figure 6-6: | 45° Biax Specimens showing delamination type failure. | 163 |
| Figure 6-7: | Self heating curves for 45° Biax specimens loaded cyclically at 5 Hz | 164 |
| Figure 6-8: | Reduction of stiffness during cyclic loading. | 164 |
| Figure 6-9: | Stress displacement curves at different displacement rates. | 165 |
| Figure 6-10: | Damage in specimens corresponding to different load states. | 165 |
| Figure 6-11: | Determination of inflexion point in a self heating curve. | 166 |
| Figure 6-12: | Determination of endurance limit using tangent to the end of best fitting quadratic curve. | 166 |
| Figure 6-13: | Rate of damage development against different applied stress levels. | 168 |
| Figure 6-14: | Wöhler curve for 0° UD specimens. | 168 |
| Figure 6-15: | Endurance limit determination using self-heating curves. | 169 |
| Figure 6-16: | Determination of endurance limit using self-heating for 90° UD specimens. | 169 |
| Figure 6-17: | Stiffness of 0° UD specimens during self-heating cycles. | 170 |

| | | |
|--------------|---|-----|
| Figure 6-18: | Failed 90° UD specimen showing pure matrix mode failure. | 171 |
| Figure 6-19: | Failed 0° UD specimen showing fiber breakage and fiber pullout. | 171 |
| Figure 6-20: | Failed 45° Biaxial specimen showing mostly delamination with some fiber sellout and breakage mode failure. | 171 |
| Figure 6-21: | Stress-strain behavior of a test piece under monotonic loading | 172 |
| Figure 6-22: | Damage Initiation of matrix in tension as predicted by Hashin's criterion | 173 |
| Figure 6-23: | Damage development of the test piece loaded at | 174 |
| Figure 6-24: | Strain plots until 1.000.000 cycles showing hysteresis in the 30 MPa loaded specimen. | 174 |
| Figure 6-25: | Wöhler curve for 45° Biaxial specimens. | 175 |
| Figure 6-26: | NORPOL Specimens instrumented with extensometers | 175 |
| Figure 6-27: | Self heating curve up to failure for NORPOL specimens. | 176 |
| Figure 6-28: | Plot of temperature rise against the maximum applied stress. | 177 |
| Figure 6-29: | Degradation of stiffness during cyclic loading. | 177 |
| | | |
| Figure 7-1: | Dimensions for 45° Biax and UD specimens used in tensile tests. | 182 |
| Figure 7-2: | Dog bone shaped NORPOL specimens. | 182 |
| Figure 7-3: | 3 point flexion sandwich specimens. | 182 |
| Figure 7-4: | Representation of plies stacked in ±45° in order to simulate a biaxial mat. | 184 |
| Figure 7-5: | Different mesh element size to specimen length ratios. | 184 |
| Figure 7-6: | Boundary conditions of the finite element model; Left edge fixed, right end being pulled with the help of a fixed displacement. | 185 |
| Figure 7-7: | Different mesh sized specimens are compared with experimental force - displacement curves. | 185 |
| Figure 7-8: | Comparison to FE models up to the first linear part of the force - displacement curves. | 186 |
| Figure 7-9: | Comparison of Stress - strain curves up to final failure and a logarithmic law. | 187 |
| Figure 7-10: | Linear softening traction-separation law defined in terms of ABAQUS parameters. | 188 |
| Figure 7-11: | DCB specimens as modeled in ABAQUS using the actual geometries and material properties. | 189 |
| Figure 7-12: | Crack tip on modeled between the two beams of the DCB model. | 190 |
| Figure 7-13: | Mesh for the DCB specimens. | 190 |
| Figure 7-14: | Simulation showing the crack propagating in the cohesive zone interface. | 191 |
| Figure 7-15: | Force-displacement curves for the monolithic composite interfaces, for mode I SERR primarily in delamination. | 192 |
| Figure 7-16: | DCB_323: Force-displacement curves for the bonded interfaces, for mode I SERR primarily in debonding. | 193 |
| Figure 7-17: | DCB_324: Force displacement curves for the bonded interfaces, for mode I SERR primarily in debonding. | 193 |
| Figure 7-18: | DCB_325: Force displacement curves for the bonded interfaces, for mode I SERR primarily in debonding. | 194 |
| Figure 7-19: | Correlation experimental/FEA force-displacement curves for sandwich beams. | 196 |

| | | |
|--------------|--|-----|
| Figure 7-20: | Schematic view of the model for Mode II SERR modeling using ABAQUS. | 197 |
| Figure 7-21: | Deformed modeled specimens after the application of load. | 198 |
| Figure 7-22: | Force-displacement curves for composite layup specimens. | 198 |
| Figure 7-23: | Force-displacement curves for bonded composite specimens. | 199 |
| Figure 7-24: | Specimen used for the characterization of strength properties of a single lap joint. | 199 |
| Figure 7-25: | FE Model of the single lap joint. | 200 |
| Figure 7-26: | FEM of bonded interface of the single lap joint. | 200 |
| Figure 7-27: | Mesh size is refined at the bonded interfaces to promote an accurate initiation of damage. | 201 |
| Figure 7-28: | Load-displacement curve of a monotonic loading on a single lap joint. | 201 |
| Figure 7-29: | Stages of failure in the single lap joint. | 203 |
| Figure 7-30: | Fiber matrix interfaces as modeled by cohesive zone elements. | 204 |
| Figure 7-31: | Steps in the force displacement curve showing damage initiation. | 204 |
| Figure 7-32: | Simple lap joint showing different phases of failure under tensile load. | 205 |
| Figure 7-33: | Failed bonded surfaces showing delamination type failure in the composite reinforcements. | 206 |
| Figure 7-34: | Modeling strategy for studying the behavior of the final structure. | 208 |
| Figure 7-35: | Creation of the geometry of the blade with CATIA. | 209 |
| Figure 7-36: | Imported and partitioned geometry in ABAQUS for FE analysis. | 209 |
| Figure 7-37: | Each of the partitions is given their proper corresponding composite layups. | 210 |
| Figure 7-38: | Highly stressed regions in the wind turbine blade, loaded in the PTS and STP regimes. | 211 |
| Figure 7-39: | Two planes 1mm apart are place on the desired blade length and cuts made to extract a section. | 212 |
| Figure 7-40: | Extracted 1mm thick blade section. | 212 |
| Figure 7-41: | Composite layups on the junction of the blade surface to the shear webs. | 213 |
| Figure 7-42: | Mesh and Boundary conditions. | 214 |
| Figure 7-43: | Maximum principal stress values for the different sections. | 215 |
| Figure 7-44: | Section model taking into account the different material thicknesses. | 216 |
| Figure 7-45: | Mesh details of the 3D blade section. | 217 |
| Figure 7-46: | Maximum principal stress when the section is subjected to PTS loading. | 218 |
| Figure 7-47: | Maximum principal stress when the section is subjected to STP loading. | 218 |
| Figure 7-48: | Maximum principal stress when the section is subjected to TTL loading. | 219 |
| Figure 7-49: | Maximum principal stress when the section is subjected to LTT loading. | 219 |
| Figure 7-50: | An example of mesh at the blade shear web interface region and at trailing edge. | 220 |
| Figure 7-51: | Boundary conditions being applied on the cut surfaces and of the sub model. | 221 |
| Figure 7-52: | Maximum principal stress distributions in the blade shear web interface loaded under PTS type loading. | 221 |

| | | |
|--------------|--|-----|
| Figure 7-53: | Maximum principal stress distributions in the blade shear web interface loaded under STP type loading. | 222 |
| Figure 7-54: | Maximum principal stress distributions in the blade trailing edge loaded under TTL type loading. | 222 |
| Figure 7-55: | Maximum principal stress distributions in the blade trailing edge loaded under LTT type loading. | 222 |
| Figure 7-56: | Zoom on the shear web blade interface to show the location of different cohesive zones | 224 |
| Figure 7-57: | Onset of damage type debonding and delaminations. | 225 |
| Figure 7-58: | Distribution of normal stresses along the outer skin of the blade section | 225 |
| Figure 7-59: | Distribution of in-plane principal stresses along the outer skin of the blade section | 226 |
| Figure 7-60: | Zoom on the outer skin where it is the highest stressed and the first interlaminar cohesive zones. | 226 |
| Figure 7-61: | Delaminations start to appear all along the length of the outer skin and the adjacent uni-directional plies. | 227 |
| Figure 7-62: | Cohesive zones in the outer skin layers show no evidence of crack initiating. | 227 |
| Figure 7-63: | Maximum in-plane principal stresses in the cohesive interlaminar cohesive zones. | 228 |
| Figure 7-64: | Distribution of normal stresses along the outer skin of the blade section | 228 |
| Figure 7-65: | Distribution of in-plane principal stresses along the outer skin of the blade section. | 229 |

| | | |
|--------------|--|-----|
| Figure A-1: | Partitions of the blade in terms of radius from the root. | 241 |
| Figure A-2: | Distribution of Material in the Section. | 241 |
| Figure A-3: | Sandwich with wooden core (balsa). | 254 |
| Figure A-4: | Structure stratifié simple avec adhésif. | 255 |
| Figure A-5: | Airfoil form used. | 255 |
| Figure A-6: | The coordinate system to determine the twist angle “ θ ”. | 255 |
| Figure A-7: | Layup of the section Shell. | 256 |
| Figure A-8: | Layup of the section Box. | 256 |
| Figure A-9: | Layup of the section Box-H. | 256 |
| Figure A-10: | Layup of the section Box-VVV. | 257 |
| Figure A-11: | Layup of the section D-Sec. | 257 |
| Figure A-12: | Layup of the section H-Sec. | 257 |
| Figure A-13: | Layup of the section V. | 258 |
| Figure A-14: | Layup of the section VV. | 258 |
| Figure A-15: | Layup of the section HV. | 258 |
| Figure A-16: | Layup of the section HVV. | 259 |
| Figure A-17: | Layup of the section VVV. | 259 |
| Figure A-18: | Partitions of the blade cross section. | 260 |
| Figure A-19: | Distribution of materials for the blade surface shell. | 261 |
| Figure A-20: | Distribution of materials for the spar. | 261 |
| Figure A-21: | Distribution of materials for the blade surface shell. | 262 |
| Figure A-22: | Distribution of materials for the spar. | 262 |
| Figure A-23: | Distribution of materials for the blade surface shell. | 263 |
| Figure A-24: | Distribution of materials for the spar. | 263 |
| Figure A-25: | Distribution of materials for the blade surface shell. | 264 |
| Figure A-26: | Distribution of materials for the spar. | 264 |
| Figure A-27: | Weight distribution along the blade length. | 266 |
| Figure B-1: | Layup plans for the GEV HP SPM184f 30m blade | 279 |
| Figure B-2: | Cross section of the GEV HP SPM184f 30m blade | 288 |
| Figure C-1: | Load and deflection measurement locations. | 289 |
| Figure C-2: | Load and deflection measurement locations. | 292 |
| Figure C-3: | Load and deflection measurement locations. | 294 |
| Figure C-4: | Load and deflection measurement locations. | 296 |

List of Tables

| | | |
|-------------|--|-----|
| Table 2-1: | Design Criteria. | 37 |
| Table 2-2: | Operating conditions of the wind turbine blade. | 39 |
| Table 2-3: | Design parameters for the blade. | 43 |
| Table 2-4: | Total power generated by the real and optimal blade. | 44 |
| Table 2-5: | Power produced by the rotor calculated with different methods. | 46 |
| Table 2-6: | Material properties for the modeling. (Advanced Materials, 2011) | 59 |
| Table 2-7: | Thicknesses of the blade elements | 62 |
| Table 2-8: | Values of damage criteria for the blades. | 68 |
| Table 2-9: | Pressure distribution on the blade elements. | 69 |
| Table 2-10: | The IEC Wind Classes. | 71 |
| Table 2-11: | Load cases according to the IEC 61400-1 Standards, according to the International Electro technical commission (1999). | 72 |
| Table 2-12: | Load cases for validating the blade design. | 73 |
| Table 2-13: | Values of Hashin's damage criteria | 76 |
| Table 2-14: | Reinforcement of sensible zones. | 77 |
| Table 2-15: | Values of Hashin's damage criteria after modifications. | 78 |
| Table 2-16: | Values of Hashin's damage model for the modified blade. | 80 |
| Table 2-17: | Variations of the initial blade design. | 80 |
| | | |
| Table 3-1: | Details of the Unidirectional (UD) mat used for composite manufacture. | 91 |
| Table 3-2: | Details of the 45° Biax mat used for composite manufacture. | 91 |
| Table 3-3: | Details of the PolyLite 413 Series polyester resin. | 91 |
| Table 3-4: | Details of the PolyLite 413 Series polyester resin. | 92 |
| Table 3-5: | Details of the NORPOL PF adhesive. | 92 |
| Table 3-6: | Details of the Divinycell® H80 PVC foam core. | 93 |
| Table 3-7: | List of equipment used for mechanical testing, testing. | 94 |
| Table 3-8: | List of equipment used for mechanical testing, instrumentation. | 95 |
| Table 3-9: | List of equipment used for mechanical testing, miscellaneous. | 95 |
| Table 3-10: | Fiber contents in UD and 45° Biax type composites. | 96 |
| Table 3-11: | Mechanical properties of composite in longitudinal direction | 100 |
| Table 3-12: | Mechanical properties of composite in transverse direction. | 100 |
| Table 3-13: | Mechanical properties of composite in shearing direction. | 100 |
| Table 3-14: | Mechanical Properties of NORPOL vinyl-ester adhesive. | 101 |
| Table 3-15: | Comparison of different analytical techniques to calculate the properties of composites in their orthotropic directions. | 103 |
| Table 3-16: | Young's modulus of the foam core used in sandwich specimens. | 106 |
| Table 3-17: | Summary of material properties in quasi-static conditions. | 109 |
| | | |
| Table 4-1: | Crack lengths to be modeled corresponding to forces applied. | 117 |
| Table 4-2: | Summary of the Mode I GIi results at crack initiation for three (3) specimens. | 121 |
| Table 4-3: | Summary of Mode I GIc results during crack propagation calculated for the laminated specimen. | 121 |
| Table 4-4: | Crack propagation at different pre-crack to span length ratios. | 123 |

| | | |
|------------|---|-----|
| Table 4-5: | Summary of the Mode I GIII results at crack initiation for three (3) specimens. | 126 |
| Table 4-6: | Summary of Mode I GIc results during crack propagation calculated for the laminated specimen. | 126 |
| Table 5-1: | Summary of Mode I GIc results for crack initiation calculated for the bonded specimens. | 140 |
| Table 5-2: | Summary of Mode I GIc results for crack propagation calculated for the bonded specimen. | 140 |
| Table 5-3: | Summary of Mode I GIi results for crack initiation calculated for the sandwich specimen. | 141 |
| Table 5-4: | Summary of Mode I GIc results for crack propagation calculated for the sandwich specimen. | 141 |
| Table 5-5: | Crack propagation at different pre-crack to span length ratios. | 144 |
| Table 5-6: | Summary of Mode I GIII results for crack propagation calculated for the bonded specimen. | 148 |
| Table 5-7: | Summary of Mode I GIIC results for crack propagation calculated for the bonded specimen. | 149 |
| Table 5-8: | Summary of SLB results calculated for the sandwich beams | 153 |
| Table 6-1: | Volume fraction of fibers in the 45° Biax and UD specimens | 159 |
| Table 6-2: | Properties of the 45° Biax specimens. | 160 |
| Table 6-3: | Properties of the 0°UD specimens. | 160 |
| Table 6-4: | Properties of the 90°UD specimens. | 160 |
| Table 6-5: | Comparison of 2 methods of curve fitting for finding the endurance limit | 167 |
| Table 6-6: | Stiffness of 0° UD specimens. | 170 |
| Table 6-7: | Comparison of endurance limits of the three types of different specimens. | 171 |
| Table 6-8: | Temperature rise for different applied maximum stresses. | 176 |
| Table 7-1: | Material properties used for modeling. | 183 |
| Table 7-2: | Summary of results of experimental and CZM mode I SERR “GI” | 194 |
| Table 7-3: | Summary of results of experimental and CZM mode I SERR “GI” | 195 |
| Table 7-4: | Maximum Principal stresses fiber direction for the different sections. | 214 |
| Table 7-5: | Summary of principal stresses applied on the blade sections. | 223 |

| | | |
|-------------|---|-----|
| Table A-1: | Properties of Fiberglass/Epoxy Composite. | 252 |
| Table A-2: | Properties of T300/5208 Carbon/Epoxy Unidirectional Prepreg | 253 |
| Table A-3: | Propriétés du composite Kevlar/époxy | 253 |
| Table A-4: | Distribution of cords and twist angles along the length of the blade. | 255 |
| Table A-5: | Zones de stratification | 260 |
| Table A-6: | Détail des épaisseurs des matériaux pour la pale | 261 |
| Table A-7: | Details of material thicknesses for the blade. | 262 |
| Table A-8: | Detail of thicknesses for the blade. | 263 |
| Table A-9: | Detail of thicknesses for the blade. | 264 |
| Table A-10: | Weight distribution along the length of the blade | 266 |
| Table A-11: | Reaction at the blade root under load case 1. | 267 |
| Table A-12: | Reaction at the root under aerodynamic loading | 267 |
| | | |
| Table C-1: | Loading point locations. | 289 |
| Table C-2: | Applied bending moments. | 210 |
| Table C-3: | Loading point locations. | 291 |
| Table C-4: | Applied bending moments. | 292 |
| Table C-5: | Loading point locations. | 293 |
| Table C-6: | Applied bending moments. | 294 |
| Table C-7: | Loading point locations. | 295 |
| Table C-8: | Applied bending moments. | 296 |

List of Symbols

Latin characters.

| | |
|---------------------|---|
| " A, B, D " | Curve fitting parameters for the Paris law |
| " a " | Factor of rotation induction for airflow |
| " a " | Factor of linear induction for airflow |
| " A_e " | Surface area of the blade element |
| " A_{11} " | Matrix of rigidity of composite plate under tension |
| " a_e " | Effective crack length |
| " a_o " | Length of pre-crack |
| " b " | Breadth of the specimen |
| " B " | No. of blades per rotor |
| " B_{11} " | Matrix of rigidity of composite plate under tension-flexion |
| " C " | Compliance of the composite layup |
| " C_{ply} " | Compressive strength of the ply |
| " c " | Cord length of the airfoil |
| " C_D " | Coefficient of drag |
| " C_L " | Coefficient of lift |
| " C_N " | Coefficient of force normal to the rotor plane |
| " C_p " | Coefficient of performance |
| " C_T " | Coefficient of force tangent to the rotor plane |
| " d_f, d_m, d_s " | Damage coefficients signifying a loss of rigidity |
| " D " | Damage developed in a specimen during cyclic loading |
| " D_{11} " | Matrix of rigidity of composite plate under flexion |
| " E_{11} " | Module of elasticity of the composite specimen in the direction of the fibers |
| " E_{22} " | Module of elasticity of the composite specimen in the direction perpendicular to the fibers |
| " E_c " | Modulus of elasticity of the core |
| " E_s " | Modulus of elasticity of face plate |
| " E_f " | Modulus of elasticity of fiber |
| " E_l " | Modulus of elasticity in the fiber direction |
| " E_m " | Modulus of elasticity of the matrix |
| " E_t " | Modulus of elasticity normal to the fiber direction |
| " E_x " | Global stiffness in the X-Direction |
| " E_y " | Global stiffness in the Y-Direction |
| " $F_{i,jj,ijk}$ " | Experimental coefficients depending on the rupture strengths of the composite materials |
| " F " | Factor of Glauret |
| " f " | Pradtl tip loss factor |
| " F_C " | Centrifugal force |
| " F_D " | Drag force |
| " F_e " | Resultant of aerodynamic load |
| " F_L " | Lift force |
| " F_N " | Normal force generated by the rotor |
| " F_T " | Tangential force generated by the rotor |

| | |
|------------------------------|---|
| " G_{13} " | Module of elasticity of the composite specimen in the in shearing |
| " G_{IC} ", " G_{IIC} " | Strain energy release rates in Mode I and Mode II |
| " $h_{1,2}$ " | Thickness of the DCB half beams used |
| " h_c " | Core thickness |
| " h_f " | Thickness of face plate |
| " I_o " | Moment of inertia of the section about the neutral axis of the section |
| " J " | J-integral |
| " $l_{1,2}$ " | Distance of the loading pin to the crack tip |
| " l " | Length of the blade element |
| " l_e " | Length of finite element mesh element |
| " l_s " | Length of specimen or structure |
| " M " | Total couple generated by the rotor |
| " M_e " | Bending moment applied to the blade element |
| " m_s " | Mass of the blade section |
| " $N_{\sigma,n}$ " | Residual life under cyclic loading |
| " P " | Power generated by the rotor |
| " p " | Coefficient of non-linear elasticity in non linear materials |
| " P " | Load applied |
| " P_e " | Pressure applied on the blade element |
| " Q_R " | Energy dissipated |
| " R_{blade} " | Length of the blade |
| " R " | Load ratio for fatigue tests |
| " r " | Radius of rotation of the blade element |
| " S " | Matrix of compliance |
| " S_s " | Shearing strength of the composite layup |
| " t_m " | Material thickness |
| " T_θ " | Matrix of transformation |
| " t " | Stress for damage/crack initiation |
| " T " | Tensile strength of ply |
| " T_0 " | Initial temperature of the specimen |
| " T_l " | Temperature of the lower grip |
| " $T_{n,t}$ " | Normal and tangential traction components |
| " T_S " | Surface temperature of the specimen |
| " T_u " | Temperature of the upper grips |
| " u " | Displacement of the beam mid-span |
| " v " | Nodal displacements normal to the crack plane measured for VCCT |
| " V_f " | Volume ratio of fiber |
| " V_m " | Volume ratio of matrix |
| " V_o " | Velocity of the incident wind |
| " w " | Nodal displacements parallel to the crack plane measured for VCCT |
| " w_{rotor} " | Rotational speed of the rotor |
| " X " | Strength in fiber direction |
| " X'_i, X'_j, Y'_i, Y'_j " | Force in the x and y direction on the " i " and " j " node in VCCT analysis |
| " Y " | Strength normal to the fiber direction |
| " y_{max} " | Maximum distance |
| " z " | Distance of ply from the neutral axis |

Greek characters.

| | |
|---------------------|---|
| " α, β " | Material constants under fatigue loading |
| " α " | Angle of attack of blade element |
| " $\delta_{n,t}$ " | Characteristic separation in cohesive zones |
| " δ " | Phase difference of the material lagging the applied load |
| " Δ " | Crack tip rotation factor |
| " δ " | Displacement through which the load is applied |
| " $\Delta_{n,t}$ " | Displacement of the cohesive zone nodes |
| " η " | Energy conversion train efficiency |
| " θ " | Angle of twist of the blade element with respect to the rotor plane |
| " λ_r " | Tip speed ratio |
| " ν_f " | Poisson's ratio of the fiber |
| " ν_{LT} " | Poisson's ratio with loading in the fiber direction |
| " ν_m " | Poisson's ratio of the matrix |
| " ν_{TL} " | Poisson's ratio with loading normal to the fiber direction |
| " ζ " | Factor of reinforcement |
| " ρ " | Air density |
| " σ_b " | Swept surface area of the blades |
| " σ " | Mechanical stress (direction and type will be defined by subscripts in subsequent sections) |
| " ε " | Mechanical strain (direction and type will be defined by subscripts in subsequent sections) |
| " ϕ_r " | Angle of relative wind to the rotor plane |
| " ϕ " | Energy released during failure of the cohesive zone |
| " ω " | Frequency of cyclic loading |
| " Φ_{ni} " | Factor of regain strength |

Abbreviations

| | |
|--------|--|
| BEM | Blade element momentum |
| Biax | Bi axial |
| CCD | Charge coupled device |
| CFD | Computational fluid dynamics |
| DCB | Double cantilever beam |
| DIC | Digital image correlation |
| ENF | End notched flexural |
| EWTTPD | European Wind Turbine Testing Procedure Developments |
| FEA | Finite element Analysis |
| HAWT | Horizontal Axis Wind Turbine |
| IEC | International electrotechnical comission |
| ISO | International standards organisation |
| NACA | National Advisory Committee for Aeronautics |
| PEEK | Poly-ether-ether-ketone |
| PVC | Poly-vinyl-chloride |
| SERR | Strain energy release rate |
| SLB | Single leg bending |
| UD | Unidirectional |
| VAWT | Vertical Axis Wind Turbine |
| VCCT | Virtual crack closure technique |

General Introduction.

Energy lies at the heart of modern society, enabling everything from heating, lighting, computers, and food production through to manufacturing, medicine, and transport. To properly appreciate the context of this thesis, consider that worldwide in 2011, wind power provided 0.5% of the 13.5% slice of electricity represented of the 125 PWh consumed at end-use from all primary sources (International Energy Agency, 2013) (Global Wind Energy Council, 2005). A growing appreciation of the deleterious climatic effects of anthropogenic greenhouse gas emissions is increasing regulatory pressure to mitigate or avoid CO₂ release into the atmosphere (Tyndall Centre, 2005). Simultaneously, many populous nations are rapidly aspiring to Western standards of living, intensifying the use of and competition for energy. The tractability of tackling stationary energy use and supply, as opposed to transport fuels, and in particular electricity production, has made this area of key public importance (Department of Trade and Industry, 2006). However, it is important to bear in mind the overall scale of our society's energy use, in all forms and with myriad correctable inefficiencies, when considering enhancement of electricity production.

Ultimately, the highly competitive electricity market will select the most cost-effective technology. Unfortunately, inclusion of externalities, e.g. a carbon tax, unknown future decommissioning costs, as well as subsidies to all forms of energy, creates an artificially skewed playing field. To compete in this economic environment, wind power must deliver power of grid-standard quality and at a competitive price relative to "conventional" generation. It is in this overall context that this thesis seeks to develop engineering tools capable of properly analyzing and optimizing a potentially much more cost-effective offshore wind turbine concept for renewable marine energies applications.

Wind Power

Wind power has for the past 5 years increased in installed capacity by 20-30% each year [2], indicating commercial viability with proper citing and regulatory framework. The turbines are among the best energy sources in terms of energy payback time (Elsam Engineering A/S., 2004). Once the turbines are built, their impact is virtually non-existent, given proper design and consideration of local communities and wildlife. These strong economic and sustainability credentials make wind power attractive from multiple perspectives.

Wind turbine design has achieved a high level of sophistication, enabling production of 120 m diameter, 5 MW machines, sited both on-shore and off-shore. Progress from the 6 m diameter, 15 kW machines of the early 1980's to today have been achieved by technical and scale evolution of the "Danish concept", typified by rigid three-bladed rotors placed upwind of the towers. In a modern machine, a gearbox transfers torque from the rotor to an actively controlled generator, although some directly drive a low-speed generator. Pitch actuators at the roots of the blades directly control the aerodynamic power input to the rotor. Almost universally, a Horizontal Axis Wind Turbine (HAWT) is chosen (i.e. the rotation axis of the rotor is near horizontal), although the Vertical Axis Wind Turbine (VAWT) with a vertical rotation axis received much attention in the past, and may still find application at extremely small and large scales.

Key modern development work is aimed at increased reliability, particularly for off-shore sites, and load mitigation to reduce structural cost. The latter is being tackled by more active control (in turn made possible by power electronics and fast actuators) and refined structural designs and materials. It should be appreciated that wind turbines, although sharing many engineering principles with aircraft design, are quite distinct in their objective (to deliver reliable energy) and therefore demand more cost-sensitive solutions.

Offshore Wind power

Offshore wind power refers to the construction of wind farms in bodies of water to generate electricity from wind. Better wind speeds are available offshore compared to on land, so offshore wind power's contribution in terms of electricity supplied is higher, (Madsen & Krogsgaard, 2010) and NIMBY opposition to construction is usually much weaker. However, offshore wind farms are relatively expensive (U.S. Department of Energy (DOE), 2011). At the end of 2012, 1,662 turbines at 55 offshore wind farms across 10 European countries are generating electricity enough to power almost five million households (European Wind Energy Association (EWEA), 2013). At the end of June 2013 total European combined offshore wind energy capacity was 6,040 MW (EWEA, 2014).

As of 2010 Siemens and Vestas were turbine suppliers for 90% of offshore wind power, while Dong Energy, Vattenfall and E.on were the leading offshore operators (Madsen & Krogsgaard, 2010). As of October 2010, 3.16 GW of offshore wind power capacity was operational, mainly in Northern Europe. According to BTM Consult, more than 16 GW of additional capacity will be installed before the end of 2014 and the United Kingdom and Germany will become the two leading markets. Offshore wind power capacity is expected to reach a total of 75 GW worldwide by 2020, with significant contributions from China and the United States (Tyndall Centre, 2005).

As of 2013 the 630 MW London Array is the largest offshore wind farm in the world, with the 504 MW Greater Gabbard wind farm as the second largest, followed by the 367 MW Walney Wind Farm. All are off the coast of the UK. These projects will be dwarfed by subsequent wind farms that are in the pipeline, including Dogger Bank at 7,200 MW, Norfolk Bank (7,200 MW), and Irish Sea (4,200 MW). In the end of June 2013 total European combined offshore wind energy capacity was 6,040 MW. UK installed 513.5 MW offshore windpower in the first half year of 2013 (European Wind Energy Association (EWEA), 2013).

The present PhD project contains a study of the structural static and fatigue strength of wind turbine blades loaded in flap-wise direction. A combination of experimental and numerical work has been used to address the most critical failure mechanisms and to get an understanding of the complex structural behavior of wind turbine blades. Different failure mechanisms observed during the tests performed for reduced scale tests (smaller test specimens) and the corresponding FE-analysis are presented.

This thesis entitled “**Identification and characterization of mechanical and structural properties against static damage and fatigue of a composite floating wind turbine blade.**” deals with the design of a 1 MW power output wind turbine blade. The core focus of this thesis is the development of engineering-level aerodynamic and structural models, suitable for the design of highly flexible wind turbines. The study includes the validation of the design against fatigue and static damage. Experimental work has been carried out during this thesis to characterize and model the materials used

for the fabrication of this wind turbine blade. The data generated during the experiments has been used to create finite element models which are used to study in detail the structural and mechanical behavior of this blade. A design process is also proposed in this thesis which answers some of the basic questions of how to design and validate a wind turbine blade from scratch.

Wind turbine blades are highly complex structures with complex 3 dimensional forms governed by their aerodynamics that allow a maximum of power output and efficiency. On the structural side there is always an immense interest in keeping the blades as light and as rigid as possible. No structure being perfectly rigid, the wind turbine blades are specifically designed to keep their deformation in check. Deflection twist couplings are also designed into the blades to have favorable aerodynamic properties even in the deformed state.

Each area within the wind turbine blade is structurally unique. The fiber orientations and the type of plies vary depending on the loads applied. To increase the rigidity, large open spans are made from foam core sandwich structures which increase the stiffness at not too high a cost in terms of increase in weight. As these are complex in terms of their forms and geometries, wind turbine blades are usually fabricated in at least 3 components which are later bonded together using adhesives. Therefore a good knowledge of the properties of all the materials being used in the turbine blades is important for a proper design.

Current work and organization of the PhD-thesis

In the present PhD-project, the structural strength of large offshore wind turbine blades with a load carrying box girder has been studied. A combination of experimental and numerical work has been used to address the most critical failure mechanisms, and to get an understanding of the complex structural behavior. The work done during this PhD thesis has been presented in the following chapters in this report.

The first chapter deals with the state of the art of wind turbine design and experimental validation. The works of different leading researchers has been studied and put together in different aspects dealing with the design and validation process of the wind turbine blades.

In **the second chapter** a design methodology is proposed based on some industry practices and academic research. A novel design method has been proposed coupling the design aspects dealing with the fluid part of the blade to their structural aspects. Different types of blade geometries and forms have been modeled to find out the best possible design solution for a wind turbine blade. This chapter deals with the basic aspects of design in a general sense and does not deal with the final blade being studied. The design methodology proposed can be applied to any design based on a few basic parameters which depend on the final expected power output and the wind conditions at the installation site.

The third chapter deals with the basic experimental characterization of the material properties. The composite materials used how they are manufactured, their quality control and the characterization of their mechanical properties when subjected to static loads up to their failure. Theories have been used to verify their validity in the prediction of composite material properties. This step in the experimental work although basic, is of importance for further more detailed experimental work, for example for determining the damage characteristics and fatigue life.

The fourth chapter deals with the problem of experimental characterization of the damage properties of the composite materials used in the wind turbine blade. The composite materials used come in 3 distinguishable classes: layups, bonded composite plate and sandwich structures. How wind turbines are fabricated, depends on these three types of material configurations. In the fourth chapter the damage and crack propagation characteristics of the composite layups are studied experimentally and the results are then analyzed mathematically.

The fifth chapter is an extension of the fourth where the problem of damage initiation and crack propagation is dealt with when it comes to bonded composite plates and sandwich structures. The experimental work and the mathematical analysis accorded follow some modifications to the composite layups as were treated in chapter 4.

The life and durability of the composite materials and the adhesives used has been discussed in **the sixth chapter**. The fatigue life of composites in different fiber orientations has been determined experimentally. The principal of relating the energy dissipated during fatigue tests and damage developments have been discussed to characterize the materials in a shorter test time.

The final seventh chapter deals with the finite element analysis of the materials, assemblies and the complete structure. The modeling approach starts with the validation of the models at the specimen level, once that is attained we moved on to a basic assembly, and from the basic assembly to the complete global model. This complete global model is then disintegrated into smaller sub models to have higher accuracy and detailed analyses. Throughout the modeling process the results have been validated through comparisons with the experimental data.

Chapter 1 State of the art

Table of Contents

| | |
|---|----|
| 1.1 Advances in Blade technology | 8 |
| 1.2 Methods of fabrication..... | 10 |
| 1.3 Resistance of composites to damage | 11 |
| 1.4 Resistance to delamination and de-bonding | 14 |
| 1.4.1 Analytical approach | 14 |
| 1.4.2 Finite Element approach using VCCT | 16 |
| 1.4.3 Numerical approach using cohesive zone models. | 17 |
| 1.5 Fatigue behavior of Materials..... | 21 |
| 1.6 Delamination fatigue | 24 |
| 1.7 Wind turbine form design..... | 25 |
| 1.8 Fabrication of Blades..... | 28 |
| 1.9 Full-scale testing of Wind Turbine Blades | 32 |
| 1.10 Finite element modeling of Wind Turbine Blades..... | 33 |
| 1.11 Discussion and Conclusions | 35 |

Wind energy is currently referred to the technology and the development of devices for extracting energy, often in the form of electricity, from the wind. For this purpose wind turbines are used, which are designed specifically for this purpose. In the present world there is a huge emphasis on the development and effective deployment of renewable energy resource based power. Among the technologies as frontrunners, that of wind energy is very important. An estimate of the evolution of the installed wind capacity in the world from 2004 till 2012 has shown an ever increasing trend (REN21, 2011), Figure 1-1.

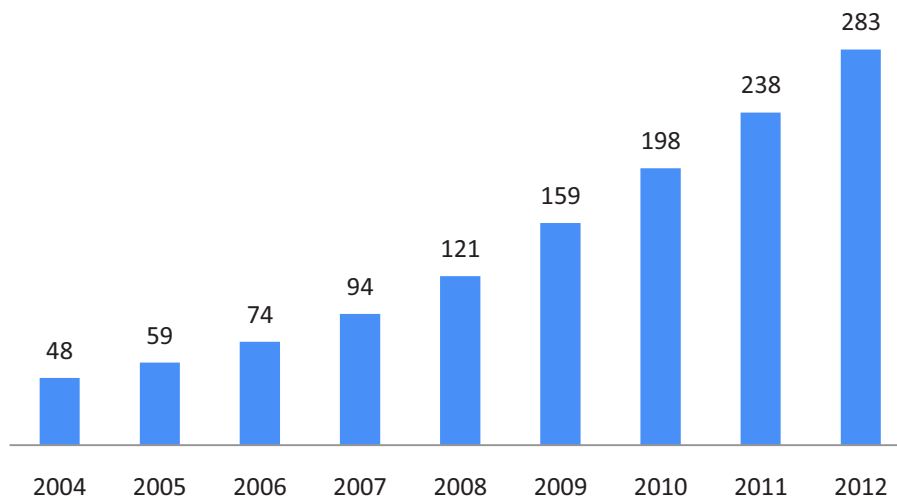


Figure 1-1 : Increase in the global installed wind energy production capacity (GW).

This trend is estimated to increase with the ever growing petroleum and energy prices, and the fact that natural resources are being exhausted at a high rate.

Different types of wind turbines have been developed for the exploitation of wind energy. Wind turbines are classified by the direction of flow of air through the turbines and by their placement. Wind turbines most commonly used are of the horizontal axis type or called HAWT (horizontal axis wind turbines).

The turbines are also classified as being offshore or terrestrial units. Although each turbine has its strong and weak points, each of these types is deployed as a function of the purpose they are supposed to serve.

As good as wind turbines are for the preservation of environment and reducing the impact and dependence on the conventional energy resources, they have certain drawbacks. The size of turbines is increasing every day, with the demand of energy going up there is a certain demand for the increase in their size. Currently wind turbines in excess of 5MW have been developed and installed sweeping at least a 50m radius, with their blades (Mason, 2004). This effect of size can be shown in Figure 1-2.

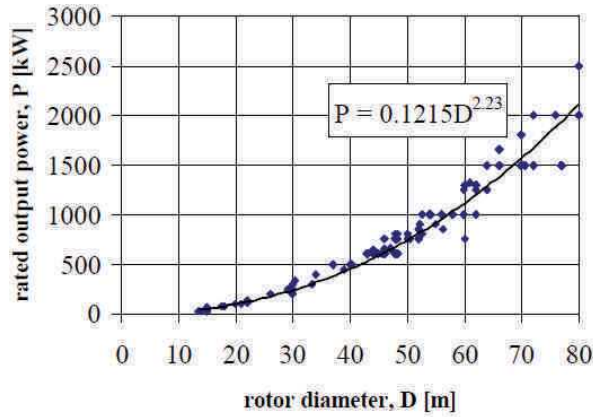


Figure 1-2 : Power output versus rotor diameter for typical commercial turbines.

Once it is well established that a higher demand of energy would put pressure to increase the density of energy developed per wind farm, the size of the turbines as a consequence would increase and hence their impact on the environment and landscape would increase as well. The effects of turbines include aesthetics i.e. the change in the natural landscapes, noise especially in sub audible range that can affect the nesting cycle of bats and other auditory sensitive animals as well as the psychological impact of moving shadows cast by the blade on the houses situated near them. Looking at the merits of large wind turbine countries like Spain who have taken the lead in Europe are already producing about 42,976 GWh and with France at about 9,600 GWh of electricity.

These reasons merit the installation of turbines in offshore wind farms. In addition the wind speeds offshore are higher and more uniform. Viewing the size of turbines needed to generate a considerable amount of energy and the available wind resources off the shore in the region of Brittany, France, in 2011 the French government decided to launch a formal appeal for projects exploiting these vast wind energy resources.

As can be seen from the Figure 1-3 the region from near Loire Atlantique all the way up to Pas-de-Calais is very favorable for exploiting wind energy, with some very high energy dense areas in the south as well.

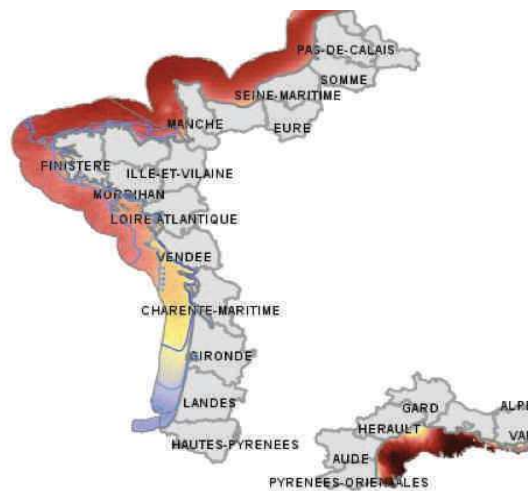


Figure 1-3 : Distribution of offshore wind resources of the coasts of France.

Among the propositions given for the development wind energy for France a project called WINFLO was launched to develop floating type wind turbines that would be moored off the Breton coast. A total of around 3000 MW of electricity is planned to be finally generated as part of this project bringing in a total of about 500 – 600 multi megawatt large floating turbines.

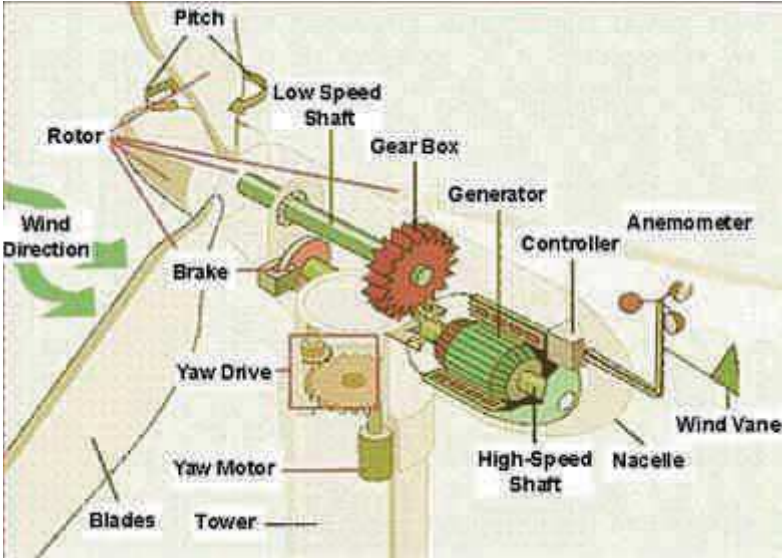


Figure 1-4 : Basic schematic of the wind turbine.

Looking at the basic schematic of the wind turbines (Figure 1-4) it can be seen that the wind turbine blades are one of the most important and expensive components. There is a lot of research going in to making the turbine blades light durable and aerodynamically efficient. Typically large scale wind turbine blades are made of composite materials, and their design and characterization takes a long time. Therefore one of the principal aims of this PhD work has been to develop methodologies to reduce the time taken for the characterization of materials. It is also the aim of this research to look into methods for reducing the amount of materials required for physical testing. In doing so, research is done to look into the mechanisms of failure of composite materials, to better predict their life. One of the important aspects of wind turbine blades is that they are at the fore front of the energy conversion chain, from wind to electricity; hence the efficiency of the whole system depends on the efficiency of these blades. Although other components have important design challenges as well. The turbine blades are also responsible (for variable pitch constant speed units) for regulating the frequency and power of the electricity produced. The turbine blades with their variable pitch control the rotational speed remains constant. Hence they deliver a constant 50 – 60Hz of alternating current based on the end user’s specifications.

1.1 Advances in Blade technology

Wind turbine blade design can be divided into two very distinct yet interdependent domains. The first is its aerodynamic design, whilst the other is its structural design. The study of performance of the turbine blades under extreme conditions, maximum deflections and the predicted life of blades are some of the important parameters need to be considered.

The study of the aerodynamic performance has been covered in this study to calculate the loads applied to the turbine blade during service and extreme stormy conditions. For this purpose the very well reputed and widely used “Blade Element Momentum Theory” or BEM for short has been used. Although other more detailed and precise methods of calculations, like Computational Fluid Dynamics using a 3 dimensional mesh to model the flow or wind over the blades and other numerical methods. As will be discussed in the sections to come that BEM is the simplest while computationally lightest method for calculating the performance and the aerodynamic geometry of a wind turbine blade. On the other hand it is rather imprecise as it is effectively a 2D computational method which does not take into account the flow of air along the length of the blade. These assumptions can cause the design to be very conservative and hence resulting in sub optimal designs. CFD techniques are very precise but at the same time very computationally demanding. Therefore certain hybrid techniques are being developed to couple the CFD’s precision with that of BEM’s speed and robustness (Esfahanian, et al., 2013). These hybrid techniques use detailed CFD and Navier Stokes equations to model the flow around the airfoil profile of the wind blade; however the complete blade is not modeled in full geometry. The Blade’s swept area is modeled as an actuator disc and boundary conditions applied to the disc to reduce the computational requirements. (Smaili & Masson, 2010).

Once the aerodynamic design of the wind turbine blade has been defined, in keeping the form the structure of the turbine blade is determined. There are different types of blade structures being used today. In general all of the blades are designed as hollow shells made from composite materials (glass-carbon fibers – epoxy/polyester matrix). In most of the cases the blade external surfaces, extrados and intrados, are joined together with adhesives. There are also stiffeners running the length of the blade glued in the interior of the blade known as spars or longerons. A typical cross section is shown in the Figure 1-5, the spar can take a number of different forms from box type as shown here to single or double bladed designs.

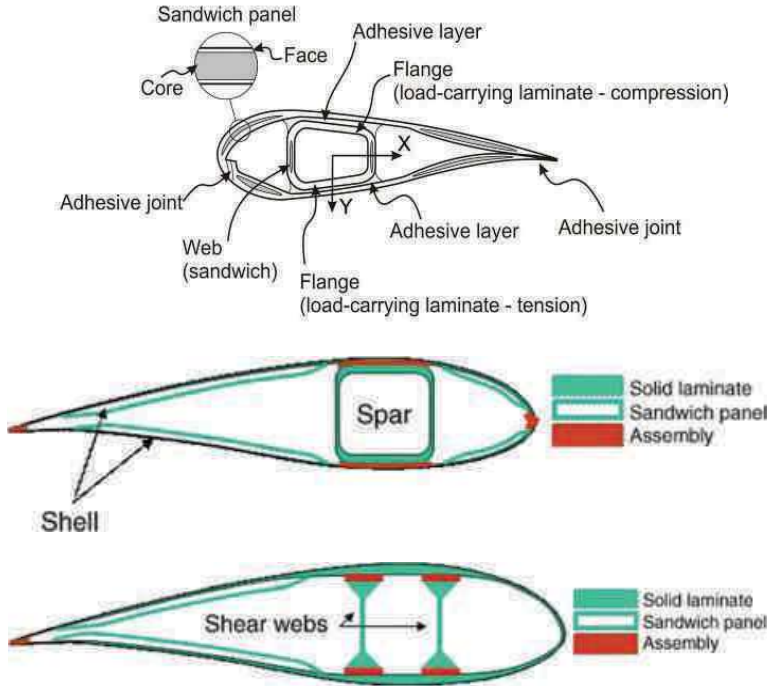


Figure 1-5: Typical wind turbine blade box and shear web, structural cross-sections.

1.2 Methods of fabrication

Recently Siemens' have come up with a one shot manufacturing procedure where an inflatable male mould is used to avoid the gluing of intrados to the extrados (Siemens, 2008). Enercon have come up with steel composite hybrid blade designs to increase the rigidity of their blade designs. In addition designers use the directional properties of the composites to create bend-torsion coupled designs, to induce twist while the blade bends under wind loads. This is done in order to automatically regulate the pitch of the blade if there is an abrupt change in wind speed, abrupt and short enough to not to give the pitch control mechanism enough time to react (Valencia, et al., 2004). Other designs look towards pre-bent blades which straighten out under operational wind loads (Verelst, 2009). There are blades manufactured with hybrid fiber mats as well. One such example shows a blade manufactured with a carbon-glass hybrid tri-axial mat with the fiber alignments given as $[-45^{\circ}_{\text{Verre}}/0^{\circ}_{\text{Carbone}}/+45^{\circ}_{\text{Verre}}]$ (Griffin & Dayton., 2002), this helps in keeping the carbon fibers straight and hence helping with buckling resistance of the blade.

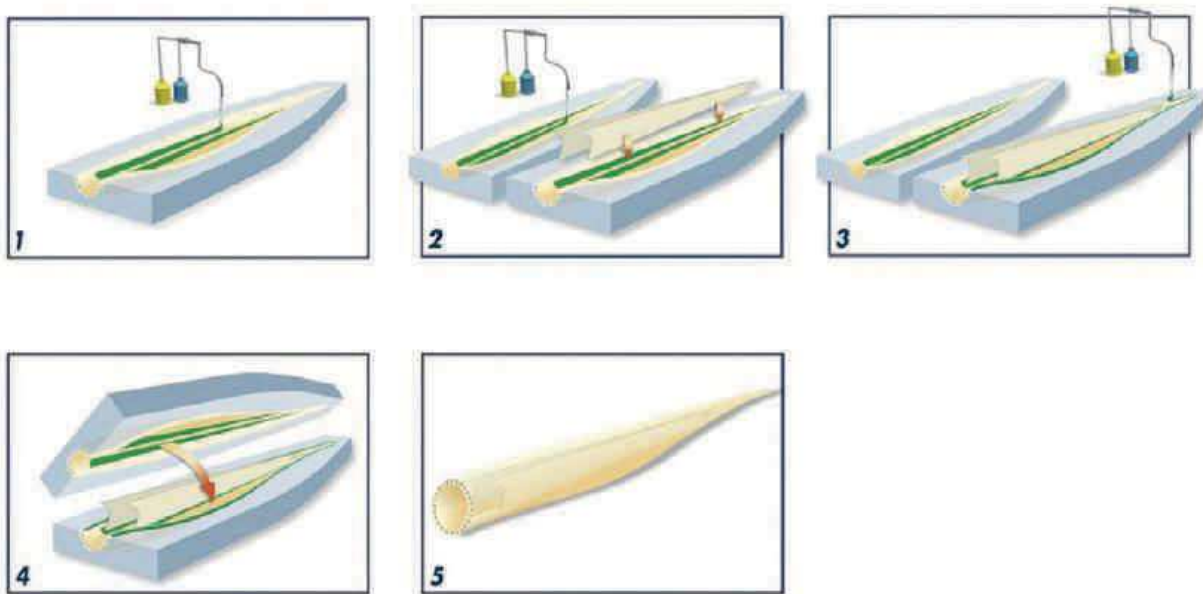


Figure 1-6: Five-step bonding process for a wind turbine blade.

The Figure 1-6 shows the different steps (phases) for manufacturing a composite blade:

1. Adhesive is applied to the first shell in the fixed part of the mould, and to the second one, at the root end of the blade.
2. The internal parts (spar or shear webs) are lifted into position.
3. Adhesive is applied to the top of the spar or shear webs for the second shell bonding.
4. The second shell is lifted over onto the spar or the shear webs.
5. The mould is closed.

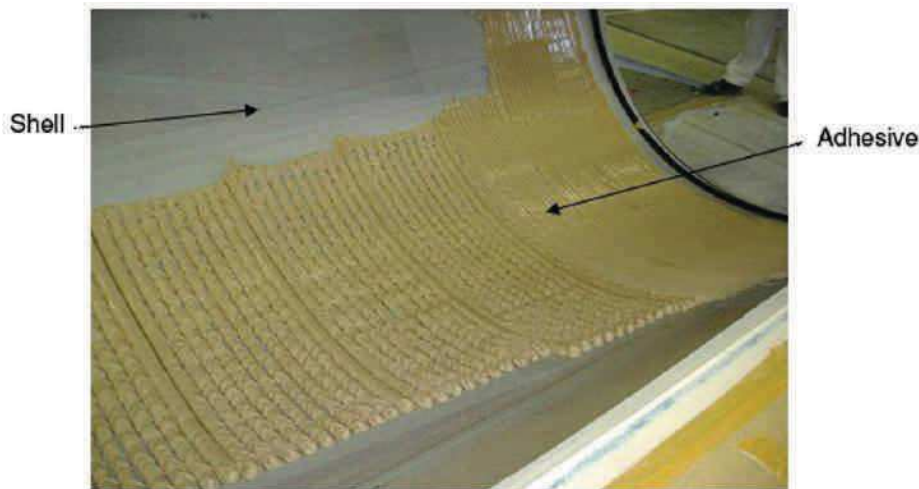


Figure 1-7: Application of the polyurethane adhesive into the first shell.

The Figure 1-7 shows the use of adhesives to join together 2 outer blade shells. These blade shells constitute the pressure and suction side of the blade.

1.3 Resistance of composites to damage

Composites used for wind turbines undergo completely reversed type cyclic loadings during their life cycles. Imagine a turbine of multi-megawatt scale turning at 11 – 16 rpm would undergo nearly 6 million cycles a year. Such loadings cause damage to take place in the turbine blade which can propagate to the extent where catastrophic failure can occur, Figure 1-8. Therefore a good knowledge of the damage characteristics is required to find the life of the wind turbine blade (Paquette, et al., 2011). In addition to the fatigue or cyclic loading based damage initiation there are other factors such as impact damage also, against which the blades should be designed. The impact resistance to composites can be improved using sandwich cores made from foam or balsa wood. Although for large size turbine blades almost always foam cores are used (Hansen, et al., 2008). The turbine blades are manufactured using the vacuum infusion process. The blades are manufactured in different parts, as Intrados, Extrados and the Longerons and then are later joined together by adhesives. Therefore the criteria of resistance of the materials to the initiation and then the propagation of cracks are very important. In general the cracks within materials appear and propagate under two different and distinct modes. The mode where the crack propagates normal to force applied is the Mode I opening type crack propagation. The other where the crack grows in the direction of the applied force is the Mode II shearing type crack propagation.

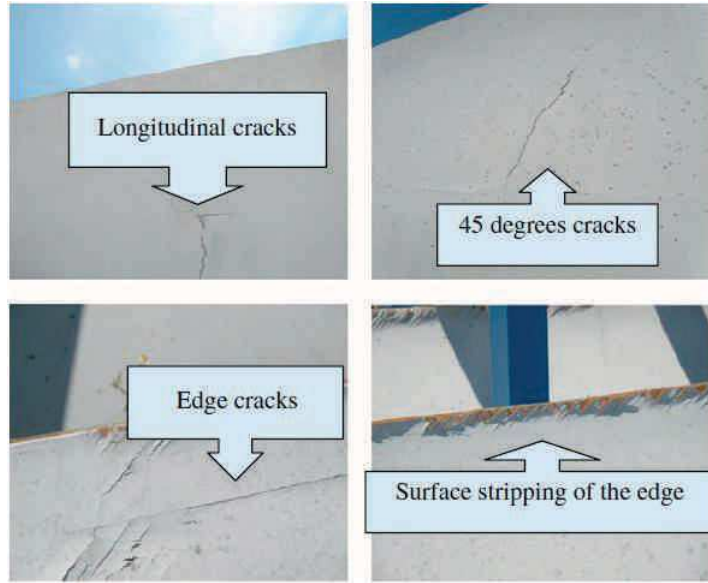


Figure 1-8: Blade damage types.

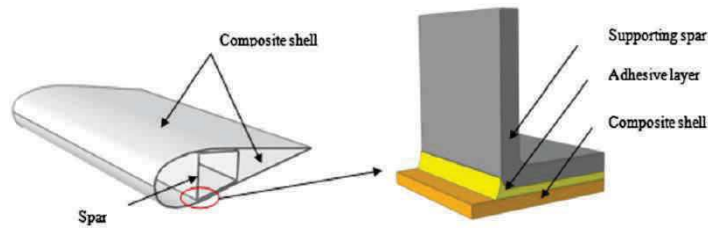


Figure 1-9: Solid model of the adhesive joint for wind turbine blade.

Once the stress – strain fields are calculated normally from Finite Element Analyses, the maximum values of stresses and strains can be used for predicting the onset of damage. The simplest approaches deal with ultimate strength of composites in tension, compression and shearing:

$$\begin{aligned}
 \bar{\sigma}_{1rc} < \bar{\sigma}_1 < \bar{\sigma}_{1rt} & \quad -\bar{\sigma}_{4rs} < \bar{\sigma}_4 < \bar{\sigma}_{4rs} \\
 \bar{\sigma}_{2rc} < \bar{\sigma}_2 < \bar{\sigma}_{2rt} & \quad -\bar{\sigma}_{5rs} < \bar{\sigma}_5 < \bar{\sigma}_{5rs} \\
 \bar{\sigma}_{3rc} < \bar{\sigma}_3 < \bar{\sigma}_{3rt} & \quad -\bar{\sigma}_{6rs} < \bar{\sigma}_6 < \bar{\sigma}_{6rs}
 \end{aligned}
 \tag{1-1}$$

where the directions 1, 2 & 3 correspond to the three spatial coordinates and 4, 5 & 6 correspond to the planes containing the axes 1-2, 2-3 and 3-1; pertaining to shearing directions. “rc”, “rt” and “rs” subscripts denote the resistance in compression, tension and shearing.

Equally these criteria can be expressed in terms of strains at failure:

$$\begin{aligned}
 \bar{\epsilon}_{1rc} < \bar{\epsilon}_1 < \bar{\epsilon}_{1rt} & \quad -\bar{\epsilon}_{4rs} < \bar{\epsilon}_4 < \bar{\epsilon}_{4rs} \\
 \bar{\epsilon}_{2rc} < \bar{\epsilon}_2 < \bar{\epsilon}_{2rt} & \quad -\bar{\epsilon}_{5rs} < \bar{\epsilon}_5 < \bar{\epsilon}_{5rs} \\
 \bar{\epsilon}_{3rc} < \bar{\epsilon}_3 < \bar{\epsilon}_{3rt} & \quad -\bar{\epsilon}_{6rs} < \bar{\epsilon}_6 < \bar{\epsilon}_{6rs}
 \end{aligned}
 \tag{1-2}$$

Following these general relations some failure relation polynomials have also been developed by researchers to base the failure of the plies on experimental data.

These relations take the general form as

$$F_i \bar{\sigma}_i + F_{ij} \bar{\sigma}_i \bar{\sigma}_j + F_{ijk} \bar{\sigma}_i \bar{\sigma}_j \bar{\sigma}_k + \dots < 1 \quad 1-3$$

where “ $F_{i,j,ijk}$ ” are the coefficients determined experimentally and depend on the rupture strengths of the composite materials. As long as the inequality above stays true there is not any onset of damage.

Using the same general form and taking into account the Von Misses criterion the Tsai-Hill damage criterion is given as:

$$\left(\frac{\bar{\sigma}_1}{\bar{\sigma}_{1rt}}\right)^2 + \left(\frac{\bar{\sigma}_2}{\bar{\sigma}_{2rt}}\right)^2 - \frac{\bar{\sigma}_1 \bar{\sigma}_2}{\bar{\sigma}_{1rt}^2} + \left(\frac{\bar{\sigma}_6}{\bar{\sigma}_{6rt}}\right)^2 < 1 \quad 1-4$$

It can be further developed to take into account the compressive strengths of the composites to get criterion of Tsai-Wu in plane stress state (Decolon & Christian, 2000):

$$F_1 \bar{\sigma}_1 + F_2 \bar{\sigma}_2 + F_{11} \bar{\sigma}_1^2 + F_{22} \bar{\sigma}_2^2 + 2F_{12} \bar{\sigma}_1 \bar{\sigma}_2 + F_{66} \bar{\sigma}_6^2 \quad 1-5$$

where

$$\begin{aligned} F_1 &= \frac{1}{\bar{\sigma}_{1rt}} + \frac{1}{\bar{\sigma}_{1rc}} & F_2 &= \frac{1}{\bar{\sigma}_{2rt}} + \frac{1}{\bar{\sigma}_{2rc}} \\ F_{11} &= -\frac{1}{\bar{\sigma}_{1rt} \bar{\sigma}_{1rc}} & F_{22} &= -\frac{1}{\bar{\sigma}_{2rt} \bar{\sigma}_{2rc}} \\ F_{12} &= \frac{1}{\sqrt{\bar{\sigma}_{1rt} \bar{\sigma}_{1rc} \bar{\sigma}_{2rt} \bar{\sigma}_{2rc}}} & F_{66} &= \frac{1}{\bar{\sigma}_{6r}^2} \end{aligned} \quad 1-6$$

These criteria are very good for predicting the onset of damage. In addition these criteria can be used in any analytical calculation. However it is seen especially in large composite structures that there can always be a certain fraction of the structure already damaged. Hence the performance especially the stiffness of the damaged structure needs to be calculated to see if the structure is usable in its damaged state. As will be explained later the structure’s damage propagation is modeled and predicted for the same exact reason to include the residual life of the damaged structure to the total usable life span. Otherwise since these large structures have some sort of damage already in them would require costly replacements as soon as damage appears which would render them financially infeasible.

For this purpose Hashin’s criteria of damage have been developed. These criteria not only represent the damaged stiffness of the structures but also have the provision to differentiate the failure in matrix and fiber mode failures.

Mode I: Fibers in tension $\bar{\sigma}_1 \geq 0$

$$\left(\frac{\bar{\sigma}_1}{\bar{\sigma}_{1rt}}\right)^2 + \alpha \left(\frac{\bar{\sigma}_6}{\bar{\sigma}_{6rt}}\right)^2 < 1; \text{ for } 0 < \alpha < 1 \quad 1-7$$

Mode 2: Fibers in compression $\bar{\sigma}_1 < 0$

$$\left(\frac{\bar{\sigma}_1}{\bar{\sigma}_{1rc}}\right)^2 < 1 \quad 1-8$$

Mode 3: Matrix in tension $\bar{\sigma}_2 \geq 0$

$$\left(\frac{\bar{\sigma}_2}{\bar{\sigma}_{2rt}}\right)^2 + \left(\frac{\bar{\sigma}_6}{\bar{\sigma}_{6rt}}\right)^2 \quad 1-9$$

Mode 4: Matrix in compression $\bar{\sigma}_2 < 0$

$$\left(\frac{\bar{\sigma}_2}{2\bar{\sigma}_{6rt}}\right)^2 + \left[\left(\frac{\bar{\sigma}_{2rt}}{2\bar{\sigma}_{6rt}}\right)^2 - 1\right]\frac{\bar{\sigma}_2}{\bar{\sigma}_{2rc}} + \left(\frac{\bar{\sigma}_6}{\bar{\sigma}_{6rt}}\right)^2 < 1 \quad 1-10$$

where $\hat{\sigma}_i$ is the effective stress of the damaged structure in 1, 2 and 6 direction.

$$\hat{\sigma}_i = \begin{bmatrix} \frac{1}{1-d_f} & 0 & 0 \\ 0 & \frac{1}{1-d_m} & 0 \\ 0 & 0 & \frac{1}{1-d_s} \end{bmatrix} \quad 1-11$$

where d_f , d_m , and d_s being the damage coefficients which signify a loss of rigidity in general;

$$d = \frac{\text{rigidity of damaged structure}}{\text{rigidity of original structure}} \quad 1-12$$

The Hashin criteria is very well adaptable to finite element models, various commercial software use the same criterion in their codes.

1.4 Resistance to delamination and de-bonding

1.4.1 Analytical approach

In general beam theories are applied to pre-cracked specimens in order to measure the energy liberated during crack propagation. This energy liberated also called the strain energy release rate, can then be used to predict the crack propagation and damage development characteristics of the material

(Holmes, et al., 2007). Following are some formulations based on simple beam theory to determine these strain energy release rates.

Mode I

$$G_{IC} = \frac{3P\delta}{2ba} \quad 1-13$$

Mode II

$$G_{IIC} = \frac{9P^2 a^2 C}{2b(2L^3 + 3a^3)} \quad 1-14$$

and for *mixed modes*.

$$G_I = \frac{12P_I^2}{b^2 h^3 E_{11}} \left(a_o^2 + \frac{2a_o}{\lambda} + \frac{1}{\lambda^2} + \frac{h^2 E_{11}}{10G_{13}} \right) \quad 1-15$$

$$G_{II} = \frac{9P_{II}^2}{16b^2 h^3 E_{11}} \left(a_o^2 + \frac{h^2 E_{11}}{5G_{13}} \right) \quad 1-16$$

$$\lambda = \frac{1}{h} \sqrt{\frac{6E_{22}}{E_{11}}} \quad 1-17$$

$$P_I = P_C \left(\frac{3c - L}{4L} \right) \quad 1-18$$

$$P_{II} = P_C \left(\frac{c + L}{L} \right) \quad 1-19$$

where “G_{IC}” and “G_{IIC}” are respectively the rate of energy release in mode I and mode II, “P” is the load applied, “δ” is the displacement through which the load is applied (opening in mode I and flexion in mode II), “b” is the breadth of the specimen, “a” is the crack length, “E₁₁”, “E₂₂” and “G₁₃” is the module of elasticity of the composite specimen in the direction of the fibers, perpendicular to them

and in shearing respectively. “C” is the compliance given by “ $C = \delta/P$ ” and “ P_I, P_{II} ” are respectively the forces applied at different location in a mixed mode bending experiment.

1.4.2 Finite Element approach using VCCT

In addition to these some modeling techniques such as “virtual crack closure technique” VCCT can also be used for the determination of the energy release rates. In general the VCCT relations are given by 1-20 and 1-21 (Krueger, et al., 2000).

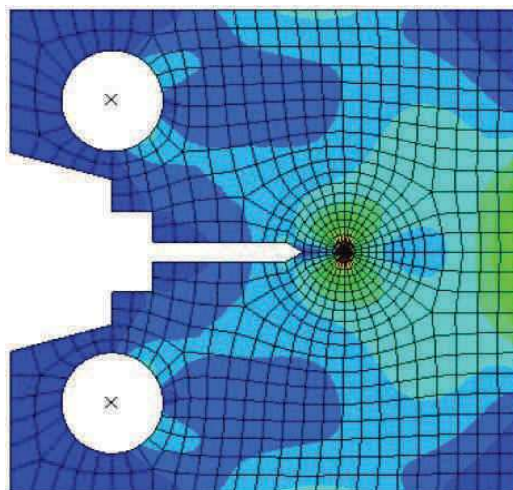
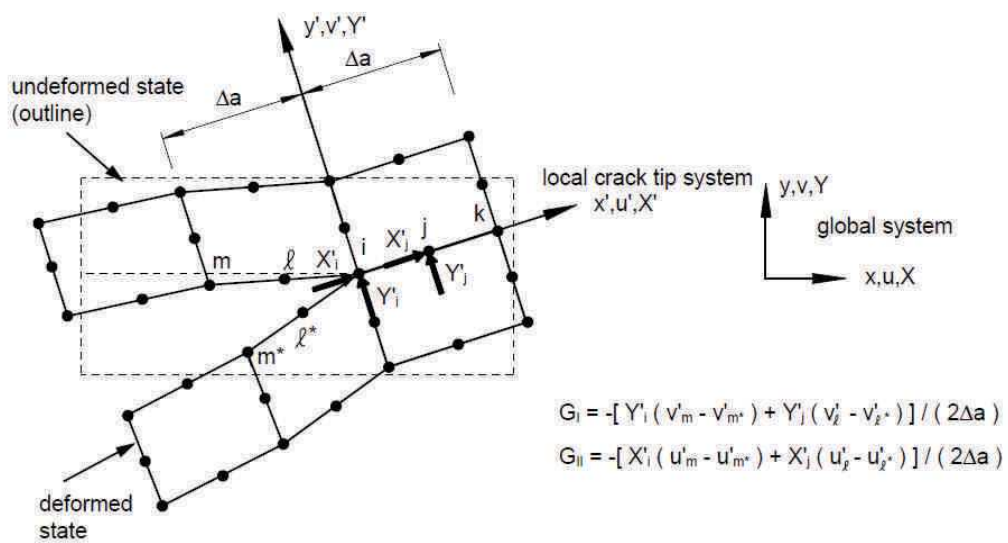


Figure 1-10 : Determination of crack energy release rates using VCCT.

$$G_{IC} = -[Y'_i(v'_m - v'_{m*}) + Y'_j(v'_l - v'_{l*})] \quad 1-20$$

$$G_{IIC} = [X'_i(u'_m - u'_{m*}) + X'_j(u'_l - u'_{l*})] \quad 1-21$$

Where X'_i, X'_j, Y'_i, Y'_j is the force in the x and y direction on the “i” and “j” node. “v” and “u” are the displacements along x and y directions of the nodes “m” and “l”

The VCCT is a good technique to couple the determination of G_I and G_{II} when the crack path and/or the loading conditions give rise to mixed mode crack propagations. VCCT is based on the basic hypothesis that the energy liberated during the propagation of a crack through a certain distance is the same as required to close the crack behind it.

1.4.3 Numerical approach using cohesive zone models

Cohesive zone models or CZM's are based on the separation of the joined interfaces. They are based on the displacement jumps that occur denoting a separation of two adjoining pieces and hence complete failure. The CZM's are based on the use of cohesive zones which can be considered to have zero thickness or in other words the whole of the CZM element acts as one entity and the whole for the element degrades and fails at once. Only the interactions of the interfaces are taken into account, which include the traction forces at the interfaces and their respective displacements. The direction of the crack growth depends on the position of cohesive elements. Different traction separation laws have been developed (Park & Paulino, 2011), but they all represent the same global behavior. The traction at the cohesive zone interface builds up to a limiting value, called crack initiation traction presented in terms of stress. Then a certain “softening” is taken into account of the cohesive zone till the traction “stress” comes down to zero (Kregting, 2005) (Hamitouche, et al., 2008).

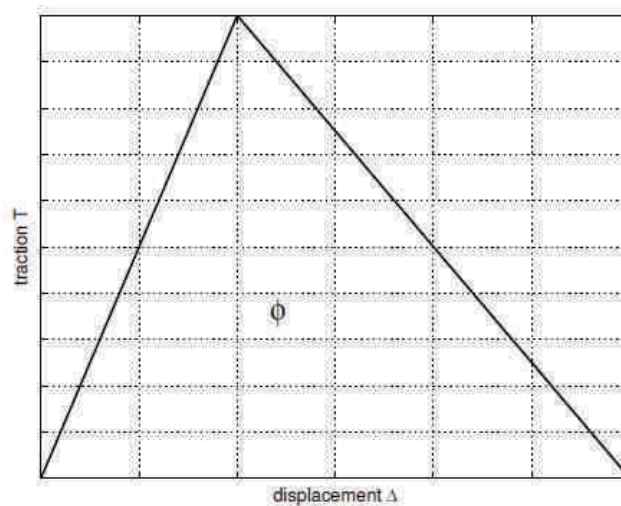


Figure 1-11 : A general traction separation behavior for CZMs

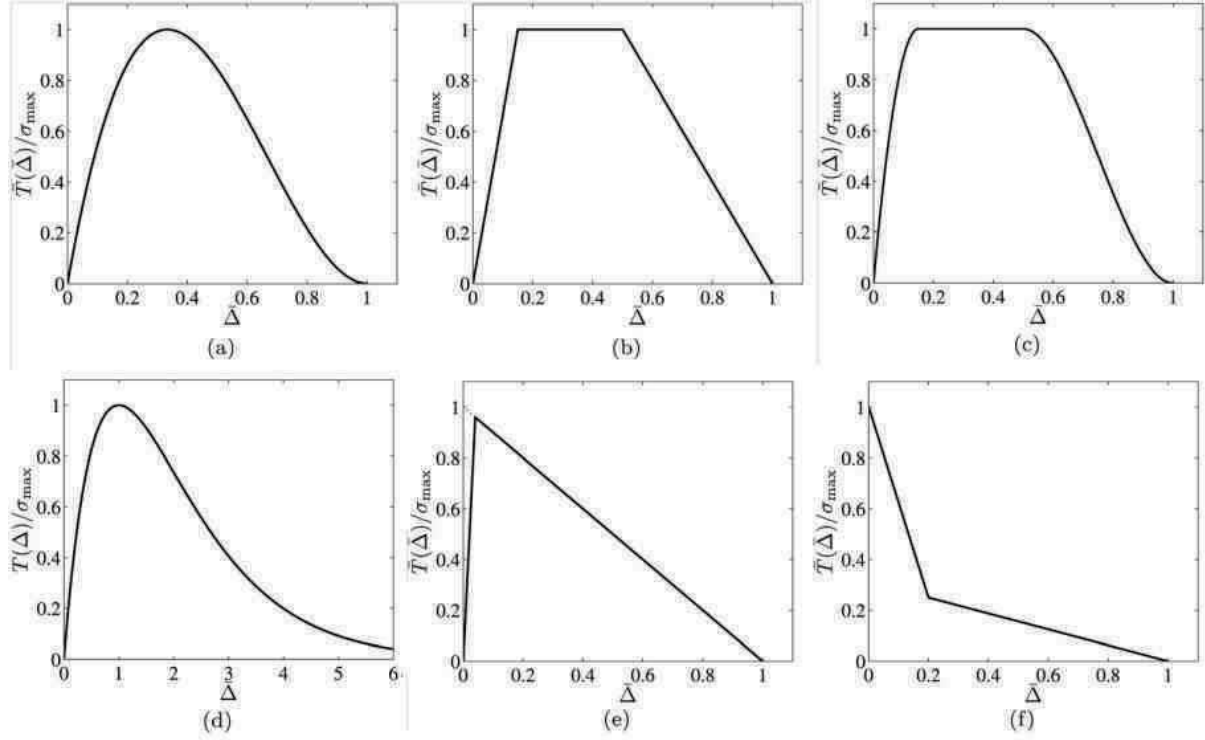


Figure 1-12 : Different one dimensional effective displacement based models.

(a) cubic polynomial, (b) trapezoidal, (c) smoothed trapezoidal, (d) exponential, (e) linear softening, and (f) bilinear softening

The area “ ϕ ” in the Figure 1-11 corresponds to the energy released during failure of the cohesive zone and depends on the stiffness of the zone. For realistic results these values are kept very high, otherwise large deformations in the cohesive zone elements take place without failure. Finite element analysis is used to simulate this aspect of cohesive zone rigidity.

In general the traction can be represented as the tangential and normal components to the cohesive zone plane. In general the traction and displacement vectors are given as under.

$$T = -\frac{\partial\phi(\Delta)}{\partial(\Delta)} \quad 1-22$$

$$\Delta = (\Delta_n, \Delta_t) \quad 1-23$$

After the application of the potential, the normal and tangential traction components are given as.

$$T_n = \frac{\phi_n}{\delta_n} \exp\left(-\frac{\Delta_n}{\delta_n}\right) \left\{ \frac{\Delta_n}{\delta_n} \exp\left(-\frac{\Delta_t^2}{\delta_t^2}\right) + \frac{1-q}{r-1} \left[1 - \exp\left(-\frac{\Delta_t^2}{\delta_t^2}\right) \right] \left[r - \frac{\Delta_n}{\delta_n} \right] \right\} \quad 1-24$$

$$T_t = 2 \left(\frac{\phi_n \Delta_t}{\delta_t^2} \right) \left\{ q + \left(\frac{r-q}{r-1} \right) \frac{\Delta_n}{\delta_n} \right\} \exp\left(-\frac{\Delta_n}{\delta_n}\right) \exp\left(-\frac{\Delta_t^2}{\delta_t^2}\right) \quad 1-25$$

Where “ $T_{n,t}$ ” are the normal and tangential traction components, “ $\phi_{n,t}$ ” is the area under the traction displacement curve for normal and tangential directions respectively, “ $\Delta_{n,t}$ ” is the displacement of the cohesive zone nodes, “ $\delta_{n,t}$ ” is the characteristic separation such that “ $T_n(\delta_n) = \sigma_{max}$ ”, “ $T_t(\delta_t/\sqrt{2}) = \tau_{max}$ ” with “ σ_{max} ” and “ τ_{max} ” being the normal and tangential maximum tractions. “ $q = \phi_t / \phi_n$ ” and “ $r = \Delta'_n / \delta_n$ ” with Δ'_n is Δ_n when complete shear separation has taken place with zero normal tension. In this case the $q = 1$ and $r = 0$.

Taking pure uncoupled traction forces where T_n and T_t are measured when $\Delta_t = 0$ and $\Delta_n = 0$ respectively. We obtain for the energies released:

$$\phi_n = \sigma_{max} \exp(1) \delta_n \quad 1-26$$

$$\phi_t = \sqrt{\exp(1)/2} \tau_{max} \delta_t \quad 1-27$$

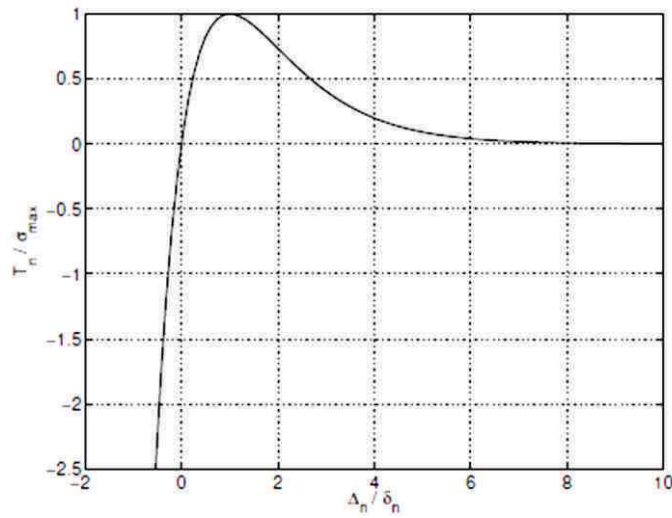


Figure 1-13: Normal traction curve

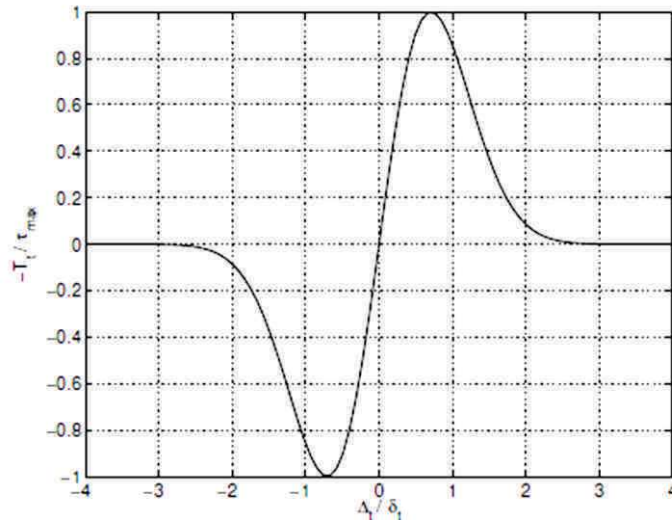


Figure 1-14: Tangential traction curve

“ T_n / σ_{max} ” and “ T_t / τ_{max} ” are the dimensionless tractions, “ Δ_n / δ_n ” and “ Δ_t / δ_t ” are the dimensionless traction openings.

Equations 1-24 and 1-25 can be used in coupled situations also when the tractions applied are not purely normal or tangential, i.e. $T_n = T_n(\Delta_n, \Delta_t)$ and $T_t = T_t(\Delta_n, \Delta_t)$.

The traction displacement surfaces in this case would become as shown in Figure 1-15.

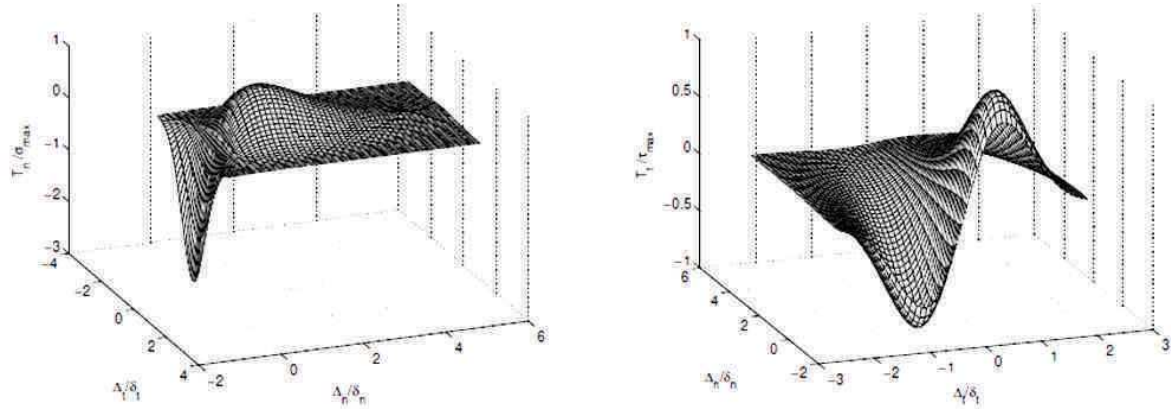


Figure 1-15: Normal and tangential traction surface

Following these general formulations of traction separation laws there has been a development of some variations in order to refine the modeling of behavior. To begin with there are one-dimensional effective displacement-based models like the cubic polynomial, trapezoidal, smoothed trapezoidal, exponential, linear softening and bilinear softening as shown in Figure 1-12 (Tvergaard, 1990)(Tvergaard & Hutchinson, 1993), (Scheider & Brocks, 2003), (Ortiz, 1999), (Camacho, 1996) (Geubelle, 1998), (Petersson, 1981). These one-dimensional effective displacement-based models have their limitations in that the stiffness of the cohesive zone may increase with an increase in the traction separation. The other limitation is that the strain release energy is constant irrespective of the mode, which makes the mixed mode calculations difficult. In addition to these constraints these models can not consider negative separations due to their formulations which take into account the square of separations and displacements (Park & Paulino, 2011).

In view of the limitations in the effective displacement models, potential based models are developed. In these models the separation is presented in terms of normal and tangential separations, instead of general effective displacements. Hence their respective derivations result in their respective tractions. Some of the models present in the literature are polynomial representations (Needleman, 1987)(Freed, 2008) and the universal binding energy models (Needleman, 1990),(Beltz, 1991),(Xu & Needleman, 1993).

The final aim of modeling cohesive zones is to simulate the path of the crack propagation (delamination) through the composite and cohesive failure in joints (assemblies). The crack would follow the path of least resistance. There are different modes in which the crack can propagate. Figure 1-16 shows one such example where the crack can take anyone of the four possible routes. It so happens that in some cases the crack is bifurcated and follow different paths at the same time.

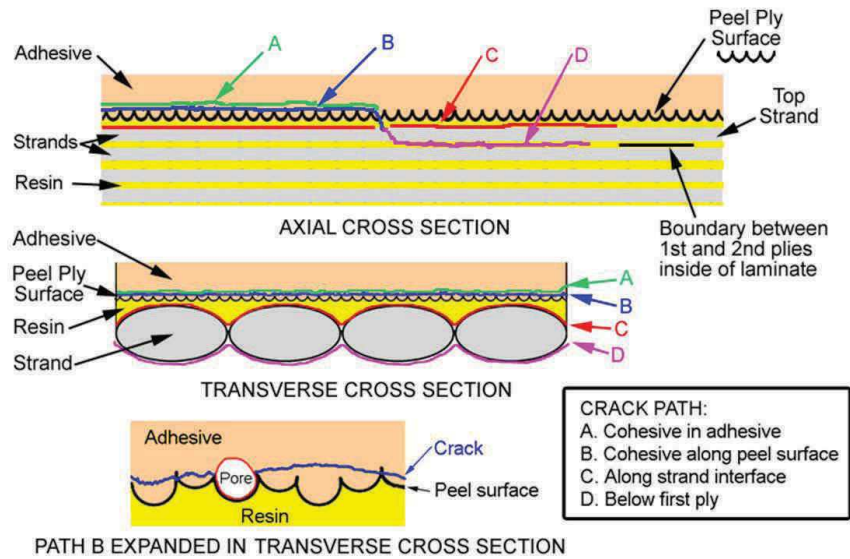


Figure 1-16: Different paths followed by a crack based on the resistance to crack propagation in each mode

1.5 Fatigue behavior of Materials

The behavior of materials in fatigue is a very important parameter in the design of mechanical components. As such for wind turbine blades, as discussed above the influence of fatigue on the degradation of stiffness and eventually strength is a very important design factor. The fatigue characteristics for composites are complicated to predict and model as a result of their multi-mode failure mechanisms. Therefore a study of the most likely mode of failure is necessary to be done before fatigue tests are carried out. The size and speed of rotation of these blades suggest that they will experience an excess of 100 million cycles during a 20 year life time. Although care must be taken while testing the materials in a controlled environment as the higher applied load cycles can cause a loss in elasticity but an increase in final failure (Hachemane & Bezzazi, 2009).

For composite materials it is seen that classic tensile tests may show a highly non linear behavior. This non linearity may be due to the damage taking place or in some cases a bi-linear behavior is shown before failure, attributed to the phase change of the composite polymer matrix during monotonic loading (Choi, et al., 2001).

For taking into the account this non-linearity in the composites behavior the stress-strain relation can be expressed as:

$$\sigma = E \varepsilon^p \quad 1-28$$

Where “ E ” is the rigidity of the material and “ p ” is a coefficient based on non-linearity.

In general in the presence of cracks within the material Paris’ law can be used to determine the remaining life of the material.

$$N = \frac{2(a_c^{\frac{2-m}{2}} - a_i^{\frac{2-m}{2}})}{(2-m)C(\Delta\sigma Y\sqrt{\pi})^m} \quad 1-29$$

Where “ a_c ” and “ a_i ” is the crack length where the material would fail under static load, applied as the load amplitude to the specimen and the initial crack length respectively. “ m and Y ” are the material constants determined by experimentation. “ N ” is the number of cycles till final failure.

The above general Paris law works well for homogenous materials. Whereas in the case of fiber reinforced composites its application needs to be modified. As already explained the failure in fiber reinforced composites is progressive. Starting from the initiation of crack at the matrix then growing and interacting with the fibers which can cause it to slow down and finally creating a sufficiently large discontinuity in the composite that the structure loses its rigidity well before final failure (Upitis, et al., 1979).

The characterization of materials in fatigue is a long and laborious process. The experiments need to be run for long periods of time as to complete the given number of cycles up to failure. To address this problem some different approaches are being developed to reduce the material testing times. One such method which can be run at accelerated rates was presented by (Sutherland, 1999) (Musial, 2000).

The equivalent damage concept presented in (Sutherland, 1999) and (Musial, 2000) states that the damaged state of a material at an equivalent number of cycles “ n ” subjected to a stress level “ σ ” can be determined which is an equivalent to a damaged state $D(\sigma_l, n_l)$ at a stress level “ σ_l ” after undergoing “ n_l ” no of cycles.

The damage at stress level “ σ_k ” is given by 1-30:

$$D_{\sigma_k} = \frac{\sum_{r=1}^k (\sigma_{res(r-1)} - \sigma_{res(r, n_r)})}{\sigma_{rupture} - \sigma_k} \quad 1-30$$

where 1-31 signifies the reduction in strength due to the spectral charge:

$$\sum_{r=1}^k (\sigma_{res(r-1)} - \sigma_{res(r, n_r)}) \quad 1-31$$

The residual strength after the stress level “ σ_i ” can be given by 1-32:

$$\sigma_{failure} - \sigma_{res(n)} = \alpha \left(\frac{\sigma_i}{\sigma_{failure}} \right)^{0.6} \left[[\sigma_i (1 - R)^{1.6}] \frac{1}{f_i^\beta} (n_i^\beta - 1) \phi_{n_i} \right] \quad 1-32$$

where $R = \left(\frac{\sigma_{min}}{\sigma_{max}} \right)$, “ α, β ” are material constants, “ σ_{max} ” is the maximum applied stress in the direction of the loading, “ $\sigma_{failure}$ ” is the ultimate strength of the undamaged material, “ $\sigma_{res(r-1)}$ ” is the residual strength after “ r^{th} ” load level, “ $\sigma_{res(r, n_r)}$ ” is the residual strength after “ n ” number of cycles “ r^{th} ” load level, “ σ_k ” is the applied stress at “ k^{th} ” load level, “ f_i ” is the frequency of load at “ i^{th} ” load level.

Following the above formulation, (Clausen & Epaarachchi, 2003) defined a factor for regain strength “ Φ_{ni} ”. Given in 1-33:

$$\phi_{ni} = 1 - \left[1 - \left(\frac{n}{N_{\sigma,n}} \right)^\beta \right]^\beta \quad 1-33$$

where “ $N_{\sigma,n}$ ” is residual life at “ σ_n ” after loading at “ $(n-1)^{th}$ ” step. “ $N_{\sigma,n}$ ” is determined as;

$$\sigma_{res(n-1)} - \sigma_n = \alpha \left(\frac{\sigma_i}{\sigma_{rupture}} \right)^{0.6} \left[[\sigma_{ni}(1-R)^{1.6}] \frac{1}{f_i^\beta} (N_{\sigma,n}^\beta - 1) \right] \quad 1-34$$

The material properties for the 1-32 can be determined using classic SN curves for the material being tested.

Finally the no of cycles “ $n_{equivalent}$ ” at stress level “ σ ”, frequency “ f ” and stress ratio “ R ” which cause the same strength degradation at an arbitrary level, as “ σ_i ”, frequency “ f_i ” and stress ratio “ R_i ”.

$$n_{equivalent} = \left(\frac{\alpha \left(\frac{\sigma_i}{\sigma_{rupture}} \right)^{0.6-R_i} [\sigma_i(1-R_i)^{1.6}] \frac{1}{f_i^\beta} (n_i^\beta - 1) \phi_{n1}}{\alpha \left(\frac{\sigma}{\sigma_{rupture}} \right)^{0.6-R} [\sigma_i(1-R)^{1.6}] \frac{1}{f^\beta} \phi_n} + 1 \right)^{1/\beta} \quad 1-35$$

Following the equivalent strength degradation technique some researchers have worked on characterizing the material’s fatigue characteristics based on their thermo mechanical behavior. Instead of considering the degradation of stiffness the heat liberated during fatigue analyses can also be used to determine the fatigue life at an accelerated rate (Curà, et al., 2005). Although these tests have been used for metallic materials but for composites especially long fiber reinforced composites, their use has been limited. Fatigue life depends on the elastic and plastic behavior and the change in the polymer microstructure taking place in the material under loading, hence materials undergoing little phase changes during loadings do not exhibit marked changes in heat generation or reduction of stiffness which can lead to inaccuracies in the fatigue life determination using accelerated techniques.



Figure 1-17: Some failed wind turbine blades during their service.

1.6 Delamination fatigue

In long fiber reinforced composites the delamination type failures are common place. Such failures take place due to stress concentrations in the interlaminar regions. In addition the locations where there is a high concentration of interlaminar tensile or shear stresses, delaminations usually occur. This type of failure is common in composites because the fibers are a lot stronger than the matrix and hence usually the matrix fails before the fibers break or get pulled out. To predict and model the delamination failures it is important to model the composite through their thickness to account for interlaminar stress concentrations. For this purpose the delamination initiation should be checked using the strain energy release rates as discussed in section 1.4 of this chapter (a detailed discussion will follow in the corresponding chapters).

In general, the crack growth per cycle can be related to the strain energy release rate by:

$$\frac{da}{dN} = A(G_{max})^B \quad 1-36$$

Since the values for the exponent “*B*” are rather high between 3 and 15 hence using the fatigue growth part of the curve any small deviation from the service load would lead to large errors in the delamination growth rate. Since the “*G*” is the square of applied load the growth rate would be raised

to the power “ $2B$ ” of the load applied(Harris, 2003). “ G_{max} ” here signifies the value of “ G ” under the applied fatigue load.

To resolve this problem the “No Growth” approach is developed, where a threshold strain energy release rate is to be determined “ G_{th} ”. This threshold is determined by cyclically loading DCB and ENF specimens for mode II and II respectively. The value of “ G ” at an applied cyclic load where the crack slows down considerably or stops completely is the “ G_{th} ” for that applied load. Different threshold “ G_{th} ” values are then plotted against their corresponding loads (Murri, 2011). The values of “ G ” can be calculated by using “VCCT” for the real structure and if at the applied load it does not attain the threshold value “ G_{th} ” he structure can be considered safe.

The no growth approach can be expressed in the Paris’ Law form as:

$$\frac{da}{dN} = A(G_{max})^B \frac{\left[1 - \left(\frac{G_{th}}{G_{max}}\right)^{D_1}\right]}{\left[1 - \left(\frac{G_{th}}{G_c}\right)^{D_2}\right]} \quad 1-37$$

Where the values of “ A ” and “ B ” are calculated by fitting to the Paris law and “ D_1 ” and “ D_2 ” are determined from the experimental data of crack growth(Murri, 2011).

1.7 Wind turbine form design

Although the optimization of the aerodynamic design is not the principal aims of this thesis but it is treated none the less as it is essential for calculating the aerodynamic loads applied. These loads are then used to simulate the blade using FEA and to find out the validity of the proposed blade designs. The loads applied on the blade can be divided in 3 principal categories:

1. Aerodynamic loading applied by the wind as lift and drag,
2. Inertial loading due to weight of the blade,
3. Centrifugal due to its rotation.

Amongst these three loads the inertial load due to the weight of the blade is perfectly cyclic at a constant wind and rotational speed. The wind loading is considered for design purposes to be constant but varies from point to point along the length of the wind blade. Especially when the blade is vertical downwards, the blade experiences a gradient of wind from it being slowest at its tip to it being highest at its root. This is due to the gradient in wind speed present as a result of resistance with the ground, although this variation is usually ignored. The blade experiences two cycles of pure flexion but reversed in direction while the rotation and one case each of pure tension and compression when the blades are vertical upwards and downwards respectively. The centrifugal force rests constant as long as the blade does not accelerate or decelerate and this is the case for constant speed turbines that for most of their service they turn at a uniform constant rotational velocity. Therefore the blades experience completely reversed fatigue loading. In addition when the blade is vertical upwards the blade experiences compression in which its resistance to buckling becomes increasingly important. Moreover the design of the wind turbine blade is done in extreme wind conditions during service and when the turbine needs to be stopped during stormy conditions. The deflections of the blade tip should

be well taking into consideration to verify the interference distance from the tower. The design regulations are given in the “IEC-61400-1 ED 3” and recommendations are made in the “Germanischer Lloyd (GL)” insurance conditions. It is seen from experience that the longerons of these blades and the outer most skin containing 45° Biax mats are the most sensitive components to fatigue failure(Kensche, 2004). The other specifications according to GL are for the admissible loads; in general the design safety factor varies between 1.02 to 1.82 of the maximum admissible load.

The most commonly used theory for the determination of charges applied on the wind turbine blade is the Blade Element Momentum theory. By this theory the blade is divided into various elements of the same length along the blade length. Depending on the length of the blade they can be divided into 10-20 elements, where a sensitivity study should be made in order to differentiate the blade (Janajreh, 2012). However this method considers each element as completely independent of the other with no flow taking place across the boundary of adjacent elements. Hence the flow is modeled as 2D in each of the elements. However the tip losses, wake losses and losses due to rotation of the wind stream can be considered in applying different correction factors which will be discussed in detail while representing the mathematical form of BEM. The total power generated by the blade can be determined by summing the power generated by each of the blade sections.

The form of the blade depends on the choice of the airfoil profile that can give a high lift at relatively low angles of attack in order to keep the overall twist of the blade low. This permits ease of manufacture and less stress concentrations. Off the various parameters that are fixed during the design the process the rotational speed is fixed also, which depends on the blade length and the final power to be generated by it. Due to the manufacturing constraints present the final design is to some extent a compromise between the optimal aerodynamic performance and structural resistance. The latter being always more important as a result of safety than the aerodynamics which usually suffer.

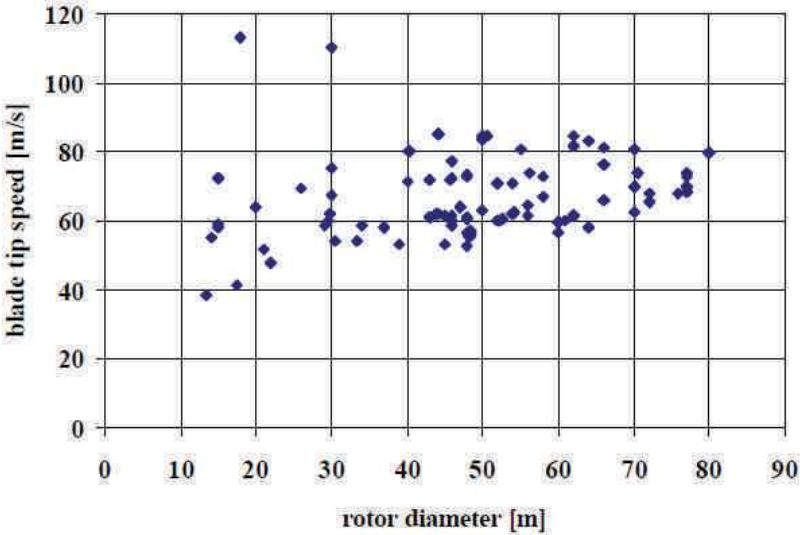


Figure 1-18 : Rotor tip speed plotted against typical rotor diameters for polymer based composite blades.

In general the BEM calculation code consists of the following steps:

1. Initialize the calculation by considering $a = a' = 0$

Calculate “ φ ” by

$$\tan\varphi = \frac{(1 - a)V_o}{(1 + a')\omega r} \quad 1-38$$

Where “ φ ” is the angle of wind with respect to the rotor plane, “ V_o ” is the velocity of the incident wind, “ ω ” is the rotational speed of the rotor in rad/s, “ r ” is the radius of rotation of the blade element being considered.

2. Calculate the local angle of the element “ θ ” by fixing the angle of attack “ α ”

$$\alpha = \varphi - \theta \quad 1-39$$

“ α ” is the angle of attack, “ θ ” is the angle of the blade element with respect to the rotor plane

3. Find out the lift and drag coefficients “ C_L ” and “ C_D ” respectively for the airfoil profile chosen using their aerodynamic graphs.
4. Calculate “ C_N ” and “ C_T ” by the equation where “ C_N ” and “ C_T ” the coefficients of normal and tangential force normal to the plane of the rotor

$$\begin{aligned} C_N &= C_L \cos\varphi + C_D \sin\varphi \\ C_T &= C_L \sin\varphi - C_D \cos\varphi \end{aligned} \quad 1-40$$

5. Re-calculate a and a' for the second iteration

$$a = \frac{1}{\frac{4 \sin^2 \varphi}{\sigma C_n} + 1} \quad 1-41$$

And

$$a' = \frac{1}{\frac{4 \sin \varphi \cos \varphi}{\sigma C_t} - 1} \quad 1-42$$

Where

$$\sigma = \frac{Bc}{2\pi r} \quad 1-43$$

“ σ ” is the solidity of the rotor i.e. the area of the blades divided by their swept area. “ B ” is the number of blades, “ r ” is the radius of rotation of the element considered.

The values of “ a ” and “ a' ” are calculated and compared with their values calculated in the previous step. Upon comparing the two values, if they fall under a certain tolerance (for example <0.0001) the computational loop is stopped. At this point the final values of “ φ ” are then considered for the aerodynamic design.

Finally the lift and drag forces “ L ” and “ D ” are then calculated respectively.

$$L = \frac{1}{2} \rho C_L c V_{rel}^2 \quad 1-44$$

$$D = \frac{1}{2} \rho C_D c V_{rel}^2 \quad 1-45$$

and

$$P_N = L \cos \varphi + D \sin \varphi \quad 1-46$$

$$P_T = L \sin \varphi - D \cos \varphi \quad 1-47$$

“ P_N ”, “ P_T ” is the force normal and tangential to the rotor rotational plane. “ c ” is the cord of the blade element.

6. Determine the total power generated by the turbine rotor as

$$M = \sum_{i=1}^n r l N P_T \quad 1-48$$

where “ M ” is the total couple produced by one blade.

The above system of equations is typically used for the determination of the form of the wind turbine blade and to calculate the loads applied on each of its elements.

1.8 Fabrication of Blades

The first problem with large wind turbine blades is their weight. With the ever increasing size of the blades their weight is bound to rise. To keep in check this increase some innovative techniques have to be used. Conventionally the blades are fabricated almost completely of glass fiber and polymer composites. Although it is debatable as to how much is the use of fiber glass really effective for their fabrication. “LM Glasfiber” has been successful in fabricating a wind turbine blade up to 54m in length with only glass fiber based composites. The design is sort of a “mono-coque” design where the outer skin is actually a load bearing component (Mason, 2004). On the other hand “Aerodyn Energie systeme GmbH (Rensburg Germany)” has been able to fabricate a blade made up of a carbon glass fiber hybrid mat, with epoxy resin used as the common matrix. Expensive carbon mats are placed in high stress areas such as the root, to give the blade a lighter and more rigid design. In addition to the choice of material the orientation of fibers plays an important role as well. For instance carbon fibers

have high resistance to buckling when loaded along their lengths in compression. Hence they are so placed near the root of the blade near the intrados. The only problem with unidirectional fibers is that they are held in place with secondary fibers knitted in the tram direction. These secondary fibers can cause waviness hence degrading the in-axis compression resistance. To address this problem SAERTEK has developed a mat called « MMWK ; Multi-Layer, Multi-Axis, Wrap-Knit » with the fiber layup as $[-45^{\circ}_{\text{Glass}}/0^{\circ}_{\text{Carbon}}/+45^{\circ}_{\text{Glass}}]$ to maintain the carbon fibers, straight(Griffin, 2002).

The resistance to delamination type fatigue failure is typically dependant on the characteristics of the matrix. The failure usually initiates at a defect usually present in the fiber-matrix interface as porosity or impurities being trapped in these locations. Once the matrix fails the fibers can no longer keep their shape and hence the structure fails to keep its geometry. Epoxies are known to have good resistance to such failures although polyesters are also finding their use due to low costs (Paquette, 2011). The fatigue experienced by wind turbine blades is usually in the high cycle region where the elasticity of the structure is never exceeded. As composites are always subject to certain defects introduced during manufacture, structures are designed with sufficient crack barriers and interfaces to slow down the crack propagations. In addition sandwich structures are used in region where buckling is an important factor and where impact damage is imminent like the leading edges. For this purpose materials ranging from balsa to hi-tech foams and honey-comb structures are used for sandwiches, although they can pose challenges during the manufacture phase(Hansen, et al., 2008).

The most commonly used matrices are the epoxies and unsaturated polymers. They are used in vacuum resin infusion. “Dow Chemicals” have been concentrating on the shelf life of resins to decrease wastage. In addition the adhesion of matrices is also important as most of the turbine blades are manufactured in parts and then joined together using adhesives.

One of the innovative techniques in matrix materials is the use of thermoplastics. Poly-ether-ether-ketone, (PEEK) has been used in the aeronautical industry but not for principal load bearing components. Although their material and processing costs are comparable or sometimes even lesser than thermosets their mechanics of damage are not well known hence their use is limited up till now. One problem that exists in the use of such materials is the fact that their injections into moulds at higher temperatures cause the fibers to expand and contract upon cooling causing voids at the fiber ends, as fiber coefficient of expansions are higher than that of the matrices. In addition to the voids residual stresses are also induced Figure 1-19 to Figure 1-22.

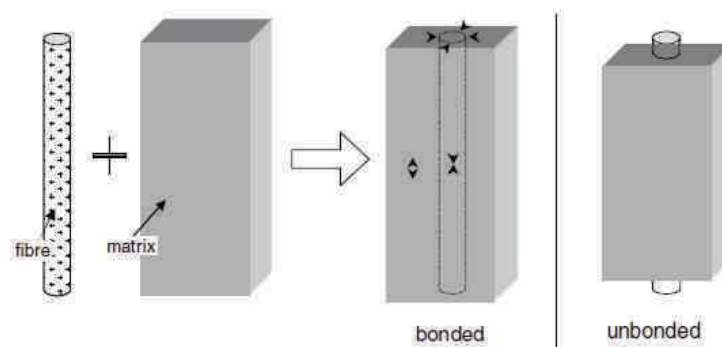


Figure 1-19: Deformation of a fiber bonded to a matrix and of a free fiber.

Each ply in the composite stack applies a stress on its adjacent ply as the coefficient of thermal expansion for each of the plies is different in a given direction.

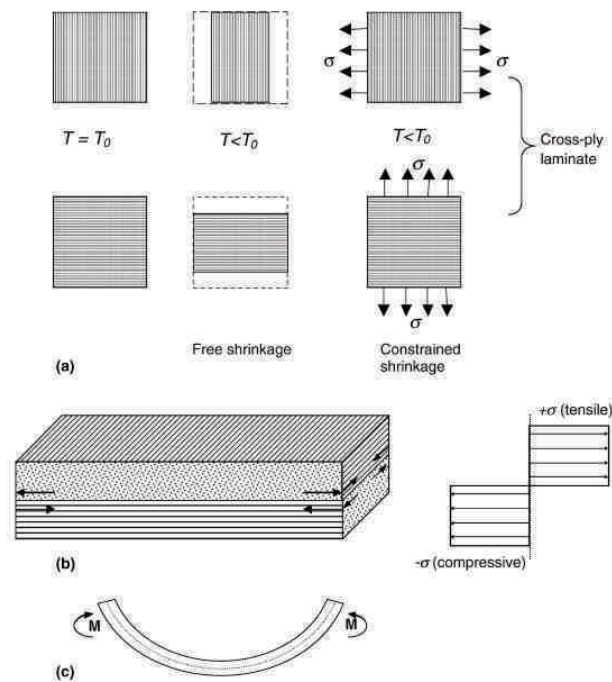


Figure 1-20: Bending moment applied due to differential shrinkage of plies.

Generally a temperature gradient, especially in thick composites can be present due to the surface cooling a lot sooner than the interior. This differential cooling gives rise to a parabolic distribution of stresses along the thickness of the composite. There are 4 important parameters to be considered which define the distribution of stresses in the composite stack, i.e. their elasticity, the temperature of curing, volume fraction of fibers and the thermal expansion coefficients of the materials. There are also semi-crystalline plastics whose rate and temperature of crystallization can have an effect on the stress distribution. In addition to these, there are conditions of injection and the overall environment of the manufacturing facility that can have an effect on these residual stresses, but their effects are not very well understood (Parlevliet & Beukers, 2006).

The advantage of using thermoplastics is their capacity of being repaired in case of damage. Generally speaking repairs done on thermosets induce stress concentrations hence affecting the fatigue life of the composite structures. The material states before and after repairs always differ and usually the repairs are in-situ hence causing defects such as pores and cracks. The repaired zones are prone to delaminations. In different studies a repaired zone on aramid fiber – epoxy composite showed a degradation of 10 – 18% in fatigue resistance. Furthermore the ultimate strength suffered a loss of around 12% as well. Whereas repaired thermoplastics show less of these tendencies (Botelho, et al., 2009).

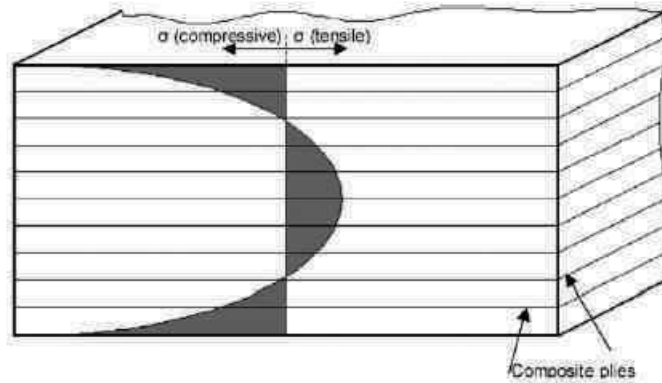


Figure 1-21 : Distribution of thermal stresses created during the hardening of matrix in a thermoplastic matrix composite.

In general there are three different methods used for the fabrication of different components of the blade. Furthermore usually the large dimension blades are manufactured in 3 parts, the Extrados the Intrados and a longitudinal stiffener called the Longeron or the Spar. For the longerons there are two types. One which gives strength to shearing stresses is in the form of a single vertical blade joining the intrados to the extrados. The other type has a more elaborate double bladed design or sometimes in the form of a box section to resist flexural stresses as well (Holmes & Brøndsted, 2007).

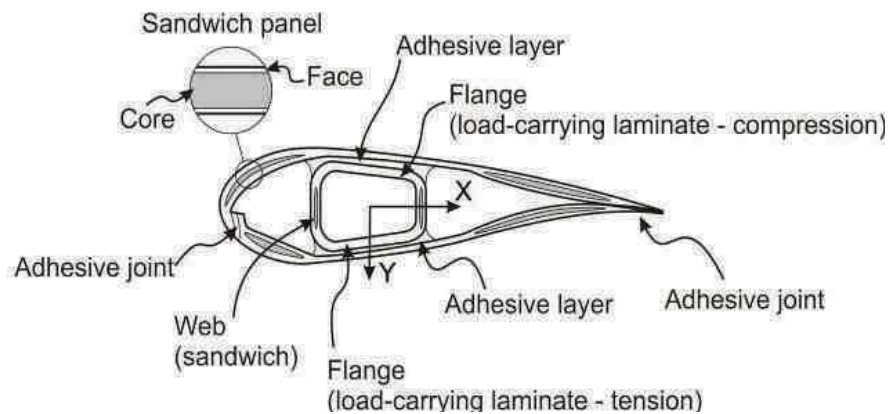


Figure 1-22: A typical box section longeron blade cross section

The three parts are usually joined together by adhesive normally of the same matrix composition. Here we discuss some of the most commonly used composite fabrication techniques used in wind turbine blade manufacture

1. Resin infusion
2. Prepreg mats
3. Hand layup

Of the three the resin infusion method is the most used. The prepreg mats are expensive and their compacting before hardening can leave voids in between the plies and can cause structural inaccurate tolerances. Here we will discuss the resin infusion technique in detail, in the context of large wind turbine blade manufacturing. In resin infusion the Resin transfer molding technique is the most precise method for composite part manufacturing. The dry mats are layered and resin is pumped into the laid plies in moulds, under vacuum and/or pressure to completely saturate the plies with resin. The parts can be fabricated by this technique in a closed mold process, where the core and cavity both give a certain finish to the surface. The resin is usually injected under pressure between the two molds. But this method is not very suitable for realizing sandwich structures with collapsible foam cores due to high forming pressures and crushing of the foam cores.

In another method the mold is open that is only a concave mould is used. The plies are then covered with a breather cloth to soak up excess resin and then lined with a plastic film to maintain vacuum. Vacuum is applied and then the resin is left to flow under low pressure into the mold.

Finally layers of dry cloth are and polymer matrix in film form are stacked alternatively. Upon the application of heat the resin film plasticizes and flows in between the dry plies. The temperature for this process can exceed 90 - 100°C causing the problems typical to the use of thermoplastics as discussed above.

Once the components are manufactured they need to be joined together. This is usually done with the help of adhesives. Due to the present manufacturing tolerances for wind turbine blades the blades joints can be very thick hence certain silicon based fillers may need to be used for the adhesives (Dubouloz, 2009).

1.9 Full-scale testing of Wind Turbine Blades

Wind turbine blade testing is fairly recent, in 1996 the European Wind Turbine Testing Procedure Developments (EWTPD) was started to bring together the various European laboratories working in this sector (Zhou, et al., 2014). Wind turbine blade testing as specified by the IEC standards are governed by the ISO 2394. The ultimate load analysis is carried out within the guidelines of the section 7.6 of the IEC 61400-1 standards, with the use of appropriate safety factors. Upon referring to these standards it can be seen that the safety factors and hence the testing limits are based on the physical properties of the materials used hence proper specimen level testing is necessary. The wind turbine blades are validated before being shipped to the client, or during their development process through full scale testing. The full scale testing can be under static loads up to the failure of the blade, or just to verify the stiffness of the blades at the predicted load levels. Full scale tests are also done under fatigue loading where low cycle high amplitude fatigue loads are applied until the blade fails. Some classic fatigue test methods include and others where the degradation in stiffness and strength is monitored to predict the fatigue life without having to use a large number of blades during testing (Freebury & Musial, 2000).

The tested blades are instrumented whether they are loaded to their final failure or to a specified value without failure. The blades are instrumented with strain gauges to note any non-linearity in their behavior, which would signify damage taking place (Zhou, et al., 2014). Furthermore the blades are instrumented using acoustic emission sensors, to sense cracking, infrared imagery also for damage identification and digital image correlation to have multiple strain measurements on the blade surface.

(Jørgensen, et al., 2004). The blades are loaded at different predefined points to a specified level, either till their final failure or until a prescribed deflection.

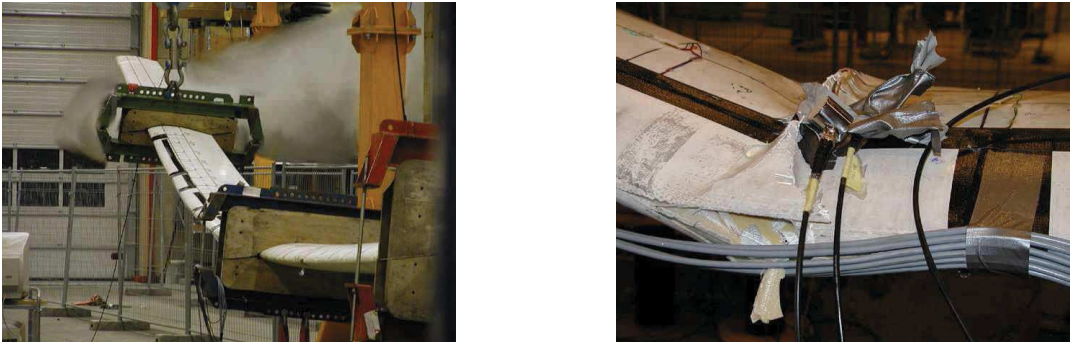


Figure 1-23: A VESTAS® 25m blade loaded till final failure

The Figure 1-23 shows an example of a VESTAS 25m long blade that was tested at the RISO laboratory in Denmark. The Figure 1-23 shows the use of strain gauges to monitor the health of the blade during the test and to ascertain the load at which the blade starts to get damaged and later fails.

1.10 Finite element modeling of Wind Turbine Blades

The wind turbine blades are complex structures in terms of their geometry and the materials used. They need to be modeled on the one hand as accurately and precisely as possible, while on the other hand the models should be light enough to be able to be run in a reasonable amount of time using reasonable computational resources. The finite element analysis is done for the validation of the structural design as well as the dynamic or modal response of the blades, as vibration at natural frequencies is an important part of blade design (Bechly & Clausen, 1997) (Hamdi, et al., 2014).

The finite element analysis of wind turbine blades can be done with varying degrees of complexity. The blade can be modeled as a beam with varying degree of complex or simple beam elements (Wang, et al., 2014) (Kim, et al., 2013)(Roth-Johnson, et al., 2014). Three dimensional shells can be used to simplify the problem field yet keeping the overall geometry of the blade. The shell elements as shown in Figure 1-24 are given material properties based on classical composite plate theory, to reduce the computational costs (Wang, et al., 2014) (Song, et al., 2011).

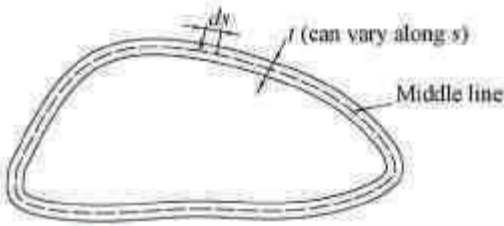


Figure 1-24: 3D Shell with classical composite plate theory definition.

Further more precise models are possible which include the thickness effects of the composite layups. But these models are usually for small portions of the blade instead of the complete structure owing to the complexity and computational costs. To this end some analytical 3D models have also been developed (Chazly, 1993).

The structural analysis of wind turbine blades although gives the overall behavior of the blade, but there is always a need to understand the limits at which the blade would fail (Wang, et al., 2014). And also to how it would fail. For this purpose, linear fracture mechanics are applied to detailed models at the sensitive zones, which include the bonded joints where the blades are assembled (Ji & Han, 2014) (Reinoso, et al., 2012).

As the wind turbines are constantly loaded with reversed loads they undergo fatigue loading at up to 4 million cycles per year. This puts a lot of emphasis on the fatigue life determination of the blades as well. Cumulative damage modeling has been used to model the life of these blades (Shokrieh & Rafiee, 2006). The application of cyclic loads may be based on measurements done in the field (Abouhnik & Albarbar, 2012).

The modeling in terms of structure is augmented with the aerodynamic analysis. Aero-elastic behavior with coupled fluid structure interactions is used to calculate the loads applied on the blade during their service (Gebhardt & Rocca, 2014) (Zhang, et al., 2014).

The finite element models of wind turbine blades, finally need to include all the structural properties and the boundary conditions applied as close as possible to the real cases. These parameters are applied in instantaneous state models or as probabilistic models, dealing with the load events taking place at some intervals of time (Lekou, 2013). The Figure 1-25 shows a typical result of a finite element model showing the blade tip deflections and the behavior of the blade under compression, against buckling.

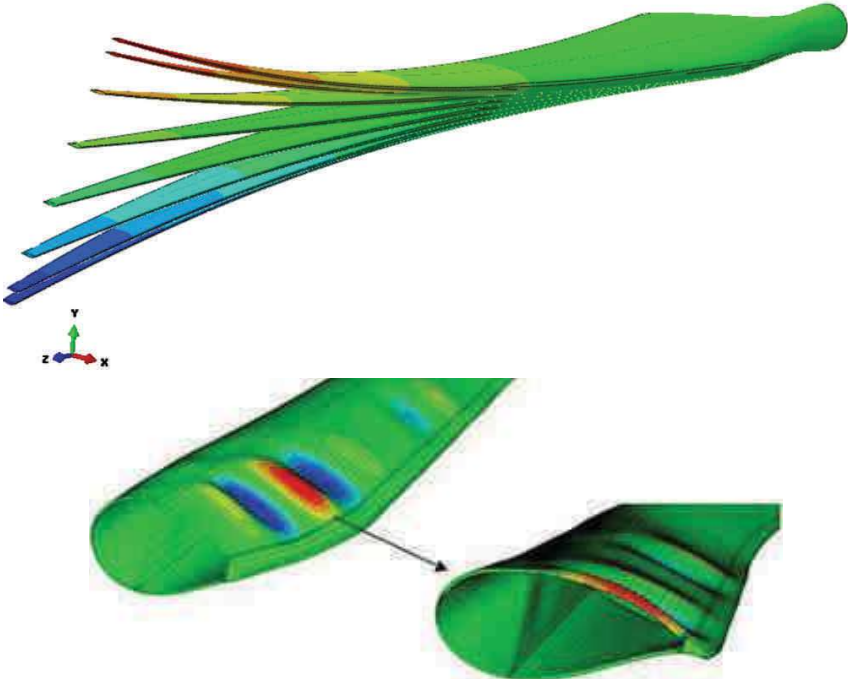


Figure 1-25: A wind turbine deformed under aerodynamic loads showing end deflections. Prediction of buckling strength based on these loads.

1.11 Discussion and Conclusions

The wind turbine blade is a complex piece of structural, material and aerodynamic engineering. The design process takes a lot of time for a new turbine blade. There is a need to choose and to focus on the best possible, time saving strategies to be put in place, which deal with the structural and aerodynamic aspects of the design. The best experimental and modeling strategies need to be identified to decrease the design cycle time while maintaining a required degree safety and accuracy in the designs. Furthermore there is a need to model the structure of these turbine blades as accurately as possible keeping in view the time consumed or computations. In the corresponding chapters all the design aspects mentioned in the current chapter would be treated and their efficiency would be gauged.

Chapter 2 --- Design methodology for Wind turbine Blades

Table of Contents

| | | |
|-------|---|----|
| 2.1 | Design Parameters..... | 38 |
| 2.1.1 | Swept area and Power generated | 38 |
| 2.1.2 | Coefficient of performance | 38 |
| 2.2 | Calculation of the shape of the wind turbine blade..... | 40 |
| 2.2.1 | Aerodynamic geometry of the wind turbine blade; Blade Element Momentum Theory | 40 |
| 2.2.2 | Optimum design of the blade..... | 43 |
| 2.3 | Power generated by the rotor | 45 |
| 2.4 | Convergence of the BEM calculation (HELICIEL)..... | 46 |
| 2.5 | Determination of the structure: | 47 |
| 2.6 | Normal Wind conditions..... | 52 |
| 2.7 | Extreme wind conditions..... | 52 |
| 2.8 | Determination of the blade cross section | 54 |
| 2.8.1 | Method of maximum stress..... | 54 |
| 2.8.2 | Method of maximum deflection..... | 55 |
| 2.9 | Finite element modeling of the blade..... | 58 |
| 2.10 | Materials used for the modeling..... | 58 |
| 2.11 | Modeling of the material..... | 59 |
| 2.12 | Determination of the initial layup | 61 |
| 2.13 | Convergence of Mesh | 63 |
| 2.14 | Modeling of the structural response of the blade using finite elements..... | 65 |
| 2.15 | Inertial loading due to blade's weight..... | 65 |
| 2.16 | Aerodynamic loading due to incident wind | 69 |
| 2.17 | Centrifugal load due to rotation of the blade..... | 70 |
| 2.18 | Behavior subject to global loading: Aerodynamic, gravitational and centrifugal..... | 70 |
| 2.19 | Modifications to the initial blade design..... | 80 |
| 2.20 | Conclusions and Discussion..... | 85 |

The design of wind turbine blades is based on a certain number of parameters. Some are calculated while others are a product of different hypothesis. The Table 2-1 shows the parameters of design as fixed by the environmental conditions while equally others chosen as the starting point of the design like the length of the blade and the power developed. The question of the choice of the airfoil profile for the blades is addressed by simplifying the design. The profile is taken as one with well known aerodynamic properties. For showing this design methodology a simple NACA 4424 profile is used. This section is chosen due to its higher thickness thus giving higher stiffness to the blade.

The aim of this study is to develop a series of calculations for the design of a wind turbine blade. Therefore we are going to define the design in terms of parameters that can be modified later for optimization.

| | |
|---|--|
| Length (m) | 50, of which 5 for the fixation and root |
| Maximum cord (mm) | 6000 |
| Fluid speed upstream of blade (m/s) | 25 |
| Extreme wind speeds for parked rotor (m/s) | 55 |
| Angular velocity (rpm) | 16 |
| Power (MW) | 5 |

Table 2-1: Design Criteria.

One of the other important factors of design is the number of blades per rotor. There are two most commonly used rotor configurations present in the world today. There are 2 and 3 blade rotors in service. The number of blades is chosen primarily on the dominant wind speeds and hence the tip speed ratios of the wind turbine blades. As a rule of thumb the faster the wind speed one needs lesser number of blades per rotor. The Figure 2-1 shows the general criteria of the choice of rotor configurations based on wind speed.

As can be seen in the Figure 2-1 that the 2 blade configuration is best suited to higher wind speeds as compared to a three rotor blade hence for our application we have chosen such a configuration.

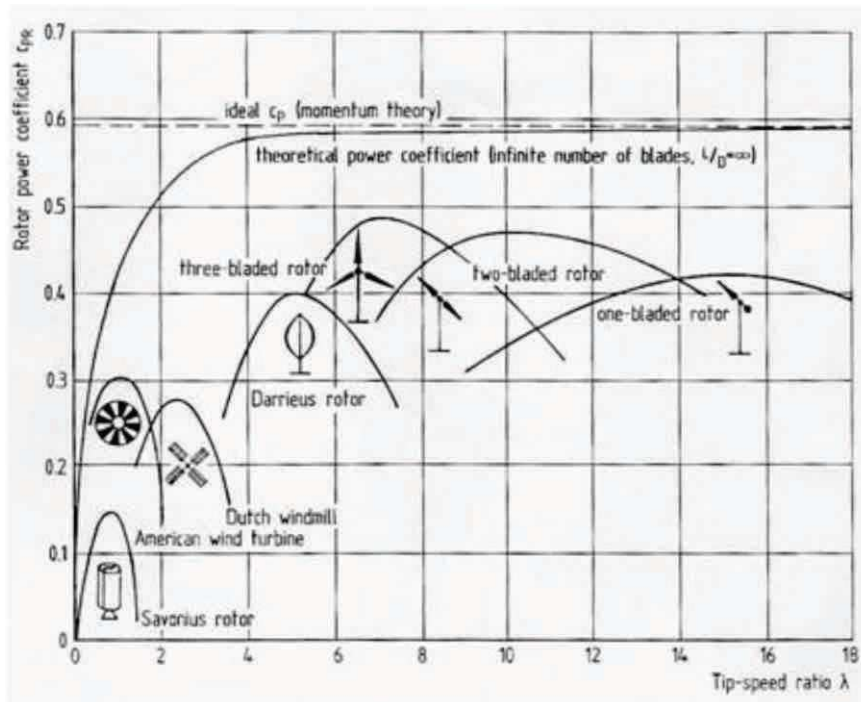


Figure 2-1: Choice of rotor based on tip speed ratios.

2.1 Design Parameters

2.1.1 Swept area and Power generated

The basic law for calculating the power generated by a rotor is given by:

$$P = \frac{1}{2} C_p \eta \rho \pi R_{blade}^2 V_o^3 \quad 2-1$$

where

“ P ” is the Power, “ C_p ” is the Coefficient of performance, “ η ” is the Energy conversion train efficiency, “ ρ ” is the Air density, “ R_{blade} ” is the Length of the blade and “ V_o ” is the Incident wind velocity.

2.1.2 Coefficient of performance

The coefficient of performance “ C_p ” is equivalent to the aerodynamic efficiency of the turbine. For a perfect turbine the maximum coefficient is given by the limit of Betz which is $C_p = 16/27$. This limit is set to have a minimum amount of wind at the exit of the turbine. The ratio of the wind speeds at the entry and exit of the turbine is given by the factor “ a ”.

$$a = \frac{V_o - V_s}{V_o} \quad 2-2$$

where “ V_s ” is the wind velocity at the exit and “ V_o ” is the velocity of the wind at the entry.

Therefore the ideal case where $C_p = 1$ is not possible as the exit velocity of the wind will drop down to zero hence there will be no flow of air through the turbine.

According to the limit of Betz the “ C_p ” is related to “ a ” by:

$$C_p = 4a(1 - a)^2 \quad 2-3$$

Therefore at $a = 0$ the $C_p = 0$ also.

Furthermore a rotor never practically achieves even the Betz limit. The rotational speeds required to get the limit of Betz up to this level are so high that the centrifugal forces involved will damage the blade. In most cases the large scale wind turbine blades turn from 11 – 16 rpm.

The equation 2-1 gives the amount of power available in the rotor disc area of the flowing wind. However the amount of energy available at the rated speed is very high ≈ 60 MW. Wind turbines are scaled according to their generator’s capacities to produce electricity. Hence only 5MW of power will be extracted from the available wind power. This is done so that the turbine produces the same amount of power from the cut-in speed, which is where it just starts to turn. For our design we have considered that the turbine will start producing its maximum output of 5MW at 12m/s wind speed.

| | |
|--|--------------|
| Vo max (m/s) | 25 |
| Power generated by the rotor (MW) | 5 |
| Efficiency “η” Wind turbine (%) | 85 |
| Typical “C_p” for commercial wind turbines (%) | 35 |
| Minimum wind velocity for 5 MW (m/s) | ≈ 15 |
| C_p required at $V_o = 25$ m/s (%) | 8 |

Table 2-2: Operating conditions of the wind turbine blade.

Using the same theory it can be seen that the C_p of the blade needs to be degraded to keep the power produced constant at 5MW as the wind speed increases. In the first part of the curve the C_p is kept constant to get the maximum possible power output, once the 5MW level is reached the C_p is degraded. This modification in the C_p is usually done with the help of blade pitch control or just by letting the excess power produced “drain off”.

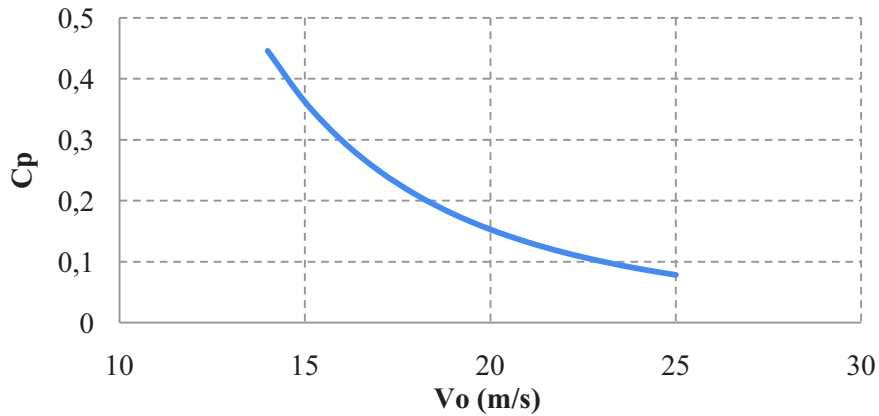


Figure 2-2: Evolution of coefficient of performance as a function of wind speed.

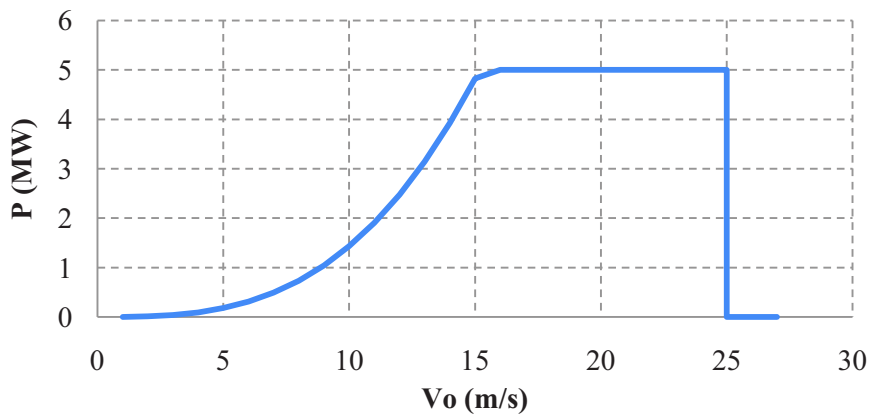


Figure 2-3 : Evolution of the power generated as a function of wind speed.

In the coming sections the wind turbine shall be designed according to 2 different wind speeds:

- A maximum wind speed where the turbine can work at 55m/s and
- Storm winds: here the blades are parked up to 70m/s.

2.2 Calculation of the shape of the wind turbine blade

2.2.1 Aerodynamic geometry of the wind turbine blade; Blade Element Momentum Theory

The aerodynamic loads applied on the blade are calculated by the BEM, whose principal equations are given as under (Abedi, 2013), (Chr., et al., 2005).

Consider an element of the blade, turning around an axis defined as the rotor rotational axis, under the wind load applied by the wind speed V_{rel} , Figure 2-4.

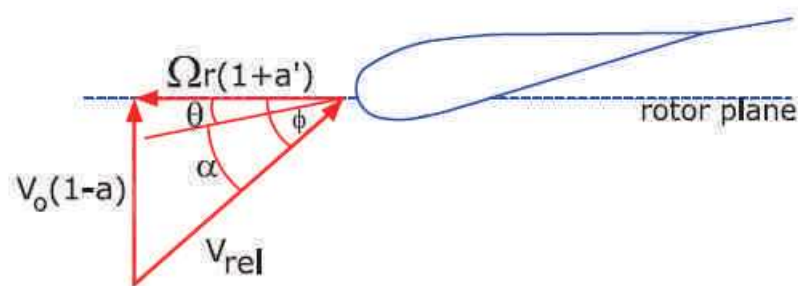


Figure 2-4: Principle of airflow around a blade section.

Here we present the different steps of the wind blade form determination.

Initialization of the calculation using the parameters “ a ” and “ a' ”: $a = a' = 0$.

Calculate “ φ ” by the 2-4 :

$$\tan\varphi = \frac{(1 - a)V_0}{(1 + a')\omega r} \quad 2-4$$

where “ φ ” is the angle of incidence of wind with the rotor plane, “ V_0 ” is the incident absolute wind in velocity in the free stream. “ ω ” is the rotational velocity of the rotor in rad/s and “ r ” is the radius of the blade section in consideration.

Calculate the local twist angle “ θ ” considering an angle of attack “ α ” as constant.

$$\alpha = \varphi - \theta \quad 2-5$$

The maximum coefficient of lift for a section at 14° varies between 1.2 and 1.4. The convention is to determine the design keeping in view a high enough coefficient of lift around at 80% that is to say 0.96 – 1.12. This consideration gives a $C_L = 1.08$ at $\alpha = 7^\circ$.

Next calculate the “ C_N ” and “ C_T ” being respectively the coefficients of normal and tangential forces to the plain of the rotor.

$$\begin{aligned} C_N &= C_L \cos\varphi + C_D \sin\varphi \\ C_T &= C_L \sin\varphi - C_D \cos\varphi \end{aligned} \quad 2-6$$

Calculate the “ a ” and “ a' ” with the equations 2-7 & 2-8:

$$a = \frac{1}{\frac{4 F \sin^2 \varphi}{\sigma C_n} + 1} \quad 2-7$$

and

$$a' = \frac{1}{\frac{4 F \sin \varphi \cos \varphi}{\sigma C_t} - 1} \quad 2-8$$

where

$$\sigma = \frac{Bc}{2\pi r} \quad 2-9$$

“ σ ” is the swept surface area of the blades, “ B ” is the number of blades per rotor, “ r ” is the position of the section considered.

If the value of “ a ” and “ a' ” changes above a certain given initial tolerance between calculation iterations the loop restarts at the first line. If not stop the loop and note the value of “ φ ”. We had chosen 0.0001 as the precision of the iteration steps.

Furthermore

$$F = \frac{2}{\pi} \cos^{-1}(\exp(-f)) \quad 2-10$$

and

$$f = \frac{B(R-r)}{2r \sin \varphi} \quad 2-11$$

Note here that “ F ” and “ f ” are the factors of Glauret and the Pradtl tip loss factor.

Calculate the loads applied to each of the blade elements using 2-12 - 2-15.

$$F_L = \frac{1}{2} \rho C_L c V_{rel}^2 \quad 2-12$$

$$F_D = \frac{1}{2} \rho C_D c V_{rel}^2 \quad 2-13$$

and

$$F_N = L \cos \varphi + D \sin \varphi \quad 2-14$$

$$F_T = L \sin \varphi - D \cos \varphi \quad 2-15$$

“ F_L ” and “ F_D ” are the Lift and drag force respectively, “ F_N ” and “ F_T ” are the forces normal and tangential to the rotor plane, “ c ” is finally the cord of the section at the blade element considered.

2.2.2 Optimum design of the blade

The optimum form of the blade is determined using the BEM method but considering maximum possible power generation according to the Betz limit.

| | |
|---|-----------|
| Airfoil type | NACA 4424 |
| Maximum thickness of the profile as a percentage of the cord (%) | 24 |
| Position of maximum thickness in cord percentage (%) | 30 |
| Angle of attack for maximum lift (deg) | 7 |
| Maximum Coefficient of lift | 1.08 |
| Coefficient of drag at angle of attack of 7° | 0.01 |

Table 2-3: Design parameters for the blade.

Therefore the cord is given by the equations 2-16 and 2-17.

$$\varphi = \tan^{-1}\left(\frac{2}{3\lambda_r}\right) \quad 2-16$$

$$c = \frac{8\pi r \sin \varphi}{3BC_l \lambda_r} \quad 2-17$$

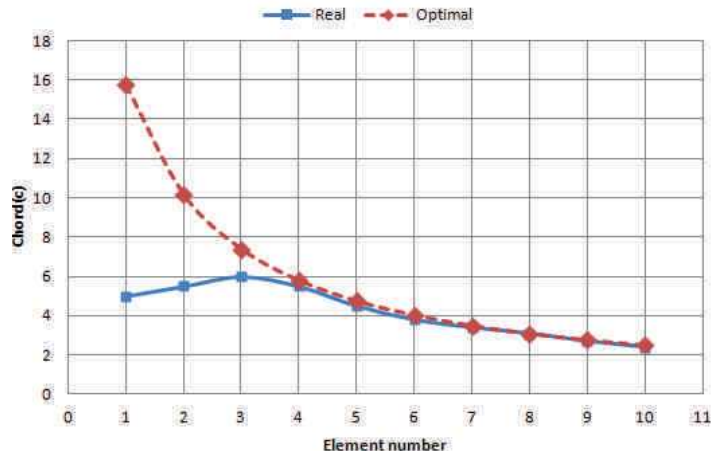


Figure 2-5: Distribution of real cord and optimal cord.

Since the optimal distribution of cord is not realizable hence a more realistic cord is chosen with the effect on power as shown in the Figure 2-6.

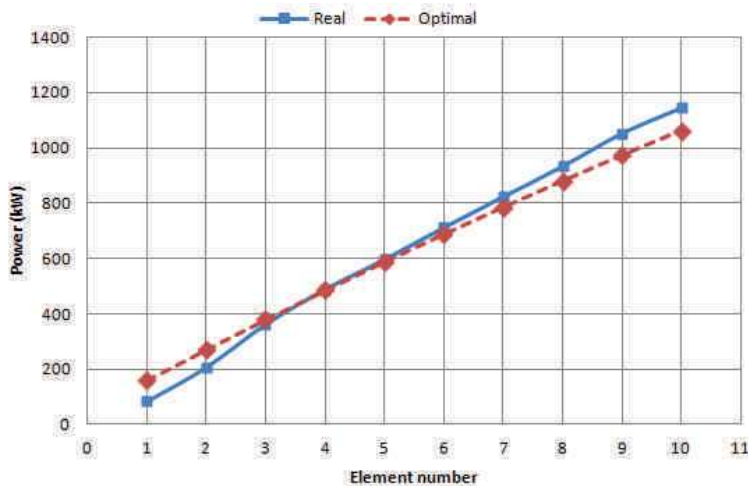


Figure 2-6: Distribution of power developed along the length of the blade.

The change of geometry causes the power generated to change as well.

| | Blade with optimal cord | Blade with real cord |
|--------------|-------------------------|----------------------|
| Power | 6.23 MW | 6.44MW |

Table 2-4: Total power generated by the real and optimal blade.

The power generated by the real blade is slightly higher, this is due to the formulation used for the power generation takes into account the power generated at all the elements, since the power generated at the root is very low the slight increase in the blade cord at the further end causes the total power to rise.

$$P_e = \omega \sigma \pi \rho V_0^2 \frac{((1-a)^2 C_l \sin \phi - C_d \cos \phi) \times r^2 dr}{\sin^2 \phi}$$

2-18

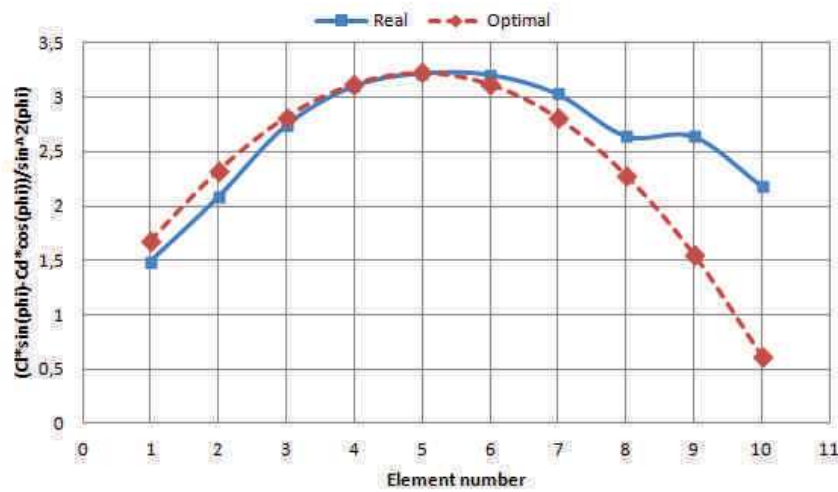


Figure 2-7: Effect of the twist on the power produced.

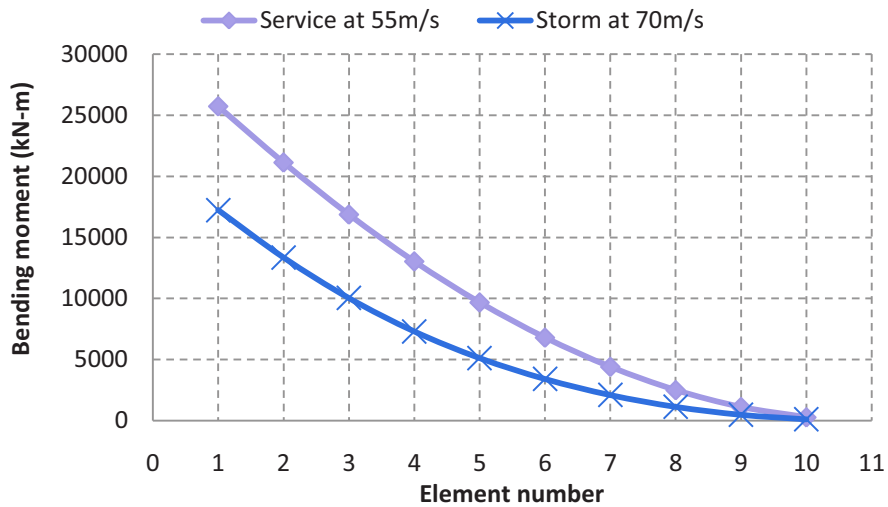


Figure 2-8: Distribution of bending moment along the blade length, 2 cases: 55m/s and 70m/s.

The bending moment for the blade in service at 55m/s is higher than that for stormy conditions at 70m/s.

2.3 Power generated by the rotor

Determine the total power of the turbine by integrating the value of the tangential force (HELICIEL, 2013) and (Ingram, Dec, 2005).

$$P_e = 4\pi r^3 \rho V_o \omega (1 - a) a' F dr$$

or

$$P_e = F_T \omega$$
2-19

“ P_e ” is the power generated by each of the elements, “ B ” is the number of blades, “ dr ” is the differential length of each element.

Here we show the power generated by the rotor as calculated by the code HELICIEL and BEM.

| $\frac{1}{2} C_p \rho \pi R^2 V_o$ | Heliciel | BEM |
|------------------------------------|--------------|--------------|
| $C_p = 0.08$ | $C_p = 0.08$ | $C_p = 0.08$ |
| 6.38 MW | 6.51 MW | 6.04 MW |

Table 2-5: Power produced by the rotor calculated with different methods.

It should be noted here that the power generated as per calculations is higher than the power required at 5MW. This is due to the fact we have for the moment ignored the mechanical inefficiencies.

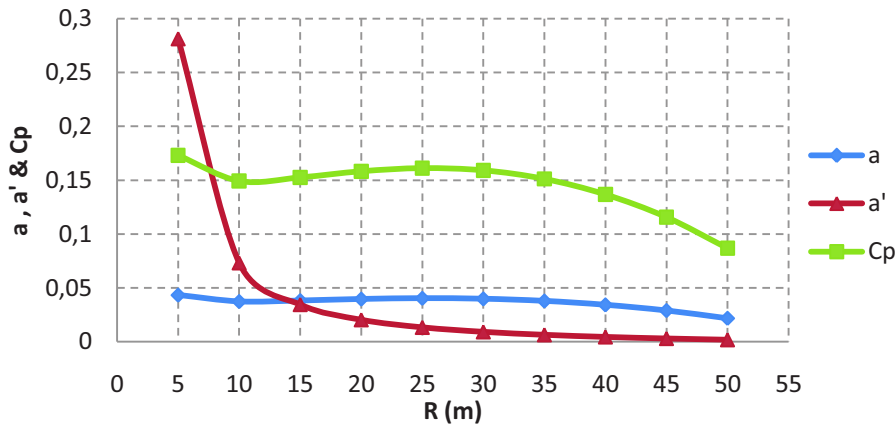
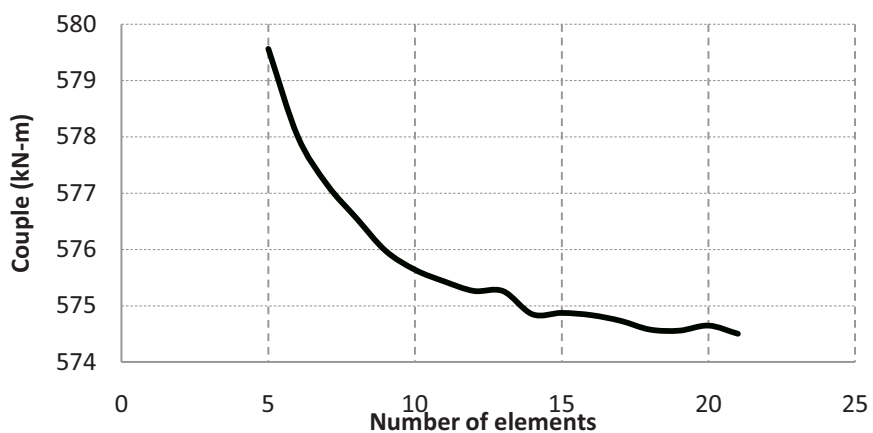


Figure 2-9: Distribution of induction factors along the length of the blade.

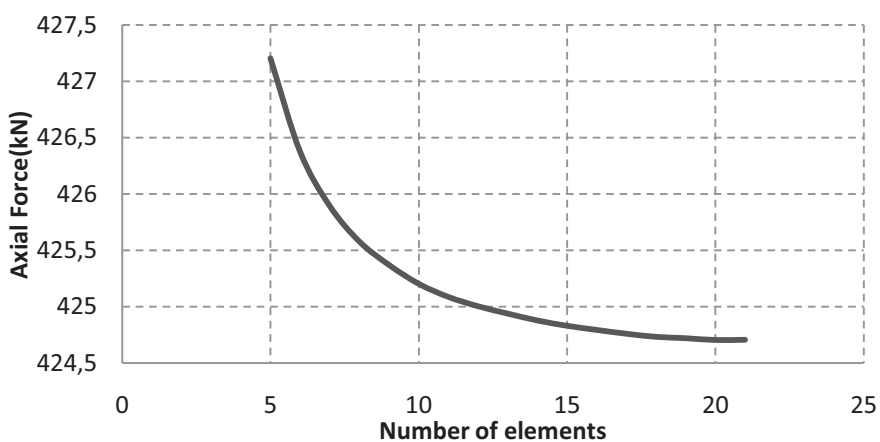
By the 2-3 we can find the “ a ” for a given “ C_p ”. In the ideal case where the $C_p = 0.59$; $a = 0.15$. On the other hand if we take, $C_p = 0.35$; which gives us $a = 0.15$. As explained the value of “ C_p ” is small hence “ a ” varies between 0.043 and 0.025.

2.4 Convergence of the BEM calculation (HELICIEL)

The BEM is a discretization method where the blade is partitioned into elements. Therefore it is important to verify the sensibility of the number and size of elements on the final results. On the other hand if the element size suitable for convergence is too small we can always use a larger element size to save on computational power provided the difference in the results is not very large. We have considered the aerodynamic load as the parameter for convergence, Figure 2-10.



(a). Evolution of couple



(b). Evolution of axial force

Figure 2-10: Convergence of BEM based on torque and axial force.

It can be seen that the BEM converges above 20 blade elements. However the difference between 10 and 20 elements should be noted in order to verify which amount of blade elements is easier to model and also to verify if a lesser number of blades would affect harshly the final results. In fact the difference in the values of the parameters considered for the two is between 0.11% and 0.17%. Therefore for the sake of simplicity we will continue to use 10 blade elements.

2.5 Determination of the structure:

There are different blade cross sections in use presently. There are designs which include just an outer shell while others consider an internal stiffener we shall call from this point onwards as the spar. There are different types of spar. The blade sections are listed in the Figure 2-11.

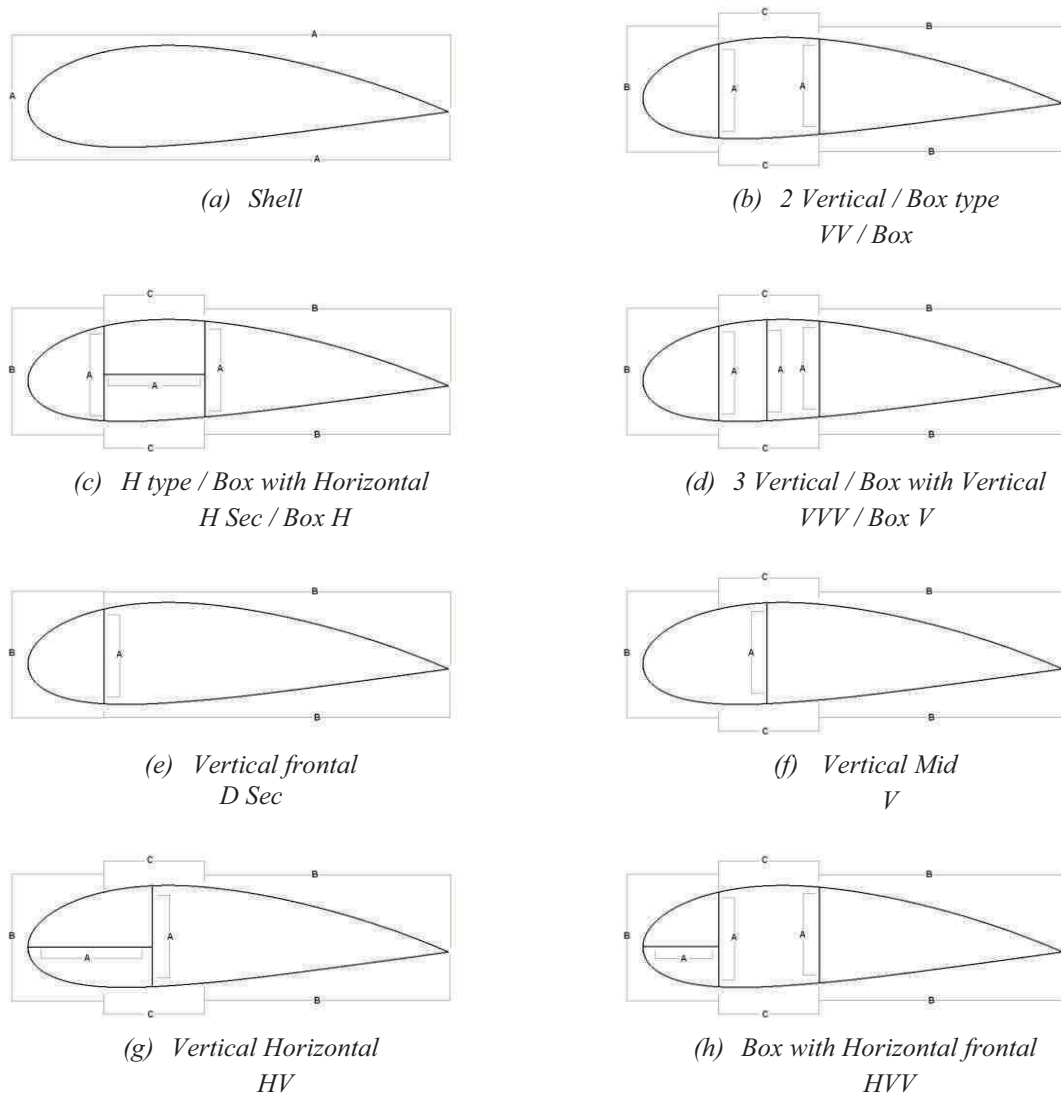
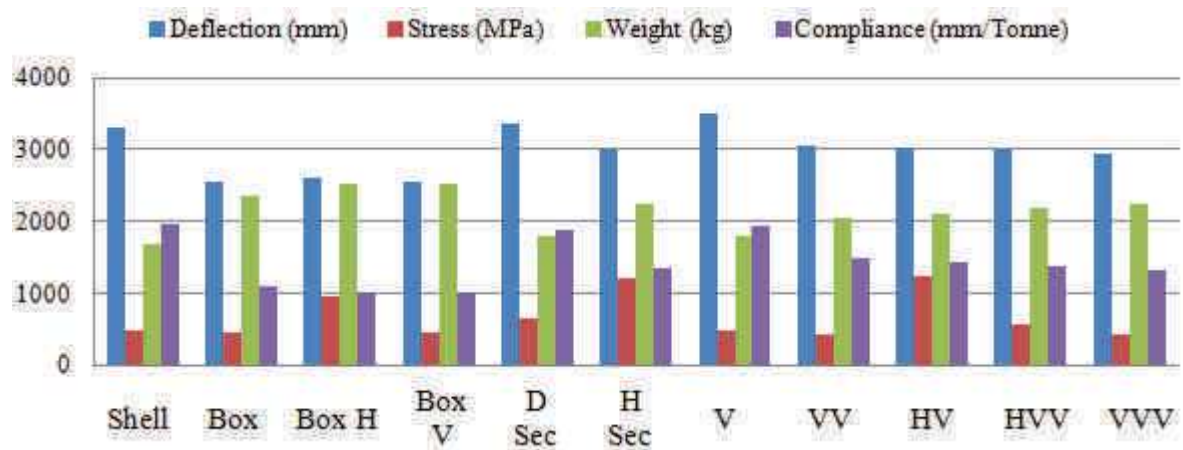


Figure 2-11: Different blade cross sections considered in the study.

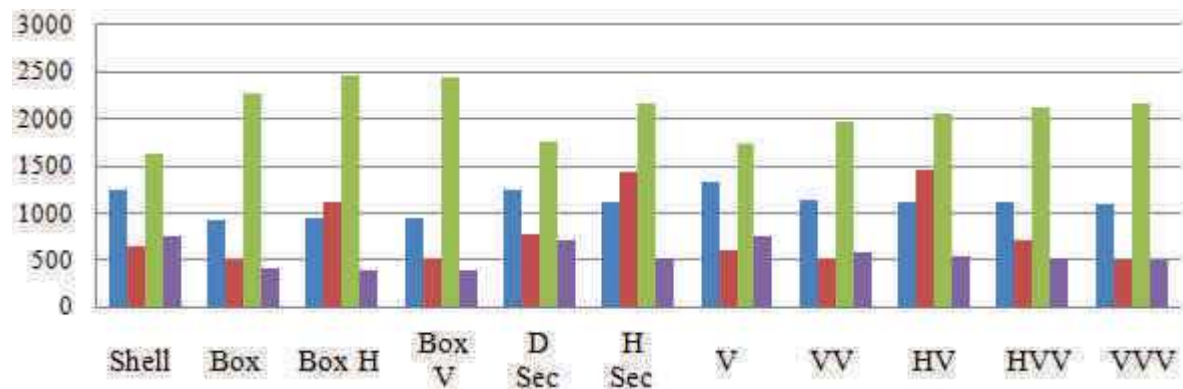
The sections chosen have 8 geometric configurations with another 3 combinations depending on the layups. The sections having the word “Box” in their nomenclature signify that the blade surface-shear-web spar interface is reinforced with extra layups.

Furthermore as part of an initial investigation the blades cross sections were modeled in ABAQUS FE software as prismatic cantilever beams with their proper layups and loaded with a uniform flap wise pressure load of 0.5 kPa. Furthermore since the specific width of each section is different hence the sectional weight was also considered in these simulations. To correlate the different types of materials used in the composite lade industry properties of Fiberglass/Epoxy, Carbon fiber/Epoxy and Kevlar/Epoxy composites were taken from the literature and applied to the simulations to ascertain which section and material showed the best performance.

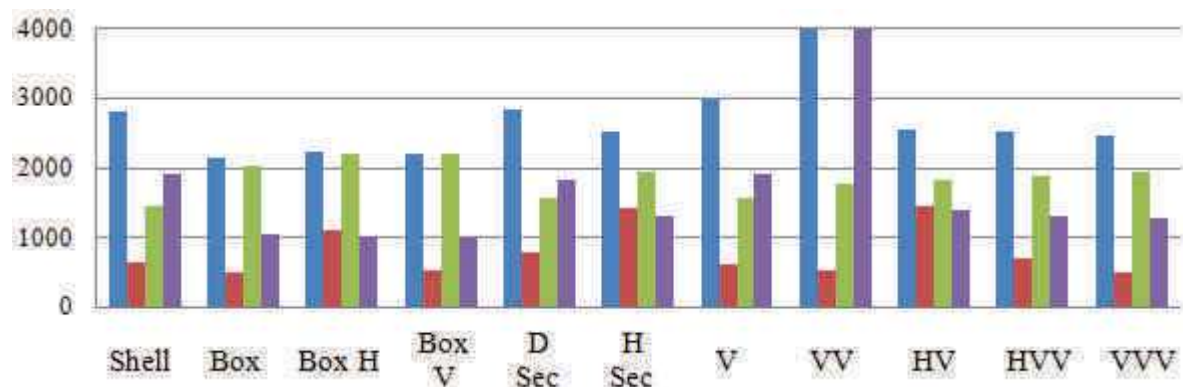
The performance of the different sections is thus illustrated in terms of their deflection at the free end, maximum stress induced, weight and compliance. The results are illustrated in Figure 2-12.



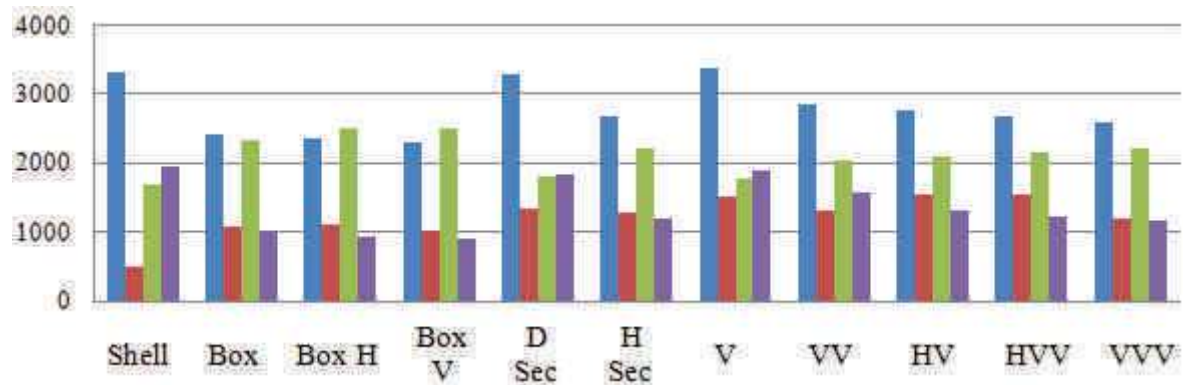
(a) Fiberglass/Epoxy S2 unidirectional vacuum infusion



(b) T300/5208 Carbon/Epoxy unidirectional prepreg



(c) Kevlar/Epoxy



(d) Fiberglass/Epoxy shell with Carbon/Epoxy spar

Figure 2-12: Different blade cross section and material configuration structural performance.

To summarize and compare the structural performance of these cross sections we shall compare the deflections at the free end, which is one of the defining parameters of any blade design.

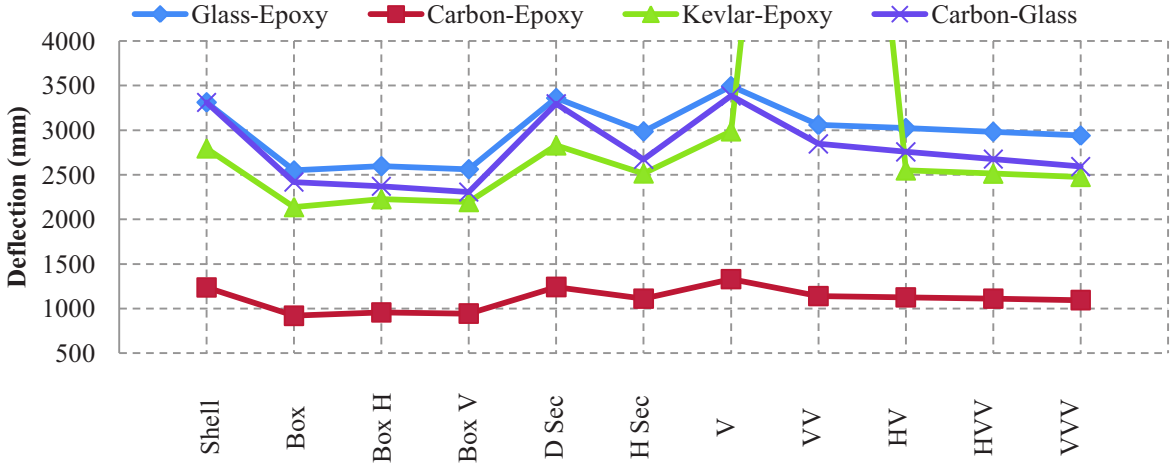


Figure 2-13: Summary of deflections of different section types of different materials in use.

The above investigation helps to determine which sort of section would be the best choice for the blade structure. We have inferred that using a box type spar in the blade as the stiffener is the best option. While carbon fiber has obvious advantages in terms of structural rigidity its use is limited due to its cost and manufacturing complexities. The study that proceeds from this point onwards will focus on the use of fiberglass/epoxy and a final note on the use of carbon fiber just as the shear-web spar is also discussed.

The following step in the design process is the determination of the bending moments produced under the effect of the wind.

For this calculation consider the blade to be a cantilever beam with its root fixed to a rigid frame. The load at of the elements can be calculated by using the equation of lift force as given before. By assuming that the effect of drag is negligible $\pm 10\%$ of the total force, the direction of application of the load is normal to the blade cord. The total load is given by:

$$F_e = \sqrt{F_L^2 + F_D^2} \tag{2-20}$$

where “ F_e ” is the magnitude of the aerodynamic load, “ F_L ”, “ F_D ” are the lift and drag forces for the section of the blade.

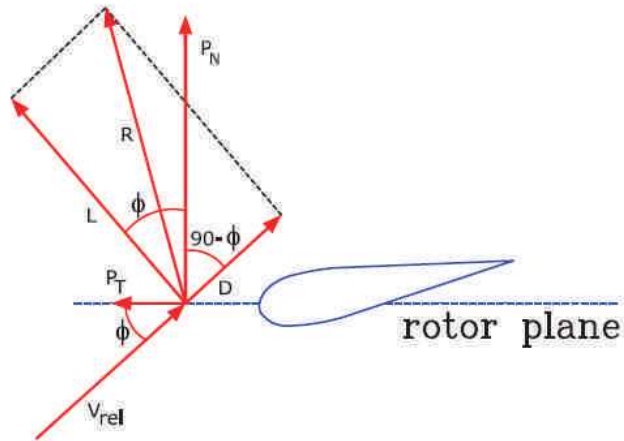


Figure 2-14: Aerodynamic loads as experienced by the blade cross section.

The cross section of the blade is given by the Figure 2-15.

“c” is the cord of the section, “t” is the thickness of the material for the blade.

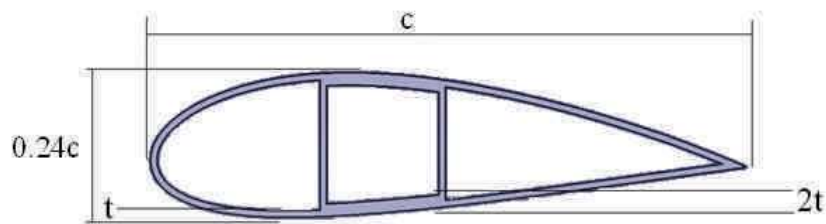


Figure 2-15: Material distribution being put in place by the present design methodology.

Since the simplified section does not consider the effect of sandwich structures the thickness of the blade surface and the spar is considered to be constant and uniform.

Once again the load calculated by the BEM will be applied to each of the elements uniformly. The blade element size here is considered to be 5m for 10 elements.

The total load per element is thus given by the 2-21.

$$F_{es} = F_e \times l \quad 2-21$$

“ F_e ” is the magnitude of load for each of the elements, “ F_{es} ” is the total load applied to the element and “ l ” is the length of the element.

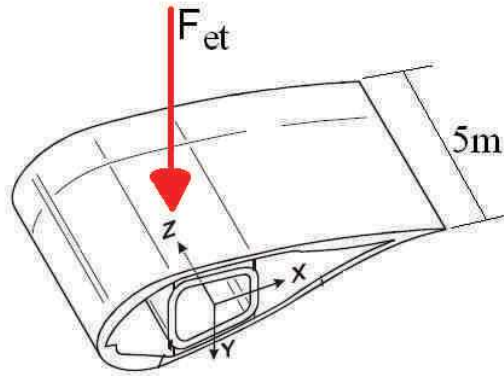


Figure 2-16: Position and orientation of the equivalent load applied on a blade element.

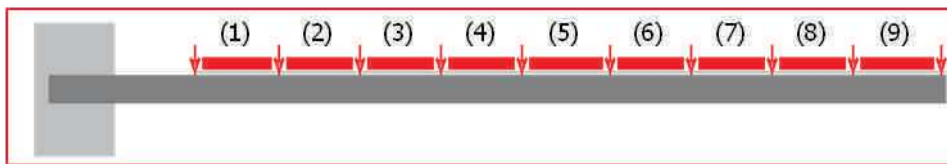


Figure 2-17: Modeling of the blade as a cantilever beam.

The different conditions of wind are given in the standards and will be explained here briefly. Again for simplicity the names and acronyms used are as-is in the standards.

We distinguish between two different states of wind: the normal and extreme wind states. The normal state gives the wind distribution and turbulence as normal. The extreme conditions are those of storms, gusts, high turbulence and highly variable wind speeds.

2.6 Normal Wind conditions

NWP: The normal wind profile defines a vertical gradient of wind up to the atmospheric boundary layer. Furthermore the wind velocity increases with an increase in height.

NTM: the normal turbulence model predicts a temporal variation in the wind speed pour taking into account their fluctuations.

2.7 Extreme wind conditions

EWM: The extreme wind model models an extreme wind condition as that of a storm.

EOG: Extreme operating gust defines a short term increase in wind as that in case of a gust and then return of wind speed to normal.

EDC: The extreme direction change is the case where the wind speed changes suddenly and then remains at the new directions.

ECG: In the extreme coherent gust case the wind speed rises sharply and stabilizes at this new speed.

ECD: The extreme coherent gust with direction change is a combination of sudden rise in wind speed and change in wind direction.

EWS: The extreme wind shear can be vertical or horizontal. These wind shears produce a sharp gradient along the radius of the rotor.

For the extreme wind model (EWM), the extreme operating gusts (EOG) and the extreme change in direction (EDC), we define two cases. One with a recurrence of one year (EWM1, EOG1, EDC1,) and the other more severe with a recurrence of 50 years (EWM50, EOG50, EDC50).

The case 6.1 of the standard IEC 61400-1 predicts a situation where the turbine would stop at an extreme wind case recurring every 50 years. Two situations are defined for this case: the first when the blade is vertical towards the top, the other where the blade is horizontal and the blade is subjected to a combined load of wind lift and its own weight.

In service the loads applied and the bending moments can be evaluated. However for the extreme wind conditions the rotor is modeled as a flat plate with the entire wind load being applied as a drag force on this plate. The force is calculated in 2-22.

$$F_{et} = \frac{1.17}{2} \rho A_e V_0^2 \quad 2-22$$

where “ F_{et} ” is the Force applied on the blade element under the action of the wind at velocity V_0 , “ A_e ” is the Surface area of the element; “ ρ ” is the density of air.

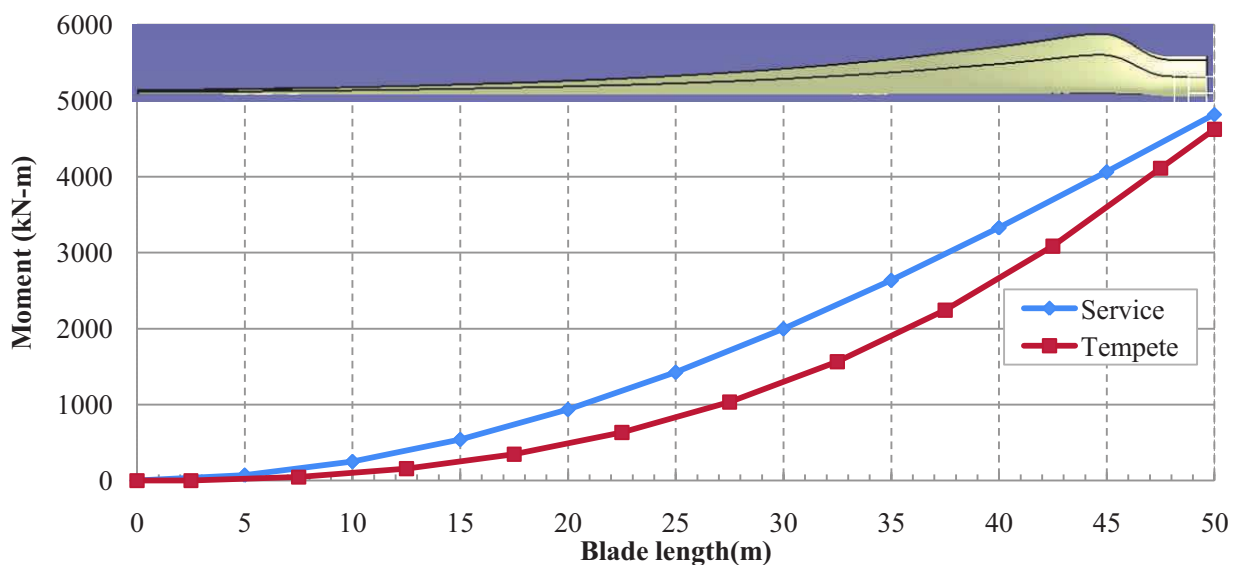


Figure 2-18: Distribution of bending moment along the length of the blade.

Once the bending moment is calculated, we can pass on to the second part of this calculation which is the determination of the geometry of the blade element cross section necessary to resist the aerodynamic loads thus applied.

Here the wind speed is considered to be 55 m/s in service and 70m/s in the storm case at which point the rotor is stopped and acts as a static flat plate, Figure 2-18.

2.8 Determination of the blade cross section

2.8.1 Method of maximum stress

In this method of basing the design on maximum permissible stress we use the equations dealing with the stress calculations on cantilever beams. Here since the materials used is a composite we shall use their homogenized properties for this phase of the design.

$$I_o = \frac{M_e 0.12 a_o}{\sigma_o} \quad 2-23$$

Where “ I_o ” is the moment of inertia of the section about the neutral axis of the section, “ M_e ” is the bending moment applied to the blade element and “ σ_o ” is the maximum admissible stress.

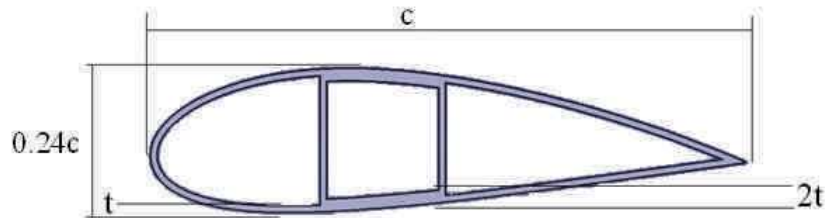


Figure 2-19: Definition of the section as a primitive

In general for a cross section the moment of inertia is given by:

$$I_o = constant \times [(width \times height^3)_{external} - (width \times height^3)_{internal}] \quad 2-24$$

Also the external width and the ratio of width/height are known. For the profile chosen as NACA 4424 an approximate analytical equation for calculating the moment of inertia is given by:

$$I_o = 0.058631 \times [(C \times 0.24C^3) - (C - 2t_m)((0.24C - 2t_m)^3)] \quad 2-25$$

Note here that this equation 2-25 is applicable only for a small change in the material thickness and where the wall thickness is relatively thin. The Figure 2-20 shows the variation of this equation 2-25 with respect to the “ I_o ” calculated by the discretized area method.

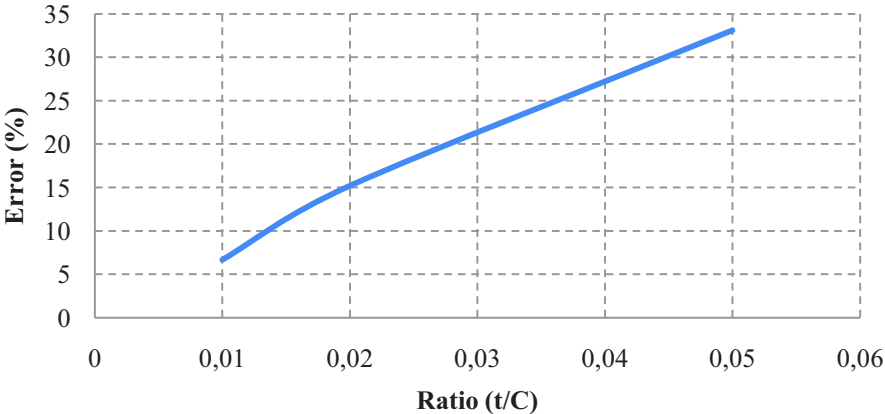


Figure 2-20: Comparison of the I_o calculated with the help of 2-25 and CATIA V5

where the ratio of “ t_m/C ” is the ratio between the thickness of the section and the cord of the profile. For our calculation the value of this ratio rests between 0.003 and 0.025 therefore the maximum error predicted would be $\approx 15\%$.

2.8.2 Method of maximum deflection

The method of maximum admissible stress does not check the deflection at the blade tip. Consider the blade modeled as a cantilever beam subjected varying distributed loads, Figure 2-21. The regions in red indicate distributed loads. Other boundary conditions include the fixed support at the blade root.

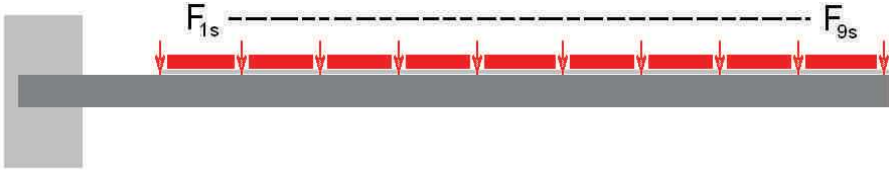


Figure 2-21: Modeling of the blade and the loads associated with it.

By convention the equation of bending moment for each of the elements (e) of this beam is given by:

$$M_e = \sum_{j=1}^e F_{js} (e + 0.5) \times l^2 \tag{2-26}$$

After applying the boundary conditions the deflection at the blade tip is:

$$y_{\max} = \frac{M_e}{3EI_o} \quad 2-27$$

where “ I_o ” is a function of “ y_{\max} ”:

$$I_o = \frac{M_e}{3Ey_{\max}} \quad 2-28$$

This equation of the bending moment is valid only for the last section of a blade discretized in 10 elements only. In effect, for each of the sections subjected to a unique loading, it is necessary to create an equation of bending moments and calculate the local deflections with the local boundary conditions considered for each of the sections separately. In general the train of calculations for this model takes the form below.

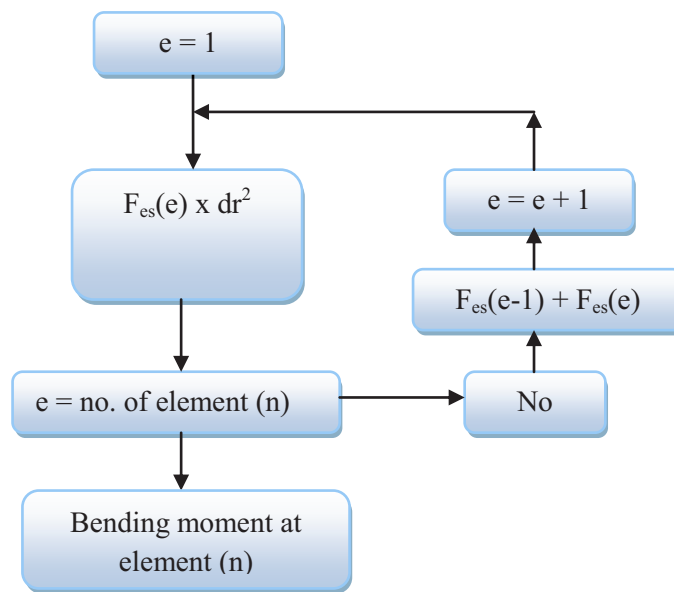


Figure 2-22 : Flow chart of the Blade Model.

$$y_{\text{Section } n} = \frac{1}{EI} \iint \text{Bending moment at the element "n"} \quad 2-29$$

After the double integration of the 2-29 of the bending moment, the constants of integration are found by the boundary conditions at each of the local elements.

By fixing the deflection for each of the elements the moment of inertia “ I_o ” for each of the sections can be evaluated.

The second parameter of interest is the rigidity in flexion of the cross section which is given by “EI” in the 2-29. The calculation of this rigidity for a beam is defined by the theory of composite plates. The equations of interest are given under 2-30 - 2-35.

Consider a ply oriented at an angle “ θ ” with respect to the global coordinate system. The relationship between the stress and strain vectors is given by:

$$\sigma = \bar{D}\varepsilon \quad 2-30$$

with

$$\sigma = \begin{Bmatrix} \sigma_1 \\ \sigma_2 \\ \tau_{12} \end{Bmatrix} \& \varepsilon = \begin{Bmatrix} \varepsilon_1 \\ \varepsilon_2 \\ 1/2 \varepsilon_{12} = \gamma_{12} \end{Bmatrix} \quad 2-31$$

where

$$\bar{D} = \bar{S}^{-1} \quad 2-32$$

$$\bar{S} = RT^{-1}R^{-1}ST \quad 2-33$$

$$S = \begin{bmatrix} 1/E_1 & -\nu_{21}/E_2 & 0 \\ -\nu_{12}/E_1 & 1/E_2 & 0 \\ 0 & 0 & 1/G_{12} \end{bmatrix} \quad 2-34$$

$$R = \begin{bmatrix} 1 & 0 & 0 \\ 0 & 1 & 0 \\ 0 & 0 & 2 \end{bmatrix} \& T = \begin{bmatrix} \cos^2\theta & \sin^2\theta & 2\cos\theta\sin\theta \\ \sin^2\theta & \cos^2\theta & -2\cos\theta\sin\theta \\ -\cos\theta\sin\theta & \cos\theta\sin\theta & \cos^2\theta - \sin^2\theta \end{bmatrix} \quad 2-35$$

Note here that the matrix “D” gives the rigidity of the ply and the element 1x1 of the matrix D this rigidity in the “x” direction (along the length of the blade).

For a composite material constituted of “N” no of plies with different orientations, the matrix of rigidity in flexion is given by:

$$C = \frac{1}{3} \sum_{K=1}^N \bar{D} (z_{k+1}^3 - z_k^3) \quad 2-36$$

For the definition of the terms used in the matrix C refer to Figure 2-23.

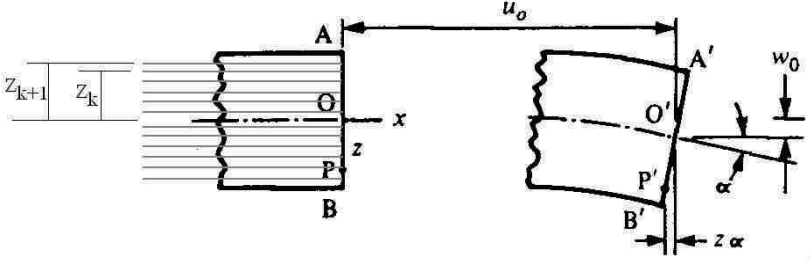


Figure 2-23: Composite plate under flexural loading

The element 1x1 of the matrix “C” gives the rigidity in bending of the beam in the x direction which corresponds to the flexion by the bending moment (Roylance, 2000).

2.9 Finite element modeling of the blade

After putting in place the schematic of the work with respect to the determination of the cross sections with BEM, we move on to the modeling of the blade’s structure in ABAQUS Finite element modeling software. The Figure 2-24 gives the flowchart for the modeling process.

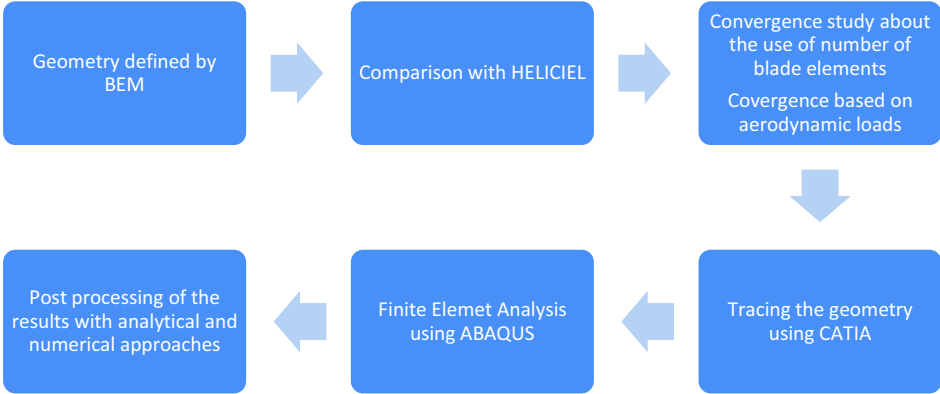


Figure 2-24: Chain of calculations for the design of blade.

2.10 Materials used for the modeling

The materials chosen for the modeling of the blade are the composite materials with glass fiber reinforcements using an epoxy resin. The material properties are given in the Table 2-6.

| Properties | Value |
|-------------------------------------|--------------|
| Physical properties | |
| Fiber Volume (%) | 57 – 63 |
| Density (kg/m ³) | 1960 – 2020 |
| Elastic constants | |
| Elastic Modulus, Longitudinal (GPa) | 53 – 59 |
| Elastic Modulus, Transverse (GPa) | 16 – 20 |
| Shearing Modulus (GPa) | 6 – 9 |
| Coefficient of Poisson | 0.26 – 0.28 |
| Strength properties | |
| Tensile Longitudinal (MPa) | 1540 – 2000 |
| Compression Longitudinal (MPa) | 690 – 1240 |
| Tensile Transverse (MPa) | 41 – 82 |
| Compression Transverse (MPa) | 110 – 200 |
| Shearing in-plane (MPa) | 62 – 165 |
| Shearing Inter-Laminar (MPa) | 55 – 103 |
| Flexural Longitudinal (MPa) | 1240 – 1720 |
| Crushing Longitudinal (MPa) | 464 – 552 |
| Strain at failure | |
| Tensile Longitudinal (%) | 2.7 – 3.5 |
| Compression Longitudinal (%) | 1.1 – 1.8 |
| Tensile Transverse (%) | 0.25 – 0.50 |
| Compression Transverse (%) | 1.1 – 2 |
| Shearing in-plane (%) | 1.6 – 2.5 |

Table 2-6: Material properties for the modeling. (Advanced Materials, 2011).

2.11 Modeling of the material

The modeling of the material in ABAQUS comprises of two parts. The first is the mechanical properties of the materials in question which include the strength for the prediction of damage. The

damage model used for composites by default in ABAQUS is the Hashin's Damage Model. This model is defined in equations 2-32 - 2-35.

The second important parameter is the ply layup, their order and their angles of orientation. In the Figure 2-27 a comparison of the effects of ply thicknesses is shown. The Figure 2-25 - Figure 2-27, show the details of the finite element model used for the ply thickness sensibility. The model used is that of a cylindrical cantilever beam. The beam is a 3D shell with no thickness. A quadrilateral shell element is used to mesh the beam model. The Figure 2-25 shows the applied boundary conditions. The beam is fixed at one end to act as a cantilever and at the other end a point force in the vertical direction is applied to produce bending.

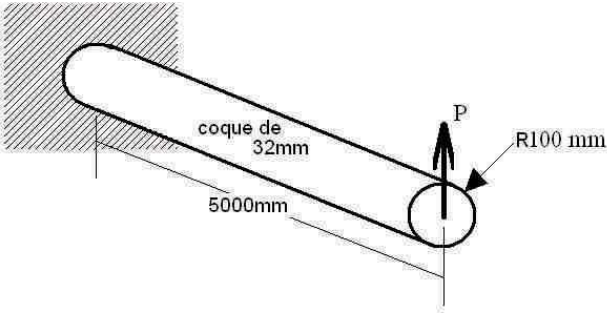


Figure 2-25: A simple composite tube loaded as a cantilever beam.

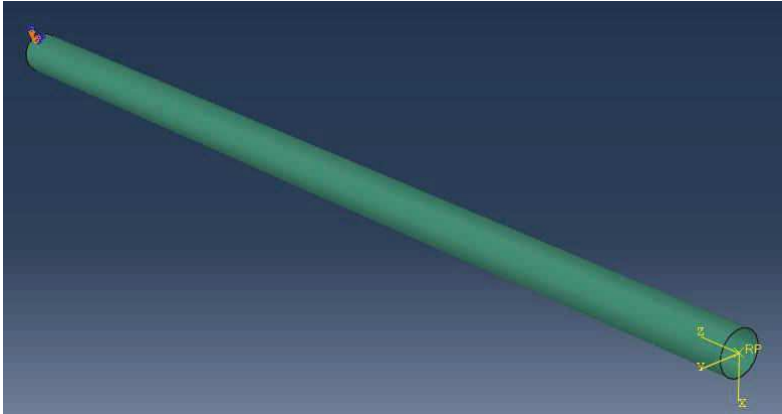


Figure 2-26: Problem as modeled in ABAQUS.

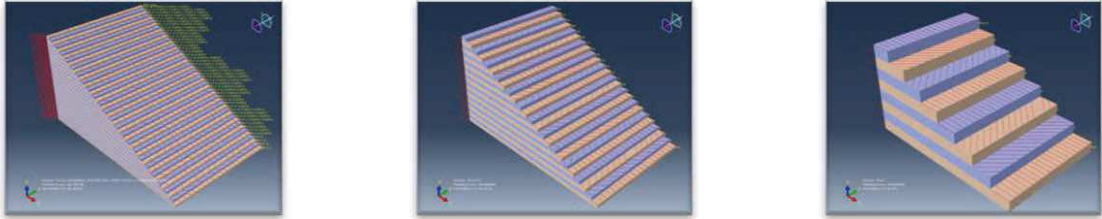


Figure 2-27: Layup models in ABAQUS, thickness of 0.1 to 2mm.

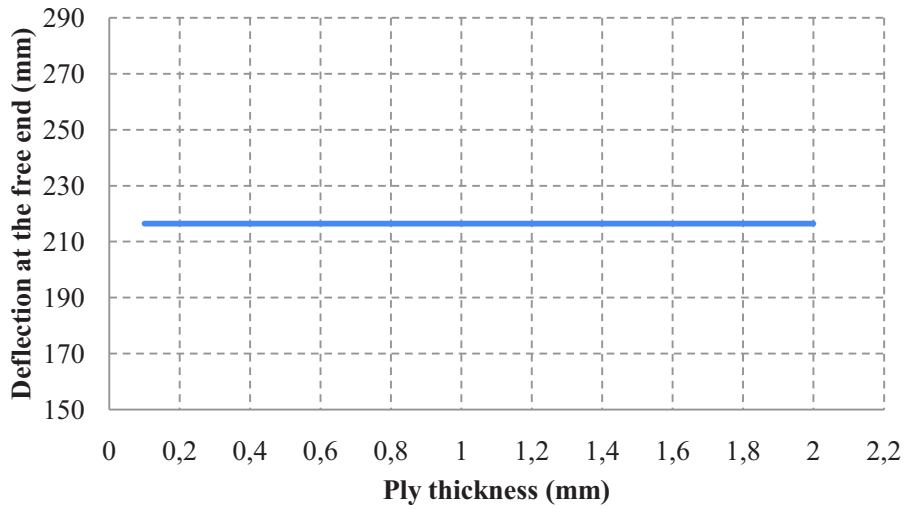


Figure 2-28: Free end deflection of the beam.

Let's consider a ply of 2mm to 0,1mm of thickness which has been used for modeling the cylindrical beam with a total thickness of 32mm and a layup of the type $[0/\pm 45/0]_n$. one can see in the Figure 2-27 that there is no effect of the tip deflection.

2.12 Determination of the initial layup

For the determination of the initial layup it is necessary to define some parameters as constants which would command the properties of the cross section. In the first step we have selected the maximum admissible stress under flexion as this parameter. The flexion is calculated by the bending moment as given in the 2-25. Then from the 2-15, we can find the value of " I_o ". For this first step we chose a value of 200MPa as the admissible stress level. This value has been derived using the damage criteria of "Yamada Sun". this criteria is usually used for unidirectional stress cases but where there is a lot of flexural stresses and the vertical shearing stresses are lower in comparison this criteria can be used.

$$\frac{\sigma_1^2}{X^2} + \frac{\tau_1^2}{S^2} < 1 \quad 2-37$$

By the criteria of Yamada Sun, we can fine the admissible values of shearing " τ " which is around 61 MPa. For a starting point this value of shearing stress is sufficient. By the 2-15, the moment of inertia " I_o " and hence the thickness of the material for each of the sections is summarized in the Table 2-7.

| r (m) | Thickness of the skin (mm) | Thickness of the sandwich core (mm) | Total thickness of the sandwich core (mm) |
|-------|----------------------------|-------------------------------------|---|
| 5-10 | 5 | 10 | 20 |
| 10-15 | 5 | 10 | 20 |
| 15-20 | 4.5 | 9 | 18 |
| 20-25 | 4.5 | 9 | 18 |
| 25-30 | 4 | 8 | 16 |
| 30-35 | 3.5 | 7 | 14 |
| 35-40 | 3 | 6 | 12 |
| 40-45 | 2 | 4 | 8 |
| 45-50 | 1 | 2 | 4 |

Table 2-7: Thicknesses of the blade elements.

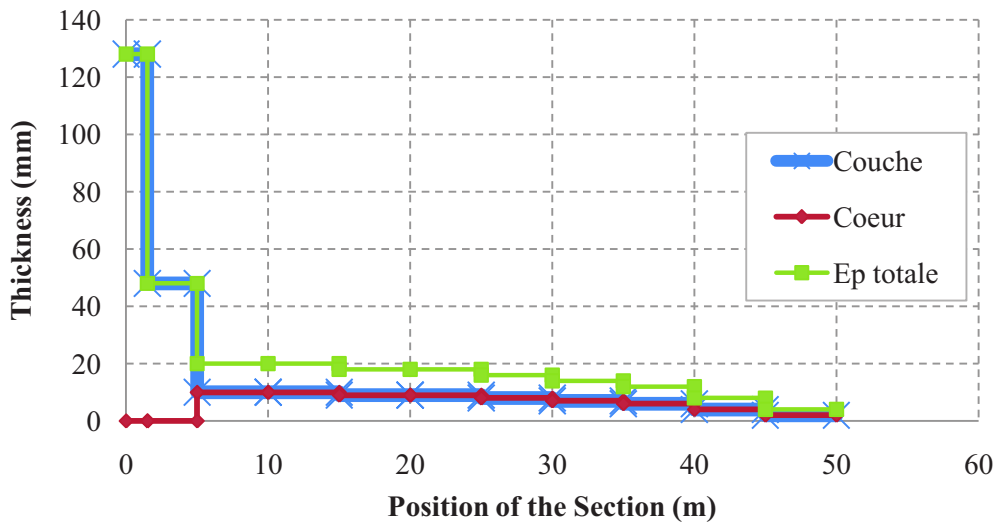


Figure 2-29: Distribution of the thickness.

It should be noted that the sections are designed to resist only the aerodynamic loads and not that of centrifugal and inertia due to the weight of the blade. The general layup plan is shown in the Figure 2-29. For details on layups see the Annex A.

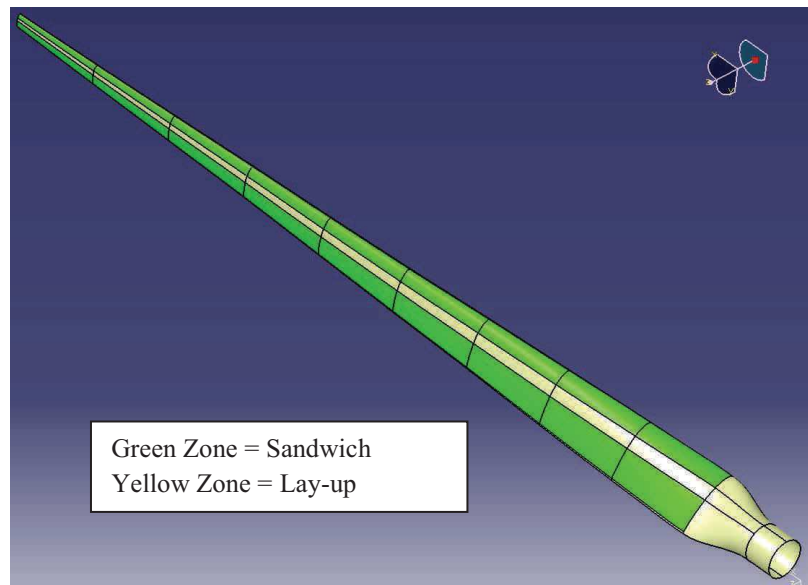
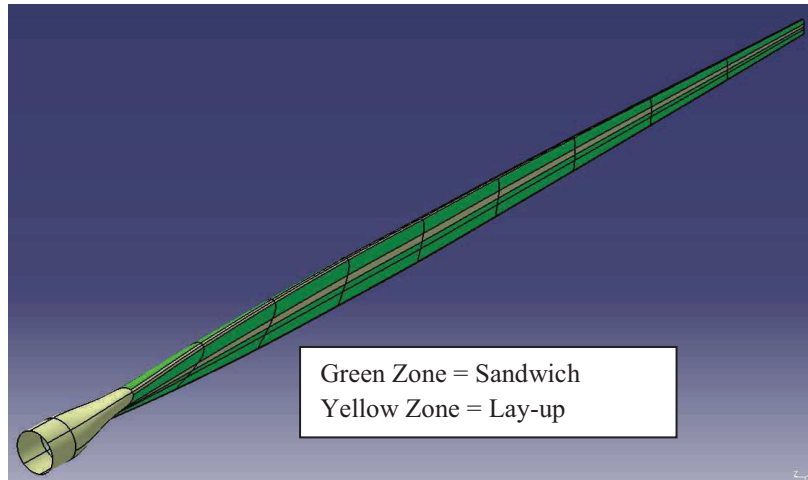


Figure 2-30: Zones of the blade partition.

2.13 Convergence of Mesh

To study the mesh convergence, we are going to base the study on the maximum deflection at the blade tip. A uniform pressure distribution of 1kPa is applied to the blade while it is fixed at the root, Figure 2-31.

The plot of the reaction force at the blade root against the mesh size shows a mesh size of 250mm and finer the size starts to converge, Figure 2-29 and Figure 2-30. This mesh size corresponds to a mesh to structure size ratio of " l_e/l_s " of 0.005. This value or smaller will be used for further studies in order to avoid mesh convergence studies for each case.

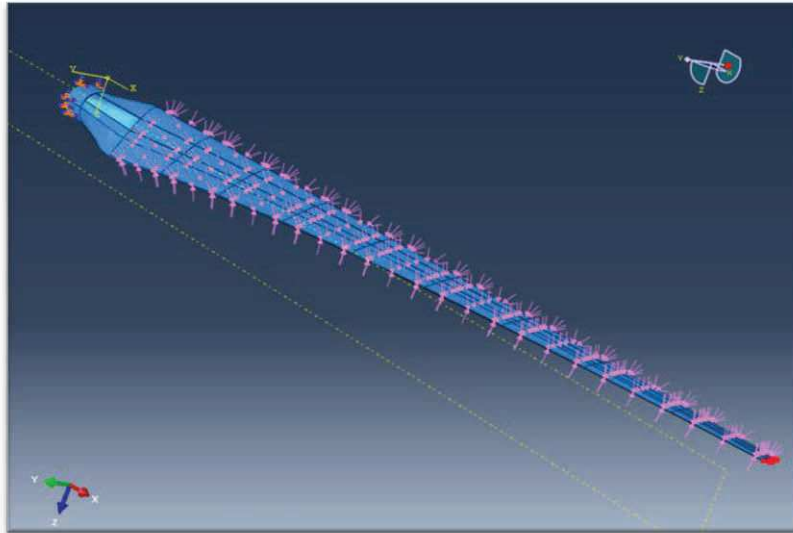


Figure 2-31: ABAQUS Blade model for the convergence study.

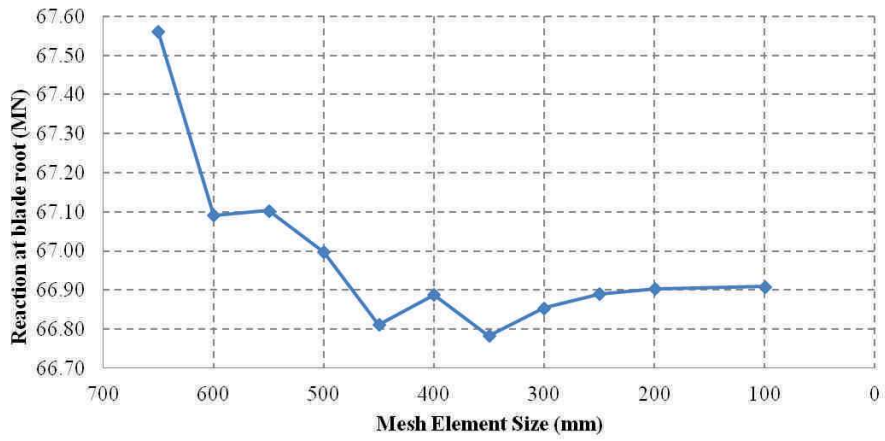


Figure 2-32: Mesh size convergence.

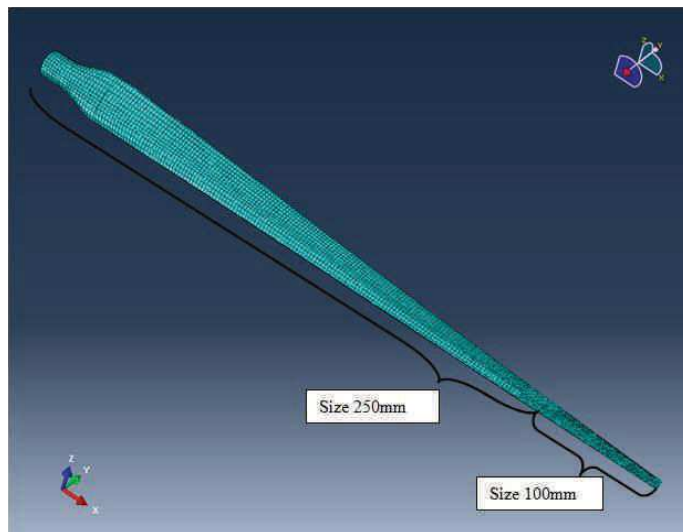


Figure 2-33: Blade Mesh.

2.14 Modeling of the structural response of the blade using finite elements

The finite element method is a lot precise than the calculation of structure using BEM sections. Nonetheless it is a lot heavier on the computational resources. Since the blades are hollow structures with thin walls, we can use 3D shell type geometry. These elements are good for applying composite layups since the wall thicknesses are very less as compared to the overall dimensions of the structure.

The modeling of boundary conditions is rather straight forward. As explained the blade is modeled as a beam. The gravitational and centrifugal forces are calculated by the software itself from the material densities and layup thicknesses.

Among the boundary conditions the aerodynamic loads are the most difficult to determine. They are in fact loads that are in the form of non uniform pressure distributions over the surface and friction or resistance forces acting along the length of the blade due to side slips. However certain designers have decided to neglect the effects of these side slip forces as they are not very high in their magnitude (Berggreen, et al., 2007). And others neglect the variation of pressure along the cord as well and apply an averaged pressure distribution along the cord of the section (Griffin & Zuteck, 2001). While (Mckittrick, et al., 2001) have chosen to apply the pressure and aerodynamic loads directly from the CFD analyses. Although this can over complicate the problem.

The design of the structures using finite element analysis is usually an iterative process: the structure is analyzed then the design is modified to satisfy the conditions of the materials or of their strengths, their deformations or their natural frequencies (Berggreen, et al., 2007).

The aim of this section is the numeric study of behavior under these 3 principal types of loadings:

1. Inertial due to Blade's weight
2. Aerodynamic due to the incident winds
3. Centrifugal forces due to their rotation.

2.15 Inertial loading due to blade's weight

The weight of the blade and the load applied due to its weight is dependent on the density of the materials making the wind blade. It depends also on the layup strategy especially how the weight is spread out over the length of the blade. Therefore once the materials have been defined the ABAQUS software can calculate the load itself according to the layups.

In general the mass of the structure is given by the equation 2-38:

$$\text{Mass} = \sum \text{Volume of material}_i \times \text{Density of material}_i \quad 2-38$$

Therefore the mass of the blade is the sum of the masses of all the materials constituting the blade

The load due to its weight is applied all over the rotational positions of the blade. For us there are 2 cases which are important:

1. When the blade is vertical upwards the blade is under compression forces
2. When the blade is horizontal and the weight causes it to bend in the flapwise direction.

When the blade is vertical with the tip upwards the weight of the blade acts to compress the blade towards its root. The geometry of the blade and that of the spar at this instance becomes very important with respect to its resistance to buckling. Here we will consider 2 types of spars depending on the sweep path followed by along the axis of the blade Figure 2-33. In addition for the instance we are concerned more with the effect of compressive stress on the damage taking place in the blade and not in the modes of buckling for the blade.

2 different geometrical forms of the spars are modeled here. The difference is based on the center of rotation of the sections of the blade to give the final twist. In one type the sections are twisted around the leading edge while in the other the rotation is done around the aerodynamic center of the sections thus rendering the spar straight and twisted, as compared to curved and twisted as in the first case. It should be remembered that according to the BEM method the center of twist has no effect on the blade performance.

Here we will study the effects of this curvature induced in the spar on the strength of the blade and also of the spar.

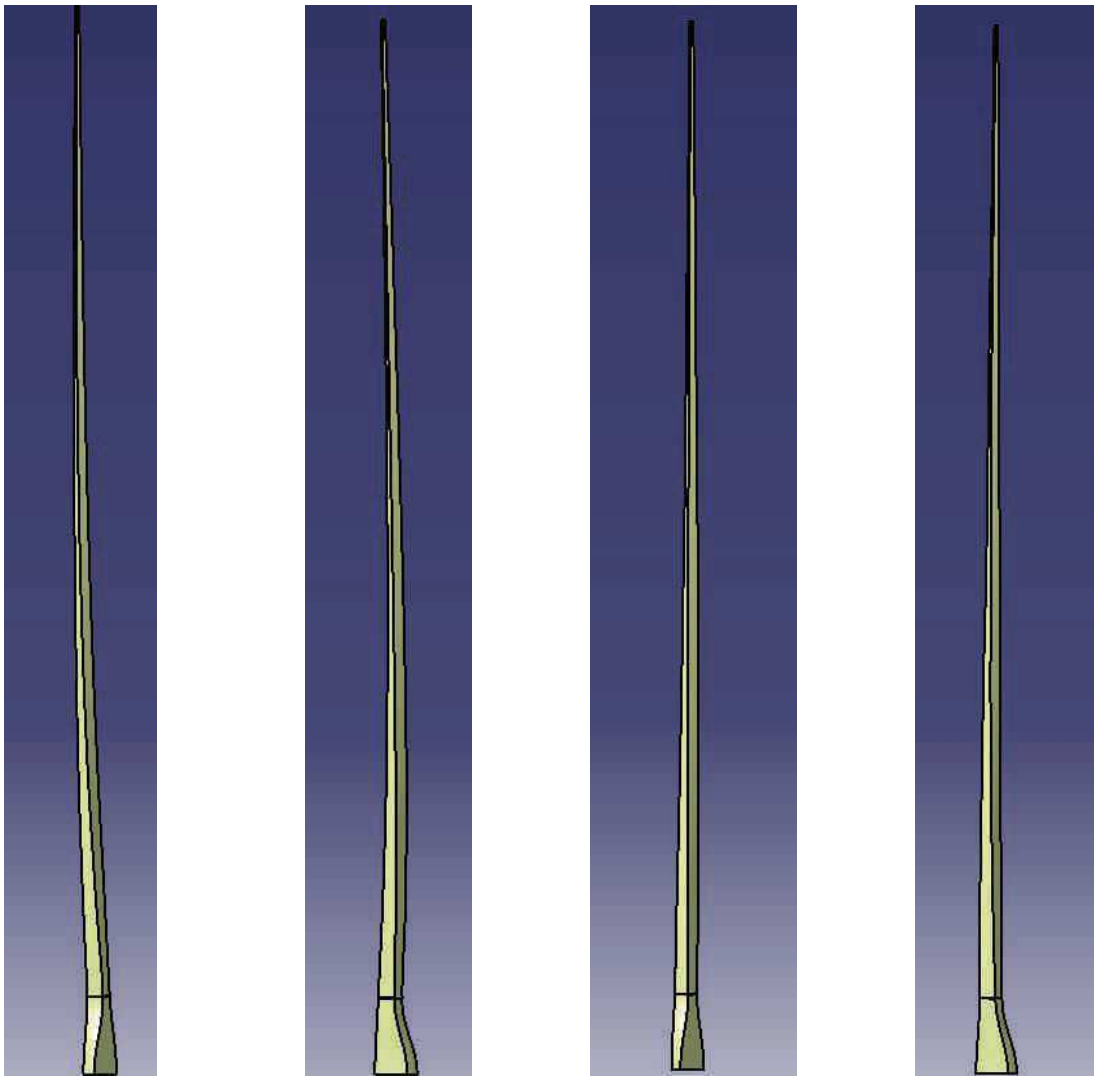
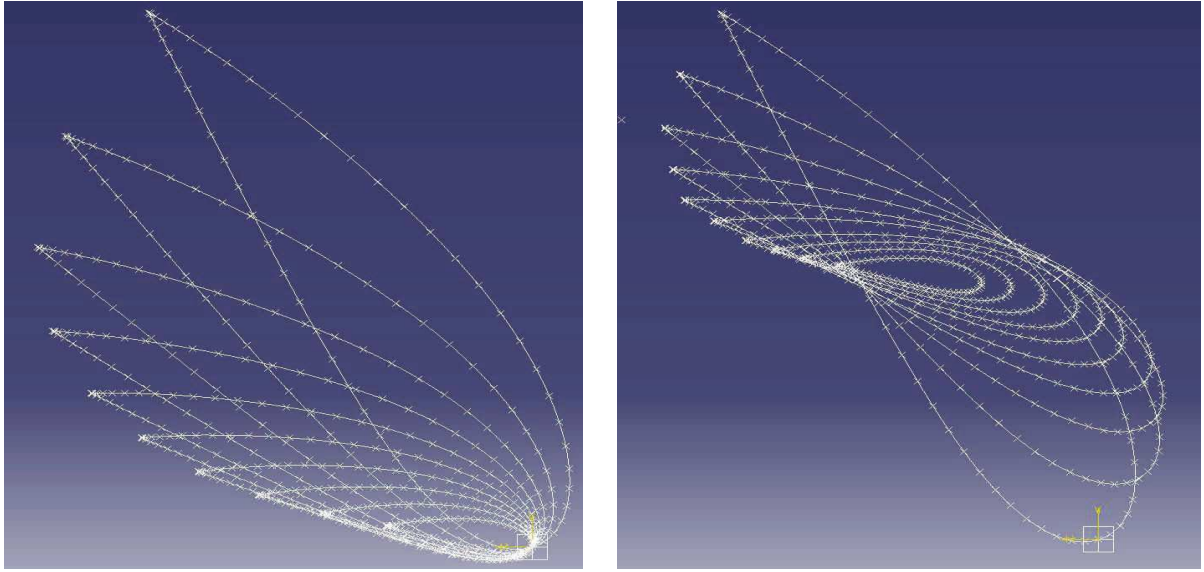
To compare the two types the blade is loaded along its axis with its weight. The zone of singularity or stress concentration is noted and the mesh is further refined to get a more detailed view of the damage taking place at this zone of singularity.

Refer to the Figure 2-34. The curved spar is referred to as “Blade 1” while the straight spar is referred to as “Blade 2”.

It should be noted here that the mode of failure which is more sensible that is, that of the matrix is more sensible to the mesh size than that of the fiber mode. In any case it is clear that the curved spar is more susceptible to damage caused due to buckling. It should be noted here that the failure mode, which is most sensitive to changes in the mesh size is one that is bound to the matrix to the fiber.

From the above results we can conclude that:

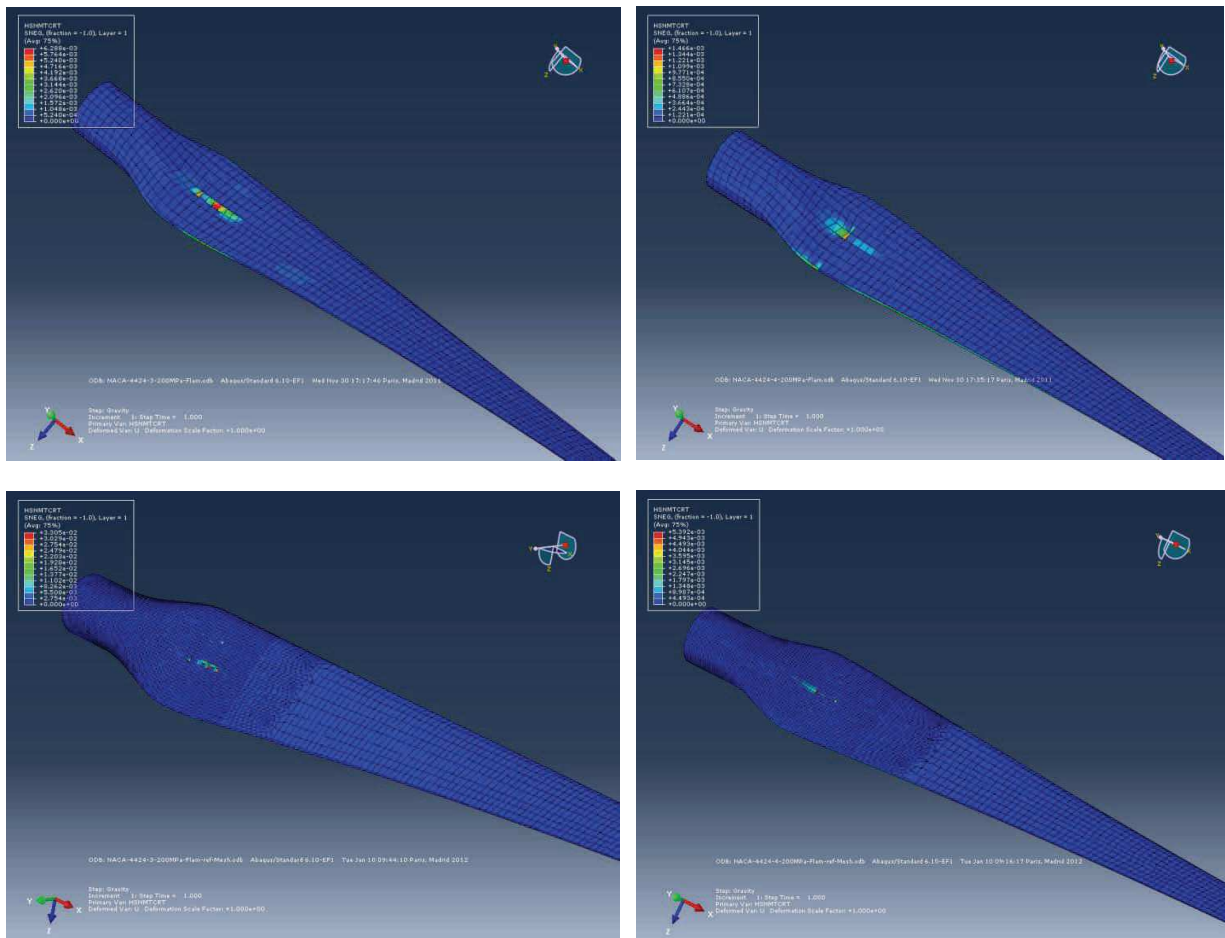
1. Under self weight there is no risk of damage taking place when the blade is parked vertical,
2. The results vary due to the mesh size therefore the mesh convergence should be well studied especially in the zone of stress singularities.



(a) Blade 1

(b) Blade 2

Figure 2-34: Effect of the twist pivot on the form of the spar.



(a) Blade 1

(b) Blade 2

Figure 2-35: Effect of mesh fineness on the damage sensitivity.

| Blade 1: Maximum value | | | | Blade 2: Maximum value | | | |
|------------------------|----------|----------|----------|------------------------|----------|----------|----------|
| Fiber | | Matrix | | Fiber | | Matrix | |
| Coarse mesh | | | | | | | |
| Tension | Comp. | Tension | Comp. | Tension | Comp. | Tension | Comp |
| 7.123e-5 | 2.139e-3 | 6.288e-3 | 3.711e-4 | 3.367e-8 | 2.019e-4 | 1.466e-3 | 8.290e-5 |
| Fine Mesh | | | | | | | |
| Tension | Comp | Tension | Comp | Tension | Comp | Tension | Comp |
| 7.609e-5 | 2.507e-3 | 3.305e-2 | 1.345e-3 | 1.685e-8 | 2.439e-4 | 5.392e-3 | 2.644e-4 |

Table 2-8 : Values of damage criteria for the blades.

2.16 Aerodynamic loading due to incident wind

As it has been explained in 2.3 the aerodynamic load is calculated from the BEM for each of the blade elements. With ABAQUS the force thus calculated is then applied in a uniform manner over the entire length of the section. However on the leading and trailing edges the pressure is applied inwards the blade to simulate incidence and effects of turbulence induced depression.

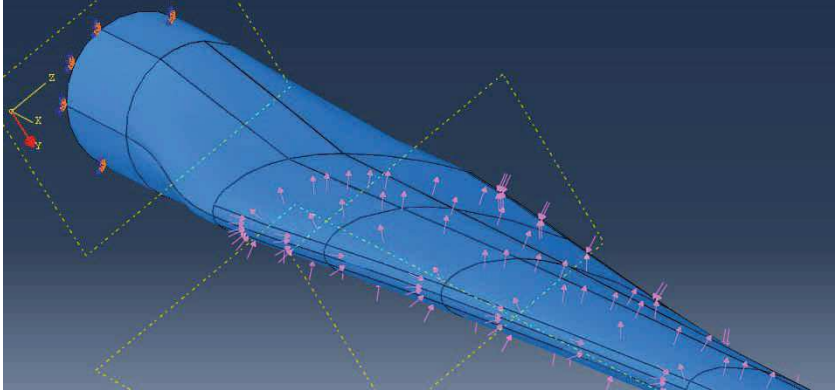


Figure 2-36: Pressures applied on the wind turbine blade elements

The uniform pressures are calculated by the equation 2-39:

$$P_e = \frac{F_{et}}{S_e} \tag{2-39}$$

where “ P_e ” is the pressure applied to the element, “ F_{et} ” is the total aerodynamic load given by the 2-39 and “ S_e ” is the total surface area of the element calculated using CATIA.

The Table 2-9 and the Figure 2-36 give the repartition of the pressure applied to the structure.

| Element | Pressure (kPa) |
|---------|----------------|
| 1 | 0.18 |
| 2 | 0.24 |
| 3 | 0.34 |
| 4 | 0.47 |
| 5 | 0.65 |
| 6 | 0.87 |
| 7 | 1.14 |
| 8 | 0.96 |
| 9 | 0.77 |

Table 2-9: Pressure distribution on the blade elements.

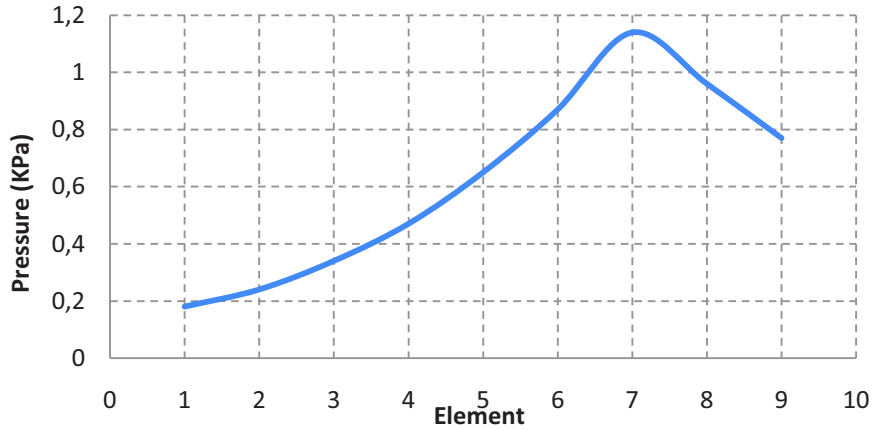


Figure 2-37: Pressure distribution on the blade.

2.17 Centrifugal load due to rotation of the blade

The centrifugal force applied on the blade depends on the mass and the rotational velocity of the blade as given in the 2-40.

$$F_c = \frac{1}{2} \text{Mass} \times \omega^2 r \quad 2-40$$

Where “ ω ” is the rotational velocity and “ r ” is the distance of the blade element from the center of rotation.

To calculate the stress due to the centrifugal force we calculate the centrifugal force at each of the elements long the blade’s length 2-41.

$$F_c = \frac{\omega^2}{2} \int m_s r dr \quad 2-41$$

where “ m_s ” is the mass of the section in kg/m^2 .

2.18 Behavior subject to global loading: Aerodynamic, gravitational and centrifugal

Before going into the case of global loadings on wind turbine blades it is important to see how in the literature different designers have addressed the problem of applying loads to the large size wind turbine blades of 5MW and up. Most of the designers follow the case 6.1 of the standards IEC 61400-1, which states that in extreme stormy conditions the rotor stops (Griffin, 2002)(Knill, 2005)(Joncas, et al., 2004)(Van Rijswijk, et al., 2005)(Veers, et al., 2003)(Hillmer, et al., 2007)(Hillmer, et al., 2007). For turbines of the class 1 which corresponds to large offshore units the extreme wind condition is 70 m/s(Joncas, et al., 2004). It is also necessary to point out here that the blade acts like a flat plate with its most drag inducing face up wind to simulate the worst case scenario. The normal stresses due to the

weight of the blade at these wind speeds become negligible (Van Rijswijk, et al., 2005). In the horizontal position the blade is simulated to be in a position where the lift generated by the extreme winds is in the direction of the weight of the blade (Griffin, 2002). Considering also that the blade acts as a flat plate and the wind direction can change $\pm 15^\circ$ is also mentioned in the standard.

The Table 2-10 shows the IEC Wind Classes and the wind speeds that the turbine must be designed to withstand.

| IEC Wind Class | | | |
|--|---------------|---------------|--------------|
| | 1 (High Wind) | 2 (Med. Wind) | 3 (Low Wind) |
| Reference Wind Speed | 50 m/s | 42.5 m/s | 7.5 m/s |
| Annual Average Wind Speed (Max) | 10 m/s | 8.5 m/s | 7.5 m/s |
| 50-year Return Gust | 70 m/s | 59.5 m/s | 52.5 m/s |
| 1-year Return Gust | 52.5 m/s | 44.6 m/s | 39.4 m/s |

Table 2-10 : The IEC Wind Classes.

Before going into the critical load evaluation for the blade of 6 MW, it is interesting to note the different cases present in the literature for the design or evaluation of the blades of large energy production. Majority of authors chose two types of load cases of which one is the case 6.1 of the IEC 61400-1 standards that is the machine stops at a high wind speed. (Griffin & Zuteck, 2001) (Hillmer, et al., 2007) (Joncas, et al., 2004) (Van Rijswijk, et al., 2005). For the class 1 turbines, usually the case for large turbines this speed corresponds to a wind speed of 70m/s. (Joncas, et al., 2004) explains that the blade is perpendicular to the wind flow, and is vertical upwards hence putting compressive stresses on the downwind side of the blade. The stresses due to the weight have also been neglected. (Van Rijswijk, et al., 2005) also puts the blade perpendicular to the wind direction but horizontal, such that the bending takes place due to the self weight of the blade. (Griffin & Zuteck, 2001) Consider the blade as a flat plate but also at a variation of 15° as explained in the standards.

The other load cases are for loads applied during operation of the blades. (Joncas, et al., 2004) defines a condition where the blade is horizontal while moving downwards with a velocity of 25 m/s according to the cut-off speed of the machine. (Van Rijswijk, et al., 2005) uses the same conditions but at a velocity of 15 m/s where the lift is theoretically maximum. Griffin & Zuteck considers a fatigue loading in bending due to the weight of the blade in the plane of rotation of the blade, (Griffin & Zuteck, 2001). simulates the velocities from 2 to 25 m/s for the case 1.1 of the IEC standards, (Hillmer, et al., 2007).

We can infer here that the authors have used the load case of the IEC standards at the stopped blade. However for the ones who study the blade in rotation or operation the load cases are simpler as compared to the ones shown in the IEC standards. Wind shearing is not considered as a constant wind profile is considered all along the length of the blade. Furthermore the effect of gusts and directional changes are not taken into consideration either. This is normal that all the load cases be not considered as the operational conditions are not always fully known at the preliminary stages of design.

| Design situation | DLC | Wind condition | | Other conditions | Type of analysis | Partial safety factors |
|---|-----|----------------|---|---|------------------|------------------------|
| 1) Power production | 1.1 | NTM | $V_{in} < V_{hub} < V_{out}$ | For extrapolation of extreme events | U | N |
| | 1.2 | NTM | $V_{in} < V_{hub} < V_{out}$ | | F | * |
| | 1.3 | ETM | $V_{in} < V_{hub} < V_{out}$ | | U | N |
| | 1.4 | ECD | $V_{in} = V_r - 2\text{m/s}, V_r, V_r + 2\text{m/s}$ | | U | N |
| | 1.5 | EWS | $V_{in} < V_{hub} < V_{out}$ | | U | N |
| 2) Power production plus occurrence of fault | 2.1 | NTM | $V_{in} < V_{hub} < V_{out}$ | Control system fault or loss of electrical network | U | N |
| | 2.2 | NTM | $V_{in} < V_{hub} < V_{out}$ | Protection system or preceding internal electrical fault | U | A |
| | 2.3 | EOG | $V_{hub} = V_r \pm 2\text{m/s}$ and V_{out} | External or internal electrical fault including loss of electrical network | U | A |
| | 2.4 | NTM | $V_{in} < V_{hub} < V_{out}$ | Control, protection, or electrical system faults including loss of electrical network | F | * |
| 3) Start up | 3.1 | NWP | $V_{in} < V_{hub} < V_{out}$ | | F | * |
| | 3.2 | EOG | $V_{hub} = V_{in}, V_r \pm 2\text{m/s}$ and V_{out} | | U | N |
| | 3.3 | EDC | $V_{hub} = V_{in}, V_r \pm 2\text{m/s}$ and V_{out} | | U | N |
| 4) Normal Shut down | 4.1 | NWP | $V_{in} < V_{hub} < V_{out}$ | | F | * |
| | 4.2 | EOG | $V_{hub} = V_{in}, V_r \pm 2\text{m/s}$ and V_{out} | | U | N |
| 5) Emergency Shut down | 5.1 | NTM | $V_{hub} = V_{in}, V_r \pm 2\text{m/s}$ and V_{out} | | U | N |
| 6) Stopped | 6.1 | EWM | 50 year recurrence period | | U | N |
| | 6.2 | EWM | 50 year recurrence period | Loss of electrical network connection | U | A |
| | 6.3 | EWM | 1 year recurrence period | Extreme yaw misalignment | U | N |
| | 6.4 | NTM | $V_{hub} < 0.7 V_{ref}$ | | F | * |
| 7) Parked and fault conditions | 7.1 | EWM | 1 year recurrence period | | U | A |
| 8) Transport, assembly, maintenance and repair. | 8.1 | NTM | V_{maint} to be stated by the manufacturer | | U | T |
| | 8.2 | EWM | 1 year recurrence period | | U | A |

Abbreviations:

| | | | |
|------------|---|---|--|
| DLC | Design load case | NWP | Normal wind profile model |
| ECD | Extreme coherent gust with direction change | $V_r \pm 2\text{m/s}$ | Sensitivity to all wind speeds in the range shall be analyzed. |
| EDC | Extreme direction change | F | Fatigue |
| EOG | Extreme operating gust | U | Ultimate strength |
| EWM | Extreme wind speed model | N | Normal |
| EWS | Extreme wind shear | A | Abnormal |
| NTM | Normal turbulence model | T | Transport end erection |
| ETM | Extreme turbulence model | * | Partial safety for fatigue |

Table 2-11: Load cases according to the IEC 61400-1 Standards, according to the International Electro technical commission (1999).

Other cases of loading are the cases for operations (Joncas, et al., 2004). Defining the blade as moving towards the ground and at that instance being horizontal under the effect of wind at 55m/s (Van Rijswijk, et al., 2005). Although the wind loading may be considered when the blade is under the influence of a 12m/s winds it is where the lift is theoretically the highest (Griffin, 2002). They consider also the flexural fatigue in the flapwise direction (Hillmer, et al., 2007). Simulating a time change series in the wind speed from 2 – 55m/s according to the case 1.1 of the standards IEC.

It is also noted that the authors cited above have used the standards IEC in the case of parked blades. However for the conditions of loadings of the blades in service the loadings are more complex, for example the wind shearing is not taken into account and the wind speed is considered constant all along the rotor, the effect of gusts is normally neglected also. This is normally the case for the initial designs that more complex combined loadings are not studied, and is left for later stages in the wind turbine blade design. In general there are a number of load combinations to be applied for validating the design of the blade. These combinations are summarized in the Table 2-12.

| Load case | Aerodynamic | Centrifugal | Inertial due to blade's weight |
|------------------|---|---|--|
| 1 | Pressure due to an incident wind at 55m/s | Load corresponding to a rotational velocity of 16 rpm | Weight applied in the 4 ortho-axial directions |
| 2 | Pressure due to an incident wind at 55m/s | - | - |
| 3 | Pressure due to an incident wind at 70 m/s, storm conditions the blade is stopped | - | Load applied in 2 directions (\pm edgewise) |
| 4 | - | - | Load applied towards the root of the blade |
| 5 | Pressure due to an incident wind at 70 m/s, storm conditions the blade is stopped | - | Load applied towards the root of the blade |
| 6 | - | - | Load applied in 2 directions (\pm flapwise) |
| 7 | - | - | Load applied in 2 directions (\pm flapwise) until final failure |

Table 2-12: Load cases for validating the blade design.

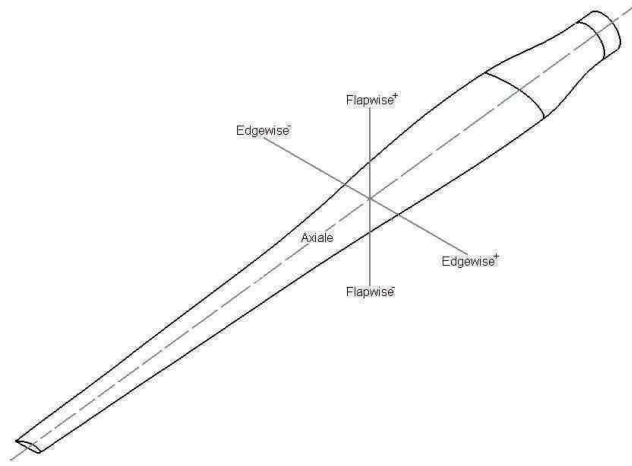


Figure 2-38: Blade relevant coordinate system.

However here we shall use the most sever loading cases for our simulations. Once the blade has been loaded with the aerodynamic, gravitational and centrifugal forces, two blade positions are simulated:

1. The blade is horizontal with the weight of the blade acting in the direction of the lift
2. The blade is vertical upwards with the flat face of the blade facing the wind.

It's important to gauge the response of the blade in light of the damage taking place within it subjected to such loadings. For this we shall use the criteria of Hashin's damage(Christensen, 2014):

Tension in the Matrix: $(\sigma_{22} + \sigma_{33}) > 0$

$$\frac{1}{T_{22}^2} (\sigma_{22} + \sigma_{33})^2 + \frac{1}{S_{23}^2} (\sigma_{23}^2 - \sigma_{22}\sigma_{33}) + \frac{1}{S_{12}^2} (\sigma_{12}^2 + \sigma_{31}^2) \leq 1 \quad 2-42$$

Compression in the Matrix: $(\sigma_{22} + \sigma_{33}) < 0$

$$\frac{1}{C_{22}} \left[\left(\frac{C_{22}}{2S_{23}} \right)^2 - 1 \right] (\sigma_{22} + \sigma_{33}) + \frac{1}{4S_{23}^2} (\sigma_{22} + \sigma_{33})^2 + \frac{1}{S_{23}^2} (\sigma_{23}^2 - \sigma_{22}\sigma_{33}) + \frac{1}{S_{12}^2} (\sigma_{12}^2 + \sigma_{31}^2) \leq 1 \quad 2-43$$

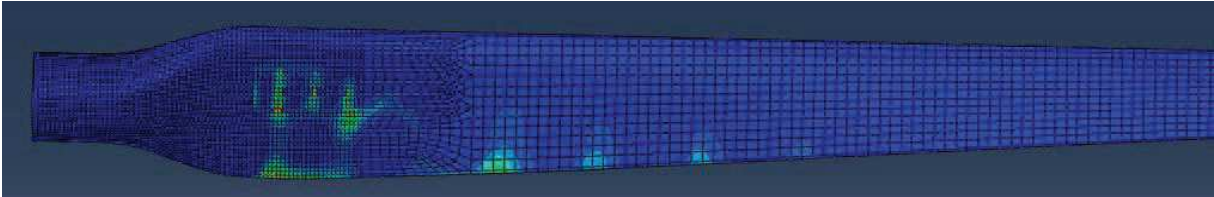
Tension in the Fiber: $\sigma_{11} > 0$

$$\left(\frac{\sigma_{11}}{T_{11}} \right)^2 + \frac{1}{S_{12}^2} (\sigma_{12}^2 + \sigma_{31}^2) \leq 1 \quad 2-44$$

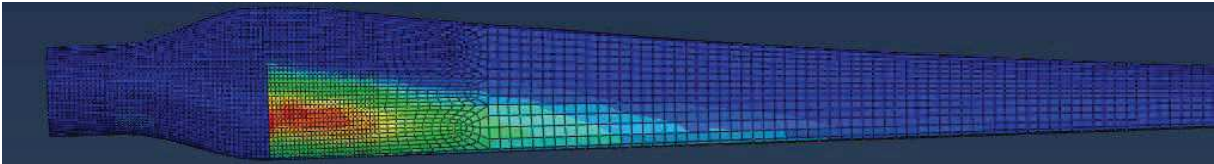
Compression in the Fiber: $\sigma_{11} < 0$

$$\left(\frac{\sigma_{11}}{C_{11}} \right)^2 \leq 1 \quad 2-45$$

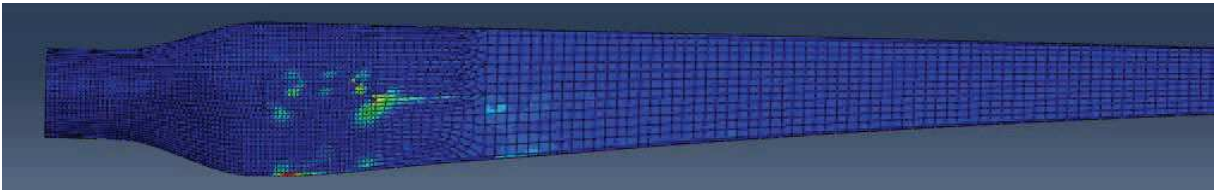
The Figure 2-39 shows the damage taking place in the Blade 1.



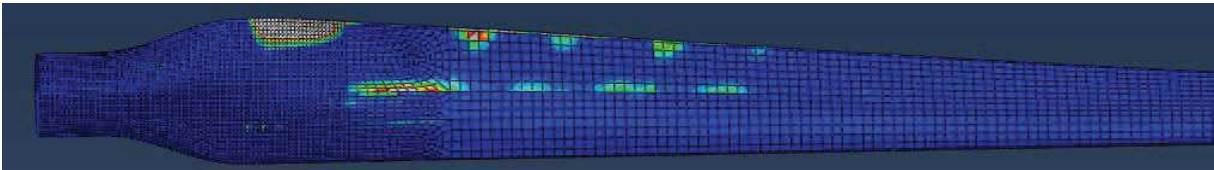
(a) *Fibers in compression.*



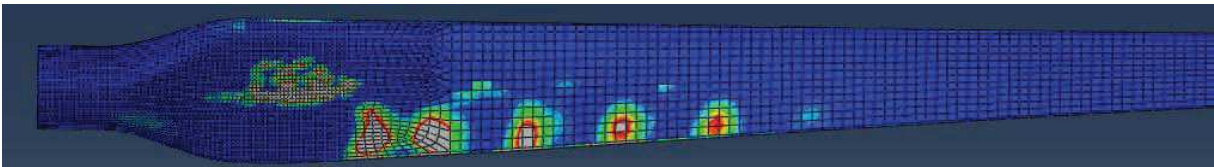
(b) *Fibers in Tension.*



(c) *Matrix in compression.*

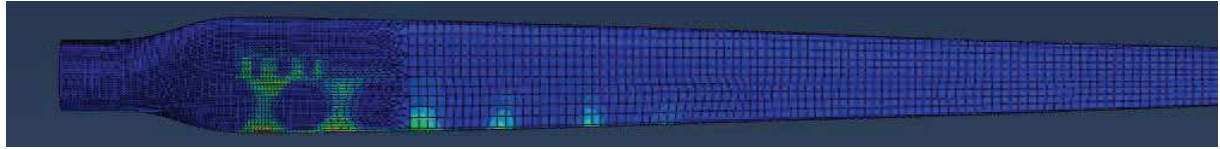


(d) *Matrix in tension, Extrados.*

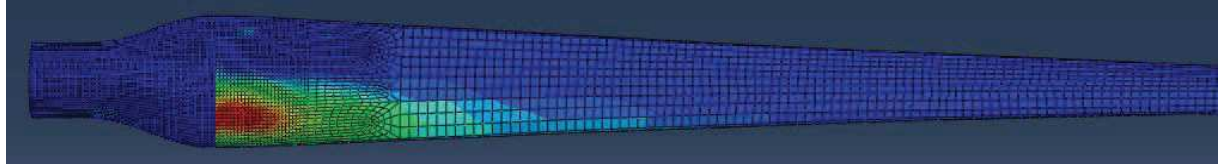


(e) *Matrix in tension, Intrados.*

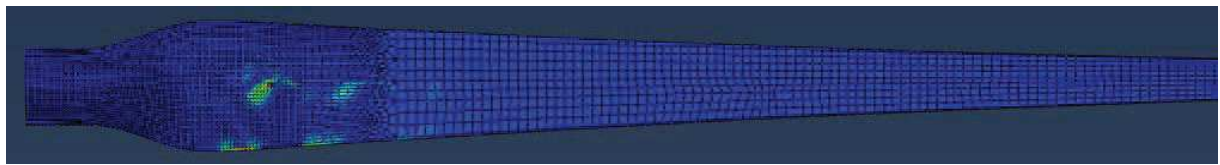
Figure 2-39: Representation of the damage in the Blade 1.



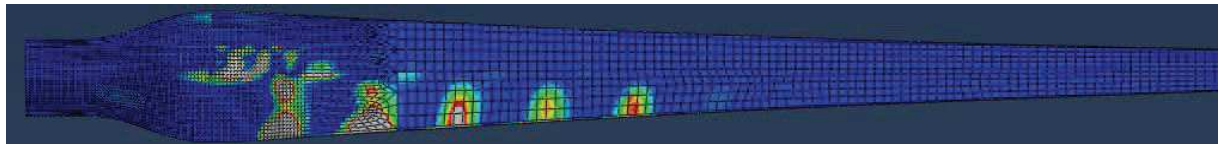
(a) *Fibers in compression.*



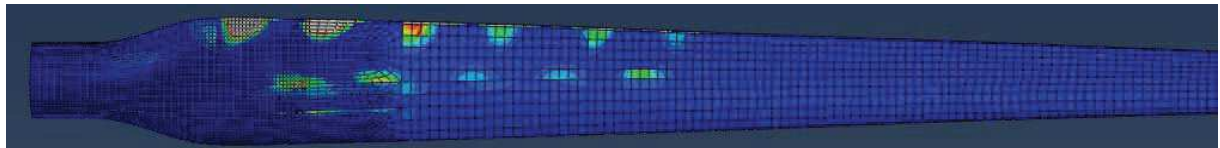
(b) *Fibers in tension.*



(c) *Matrix in compression.*



(d) *Matrix in tension, Extrados.*



(e) *Matrix in tension, Intrados.*

Figure 2-40: Representation of the damage in the Blade 2.

In the Figure 2-40 the zones red and grey are the zones which satisfy the conditions of failure according to the Hashin's damage criteria.

| Blade 1: Maximum Value | | | | Blade 2: Maximum Value | | | |
|------------------------|----------------|--------------|-----------------|------------------------|----------------|-----------------|-----------------|
| Fibers | | Matrix | | Fibers | | Matrix | |
| <i>Comp.</i> | <i>Tension</i> | <i>Comp.</i> | <i>Tension</i> | <i>Comp.</i> | <i>Tension</i> | <i>Comp.</i> | <i>Tension</i> |
| 9.021e-1 | 6.275e-2 | 8.813e-1 | 1.088e+1 | 7.275e-1 | 6.104e-2 | 1.177e+0 | 1.514e+1 |

Table 2-13 : Values of Hashin's damage criteria

It is important to note here that the damage criterion is not satisfied for the 2 blades especially in the matrix mode. The Blade 2 shows a better resistance to damage in the fiber mode. Also although the intensities of damage are higher for the Blade 2 but the damage zones are a lot more localized. Therefore from this point on we shall concentrate on the design of the Blade 2.

The Figure 2-41 shows that the damage is localized in the first 3 blade elements. Furthermore it is close to the trailing edge. Therefore reinforcements are proposed for this zone.

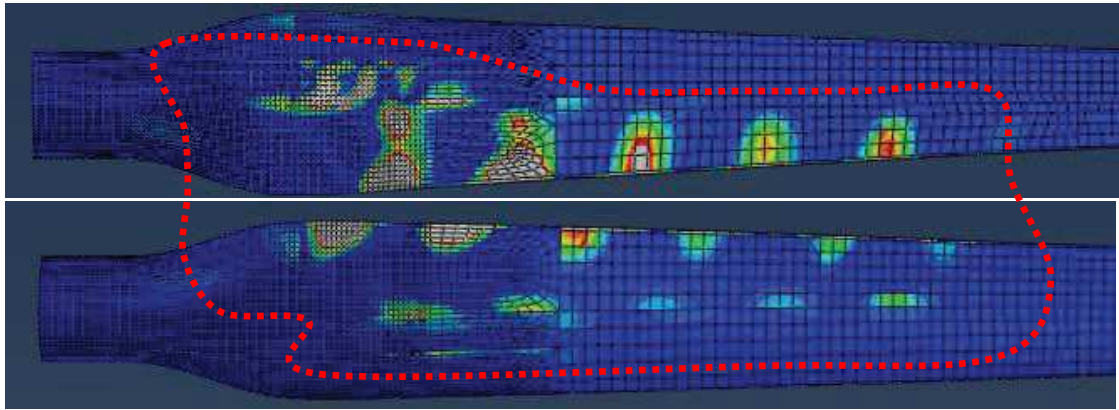


Figure 2-41: Damaged Zones.

The way to reinforce the blade in increasing the material thickness should be such that it should not increase substantially the weight of the blade. Since most of the stresses are inversely proportional to the moment of inertia of the sections there would be found ways to increase the moment of inertia without increasing its weight.

Fortunately, with composite materials we have this liberty. The use of sandwiches with light weight cores the order of 0.1 of the weight of the composite increase substantially the moment of inertia while not substantially affecting the weight of the structure. Hence if the moment of inertia is doubled the mass would increase by a factor of $2^{1/3} = 1.2599$ since;

$$\text{Moment of inertia} = \text{Constant} \times \text{Width of the section} \times \text{Thickness of the section}^3$$

The Table 2-14 shows the procedure of increasing the thickness of the sensitive zones by using sandwich cores.

| Thickness Zones | Core (mm) | | Total mass of the Blade (tons) | |
|--------------------|---------------------------|---------------------------|---|---------------------------|
| | 1 st Iteration | 2 nd Iteration | 1 st Iteration | 2 nd Iteration |
| 5-10 (m) | 10 | 41 | 9.48 | 9.83 |
| 10-15 (m) | 10 | 41 | Percent increase of mass between the two iterations $\approx 3.7\%$ | |
| 15-20 (m) | 9 | 40 | | |

Table 2-14 : Reinforcement of sensible zones.

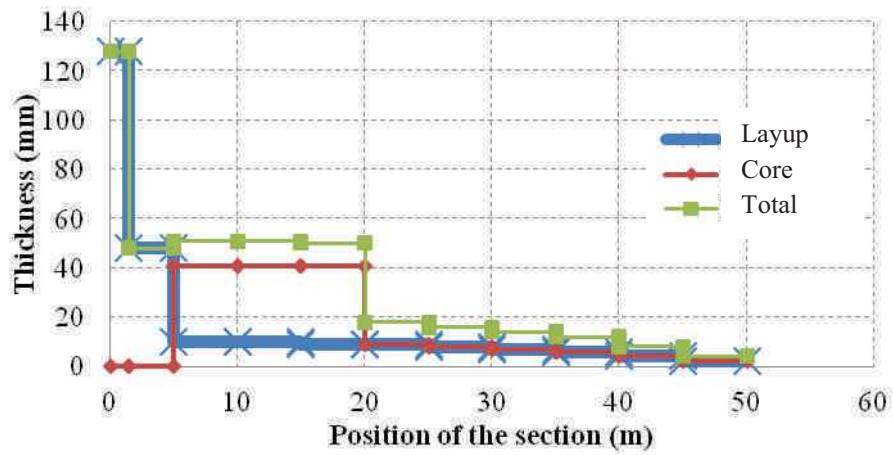


Figure 2-42: Distribution of thickness.

The Figure 2-43 illustrates the incidence of change in the thickness on the damage behavior of the Blade.

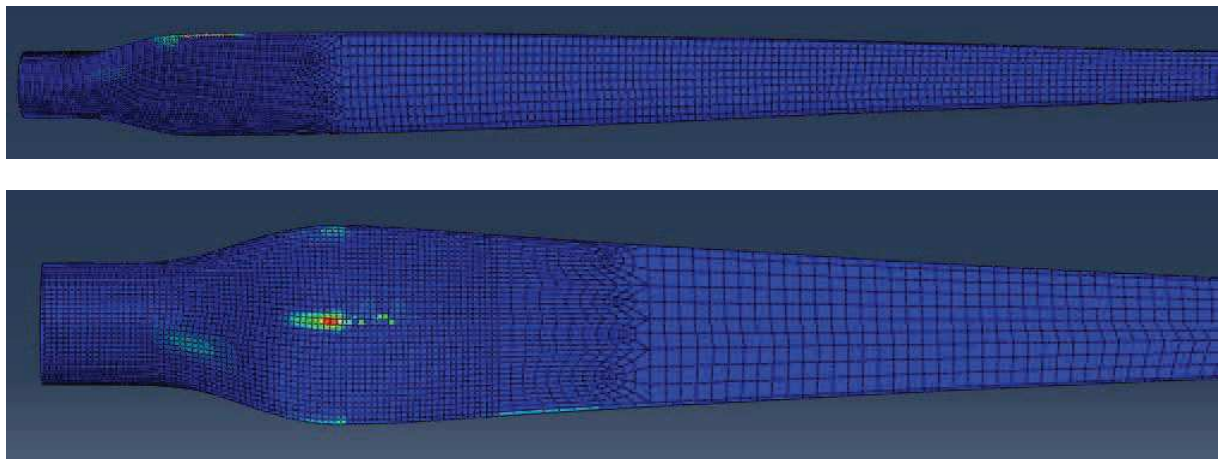


Figure 2-43: Damaged zones after modifications.

| Blade 2: Maximum Value Thin Core (10mm) | | | | Blade 2: Maximum Value Thick Core (40mm) | | | |
|--|----------------|-----------------|-----------------|---|----------------|--------------|----------------|
| Fibers | | Matrix | | Fibers | | Matrix | |
| <i>Comp.</i> | <i>Tension</i> | <i>Comp.</i> | <i>Tension</i> | <i>Comp.</i> | <i>Tension</i> | <i>Comp.</i> | <i>Tension</i> |
| 7.275e-1 | 6.104e-2 | 1.177e+0 | 1.514e+1 | 2.017e-1 | 4.936e-2 | 1.697e-1 | 3.710e0 |

Table 2-15: Values of Hashin's damage criteria after modifications.

Note here that the skin thickness has remained the same while the damage resistance has greatly increased, as shown in the Table 2-15. For achieving this, the trailing edge and the zone of the blade's surface in contact with the spar have been reinforced.

After having doubled the thickness of the core, Figure 2-44, the damage zones have practically all been removed - Figure 2-45 – Figure 2-46. However there is still one element showing high stress gradients and damage this is an artifact of simulation due to the insufficient meshing finesse at this point.

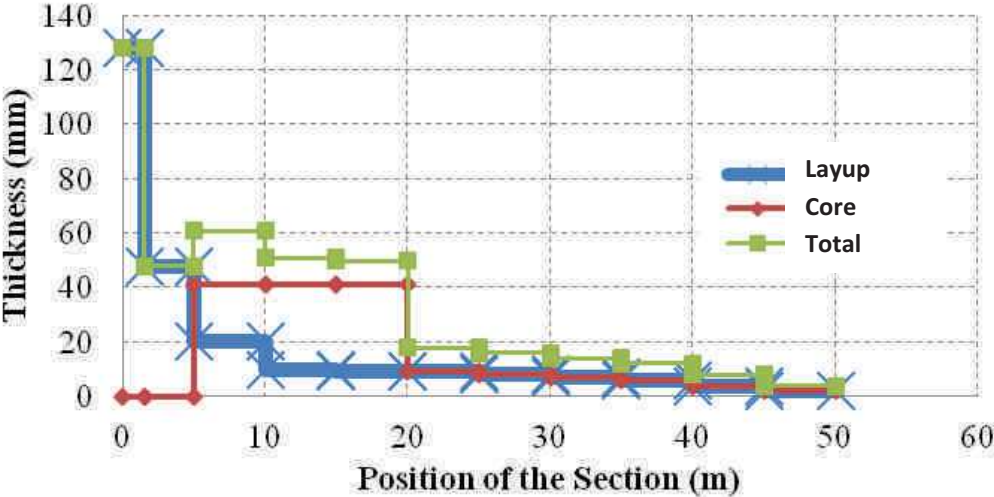


Figure 2-44: Distribution of thickness.

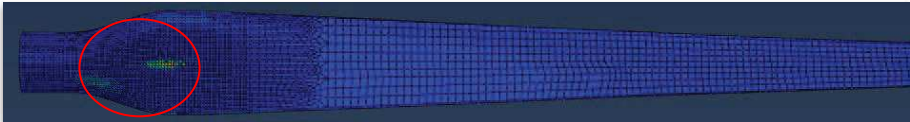


Figure 2-45: Final damaged zones.

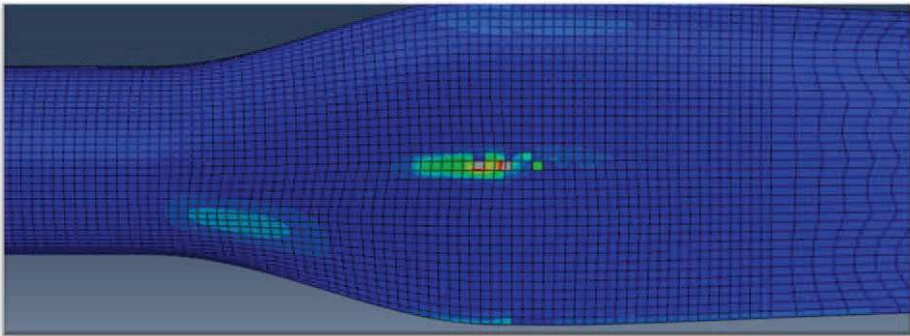


Figure 2-46: Zoom of damaged zone.

| Blade 2: Maximum Value Thick Core (40mm) | | | | Blade 2: Maximum Value Thick Core (40mm), Thick skin | | | |
|---|----------------|--------------|-----------------|---|----------------|--------------|-----------------|
| Fibers | | Matrix | | Fibers | | Matrix | |
| <i>Comp.</i> | <i>Tension</i> | <i>Comp.</i> | <i>Tension</i> | <i>Comp.</i> | <i>Tension</i> | <i>Comp.</i> | <i>Tension</i> |
| 2.017e-1 | 4.936e-2 | 1.697e-1 | 3.710e+0 | 1.259e-1 | 3.704e-2 | 8.85e-2 | 2.899e+0 |

Table 2-16: Values of Hashin's damage model for the modified blade.

2.19 Modifications to the initial blade design

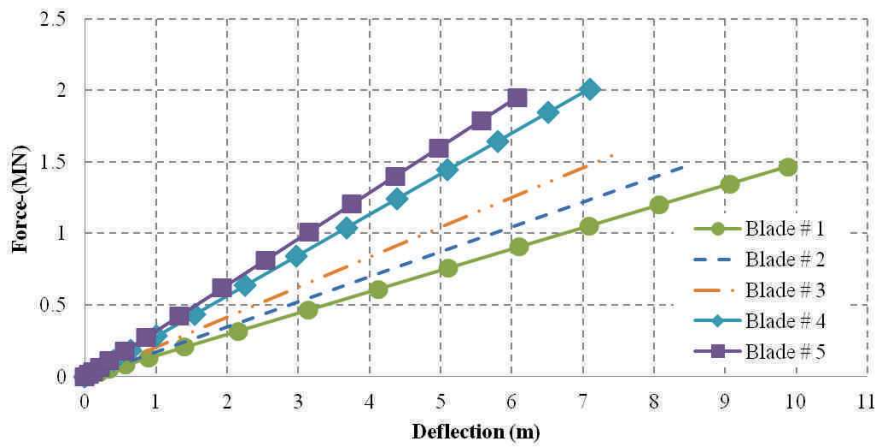
Although from the previous section it can be seen that the increase in the overall moment of inertia of the blade cross sections in the sensitive regions can lead to higher stiffness, without necessarily increasing the overall weight of the blade. In this section however, we shall discuss some other options to increase the overall stiffness of the blade, their strength and their post failure behavior.

Here 5 variations of the initial design are proposed as given in the Table 2-17.

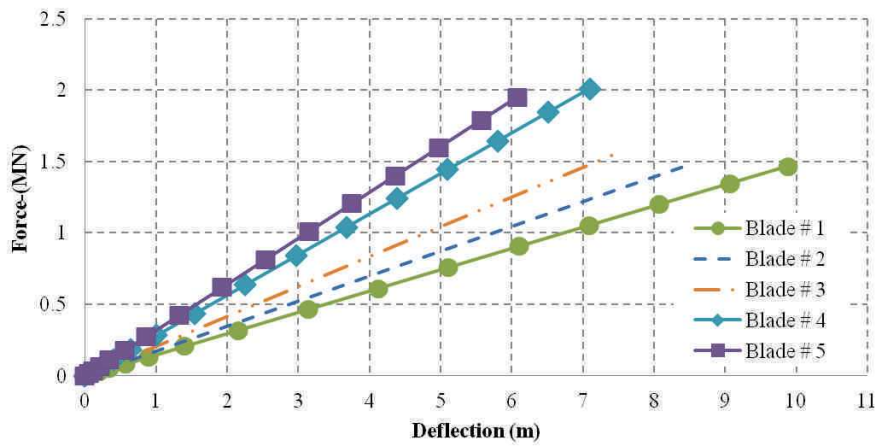
| No. | Blade Designation | Material | | Material Thicknesses |
|-----|------------------------------|------------------|------------------|---|
| | | Blade surface | Spar | |
| 1 | NACA-4424-60m-200MPa | Fiberglass/Epoxy | Fiberglass/Epoxy | As per initial design |
| 2 | NACA-4424-60m-CL-200MPa | Fiberglass/Epoxy | Carbon/Epoxy | As per initial design |
| 3 | NACA-4424-60m-CLE-200MPa | Fiberglass/Epoxy | Carbon/Epoxy | Blade No. 2 with sparspar reinforced with a thicker sandwich core |
| 4 | NACA-4424-60m-AE-200MPa | Fiberglass/Epoxy | Fiberglass/Epoxy | Blade No. 1 with sparspar reinforced with a thicker sandwich core |
| 5 | NACA-4424-60m-CLE-200MPa-SEC | Fiberglass/Epoxy | Carbon/Epoxy | Blade No. 2 with blade surface and sparspar reinforced with a thicker sandwich core |

Table 2-17: Variations of the initial blade design.

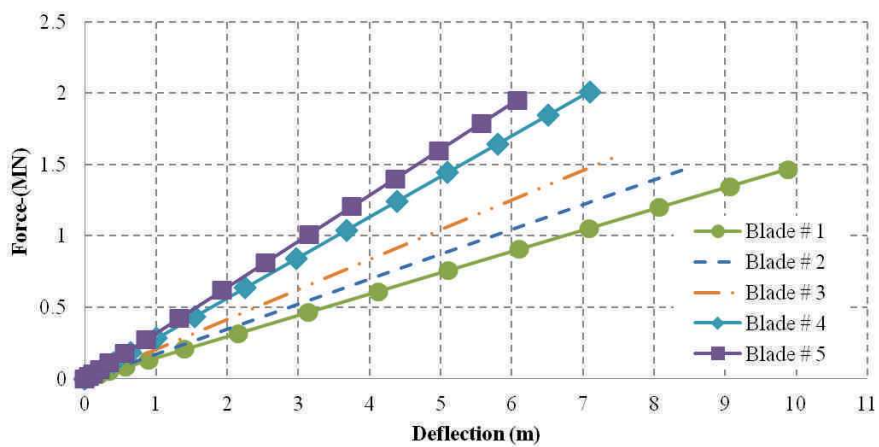
All these blades are then loaded with the load cases as shown in the Table 2-12. The behavior of these blades under the first 6 load cases is thus shown in the Figure 2-48.



(a) Load case 1

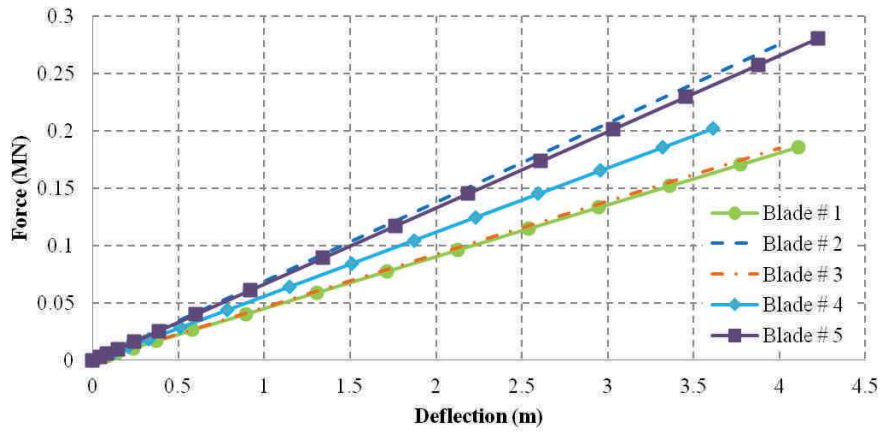


(b) Load case 2

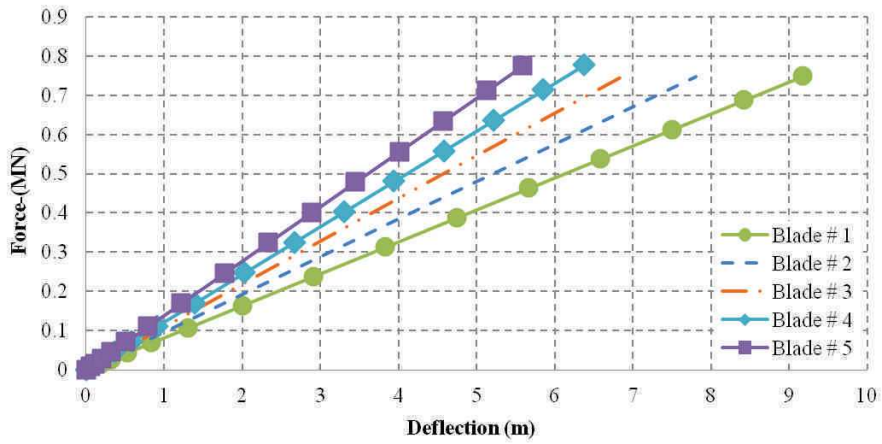


(c) Load case 3

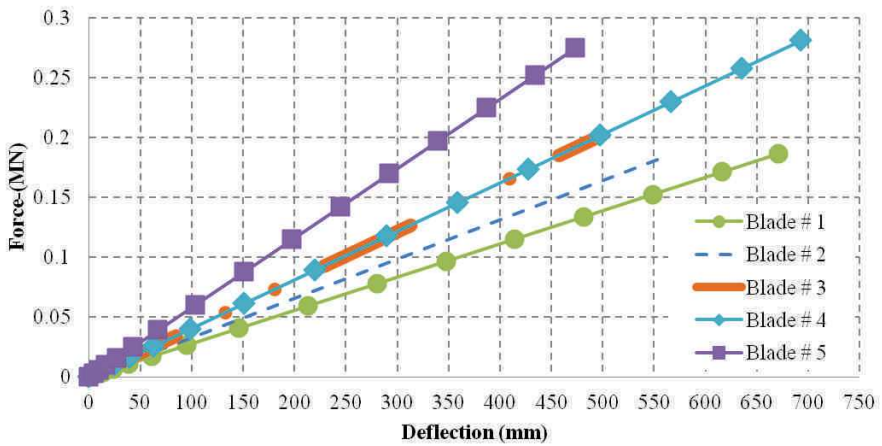
Figure 2-47: Reaction force measured at the root of the blade against the blade tip deflection (load case 1-3).



(d) Load case 4



(e) Load case 5



(f) Load case 6

Figure 2-48: Reaction force measured at the root of the blade against the blade tip deflection. (load case 4-6).

Here it can be seen that from a strength point of view all the blade variations hold good, they deform without showing any damage. However, as explained in the previous sections that strength is not always the best parameter to gauge a blades structural performance, the tip deflection should also be limited. This deflection can be of the order of 10% of the blade length depending on the blade design specifications. The blades are then loaded up to their failure in the 7th load case. The results are summarized in the Figure 2-49.

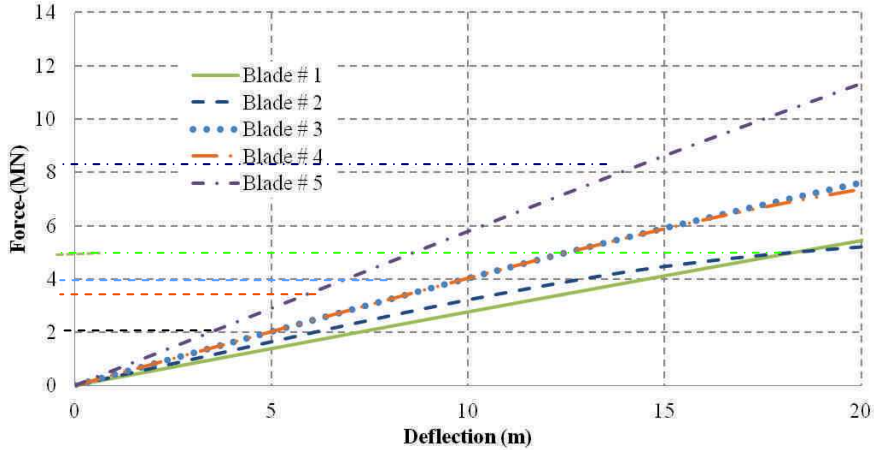


Figure 2-49: Point of damage in the loads deflection graphs under load case 7.

From the Figure 2-49 one can see that the thicker blade sections are stiffer and more resistant to damage. However for the first 2 designs where we used a carbon Spar for the second we see that the blade although is much stiffer but fails at a lower load as compared to it all fiberglass counterparts. Upon close inspection it was revealed that the stiff carbon fiber spar induces high stress concentrations at the blade surface which acts as a point of initiation of damage thus the structure fails at a much lower load.

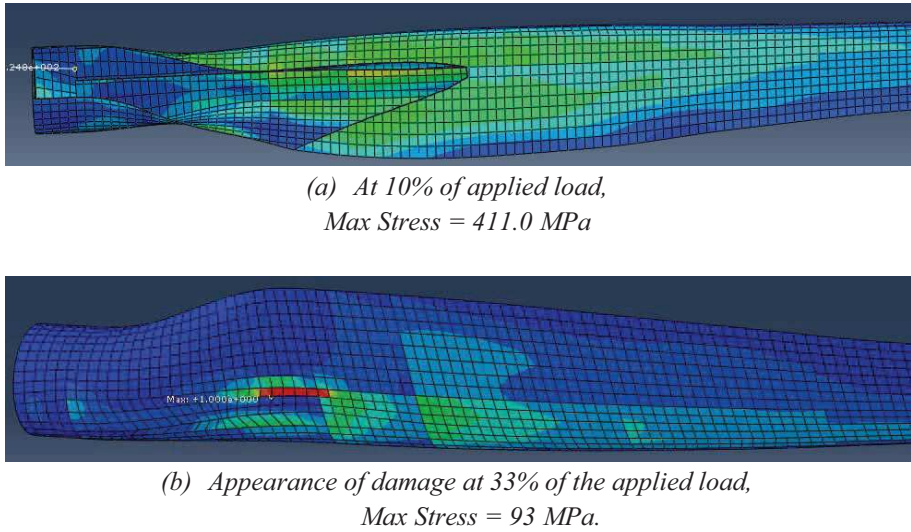
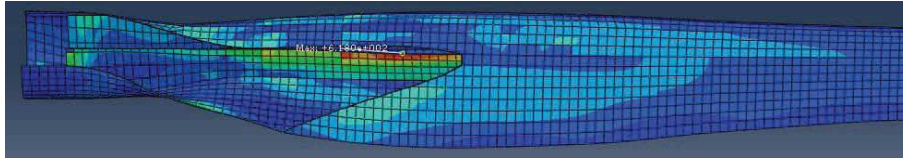
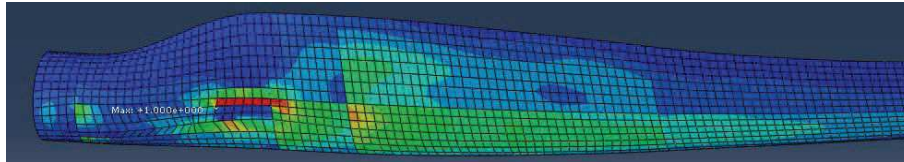


Figure 2-50: Onset of damage in Blade 1 -NACA-4424-60m-200MPa- at different stages during the loading until complete failure.

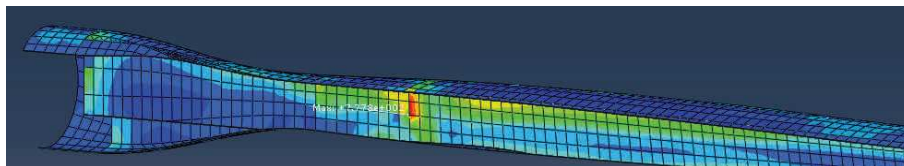


(a) At 10% of the applied load,
Max Stress = 618.4 MPa.

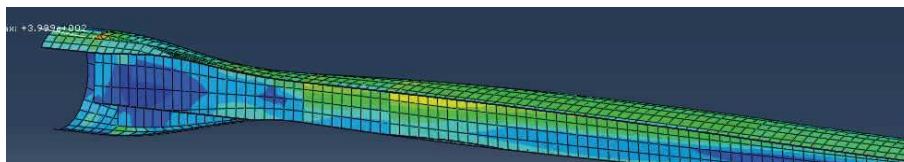


(b) Appearance of damage at 1.5% of the applied load,
Max Stress = 100 MPa.

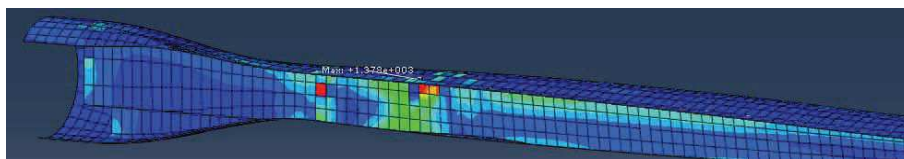
Figure 2-51: Onset of damage in Blade 2 - NACA-4424-60m-CL-200MPa- at different stages during the loading until complete failure.



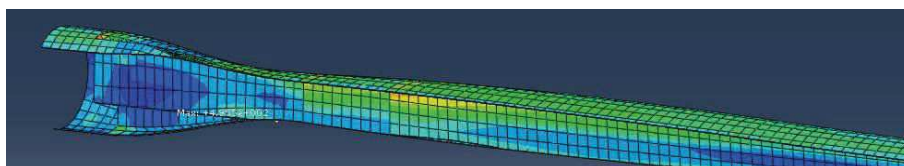
(a) Blade 2: Spar of NACA-4424-60m-CL-200MPa at 60% of the applied,
Max Stress = 778 MPa



(b) Blade 1: Spar of NACA-4424-60m-200MPa at 60% of the applied load,
Max Stress = 400 MPa



(c) Blade 2: Spar of NACA-4424-60m-CL-200MPa at 70% of the applied load,
Max Stress = 1378 MPa



(d) Blade No. 1: Spar of NACA-4424-60m-200MPa at 70% of the applied load,
Max Stress = 495 MPa

Figure 2-52: Onset of damage in Blade 1 and Blade 2 Spar at different stages during the loading until failure.

The Figure 2-50 to Figure 2-52 show how a stiffer spar causes the more compliant bade surface to deform beyond its damage limit and the blade fails at a much lower value than if the blade was entirely made up of a softer material. However this result can be exploited in the sense that care should be taken especially in the interfaces of soft and hard materials to sufficiently reinforce the softer interface sides.

2.20 Conclusions and Discussion

After having done the modeling of the blade being designed by the method explained in this chapter it is clear that the maximum admissible stress state considered towards the tip of the blade tends to diminish, Figure 2-53. This is due to the fact that the material thickness at the tip is always thicker than that determined by design for practical purposes.

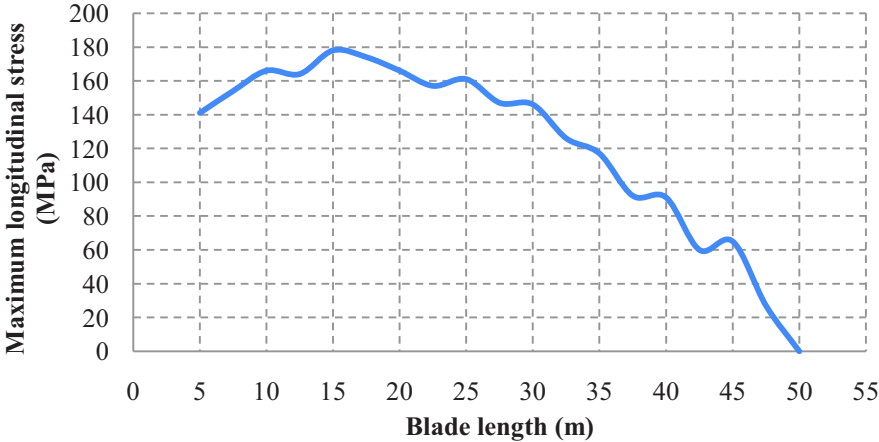


Figure 2-53: Maximum stress calculated by ABAQUS along the length of the blade.

It is also noted that treating the blade as a simple beam for more detailed studies is not sufficient. The sections when treated as one entity swept in 1D introduce a lot of assumptions and simplifications which can lead to over confident or over designed structures.

The blade deflections should be checked for the designs to be proposed. Many composites fail at a much higher strain where the blades may not be usable due to their overly deformed geometries.

In the case of using stiffer more expensive materials selectively in sensitive zones care should be taken not to create high stiffness gradients. The stiffness changes across interfaces should be gradual in order to limit the effect of stress concentrations.

Following this chapter we shall discuss the various experiments done on the material specimens in order to determine their mechanical properties. The development of a material property profile is important to be able to model the wind turbine blade more accurately.

Chapter 3 --- Experimental characterization of material properties

Table of contents

| | |
|--|-----|
| 3.1 Fabrication of composite panels | 88 |
| 3.2 Materials | 91 |
| 3.3 Equipment used for mechanical testing..... | 93 |
| 3.4 Determination of fiber content..... | 96 |
| 3.5 Quasi static material properties | 96 |
| 3.5.1 Tensile tests..... | 96 |
| 3.5.2 Flexural tests | 103 |
| 3.6 Discussion on results | 107 |
| 3.7 Summary of test results | 109 |

The next step in the design process is the determination of the material properties. The material properties of composite materials need to be determined in order to model the structure precisely and for doing further more detailed delamination and fatigue failure investigations. The composites were fabricated in the form of 2 m² (2x1m) plates using unidirectional and 45° biaxial mats, in different thicknesses. Furthermore the 45° biaxial type composite plates in different thickness were joined with “NORPOL” vinyl-ester adhesives of different thicknesses for the characterization of resistance in de-bonding type failures. Sandwich structures with 2mm face thicknesses and 10 – 30mm thick 80gm/m³ PVC foam cores were also used for the characterization of sandwiches in flexion and delamination properties.

The Figure 3-1 shows the general hierarchy of a Wind turbine design process. The base of any design is the performance and the power output parameters. It is based on these parameters that the overall dimensions of the blade are ascertained. After which a more detailed structural design is done based on the forces applied as determined by the operational parameters of the turbine blade. The structure then needs to be modeled more accurately using the real material properties, the materials which will be used in the fabrication of the turbines. Therefore experiments and mechanical tests are done on the material specimens to develop a material properties profile, which this chapter in part will deal with. The final stage is the numerical modeling of the complete wind turbine blade taking into account the physical material properties.

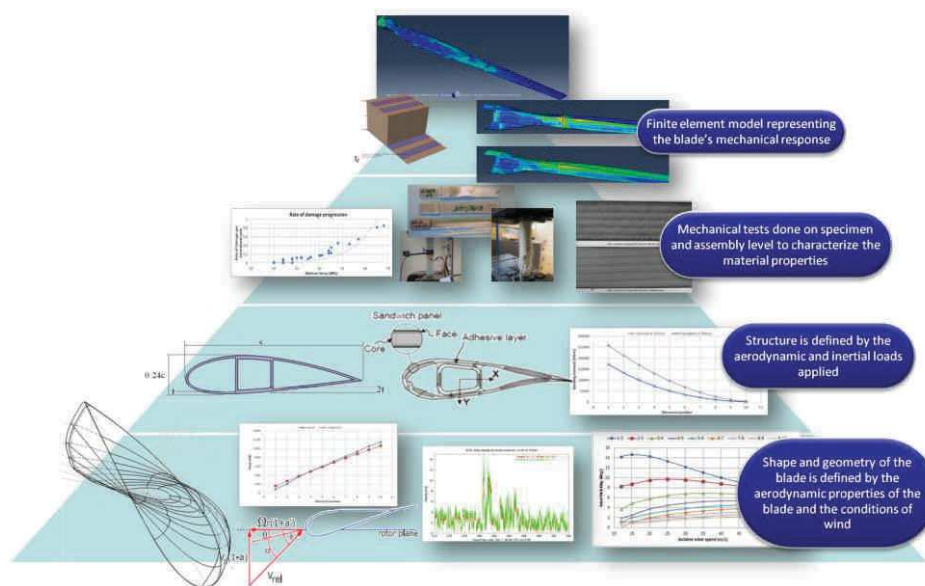


Figure 3-1: The general design process shown in hierarchy where the specimen level material testing lies at the fourth tier.

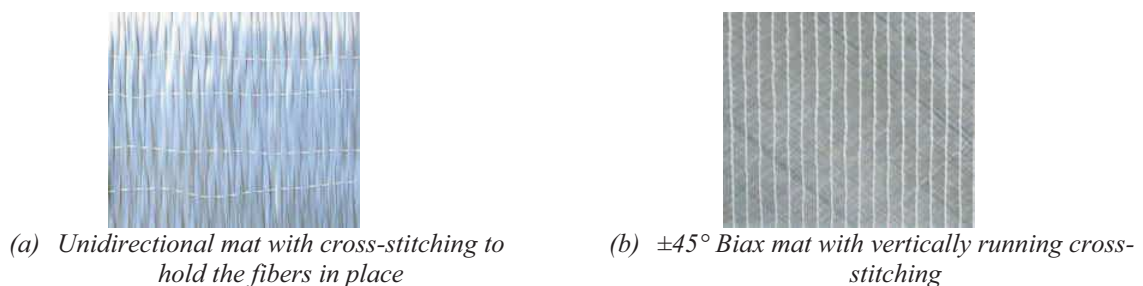


Figure 3-2 : Woven structures for the production and manufacture of specimens.

The two principal types of mats used for the composite specimens are shown in the Figure 3-2. Both the mats as can be seen contain the principal fibers in either single direction (UD mats) or in alternating 45° directions (45° Biax mats). The principal fibers are then held in place with stitches the amounts and types of which are given in the Table 3-1 and Table 3-2.

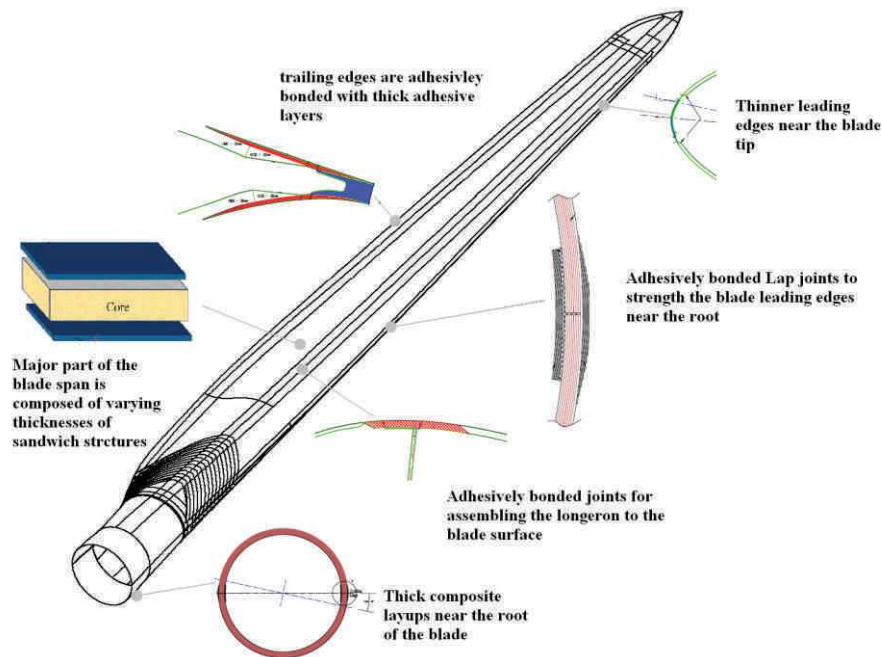


Figure 3-3: Different types of layups and composite layup configurations at different locations within a wind turbine blade.

Furthermore as depicted in the Figure 3-3 the wind turbine blade consists of varying thicknesses of different materials. These materials are in the form of different types of composite layups as well as sandwich structures. The different components of the blade are then assembled together with the help of adhesive bonding.

3.1 Fabrication of composite panels

The panels as explained were fabricated in large panels at the ASTRIUM Composites manufacturing facility, before being cut down to size for transport (500mm x 250mm), as shown in the Figure 3-4 and Figure 3-5. The plates are manufactured using the vacuum resin infusion process. In this process firstly the proper thickness of the composite mat is laid out with the sandwich core included on a glass table to check the completion of resin infusion, as the resin is injected from the top and flow down to the glass table in the bottom. Then the stacking is covered with a breather cloth. The whole of the stacking is then covered with a plastic film. This plastic film acts as the vacuum bag. The bag is then vacuumed out before infusion is commenced at the top middle part of the composite stacking. The use of closed pore PVC foam core permits the use of this method to avoid the absorption of resin by the foam core, in the case of sandwich structures. After a period of polymerization at room temperature for more than 8 hours the vacuum in the bag is released, the breather cloth removed and the plates are de-molded before being cut to specifications.



(a) Composite layers being laid out



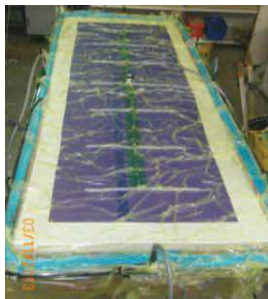
(b) Sizing of the layers after layup to +25mm of final size



(c) Laying up of a breather cloth to drain the excess resin



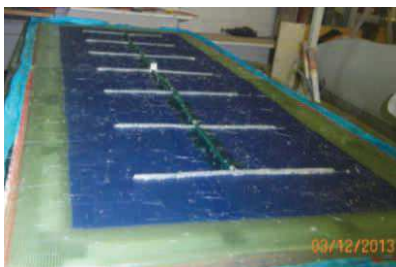
(d) Checking for air tightness under vacuum



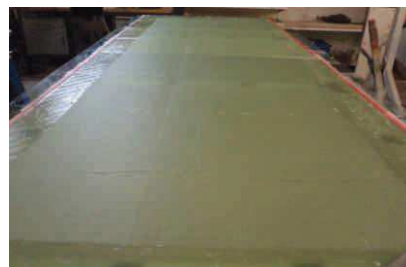
(e) Complete vacuum bag setup before resin infusion.



(f) Vacuum bag during infusion



(g) Removal from the vacuum bag after polymerization at room temperature



(h) Final composite panel after demolding and before final trimming and sizing

Figure 3-4: Fabrication of composite panels.



(a) Completed vacuum bag before the start of infusion



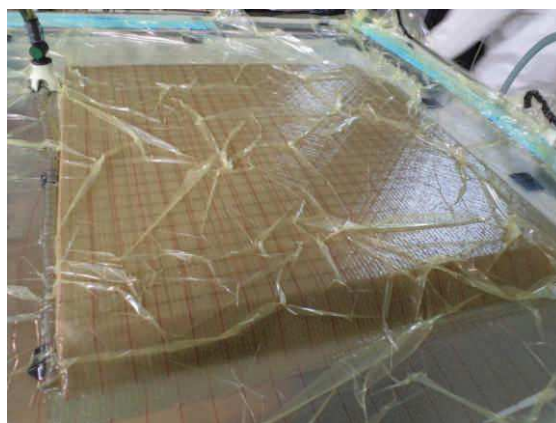
(b) Runners in place for infusion to commence at the middle top of the stacking



(c) View of the infusion process from under the bottom glass mold



(d) Completion of infusion process as viewed from the bottom of the glass mold



(e) Complete sandwich panel before de-molding and sizing.

Figure 3-5: Fabrication of sandwich panels.

3.2 Materials

The materials used for the preparation of the composite panels are E-Glass fiber mats in polyester resin. The details for the two types of mats used are listed in the Table 3-1 and Table 3-2.

| Construction | Areal Weight (g/m ²) | Tolerance (±%) | Material | Linear Density (tex) |
|--------------------|----------------------------------|----------------|--------------|----------------------|
| 0° | 1152 | 5 | E – Glass | 2400 |
| 90° | 49 | 5 | E – Glass | 68 |
| Stitching | 12 | 5 | PES 110 dtex | |
| Total Areal weight | 1213 | 5 | Binder | Warp-Tricot |

Table 3-1: Details of the Unidirectional (UD) mat used for composite manufacture.

| Construction | Areal Weight (g/m ²) | Tolerance (±%) | Material | Linear Density (tex) |
|--------------------|----------------------------------|----------------|-------------|----------------------|
| +45° | 451 | 5 | E – Glass | 600 |
| -45° | 451 | 5 | E – Glass | 600 |
| Stitching | 12 | 5 | PES 76 dtex | |
| Total Areal weight | 912 | 5 | Binder | Warp |

Table 3-2: Details of the 45° Biax mat used for composite manufacture.

| Physical data in liquid state at 23°C | | | |
|--|-------------------|------------|----------------|
| Properties | Unit | Value | Test method |
| Viscosity cone and plate at 23°C | mPas (cps) | 140-160 | 2460-001 |
| Specific gravity | g/cm ³ | 1.11 ±0.02 | ISO 2811-2001 |
| Acid number | mgKOH/g | 20 | 2000-001 |
| Styrene content | % | 44-48 | 2230-001 |
| Flash point | °C | 32 | ASTM D 3278-73 |
| Gel time +1.5% NORPOL Peroxide2 | Minutes | 135-145 | 2160-001 |
| +1.5% NORPOL Peroxide1 | Minutes | 115-140 | 2160-001 |
| Volume shrinkage | % | <9 | ISO 3521-1997 |
| Storage stability from date of manufacture | months | 6 | G 180 |

Table 3-3: Details of the PolyLite 413 Series polyester resin in liquid state.

| Non reinforced casting properties | | | |
|--|-------------------|--------------|--------------------|
| Post curing at room temp, 24h then at 60°C for 24h then at 100°C for 3h | | | |
| Properties | Unit | Value | Test method |
| Tensile strength | MPa | 67 | ISO 527-1993 |
| Tensile elongation at break | % | 3.5-4.5 | ISO 527-1993 |
| Tensile modulus | MPa | 3300 | ISO 527-1993 |
| Flexural strength | MPa | 125 | ISO 178-2001 |
| Flexural modulus | MPa | 3500 | ISO 178-2001 |
| Impact Strength (Charpy P4) | kJ/m ² | 6-9 | ISO 179-2001 |
| Heat distortion temp | °C | 85 | ISO 75-1993 |
| Hardness Barcol. 934-1, min | - | 45 | ASTMD 2583-99 |

Table 3-4: Details of the PolyLite 413 Series polyester resin post cure.

| Physical data in liquid state at 23°C | | | |
|--|-------------------|--------------|--------------------|
| Properties | Unit | Value | Test method |
| Viscosity Brookfield HBT sp B/5 rpm | poises | 1350 – 1500 | 2460-001 |
| Density | g/cm ³ | 1.12 - 1.15 | 2100-001 |
| Gel time, 2% NORPOL N°24 | minutes | 55 – 65 | 2160-006 |
| Exothermic peak with 2% NORPOL N° 24 | °C | 90 – 120 | 2340-002 |
| Storage stability from date of manufacture | months | 4 | |
| Non reinforced casting properties | | | |
| Properties | Unit | Value | Test method |
| Tensile strength | MPa | 35 – 40 | ISO 527-1/2-93 |
| Tensile elongation at break | % | 2.5 - 3.5 | ISO 527-1/2-93 |
| Flash point | °C | 70 | ISO 75-1/2-93 |
| Linear shrinkage | % | 1.8 | ASTMD2566-69 |

Table 3-5: Details of the NORPOL PF adhesive.

| Property | Unit | Value | Test Method |
|--|-------------------|--------------|--------------------|
| Nominal Density ¹ | Kg/m ³ | 80 | ISO 845 |
| Compressive Strength ² | MPa | 1.4 | ASTM D 1621 |
| Compressive Modulus ² | MPa | 90 | ASTM D 1621 |
| Tensile Strength ² | MPa | 2.5 | ASTM D 1623 |
| Tensile Modulus ² | MPa | 95 | ASTM D 1623 |
| Shear Strength | MPa | 1.15 | ASTM C 273 |
| Shear Modulus | MPa | 27 | ASTM C 273 |
| Shear Strain | % | 30 | ASTM C 273 |
| 1) Typical density variation of ±10% | | | |
| 2) Perpendicular to plane. All values measured at 23°C | | | |

Table 3-6: Details of the Divinycell® H80 PVC foam core.

The materials properties given in Table 3-1 - Table 3-6 are properties taken from material data sheets provided by the manufacturers. The fiberglass cloth comes from Saertek GmbH & Co. the stitches are from Owens Corning Composite Materials, Polyester resin and NORPOL Adhesive from Reichhold A. S.

3.3 Equipment used for mechanical testing

In general the equipment used for the testing of material properties can be divided into 2 categories. The first are the machines used for loading the equipment and the second is the apparatus used for instrumentation. The equipment used for loading the specimens in tension and flexion are used depending upon their capacity, their capability to load specimens repeatedly and the degree of precision required for each test.

For instrumentation biaxial strain gauges with their data acquisition and treatment system, thermocouples, CCD camera and a Thermal camera are used for monitoring the tests and taking measurements. The equipment and their use are summarized in Table 3-7 –Table 3-9.



UTS tri-column screw type tensile test machine (250kN):
 → Quasi static tensile tests



Adamel bi-screw type tensile test machine (50kN):
 → Delamination and Quasi-static flexion tests

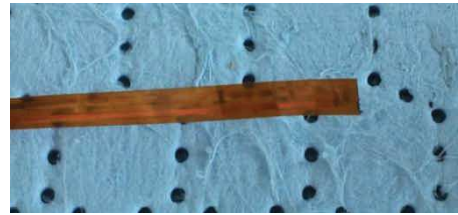


Instron hydraulic fatigue test machine (150kN):
 → Fatigue and Cyclic loading tests.

Table 3-7 : List of equipment used for mechanical testing, testing.



Biaxial strain gauges (2mm):
→ Linear strain measurement



T- Type thermocouples (-40 – 100°C with ±0.01°C precision)
→ Temperature measurement



Spider 8 data acquisition system (8 channel):
→ Linear strain and Thermocouple temperature data acquisition and processing



FLIR systems thermal camera:
→ Temperature profile and distribution measurement.



Retiga 1300 CCD Camera:
→ Visual measurements and Digital image correlation for linear strain field measurement

Table 3-8: List of equipment used for mechanical testing, instrumentation.



Nabertherm 1000°C furnace:
→ Calcination of composites



Diamond wheeled circular saws:
→ Sizing of specimens

Table 3-9: List of equipment used for mechanical testing, miscellaneous.

3.4 Determination of fiber content

The fiber content in any composite layup is an important factor used for determining the strength of these materials. It permits to model and to determine analytically the properties of the layup. Furthermore as will be shown later on it helps in the finite element modeling with accuracy. Defining the fiber content in terms of volume gives the effective cross section of fibers supporting the applied loads on the structure.

To determine the fiber content in percentage of mass of the composite a small piece of the composite is cut, measured to determine its volume, weighed and then calcinated in an oven at 650°C for about 4 hours to burn away all the polymer resin thus leaving behind just the fibers, which are again weighed. The difference in the weight gives the weight of the resin thus burnt away. Since the density of both the fibers and the resin is known, the fiber content can be calculated in terms of volume, Table 7.

| Composite type | Volume fiber content (%) | Mass fiber content (%) |
|----------------|--------------------------|------------------------|
| UD | 54 ± 0.5 | 74 ± 1.0 |
| 45° Biax | 55 ± 1.0 | 73 ± 1.0 |

Table 3-10: Fiber contents in UD and 45° Biax type composites.

As expected the UD type layup shows slightly higher fiber packing due to lesser voids between the crisscrossing fibers.

3.5 Quasi static material properties

3.5.1 Tensile tests

Tensile tests are done on the composite specimen's oriented parallel, normal and at an angle of 45° to the direction of the applied force, for determining their properties in longitudinal, transverse and pure shearing directions. Furthermore adhesive massive specimens are tested in longitudinal direction for their tensile properties, Table 3-7 and Table 3-8.

Specimens of 250x25mm equipped with biaxial strain gauges are loaded till final failure. For the NORPOL adhesive specimens we used digital image correlation to measure the strains in the longitudinal and transverse directions, Table 3-9. The apparatus for traction tests is shown in Figure 3-6, with the specimens failing as shown in Figure 3-7.



Figure 3-6: A composite specimen loaded into the UTS tensile test machine, instrumented with a biaxial strain gauge for the measurement of longitudinal and transverse strains.



(a) Unidirectional specimen loaded at 90° to the fiber direction for determining " E_t "



(b) Unidirectional specimen loaded at 45° to the fiber direction for determining " G_{lt} "



(c) Unidirectional specimen loaded at 0° to the fiber direction for determining " E_l "

Figure 3-7: Failed specimens after traction tests used for the characterization of the materials.

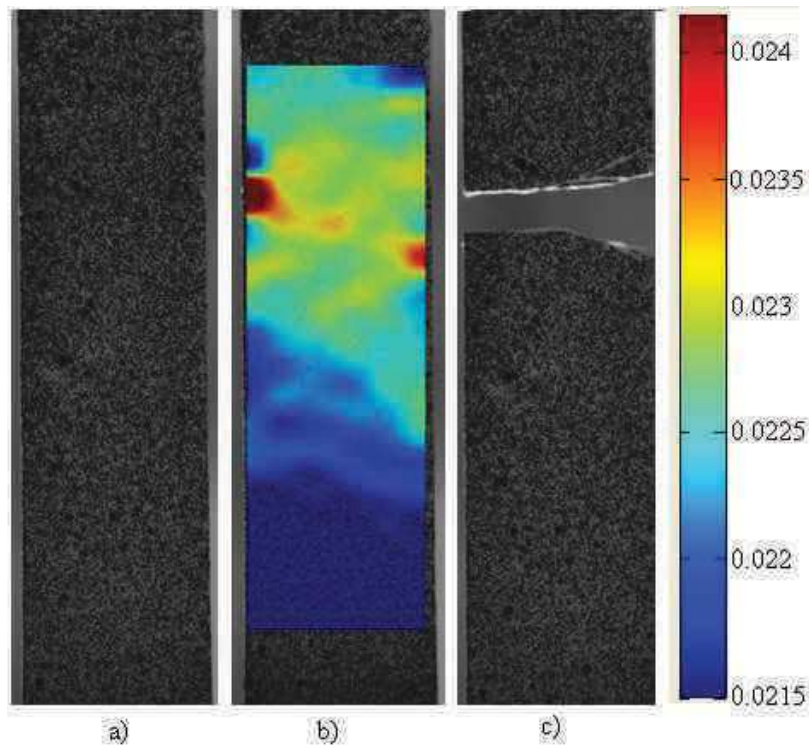


Figure 3-8: NORPOL Adhesive specimen

(a) at initial state, (b) DIC showing higher strains along the application of the force (vertical direction) where failure is about to occur (in red), (c) failed specimen shows cracks starting at the higher strained regions.

Figure 3-8 shows a NORPOL specimen loaded till failure under monotonic tension. The specimen is coated with a special paint to follow the deformation using digital image correlation.

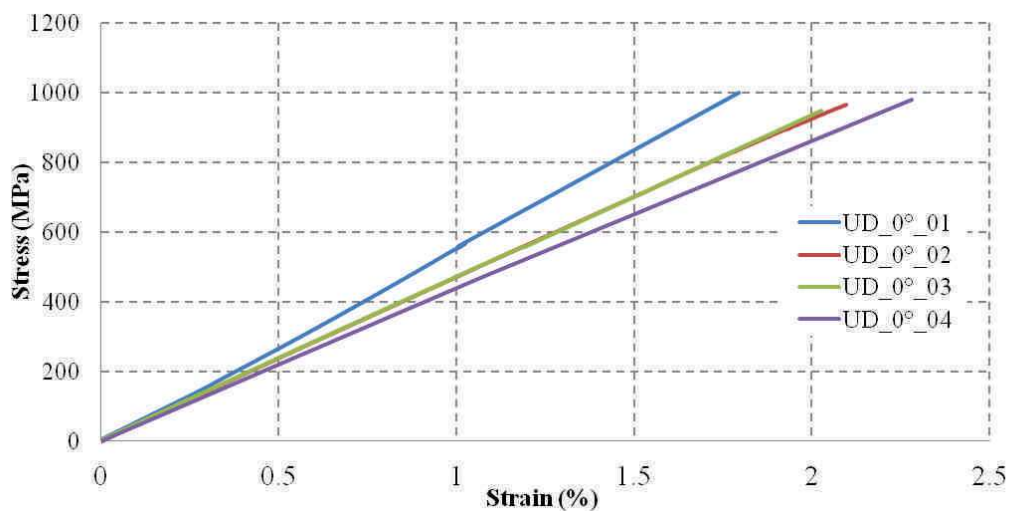


Figure 3-9: Longitudinal elastic properties of E-Glass/polyester lamina.

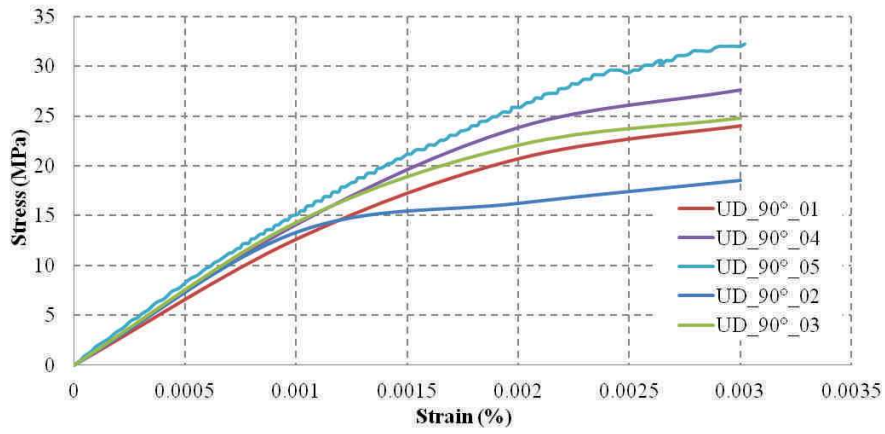


Figure 3-10: Transverse elastic properties of E-Glass/polyester lamina..

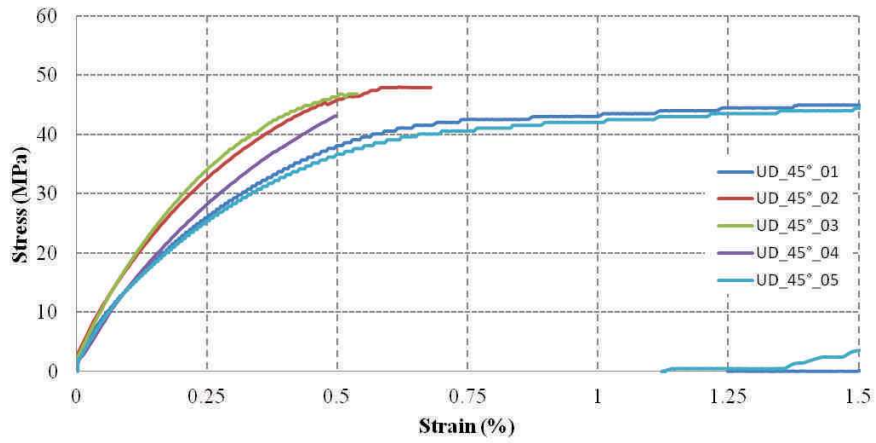


Figure 3-11: Shearing properties of E-Glass/polyester lamina.

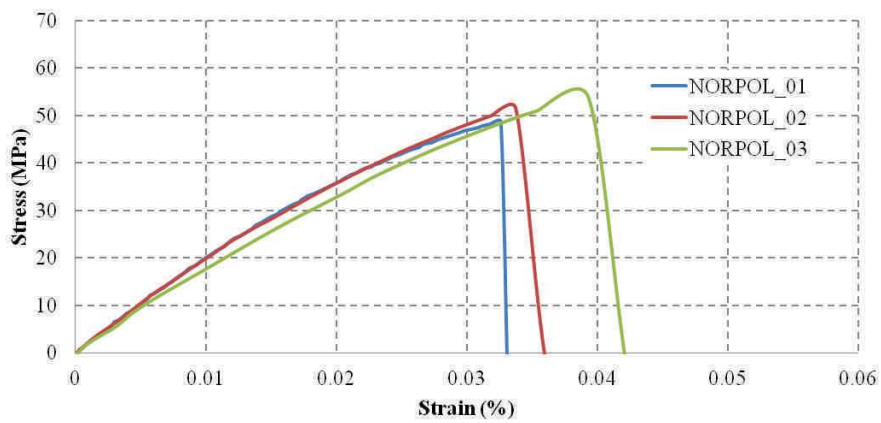


Figure 3-12: Tensile properties for NORPOL adhesive.

| Specimen | E_L (GPa) | E_{Lavg} | v_{LT} | v_{LT avg} | X (MPa) | X_{avg} (MPa) |
|-----------------|----------------------------|-------------------------|-----------------------|---------------------------|----------------|------------------------------|
| UD_0°_01 | 55.02 | 48.11 | 0.31 | 0.28 | 990.65 | 965.50 |
| UD_0°_02 | 46.24 | | 0.25 | | 934.80 | |
| UD_0°_03 | 47.24 | | 0.27 | | 956.55 | |
| UD_0°_04 | 43.98 | | 0.29 | | 980.00 | |
| IMA Dresden | | 45.78 | - | | 1021.3 | |

Table 3-11: Mechanical properties of composite in longitudinal direction

| Specimen | E_T (GPa) | E_{Tavg} | v_{TL} | v_{LT avg} | Y (MPa) | Y_{avg} (MPa) |
|-----------------|----------------------------|-------------------------|-----------------------|---------------------------|----------------|------------------------------|
| UD_90°_01 | 10.66 | 11.21 | 0.086 | 0.096 | 32.50 | 33.50 |
| UD_90°_02 | 10.4 | | 0.094 | | 34.60 | |
| UD_90°_03 | 11.04 | | 0.095 | | 37.20 | |
| UD_90°_04 | 11.21 | | 0.098 | | 31.40 | |
| UD_90°_05 | 12.76 | | 0.107 | | 31.80 | |
| IMA Dresden | | 10.21 | - | | 40.9 | |

Table 3-12: Mechanical properties of composite in transverse direction.

| Specimen | G_{LT} (GPa) | G_{LTavg} | S (MPa) | S_{avg} (MPa) |
|-----------------|-----------------------------|--------------------------|----------------|------------------------------|
| UD_45°_01 | 4.36 | 4.42 | 45.68 | 48.69 |
| UD_45°_02 | 8.52 | | 50.55 | |
| UD_45°_03 | 4.53 | | 48.37 | |
| UD_45°_04 | 4.52 | | 49.35 | |
| UD_45°_05 | 4.29 | | 49.50 | |
| IMA Dresden | | 4.21 | - | 35.30 |

Table 3-13: Mechanical properties of composite in shearing direction.

| Specimen | E (GPa) | E _{avg} (GPa) | ν | ν _{avg} | X _(NORPOL) (MPa) | X _{avg(NORPOL)} (MPa) |
|-----------|---------|------------------------|------|------------------|-----------------------------|--------------------------------|
| NORPOL_01 | 1.65 | 1.82 | 0.34 | 0.34 | 52.50 | 51.25 |
| NORPOL_02 | 1.83 | | 0.32 | | 51.29 | |
| NORPOL_03 | 1.83 | | 0.35 | | 49.96 | |

Table 3-14: Mechanical Properties of NORPOL vinyl-ester adhesive.

It may be noted for all the curves shown above that we consider only the first linear part of the curve for the calculation of mechanical properties.

Using the different laws for analytically calculating the properties in different direction we can measure their accuracy in measuring. The formulations of the laws are briefly shown below.

The Figure 3-9 - Figure 3-12 show the real stress strain curves until failure, of composite specimens in different orientations and of the NORPOL adhesive. The Table 3-11 - Table 3-14 summarize the material properties described by the above mentioned Figure 3-9 - Figure 3-12.

3.5.1.1 Law of mixtures

According to the law of mixtures the various engineering constants are calculated for the composite layups and are described as under.

$$E_l = E_f V_f + E_m V_m \quad 3-1$$

$$\frac{1}{E_t} = \frac{V_f}{E_f} + \frac{V_m}{E_m} \quad 3-2$$

$$\nu_{lt} = \nu_f V_f + \nu_m V_m \quad 3-3$$

$$\frac{1}{G_t} = \frac{V_f}{G_f} + \frac{V_m}{G_m} \quad 3-4$$

where the “ E_l ”, “ E_t ” and “ G_t ” are the longitudinal transverse and shearing young’s moduli respectively. “ V_f ” and “ V_m ” are the volume fractions of fibers and matrix. ν_{lt} , ν_f and ν_m , are the poisson’s ratio of the composite fiber and the matrix respectively.

3.5.1.2 Model of Hapin-Tsai

Similarly the law of Hapin – Tsai has been formulated to take into account the imprecision of the Law of mixtures in the transverse and shear directions. the details of this method can be found in (Halpin & Kardos, 1976).

$$\eta = \frac{\frac{M_f}{M_m} - 1}{\frac{M_f}{M_m} + \xi} \quad 3-5$$

$$\frac{M}{M_m} = \frac{1 + \xi \cdot \eta \cdot V_f}{1 - \eta \cdot V_f} \quad 3-6$$

where “ M ” is the modulus considered, “ η ” is the factor given in the 3-6 and “ ξ ” is the factor of reinforcement and is determined empirically. Its value typically varies from 1 to 2.

3.5.1.3 Model of Chamis

The model of Chamis is also another law for determining the material properties of composites from the mixture ratios (Chamis, 1984).

$$E_l = E_f V_f + E_m V_m \quad 3-7$$

$$E_t = \frac{E_m}{1 - \sqrt{V_f} \left(1 - \frac{E_m}{E_f}\right)} \quad 3-8$$

$$G_{lt} = \frac{G_m}{1 - \sqrt{V_f} \left(1 - \frac{G_m}{G_f}\right)} \quad 3-9$$

$$v_{lt} = v_f V_f + v_m V_m \quad 3-10$$

The different laws used for the prediction of composite properties are summarized in the Table 3-15.

| Theories | E_l (GPa) | E_t (GPa) | G_{lt} (GPa) | v_{lt} |
|--|--------------------------------|--------------------------------|---------------------------------|-----------------------|
| Law of Mixtures | 47.41 | 6.81 | 3.29 | 0,28 |
| Hapin-Tsai | 47.41 | 12.45 | 3.73 | - |
| Chamis | 47.41 | 11.24 | 4.24 | 0,28 |
| Experimental | 48.16 | 11.21 | 4,42 | 0,28 |
| % error compared to experimental values | | | | |
| Law of Mixtures | 1.5% | 39% | 25.6% | 0% |
| Hapin-Tsai | 1.5% | 9% | 15.6% | - |
| Chamis | 1.5% | 0.3% | 4.1% | 0% |

Table 3-15: Comparison of different analytical techniques to calculate the properties of composites in their orthotropic directions.

3.5.2 Flexural tests

The flexural tests are done to find out the properties of the sandwich core in tension. Since testing the foam core independently is very difficult due to its low strength. 100 x 25mm long beams are tested in flexion and upon applying simply supported beam theory the young' Modulus of the core material is found out.

For this purpose 3 different beams are tested. Each with a composite face thickness of 2mm and the foam core thicknesses of 10, 20 and 30mm. same as for the preceding case we will take only the first linear part of the curve for the calculation of mechanical properties.

The flexural tests (as well as tensile tests) are done at different cross head velocities to check the effect of loading rates on the mechanical properties, and up to which speeds the tests can be considered quasi-static as the reduction in test times is also one of the associated aims of this PhD work.



Figure 3-13: Sandwich specimens used for the characterization of the foam core (a) 10mm, (b) 20mm and (c) 30mm foam cores.

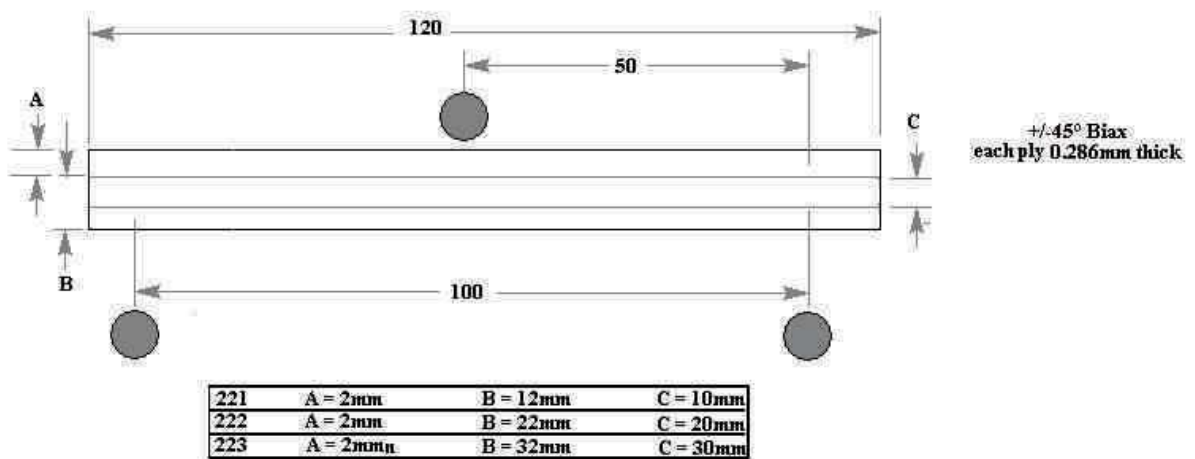


Figure 3-14: Schematic of flexion test specimens.

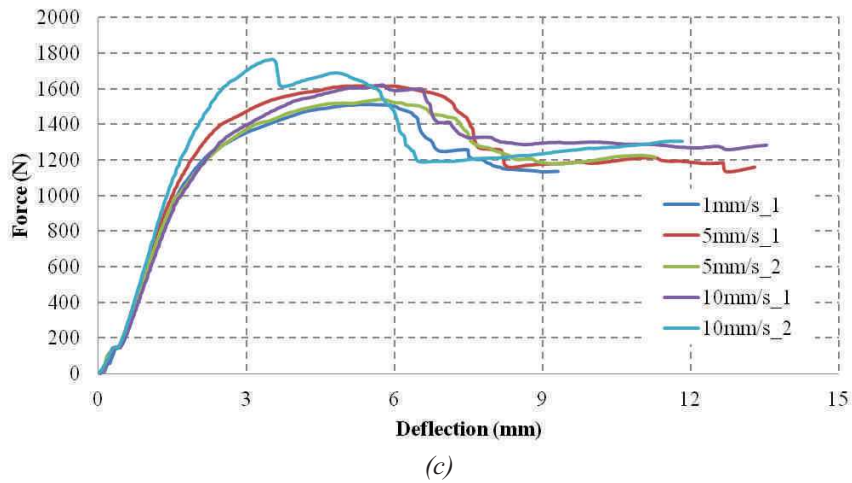
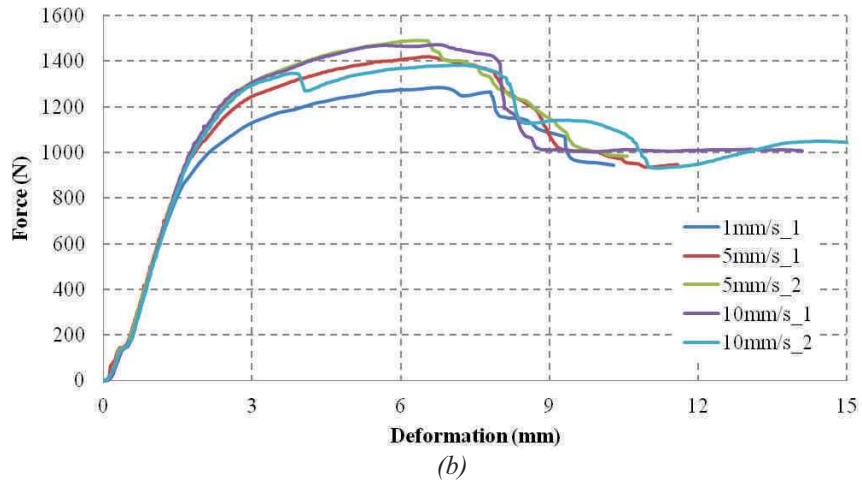
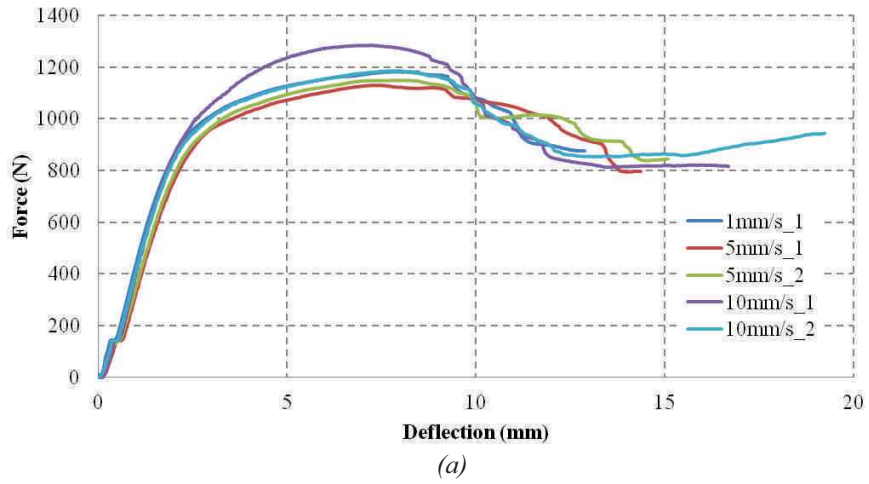


Figure 3-15: Force-displacement curves for (a) 10, (b) 20 and (c) 30mm thick core sandwich specimens.

For the calculation of the Young's modulus of the sandwich foam core we use the theory of simply supported beam in flexion. In general for a beam under 3 point bending, the deflection at its mid span is given by 3-11(Russel, et al., 2011).

$$(EI)_{eq} = \frac{PL^3}{48u} \quad 3-11$$

where “ u ” is the displacement of the mid span, “ P ” the load applied, “ L ” the span of the beam, “ $(EI)_{eq}$ ” is the equivalent flexural rigidity of the beam.

The “ $(EI)_{eq}$ ” is further given by the sum of the flexural rigidities of the constituents of the beam material.

$$E_c = \left[(EI)_{eq} - \frac{E_s b t_s^3}{6} - \frac{E_s b t_s (h_c + t_s)^2}{2} \right] \frac{12}{b h_c^3} \quad 3-12$$

where “ E_c ” is the young's modulus of the foam core, “ E_s ” the young's modulus of the face, “ b ” is the width of the specimens, “ t_s ” the thickness of the faces and “ h_c ” is the thickness of the foam core.

From the different specimens tested the calculated values of the core's young modulus are given in the Table 3-16.

| Specimen | “ h_c ” Foam Core thickness (mm) | “ E_c ” Foam core Young's Modulus (MPa) | |
|----------|--|---|-----------|
| | | Mean | Std. Dev. |
| 221 | 10 | 27.00 | 0.17 |
| 222 | 20 | 11.84 | 0.01 |
| 223 | 30 | 7.51 | 0.03 |

Table 3-16: Young's modulus of the foam core used in sandwich specimens.

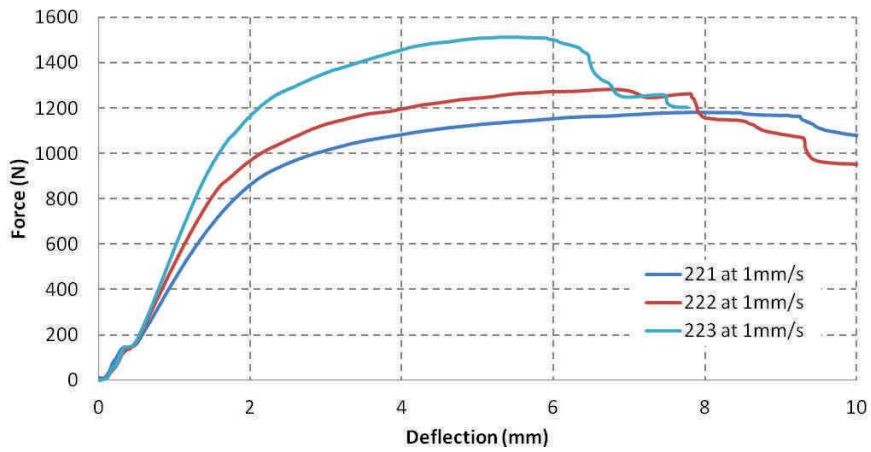
3.6 Discussion on results

1. The vacuum resin infusion process gives consistent quality of the composite panels fabricated.
2. The results correspond well when calculated analytically using the Chamis law of stratified plates. The errors for other laws seem to be on the higher side.
3. The determination of the Foam core's elasticity proved to be challenging from flexural tests, on close inspection it is revealed that there is a certain degree of resin penetrating the foam core during the infusion process which creates a different rigidity profile for each different thickness of the foam core thus giving different results, Figure 3-16. For the simulations the foam core stiffness calculated as is for each thickness would be used.

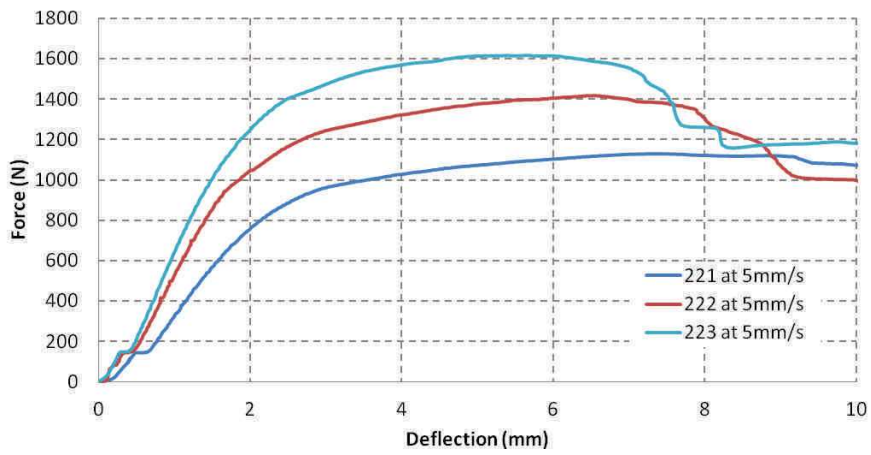


Figure 3-16: Presence of resin in the core of the sandwich.

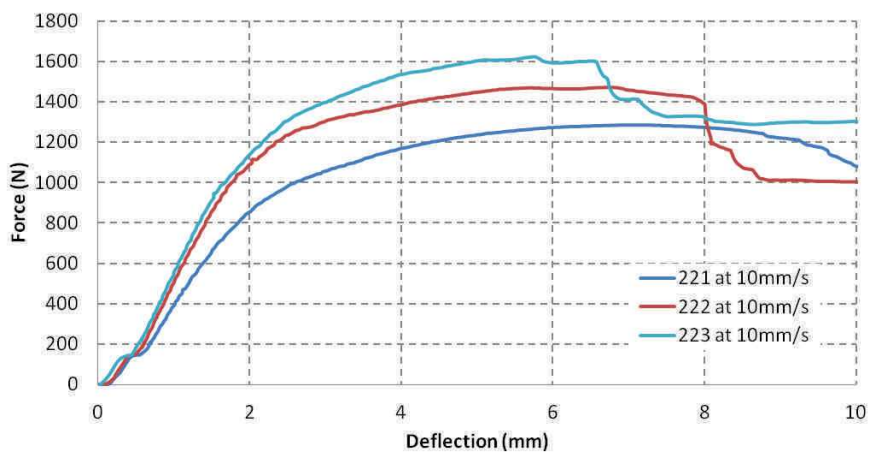
4. The Figure 3-17 shows the effect of thickness on the bending stiffness of the beam specimens. As can be seen by the specimens that the stiffness rises with a rise in the core thickness although the face thickness is the same for the three specimens. It is also important to note that the thicker specimens start to fail a lot later also, that is at a higher force and displacement.



a) Sandwich specimens under bending loaded at 1mm/s.



b) Sandwich specimens under bending loaded at 5mm/s.



c) Sandwich specimens under bending loaded at 10mm/s.

Figure 3-17: A comparison of the three sandwich thicknesses under bending.

3.7 Summary of test results

The mechanical tests done to determine the material properties are used as a precursor to every design process. Their reproducibility and accuracy is important. Although there have been some variations in the results they have been discussed in the corresponding sections. Here a summary of all the material properties determined shall be presented in Table 3-17.

| Material | Average Modulus of Elasticity/Shearing (E/G) (GPa) | Poisson's Ratio $\nu_{LT/TL \text{ avg}}$ | Stress at Failure X/Y (MPa) |
|--|---|---|------------------------------------|
| Uni-directional mat - Fiber direction - Transverse direction | $E_L = 48.11$ $E_T = 11.21$ | $\nu_{LT} = 0.280$ $\nu_{TL} = 0.096$ | X = 965.50 Y = 33.50 |
| Uni-directional mat in shearing direction (G_{LT}) | 4.42 | - | 48.69 |
| NORPOL Adhesive | 1.82 | 0.35 | 51.25 |
| PVC Foam core | (MPa) | | |
| - 10mm thickness | 27.00 | - | - |
| - 20mm thickness | 11.84 | | |
| - 30mm thickness | 7.51 | | |

Table 3-17: Summary of material properties in quasi-static conditions.

Chapter 4 Fracture Resistance in Monolithic Interfaces

Table of Contents

| | | |
|-------|--|-----|
| 4.1 | Mode I opening mode: Experimental setup..... | 112 |
| 4.2 | Analytical calculation of Strain energy release rate for Mode I (G_I)..... | 114 |
| 4.2.1 | MBT 1 (Modified Beam Theory 1)..... | 114 |
| 4.2.2 | MBT 2 (Modified Beam Theory 2)..... | 114 |
| 4.2.3 | CBBM (Compliance Based Beam Method)..... | 115 |
| 4.2.4 | CC (Compliance Calibration Method)..... | 115 |
| 4.2.5 | Calculation using J-integral | 116 |
| 4.2.6 | Virtual crack closure technique (VCCT) | 116 |
| 4.3 | Results of Mode I DCB tests | 120 |
| 4.4 | Mode II shearing mode: Experimental setup..... | 122 |
| 4.5 | Analytical calculation of Strain energy release rate for Mode II (G_{II})..... | 124 |
| 4.5.1 | Beam theory (BT) | 124 |
| 4.5.2 | Shearing Height theory (SH) | 125 |
| 4.5.3 | Compliance Calibration (CC) | 125 |
| 4.5.4 | Virtual Crack Closure Technique (VCCT) | 125 |
| 4.6 | Conclusions and Discussion | 127 |

Following the material properties characterization it is important to study the resistance of the materials under delaminations and also to ascertain their fracture resistance. The delamination of composite materials is one of the main sources of failure (Park, et al., 2014)(Damghani, et al., 2014)(Zhuang & Talreja, 2014)(Parida & Pradhan, 2014). During service the composite components undergo solicitations which can be normal and parallel to the fiber directions. These solicitations cause transverse and in plane stresses. This stresses therefore, when attain a certain value can cause the initiation of cracks. These fissures usually originate at internal defects present within the structure or singularities due to stress concentrations as a result of design. Furthermore the internal structure such as ply stacking and fiber configurations such as weaved mats can be a source of initiation as well (Carvalho, et al., 2011).

The most common type of failure in composite is that of delamination (Li, et al., 2014), (Pereira & De Morais, 2004). This is usually due to the fact that the matrix is a lot weaker in strength and stiffness than the fibers hence under the applied loads they tend to fail first. The same in tension matrix failures apply to in-plane compression; where the load is applied in the plane of the plies. Kink band formations cause tensile stresses in the matrix thus causing it to fail, eventually giving rise to damage nuclei (Camanho, et al., 2014).

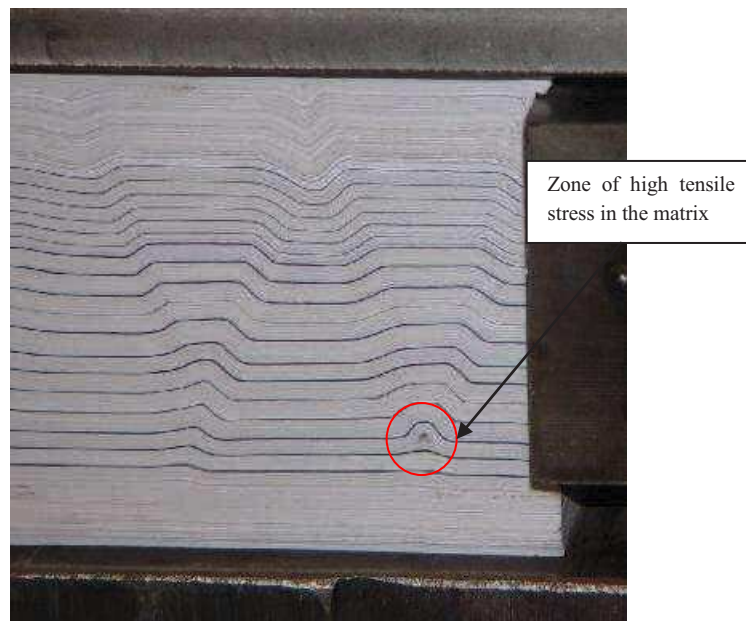


Figure 4-1: Kink band formation demonstrated with the help of a stack of paper under in-plane compressive load.

Since the failure as explained initiates at the matrix phase and for the most part, the crack propagation rests in the matrix phase hence the accurate characterization of these interfaces is necessary. The interfaces are characterized in normal and parallel to the ply planes. The mode normal to the stacking plane is called the opening, peeling or simply first mode (Mode I). The mode parallel to the stacking planes is called in plane and transverse shearing modes respectively (Mode II) and (Mode III). Although for most practical purposes for orthotropic composite plies the mode II and mode III are considered to be the same.

4.1 Mode I opening mode: Experimental setup

As explained above the mode I failure is the result of opening up of the interfaces where the load applied is normal to the plies. For characterizing the materials in mode I type failure modes it is important to isolate the crack propagation to take place under a force normal to the stacking planes. For this purpose a standard double cantilever beam (DCB) specimen is proposed. This specimen consists of a rectangular piece of composite with a crack of a specified length already introduced to provoke cracking in a know location. Usually the crack is at the mid height of the specimen, but can be to one side as well in order to accommodate for manufacturing constraints.

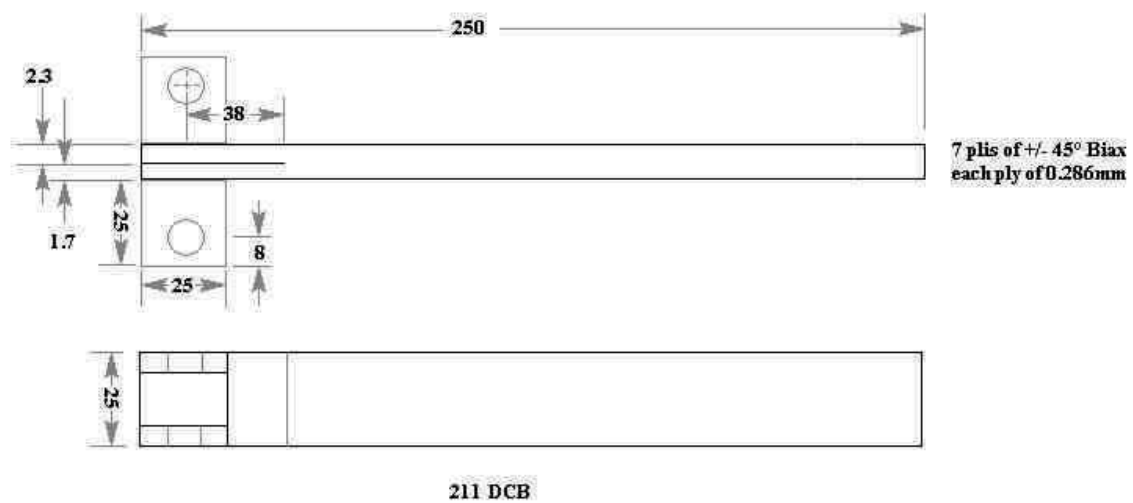


Figure 4-2: DCB specimen used for Mode I fracture resistance tests.

The specimens are cut from a composite plate laid up with 0.572mm thick 7 layers. A 20 μ m thick Teflon film is inserted to create the 52.5mm long pre-crack. U shaped pieces machined from mild steel are then glued to the 2 half cantilevers to be pulled by the traction machine. Pins are driven through holes, drilled in the U blocks to act as pivots ensuring rotational degree of freedom.

The tests are done on a tensile test machine loading the specimen at a rate of 1mm/s. this ensures quasi static crack growth. The crack length is recorded using a CCD camera which can take photographs at a given frequency for example 1 Hz (seen that the crack growth is rather slow), Figure 4-3. The typical image recorded by the camera is shown in Figure 4-4.

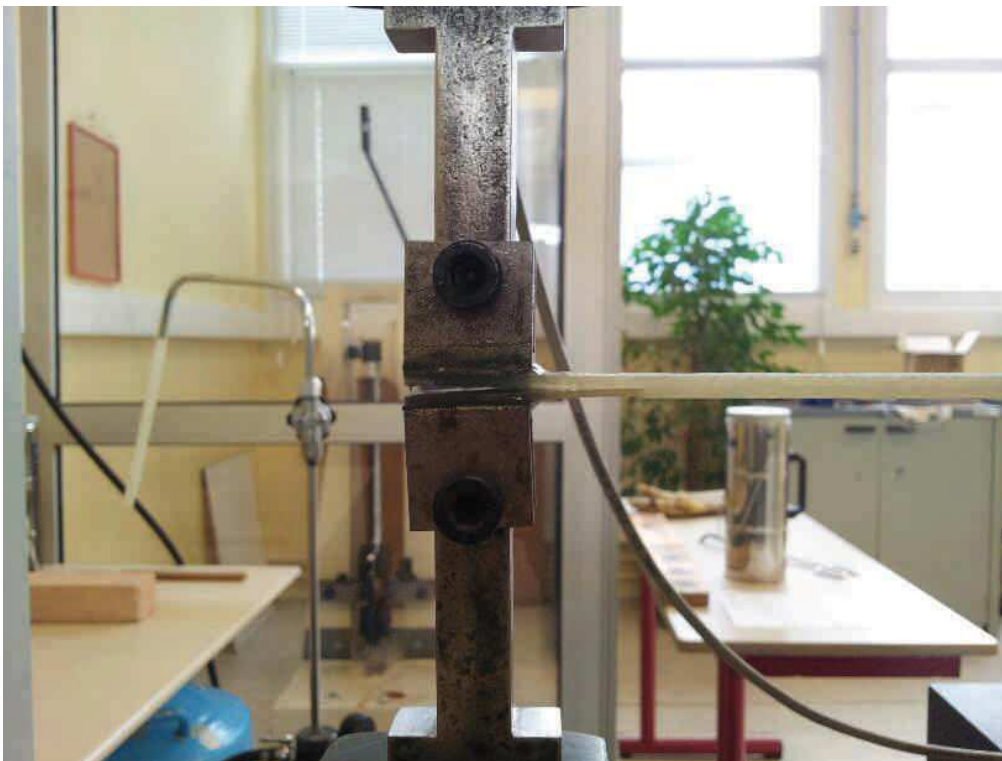


Figure 4-3: Experimental setup to calculate/measure the crack growth in DCB tests.

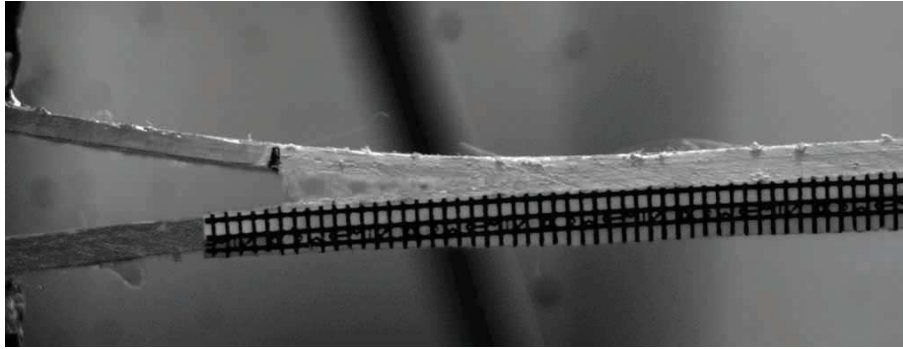


Figure 4-4: Image used for the identification of crack tip

4.2 Analytical calculation of Strain energy release rate for Mode I (G_I)

Based on the beam theory there are different analytical approaches that have been formulated for the calculation of the strain energy release rate in mode I " G_I ".

4.2.1 MBT 1 (Modified Beam Theory 1)

The modified beam theory models the DCB specimen as a simple cantilever beam based on the Timoshenko beam theory:

$$G_I = \frac{3P\delta}{2ba} \quad 4-1$$

where " P " is the load to give a " δ " displacement, " b " is the specimen width and " a " is the crack length. This theory calculates the G_I considering the compliance of the cracked beam. This basic law is easy to implement but can be inaccurate.

4.2.2 MBT 2 (Modified Beam Theory 2)

In the modified beam theory 2 we take into account the rotation of the crack front as well as the partially cracked interface to account for the fiber bridging.

$$G_I = \frac{3P\delta}{2b(a + |\Delta|)} \quad 4-2$$

This theory takes into account the rotation of the crack tip. Also it was seen during the experiments that the DCB specimens underwent large displacements to propagate the crack, hence a correction factor should be included to take into account the turning effects of the U blocks.

$$N = 1 - \left(\frac{l_2}{a}\right)^3 - \frac{9}{8} \left[1 - \left(\frac{l_2}{a}\right)^2\right] \frac{l_1 \delta}{a^2} - \frac{9}{35} \left(\frac{\delta}{a}\right)^2 \quad 4-3$$

$$F = 1 - \frac{3}{10} \left(\frac{\delta}{a}\right)^2 - \frac{3}{2} \left(\frac{l_1 \delta}{a^2}\right) \quad 4-4$$

where “P” is the force applied, “δ” the displacement of the two beams, “b” is the width of the specimen, “a” the length of the crack, “Δ” is the crack front rotation correction factor, “l₁” is the distance of the loading pin to the mid plane of the specimen and “l₂” is the distance from the center of the pin to the end of the U-block.

4.2.3 CBBM (Compliance Based Beam Method).

This method is formulated based on the apparent crack length. Here we consider the modified flexural stiffness of the beam specimen:

$$\bar{E}_f = \frac{8(a_0 + |\Delta|)^3}{bh^3} \left(C_0 - \frac{12(a_0 + |\Delta|)}{5bhG_{xy}} \right) \quad 4-5$$

Hence the value of G_I can be calculated as under.

$$G_I = \frac{6P^2}{b^2h} \left(\frac{2}{\bar{E}_f} \left(\frac{a_e}{h}\right)^2 + \frac{1}{5G_{xy}} \right) \quad 4-6$$

$$a_e = a_0 + |\Delta| \quad 4-7$$

This method has the advantage of not having to monitor the crack length as it propagates through the specimen.

4.2.4 CC (Compliance Calibration Method).

With the compliance calibration method the compliance is considered to be a function of the crack beam. The formulation for G_I is thus given by 4-8.

$$G_I = \frac{nP^2 R a^{n-1}}{2b} \quad 4-8$$

where “ R ” is anti natural log of the intersection of a plot between “ $\ln(C)$ ” and “ $\ln(a)$ ”.

4.2.5 Calculation using J-integral

One other method for the calculation of “ G_I ” is the use of J-Integral. The J-integral calculated at the crack tip gives the Mode I fracture resistance when applied to a DCB test. In general the J-Integral for a DCB type test can be calculated using the displacement of the two cantilever beams and the angle of rotation of the beam ends (Gunderson, et al., 2007).

$$J_I = \frac{2b}{P} \sin(\theta/2) \quad 4-9$$

where “ θ ” is the included angle between the two half beams.

4.2.6 Virtual crack closure technique (VCCT)

All the above formulations whether they require crack lengths to be measured or not depend on various factors for their accuracy. These can be the position of the pre-crack, the position of clamping points etc. Therefore a method known as VCCT has been developed which is coupled to a finite element model to directly get information about the forces and displacements at nodes near and at the crack tip to get the most accurate results. The theory has been already treated in detail here its implementation using ABAQUS finite element code will be shown. For simplification the law used to calculate G_I are given in the equation as follows:

$$G_I = \sigma_{M3}(w_U - w_L)/2 \quad 4-10$$

where “ σ_{M3} ” is the maximum stress at the crack tip, “ $w_{U,L}$ ” is the nodal displacements of node U and L in the horizontal direction.

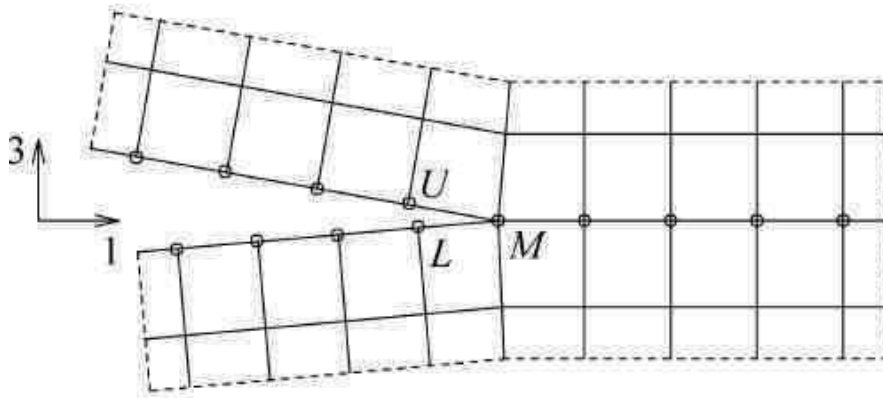


Figure 4-5: Schematic for VCCT used in equation 4-10.

For the calculations of G_I , DCB model is created in ABAQUS. The model has the same type of stratification and material properties to simulate the true rigidity. The model is modified for each crack length that corresponds to actual experimental observations. The forces experienced at each of these crack lengths are applied to record the displacements of the nodes U and L, and the stress along the vertical direction at node M, to be used in the VCCT law, Figure 4-5.

| Force (N) | Displacement (mm) | Crack length (mm) |
|-----------|-------------------|-------------------|
| 56.00 | 5.916 | 39.00 |
| 53.00 | 6.489 | 41.00 |
| 54.00 | 11.015 | 47.00 |
| 47.00 | 12.334 | 49.00 |
| 47.00 | 12.417 | 54.00 |
| 47.00 | 12.501 | 55.00 |
| 39.00 | 14.663 | 57.00 |
| 40.00 | 15.001 | 62.00 |
| 41.00 | 15.416 | 64.00 |
| 32.00 | 23.498 | 66.00 |
| ... | ... | ... |

Table 4-1: Crack lengths to be modeled corresponding to forces applied.

Table 4-1 shows an example of a specimen modeled with different crack lengths and the forces experienced at these crack lengths by the specimen.

VCCT: Mesh sensitivity

The first step in any finite element modeling technique is the study of the mesh size and type on the results being calculated. For this purpose a mesh sensitivity analysis is done where mesh size is reduced until a globally acceptable maximum or minimum value of the relevant parameter is found. The DCB specimens are modeled in plain stress two dimensional models. The mesh sensitivity is studied in the first phase to see the global behavior, if it meets the experimental results in terms of rigidity. Then the mesh at the crack front is refined to see the effect of different crack tip meshes on the calculated values of “ G_I ”. The mesh distribution is shown in the Figure 4-6.

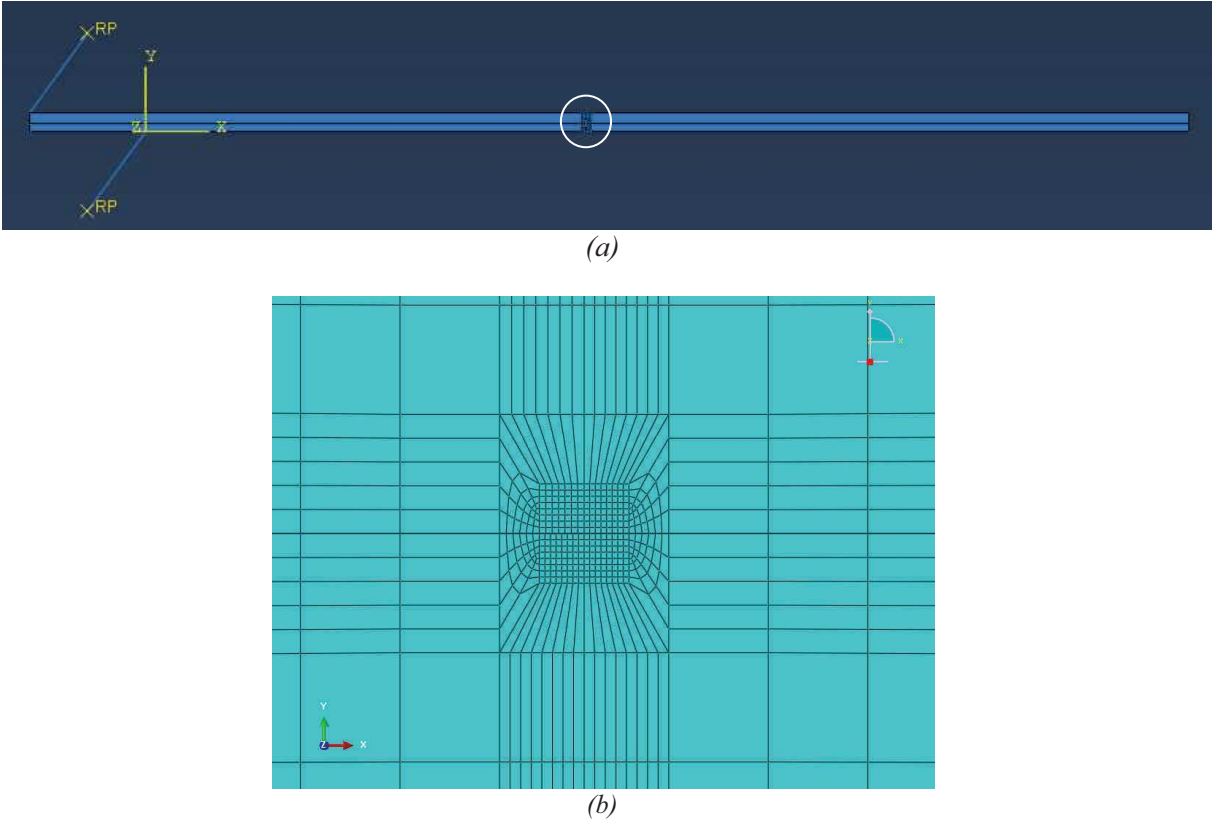


Figure 4-6 : Mesh distribution for the DCB specimen: (a) Complete specimen and (b) Zoom on the crack tip.

Once the model is meshed with a starting mesh size it boundary conditions at one of the experimentally measured displacement, crack length curves are applied. The mesh size is varied to find the maximum or minimum value of the measured quantity. For our analysis a crack length of 120mm for an opening of 37.331mm is modeled which corresponds to an actual experiment and the value G_I is calculated. The Figure 4-7 shows the results of the sensitivity analysis.

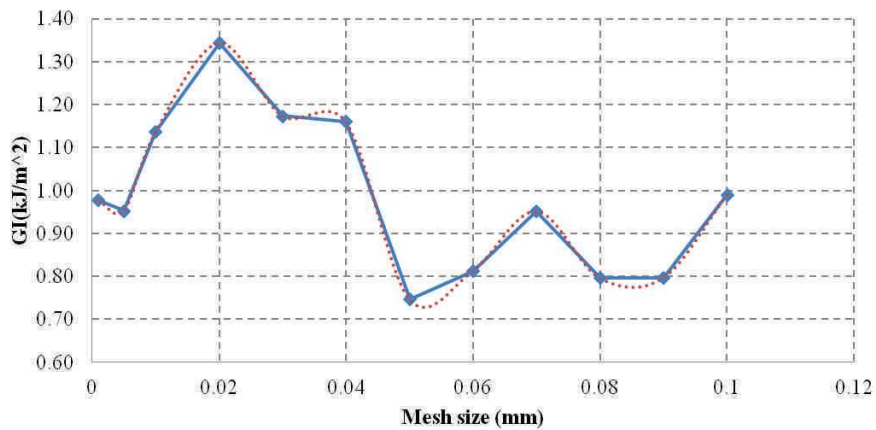


Figure 4-7: Mesh sensitivity for the calculation of G_I , mesh size as on crack tip.

The sensitivity graph shows that at a mesh size of 0.05mm at the crack tip the value measured is the least hence a global convergence can be seen. There can be seen several local convergent points but none as remarkable as that for 0.05mm mesh size. Mesh sizes have been varied from 0.001mm to 0.1mm where any smaller or larger values would either make the model too heavy computationally or would make it too coarse to be practically usable.

Calculating VCCT

Once a suitable mesh size is found out the beam is modeled with different crack lengths and each crack length is modeled with its opening as the boundary condition. The stress at the crack tip is measured using FE results and the vertical displacements of the nodes adjacent to the crack also noted as shown in Figure 4-5.

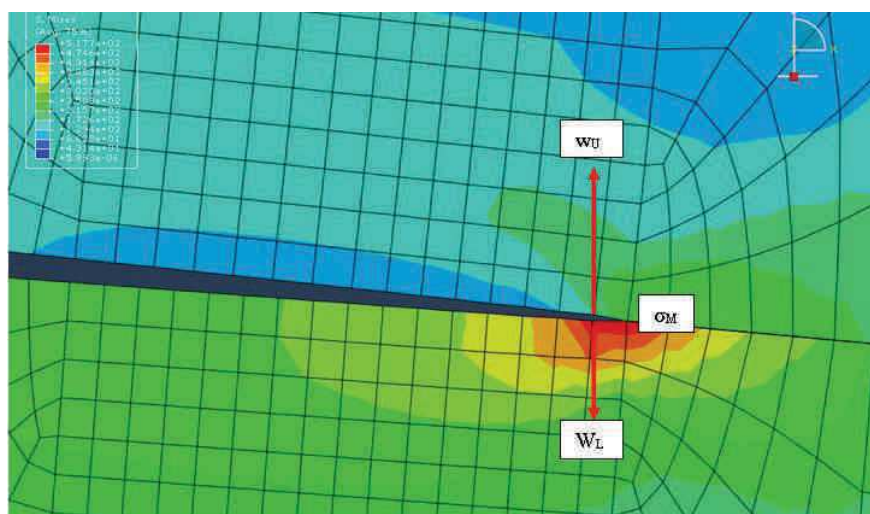


Figure 4-8: Nodal variables for calculating G_I

Employing the equation 4-10 the values of “ G_I ” can be calculated.

4.3 Results of Mode I DCB tests

In the experiments done for determining the mode I fracture resistance the crack length is monitored using a CCD camera. A lens with a sufficiently high magnification is used to get a close up view of the crack tip. The crack tip is measured manually for each load step applied by the tensile test machine. A scale can be fixed on the specimen to record the length of the crack as it advances during the test.

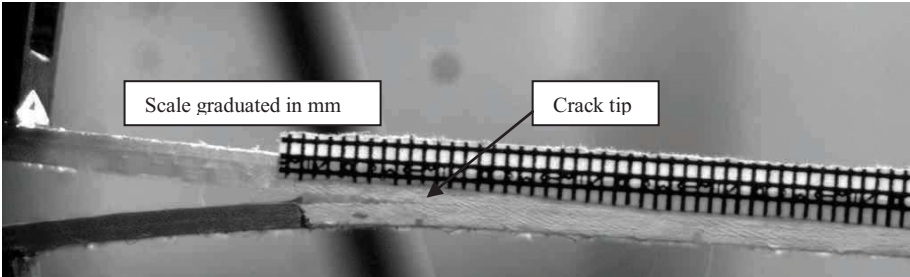


Figure 4-9: Typical image taken by the CCD camera for tracking the crack length.

The tests are done on 3 specimens for calculating the G_I using the crack tracking methods and another one test done for measuring the rotation of the two half beams. For this last method the camera is trained to photograph just the opening ends of the two half beams.

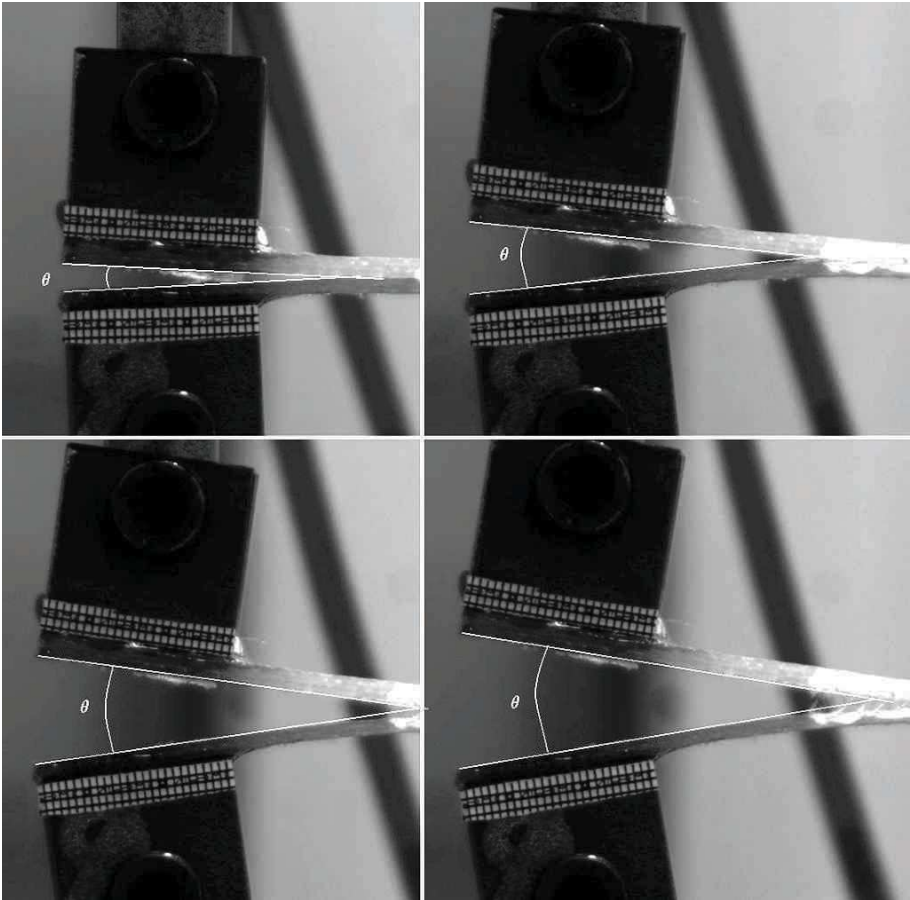


Figure 4-10: Included angle of the two half beams at each applied load step.

The results from the various methods presented in equations 4-2 to 4-10 are presented in Table 4-3, while Table 4-2 the mode I SERR at initiation “ G_{II} ” is summarized.

| Theory | MBT 1 | | MBT 2 | | CC | | VCCT | |
|--------|-------------------------------|---------|-------------------------------|---------|-------------------------------|---------|-------------------------------|---------|
| | G_{II} (kJ/m ²) | | G_{II} (kJ/m ²) | | G_{II} (kJ/m ²) | | G_{II} (kJ/m ²) | |
| | Mean | Std Dev |
| | 0.365 | 0.133 | 0.424 | 0.161 | 0.359 | 0.146 | 0.547 | 0.214 |

Table 4-2: Summary of the Mode I G_{II} results at crack initiation for three (3) specimens.

| Theory | MBT 1 | | MBT 2 | | CC | | VCCT | | J-Integral | |
|---------------|-------------------------------|---------|-------------------------------|---------|-------------------------------|---------|-------------------------------|---------|-------------------------------|-------|
| | G_{Ic} (kJ/m ²) | | G_{Ic} (kJ/m ²) | | G_{Ic} (kJ/m ²) | | G_{Ic} (kJ/m ²) | | G_{Ic} (kJ/m ²) | |
| | Mean | Std Dev | 1.285 | 0.280 |
| 1 | 1.223 | 0.216 | 1.091 | 0.373 | 0.958 | 0.216 | 1.015 | 0.136 | | |
| 2 | 1.255 | 0.233 | 1.134 | 0.321 | 1.060 | 0.238 | 1.022 | 0.113 | | |
| 3 | 0.888 | 0.183 | 0.674 | 0.242 | 0.819 | 0.224 | 0.822 | 0.076 | | |
| Result | | | | | | | | | | |
| | Mean | Std Dev | | |
| | 1.122 | 0.203 | 0.966 | 0.254 | 0.946 | 0.121 | 0.953 | 0.113 | 1.285 | 0.280 |

Table 4-3: Summary of Mode I G_{Ic} results during crack propagation calculated for the laminated specimen.

To explain Table 4-3, consider for example the Figure 4-11 shown below.

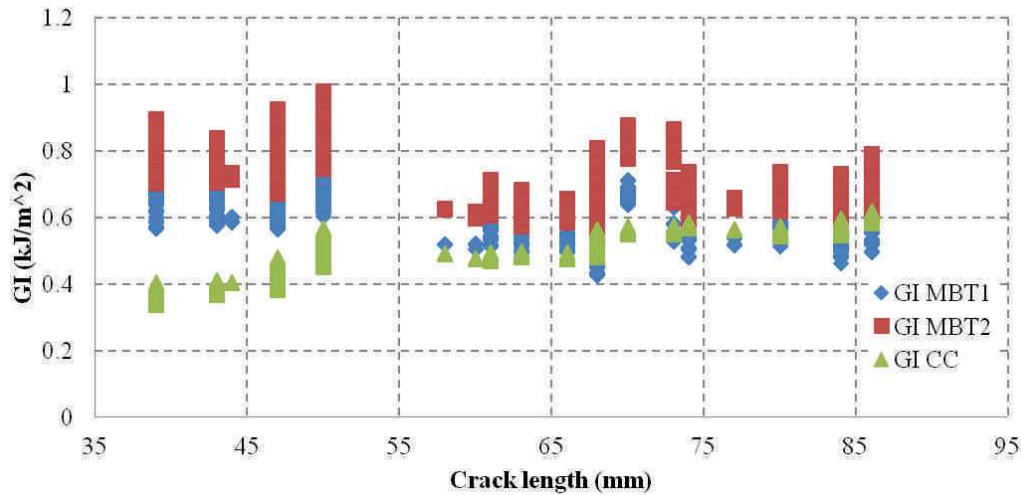


Figure 4-11: Evolution of G_I against crack propagation

In the Figure 4-11, it can be seen that the value of G_I is either higher or lower in the first part for short crack, it is the region where the crack begins to propagate hence a lot of energy is already stored which releases in a progressive manner. Hence only the region where the energy released stabilizes to a more uniform value is considered. In the Table 4-3, the mean and standard deviation of all of the G_{Ic} vs. Crack length curve is taken for each of the specimens during their crack propagation, while in the results part only the mean and standard deviation of the all the specimens taken at once are shown. These results values will be used in further calculations and modeling.

4.4 Mode II shearing mode: Experimental setup

For the mode II shearing mode strain energy release rate (SERR) measurement an end notched beam specimen (ENF) has been used. These ENF specimens are simply supported beams under three points flexion. The pre crack at the end of the specimen thus propagates under shearing of the top and bottom part of the half beams. For facilitating the sliding of the two half beams one over the other a glass fiber is inserted in the pre-crack to relieve the pressure, reducing friction and to give a rolling surface again to reduce the “stiction” between the two half beams.

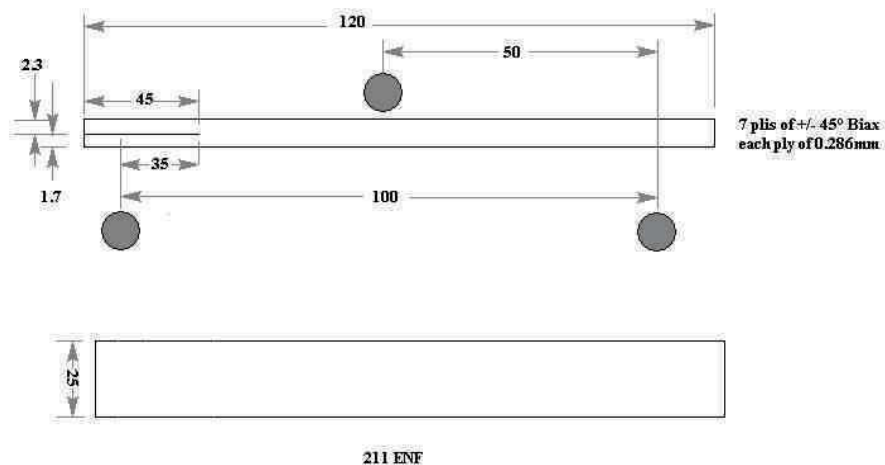


Figure 4-12: ENF specimen used for Mode II fracture resistance tests.

With ENF specimens it is important to note a stable propagation of cracks. The crack propagation depends on the ratio of the pre-crack length to the span length of the beam specimen. Hence different ratios for different lengths have been used at first to get stable crack propagation.

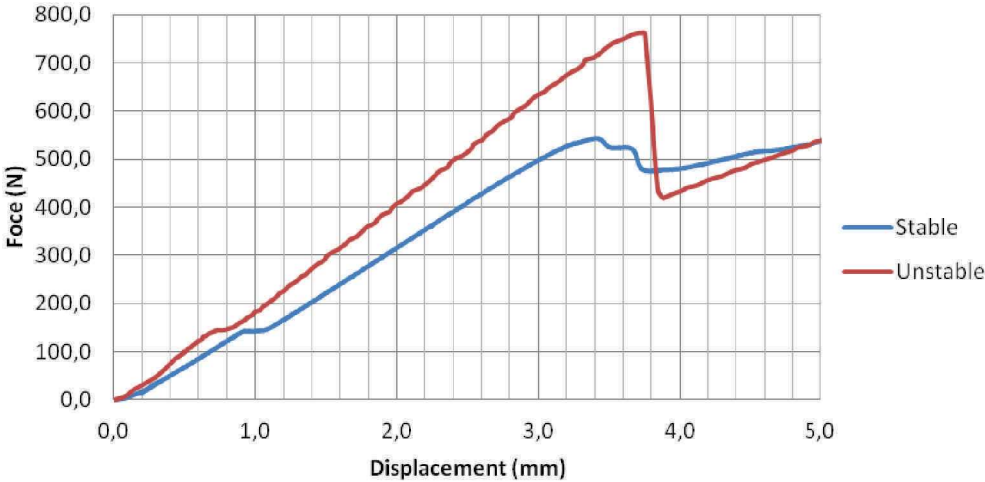


Figure 4-13 : Force-displacement curves for stable and unstable crack growth.

Figure 4-13 shows a comparison of two such experiments that were done on different pre-crack to span length ratios of 0.35 and 0.25, respectively. The ratio “ a_0/L ” is usually set to 0.25 at the start (specified by ASTM standards) but can later be modified seen that the propagation is stable or not. For example in our case it can be clearly seen that the 0.25 ratio was insufficient for stable propagation. In general, different ratios were tried and a summary is shown below in Table 4-4.

| Specimen | Pre crack “ a_0 ” (mm) | Specimen span length “ L ” (mm) | “ a_0/L ” Ratio | Propagation type |
|--------------|--------------------------|-----------------------------------|-------------------|-------------------------------|
| ENF-100-4-25 | 25 | 100 | 0.25 | Unstable |
| ENF-100-4-35 | 35 | 100 | 0.35 | Stable |
| ENF-100-4-40 | 40 | 100 | 0.40 | Stable |
| ENF-120-4-25 | 25 | 120 | 0.21 | Unstable |
| ENF-120-4-42 | 42 | 120 | 0.35 | Stable |
| ENF-150-4-25 | 25 | 150 | 0.17 | Unstable |
| ENF-150-4-60 | 60 | 150 | 0.40 | Stable |
| ENF-220-4-25 | 25 | 220 | 0.11 | No propagation until buckling |

Table 4-4: Crack propagation at different pre-crack to span length ratios.

From the discussion above it can be deduced that for this type of material and beam thickness and “ a_0/L ” ratio of 0.35 – 0.40 is where we observe smooth and stable crack propagation.

The stability of the crack propagating can also be determined analytically. The equations relating to the stability show that for a stable propagation, the ratio of “ dG/da ” should be non positive.

$$\left. \frac{dG}{da} \right|_p = \frac{P^2}{2b} C'' \leq 0$$

4-11

$$\left. \frac{dG}{da} \right|_u = \frac{u^2}{2bC^2} \left(C'' - \frac{2C'^2}{C} \right) \leq 0$$

where “ C ” is the compliance and C' is the derivative of “ C ” with respect to crack length. The two conditions are given at constant force and constant displacement crack propagation. Although in real practice one rarely sees such pure fracture modes. The equations 4-11 can be calculated to determine a crack length ratio that would give stable crack propagation.

$$C = \frac{L^3 + 12a^3}{384E_{11}I}, \quad u = \frac{PL^3}{384E_{11}I} + \frac{16\sqrt{E_{11}I}}{P^2} \left(\frac{bG_{II}}{3} \right)^{3/2}; 0 \leq a \leq L/2$$

4-12

$$C = \frac{L^3 - 3(L-a)^3}{96E_{11}I}, \quad u = \frac{PL^3}{96E_{11}I} - \frac{16\sqrt{E_{11}I}}{P^2} \left(\frac{bG_{II}}{3} \right)^{3/2}; 0 \leq a \leq L/2$$

The equations 4-12 are derived from the Euler-Bernouli’s beam theory. They give the compliance and the displacement of the point of application of force ($L/2$ in our case). (Allix, et al., 1995).

4.5 Analytical calculation of Strain energy release rate for Mode II (G_{II})

Based on the beam theory there are different analytical approaches that have been formulated for the calculation of the strain energy release rate in mode II “ G_{II} ”.

4.5.1 Beam theory (BT)

In general the mode II SERR is given by $G = \frac{P^2}{2b} \frac{dC}{da}$ where C can be calculated from the equations 4-12.

$$G_{II} = \frac{9a^2P^2}{16E_{11}b^2h^3}$$

4-13

4.5.2 Shearing Height theory (SH)

$$G_{II} = \frac{9a^2 P^2}{16E_{11} b^2 h^3} \left(1 + 0.2 \frac{E_1}{G_{13}} \left(\frac{h}{a} \right)^2 \right) \quad 4-14$$

where “ G_{13} ” is the shearing modulus which takes into account the shearing deformation of the crack front in the calculation of the Mode II SERR.

4.5.3 Compliance Calibration (CC)

$$G_{II} = \frac{1.5ma^2 P^2}{b^2} \quad 4-15$$

where “ m ” is a coefficient which depends on the function “ $C = f(a^3)$ ”.

4.5.4 Virtual Crack Closure Technique (VCCT)

The VCCT can be used for any fracture SERR calculation in any mode. In general the 4-10 holds true for Mode II fracture also with a modification in the direction of displacements and stresses taken.

$$G_{II} = \tau_{M1}(v_U - v_L)/2 \quad 4-16$$

with the “ v ” being the horizontal displacements of nodes “ u ” and “ l ”. The steps previously explained are taken in the modeling of the specimens including a mesh sensitivity analysis both for the load-displacement curves of the specimens globally as well as the local sensitivity of the mesh at the crack tip.

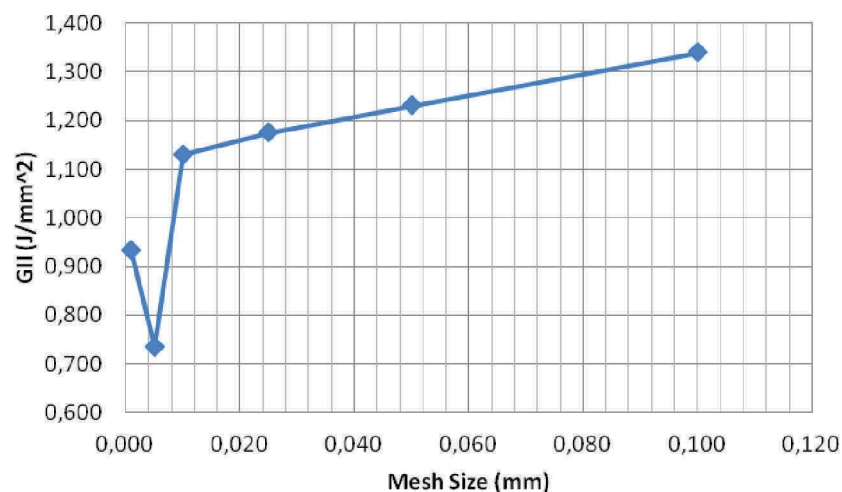


Figure 4-14: Mesh sensitivity for calculating G_{II} SERR.

Figure 4-14 gives a global minimum at a mesh size of 0.005mm. Therefore this mesh size will be used for all subsequent VCCT calculations.

| Theory | BT | | SH | | CC | | VCCT | |
|---------|--------------------------------|---------|--------------------------------|---------|--------------------------------|---------|--------------------------------|---------|
| | G_{Iii} (kJ/m ²) | |
| | Mean | Std Dev |
| a_0/L | | | | | | | | |
| 0.35 | 0.556 | 0.036 | 0.561 | 0.036 | 0.558 | 0.036 | 0.460 | 0.042 |
| 0.40 | 0.509 | 0.126 | 0.513 | 0.128 | 0.510 | 0.127 | 0.485 | 0.009 |

Table 4-5: Summary of the Mode I G_{Iii} results at crack initiation for three (3) specimens.

| Theory | BT | | SH | | CC | | VCCT | | |
|---------|--------------------------------|---------|--------------------------------|---------|--------------------------------|---------|--------------------------------|---------|-------|
| | G_{Iic} (kJ/m ²) | | |
| | Mean | Std Dev | |
| a_0/L | | | | | | | | | |
| 0.35 | 1 | 0.786 | 0.204 | 0.791 | 0.205 | 0.789 | 0.205 | 0.651 | 0.187 |
| | 2 | 0.578 | 0.100 | 0.582 | 0.100 | 0.580 | 0.100 | 0.474 | 0.018 |
| | 3 | 0.825 | 0.099 | 0.830 | 0.099 | 0.827 | 0.099 | 0.721 | 0.580 |
| 0.40 | 1 | 0.555 | 0.099 | 0.559 | 0.092 | 0.557 | 0.093 | 0.551 | 0.057 |
| | 2 | 0.710 | 0.114 | 0.714 | 0.114 | 0.713 | 0.114 | 0.533 | 0.190 |
| | | | | | | | | | |
| | Mean | Std Dev | |
| | 0.691 | 0.121 | 0.695 | 0.122 | 0.693 | 0.121 | 0.586 | 0.099 | |

Table 4-6: Summary of Mode I G_{Iic} results during crack propagation calculated for the laminated specimen.

4.6 Conclusions and Discussion

The results as summarized in Table 4-6 show a good correspondence in the different methods. There are some refinements seen in the results when more comprehensive theories other than simple beam theories are used. One point to consider here also is the utilization of techniques that do not require the tracking the crack lengths. For example the J-integral technique which has shown a good correspondence to the results.

However there are a certain number of inaccuracies that still exist. These are evident in the difference between analytical theories and the VCCT method. The reasons can be summarized as under:

1. The beams are seen to be undergoing a lot of flexion (in ENF) and hence do not remain in the small deformation problem field. With a maximum deflection of about 6% of the span length and the crack initiating at a deflection of about 3% deflection. These curvatures can cause inaccurate results. For DCB results the flexion is well above 20% at initiation of cracking.
2. There is a fair amount of fiber bridging taking place in the DCB specimens. Although this may not be evident by seeing the force displacement curves as the machine sensitivity may not sufficiently high, but close inspection of the beam profiles show fibers being broken at each step in the advance of the crack. Although the cracks are not open in the ENF specimens so fiber bridging cannot be viewed, but it is still present.

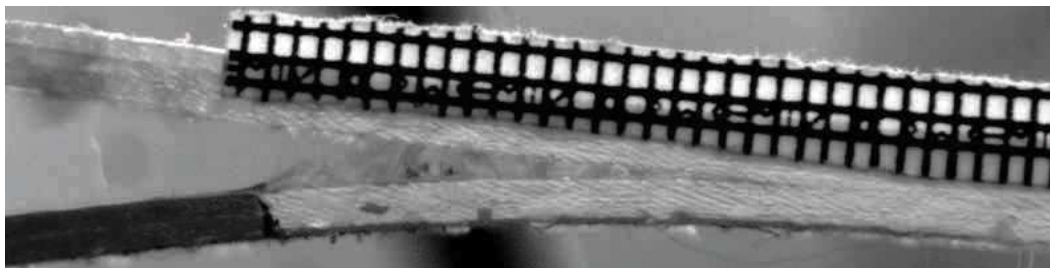


Figure 4-15: Unbroken fibers connecting the lower and upper half beams well behind the crack tip.

3. In ENF tests friction between the crack surfaces was a dominating problem. So much so that in initial tests a stable propagation of cracking was very difficult to obtain. It was viewed that as soon as the machine loaded to overcome the static friction the crack propagated in a very abrupt manner hence not giving ample propagation points for the calculation of G_{II} . This problem was rectified to a certain extent using a glass fiber bead inserted in between the two half beams to allow the surfaces to roll on each other instead of sliding. This is one of the principal reasons why the G_{II} calculated through VCCT is slightly lower than for analytical methods because in VCCT friction is not considered between the sliding surfaces.
4. The effect of a curved crack tip is also present which can cause a certain inaccuracy in the results. The crack tips especially for the ENF tests were seen to be either slightly convex or turned towards an edge, Figure 4-16.

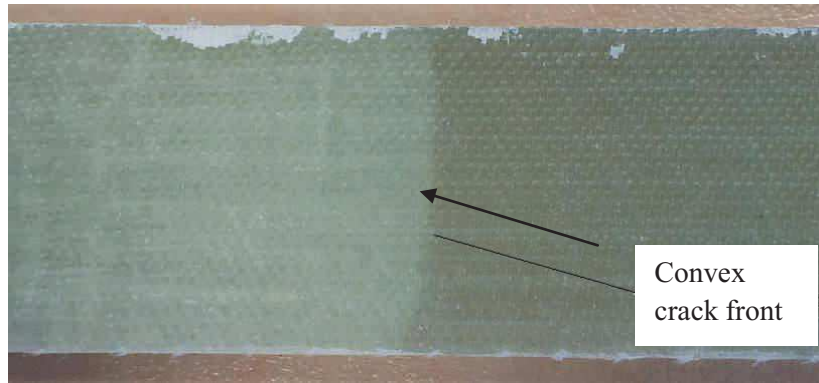


Figure 4-16: Crack front in DCB specimens.

5. The pre-crack is also not always at the mid height of the beam. But since one end of the beam is free therefore there are no forces parallel to the crack plane being induced in the beam.

$$M_T = M_1 + M_2 + \frac{h_1 + h_2}{2} N_1 \quad 4-17$$

where “ M_T ”, “ M_1 ” and “ M_2 ” is the total moment and the moments in the upper and lower half beams, “ N_1 ” is the force parallel to the crack plane and “ h_1 ” and “ h_2 ” are the half beam thicknesses. Since the force “ N_1 ” = 0, and that as M_1 and M_2 are equal hence there is no or very little mode mixing.

6. Manufacturing and fabrication discrepancies are another source of inaccuracy. When using thick composite plies in the order of 1000+ gm/mm² ply waviness and voids can occur. These cause the crack to propagate in a non-uniform manner thus giving higher or lower than expected SERR values.

Chapter 5 Fracture Resistance in Bonded Interfaces and Sandwich Structures

Table of Contents

| | |
|---|-----|
| 5.1 Mode I opening mode: Experimental setup | 131 |
| 5.2 Analytical calculation of Strain energy release rate Mode I (G_I) | 133 |
| 5.2.1 MBT 1 (Modified Beam Theory 1)..... | 134 |
| 5.2.2 MBT 2 (Modified Beam Theory 2)..... | 134 |
| 5.2.3 CC (Compliance Calibration Method)..... | 135 |
| 5.2.4 Virtual crack closure technique (VCCT) | 135 |
| 5.3 Results of Mode I DCB tests | 137 |
| 5.4 Mode II shearing mode bonded beams: Experimental setup | 143 |
| 5.5 Analytical calculation of Strain energy release rate Mode II (G_{II}): Bonded Beams..... | 145 |
| 5.5.1 Beam theory (BT) | 148 |
| 5.5.2 Compliance calibration (CC) | 148 |
| 5.6 Results of Mode II ENF tests for bonded beams | 148 |
| 5.7 Mode II shearing mode of sandwich beams: Experimental setup | 149 |
| 5.8 Analytical calculation of Strain energy release rate Mode II (G_{II}): Sandwich Beams | 151 |
| 5.9 Mode II SLB results for Sandwich beams | 152 |
| 5.10 Observations on Results | 153 |

Continuing with the fracture resistance of materials the resistance of bonded and sandwich structures will be discussed here. Wind turbine blades like most composite structures are bonded with adhesives. They are manufactured in several different components then they are assembled together with the help of adhesives. In the particular case for wind turbine blades it should be noted that, due to the quality of manufacturing, the adhesive thicknesses vary from position to position, Figure 5-1. One often finds thicknesses upwards of 35mm. therefore the effect of thickness on the behavior of the bonded joints is a very important factor to be studied. In addition, there are locations within the wind turbine blade where sandwich type structures are used to increase the rigidity. The sandwich core varies in both thickness and density Figure 5-2. However for our experiments we have used the same density of foam core used for the most part of the turbine blade. Different thicknesses of the foam cores are used to determine the effect of scale on the SERR properties.

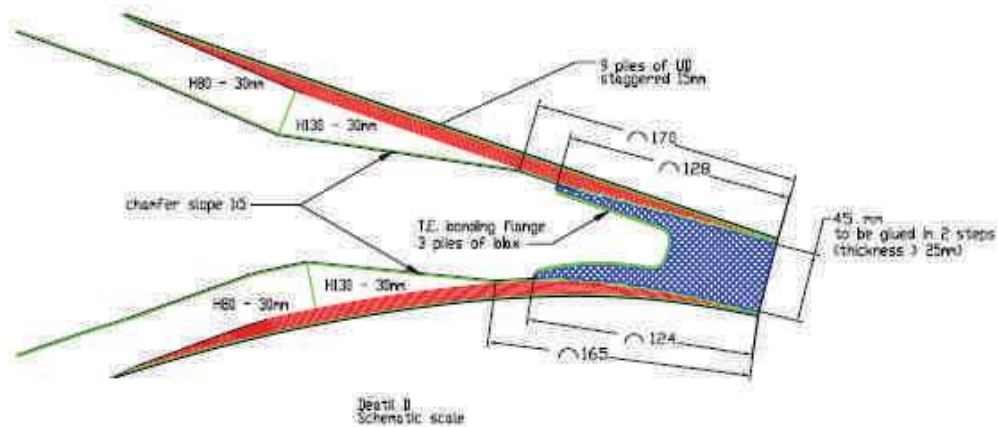


Figure 5-1: Example of a bonded joint at the trailing edge of the wind turbine (Nass & Wind, s.d.).

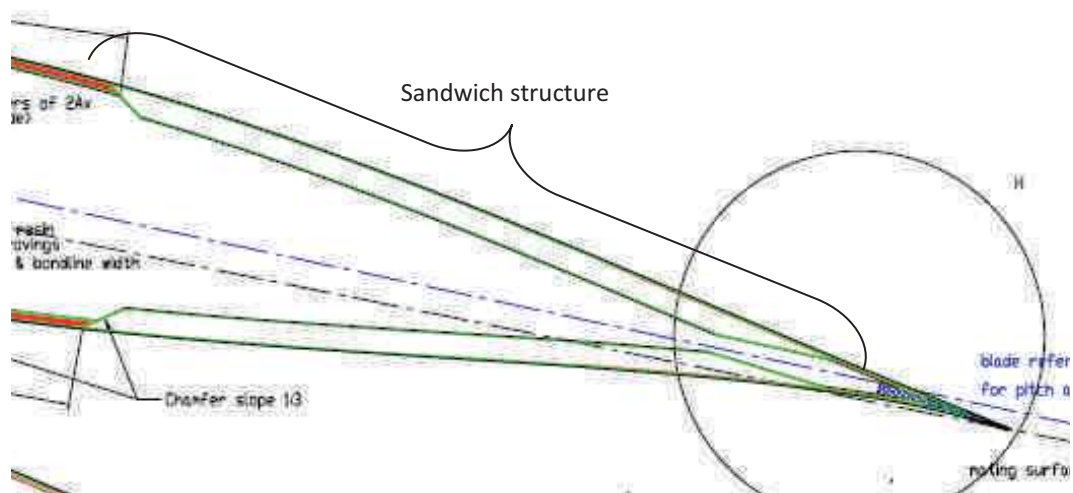
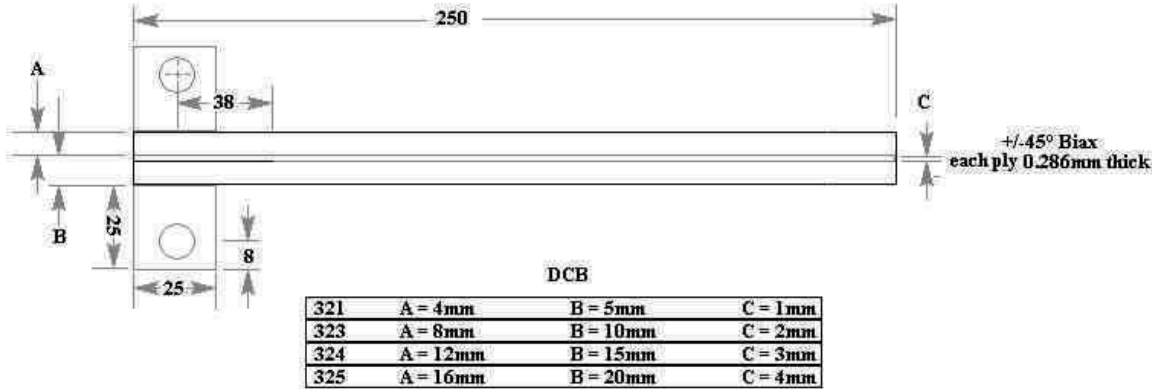


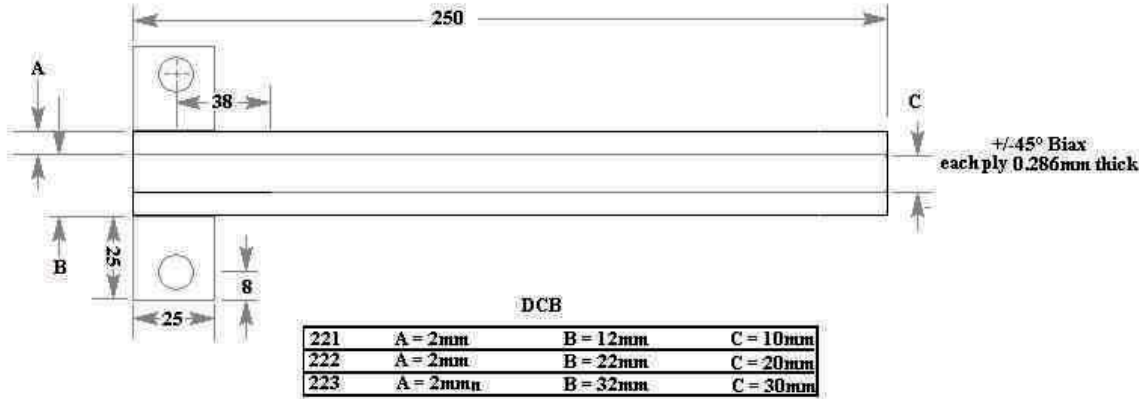
Figure 5-2: Sandwich structures used to stiffen the unsupported spans of the wind turbine blade sections.

5.1 Mode I opening mode: Experimental setup

The specimens used for the characterization of adhesive bonds and the sandwich structure core-face interfaces are shown schematically in the Figure 5-3. The adhesive bonded specimens are made up of a 45° Biax type composite bonded together with varying thicknesses of NORPOL adhesive. The faces plates for the composite sandwich specimens are equally made up of 45° Biax type composites. The faces for all of the specimens are 2mm thick.



(a) Bonded composite beams



(b) Sandwich structures

Figure 5-3: DCB specimen used for Mode I fracture resistance tests.

The Figure 5-4 shows the different types of DCB specimens used for the characterization of interfaces. The interfaces in question are bonded ones and between the foam core and face plates for the sandwich structures.



(c) Bonded composite beams



(a) Sandwich structures

Figure 5-4: DCB specimen used for Mode I fracture resistance tests.



Figure 5-5: Experimental setup to calculate/measure the crack growth in DCB tests.

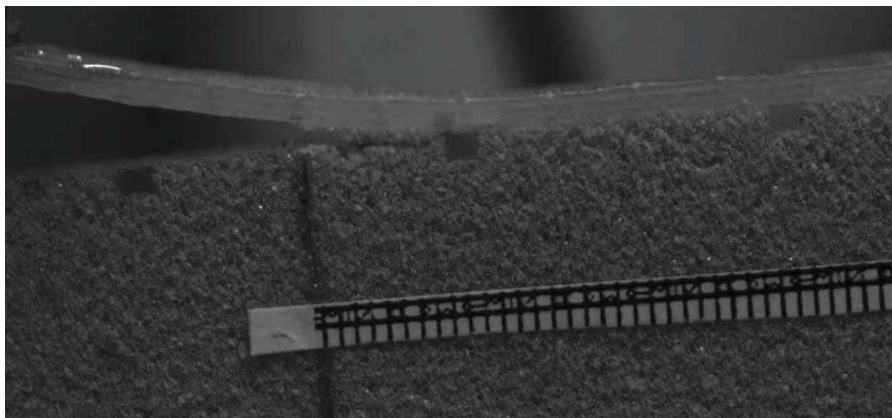


Figure 5-6: Image used for the identification of crack tip.

The Figure 5-4Figure 5-5 shows the experimental setup for determining the mode I SERR, a DCB sandwich specimen is being loaded in tension and in the Figure 5-6 the recording of the CCD camera is shown to determine the crack length.

5.2 Analytical calculation of Strain energy release rate Mode I (G_I)

The mode I crack resistance calculations are done using MBT1, MBT2 and CC formulations (See Chapter 4). Their mathematical representations are given here under for reminding. The formulations require the load and displacement data as well as the crack length for each of the specimens.

5.2.1 MBT 1 (Modified Beam Theory 1)

This theory is based on the classical Timoshenko beam theory. (as explained in chapter 4, here it is shown as a reminder).

$$G_I = \frac{3P\delta}{2ba} \quad 5-1$$

5.2.2 MBT 2 (Modified Beam Theory 2)

$$G_I = \frac{3P\delta}{2b(a + |\Delta|)} \quad 5-2$$

This theory takes into account the rotation of the crack tip. Also it was seen during the experiments that the DCB specimens underwent large displacements to propagate the crack, hence a correction factor should be included to take into account the partially separated interfaces. For this correction we shall treat the problem using elastic foundation analysis as developed in (Avilés & Carlsson, 2008).

$$\Delta = \left[a^3 + \frac{3aF_1}{2\lambda^2} + \frac{3F_2}{2\lambda^3} \right]^{1/3} - a \quad 5-3$$

$$F_1 = \frac{\sinh^2(\lambda c) + \sin^2(\lambda c)}{\sinh^2(\lambda c) - \sin^2(\lambda c)} + 2a\lambda \frac{\sinh(\lambda c)\cosh(\lambda c) + \sin(\lambda c)\cos(\lambda c)}{\sinh^2(\lambda c) - \sin^2(\lambda c)} \quad 5-4$$

$$F_2 = \frac{\sinh(\lambda c)\cosh(\lambda c) - \sin(\lambda c)\cos(\lambda c)}{\sinh^2(\lambda c) - \sin^2(\lambda c)} + a\lambda \frac{\sinh^2(\lambda c) + \sin^2(\lambda c)}{\sinh^2(\lambda c) - \sin^2(\lambda c)}$$

where “P” is the force applied “δ” the displacement of the two beams, “b” is the width of the specimen, “a” the length of the crack, “Δ” is the crack front rotation correction factor, “c” is the length of the partially unbounded interface in general taken as (L-a). For the definition of λ refer to equations 5-5.

$$\lambda = \sqrt[4]{\frac{6E_c}{E_f h_f^3 h_c}} \quad 5-5$$

where “E_c” is the modulus of elasticity of the core “E_f” is the flexural modulus of the face plate, “h_f” is the thickness of the face and “h_c” is the thickness of the core.

5.2.3 CC (Compliance Calibration Method)

With the compliance calibration method the compliance is considered to be a function of the crack beam. The formulation for G_I is thus given by:

$$G_I = \frac{nP^2 R a^{n-1}}{2b} \quad 5-6$$

where “ R ” is anti natural log of the intersection of a plot between “ $\ln(C)$ ” and “ $\ln(a)$ ”.

5.2.4 Virtual crack closure technique (VCCT)

The Figure 5-7 shows the simplified view of a VCCT analysis used for the determination of mode I SERR. The nodes “ U ” and “ L ” are displaced through “ w_U ” and “ w_L ” in the vertical direction which is then used in the equation 5-7 to determine G_I (mode I SERR). Figure 5-8 shows the same technique being implemented in Finite Element Analysis. The figure shows in different orders of magnification the mesh used for this analysis.

$$G_I = \sigma_{M3}(w_U - w_L)/2 \quad 5-7$$

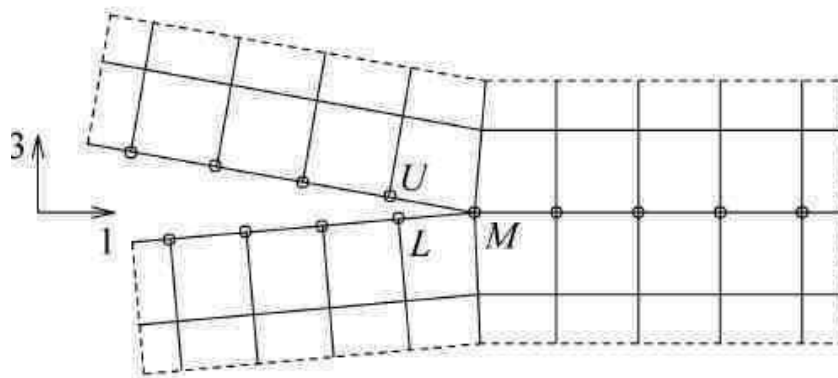


Figure 5-7: Schematic for VCCT used in equation 5-7.

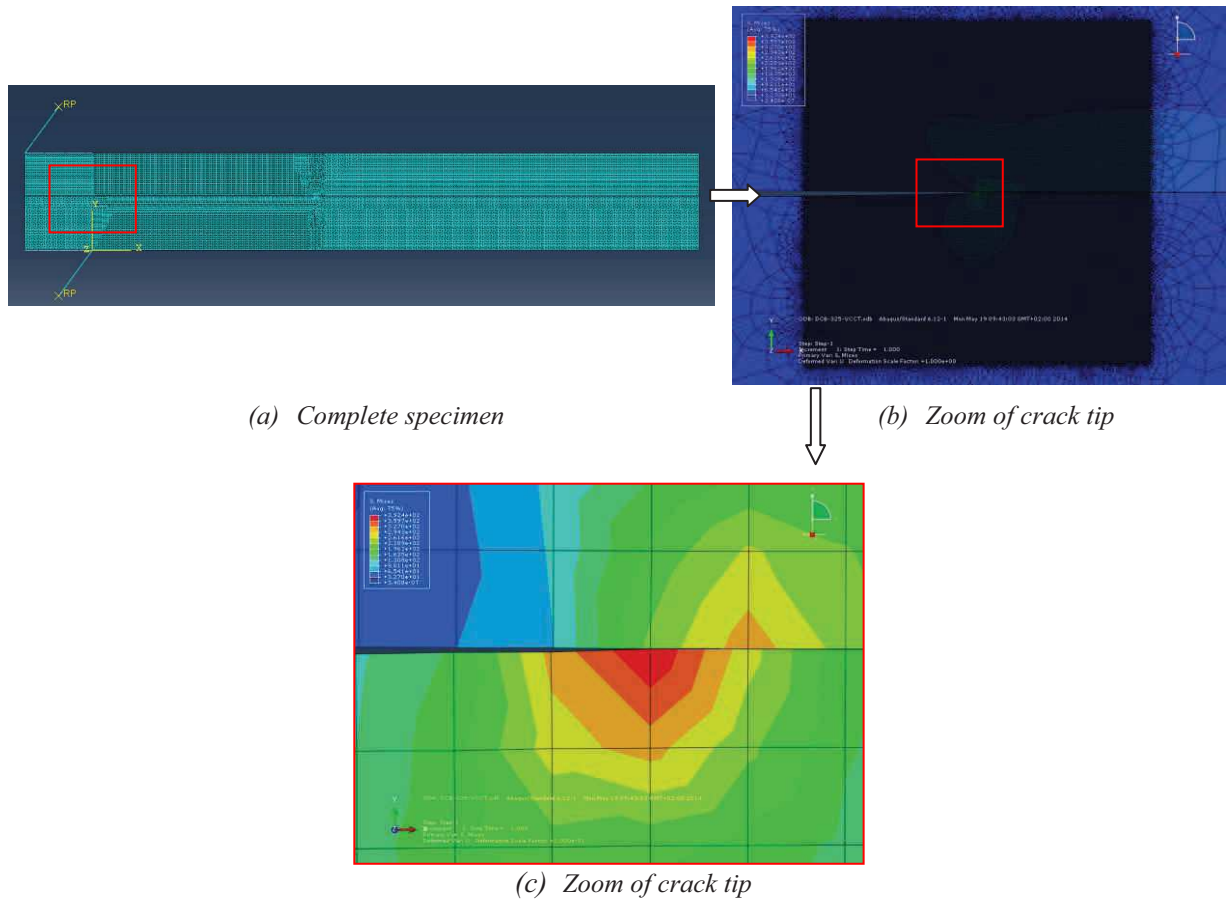


Figure 5-8: Mesh distribution for the DCB specimen..

5.2.4.1 Calculating VCCT

The SERR is calculated by taking into account the stress at the crack front and the displacements at the neighboring nodes as shown in the Figure 5-9.

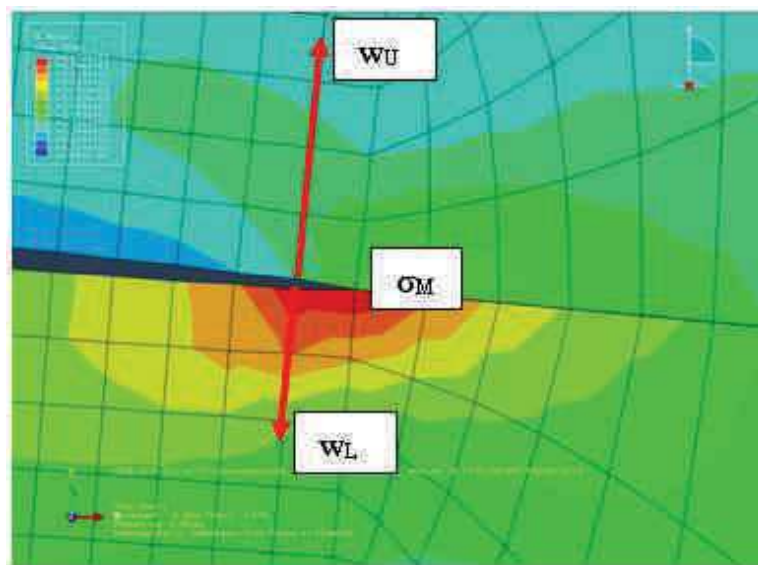


Figure 5-9: Nodal variables for calculating G_I .

5.3 Results of Mode I DCB tests

The results of the DCB tests will be discussed in this section. The Figure 5-10 shows the crack tip as photographed at each step along its propagation through a CCD camera. Figure 5-11 shows the force displacement curves for the different types of specimens tested to determine the mode I SERR, at initiation " G_{Ii} " and " G_{Ic} ".

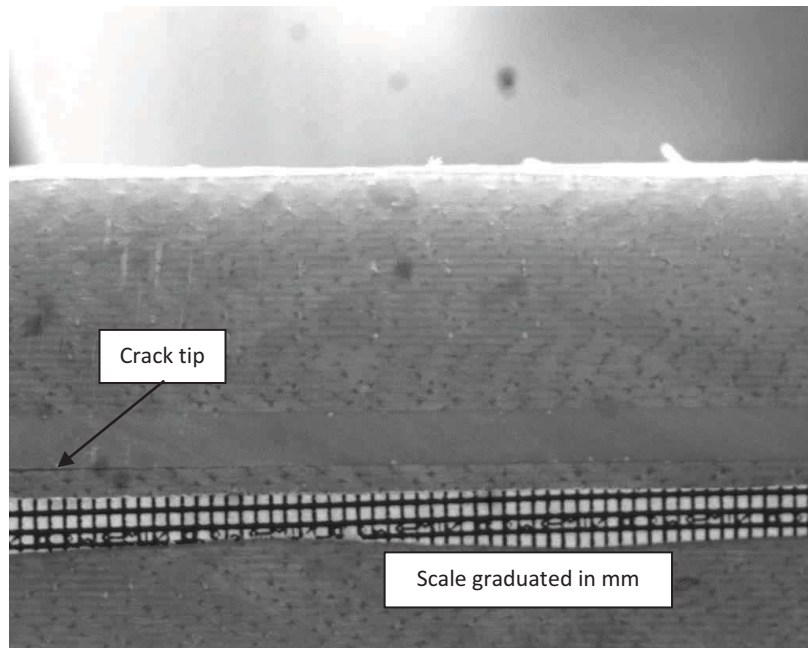
The force displacement curves show variations between different tests. The reproducibility of these tests can be seen to vary from specimen to specimen. It can be further seen that the reproducibility is rather weak on the case of specimen type 325 as compared to the type 321. Therefore a definite link of reproducibility is seen with the specimen thickness.

To explain these reproducibility variations refer to the Figure 5-11c for example. The curves can be divided into two parts. The first is the bending of the half beam up to initiation of crack and the later is the evolution of force with the growing crack length. It can be seen that the crack initiation G_{Ii} is different for each specimen. This is attributed to the stiffness of the specimens and the pre-crack quality. The stiffer the specimen the variations at the crack initiation increase due to crack tip quality (shape, length and surface adhesion). The second part of the curve which determines the G_{Ic} at the propagation stage has very little variation from specimen to specimen and the curves can be seen to have the same curvature throughout this region.

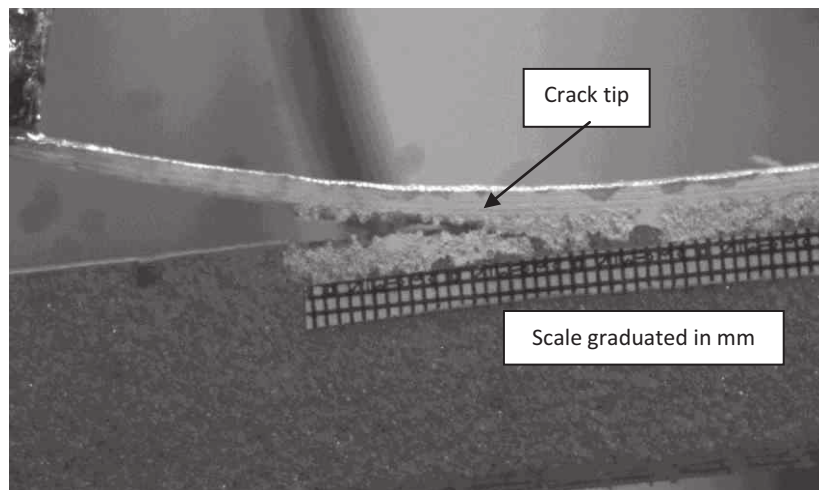
This reflected in the Table 5-1 and Table 5-2 where we can see that the standard deviation in the results is higher for initiation than for propagation. The variation of the G_{Ii} at the initiation stage is pronounced for stiffer specimens and is reflected in the compliance calibration calculations. It can be seen that as at the initiation the bending on the specimen is very low hence the compliance calibration technique over corrects the compliance and hence we see very low G_{Ii} values calculated with the help of compliance calibration.

The Table 5-3 and Table 5-4 for the sandwich specimens where the face is lower in overall stiffness the variations in the G_{Ii} is a lot lower as shown by their standard deviations.

The results from the various methods presented in 5-2 to 5-7 are presented in Tables 5-1 and 5-2 and in Figure 5-11.

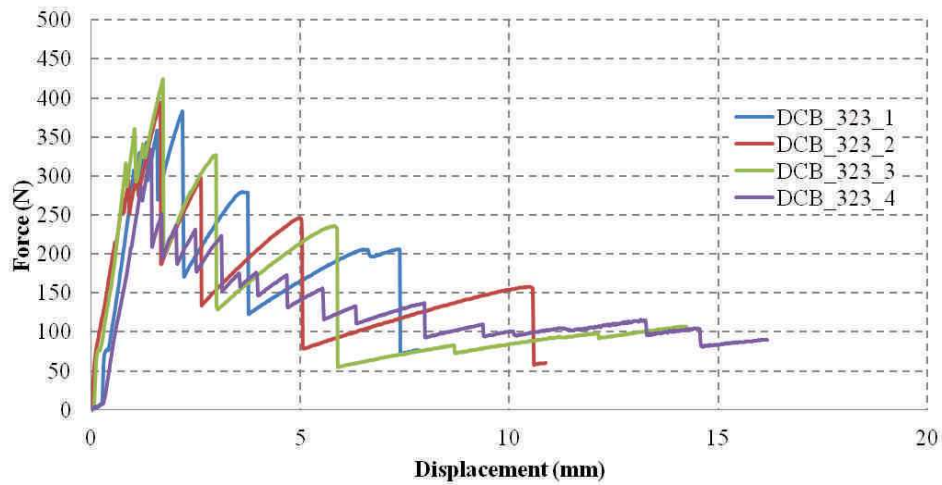


(a) Bonded beams

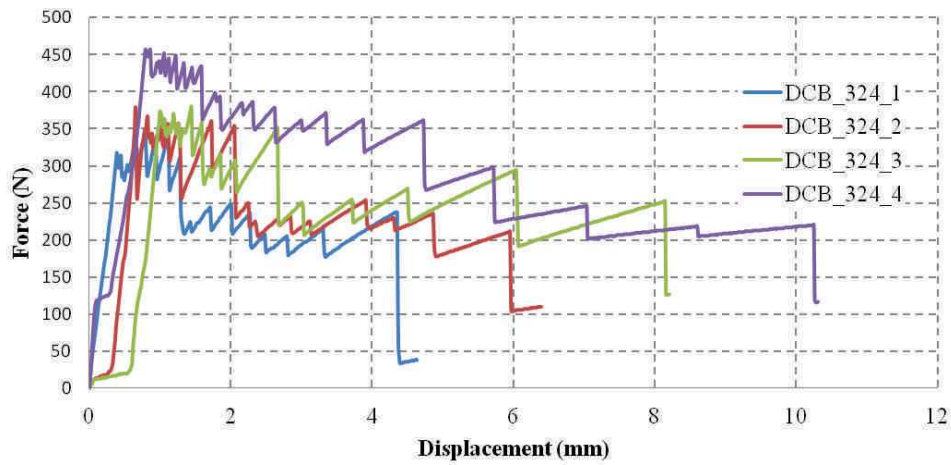


(b) Sandwich specimens

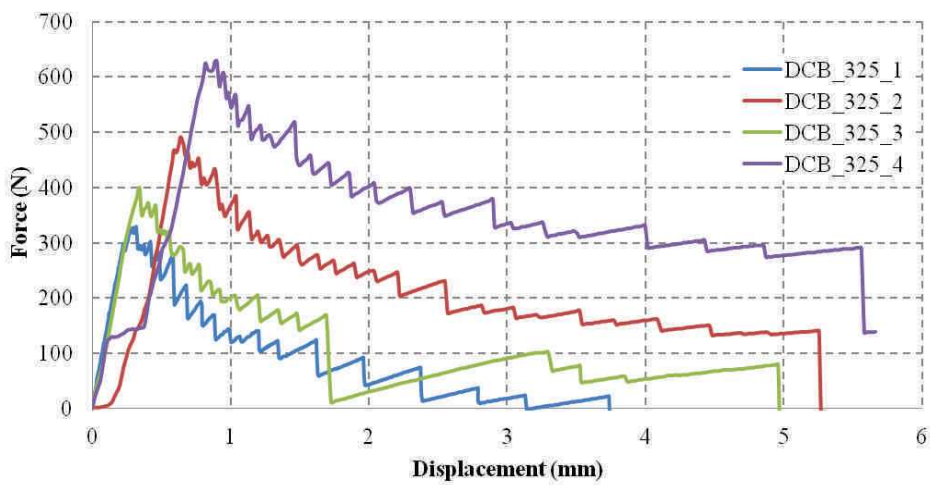
Figure 5-10: Typical image taken by the CCD camera for tracking the crack length.



(a) 2mm thickness of adhesive layer



(b) 3mm thickness of adhesive layer



(c) 4mm thickness of adhesive layer

Figure 5-11: Force displacement curves for bonded specimens.

| Theory | MBT 1 | | MBT 2 | | CC | | VCCT | |
|---|--|---------|-------------------------------|---------|-------------------------------|---------|-------------------------------|---------|
| | G_{II} (kJ/m ²) | | G_{II} (kJ/m ²) | | G_{II} (kJ/m ²) | | G_{II} (kJ/m ²) | |
| | Specimen: 323, Bonded Beam specimens: Substrate 8mm, Adhesive 2mm | | | | | | | |
| | Mean | Std Dev | Mean | Std Dev | Mean | Std Dev | Mean | Std Dev |
| | 0.738 | 0.252 | 0.575 | 0.260 | 0.030 | 0.048 | 0.749 | 0.422 |
| Specimen: 324, Bonded Beam specimens: Substrate 12mm, Adhesive 3mm | | | | | | | | |
| Mean | Std Dev | Mean | Std Dev | Mean | Std Dev | Mean | Std Dev | |
| | 0.358 | 0.144 | 0.168 | 0.029 | 0.022 | 0.019 | 0.533 | 0.322 |
| Specimen: 325, Bonded Beam specimens: Substrate 16mm, Adhesive 4mm | | | | | | | | |
| Mean | Std Dev | Mean | Std Dev | Mean | Std Dev | Mean | Std Dev | |
| | 0.344 | 0.202 | 0.146 | 0.026 | 0.043 | 0.034 | 0.768 | 0.555 |

Table 5-1: Summary of Mode I G_{Ic} results for crack initiation calculated for the bonded specimens.

| Theory | MBT 1 | | MBT 2 | | CC | | VCCT | |
|---|--|---------|-------------------------------|---------|-------------------------------|---------|-------------------------------|---------|
| | G_{Ic} (kJ/m ²) | | G_{Ic} (kJ/m ²) | | G_{Ic} (kJ/m ²) | | G_{Ic} (kJ/m ²) | |
| | Specimen: 323. Bonded Beam specimens: Substrate 8mm. Adhesive 2mm | | | | | | | |
| | Mean | Std Dev | Mean | Std Dev | Mean | Std Dev | Mean | Std Dev |
| | 0.609 | 0.158 | 0.535 | 0.110 | 0.226 | 0.025 | 0.513 | 0.183 |
| Specimen: 324. Bonded Beam specimens: Substrate 12mm. Adhesive 3mm | | | | | | | | |
| Mean | Std Dev | Mean | Std Dev | Mean | Std Dev | Mean | Std Dev | |
| | 0.365 | 0.042 | 0.267 | 0.022 | 0.166 | 0.032 | 0.290 | 0.031 |
| Specimen: 325. Bonded Beam specimens: Substrate 16mm. Adhesive 4mm | | | | | | | | |
| Mean | Std Dev | Mean | Std Dev | Mean | Std Dev | Mean | Std Dev | |
| | 0.205 | 0.089 | 0.115 | 0.018 | 0.061 | 0.040 | 0.296 | 0.052 |

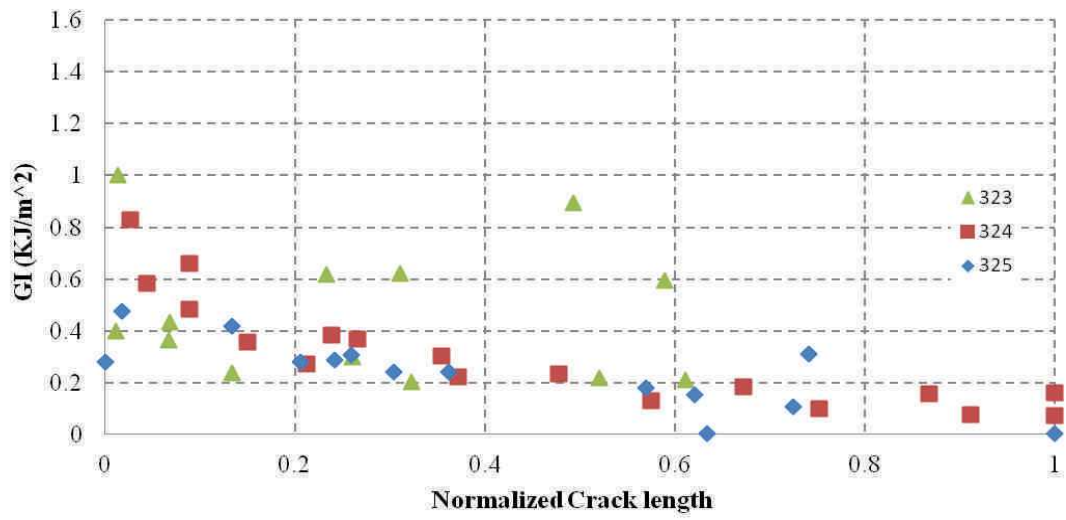
Table 5-2 : Summary of Mode I G_{Ic} results for crack propagation calculated for the bonded specimen.

| Theory | MBT 1 | | MBT 2 | | CC | | VCCT | |
|---|---|---------|-------------------------------|---------|-------------------------------|---------|-------------------------------|---------|
| | G_{II} (kJ/m ²) | | G_{II} (kJ/m ²) | | G_{II} (kJ/m ²) | | G_{II} (kJ/m ²) | |
| | Specimen: 221, Sandwich Beam specimens: Face 2mm, Core 10mm | | | | | | | |
| | Mean | Std Dev | Mean | Std Dev | Mean | Std Dev | Mean | Std Dev |
| | 0.452 | 0.229 | 0.520 | 0.297 | 0.563 | 0.201 | 0.488 | 0.348 |
| Specimen: 222, Sandwich Beam specimens: Face 2mm, Core 20mm | | | | | | | | |
| Mean | Std Dev | Mean | Std Dev | Mean | Std Dev | Mean | Std Dev | |
| | 0.436 | 0.082 | 0.446 | 0.164 | 0.405 | 0.067 | 0.593 | 0.177 |
| Specimen: 223, Sandwich Beam specimens: Face 2mm, Core 30mm | | | | | | | | |
| Mean | Std Dev | Mean | Std Dev | Mean | Std Dev | Mean | Std Dev | |
| | 0.533 | 0.063 | 0.571 | 0.073 | 0.813 | 0.209 | 0.662 | 0.225 |

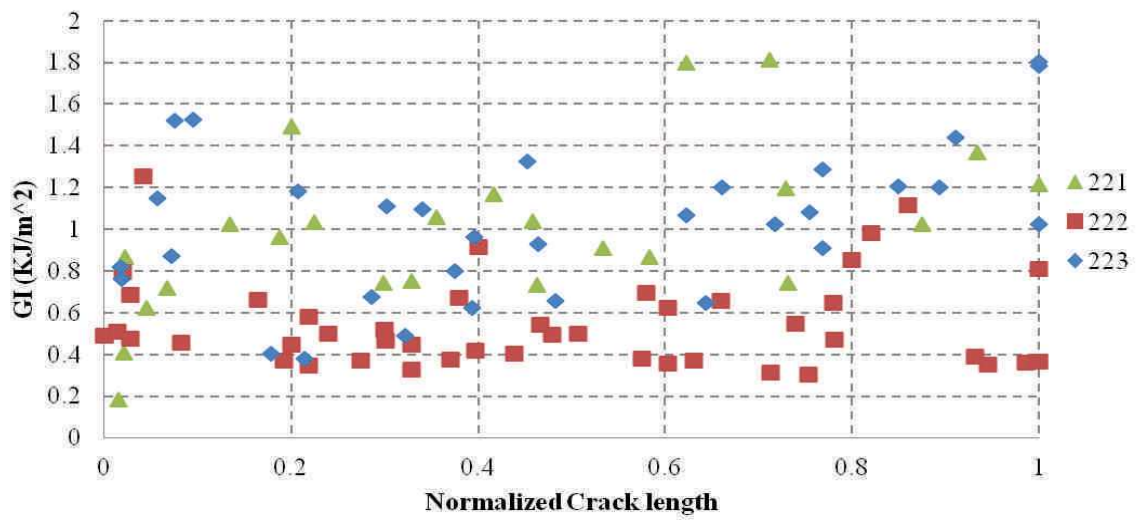
Table 5-3 : Summary of Mode I G_{II} results for crack initiation calculated for the sandwich specimen.

| Theory | MBT 1 | | MBT 2 | | CC | | VCCT | |
|---|---|---------|-------------------------------|---------|-------------------------------|---------|-------------------------------|---------|
| | G_{Ic} (kJ/m ²) | | G_{Ic} (kJ/m ²) | | G_{Ic} (kJ/m ²) | | G_{Ic} (kJ/m ²) | |
| | Specimen: 221, Sandwich Beam specimens: Face 2mm, Core 10mm | | | | | | | |
| | Mean | Std Dev | Mean | Std Dev | Mean | Std Dev | Mean | Std Dev |
| | 0.604 | 0.063 | 0.692 | 0.130 | 0.691 | 0.085 | 1.035 | 0.290 |
| Specimen: 222. Sandwich Beam specimens: Face 2mm. Core 20mm | | | | | | | | |
| Mean | Std Dev | Mean | Std Dev | Mean | Std Dev | Mean | Std Dev | |
| | 0.498 | 0.101 | 0.484 | 0.054 | 0.431 | 0.028 | 0.551 | 0.152 |
| Specimen: 223. Sandwich Beam specimens: Face 2mm. Core 30mm | | | | | | | | |
| Mean | Std Dev | Mean | Std Dev | Mean | Std Dev | Mean | Std Dev | |
| | 0.646 | 0.111 | 0.690 | 0.094 | 0.870 | 0.077 | 1.005 | 0.131 |

Table 5-4: Summary of Mode I G_{Ic} results for crack propagation calculated for the sandwich specimen.



(a) Bonded specimens

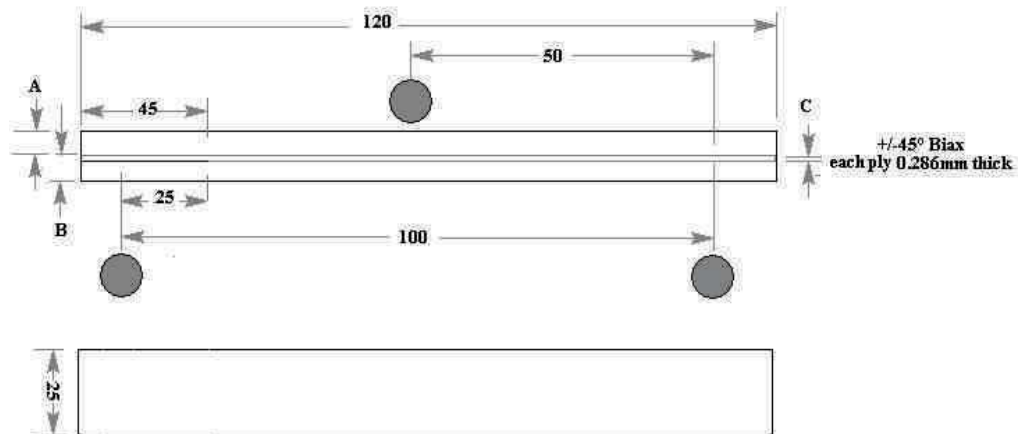


(b) Sandwich specimens

Figure 5-12: Evolution of G_I against crack propagation.

5.4 Mode II shearing mode bonded beams: Experimental setup

The mode II SERR is found out by subjecting the crack plane to pure shearing stress. The crack is propagated under shearing forces along the crack. To get a stable and uniform crack growth 3 points bending tests are chosen. The specimens used for this type of testing are called end notched flexural tests specimens or ENF specimens. The specimens are shown in the Figure 5-13.



ENF

| | | | |
|-----|----------|----------|---------|
| 321 | A = 4mm | B = 5mm | C = 1mm |
| 323 | A = 8mm | B = 10mm | C = 2mm |
| 324 | A = 12mm | B = 15mm | C = 3mm |
| 325 | A = 16mm | B = 20mm | C = 4mm |

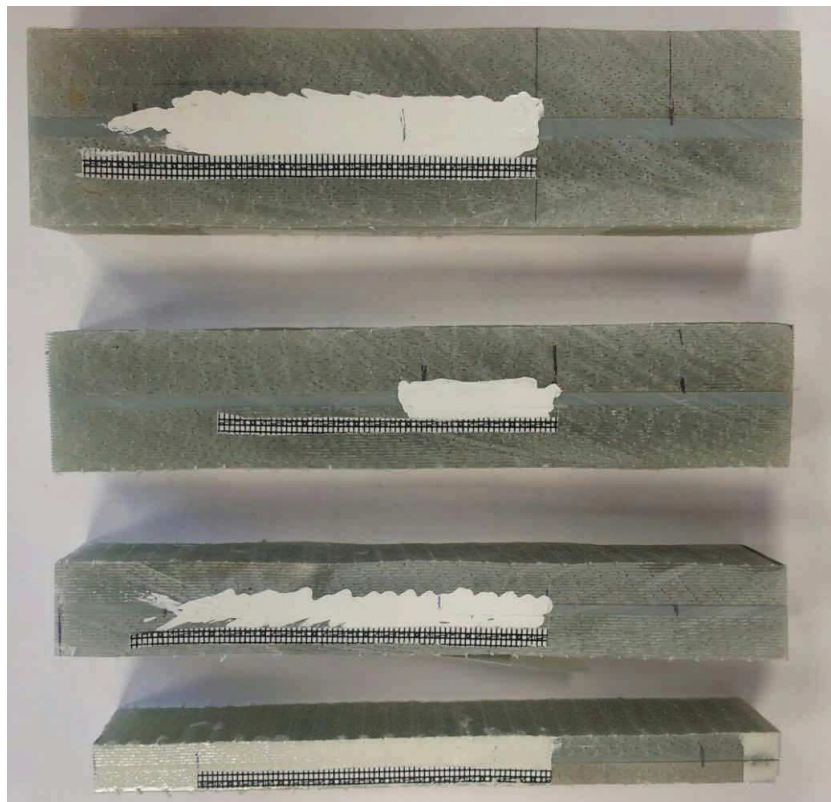


Figure 5-13: ENF specimen used for Mode II fracture resistance tests.

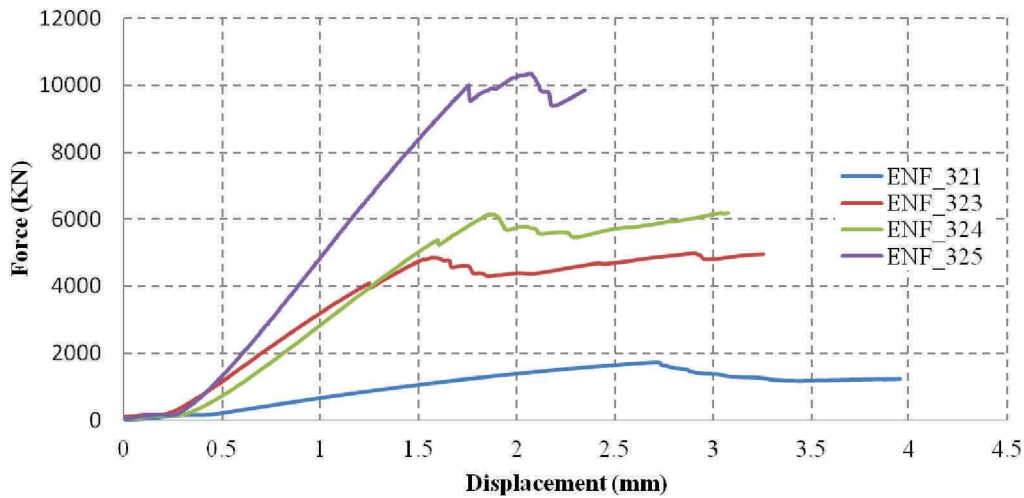


Figure 5-14: Force displacement curves for different specimens showing a stable crack growth at a a_0/L ratio of 0.25.

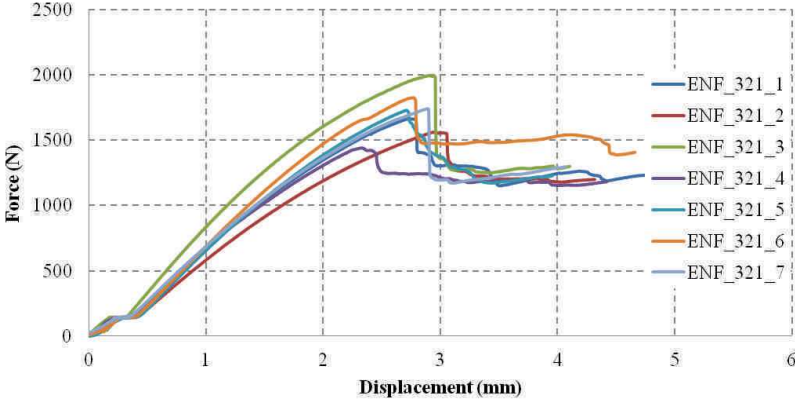
| Specimen | Pre crack “ a_0 ” (mm) | Specimen span length “L” (mm) | “ a_0/L ” Ratio | Propagation type |
|----------|--------------------------|-------------------------------|-------------------|------------------|
| 321 | 25 | 100 | 0.25 | Stable |
| 323 | 25 | 100 | | |
| 324 | 25 | 100 | | |
| | 35 | 140 | | |
| 325 | 25 | 100 | | |
| | 35 | 140 | | |

Table 5-5: Crack propagation at different pre-crack to span length ratios.

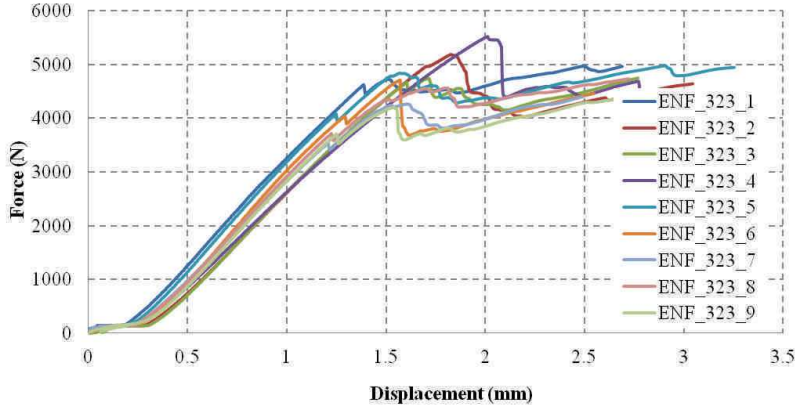
For the crack propagation to be smooth we used a ratio of a_0/L of 0.25. This ratio gave a stable and progressive crack growth. Although for thicker specimens 324 and 345 we used 2 different specimen lengths of 100 – 140 mm, just from a practical point of view as the specimens are thick and rigid a longer specimen gives more room for crack growth, hence makes it easier for tracking. Table 5-5 shows a summary of different length specimens used for a stable crack growth. Tests were done on shorter specimens also; the difference in structural behaviors will be presented in the results summary. Using the same conditions as explained in the previous chapter 4 the ratio of dG/da where non-positive will show a stable propagation of crack.

5.5 Analytical calculation of Strain energy release rate Mode II (G_{II}): Bonded Beams

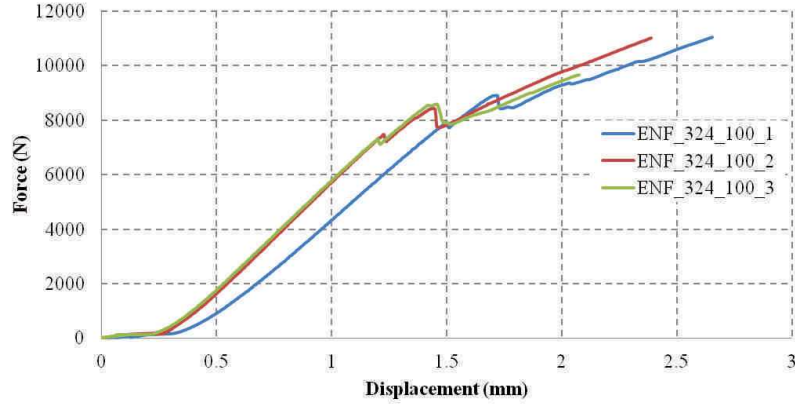
The following analytical models used for the calculation of Mode II SERR require the force applied against the deflection produced in the specimens as parameters to allow the calculations. The force displacement curves are also important to verify the crack propagation is stable. The following Figure 5-15 - Figure 5-17 show the force-displacement curves for the bonded specimens.



(a) 1mm adhesive.

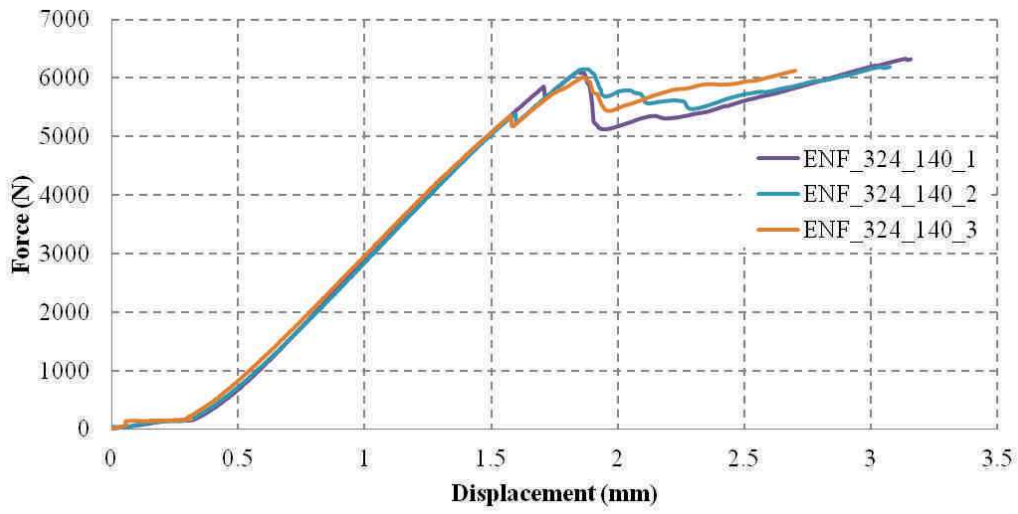


(b) 2mm adhesive.

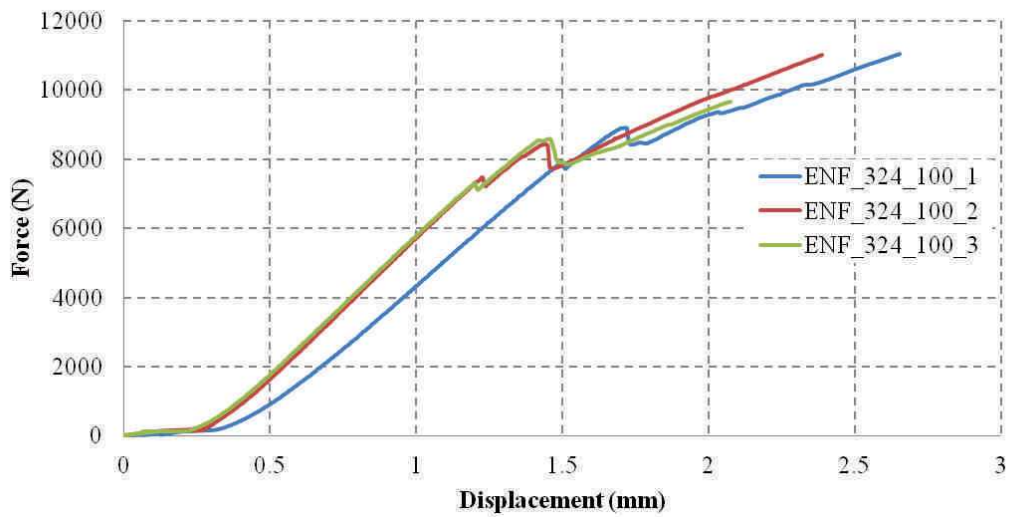


(a) 3mm adhesive.

Figure 5-15: Force-displacement curves for a 100mm long supported length of bonded specimens.

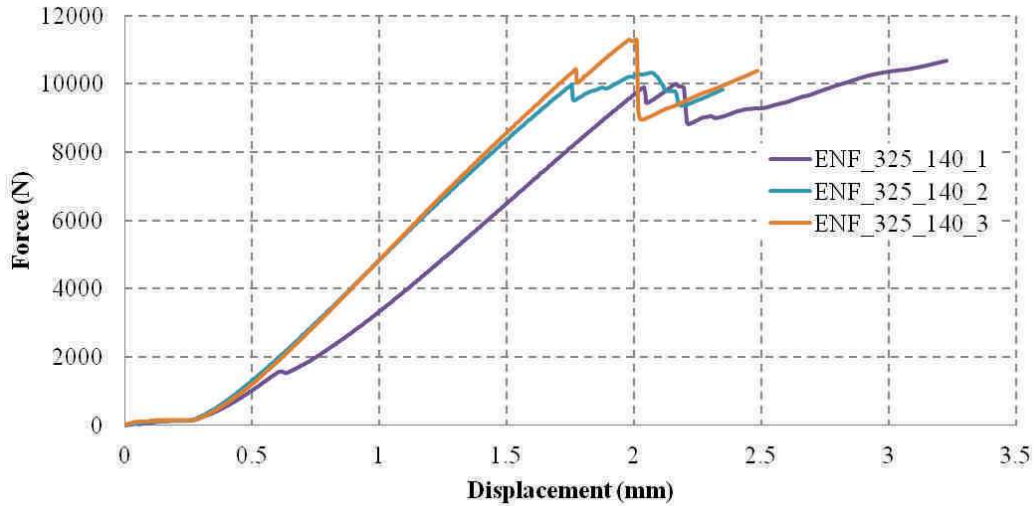


(b) 140mm long specimens.

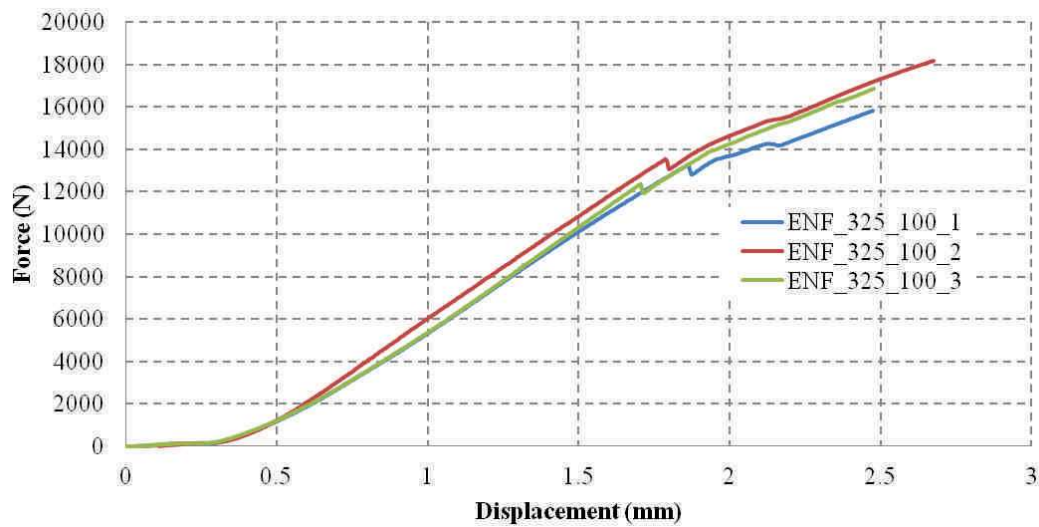


(c) 100mm long specimens.

Figure 5-16: Force-displacement curves bonded specimens, 3mm adhesive thickness.



(d) 140mm long specimens



(e) 100mm long specimens

Figure 5-17: Force-displacement curves for bonded specimens, 4mm adhesive thickness.

For the thicker specimens since their compliance is rather low we used 140mm long specimens also to monitor the crack growth over a longer length, thus giving more data points. The reproducibility of the force displacement curves follows a trend where it is seen to be dependent on specimen thickness. It is seen that for thinner specimens there are a lot more variability due to the bending of the specimens to a higher curvature thus causing rotation at the crack tip and producing higher normal forces at the crack plane. These higher normal forces cause the effects of friction to increase the variation in the test results. However as for the previous case this problem is only in the initiation phase and for the propagation phase the standard deviation in the test results is a lower level.

5.5.1 Beam theory (BT)

As given for the previous cases the classical beam theory is used to determine the value of mode II SERR G_{II} as in equation 5-8.

$$G_{II} = \frac{9a^2 P^2}{16E_{11} b^2 h^3} \quad 5-8$$

5.5.2 Compliance calibration (CC)

Using compliance calibration to correct for the effects of change in compliance with the increase in the crack length.

$$G_{II} = \frac{1.5ma^2 P^2}{b^2} \quad 5-9$$

where “ m ” is a coefficient which depends on the function “ $C = f(a^3)$ ”.

5.6 Results of Mode II ENF tests for bonded beams

The mode II SERR is calculated using two different theories taking into account the simple beam theory and the compliance calibration. As can be seen from the Table 5-6 and the

Table 5-7 that the beam theory has high standard deviation as the beam theory fails to correct for the neutral plane offset created due to thick adhesive joints. However the CC technique takes into account this effect of offset and the standard deviation is a lot lower.

| Theory | BT | | CC | |
|----------|--------------------------------|---------|-------------------------------|---------|
| | G_{III} (kJ/m ²) | | G_{II} (kJ/m ²) | |
| | Mean | Std Dev | Mean | Std Dev |
| Specimen | | | | |
| 321 | 0.571 | 0.101 | 0.607 | 0.179 |
| 323 | 0.629 | 0.159 | 0.440 | 0.107 |
| 324 | 1.263 | 0.100 | 1.211 | 0.578 |
| 325 | 2.710 | 0.324 | 1.321 | 0.367 |

Table 5-6: Summary of Mode I G_{III} results for crack propagation calculated for the bonded specimen.

| Theory | MBT1 | | CC | |
|----------|--------------------------------|---------|--------------------------------|---------|
| | G_{IIC} (kJ/m ²) | | G_{IIC} (kJ/m ²) | |
| | Mean | Std Dev | Mean | Std Dev |
| Specimen | | | | |
| 321 | 3.576 | 1.076 | 0.919 | 0.294 |
| 323 | 4.097 | 1.851 | 1.137 | 0.503 |
| 324 | 2.455 | 3.045 | 1.265 | 0.652 |
| 325 | 6.325 | 2.848 | 1.456 | 0.655 |

Table 5-7: Summary of Mode I G_{IIC} results for crack propagation calculated for the bonded specimen.

5.7 Mode II shearing mode of sandwich beams: Experimental setup

For sandwich structures an attempt was made for the calculation of Mode II SERR using ENF specimens. However due to the low strength of the foam core in crushing the crack cannot propagate in the shearing direction, Figure 5-18.

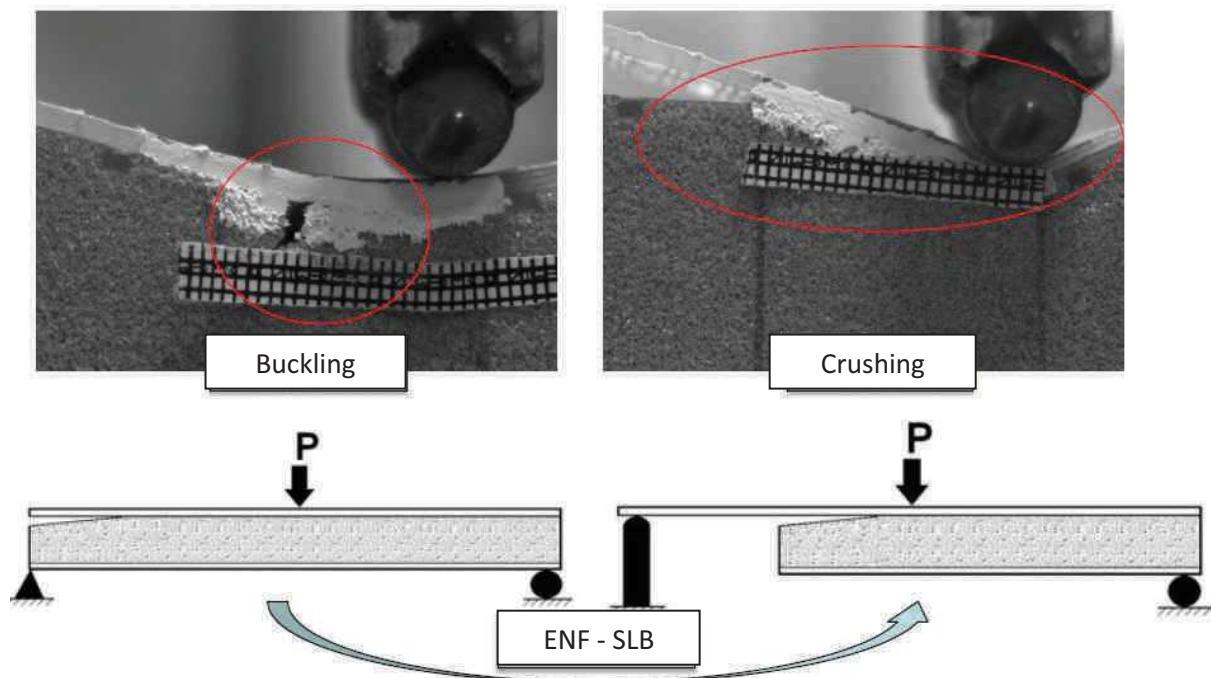


Figure 5-18: Foam core being buckled and crushed in ENF tests due to weak compressive properties.

Due to the problems encountered for sandwich structures we have chosen to use Single (Over) Leg Bend tests (SLB). SLB specimens promote opening as well as shearing thus taking the pressure off the

crack surface, the values of SERR thus calculated are that of mixed mode, that is there is a component of opening and shearing SERR in the total energy calculated. The mode II SERR can be calculated by subtracting the Mode I SERR from the total energy thus calculated (Davidson & Sunderaman, 1996).

Schematically the SLB specimens used for the calculation of SERR are shown in the Figure 5-19.

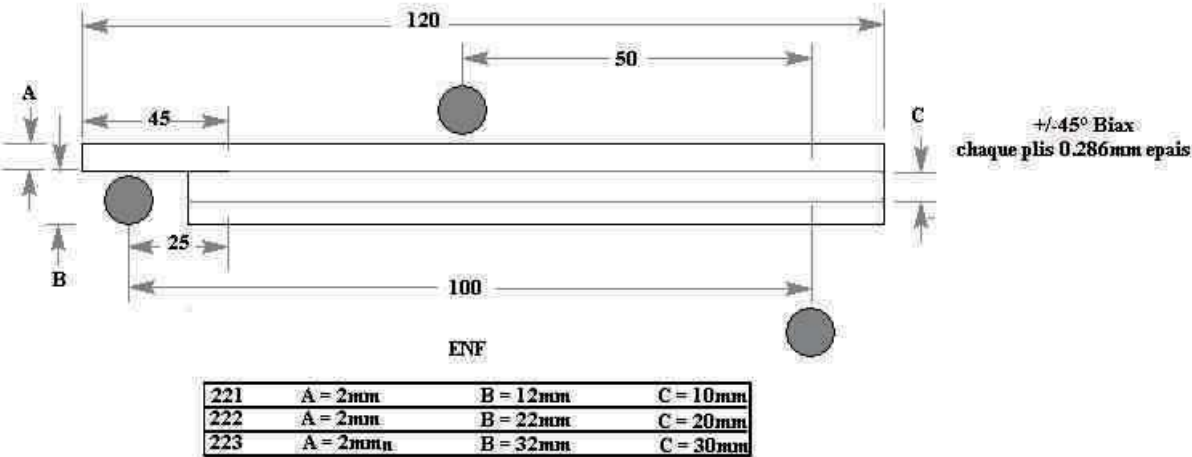


Figure 5-19: SLB specimen geometry.

5.8 Analytical calculation of Strain energy release rate Mode II (G_{II}): Sandwich Beams

The theory of composite beams is used for calculating the energy released during the propagation of crack. Where the mixed mode SERR $G_{I/II}$ is given by:

$$G_{I/II} = \frac{3P\delta a^2}{2b} \left[\frac{R-1}{2L^3 + a^3(R-1)} \right] \quad 5-10$$

with the definition of R being

$$R = \frac{D}{D_s} \quad 5-11$$

and “ D ” and “ D_s ”, are factors calculated by the rigidity of the composite beam in “ A_{11} ” tension, “ B_{11} ” tension-flexion and “ D_{11} ” flexion which is described in the system of equations below.

$$D_s = \frac{E_s t_s^3}{12}$$

$$D = D_{11} - \frac{B_{11}^2}{A_{11}}$$

$$A_{11} = 2E_s t_s + E_c t_c \quad 5-12$$

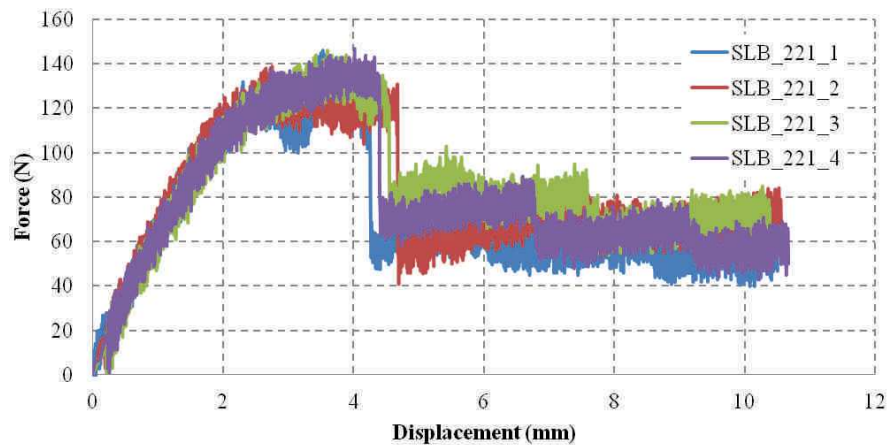
$$B_{11} = \frac{(E_c - E_s) t_s t_c}{2}$$

$$D_{11} = \frac{E_s t_s (2t_s^2 + 3t_s^2) + E_c t_c (t_c^2 + 6t_c^2)}{12}$$

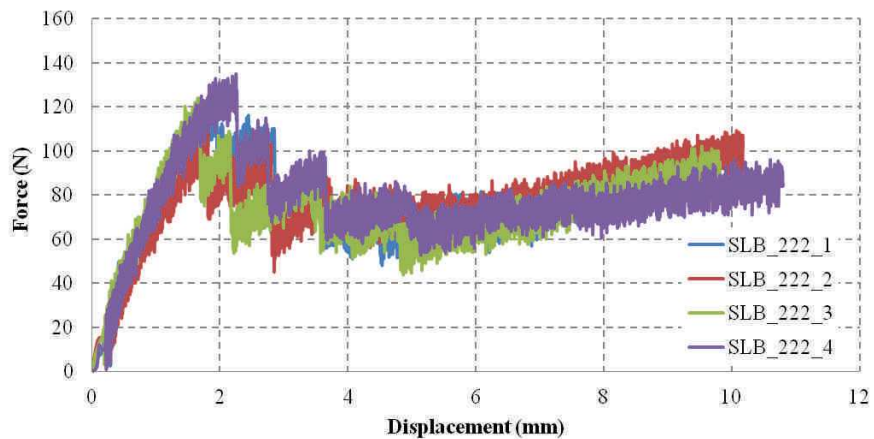
with the “ E ” being the Young’s modulus of the Face and Core (subscript “ s ” and “ c ”), “ t ” is the thickness of the Face and Core (subscript “ s ” and “ c ”)

5.9 Mode II SLB results for Sandwich beams

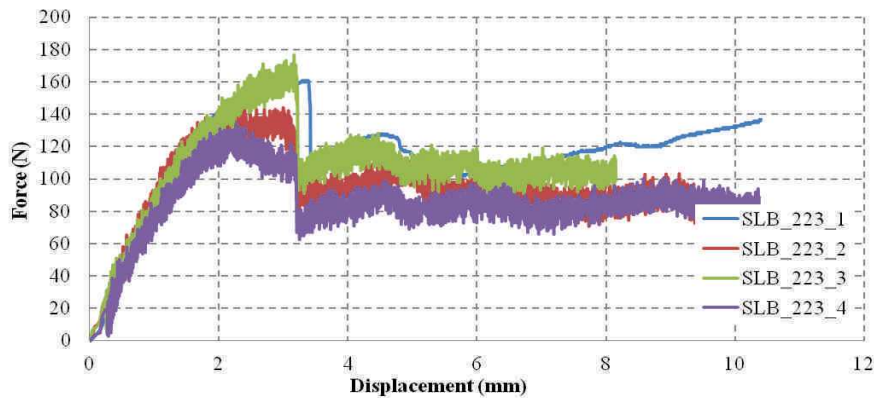
Using the formulation devised in (Davidson & Sunderaman, 1996) we can proceed to calculate the Mode I/II mixed SERR for the SLB specimens. Furthermore the force displacement curves are required to calculate the SERRs, Figure 5-20.



(a) 10mm core thicknesses



(b) 20mm core thicknesses



(c) 30mm core thicknesses

Figure 5-20: Force displacement curve for sandwich SLB specimens.

Once the mixed mode SERR $G_{I/II}$ is calculated we can proceed to calculating the mode II SERR. Since the total energy released in the mixed mode is arithmetic sum of the mode I and mode II SERR therefore the mode II SERR in this case would be the value of the mean of mode I SERR subtracted from the total energy, Table 5-8.

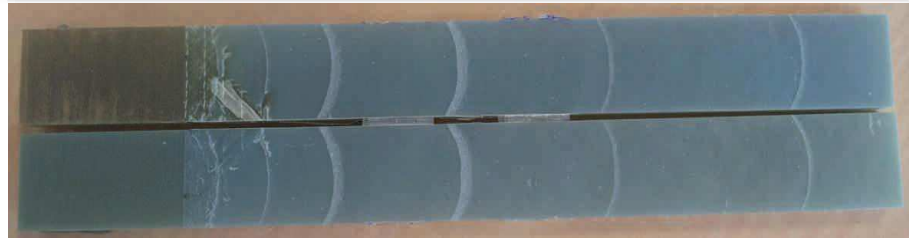
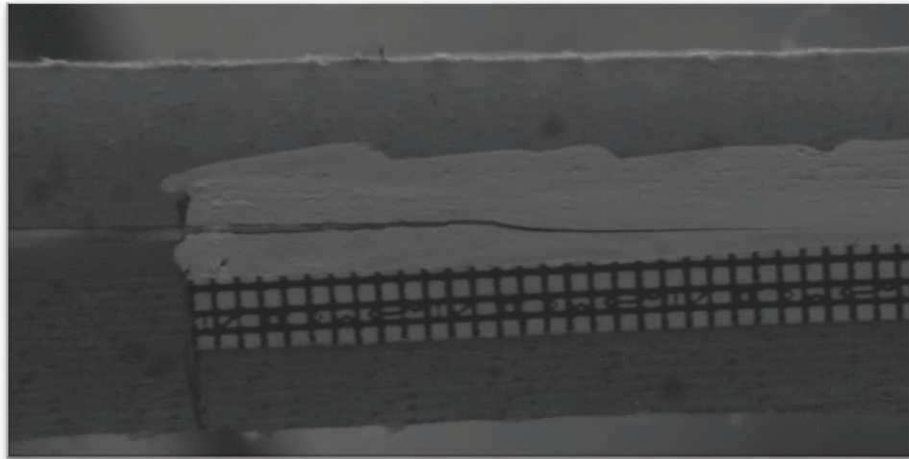
| | $G_{I/II}$ (kJ/m ²) | | G_{II} (kJ/m ²) |
|----------|---------------------------------|---------|-------------------------------|
| | Mean | Std Dev | Mean |
| Specimen | | | |
| 221 | 0.950 | 0.074 | 0.346 |
| 222 | 0.793 | 0.030 | 0.296 |
| 223 | 1.179 | 0.167 | 0.533 |

Table 5-8: Summary of SLB results calculated for the sandwich beams

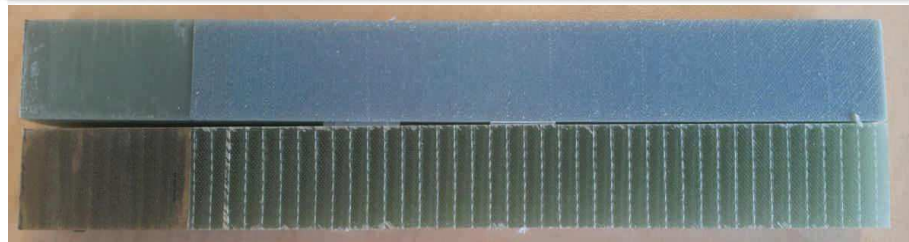
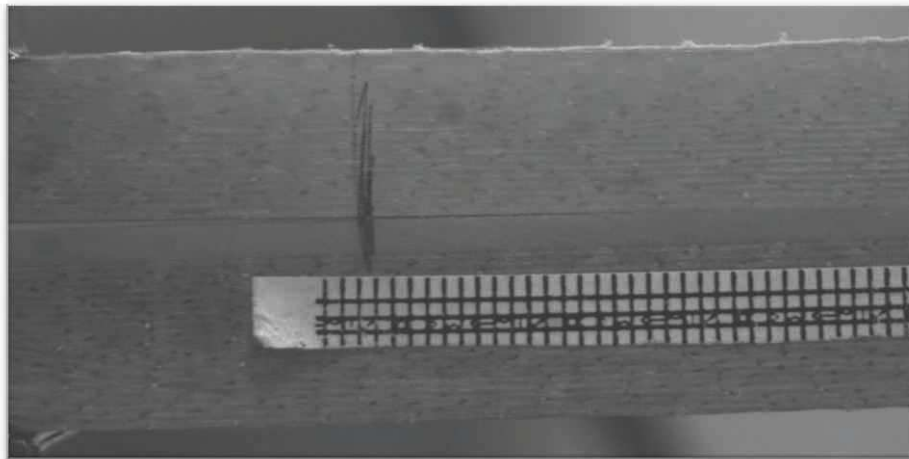
5.10 Observations on Results

The results from experiments show some deviation. There are some sources of error which are introduced directly from the experiments. These are discussed here in this section.

1. The Mode I SERR values for bonded and sandwich specimens show good correlation and as expected for thinner specimens the deviation between analytical methods and the VCCT is not very high.
2. The degree of deviation in the results can be accredited to the fact that, especially for bonded beams, since the specimens are thicker there is not lot of curvature in the beams while flexion, hence MBT1 and CC results match to each other and to the VCCT results.
3. In the DCB results for bonded beams it is seen that the Mode I SERR for specimens 323 was a lot higher than for other two specimen types. On close inspection of the crack surface it was revealed that the crack propagated within the adhesive instead of the interface thus giving (different) higher values of SERR for these specimens. This had the added advantage of measuring cracking in the adhesive itself.



(a)



(b)

Figure 5-21 : Crack growing within the (a) Adhesive layer, (b) Substrate-Adhesive interface.

4. Upon closer inspection of the cracked surfaces in Figure 5-21 it can be seen that the crack front is convex hence calling the need for curvature correction as in MBT2 theory. Moreover the cracks are also less stable in propagation in the adhesive layer, Figure 5-21a. This is also due to the fact that the cross filaments in composites act as crack-stoppers when the crack

propagates at the substrate-adhesive interface thus giving a higher Mode I SERR value, Figure 5-21b. This shall be discussed in more detail in the cohesive zone modeling section.

5. The values of Mode I SERR for bonded specimens shows a definite reduction as the crack length grows, which is to be expected, however for the sandwich specimens, the SERR fluctuates almost randomly from higher to lower values. This is explained from the nature of the foam core. Since the structure of the core is porous hence it tends to make the crack “stop and go” as the crack propagates. The cracks almost always pass in a region near the pre-crack but almost entirely in the foam core.
6. There have been studies to deal with the mode mix introduced due to dissymmetry of the crack plane. These methods are used especially for sandwich structures of high dissymmetry. (Manca, et al., 2012) (Wang & Qiao, 2003) These methods include some empirical constants that take into consideration the difference of stiffness in the different materials and also the distance of the dissymmetry plane. However we have found that for the case of Mode II SERR of bonded specimens these theories over estimate the SERR values. Refer to the Figure 5-22.

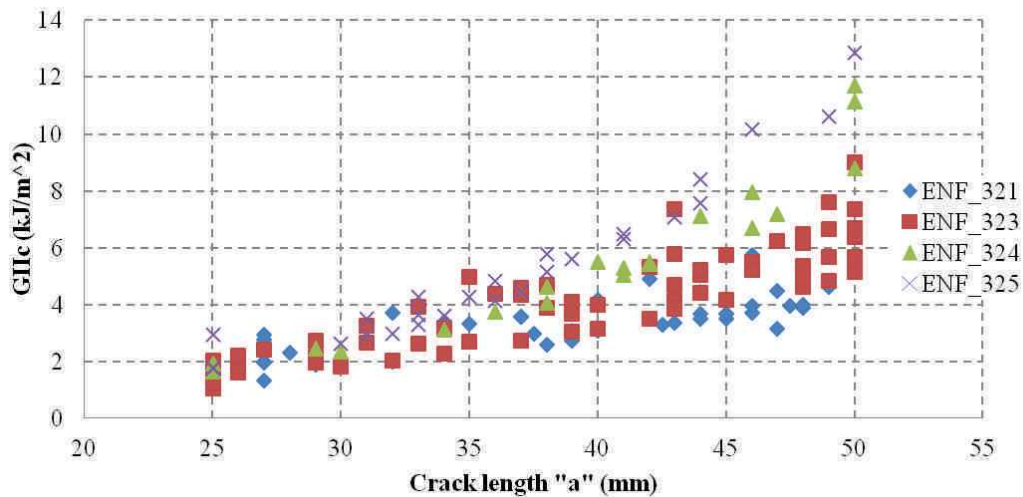


Figure 5-22: Values of Mode II SERR G_{IIc} calculated using the formulation developed in (Manca, et al., 2012).

The Figure 5-22 shows that although the consideration of the dissymmetry of the crack plane helps in correcting the values of the calculated SERR values, but as mentioned above these are still over-estimated. This over estimations is due to very low compliance of the beam specimens as the specimens used are very thick. This fact can be confirmed from the fact that the SERR values are seen to increase with the thickness of the beams. Therefore finally the compliance calibration techniques should be used to get lesser imprecision in the calculation of SERR values.

Chapter 6 --- Experimental study of behavior of materials under cyclic loading

Table of contents

| | |
|---|-----|
| 6.1 Composite material..... | 158 |
| 6.1.1 Test procedure..... | 159 |
| 6.1.2 Measurements | 162 |
| 6.1.3 Self heating and degradation of stiffness | 163 |
| 6.1.4 Effect of loading rate | 164 |
| 6.1.5 Endurance limit using self heating..... | 166 |
| 6.1.6 Rate of damage progression..... | 167 |
| 6.2 Fatigue tests on UD specimens..... | 168 |
| 6.2.1 Degradation of stiffness | 169 |
| 6.2.2 Failure Modes | 170 |
| 6.3 Discussion..... | 172 |
| 6.4 Self heating tests on NORPOL..... | 175 |
| 6.5 Conclusions and Discussion | 178 |

Once the static strength of the materials has been identified the behavior of material under cyclic loading is to be considered also. The design of wind turbines typically takes a long period of time due to the different steps involved. There are several very discretized yet interdependent design domains. Two of those are outstanding: Wind turbine blade aerodynamic design and its structural design. The design offices need practical day-to-day tools allowing them designing tailor-made solutions as fast as possible. A key data for such tools is the behavior of the material. It is especially true for large composite structures for which the feedback from real farms is rather small. The aim of this PhD work is to focus on the structural design of a 1 MW 35m long wind turbine blade, with the main aim of reducing the design time. One of the main time consuming steps in structural design is the characterization of materials. This characterization is carried out in several well defined steps. In the beginning basic material properties are defined using simple monotonic static tests. The next step especially for composites is to characterize their resistance to fracture and damage. By nature composite structures do not fail as brittle materials but rather fail in a progressive manner. Hence unlike brittle or hard materials one of the quality of composites is to be able to perform and resist the loads in a damaged state. Therefore the resistance and the residual life of composites in damaged states is an important step in their characterization. Lastly but equally important as the formers, is the characterization of composites in fatigue or cyclic loading conditions. This takes two different forms as well. The first part is the determination of visco-plastic behavior response to ascertain if the materials tested at an accelerated pace in the laboratory would have an equivalent response in the real life scenario where the solicitations are at a much lower pace.

In the precedent reports/communications the problems related to design and material characterization were addressed, in this report however the characterization of materials under cyclic loading is discussed. In addition keeping in view the aim of PhD work a methodology is developed to characterize the materials under cyclic loadings at an accelerated level with the goal of minimizing the material characterization time cycle.

Materials undergoing repetitive cyclic loadings undergo fatigue damage. It is important to note the effects of such cyclic loads on the health of structures. In addition, a good understanding of the damage taking place due to cyclic loadings leads to better prediction of the life of the structure.

Typically fatigue tests take a very long time for characterizing materials as they need to run until the specimens or structures fail. However there is a lot of attention going into searching methods which would eventually reduce the time taken for these tests. In addition to the added difficulties with long duration testing there is a question off judgment as what constitutes a fatigue limit. A material can have a fatigue endurance limit based on anywhere from 1 to 10 million cycles.

In this chapter results from fatigue tests based on tension-tension stress-cycle have been reported. In addition new approaches based on the self-heating of specimens have been treated. A comparison is also included between the two approaches to validate the self-heating technique.

Currently self heating tests have been done for metals, and to some extent to short fiber composites. However for long fiber composites, there is a need for detailed investigations to be done (Fern, et al., 2012) (Talreja, 2008) (Kordatos, et al., 2013) (Lorca, 2000) (Huang, 2002) (Rosa & Risitano, 2000) (Montesano, et al., 2013) (Fargione, et al., 2002).

Self heating fatigue tests are based on the general assumption that all materials generate (dissipate) heat due to micro/macrosopic changes taking place in their structures during loadings. Thus their dynamic Young's modulus can be related to the heat generated by equation 6-1 (Vasconcellos, et al.,

2013) (Stanely, 1997) (Krstulovic-Opara, et al., 2011) (Haj-Ali, et al., 2008) (Williams, 1974) (Emery & Dulieu-Barton, 2010) (Wu & Yao, 2010).

$$Q_R = E\varepsilon_a^2\omega\sin\delta \tag{6-1}$$

In the equation 6-1 “ Q_R ” is the energy (primarily heat) dissipated, “ E ” is the module of young, “ ε_a ” is the strain, “ ω ” is the frequency of cyclic loading and “ δ ” being the phase difference (lag in the case of polymers) between the applied load and the load transmitted through the specimen.

Although there are different regimes for material characterization in fatigue loadings like tension – tension, tension – compression, compression – compression and shearing types, but we have for the moment chosen simple tension – tension regimes as these are the types of loads most experienced by the structure and in compression type regimes buckling is more critical.

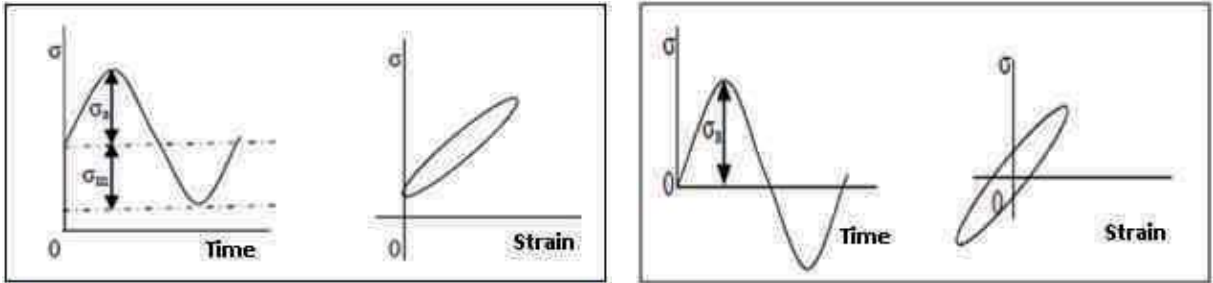


Figure 6-1: Types of fatigue loading

6.1 Composite material

The specimens are made from the same material as that to be used in the real full scale wind turbine blade. Following the standards, fiber glass mat has been used as fiber reinforcements. They were then impregnated with a polyester resin, vacuum bagged and cured at room temperature for fabricating rectangular panels. The specimens have then been cut down to size using a lubricated diamond cutting wheel to reduce manufacturing induced stresses and damage.

There are two types of specimens used for fatigue analysis. The difference in the specimen types lies with the arrangement of fibers within these specimens. One type of specimens are manufactured using uni-directional fiber mats, and would be subsequently referred to 0°UD and 90°UD specimens depending on the direction of load application. If the loads are applied along the direction of the fibers the specimens are referred to as 0°UD in the case the load is applied perpendicular the specimens are referred to as 90°UD.

The second type of specimens is made up of a bi-axial mat. The Bi-axial mat has uni-directional fiber mats superposed on one another with alternating mats at 90° to the former. This mat is then layered to give a ±45° orientation with respect to the direction of the load applied. The specimens made up of this type of fiber arrangement are referred to as 45° Biax specimens in the text that follows.

For calculating the fiber volume ratio, specimens are heated in an oven at 650°C for 3 hours to evaporate the entire resin matrix. The specimens are weighted before and after heating them. The fiber volume and mass percentages are given in the Table 6-1 as follows.

| Specimens | Volume fraction of fibers (%) |
|-----------|-------------------------------|
| 45° Biax | 55.24 |
| UD | 53.92 |

Table 6-1: Volume fraction of fibers in the 45° Biax and UD specimens

6.1.1 Test procedure

For the mechanical fatigue testing the specimens used are rectangular as use of necked specimens causes failure cracks to develop on the shoulders of the necks and one is left with an effective rectangular specimen. In case of 45° Biax composite materials, the stress distributions are such that the maximum stress is seen to be at mid span. The tests specimens are chosen intentionally large enough to limit the edge effects and defect induced stress concentrations, which can lead to premature failure and hence affect the quality of test data. Keeping in view that the composite material has a specific weight of 1152 gm/m² and that at least 5 plies are needed to reduce the statistical risk of defects affecting the test results, a specimen thickness of more than 4mm has been chosen. Keeping in line with standards, the length and breadth of the specimens is kept at 250mm x 25mm as shown in Figure 6-2. The material properties of the composite laminate are given in the Table 6-1.

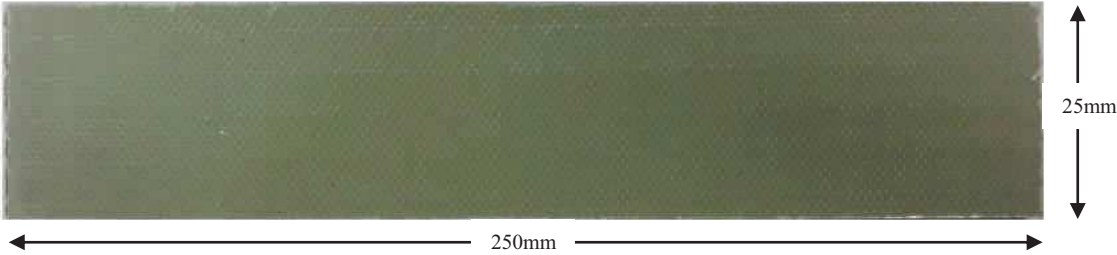


Figure 6-2 : Dimensions of the specimens used for fatigue tests

The tests are run under load controlled tension – tension regimes at $R = 0.1$, where R is the ratio of maximum and minimum applied stress. For example if we take a maximum tensile stress 30MPa then for an $R = 0.1$ the minimum tensile stress applied would be 3MPa for each cycle. A hydraulic fatigue test machine (INSTRON 150KN) is used for this experiment, as shown in Figure 6-4. The loading rate has been chosen based on two parameters. The first is that during fatigue tests the self-heating should be contained to a reasonable level. The relevant standard (ISO 13003) proposes a temperature rise of 10°C as the limit for these tests however we have kept the temperature rise to below 10°C and below 50% of the glass transition temperature T_g of the polyester resin (Harris, s.d.). From the above limits, keeping in view the T_g for polyester to be at 85°C and the ambient laboratory conditions at the time of

testing to be at around 25°C the limit maximum temperature would be 35°C. However all the tests have been run below this limiting criterion, the maximum temperature recorded during the tests was 28°C. The other limiting parameter is the loading rate.

| Specimen properties for 45° Biax | |
|--|----------------------|
| Ultimate strength (MPa) | 110 |
| Elastic limit (MPa) | 18.5 |
| Young's modulus in elastic (GPa) | 19 |
| Glass transition temperature of matrix (°C) | 80 – 89 |
| No. of plies | 7 |
| Dimensions of specimens (mm) | 250 x 25 x 4.5 - 4.7 |

Table 6-2: Properties of the 45° Biax specimens.

| Specimen properties for 0° UD | |
|--|----------------------|
| Ultimate strength (MPa) | 965 |
| Young's modulus in elastic (GPa) | 48.11 |
| Glass transition temperature of matrix (°C) | 80 – 89 |
| No. of plies | 7 |
| Dimensions of specimens (mm) | 250 x 25 x 4.5 - 4.7 |

Table 6-3: Properties of the 0°UD specimens.

| Specimen properties for 90° UD | |
|--|----------------------|
| Ultimate strength (MPa) | 33.5 |
| Elastic limit (MPa) | 30 |
| Young's modulus in elastic (GPa) | 11.21 |
| Glass transition temperature of matrix (°C) | 80 – 89 |
| No. of plies | 7 |
| Dimensions of specimens (mm) | 250 x 25 x 4.5 - 4.7 |

Table 6-4: Properties of the 90°UD specimens.

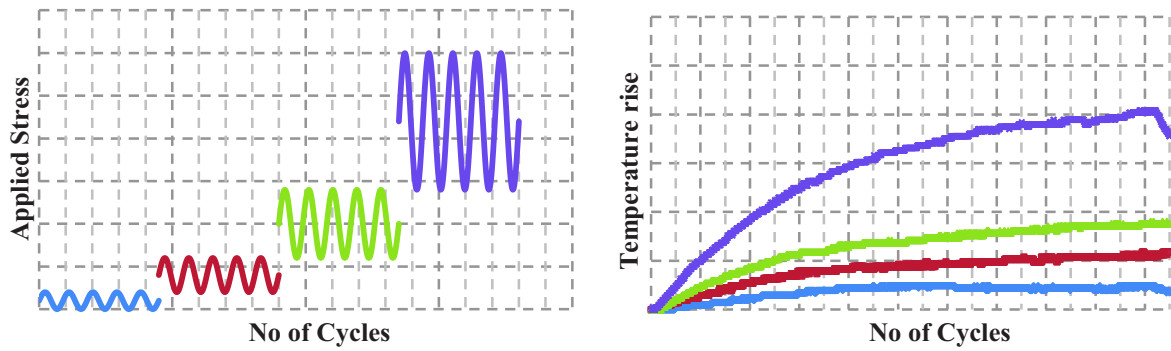


Figure 6-3: Applied stress steps and the corresponding heat generated.

Different loading rates are used in monotonic tests to study their effects on the material behavior. The loading rate, chosen for fatigue tests, shows a certain degree of hardening where the onset of damage is delayed. The results of loading rates are discussed in more detail in section 6.1.4. The loading rates had to be reduced for high loads to minimize the risk of “overheating” where the specimen is getting close to glass transition temperatures. Hence the loads have been run on 2.5 to 5 Hz. As will be shown in the section pertaining to the visco-plastic behavior of the composite for the loading rates from 60 to 150 mm/s the material response does not change. The loading rates 60 – 150 mm/s corresponds to loading rates of 2.5 and 5 Hz respectively. Hence we can deduce that for all practical purposes the effect of loading rates on the material dynamic Young’s modulus can be ignored.

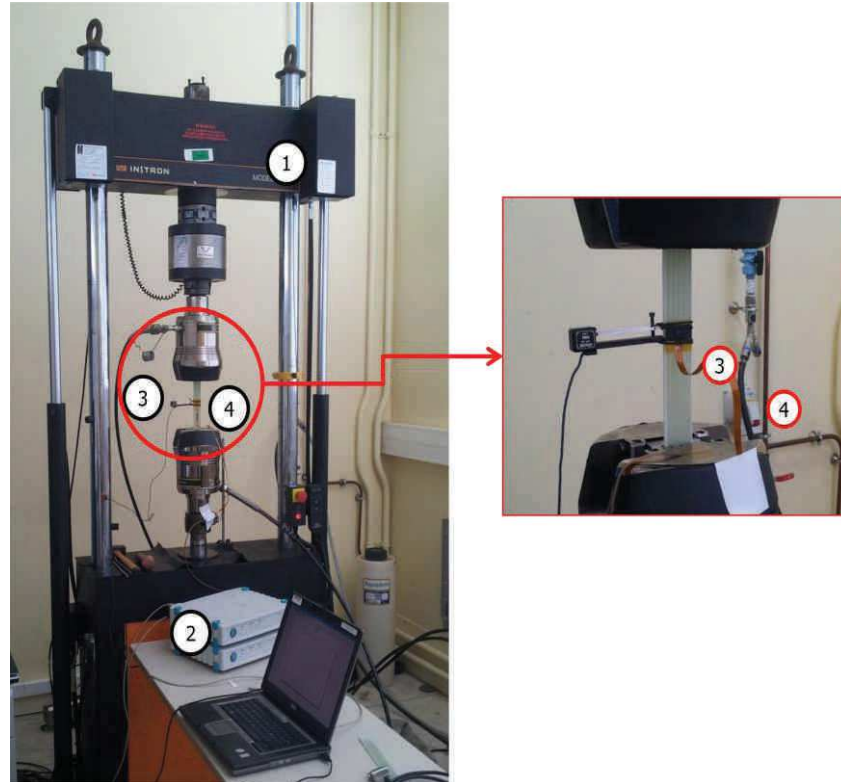


Figure 6-4: Test setup for fatigue tests. 1) Instron fatigue test machine, 2) Data acquisition system, 3) Extensometer, 4) T-type thermocouples.

The specimens are equipped with T type thermocouples having a measurement resolution of 0.1°C, which for our experimental setup, is sufficiently fine. To record the evolution of stiffness of the specimens a linear extensometer is placed at the mid span of the specimens. In addition to the instrumentations of the specimen the machine grips are instrumented with thermocouples as well to record the temperature rise of the machine. This is later used to correct for the temperature rise taking place due to the fatigue phenomenon.

The extensometer used has a gauge length of 12.5mm which is so chosen based on the stress fields for a loaded 150mm gauge length specimen.

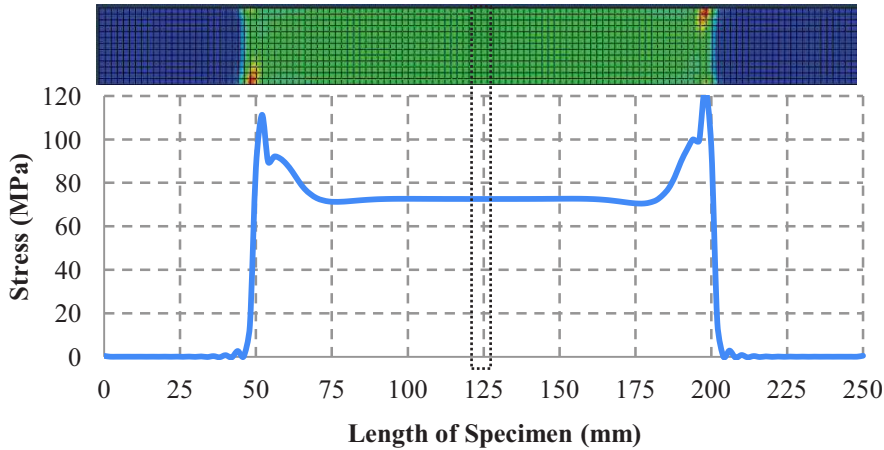


Figure 6-5 : Stress distributions on a rectangular test specimen.

As shown in the Figure 6-5 the strain field for the region chosen is uniform at the 12.5mm mid span of the specimen and thus can be used for making uniform stress-strain field measurements.

6.1.2 Measurements

For the temperature and the strain measurements, as explained above, the instruments are placed at the mid span of the specimens. The temperature rise in the specimens is isolated from the rise of the machine by the relation given as under.

$$T_{rise} = \theta = T_s - T_0 - \left(\frac{(T_l - T_{0l}) + (T_u - T_{0u})}{2} \right) \tag{6-2}$$

where “ T_0 ” is the initial temperature of the specimen, “ T_l ” and “ T_u ” the temperature of the lower and upper grips respectively and “ T_s ” is the surface temperature of the specimen. In addition to the temperature strain as expressed in percentage is also measured at the mid span. In general strain can be measured by:

$$\varepsilon_x = \frac{dL}{12.5} \times 100 \quad 6-3$$

Where ε_x is the longitudinal strain measured in the direction of the load applied and, dL is the variation in length measured by the extensometer. The strain measurements made are used to determine the degradation of stiffness of the specimens during fatigue tests.

6.1.3 Self heating and degradation of stiffness

As shown by the equation 6-1, the materials exhibit degradation in stiffness during fatigue tests. This reduction of stiffness is linked to the heat liberated during these tests. For self heating tests the degradation of stiffness is considered to be as a result of different damage mechanisms, including fibre breakage, delaminations, de-bonding and plastic deformation of the polymer matrix. On close inspection the final failure of specimens shows mostly delamination type failure, hence most of the degradation of the stiffness is attributed to matrix failure, Figure 6-6.

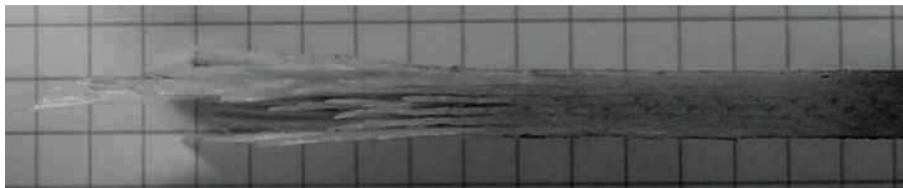


Figure 6-6: 45° Biax Specimens showing delamination type failure.

The specimens used for testing are loaded from a 2.5kN to a 6.0kN load level, which is equivalent to 25 to 60% of the static ultimate strength when loaded at loading rates corresponding to 2.5Hz and 5.0Hz cyclic loading. Some problems have been encountered in testing composites in this manner as a sufficiently long number of cycles are required to get the stabilization in temperature, at each given load step. However the longer each load step lasts the more the material gets damaged thus not leaving enough residual strength in the specimen for the next load step. Therefore a balance has to be found between the number of cycles, the heat generated and the maximum load applied. Therefore after a few tests it was found out that loading the specimens till 10,000 cycles and a load step of around 10% of the ultimate strength gave us enough resolution to plot the behavior of these specimens, furthermore it gave us enough residual strength left in the specimens to be able to load them up to 60 – 70% of the ultimate strength at final failure.

Figure 6-7 and Figure 6-8 show respectively the typical self heating and reduction of stiffness curves for the specimens, although the heat generated during tests stabilizes after a certain limit but the stiffness of the specimens keep on decreasing. This is as a result of the temperature of the experimental setup keeps on rising. This rise in temperature, although far below the glass transition temperature of the material, does cause certain matrix softening. As will be shown in a later section,

most of the significant degradation of stiffness comes from the degradation of the matrix hence it can be inferred that rise in temperature does effect the degradation of the polyester matrix.

It can be seen that above a 5.0 kN load the degradation in stiffness is highly accelerated and does not stabilize even after 10,000 cycles. Some tests were done till the final failure and the temperature rise never leveled out till final failure. Again from equation 6-1 it can be seen that since the heat liberated can be equated to the evolution of the stiffness and from the curves it is seen that although the temperature rise stabilizes but the stiffness keeps on degrading, we can infer that the temperature rise is a more reliable parameter to measure the intensity of damage in the specimen.

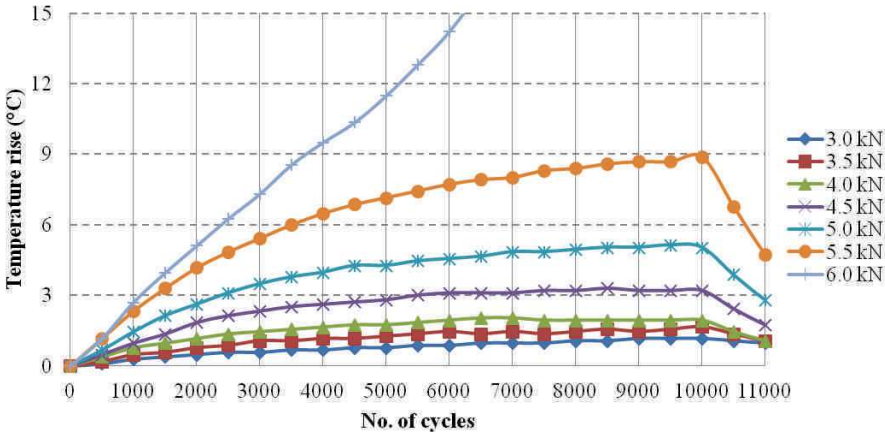


Figure 6-7: Self heating curves for 45° Biax specimens loaded cyclically at 5 Hz

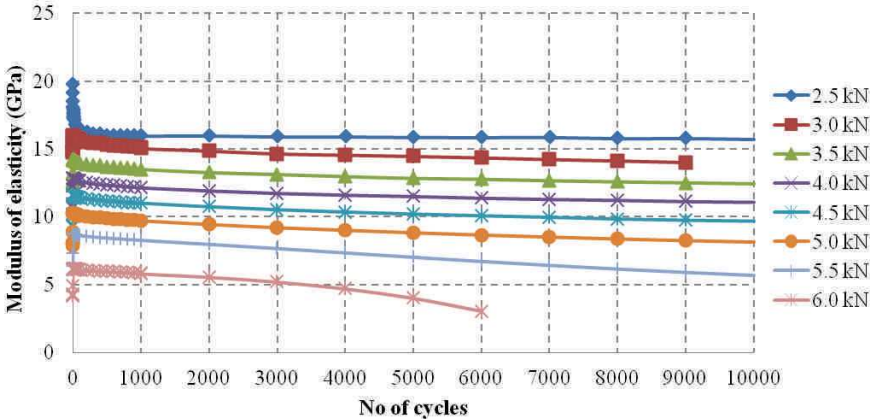


Figure 6-8: Reduction of stiffness during cyclic loading.

6.1.4 Effect of loading rate

As mentioned in preceding sections, the effect of loading rates on the behavior of the specimens is an important factor. Factors such as visco-plasticity can play an important role in the materials characterization under fatigue loading. The specimens are therefore loaded at different loading rates in monotonic tests to measure their behavior. It is seen that above a certain loading rate the material

response starts to converge. The loading rates for fatigue tests are hence chosen among these to minimize the effects of loading rate differences.

The monotonic tests are carried out at 5, 15, 30, 45, 60 and 150 mm/s. As already explained above there is a certain loading rate after which the material response converges and changes to the loading rates with a reduced effect on material response. From the Figure 6-9 it can be seen that any loading rate above 15mm/s gives effectively the same response. Hence for all practical purposes of fatigue testing between 2.5Hz and 5Hz which corresponds to 60 mm/s and 120 mm/s maximum loading rate, the response can be regarded as uniform.

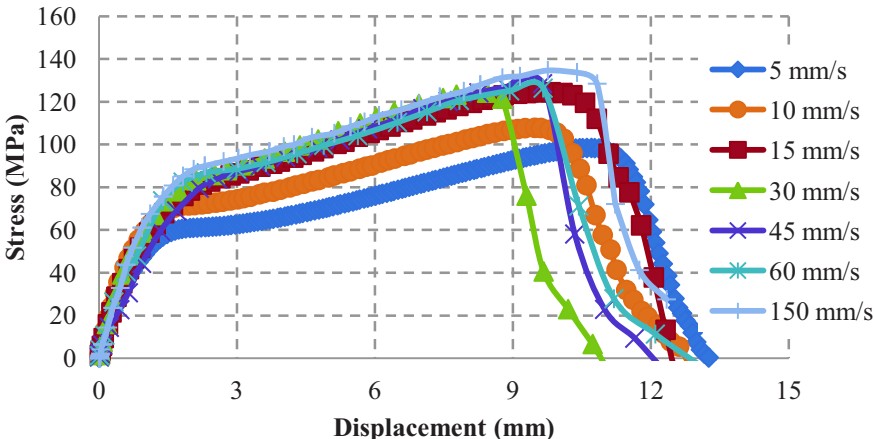


Figure 6-9: Stress displacement curves at different displacement rates.

To further understand the behavior of the material especially in the non linear response zone, the specimens have been visually inspected to check for damage.

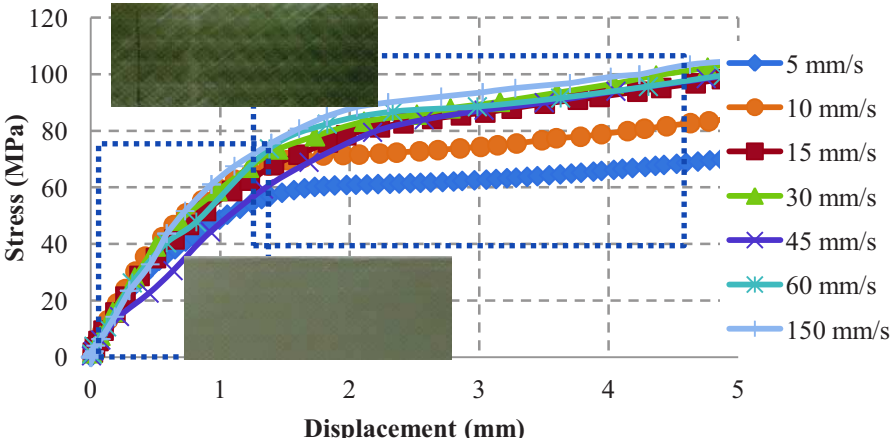


Figure 6-10: Damage in specimens corresponding to different load states.

As shown in the Figure 6-10 the two regions in the stress displacement curves, show the damaged and undamaged state of the specimens. It can be clearly seen from the specimens that as soon as the stress

displacement curve shows strong non-linearity, damage starts to appear. The damage is caused by a fiber matrix separation. Regarding the presence of such fiber matrix separation most of the non-linearity comes from physical damage and is not due to the plasticity of the matrix. Moreover the matrix fiber separation starts at around 0.1% strain.

6.1.5 Endurance limit using self heating

The principle behind using self-heating as an indicator of endurance limit is that as long as the damage progresses through the materials, there would always be some energy dissipated to the surroundings. The fact that at certain load levels the heat generated becomes equal to the heat dissipated means that the damage has stopped progressing. Hence the specimen can be loaded at this level for a very long period of time (infinite in practical terms) without it failing. Due to this fact the specimens keep on generating heat. Although the heat generation may slow down to a level where it dissipates all the energy gained to the surroundings. It is important to note the increase in heat liberated, this gives a point of inflexion beyond which the damage increases at a very rapid rate and the material damage progression becomes unstable. This unstable stage of damage progression is the limit above which materials cannot be loaded with a high level of confidence.

From the data generated in the above experiments the fatigue or endurance limit of the material can be found. For this purpose, two different approaches are used; see Figure 6-11 & Figure 6-12 below.

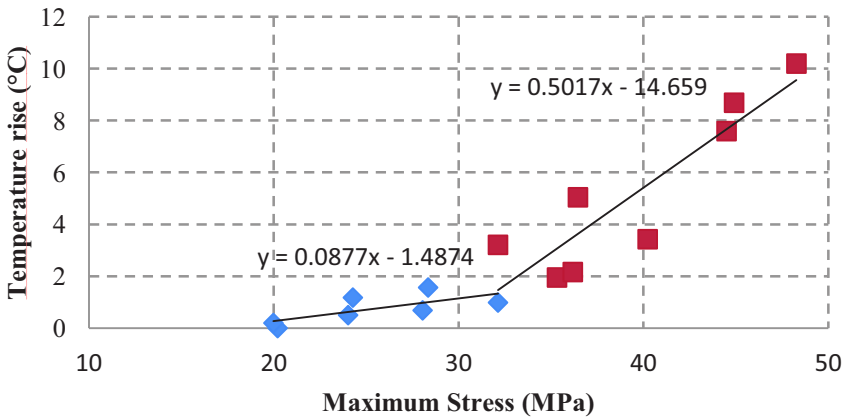


Figure 6-11: Determination of inflexion point in a self heating curve.

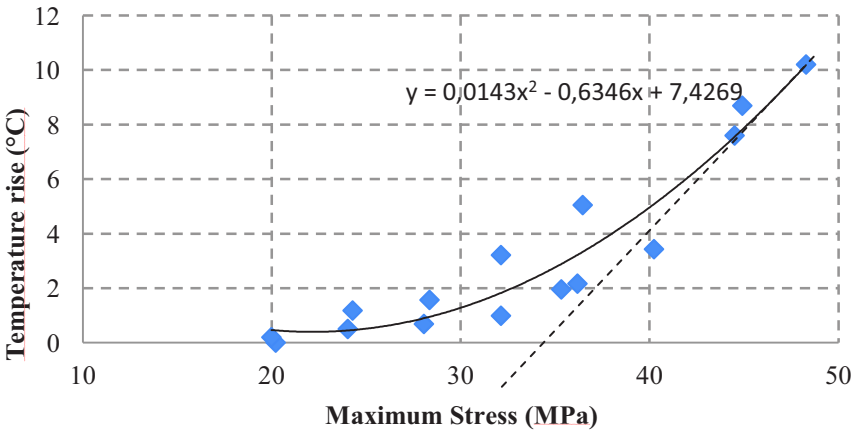


Figure 6-12: Determination of endurance limit using tangent to the end of best fitting quadratic curve.

Different authors have reported different methods for determining the endurance limit from the above given graphs (Emery & Dulieu-Barton, 2010) (Fargione, et al., 2002). There are a number of parameters to be understood about plotting the straight fitting lines for the above data. We have chosen the higher temperature rise stress levels as one region for curve fitting while the other low temperature rise as the second. Even after these fittings are done one can either choose the intersection of the two straight lines to give a unique value of endurance limit or find the x-intersects for both straight lines to get a range of endurance limit. Furthermore a tangent at the last point to a quadratic best fitting curve through all the points gives a fairly close value to the aforementioned method as shown in Table 6-5.

| Endurance limit in terms of maximum applied stress (MPa) | | |
|---|------------------------|-------|
| Self heating | Curve fitting method 1 | 34.62 |
| | Curve fitting method 2 | 33.46 |

Table 6-5: Comparison of 2 methods of curve fitting for finding the endurance limit

6.1.6 Rate of damage progression

As reported by (Stanely, 1997) (Andersons, et al., 2004) the rate of damage development can be seen to vary during a fatigue loading cycle. However the damage development measurements when done during self-heating tests are done for a specified number of cycles and are not till final failure. Hence here we will consider only the damage progression phase, where it is constant. It is known that the damage progression is much accelerated in the beginning cycles, and then it stabilizes before increasing again rapidly before final failure.

The rate of damage development can be seen to increase exponentially with the increase of the maximum applied stress, it can be said to follow a curve fitting rule as:

$$\dot{D} = \alpha e^{\beta \sigma_m} \tag{6-4}$$

Where \dot{D} the rate of damage development, α , β and σ is are curve fitting parameters and the maximum applied stresses respectively. This relation just shows the approximate exponential relation that can be used as an estimate for intermediate values of damage progression.

Furthermore it can be shown that the rate of progression of damage remains rather low, below the limit of endurance determined through self heating. After this threshold value the progression of damage starts to increase exponentially. Figure 6-13 shows results of some tests that had been run at higher load levels and at lower frequency, until failure. The frequency of loading was reduced to 2.5Hz above a stress level of 45MPa to limit the self heating, so that the temperature of the specimen stays well below the glass transition temperature.

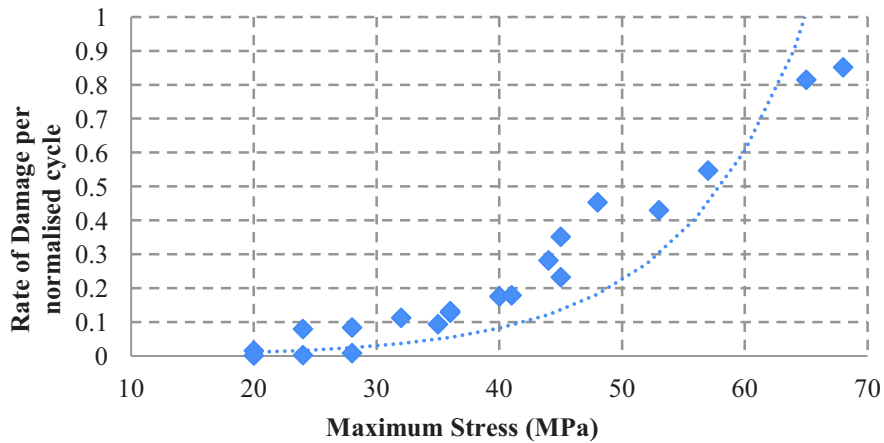


Figure 6-13: Rate of damage development against different applied stress levels.

In other reported tests on polyester resin matrices (Andersen, et al., s.d.), polyester resins show very little plasticity. The brittle fracture in the case of composite materials can be attributed to crack initiations at the fiber matrix interfaces. A close study of the failed surfaces shows a predominantly delamination type failure with some fiber pull out and almost negligible fiber breakage. This mode of failure is as expected as all the fibers are oriented at $\pm 45^\circ$ with no continuity in fibers between the two machine jaws. This has been shown in similar experimental work (Bizeul, et al., 2011) (Xiang, et al., 2014) (Colombo & Vergani, 2014) (Argüelles, et al., 2013).

6.2 Fatigue tests on UD specimens

After having developed the method for rapid characterization of composites in fatigue, we have applied the same testing procedure to uni-directional (UD) specimens. For these tests SN data was already available for the UD specimens loaded along the fiber direction. Some self-heating tests have been done to determine if the specimens show the same endurance limit.

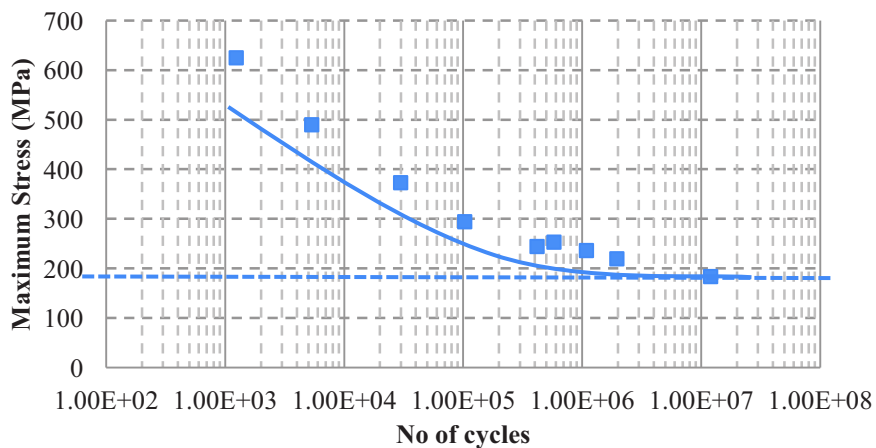


Figure 6-14: Wöhler curve for 0° UD specimens.

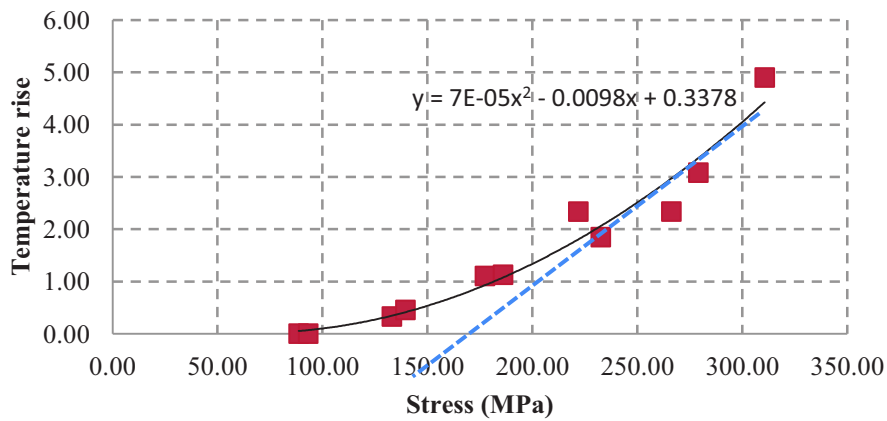


Figure 6-15: Endurance limit determination using self-heating curves.

From the two approaches shown above namely, Wöhler curve (Figure 6-14) and Self-heating (Figure 6-15) the endurance limit calculated is 183.30 MPa and 165.24 MPa respectively. Although there is a difference of about 10% maximum load but this falls within the statistical uncertainty of the fatigue tests. In addition the two types of tests were done at two different locations with the specimens although having the same materials they were of different thicknesses, thus causing some differences in the results. Another study would be done under same conditions, with the specimens fabricated from the same stock to have a better control comparison. The same procedure is used to determine the endurance limit of the specimens loaded at 90° to the fiber direct as shown in the Figure 6-16.

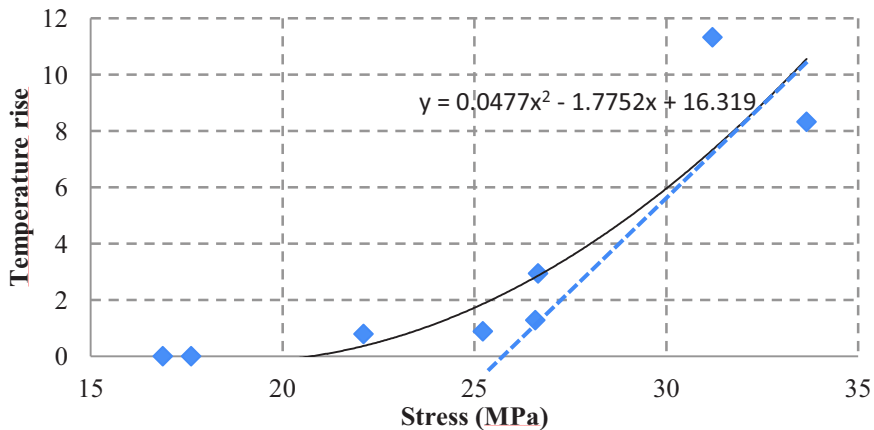


Figure 6-16 : Determination of endurance limit using self-heating for 90° UD specimens.

6.2.1 Degradation of stiffness

Unlike the specimens made up of 45° Biax, the 0° UD material specimens show almost no degradation of stiffness during the cyclic loads. This is due to the fact that although damage does exist within the specimens but the entire load is supported by the fibers hence in tension- tension tests the stiffness does not change. This further strengthens the need to use heat liberated during fatigue tests as a marker

of damage taking place within composites as compared to reduction of stiffness Table 6-6. The same principle is used to find out the endurance limit that is whenever there is a jump in the heat liberates it signifies unstable and continuous crack or damage propagation. Hence any structure loaded above this limit will not be able to perform well under cyclic loads. This by our definition is set as the endurance limit of the material.

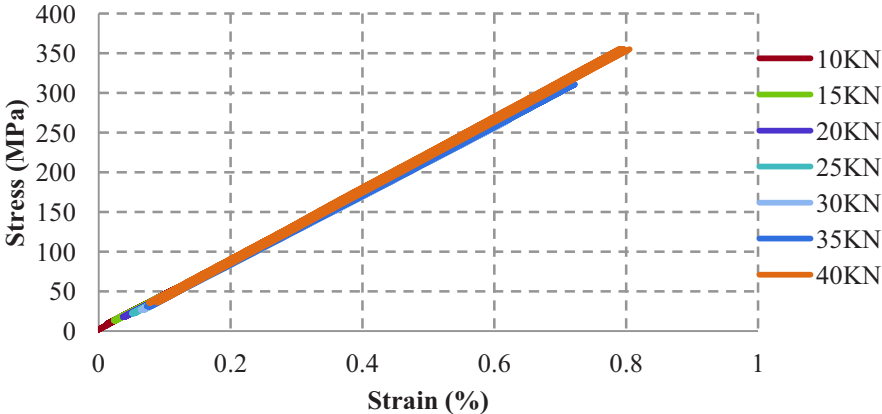


Figure 6-17: Stiffness of 0° UD specimens during self-heating cycles.

| Charge (kN) | Max. Stress (MPa) | % of failure stress | Elasticity modulus (GPa) |
|-------------|-------------------|---------------------|--------------------------|
| 15.00 | 133.04 | 13.78 | 52.23 |
| 20.00 | 177.38 | 18.37 | 46.10 |
| 25.00 | 221.87 | 22.98 | 43.45 |
| 30.00 | 266.19 | 27.57 | 42.67 |
| 35.00 | 310.67 | 32.18 | 42.99 |
| 40.00 | 355.00 | 36.77 | 45.33 |

Table 6-6: Stiffness of 0° UD specimens.

6.2.2 Failure Modes

As can be seen from the above shown results that 45° Biaxial materials are capable of being loaded to a higher percentage of their respective ultimate strengths as compared to 0° UD materials. This can be explained with the help of failure modes of the specimens.

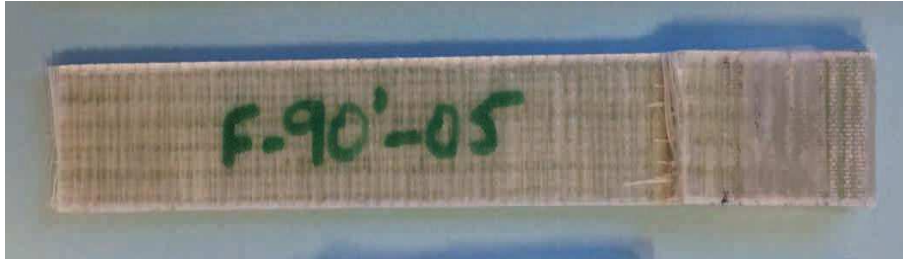


Figure 6-18: Failed 90° UD specimen showing pure matrix mode failure.



Figure 6-19: Failed 0° UD specimen showing fiber breakage and fiber pullout.



Figure 6-20: Failed 45° Biaxial specimen showing mostly delamination with some fiber sellout and breakage mode failure.

As can be seen from Figure 6-18, Figure 6-19 and Figure 6-20 the failure mode in each of the specimens is different. From pure failure of the matrix in the case of 90° UD to a Pull-out / Fiber-breakage in the 0° UD case. Furthermore the 45° Biaxial specimens show pure delamination type failure. Referring to the endurance limits measured for these different types of specimens in Table 6-7 it can be inferred that the matrix has a higher endurance limit in terms of load being supported as a percentage of its ultimate strength.

| Specimen | Endurance limit | |
|----------|----------------------|-------------------------------------|
| | Maximum stress (MPa) | Percentage of Ultimate strength (%) |
| 90° UD | 26.11 | 58 |
| 0° UD | 165.24 – 183.30 | 17 – 19 |
| 45° Biax | 32.61 – 35.62 | 23 – 25 |

Table 6-7: Comparison of endurance limits of the three types of different specimens.

In terms of absolute magnitude of stress, the 0° UD material shows the highest endurance limit. As discussed in the degradation of stiffness section the 0° UD specimens almost no degradation of stiffness until failure. However when viewed during actual tests it was seen that even at highly damaged conditions the specimens showed no or very little softening. This is attributed to the fact that in tension – tension cycles the loads are almost entirely carried by the fibers. On the other hand as soon as some of the fibers fail due to cyclic loadings the crack propagates brutally across the entire specimen and an immediate failure is experienced without a noticeable reduction in stiffness. There is an obvious reduction in endurance limits measured by the tests due to failure near the grips but that is an experimental anomaly that always exists. For us the important issue is the abrupt failure of the components loaded in the direction of the fibers is more important.

Another important point to consider here is the damage taking place in the matrix phase as shown in the 90° UD specimens. Refer to Figure 6-15 in the section of fatigue tests on UD specimens it can be seen that the heat liberated increases very rapidly near the endurance limit loading, signifying an increase in damage progression. Thus although we have a certain softening of the specimens up to the endurance limit loading cycles the failure is rather abrupt and unpredictable.

6.3 Discussion

The above mentioned investigation shows that for certain commercially used and manufactured composites a sharp increase in the damage progression can be used globally to determine a threshold for safe loading and for the characterization of materials. The investigations show that the heat generated due to damage progression follows a direct relation with the reduction in stiffness. Although the stiffness reduces as a result of heating as well but the rise in temperature of the machine was very little as compared to the heat generated by damage and the temperature rise was seen to be linear with each increase of load step. Hence this linearity of temperature rise can be taken into consideration when we see a constant reduction in stiffness even at below endurance limit stress levels.

Referring to the Figure 6-9 & Figure 6-10 it can be noted that the threshold for visible damage increases with an increase in displacement rate up to 15mm/s – 30mm/s and then levels for higher displacement rates. Hence for our experiments which lay in between 75 mm/s – 150 mm/s the effect of visco-plasticity can be regarded as constant.

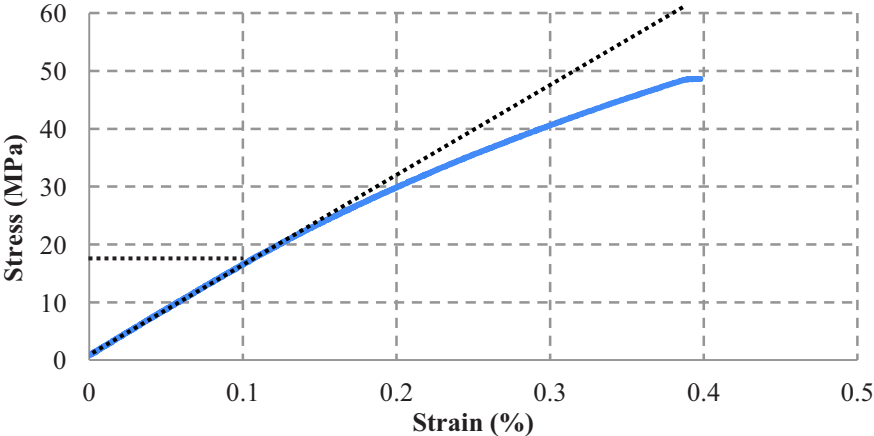


Figure 6-21: Stress-strain behavior of a test piece under monotonic loading

It can be seen that the material behaves non-linearly above ≈ 18.5 MPa. This can be shown by an 2D plane stress FEA model using Hashin's damage criteria to see the matrix failure in tension occurs at roughly the same value (uniform stress measured in the central region = 18.9 MPa), although more detailed approaches [(McCartney, 2008) (Bizeul, et al., 2011)] exist but for simple cases this suffices. It should also be noted here that the non linearity comes not only for damage taking place but due to the exponential elastic behavior of the matrix as well. Though this has not been included in the FEA. The model setup is a 2D plane model which models all the ply layup and Hashin damage criteria is used in each ply, to determine which ply would fail the first. The model simulates a simple traction test, i.e. one end is fixed while the other is given a displacement to create tension in the specimen.

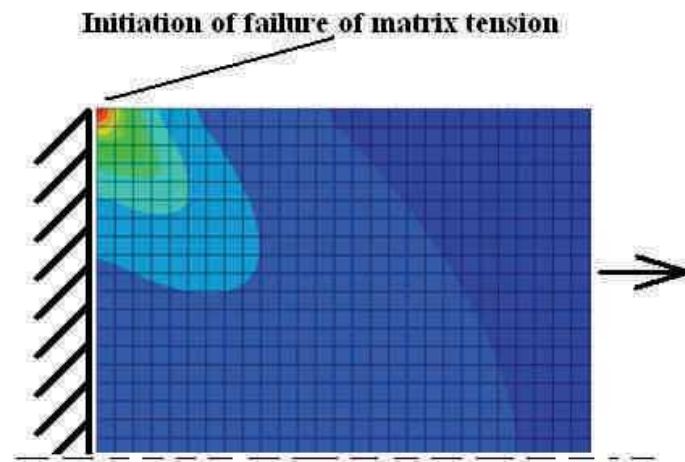
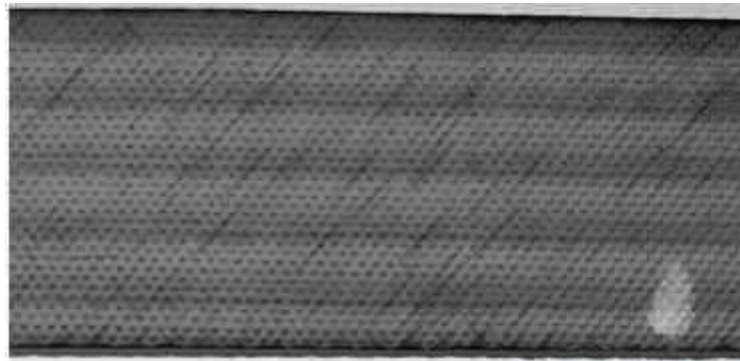


Figure 6-22: Damage Initiation of matrix in tension as predicted by Hashin's criterion

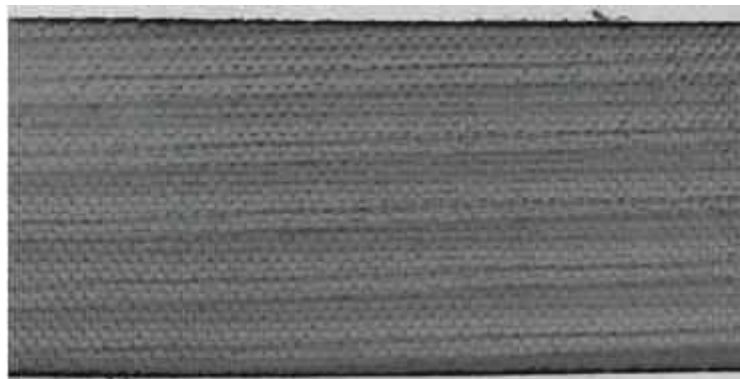
However visual inspection of the test pieces reveals that at a maximum applied stress level of 30 MPa and even after 1,000,000 cycles there is no visible damage or cracking taking place, on the other hand another specimen tested at 45 MPa for 400,000 cycles shows visible cracks appearing at the fiber-matrix interfaces, Figure 6-23. These cracks are throughout its thickness when viewed using backlighting.

It is well seen by the monotonic loading curves that the specimen will be damaged at this load level. However the damage progresses very slowly under cyclic loading below the threshold value shown in Figure 6-21 and there is a less significant degradation of stiffness.

This can be confirmed by the strain curves of this test traced during the cyclic loading. Since the loading regime is force controlled hence we consider the strain curves as better representatives of this behavior.



(a) 40% of ultimate strength (45 MPa) for 400,000 cycles



(b) 28% of ultimate strength (30 MPa) for 1,000,000 cycles

Figure 6-23: Damage development of the test piece loaded at (a) 45 MPa for 400,000 cycles and (b) 30 MPa for 1,000,000 cycles.

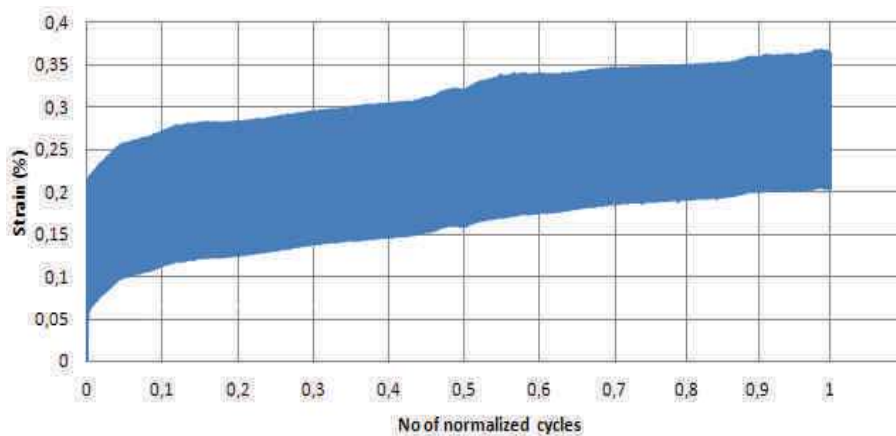


Figure 6-24: Strain plots until 1.000.000 cycles showing hysteresis in the 30 MPa loaded specimen.

It can be seen from Figure 6-24 that the material shows a certain hysteresis and even though it had been loaded beyond its elastic limit it holds for this regime of cyclic loading without visible damage or cracking. This reduction in stiffness is hence attributed to the hysteresis of the polyester matrix. Although the Wöhler curves are the most acceptable forms of representing fatigue life but they might pose difficulties when it comes to composites. As with composite materials the dispersion in test results is very high. A few tests were run to develop the Wöhler curve on the 45° Biax material as

shown on Figure 6-25. The results show one data point for each load step. This Wöhler curve can be used to estimate the endurance limit, but as explained before a higher number of tests are needed to develop a presentable data set. Instead of using asymptotes from Wöhler curves we have tested a specimen just below the endurance limit for 1 million cycles and monitored it for its damage.

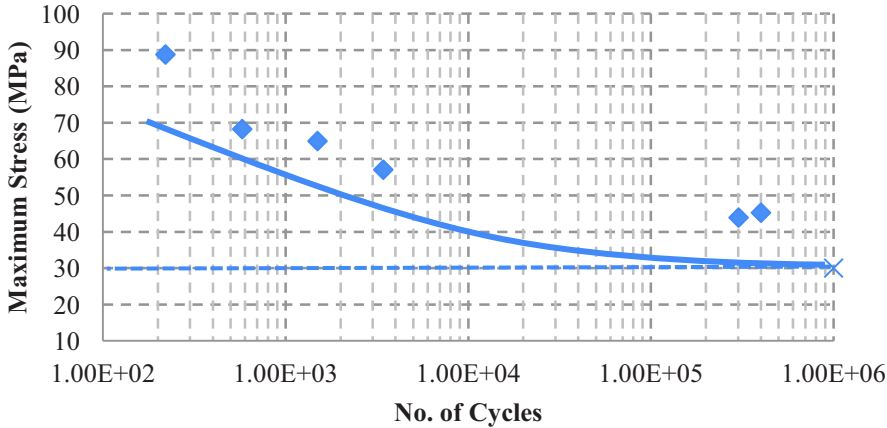


Figure 6-25: Wöhler curve for 45° Biaxial specimens.

6.4 Self heating tests on NORPOL

The same procedure adopted for the 45° biax composite specimens was applied to the NORPOL Polyvinylester specimens as well to study the correlation of self heating and the degradation of stiffness in the specimens. The same mode of experimentation has been applied to study the phenomena of self heating, Figure 6-26.



Figure 6-26: NORPOL Specimens instrumented with extensometers
 (a) Bare extensometer knives, (b) padded knives.

The strain measurements were done using an extensometer and care had to be taken because the surface hardness of the NORPOL specimens is fairly low. This causes the knife edges of the extensometer to engrave lines into the specimens causing them to fail at these scratch marks.

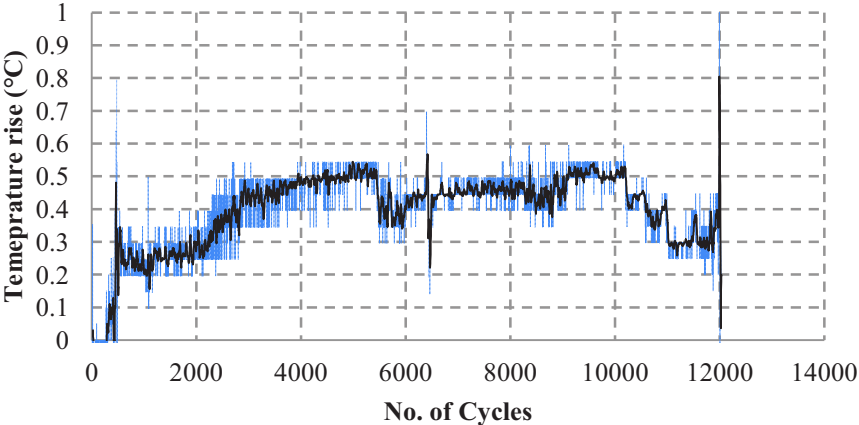


Figure 6-27: Self heating curve up to failure for NORPOL specimens.

| Specimen | Maximum applied stress (MPa) | Temperature rise up to stabilization (°C) |
|-------------|------------------------------|---|
| AF-Colle-01 | 8.75 | 0.35 |
| AF-Colle-04 | 8.75 | 0.35 |
| AF-Colle-09 | 15.0 | 0.6 |
| AF-Colle-10 | 17.5 | 0.7 |
| AF-Colle-05 | 20.0 | 0.8 |
| AF-Colle-11 | 20.0 | 0.8 |
| AF-Colle-02 | 22.5 | 0.9 |
| AF-Colle-12 | 22.5 | 0.9 |
| AF-Colle-13 | 25.0 | 1 |
| AF-Colle-06 | 27.5 | 1.1 |
| AF-Colle-14 | 27.5 | 1.1 |
| AF-Colle-15 | 30.0 | 1.2 |
| AF-Colle-03 | 32.5 | 1.3 |
| AF-Colle-17 | 32.5 | 1.3 |
| AF-Colle-07 | 35.0 | 1.4 |

Table 6-8: Temperature rise for different applied maximum stresses.

The tests were run at 5 Hz to promote self heating for only 3750 cycles per load step. It was seen that the specimens heated very readily as compared to the composite specimens. This can be attributed to the material properties of the specimens.

The self heating curves show a very slight rise in temperature and then stabilize almost immediately. The typical temperature rise is shown in the Figure 6-27 and the temperature rises for each of the stress levels is summarized in Table 6-8.

The temperature rise against the Maximum applied stress is plotted to find the endurance limit as in the previous case. The tangent thus drawn at the final point gives a maximum load value of 0.65 kN corresponding to a stress of 16.25 MPa.

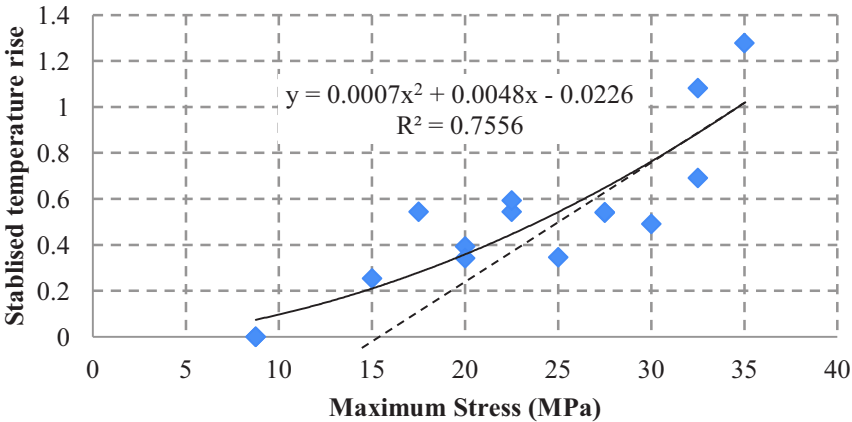


Figure 6-28: Plot of temperature rise against the maximum applied stress.

The results shown in the Figure 6-28 shows the level of stress to which if the specimen is loaded should not fail prematurely. Specimens were thus chosen and loaded at 0.7 kN and 0.6 kN a 5 Hz until failure, which is just above and below the load level of 0.65 kN calculated by the self heating curve. It was seen that the 0.7 kN specimens failed anywhere from 250000 to 400000 cycles. However the specimens loaded this load did not show a significant decrease in stiffness before failing.

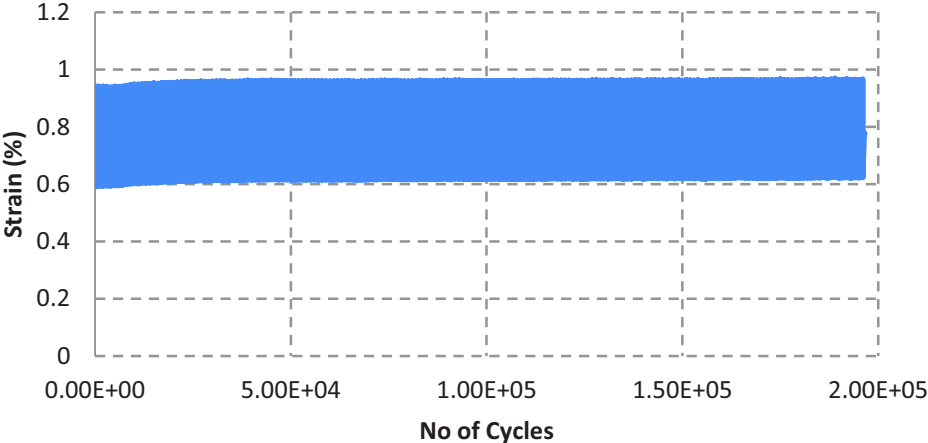


Figure 6-29: Degradation of stiffness during cyclic loading.

The Figure 6-29 shows the degradation of stiffness during a test when the specimen is loaded at 0.7 kN where it will eventually fail before 1 million cycles. As can be seen the specimen does not show a high degree of loss of stiffness during the tests and fails abruptly. This brittle failure may be due to unstable crack propagation at these load levels.

However the specimen loaded at 0.6 kN surpassed 1 million cycles and again no degradation in stiffness was seen, apart from the first few 1000 cycles where the specimen comes into the dynamic stiffness state. This result suggests that self heating tests can be used for the estimation of fatigue life of such polymer materials as well.

6.5 Conclusions and Discussion

The present study shows a definite relationship between the heat generated and the damage taking place in long fiber polymer composite material. The self-heating tests experimentally show that they can be used as a good estimate of the material's endurance limit. However there is always certain level of hysteresis effects due to plastic deformation and visco-elastic behaviors, which shall be investigated next. The test 45° Biaxial specimen loaded to 30 MPa near to the endurance limit determined by self heating (34 MPa) bore 1,000,000 cycles without any visible damage, although a reduction in elasticity was seen.

From this investigation, although difficult to define endurance limit, it can be inferred that any sharp decrease in rigidity or increase in heat generation are signs of the material fiber-matrix interfacial crack growth, in addition to hysteresis in the polymer matrix. As far as the structure is loaded cyclically under the elastic limit of the material, no sudden fatigue failure should occur. Hysteresis in polymer would also not cause sudden failures, but the rigidity of the structure would need to be checked.

Another important aspect of this investigation is that, by using plasticity curves one can determine the load threshold even in the damaged state where the structure would sustain under cyclic loading. Further investigations would be made to determine whether this holds for other materials and layups.

Taking into account the failure modes and the reduction in stiffness before failure for Biaxial as well as UD specimens, it can be concluded that any structures where the loadings are along or perpendicular to the fiber directions may cause rather unexpected fatigue failures. Hence the degree of security and early warning may be rather limited. Whereas for multi-axial composite materials and/or materials loaded at different angles as to those of their fibers the mixing of failure modes gives rise to a rather progressive softening and hence a predictable failure with early warning indicators can be accepted.

Although these tests are not completely conclusive and further experiments should be done in different loading regimes, we have a better knowledge of the behavior of the composite materials to be used on floating wind turbine blades. These results may lead to the following practical results:

- Establishment of a reliable way to define the behavior laws to be included in the design office tools (such as FEM analysis tools).
- Trends on better production processes and design approaches.

- Interesting and innovative methods to predict the lifecycle behavior of the composite blades that can be used on a regular basis for instance to carry out predictive tests on samples within the production facilities.

Furthermore the tests on NORPOL showed encouraging results as well showing fairly good correlation between the self heating curves and the defined fatigue life criteria. Although there was no loss in stiffness hence there is no direct correlation to be drawn between the heat generated and the damage taking place in the specimen in terms of degradation of stiffness.

Chapter 7 --- Finite element modeling of the wind turbine blade

Table of Contents

| | | |
|-------|---|-----|
| 7.1 | Characterization of materials..... | 181 |
| 7.1.1 | Modeling..... | 183 |
| 7.1.2 | Discussion..... | 186 |
| 7.2 | Characterization of interfaces..... | 187 |
| 7.2.1 | Model setups for DCB tests..... | 189 |
| 7.2.2 | Discussion on Results..... | 192 |
| 7.2.3 | Model setups for ENF tests..... | 197 |
| 7.3 | Modeling of single lap joints..... | 199 |
| 7.3.1 | Modeling strategy..... | 200 |
| 7.3.2 | Discussion on Results..... | 202 |
| 7.4 | Modeling of the complete blade..... | 207 |
| 7.4.1 | Modeling strategy..... | 207 |
| 7.4.2 | Tier 1: Complete blade model..... | 208 |
| 7.4.3 | Tier 2: 3D Shell blade section..... | 211 |
| 7.4.4 | Tier 3: 3D Solid blade section..... | 215 |
| 7.4.5 | Tier 4: Sub model of the Tier 3 solid model..... | 220 |
| 7.4.6 | Tier 5: Sub model of Tier 4 including cohesive zones..... | 223 |
| 7.5 | Conclusions and Discussion..... | 229 |

The modeling of the wind turbine blade under Finite Element methods is done using the ABAQUS software. The modeling takes a pyramidal approach. At the first stage the specimens used for the characterization of the materials are simulated in finite elements. Their behaviors are noted and compared to the experimental results. The basic criterion for comparison is taken as the global behavior of the specimens. In our case this global behavior is taken as the force transmitted through the material. Or in other words the reaction on the fixations, used to hold the specimens in the test machines.

The materials are characterized using mono-material specimens. Further their assemblies are tested using specimens which use a number of combinations of the constituent materials. Namely composite layups in combination with foam cores for sandwich structures and specimens bonded together for the determination of the interfacial de-bonding properties.

In the third tier the bonded lap joint specimens are used for the determination the strength of bonded joints under mixed mode failure. This is taken as a representation of an assembled joint in the real structure. The comparison of final strength and especially the mode(s) of failure as predicted by ABAQUS and as those seen in the real tests serve to validate the finite element model strategy used.

Once the validation of the tests up to the third tier (assembly level) has been done we move on to a global model of the entire wind turbine blade. This global model (referred to as parent also in later sections) serves only as a model to which the global boundary conditions are applied. These boundary conditions include the aerodynamic and inertial loads. The modeling of the blade with the real stratification is important to measure the centrifugal and gravitational inertial loads; however for the aerodynamic loads a model of the outer surface is sufficient.

Once the global response of the model is determined the zones within the blade which are the most stressed are extracted and modeled as short sub-sections of the entire blade. On these short sub sections the mesh size can be reduced keeping the stress fields of the parent model. Once sufficient mesh refining is done to localize the highly stressed regions their sensitivity to damage is ascertained. The sensitive regions are then modeled in further thinner sections with the layers modeled in three dimensions to visualize the failure modes and their initiation. This detailed analysis in the final step will show the weak spots to be reinforced in the final turbine blade.

7.1 Characterization of materials

The specimens used for the characterization of composites, adhesive and the foam core are as follows, shown in Figure 7-1 - Figure 7-3.

1. 250 x 25mm UD and Biax specimens each of 4mm thick for tensile tests.
2. Dog-bone shaped specimens for NORPOL adhesive with a 10mm wide neck and overall thickness of 4mm
3. Sandwich beams used for the characterization of the PVC foam core under flexion tests.

The specimens are used for the determination of the ply properties. Then these properties are used to model the Biax and Triax composite specimens. The Biax composite specimen models are then compared to the experiments for their validation.

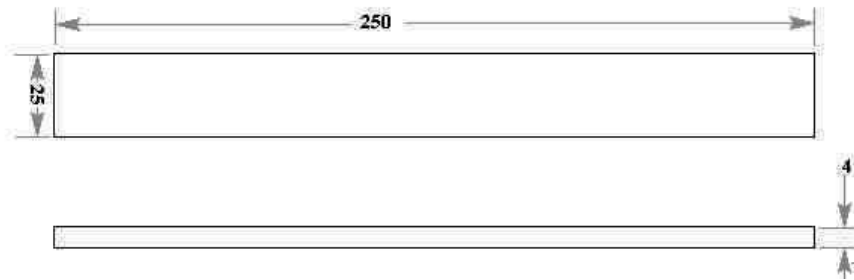


Figure 7-1: Dimensions for 45° Biax and UD specimens used in tensile tests.

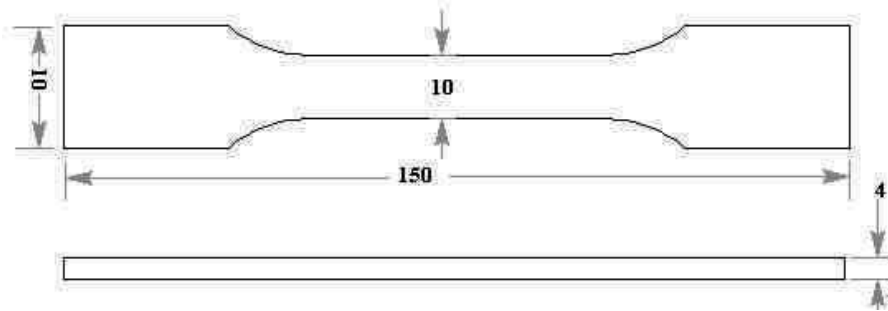


Figure 7-2: Dog bone shaped NORPOL specimens.

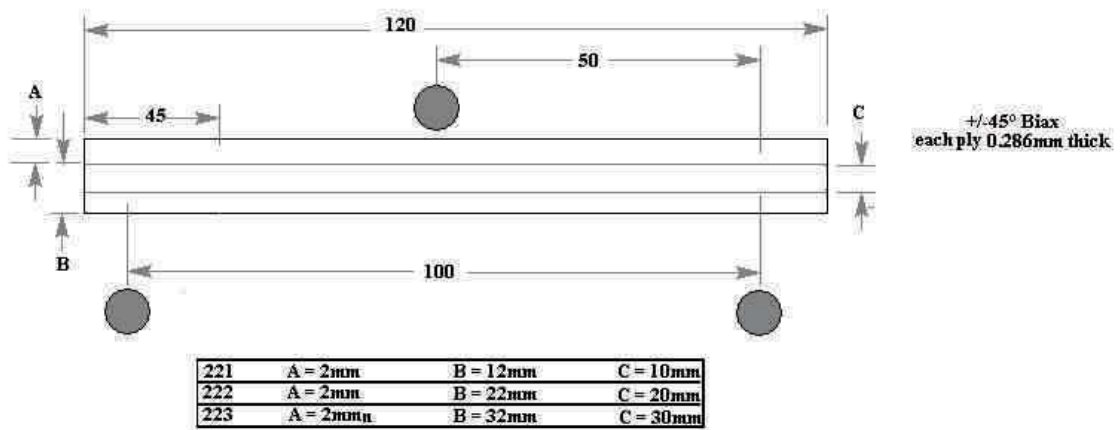


Figure 7-3: 3 point flexion sandwich specimens.

7.1.1 Modeling

The modeling of the specimens to be tested under simple tensile tests is done using 3D shell elements for the sake of simplicity and for the sake of saving on computational resources. The properties of the plies along and perpendicular to the fiber direction are taken from tests done on UD specimens. Here we shall not model the tensile tests of these UD specimens however they shall be used to model the tensile tests done on 45° Biax type composites to show the validity of the modeling technique.

As already explained the models are made of 3D shell elements. The 3D shells give the liberty to make fiber layups. The material properties are summarized in Table 7-1.

| Fiber glass – Polyester Composite | | |
|--|----------------|-------|
| Young' modulus in the fiber direction | E_1 (MPa) | 48160 |
| Young' Modulus in the layup plane and perpendicular to the fiber direction | E_2 (MPa) | 11210 |
| Young's Modulus normal to the fiber layup plane and perpendicular to the fiber direction, assuming perfect transverse orthotropy | E_3 (MPa) | 11210 |
| Poisson's ratio in the fiber direction to perpendicular on it | ν_{12} | 0.274 |
| Poisson's ratio in the fiber direction and perpendicular to the layup plane | ν_{13} | 0.096 |
| Poisson's ratio perpendicular to the fiber direction and normal to the layup plane | ν_{23} | 0.096 |
| Shearing Modulus in the plane containing the layup | G_{12} (MPa) | 4420 |
| Shearing Modulus normal to the plane containing the fiber | G_{13} (MPa) | 4420 |
| Shearing Modulus in the plane normal to the plane of layup in the direction of the fibers | G_{23} (MPa) | 9000 |
| Adhesive NORPOL – Polyester | | |
| Young's Modulus in isotropic direction | E (MPa) | 3100 |
| Poisson's ratio | ν | 0.3 |
| Strength to final failure | (MPa) | 51.25 |
| Strength of Fiber glass – Polyester Composite | | |
| Tensile in fiber direction | X_t (MPa) | 965.5 |
| Compression in fiber direction | X_c (MPa) | 978 |
| Tension in transverse direction | Y_t (MPa) | 33.5 |
| Compression in transverse direction | Y_c (MPa) | 171.8 |
| Shearing in and transverse to the fiber direction | S (MPa) | 48.69 |

Table 7-1: Material properties used for modeling.

Once the geometry is drawn taking into account just the span length of the specimen of 150 x 25mm composite layups are applied. These layups are applied in the form of stacked plies to the shell elements, Figure 7-4. The meshing is a critical step in any finite element analysis, for this purpose a mesh sensitivity analysis needs to be done. The mesh sensitivity analysis is done hence to compare the actual force displacement behavior with that of the finite element models. For the nomenclature of mesh sizing refer to Figure 7-5.

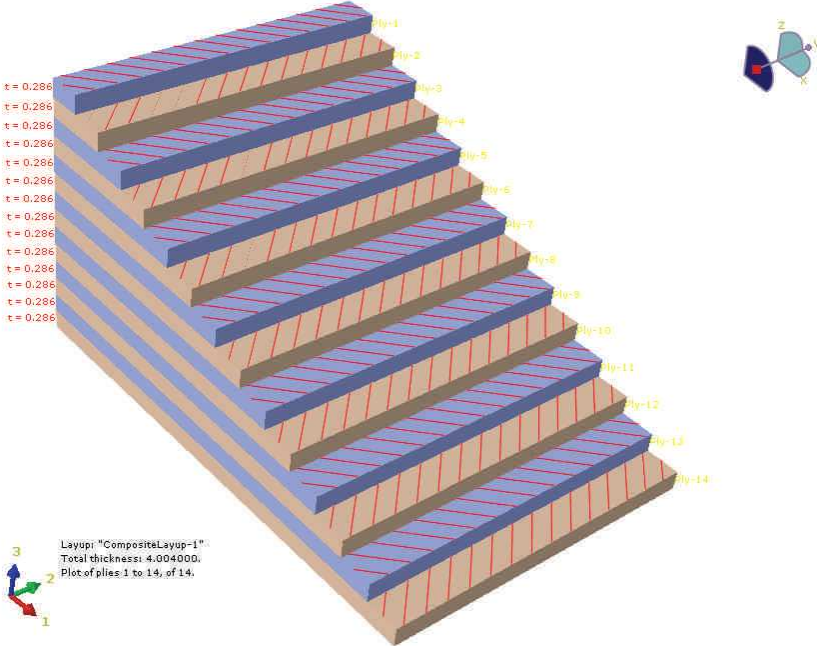


Figure 7-4: Representation of plies stacked in $\pm 45^\circ$ in order to simulate a biaxial mat.

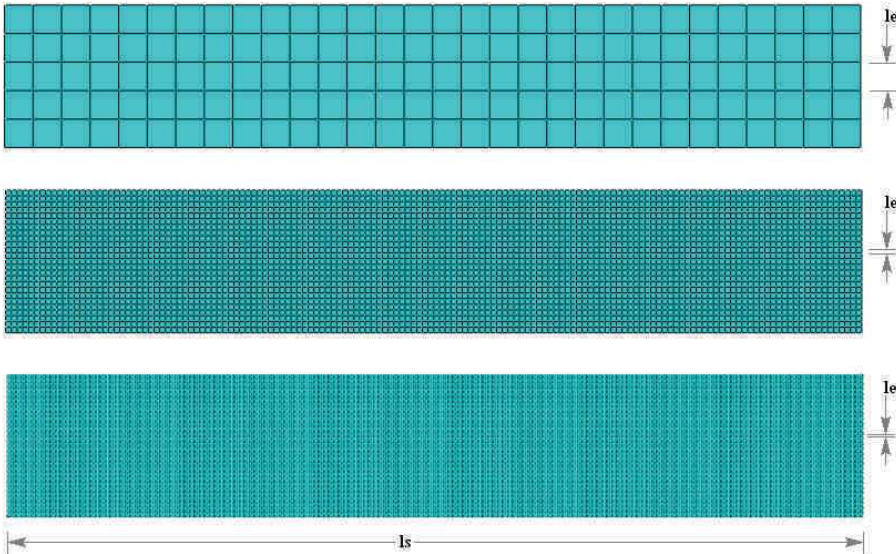


Figure 7-5: Different mesh element size to specimen length ratios.

We have chosen a mesh size of 5, 1 and 0.25mm for a span of 150mm giving us “ l_e/l_s ” ratios of 0.03, 0.006 and 0.0017 respectively.

After applying a displacement to one end while fixing the other a tensile test is simulated.



Figure 7-6: Boundary conditions of the finite element model; Left edge fixed, right end being pulled with the help of a fixed displacement.

For the validation of the model it is important to compare them with experimental results. Here 5 curves of 5 different experimental tensile tests are used for the determination of the validity of the results. Note here that we have chosen the stress – displacement curves as the representative comparison standards instead of stress-strain analyses because stress – displacement graphs show the onset of damage better than stress-strain curves. Also the fact that the use of CZM is important in the failure modeling hence we are staying within the parameters of stress – displacement (traction separation) although stress-displacement curves are also often seen in other studies.

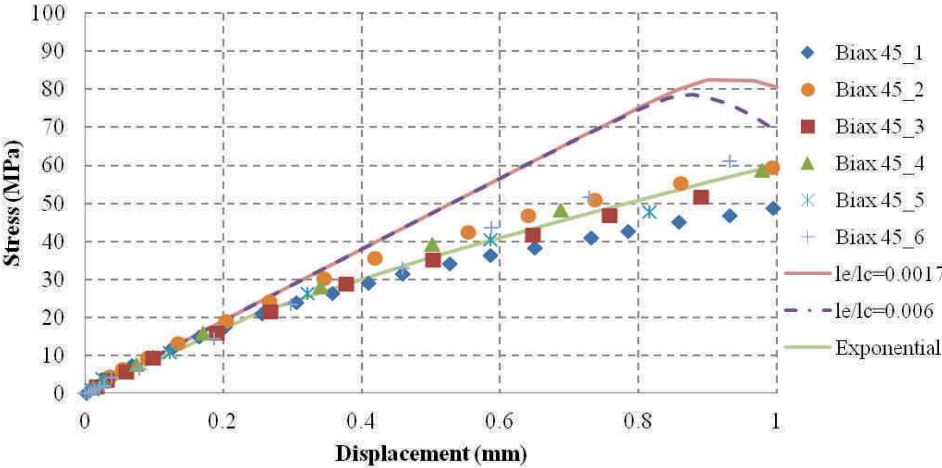


Figure 7-7: Different mesh sized specimens are compared with experimental force - displacement curves.

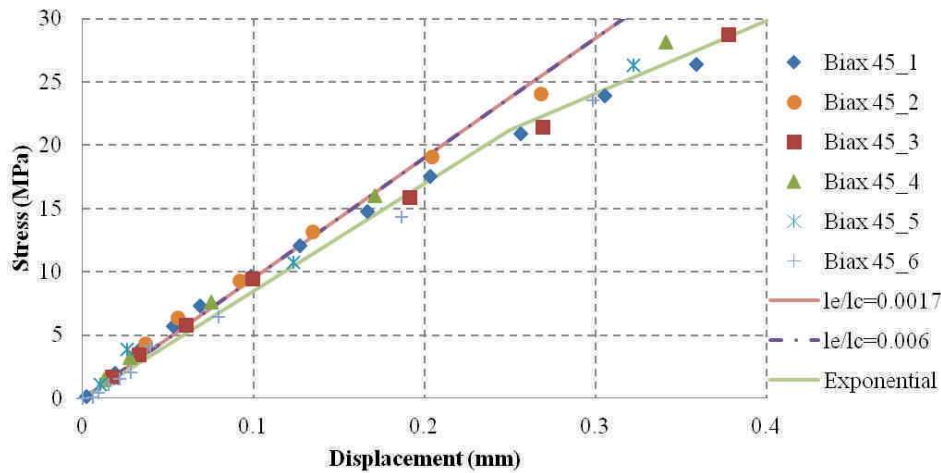


Figure 7-8: Comparison to FE models up to the first linear part of the force - displacement curves.

The results shown in Figure 7-7 and Figure 7-9 are a comparison of different mesh sizes to the experimental results. These graphs serve to set the mesh size ratio for convergence and also show the prediction of linear properties as well as the damage response of the composite specimens. An exhaustive discussion follows to explain the graphs thus shown.

7.1.2 Discussion

The results shown in the Figure 7-7 and Figure 7-8 have the following important points to consider:

1. To keep within the limits of allowed complicity for large structural models a global modified Young's law can be defined. Instead of using a linear force-displacement or stress - strain relationship, a logarithmic relationship is formulated of the form given in the equation 7-1. It should also be noted from the Figure 7-7 that the first elastic part of the curve shows an exponential elastic law, however for our design the stress limits never exceed the 30 MPa level hence a linear elastic law can be used without a great deal of inaccuracy.

$$\sigma_l = A \ln(\varepsilon_l) \quad 7-1$$

The logarithmic law as given in the equation 7-1, relates the applied stress to the strain in the specimen. However this law relates the two through a rigidity constant "A" which is not the same as the young's modulus as given in some exponential laws as in section 1.8. The other problem with logarithmic laws is that they need to be set to be corrected for each type of structure and do not follow intrinsic material properties hence they are empirical laws suitable for global structural responses.

2. In Figure 7-8, Hashin's Damage model has been used to determine the damage characteristics of the material specimens. However it can be seen even at very refined mesh sizes this model does not succeed to take into account the progressive softening of the specimens. Rather there is an abrupt fall in the rigidity. This abrupt fall is attributed to the sudden failure of matrix in

tension predicted by the Hashin's Damage model; refer to section 1.3 for the details on this model. It is well known for polyester based composites that there is a definite reduction in elasticity within the matrix before failure. This plasticity is not modeled here with Hashin's damage model. Furthermore the modeling of plasticity within the matrix in the composites tends to complicate the model which can lead to excessive need of computational resources when talking in terms of modeling of the structure.

- Referring back to the Figure 7-7 and Figure 7-8, it can be seen that the mesh size with a " l_e/l_s " ratio of 0.0017 or less shows the best correlation between modeled and experimental results. Furthermore since most of our final design is based on fatigue life of the materials in question whose mechanisms lie near the elastic portion of the behavior shown above hence we need not develop very much on the non-linear behavior of the materials used.

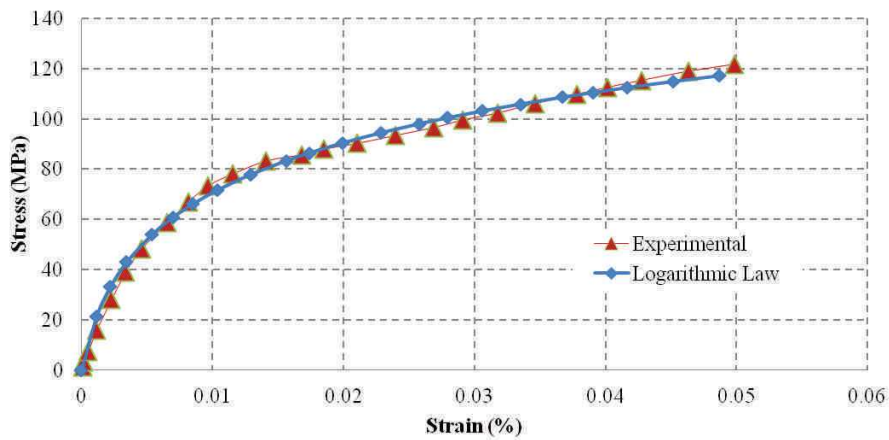


Figure 7-9: Comparison of Stress - strain curves up to final failure and a logarithmic law.

7.2 Characterization of interfaces

The characterization of interfaces and bonded assemblies are done using DCB, ENF and SLB specimens, chapter 4 and 5. Once the values of the corresponding SERR's are calculated from tests, the models are used to compare the validity of the CZM used in the finite element code.

As explained in the different approaches used for CZM modeling, ABAQUS uses a linear softening approach, Figure 1-12e of Chapter 1.

According to this law the traction-displacement curve is divided into 2 regions and further there are 3 parameters which define the traction-separation curve. The first part of the curve is the elastic force displacement part, or in terms of CZM the traction separation part. This part ends when the traction or specifically the stress at this traction reaches the value " t " which signifies the stress condition at the initiation of crack propagation. The slope of this traction-separation curve is defined in the first undamaged region by the rigidity of the CZM element " E/K_m " and in the second or damaged region from the mode I, II or III SERR " G_I, G_{II} or G_{III} ". Refer to Figure 7-10 for the complete definition of the law used by ABAQUS.

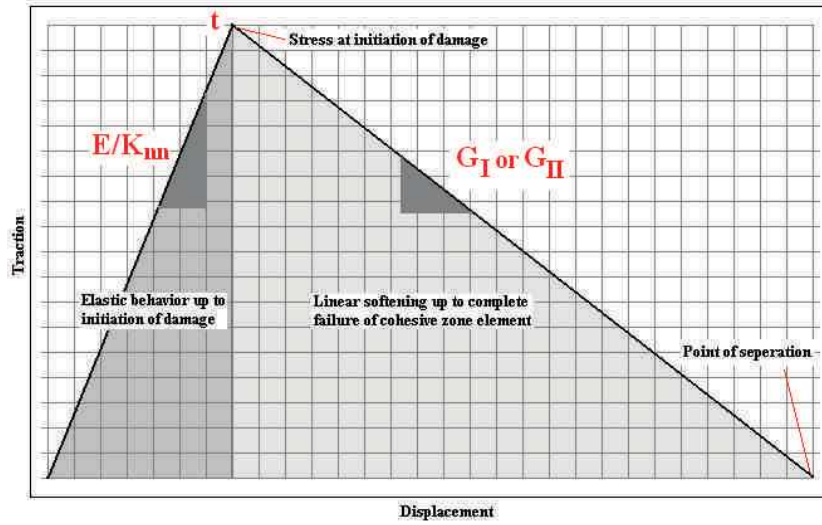


Figure 7-10: Linear softening traction-separation law defined in terms of ABAQUS parameters.

It is important to note here that the traction-separation law for the three modes of SERR follows the same tendency. Further more in the text to follow we shall use separation instead of displacement although separation is the actual failure of the CZM element where the cohesion in the elements degrades to zero. For our purposes, especially for the validation of structures, the softening part of this curve is of less importance and the value of SERR helps in displacing the point of separation to more or less displacement or strain. Hence the SERR in these terms can be considered as the residual rigidity of the damaged / softening part of the structure.

One of the features of weak cohesive zone model formulations is the introduction of viscosity for attaining static equilibrium across the CZM at the start of the failure. In general the problem of convergence can be solved by adding small viscosity to the traction-separation constitutive laws. The equations 1-24 and 1-25 are hence modified to contain the dissipative viscosity terms in them. These equations are thus shown in equations 7-2 and 7-3.

$$T_n = \frac{\phi_n}{\delta_n} \exp\left(-\frac{\Delta_n}{\delta_n}\right) \left\{ \frac{\Delta_n}{\delta_n} \exp\left(-\frac{\Delta_t^2}{\delta_t^2}\right) + \frac{1-q}{r-1} \left[1 - \exp\left(-\frac{\Delta_t^2}{\delta_t^2}\right) \right] \left[r - \frac{\Delta_n}{\delta_n} \right] \right\} + \xi_n \frac{d}{dt} \left(\frac{\Delta_n}{\delta_n} \right) \quad 7-2$$

$$T_t = 2 \left(\frac{\phi_n \Delta_t}{\delta_t^2} \right) \left\{ q + \left(\frac{r-q}{r-1} \right) \frac{\Delta_n}{\delta_n} \right\} \exp\left(-\frac{\Delta_n}{\delta_n}\right) \exp\left(-\frac{\Delta_t^2}{\delta_t^2}\right) + \xi_t \frac{d}{dt} \left(\frac{\Delta_t}{\delta_t} \right) \quad 7-3$$

where the “ $\xi_{n,t}$ ” are the viscosity parameters which govern the viscous energy dissipation in the normal and tangential direction. The viscosity does not represent any physical energy dissipation but is just to stabilize the instabilities when the crack initiates at the weak plane. However in ABAQUS, the value of both the viscosity parameters is the same for the calculations. Furthermore it is seen that viscosity problems are more important in shearing or mode II failure initiation as compared to mode I failure initiations. Usually the value of this viscosity is to be taken as small as possible but a rough guide to help selecting an appropriate value is to use the relation in equation 7-4.

$$\frac{\xi a V_0}{E' \delta_n^2} \ll 1 \quad 7-4$$

where “ E ” depends on the stiffness of the 2 materials in the interface “ a ” is the material height and “ V_0 ” is the vertical velocity of the deformation,(Gao & Bower, 2004).

7.2.1 Model setups for DCB tests

One of the salient features of interfacial characterization tests is that they are predominantly flexion type tests. The flexural properties of materials thus play an important role in their determination. For the sake of saving on computational time, the DCB specimens are modeled using continuum shell elements. They show a good correlation in flexural response to the experimental results.

The material properties are the same as defined for the previous example and given in Table 7-1. The CZM are modeled into the specimen models using cohesive elements. Each of the geometry is accurately modeled for best correlation to the experimental results.

The double cantilever beams are modeled in mono material composite type beams for the characterization of interlaminar interfaces, Figure 7-11. For the bonded joints the real adhesive thicknesses are modeled and same for the sandwich structures, their foam cores are modeled with real thicknesses.

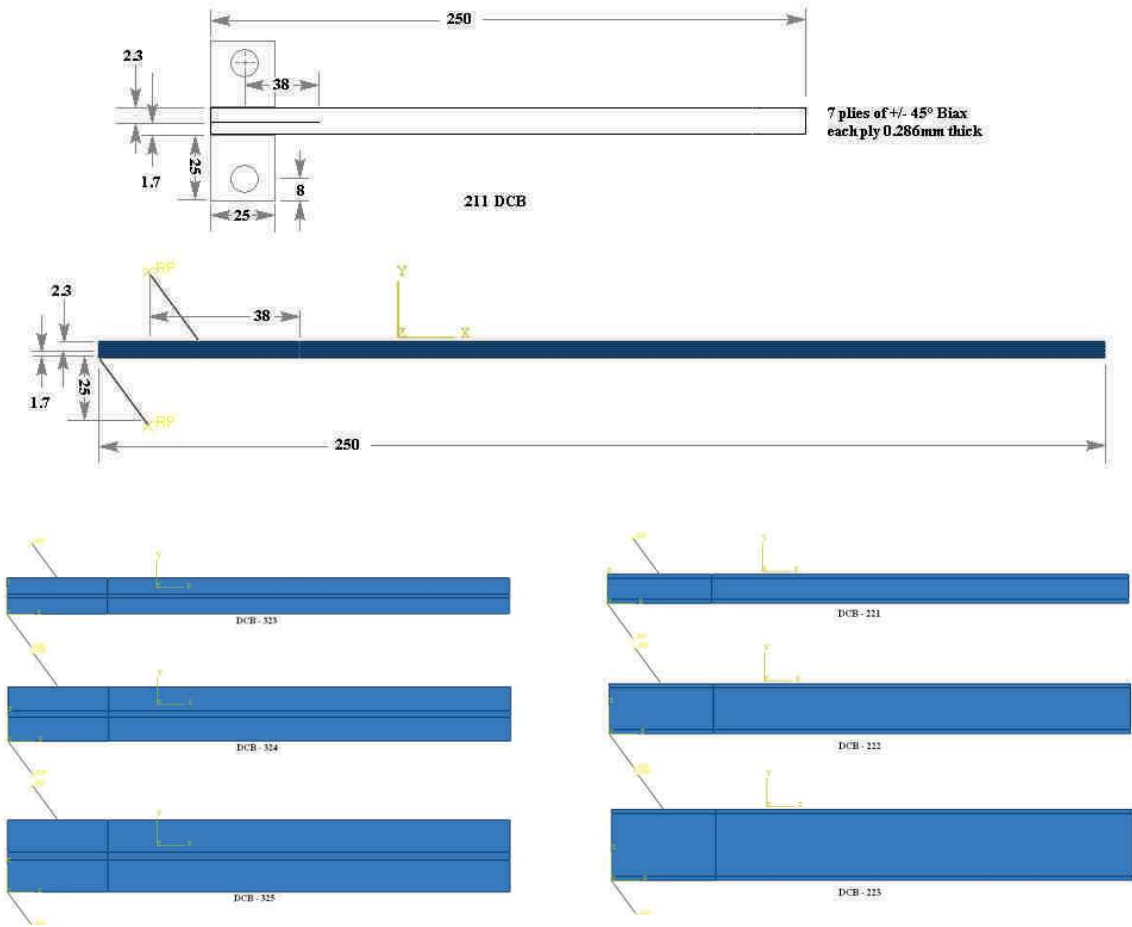


Figure 7-11: DCB specimens as modeled in ABAQUS using the actual geometries and material properties.

In addition the models contain a pre-crack at the tip of the cohesive zone which defines the plane of delamination or separation in the interface. The pre-crack is modeled with the help of a fine gap between the two beams as shown in the Figure 7-12.

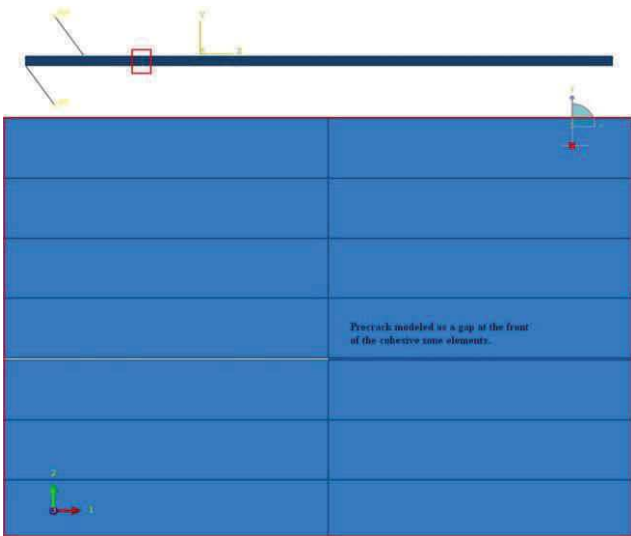


Figure 7-12 : Crack tip on modeled between the two beams of the DCB model.

For the mesh size a “ l_e/l_s ” ratio of 0.004 is chosen which is sufficiently fine for the flexion results to be in good correspondence with the experimental results.

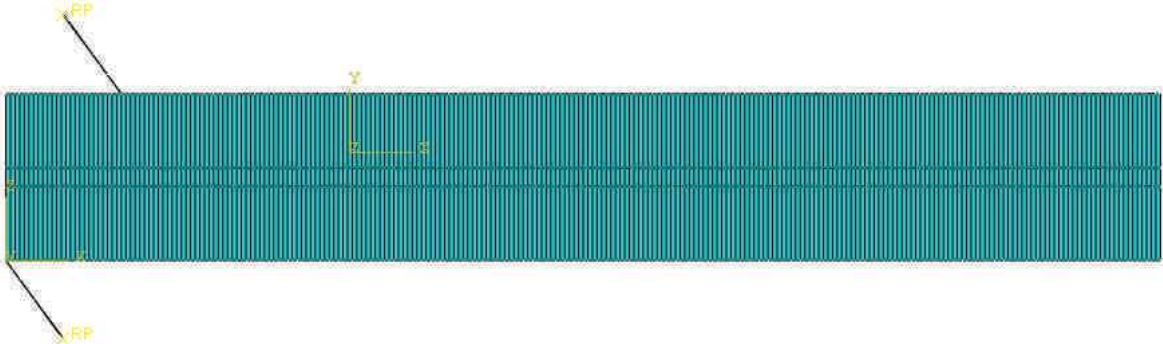


Figure 7-13: Mesh for the DCB specimens.

For the continuum shell elements there is only one element through the thickness of the beams. This helps in simplifying the computations.

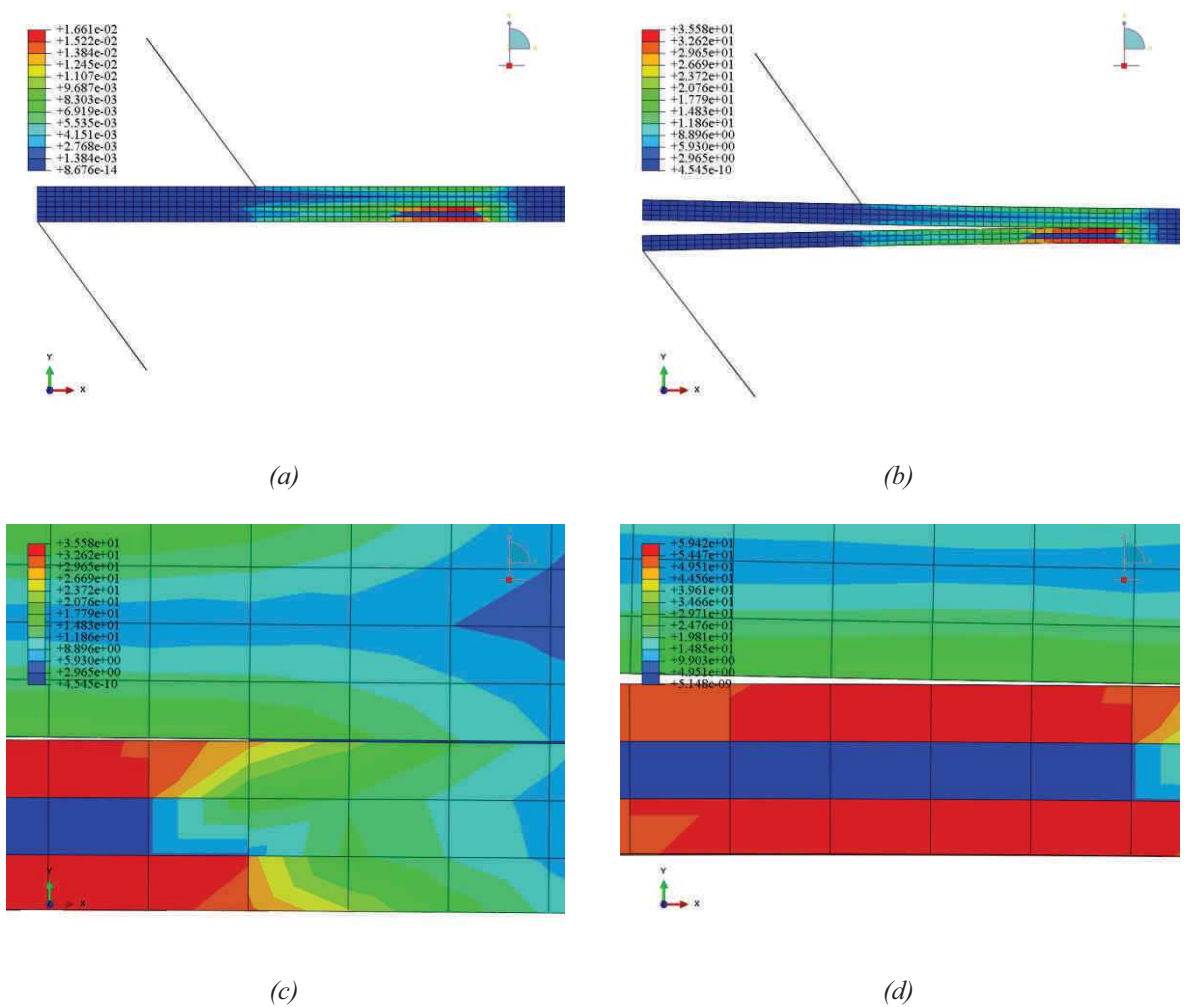


Figure 7-14: Simulation showing the crack propagating in the cohesive zone interface.

In addition the mesh types are put different for the beams and the interface. The interfacial mesh elements are directional to be able to define the SERR values in the different directions.

The bottom pivot is allowed to rotate in the plane of the specimen while the upper one is allowed to rotate in the same plane as well as it is given a certain displacement up to the crack tip reaches the end of the specimen.

The simulation at its different steps during the progression of the damage is shown in the Figure 7-14:

- The stress state at the start of crack propagation,
- Stress state during crack propagation,
- Zoom on the crack head at a given instance, crack head shown by un-failed cohesive elements in blue,
- Crack propagated through these cohesive elements showing a crack opening.

7.2.2 Discussion on Results

Upon comparing the results of the SERR values calculated in Chapters 4 – 5 with the response of CZM's at these values, the following observations can be made. Refer to the force-displacement curves for each of the test specimens and the results thus obtained from the CZM simulations.

1. *Monolithic composite DCB specimens*

Referring to the Figure 7-15 the curves with the prefix DCB show the force-displacement response of experimental tests whereas the labels ABAQUS are for the finite element simulations. The values of “ t ” the stress at the crack tip sufficient to initiate the cracking is reworked from the experimental curves in FE modeling, whereas the “ G_I ” is taken as the general range of values for these types of specimens. The last character 1mm is the mesh element size used for this simulation.

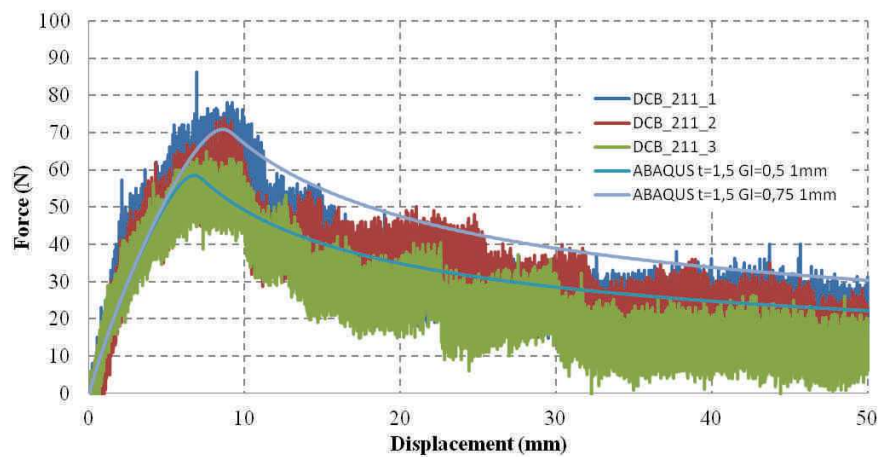


Figure 7-15: Force-displacement curves for the monolithic composite interfaces, for mode I SERR primarily in delamination.

Although from the SERR values when measured by the experimental tests vary from 0.8 to 1 J/mm^2 but here the simulations show lower values. This is attributed to the fiber bridging happening in physical tests. The fiber bridges increase the measured values of SERR as they act as crack stoppers hence effectively causing more energy to be spent on advancing the crack. CZM models do not have the provision to model fiber bridges or other types of crack stoppers. There are models present which model the crack stoppers as purely elastic elements which fail at the fiber bridge break strength.

2. *Bonded DCB_323 specimens (adhesive thickness 2 mm)*

The same results as above are simulated using FE in the case of bonded beams. In this example it can be seen that the values of the SERR calculated from VCCT and experiments lie between 0.4 and 0.6 where as the values simulated using FE is also in the same range giving good correspondence. This is already explained in Section 5.11 since there is no fiber bridging the

CZM follows the real test cases. However there is always a problem of unstable crack growth but the total energy dissipated during propagation remains identical.

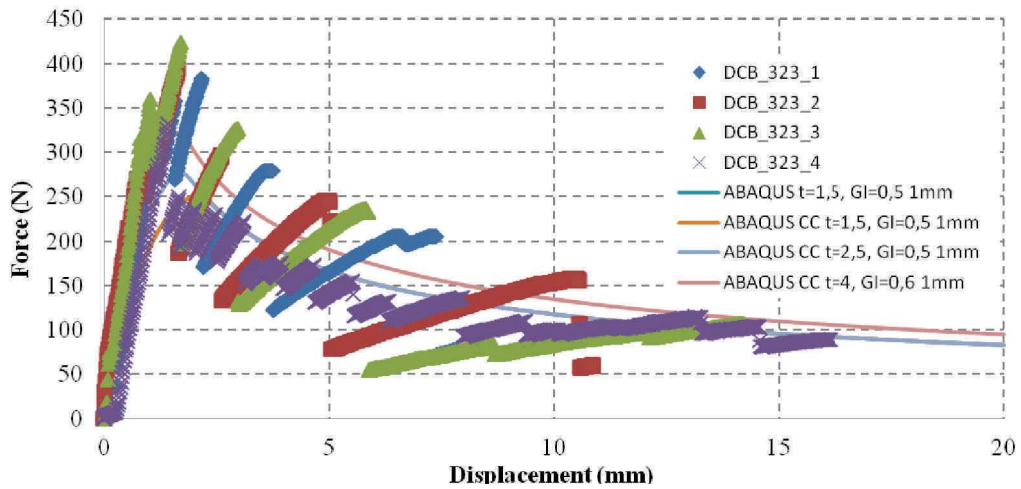


Figure 7-16: DCB_323: Force-displacement curves for the bonded interfaces, for mode I SERR primarily in debonding.

3. Bonded DCB_324 specimens (adhesive thickness 3 mm)

In this case the SERR values range from 0.25 to 0.31 for the experimental tests and the CZM models showing close correspondence to the experimental force displacement curves at 0.26 – 0.4 J/mm^2 . However there is the usual instability in the crack propagation especially when the crack length is long, there is some spring back effect in the beams as they get loaded and unloaded abruptly upon each step in the crack propagation.

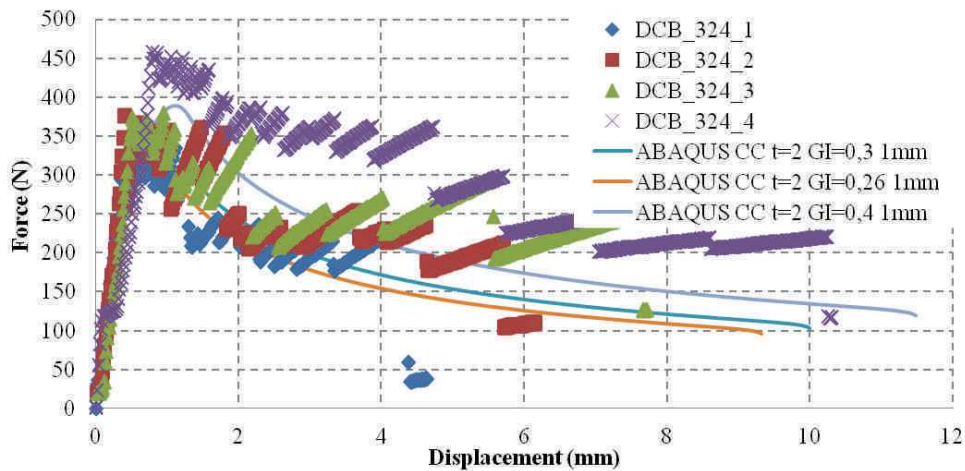


Figure 7-17: DCB_324: Force displacement curves for the bonded interfaces, for mode I SERR primarily in debonding.

4. Bonded DCB_325 specimens (adhesive thickness 4mm)

The same goes for these specimens where the values of SERR measured through experiments is roughly around 0.3 J/mm^2 and as the response goes the FE shows a values ranging from $0.2 - 0.3 \text{ J/mm}^2$, Figure 7-18.

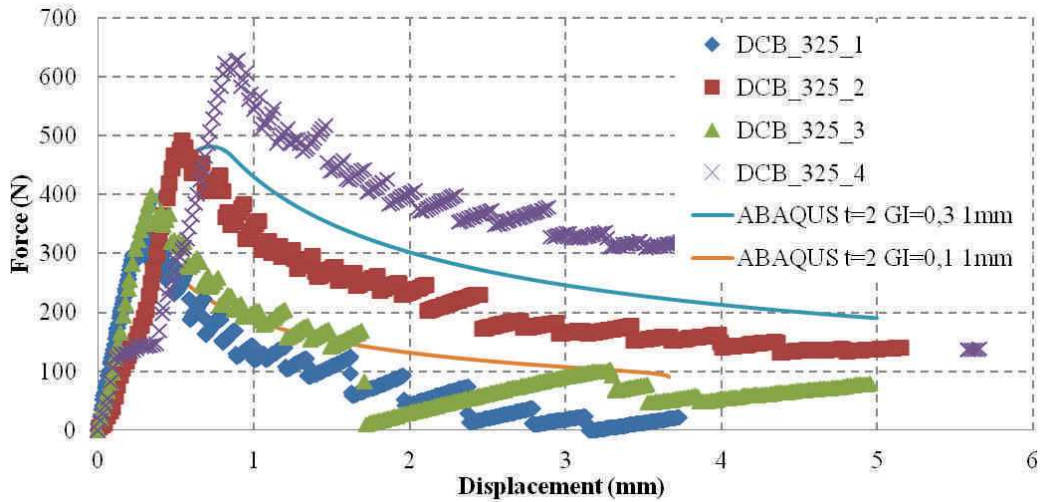


Figure 7-18: DCB_325: Force displacement curves for the bonded interfaces, for mode I SERR primarily in debonding.

The Table 7-2 gives the summary of the comparisons between the force displacement behavior of DCB specimens experimentally and modeled with ABAQUS cohesive zone elements.

| Specimen | Experimental G_I (kJ/m ²) | ABAQUS G_I (kJ/m ²) |
|----------|--|--------------------------------------|
| 323 | 0.4 – 0.6 | 0.5 – 0.6 |
| 324 | 0.25 – 0.31 | 0.26 – 0.4 |
| 325 | 0.3 | 0.2 – 0.3 |

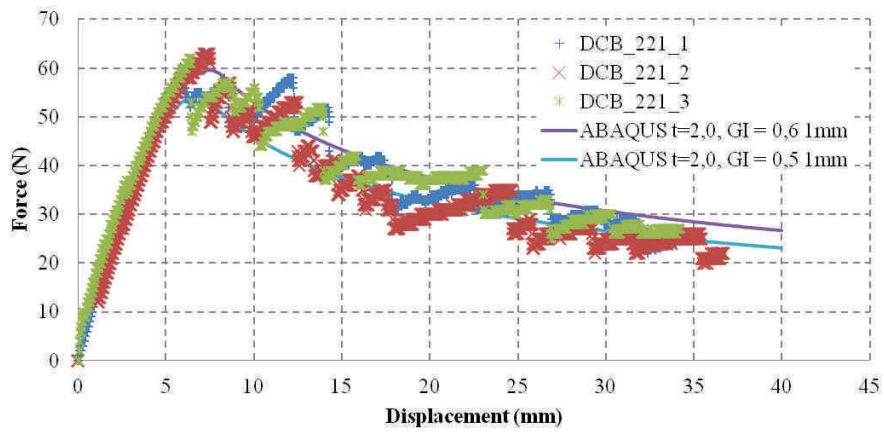
Table 7-2: Summary of results of experimental and CZM mode I SERR “ G_I ” for bonded specimens

5. Sandwich beams DCB_221, 222 and 223

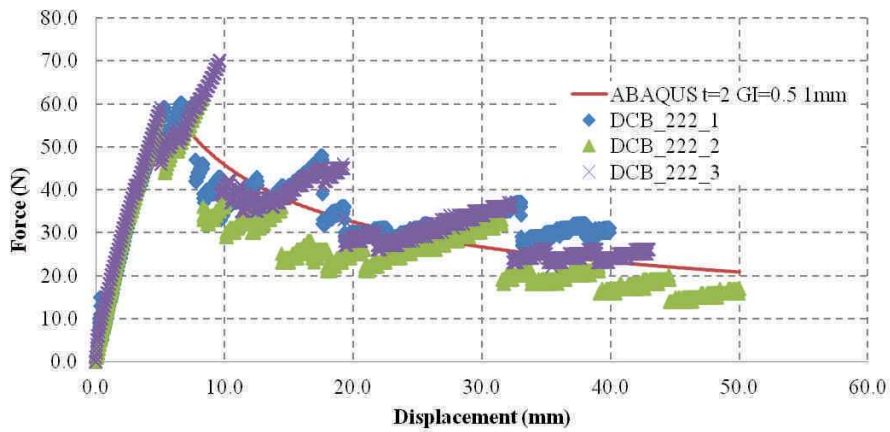
Three different sandwich beams are tested having a core thickness of 10, 20 and 30mm each with 2mm face plates, or skins. The three were subjected to the same tests as for other specimens and their modeled results compared to Table 7-3.

| Specimen | Experimental G_I (kJ/m²) | ABAQUS G_I (kJ/m²) |
|-----------------|---|---|
| 221 | 0.7 – 1.0 | 0.5 – 0.6 |
| 222 | 0.45 – 0.7 | 0.5 |
| 223 | 0.8 – 1.0 | 0.68 |

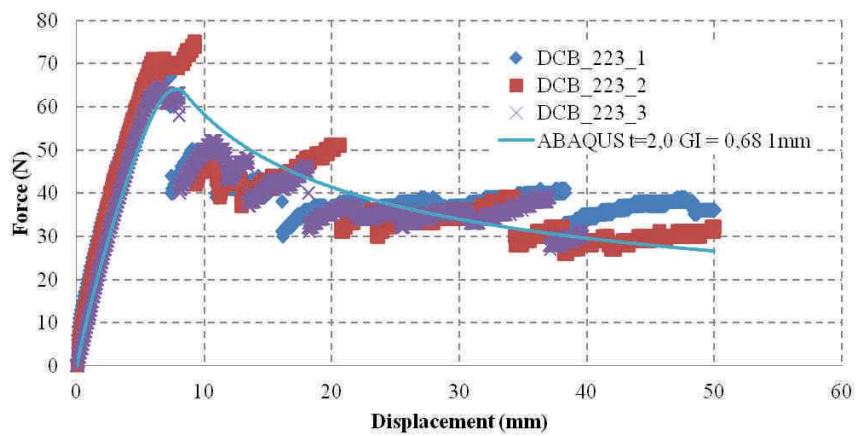
Table 7-3: Summary of results of experimental and CZM mode I SERR “ G_I ” for sandwich specimens



(a) 10mm core thickness



(b) 20mm core thickness



(c) 30mm core thickness

Figure 7-19: Correlation experimental/FEA force-displacement curves for sandwich beams.

7.2.3 Model setups for ENF tests

The ENF tests are done for the characterization of Mode II SERR or “ G_{II} ”. Here we shall present some of the results of ABAQUS modeling on the ENF tests done on composite layups and as well on the adhesive bonded specimens. The geometry in schematic view is shown in the Figure 7-20.

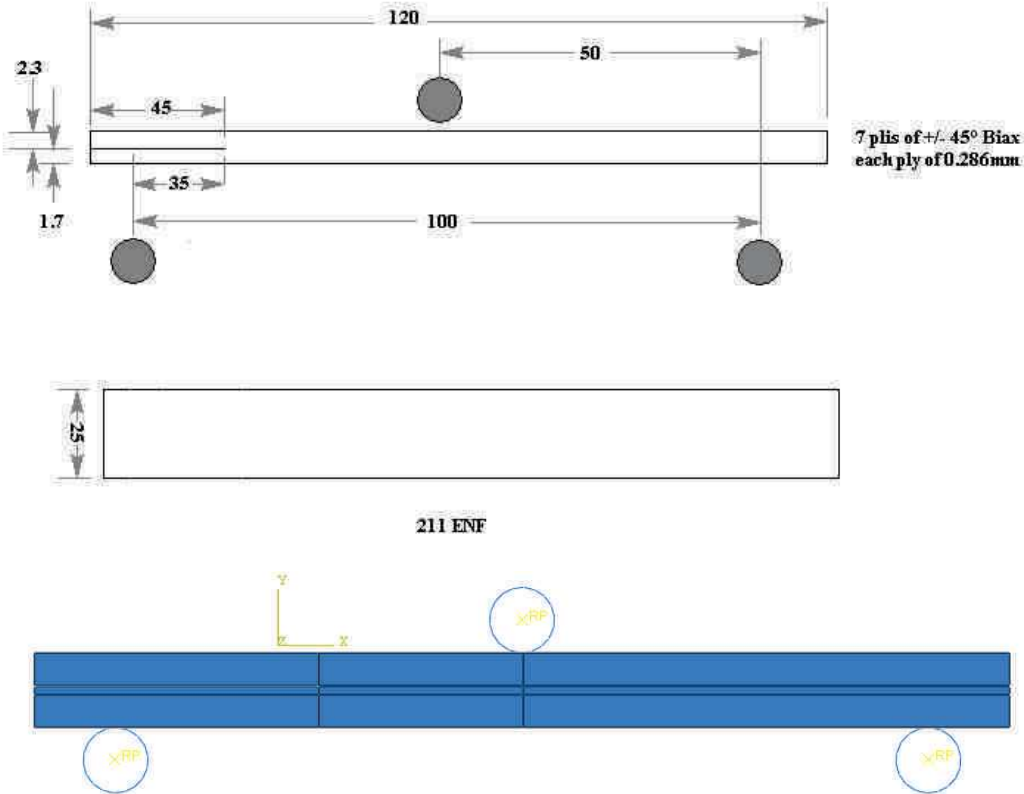


Figure 7-20: Schematic view of the model for Mode II SERR modeling using ABAQUS.

The models of the beams are modeled in 2D with a cohesive zone between the two half beams. The material properties are defined in Table 7-1 for the reinforcements and the SERR values are taken directly from the experiments. Since the models are 2D hence the material properties are transformed to the loading direction from the $\pm 45^\circ$ fiber direction. The transformation of the material properties is done using the classical composite plate theory. Consider that the fibers are oriented at $\pm 45^\circ$ to the loading direction, also considering that the materials are transverse orthotropic, hence the material properties normal to the ply plane and the fiber plane are considered the same.

$$E_x = E_y = \frac{1}{\frac{\cos^4 \theta}{E_l} + \frac{\sin^4 \theta}{E_t} + \cos^2 \theta \sin^2 \theta \left(\frac{1}{G_{lt}} - 2 \frac{\nu_{lt}}{E_t} \right)} \tag{7-5}$$

where “ $E_{x,y}$ ” is the stiffness in the loading direction and normal to it respectively.

The values of “ t ” the stress at the initiation of damage play an important role in determining where the crack will start to develop within the model.

A mesh size of 0.5mm has been used all over the models based on previous convergence studies. It should be noted that finer mesh sizes lead to a more uniform propagation of the crack but doesn't largely affect the global behavior of the specimen models.

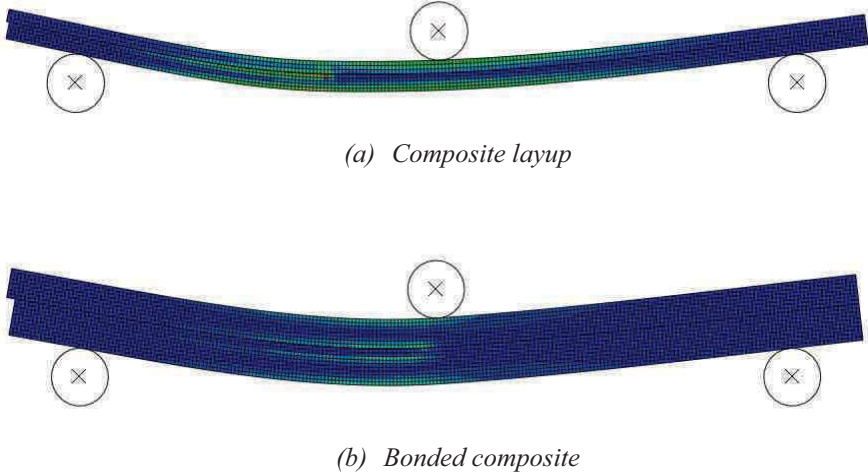


Figure 7-21: Deformed modeled specimens after the application of load.

From the Figure 7-21, ENF specimens are shown in their deformed state. The free cracked end can be seen projecting thus giving rise to shear. The areas of high stresses shown in red or dark green are the locations of the crack tips.

Discussion on Results

Upon comparing the results in terms of force-displacement curves, refer to Figure 7-22 and Figure 7-23.

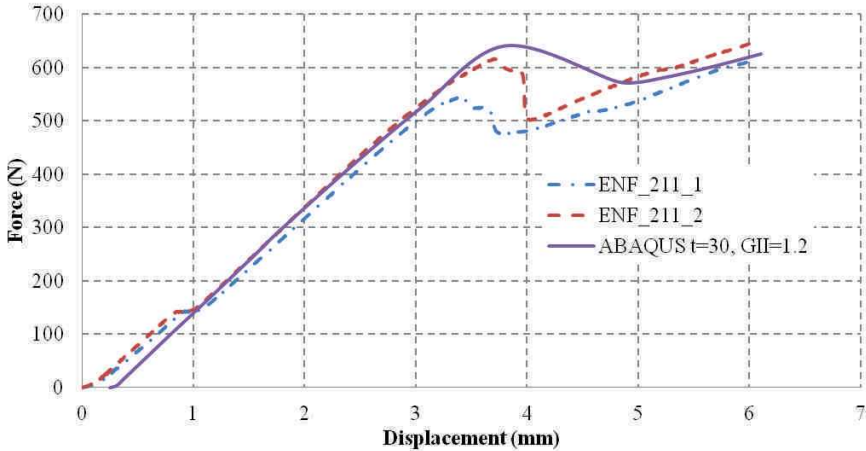


Figure 7-22: Force-displacement curves for composite layup specimens.

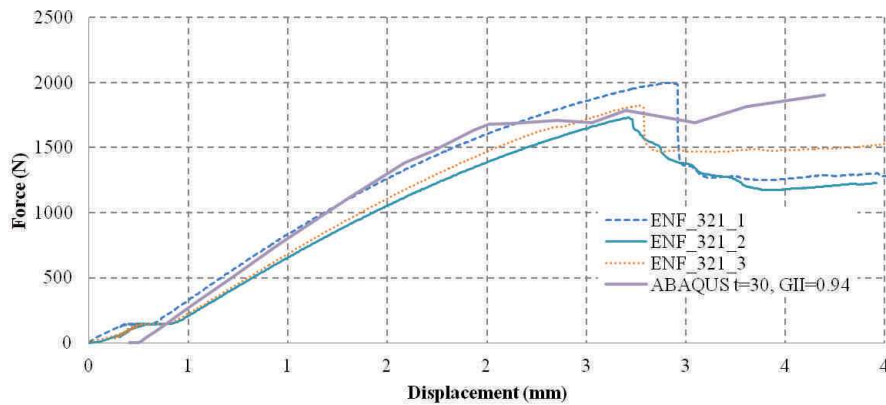


Figure 7-23: Force-displacement curves for bonded composite specimens.

From the force-displacement curves the following conclusions are drawn:

1. The value of “ t ” that is the stress value at the initiation of the damage determines the start of the damage hence it is an important parameter in determining the global behavior of the specimens.
2. The initial undamaged part shows some non-linearity. It is normal and to be expected as in flexion the material behaves with an exponential elastic law. Although this has not been taken into account in the FE model hence the damage starts at a lesser total tool displacement but the same charge.
3. Once the crack has initiated especially in the case of the bonded specimens it is very difficult to trace the damage progression using cohesive elements. Since the nature of crack propagation can be at constant load or constant displacement but as can be seen in the real experiments there is no real tendency for the crack to develop hence it progresses in a rather random fashion.
4. The loss in applied force gives a similar global value but as explained above, does not follow the real tendencies.

7.3 Modeling of single lap joints

To move up one level in modeling, the bonded joints are tested and then simulated using single lap joints. Two 160mm x 25mm composite plates are joined together using a simple overlap of 40mm long. The adhesive used is 2mm thick whereas the composite plates are 4mm in thickness. The specimen is shown in Figure 7-24.

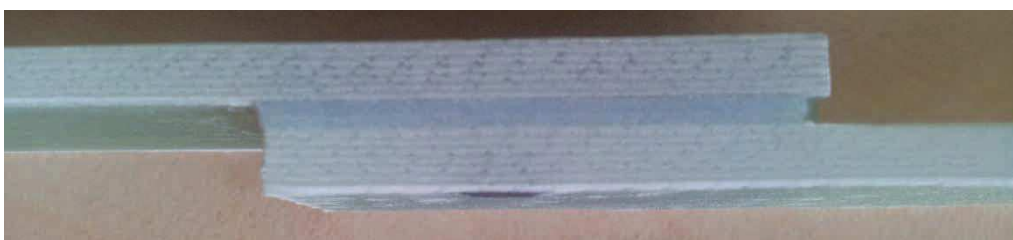


Figure 7-24: Specimen used for the characterization of strength properties of a single lap joint.

These specimens are tested in traction. During their loading, the bonded zones deform thus applying a mixed mode loading on the composite – adhesive interfaces. These specimens are monitored during the loading phase using DIC and Infrared imagery to localize the initiation and propagation of the damage taking place.

Tests on single lap joints are done to validate the mode of failures happening in the assembled geometries. This would finally lead to the modeling of the full scale wind turbine blade. The model is shown in the Figure 7-25.

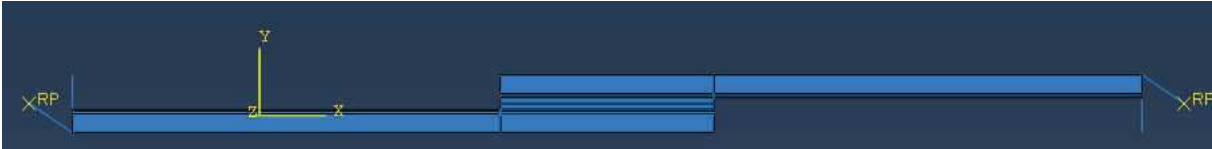


Figure 7-25: FE Model of the single lap joint.

7.3.1 Modeling strategy

The modeling of these joints has been done considering the material and fracture resistance properties of the actual materials used.

There are two models used for the validation of the FE analysis. We start off with a 2D model to localize the crack initiation zones. Since 2D models cannot simulate the gradual propagation of the cracks along the thickness of the specimens hence the specimen fails suddenly at the onset of the crack initiation. Therefore once the crack initiation modes are validated the specimen is modeled in 3D to account for the gradual decrease in the global strength of the specimens.

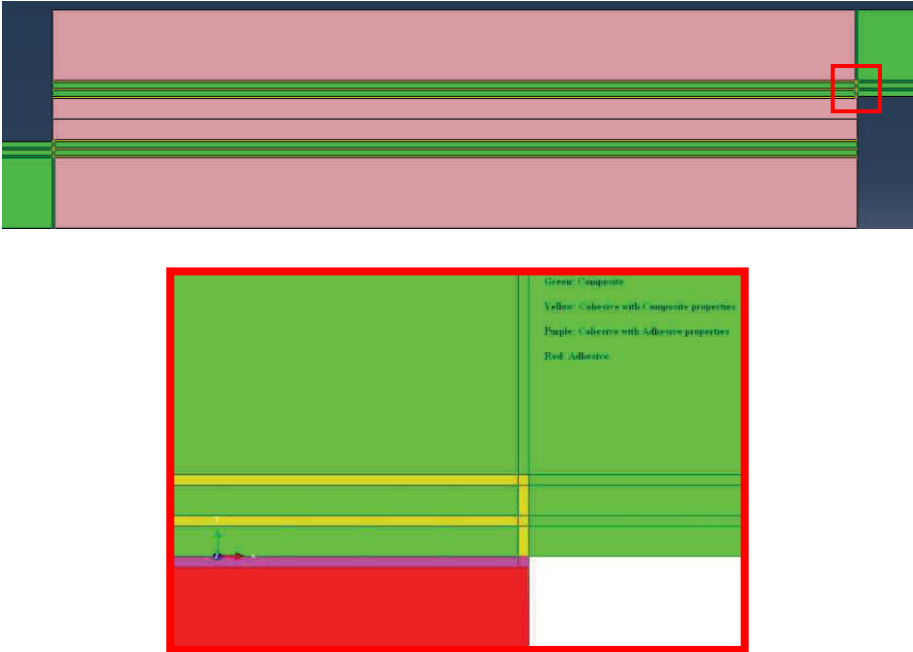


Figure 7-26: FEM of bonded interface of the single lap joint.

The 2D model is partitioned as shown in the Figure 7-26. The zones are divided into cohesive and plane stress elements. Furthermore there are 2 different types of cohesive zones. One is modeled between the first 2 plies of the composite to model delamination and the second is the interface between adhesive and the composite plate.

One important aspect to note here is that the composite cohesive zone has been modeled to separate the bonded interface once the crack has grown. This allows for simulating delamination just in the bonded place.

Once the material properties have been applied, it should be mentioned here that the mesh size has been chosen based on past DCB models and further mesh sensitivity has not been carried out.

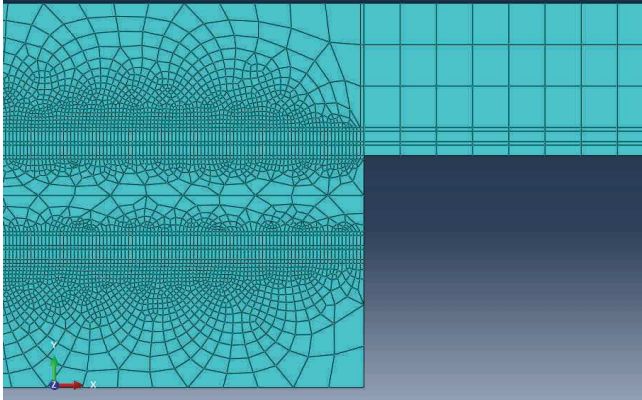


Figure 7-27: Mesh size is refined at the bonded interfaces to promote an accurate initiation of damage.

The mesh size varies from 1mm on the composite plate portions to 0.05mm at the bonded interfaces.

7.3.1.1 Boundary Conditions

As for the real case the specimens are constrained the two ends using fixed supports which at one end allow the movement only along the length of the specimens, a displacement of 5mm is given to attain complete separation of the two bonded plates. The other fixed end is completely constrained.

For comparing the simulation results with the actual physical tests consider a representative loading graph as shown in Figure 7-28.

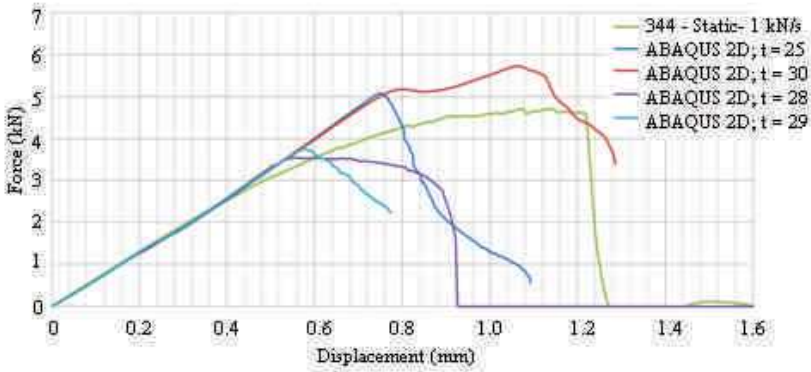


Figure 7-28: Load-displacement curve of a monotonic loading on a single lap joint.

7.3.2 Discussion on Results

The curves show the results of the FE analysis done by ABAQUS at different values of “ t ” stress at initiation of damage. As can be seen from the curves that the different values of “ t ” although do have an effect on the point of damage initiation but their tendency is rather random. This has been explained by the fact that the stress at which some of the elements fail can be different and the first few gradual failures though predictable do not count for a change in the curves above. Its only when a large portion of the elements fail that we begin to see a deviation in the curves and that point can come rather abruptly as in the case of 2D models there is no “through thickness” crack growth.

To explain further the curves shown above we shall refer to the following description with Figure 7-29.

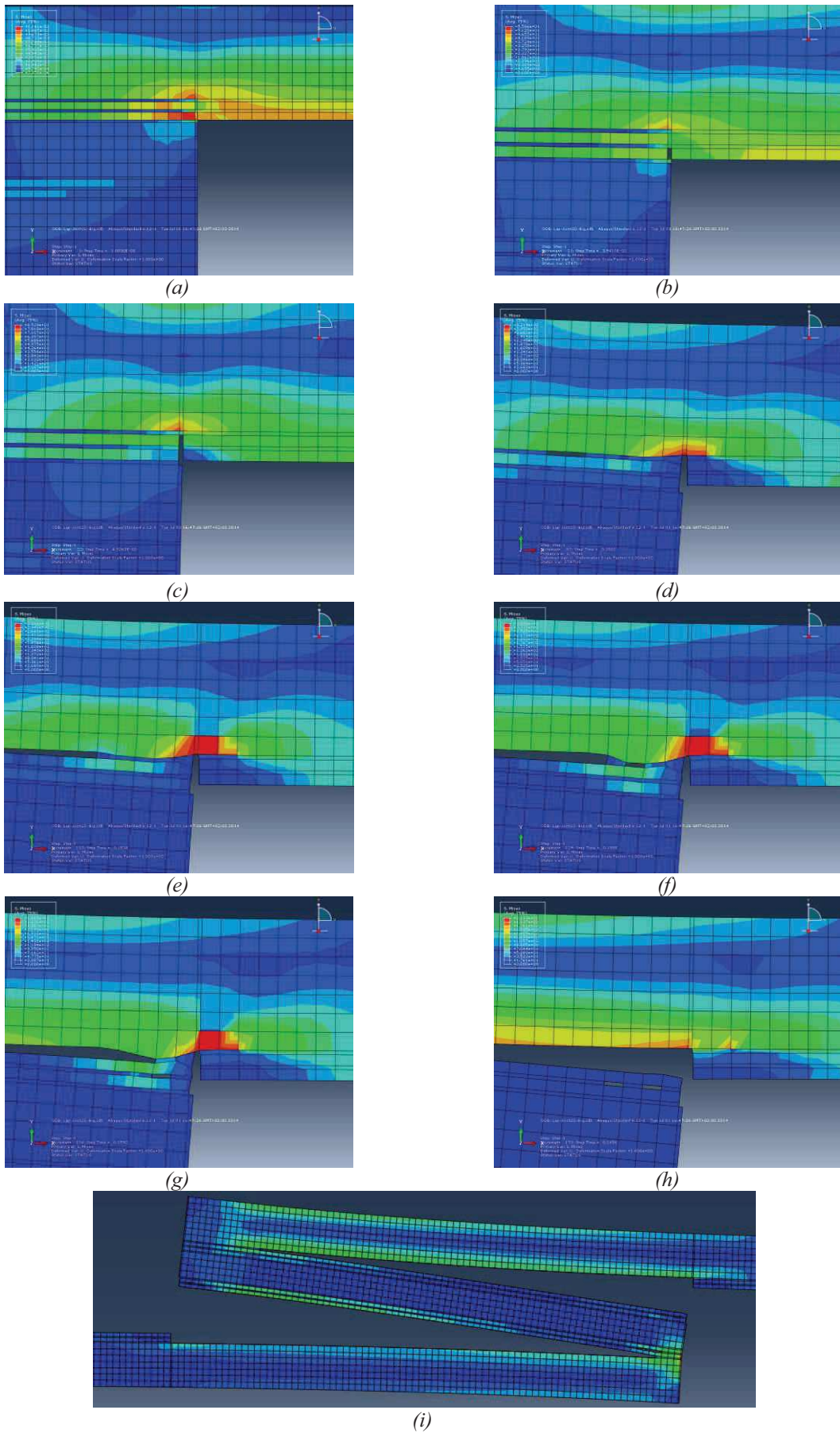


Figure 7-29: Stages of failure in the single lap joint.

Referring to the Figure 7-29 we can see in detail the different stages of damage initiation and its propagation.

- a) The specimen is loaded and the stress distributions are shown in the different plies and cohesive zones. The vertical cohesive zones are modeled to account for the fiber matrix separation due to failure. Although the fibers are at 45° to the pulling direction but for the 2D model the fibers are modeled to be normal to the plane of the model and the interlaminar properties of damage propagation are used. Figure 7-30 shows the schematic representation of modeling fiber – matrix interfaces with the help of cohesive zones. For reminding it should be noted that the interfaces in the real specimens are at 45° and in the model are normal to the application of the force.

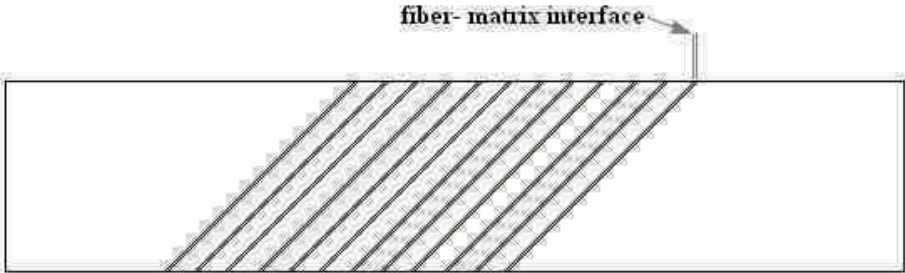


Figure 7-30: Fiber matrix interfaces as modeled by cohesive zone elements.

- b) Once the load reaches where the stress required for the initiation of the damage is attained, the failure begins at the CZE (cohesive zone element) representing a fiber matrix interface. These failures show up as small steps in the force displacement curves well before a large divergence in these curves as shown in Figure 7-31.

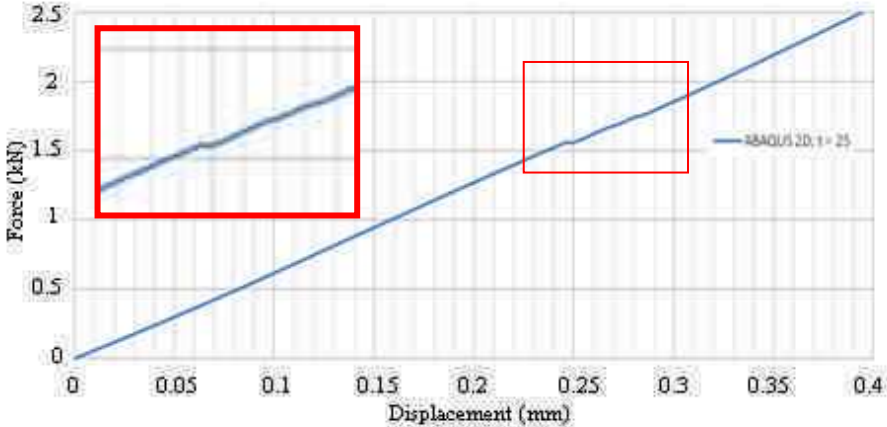
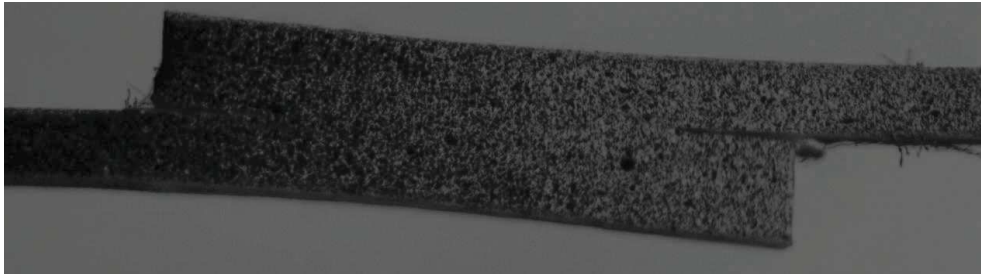


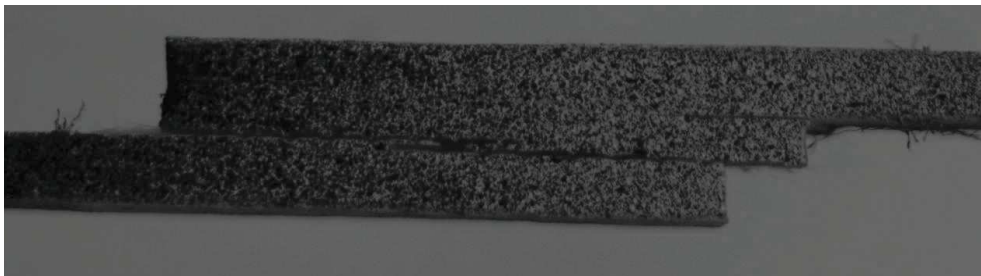
Figure 7-31: Steps in the force displacement curve showing damage initiation.

- c) Here the fiber matrix CZE has completely failed and the interlaminar and bonded CZEs are under a predominantly shearing or Mode II type loading.

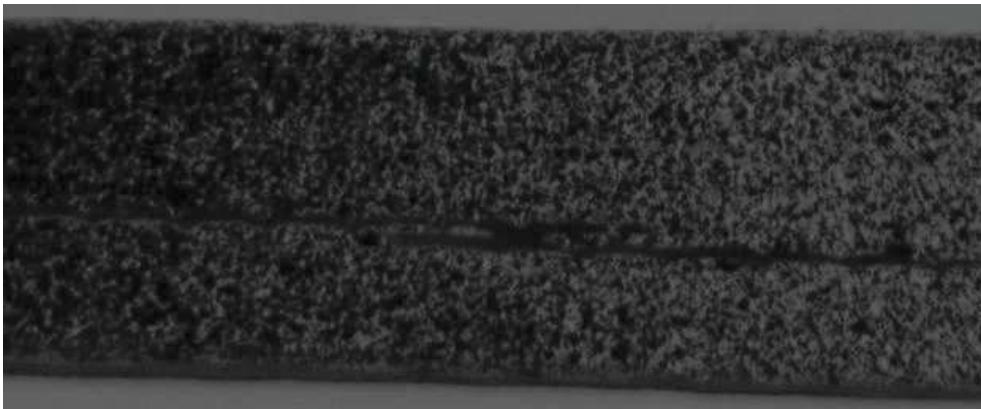
- d) The interlaminar CZE start to degrade and damage starts to initiate at these interfaces. This as will be shown is typical of what is seen experimentally. It should be noted further that there is not necessarily a continuation between the failed fiber matrix CZE and the damage initiating at the interlaminar CZE.



(a) *Initiation of damage*



(b) *Final failure state*



(c) *Zoom on the failed region*

Figure 7-32: simple lap joint showing different phases of failure under tensile load.

- e) The interlaminar crack has propagated well away from the bonded joint and into the composite reinforcement.
- f) A local crack starts developing due to opening or Mode I failure near the bonded zone. This is typical of delamination type failure.
- g) The crack started in step (f) has now joined the first delamination crack. Thus now we have a continuous crack going well into the composite reinforcement. There is another appearance of

damage in the interlaminar CZE adjacent to the first one. This shows the nature of cracks developing in equal strength interlaminar interfaces.

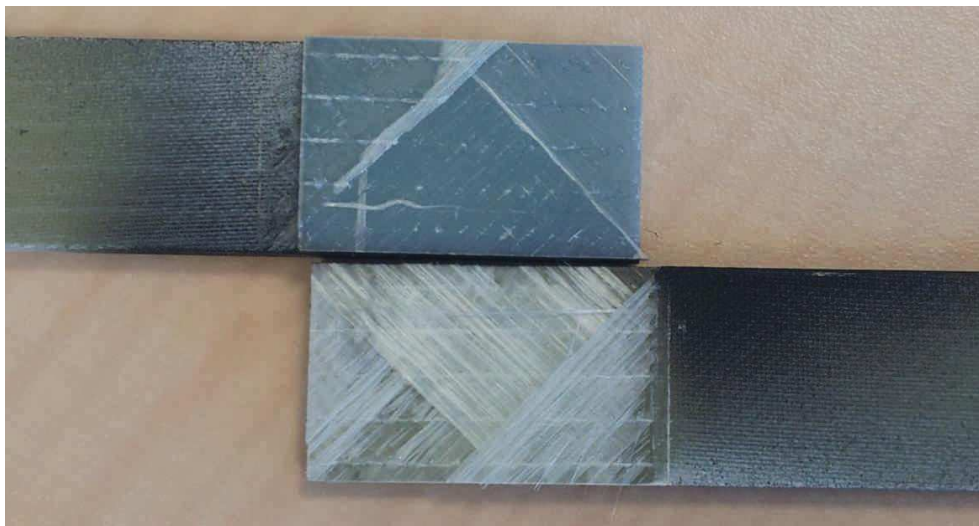
- h) The crack at this point has reached the free edge and hence there is no material holding the two specimen parts in place thus the first interlaminar crack will propagate until complete separation of the two joined composite pieces as shown in (i).

For a comparison with the experimental observations, an illustrative description is presented here using Figure 7-32.

The Figure 7-32a shows the region of crack initiation. The crack begins at the bonded end near the interface and the interlaminar region at the same time. The crack then propagates to the far end bifurcating in the two first interlaminar regions. The transfer of crack from one interlaminar region to the other depends on the arrangement of fibers thus it can be variable from specimen to specimen.



(a)



(b)

Figure 7-33: Failed bonded surfaces showing delamination type failure in the composite reinforcements.

Finally a view of the failed surfaces in Figure 7-33 showing a definite delamination or interlaminar type failure for these types of single lap joints.

The fact that in the Figure 7-30, the modes of failure have been well predicted however the load displacement graphs in the Figure 7-28 do not correspond well to the experiment. This has been attributed to how the damage progresses in a 2D model. There is no progression of damage in the width direction of the specimen hence the failure is rather abrupt. Secondly the values of Hashin failure criteria are input using a homogenized approach, since into the plane $\pm 45^\circ$ direction cannot be simulated using 2D models. For now the damage initiation and failure modes are of interest and the modeling to follow will be based on these criteria.

7.4 Modeling of the complete blade

7.4.1 Modeling strategy

The modeling strategy to determine the behavior of the complete wind turbine structure can be divided into 5 different tiers. On the bottom most tier we have the finite element model of the entire blade. This model is drafted in CATIA software and then the geometry is imported into ABAQUS where it is further partitioned to apply the different types of stratifications at different zones. Once the material assignments are complete the model is meshed depending on the geometry regions using S4R and S3R elements (quadrilateral and triangular). The **first tier** model is a 3D shell model to reduce the time for calculations. For the boundary conditions the real full scale test forces are applied to this first tier model. This phase is used as a validation of the modeling strategy, having the bending moments at each of the sections the following tiers of models will have the applied bending moments applied directly to the sections.

In the **second tier** model, the blade is partitioned into 1mm thick sections which are modeled as a shell. The bending moments as given in Annex B are applied to the sections to determine which section would be under the highest applied stress.

The section experiencing the highest amount of applied stress is then modeled in 3D as a 1mm thick blade section, but having its thickness accurately modeled as the layups in the real case. This gives a deeper insight into the through the thickness stresses taking place. This **3rd tier** model is again loaded with the bending moments applied to the two blade cross sectional faces in order to calculate the stresses applied on each of the layers of the blade section.

The **4th tier** of the blade model is where a sub model of the 3rd tier complete blade section 3D model is generated. The sub models are of the junctions at the blade surface and the shear webs (pressure side since it is the highest stressed) and the trailing edge. Furthermore the mesh in these sub models is refined and the layups are precisely modeled.

Finally the **5th tier** model is where a further sub model of this 4th tier model is generated including cohesive zones with the properties as determined by the modeling of the various bonded and sandwich specimens. This is necessary to assure the strength of the interfaces and to propose changes.

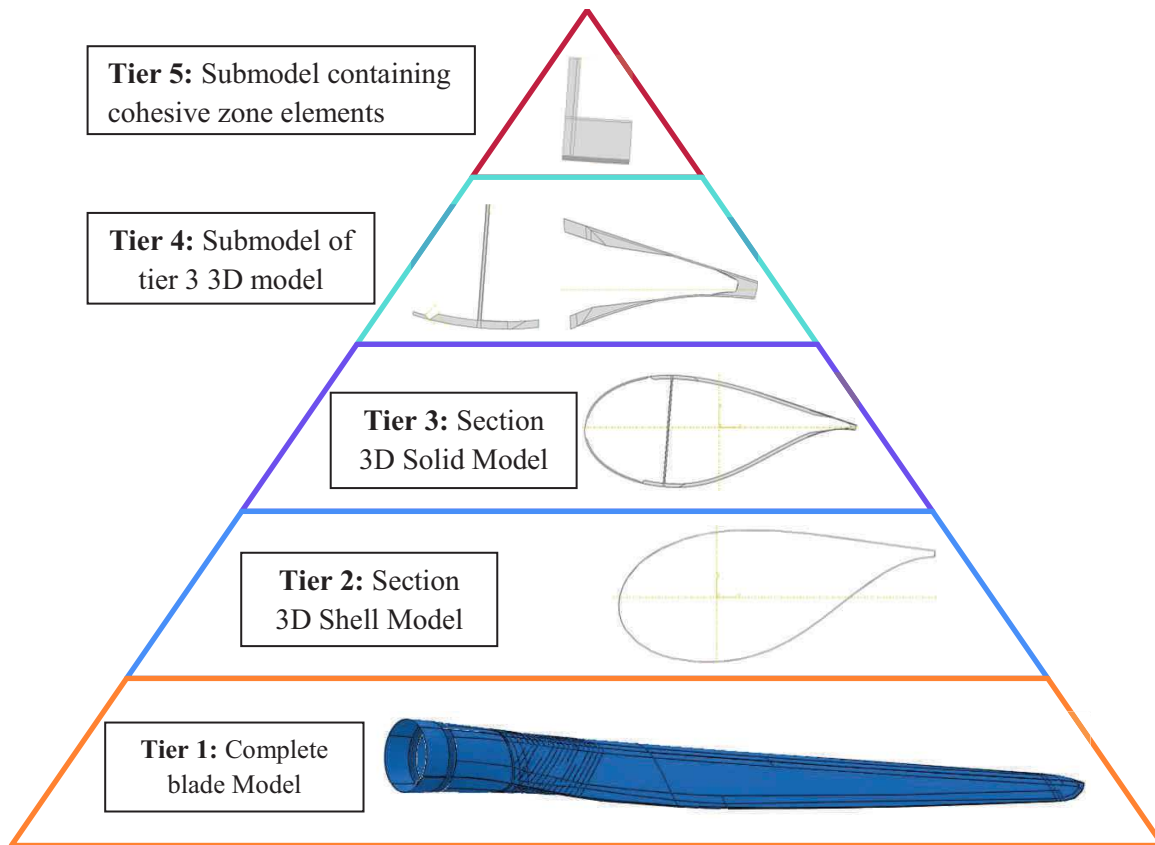
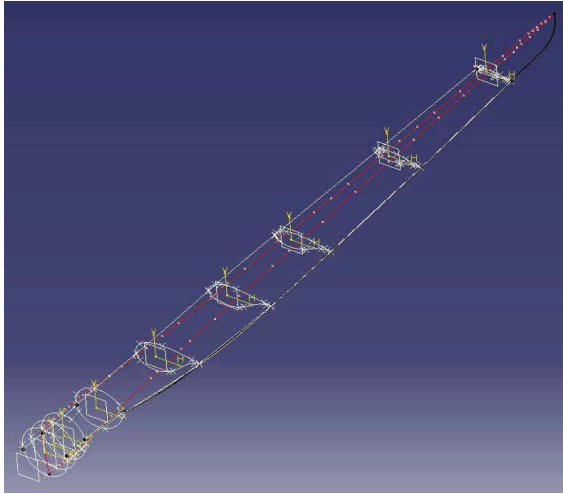


Figure 7-34: Modeling strategy for studying the behavior of the final structure.

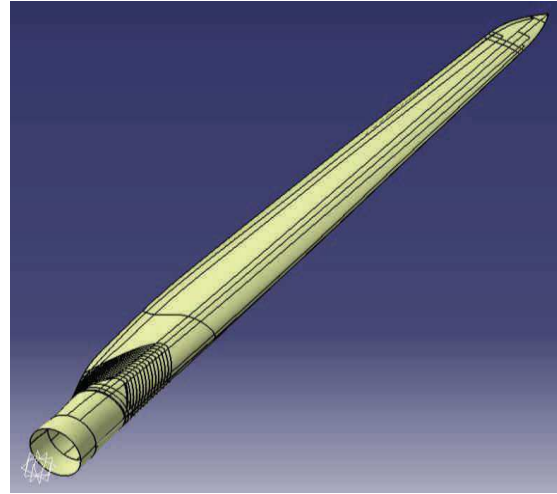
7.4.2 Tier 1: Complete blade model

7.4.2.1 Geometry and material assignment

As explained the blade geometry was modeled in CATIA using the cross sectional drawings provided in the blade design in Annex B. Firstly the skeleton of the blade is produced using 2D curves placed at the proper blade radiuses. Once the skeleton is developed it is “draped” with 3D surfaces to get the outer geometry of the required wind turbine blade. Once we have the outer surface geometry of the wind turbine blade, the surface is cut into patches corresponding to the layup plan given in Annex B.



(a) Blade skeleton drawn in 3D spline curves



(b) Filled in with surfaces and the surfaces cut to account for the layup order and placing

Figure 7-35: Creation of the geometry of the blade with CATIA.

The shell model is then exported to ABAQUS for the setup of the finite element model. In ABAQUS the model is imported in the form of multiple surfaces which need to be repaired and welded together to get a finished final part. Some of the partitioning is then later done in ABAQUS to keep the data loss during importation to a minimum.

Some final partitioning is done on the model to be able to apply the composite layups according to the Annex B. This step helps to determine the layups for the following tiers of models when we shall cut this blade into smaller sections.



Figure 7-36: Imported and partitioned geometry in ABAQUS for FE analysis.

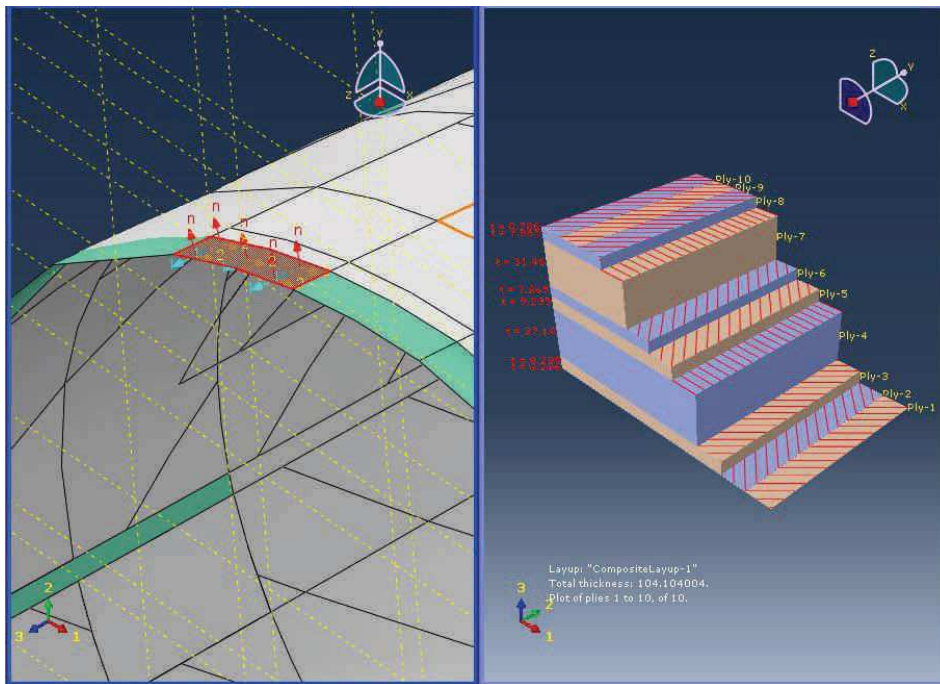


Figure 7-37: Each of the partitions is given their proper corresponding composite layups.

7.4.2.2 Boundary conditions

The blade as in given in chapter 2 has been modeled as a cantilever beam. The blade is fixed at the root constraining all 6 degrees of freedom.

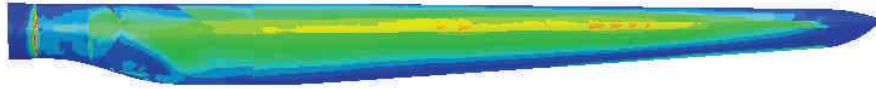
The blade model is loaded with the full scale experimental setup as detailed in the Annex C. The model is loaded in all the loading conditions, as PTS, STP, TTL and LTT details of which are given in the section 7.4.3.2.

7.4.2.3 Meshing

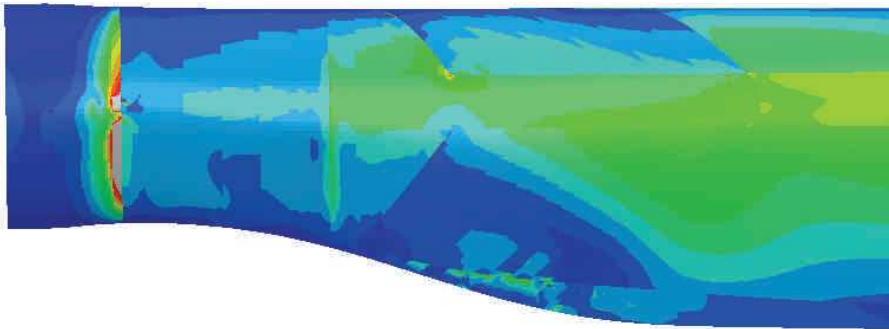
The model is meshed using quadrilateral shell type elements for the most part with a few triangular elements where the geometry is complicated and the quadrilateral elements would be excessively deformed. Keeping in with the size constraints of the blade modeled in Chapter 2 Section 2.13 a mesh size has been chosen to be less than the l_s/l_s ratio of 0.006. For a blade of 35m length, any length lesser than 200mm falls below this limit, hence we have chosen a mesh size of 100mm.

7.4.2.4 Results

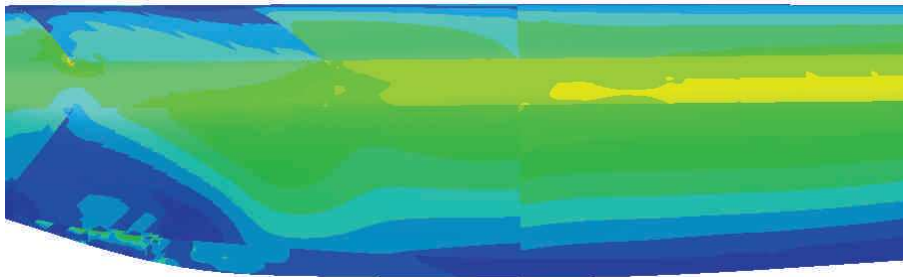
The Figure 7-38 shows the stress concentration regions to be in the blade surface and spar interface regions. The other region which shows higher stress concentration is the root-blade transition region.



(a) *A view of the complete blade.*



(b) *Zoom on the blade root-blade transition region.*



(c) *Zoom on the blade surface – spar interface.*

Figure 7-38: Highly stressed regions in the wind turbine blade, loaded in the PTS and STP regimes.

7.4.3 Tier 2: 3D Shell blade section

7.4.3.1 Geometry and material assignment

The geometry and the material assignment are directly taken from the Tier 1 complete blade model. The blade at high layup transition positions is cut and a 1mm thick blade section is extracted. This gives the advantage of visualizing the areas of high ply drops or transitions and to focus the analysis at these regions for account for stress concentrations.

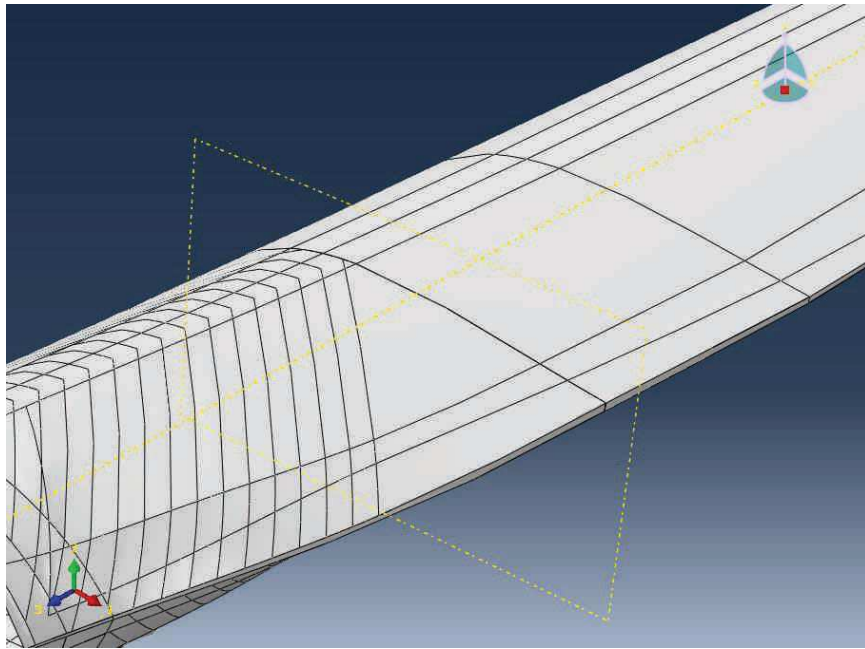


Figure 7-39: Two planes 1mm apart are placed on the desired blade length and cuts made to extract a section.

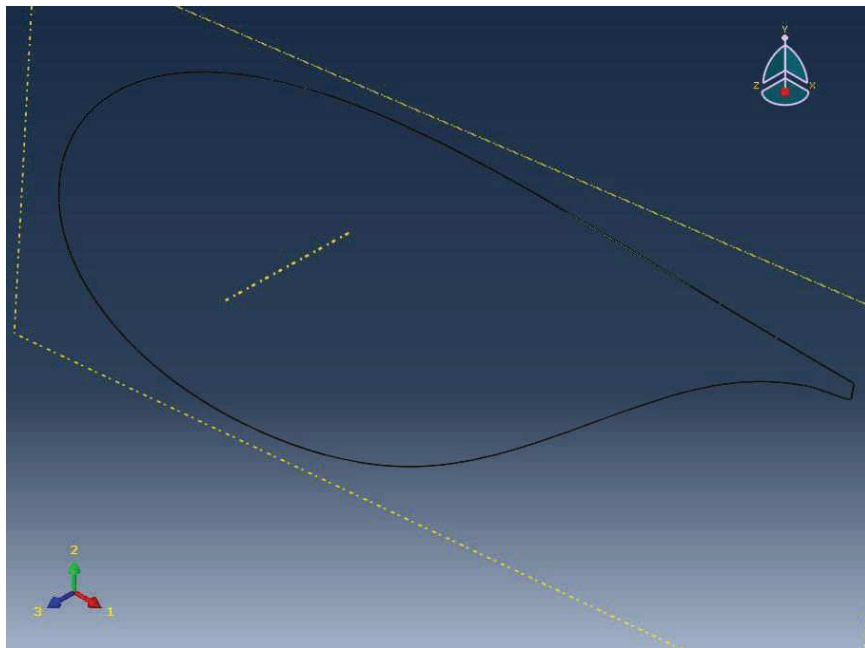


Figure 7-40: Extracted 1mm thick blade section.

Once the section is extracted as explained by the process in Figure 7-39 and Figure 7-40, the material assignments are rechecked for accordance to the layup drawings, Figure 7-41.

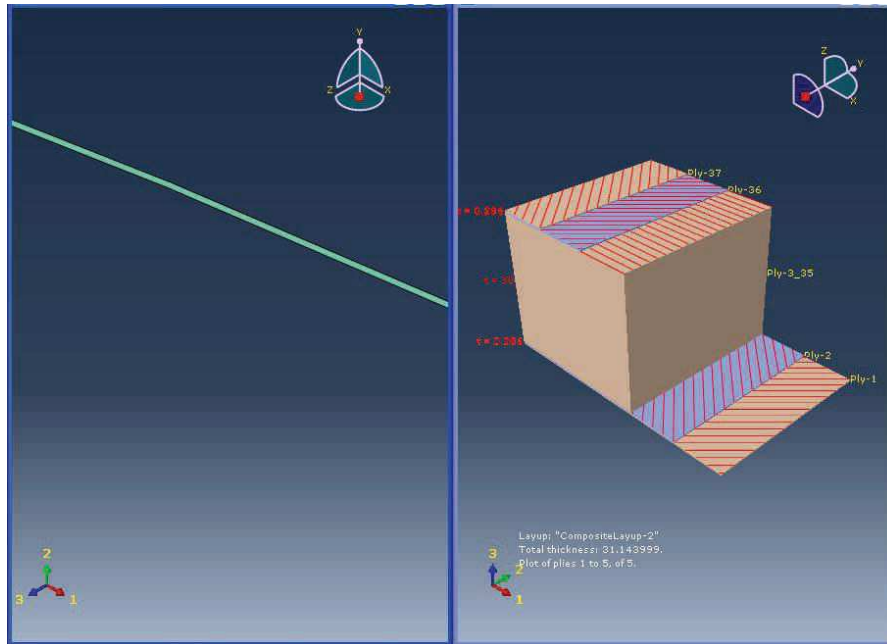


Figure 7-41: Composite layups on the junction of the blade surface to the shear webs.

It should be noted that all the steps are repeated for the shear web as well to get the geometry and material assignments accurate from the complete model.

7.4.3.2 Meshing and Boundary conditions

The mesh size is taken to be fairly fine due to 2 considerations. Firstly the geometry can be fairly complicated especially with layups being at angles not always normal to the cut cross sections. Furthermore since the section thickness is only 1mm hence the aspect ratio of the elements needs to be kept as close to 2 – 3 as possible. Keeping in view the curvature of the models we have taken a mesh size of 1mm which does not generate distorted elements and resolves finely the curved parts of the blade section. It should be also noted that this mesh size corresponds to a mesh size ratio (mesh element length to structure length) of 0.0004 which is far smaller than 0.0016 required for convergence.

The boundary conditions are applied according to the bending moments measured from the full scale tests. There are 4 different bending moments measured depending on the direction of loadings. They are listed as under. The bending moment distributions are given in the Annex C.

1. **PTS Flapwise**: bending moment applied in the flapwise direction from the pressure side (intrados) of the blade towards its suction side (extrados).
2. **STP Flapwise**: bending moment applied in the flapwise direction from the suction side (extrados) of the blade towards its pressure side (intrados).
3. **TTL Edgewise**: bending moment applied in the edgewise direction from the trailing edge of the blade towards its leading edge.
4. **LTT Edgewise**: bending moment applied in the edgewise direction from the leading edge of the blade towards its trailing edge.

The boundary conditions are applied such that one of the cross sectional faces is constrained in all degrees of freedom, while the moment is applied to the other. The moments are applied using planar rigid bodies to limit stress concentrations, Figure 7-42.

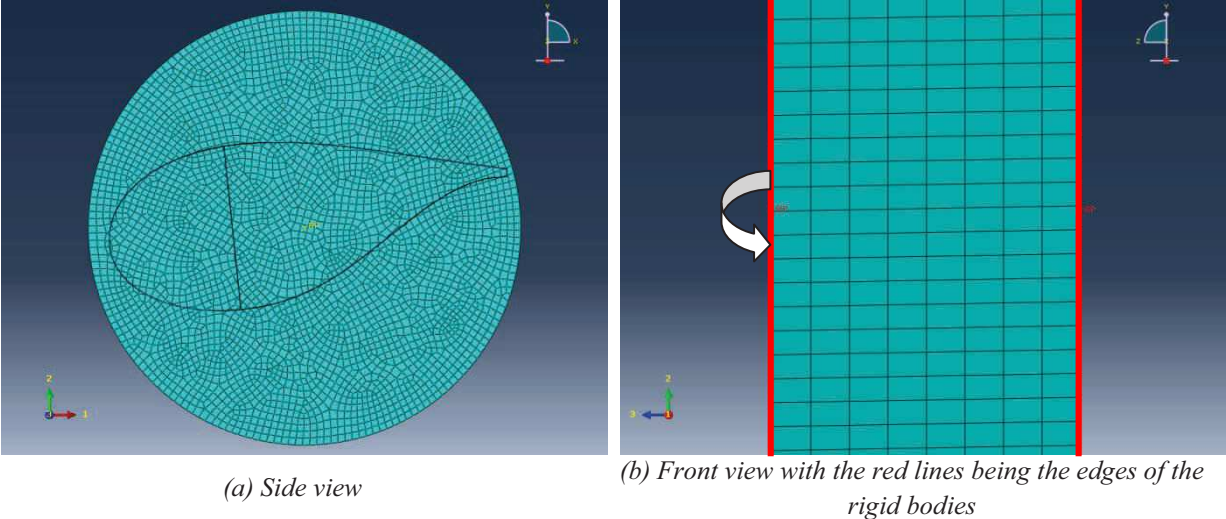


Figure 7-42: Mesh and Boundary conditions.

7.4.3.3 Selected sections and results

From the stratification and bending moment plots in Annex B and Annex C it's was judged that the sections at 3.22m, 4.05m, 7.55m and 11.72m from the root should be checked for stress levels as the ply drops in these regions would give rise to stress concentrations. The results of the first bending moment induced stresses are shown in the Figure 7-43 and Table 7-4.

| Section location (m) | Maximum Principal Stress in fiber direction (MPa) |
|----------------------|---|
| 3.22 | 53.40 |
| 4.05 | 26.85 |
| 7.55 | 155.50 |
| 11.72 | 58.99 |

Table 7-4: Maximum Principal stresses fiber direction for the different sections.

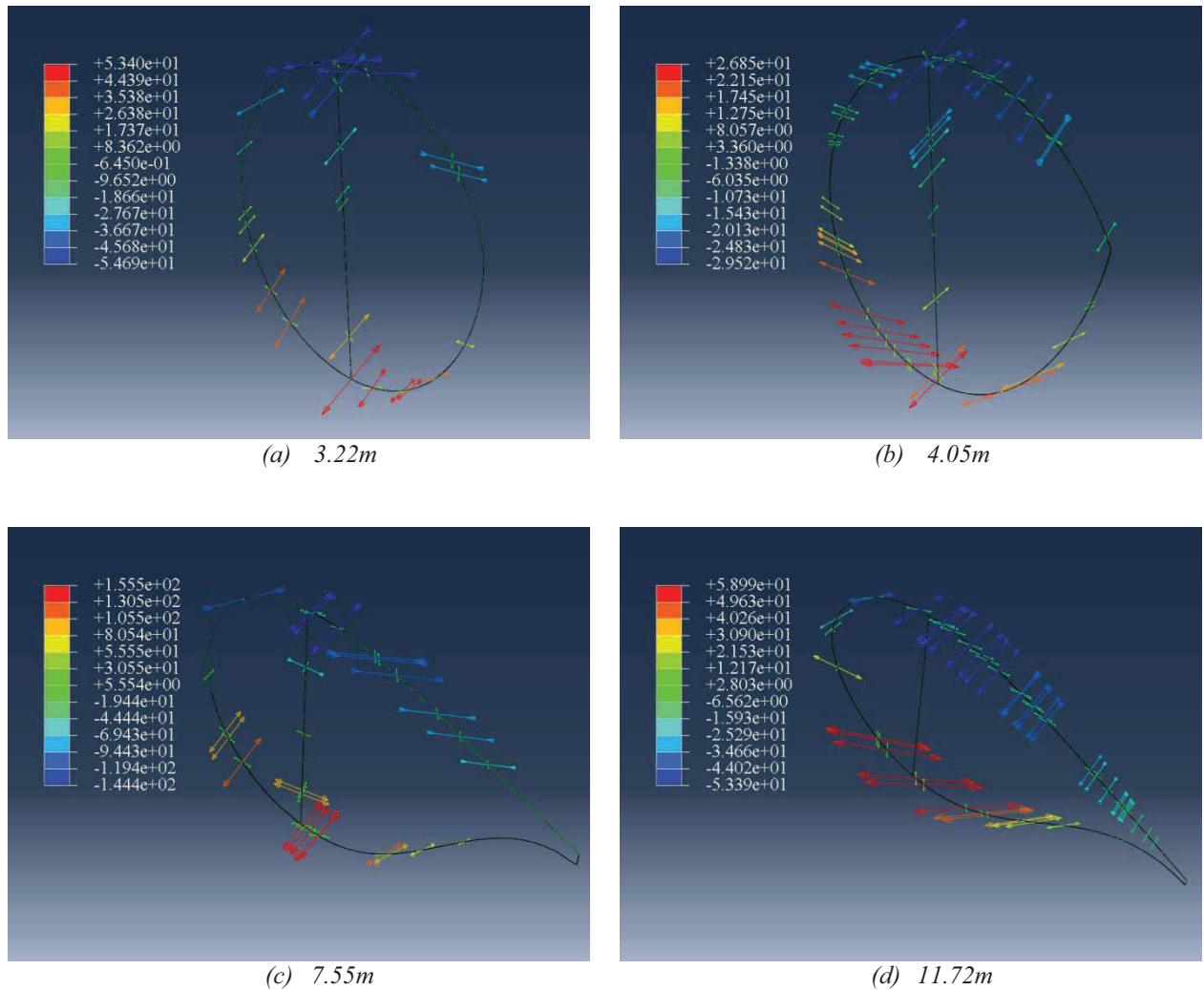


Figure 7-43: Maximum principal stress values for the different sections.

As can be seen from the Figure 7-43 and Table 7-4; the section at the 7.55m mark along the radius shows a marked increase in principal stresses in the fiber direction. Therefore now we can study this section in detail to see if there is a risk of failure or delamination taking place in the joints include within this section.

7.4.4 Tier 3: 3D Solid blade section

7.4.4.1 Geometry and material assignment

As the section at 7.55m experiences the highest amount of stress thus we shall base our “3rd tier modeling on this section to see whether there is a risk of failure. Verify whether the section can be lightened by removing material in case of too high a material thickness. The geometry follows the outer profile of the blade section while the inner section takes into consideration the thicknesses of the various layup regions. Furthermore the geometry is partitioned along the thickness to account for the different ply regions, Figure 7-44.

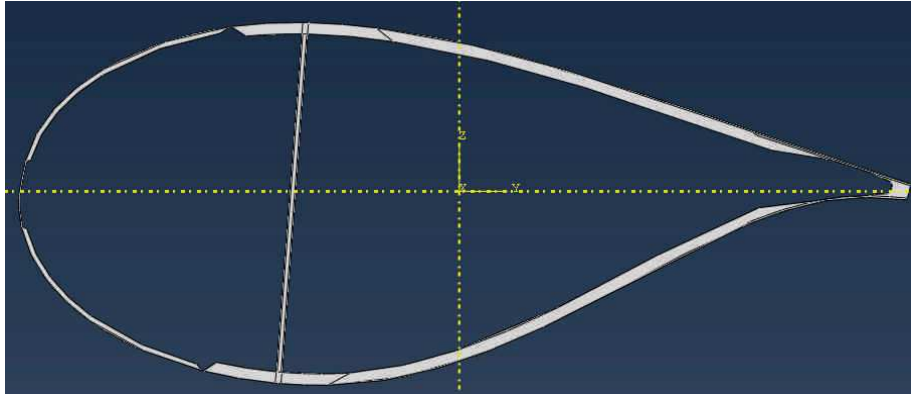
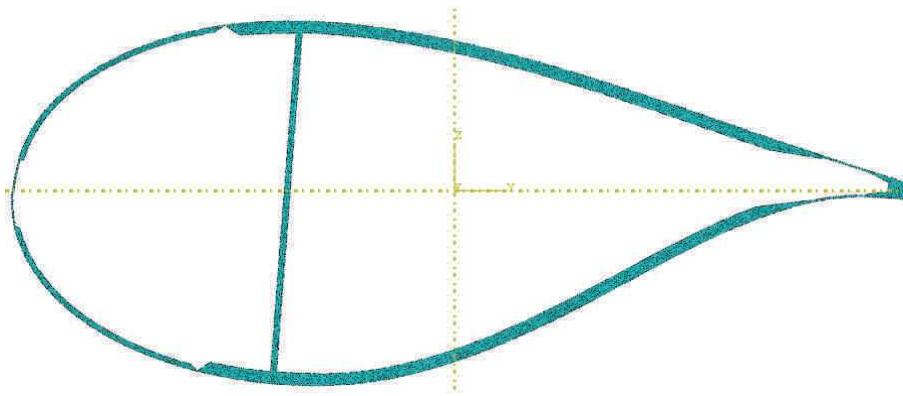


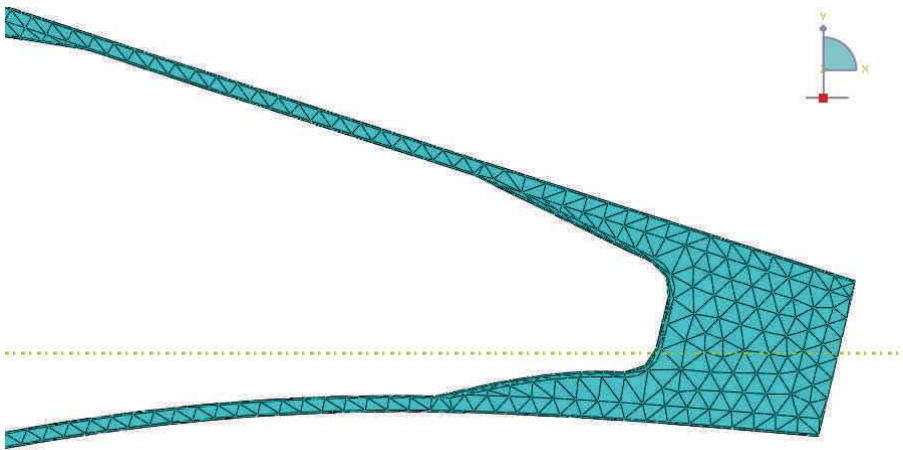
Figure 7-44: Section model taking into account the different material thicknesses.

7.4.4.2 Meshing and boundary conditions

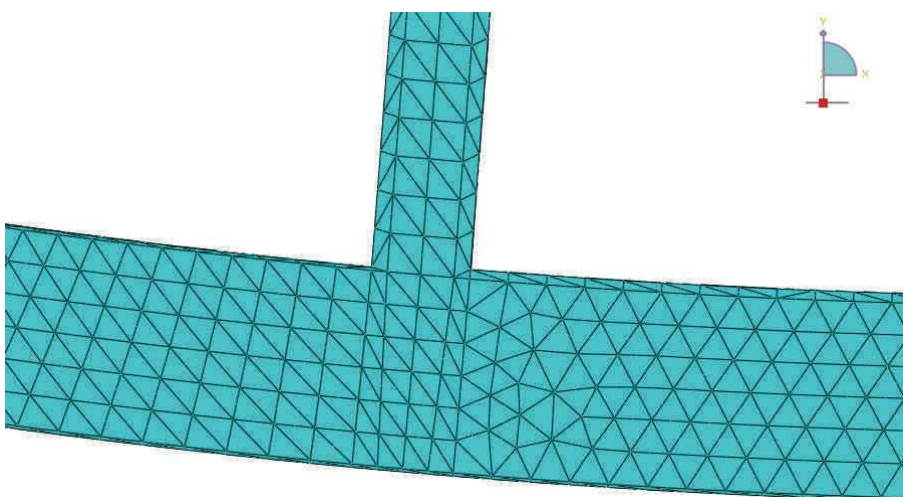
The mesh size chosen for this example is the same as for the previous 3D shell case. A mesh size of 1mm is chosen. The elements are all C3D10 type hexahedral solid elements with 3D properties. The foam core and adhesive joint due to their complex geometry have been meshed using tetrahedral elements. The boundary conditions applied are the same as for the previous case of 3D shell sections, Figure 7-45.



a) Mesh of the complete section in 3D.



b) Mesh details on the trailing edge.



c) Mesh details on the Blade surface Spar interface.

Figure 7-45: Mesh details of the 3D blade section.

7.4.4.3 Results under different load cases

In the Figure 7-46 to Figure 7-49 are presented the maximum principal stresses for the 4 load cases as explained in section 7.4.3.2 applied to the 3D blade section.

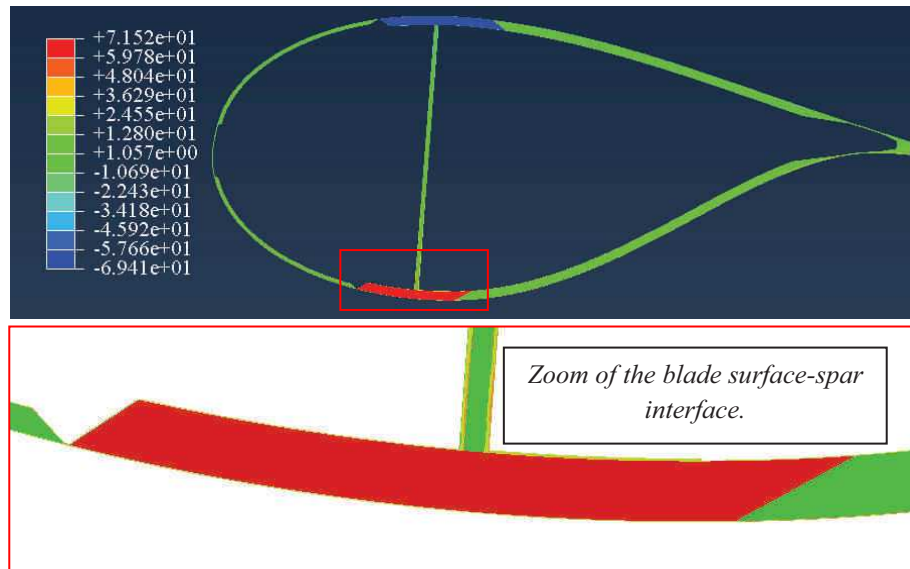


Figure 7-46: Maximum principal stress when the section is subjected to PTS loading.

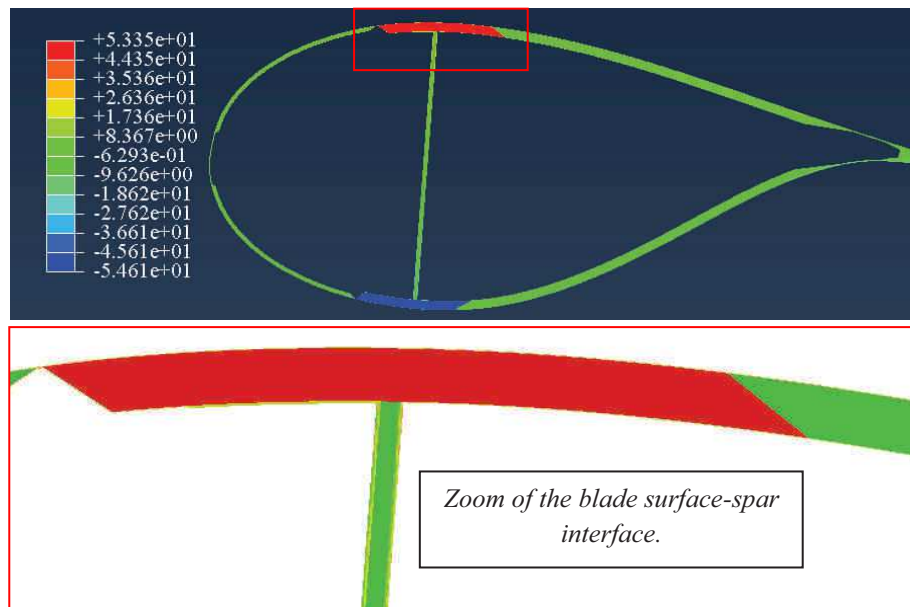


Figure 7-47: Maximum principal stress when the section is subjected to STP loading.

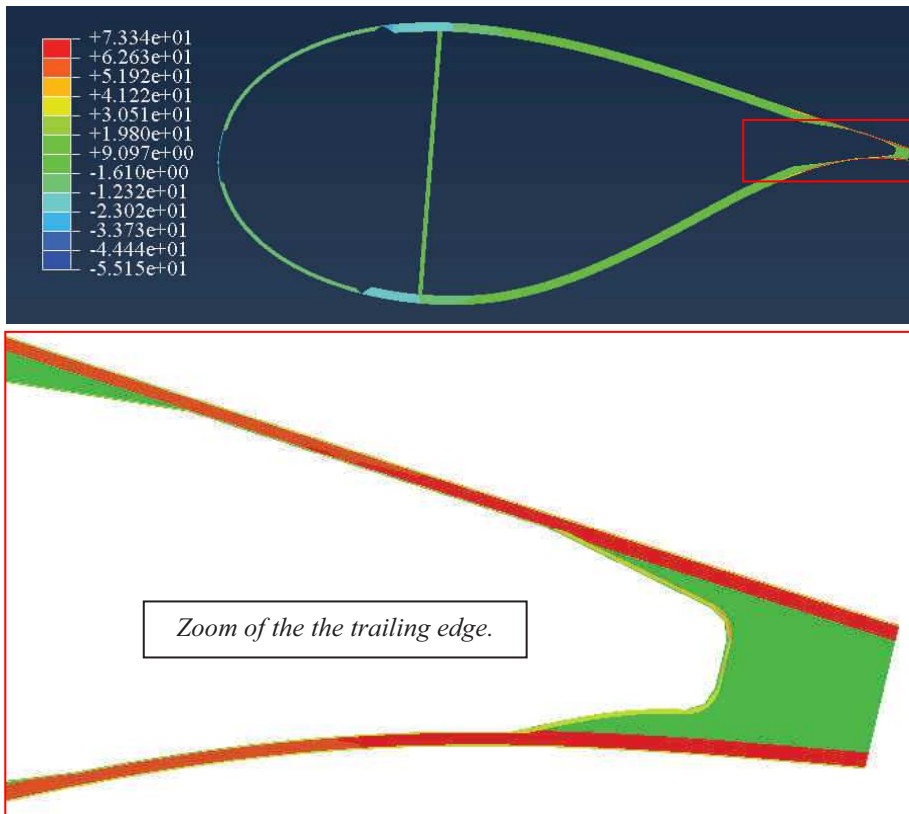


Figure 7-48: Maximum principal stress when the section is subjected to TTL loading.

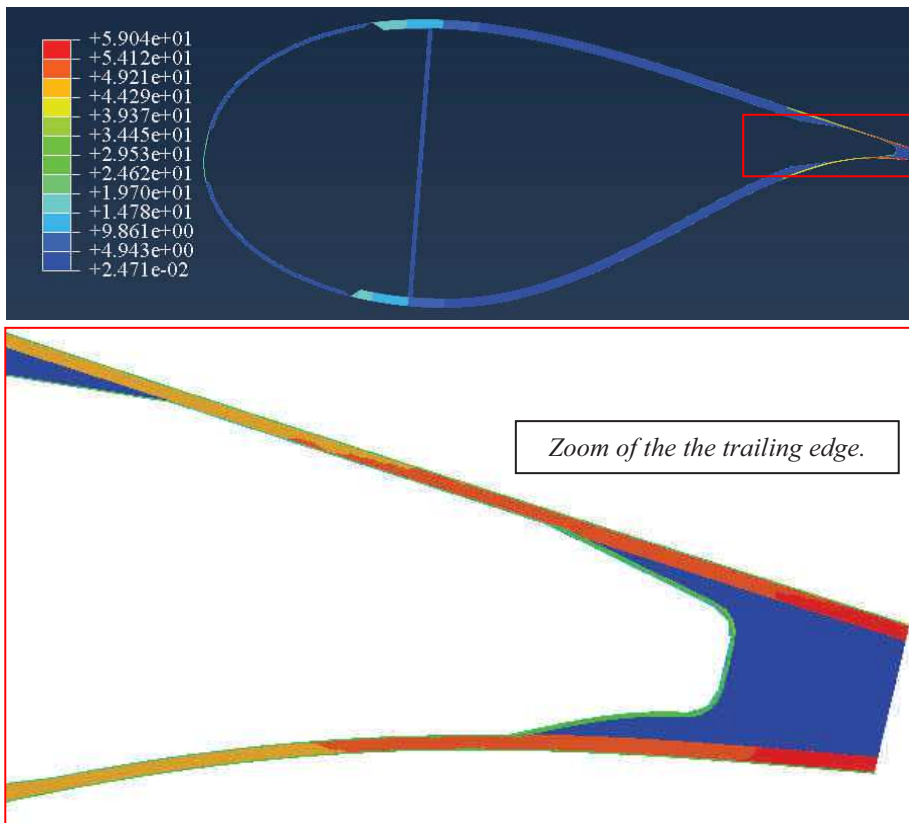


Figure 7-49: Maximum principal stress when the section is subjected to LTT loading.

7.4.5 Tier 4: Sub model of the Tier 3 solid model

For the tier of models we have chosen to model the pressure side blade-shear web interface and the trailing edge for the 4 types of load cases. The pressure side blade-shear web interface is models under PTS and STP loading regimes while the trailing edge is loaded under the TTL and LTT regimes.

7.4.5.1 Geometry and Material assignment

The model for this type of sub modeling is basically a section cut from the original 3 tier model. The model is partitioned more precisely to account for all the layups separately and the mesh is also refined to a further extent. Furthermore the material orientations in the different regions have been chosen according to the different layup regions.

7.4.5.2 Meshing and boundary conditions

The mesh type used is 3D hexahedral elements of 1mm mesh size to get the maximum fineness especially in the curved regions of the model. The loads and boundary conditions applied are directly from the parent model. The regions having triangular shape have been meshed using tetrahedral elements.

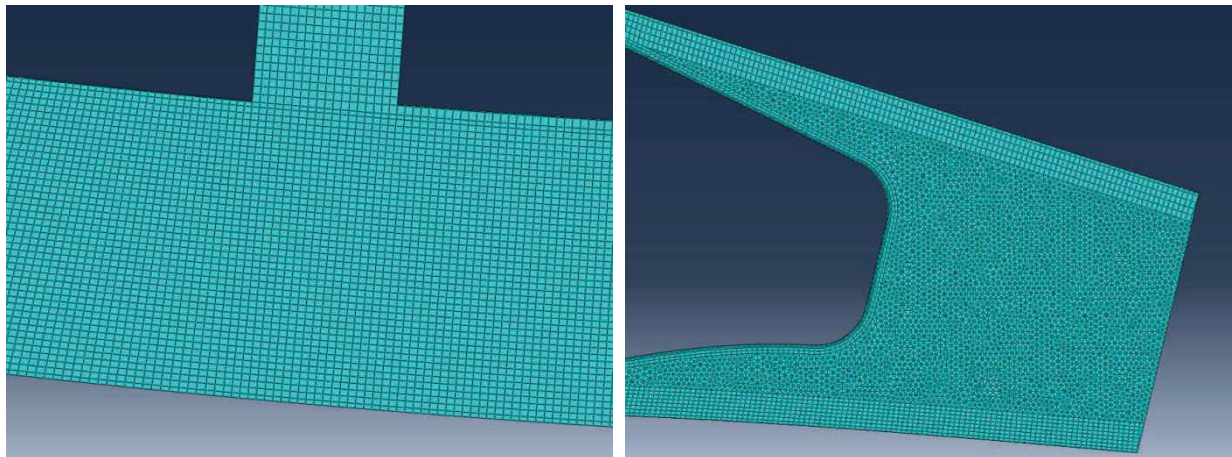
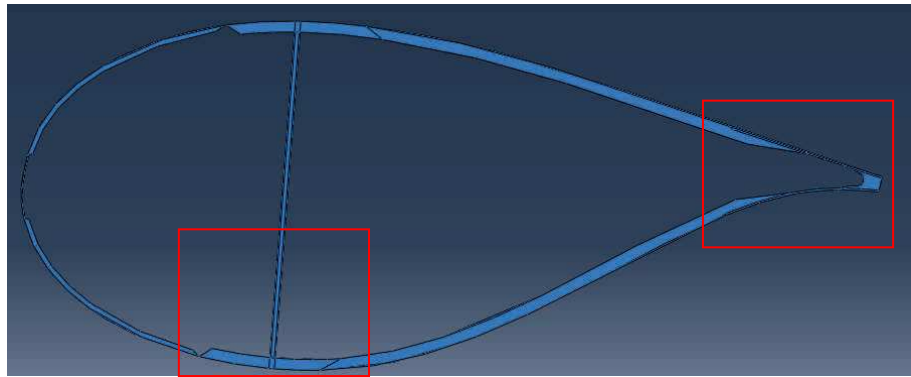
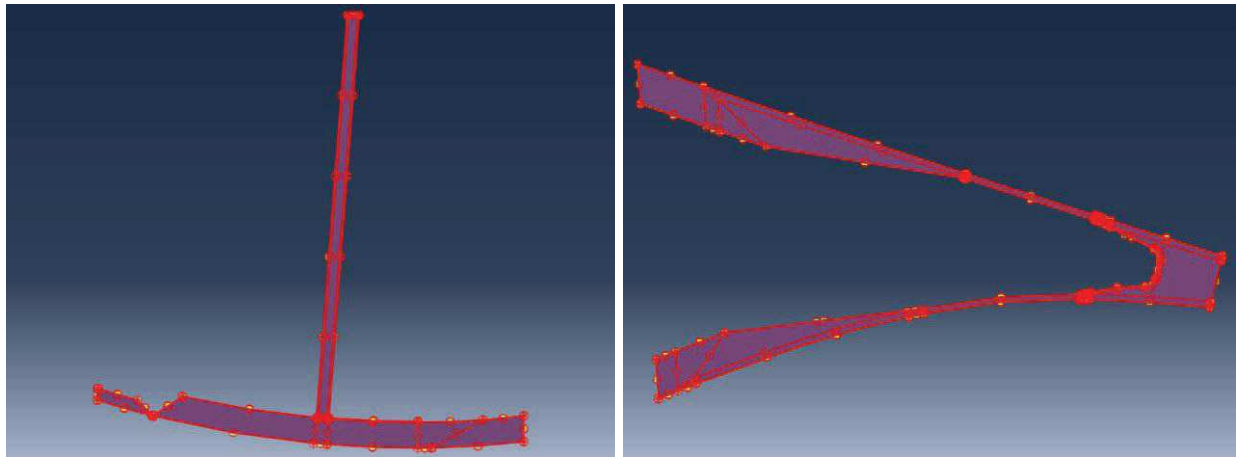


Figure 7-50: An example of mesh at the blade shear web interface region and at trailing edge.

We have chosen to use surface based strain field application, in which the strain field measured on the cut surfaces of the original model are applied as-is on the new cut surfaces of the submodel.



(a)



(b)

Figure 7-51: Boundary conditions being applied on the cut surfaces and of the submodel.

7.4.5.3 Results under different load cases

As explained previously the blade sub models have been simulated under different load conditions, including PTS, STP, TTL, and LTT. As can be seen from the tier 3 models the pressure side and the trailing edge of the blade experiences the most stresses. Therefore we have modeled these 2 regions in greater detail instead of the other ones.

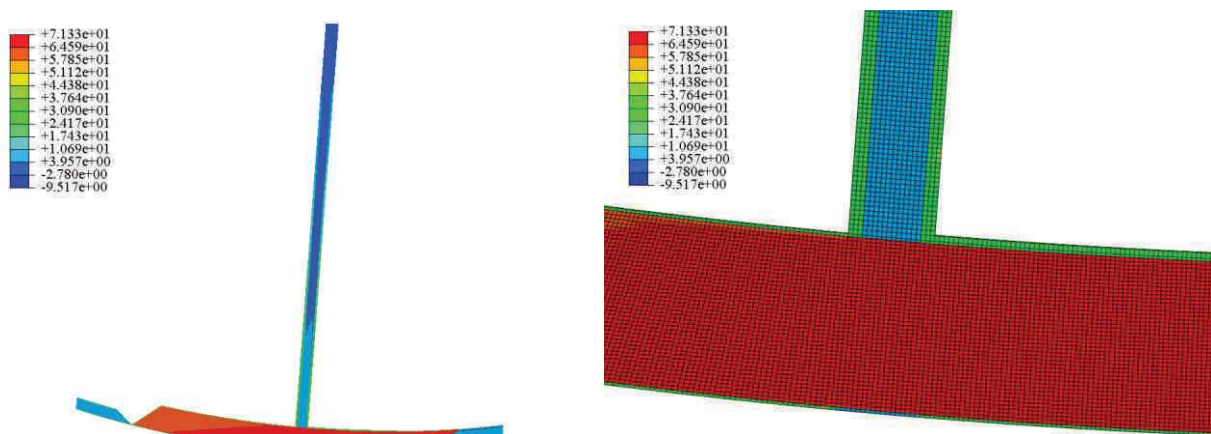


Figure 7-52: Maximum principal stress distributions in the blade shear web interface loaded under PTS type loading.

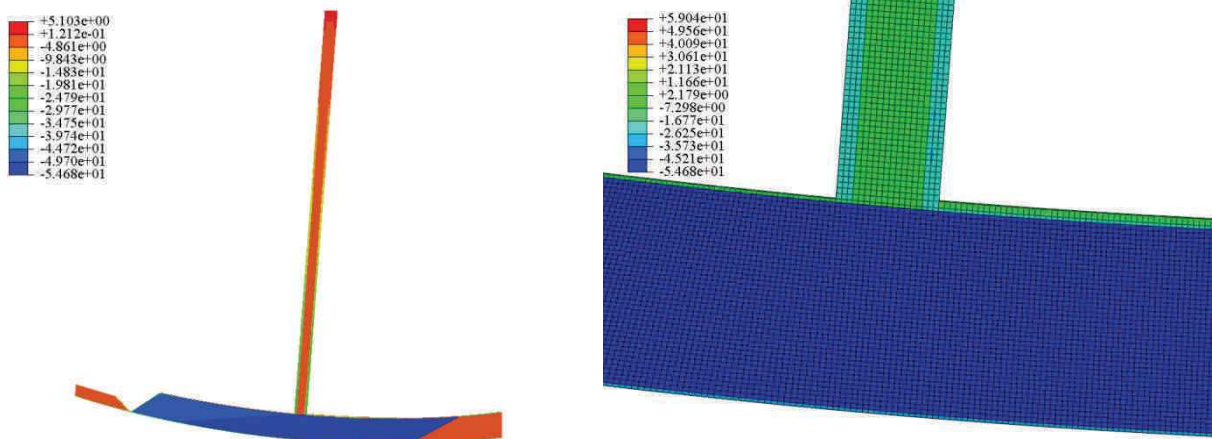


Figure 7-53: Maximum principal stress distributions in the blade shear web interface loaded under STP type loading.

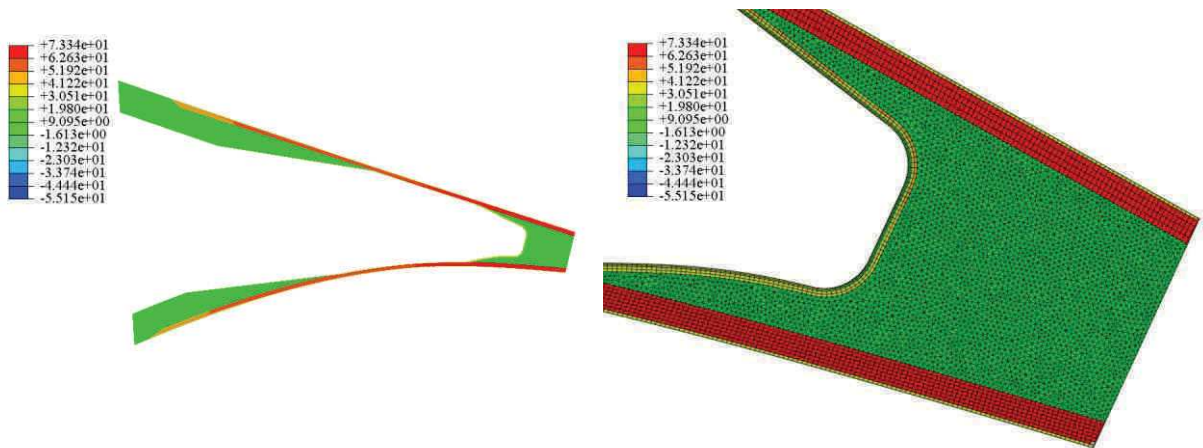


Figure 7-54: Maximum principal stress distributions in the blade trailing edge loaded under TTL type loading.

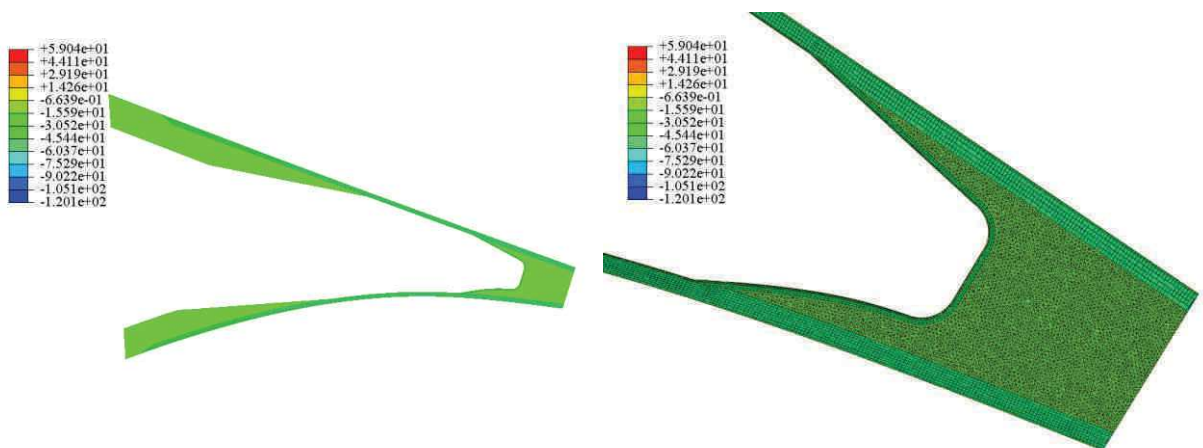


Figure 7-55: Maximum principal stress distributions in the blade trailing edge loaded under LTT type loading.

The Figure 7-52 - Figure 7-55 show the distribution of the maximum principal stress in the normal direction of the blade section. This is one of the stresses that need to be verified for the strength of the blade element. Stresses like the shearing and the in-plane (in the plane of the section) stresses need to be check as well. Their values are recapitulated in the Table 7-5.

| Section Loading | Max Principal Stress normal to the section surface S_{11} (MPa) | Max Principal Stress in plane to the section surface shearing the section S_{22} (MPa) | Max in-plane Shear Stress in plane to the surface shearing the section S_{12} (MPa) |
|-----------------|---|--|---|
| | tension/compression | | |
| PTS | 71.52 / 69.41 | 11.64 / 11.64 | 8.3 / 8.8 |
| STP | 53.35 / 54.60 | 9.59 / 9.50 | 7.17 / 6.99 |
| TTL | 73.34 / 54.48 | 12.08 / 18.34 | 8.15 / 11.11 |
| LTT | 44.98 / 60.55 | 15.14 / 9.97 | 9.17 / 6.73 |

Table 7-5: Summary of principal stresses applied on the blade sections.

It should be noted that however not explained in the Table 7-5, the location of maximum stresses taken are as shown in the Figure 7-52 - Figure 7-55. In the following section we shall see how to use these results in further sub modeling.

7.4.6 Tier 5: Sub model of Tier 4 including cohesive zones

The highest level sub model consists of cohesive zones at the ply interfaces and at the shear web blade interface, for the PTS type loading.

7.4.6.1 Model setup

The model geometry is another section of the tier 4 model. This model has only one side of the shear web to be able to model with ease. The shear web and the blade surface and the outer skin to the inner UD layups are joined together with cohesive zones. Ideally all the plies should be modeled with cohesive layers in between them but we have chosen to take the regions where there is the highest stress variation, delamination or debonding is expected. Each of the interfaces is modeled according to their proper cohesive zone properties as determined experimentally.

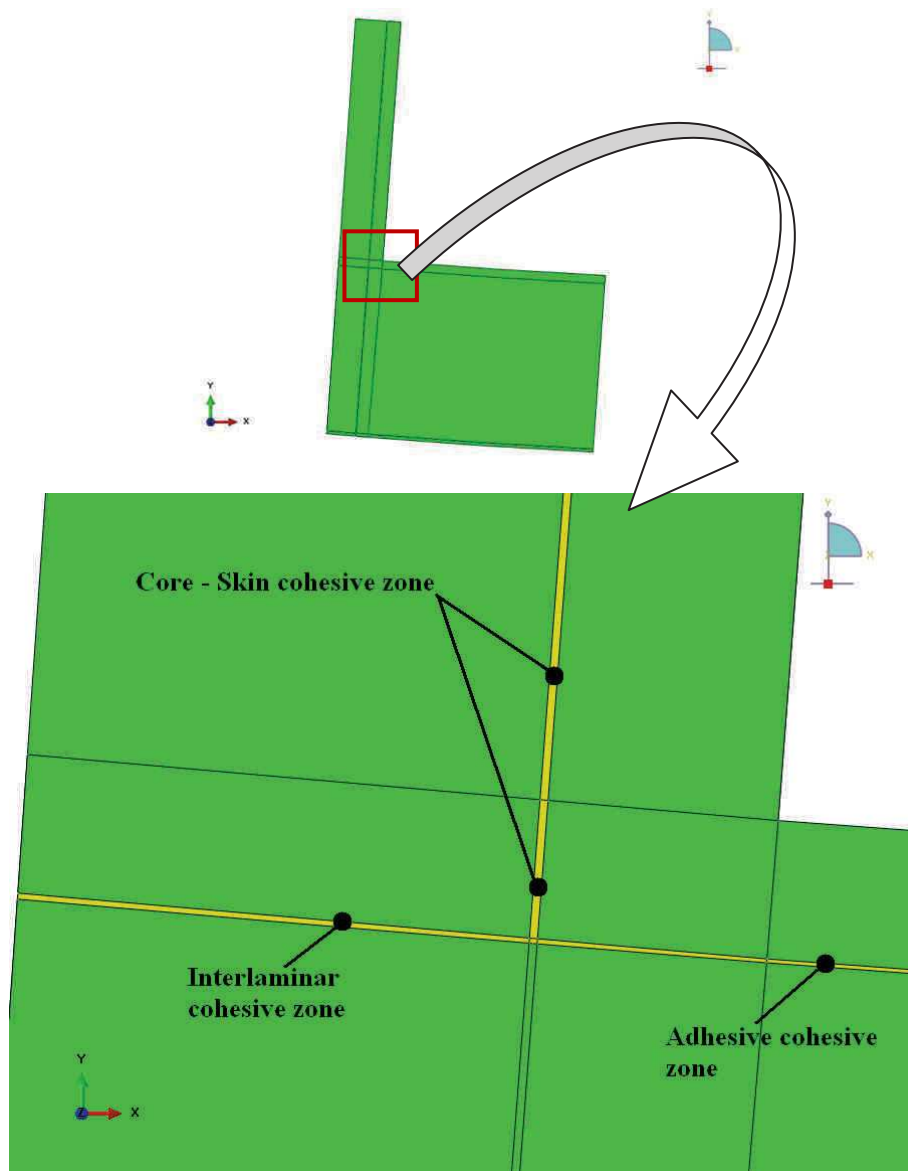


Figure 7-56: Zoom on the shear web blade interface to show the location of different cohesive zones

The same is done for the outer skin although here it is not shown.

7.4.6.2 Stress analysis results

The results of the stress analysis at the prescribed loads do not show any signs of delamination or debonding of the outer skins. However for the sake of showing how the weak spots which should be strengthened in the case of optimization of the blade are identified by loading the blade until the cohesive zones start to fail. It is seen that the cohesive zones at the shear web blade surface interface start to fail and the outer skin also starts to fail first. However the core in the shear web does not show signs of de bonding from its skin during loading up to failure.

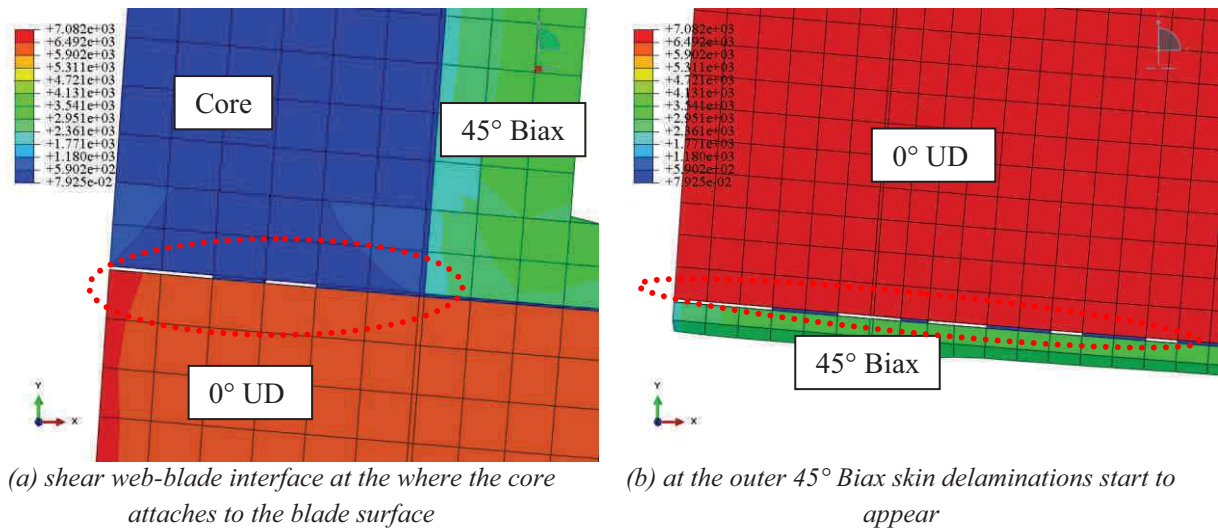


Figure 7-57: Onset of damage type debonding and delaminations.

The above failure is shown at tests up to failure, such loads are never to be expected to be applied during the life of the wind turbine blade, however at prescribed loads as explained there is no evidence of initiation of failure under static conditions.

The Figure 7-58 shows the distribution of the normal stresses at the cohesive zone elements. The stresses are measured in the opening direction as delaminations are dominant in this direction. However as can be seen from the Figure 7-58 that the maximum value of normal stresses attained remains below 2.5 MPa which has been determined experimentally where the delamination or crack begins to propagate.

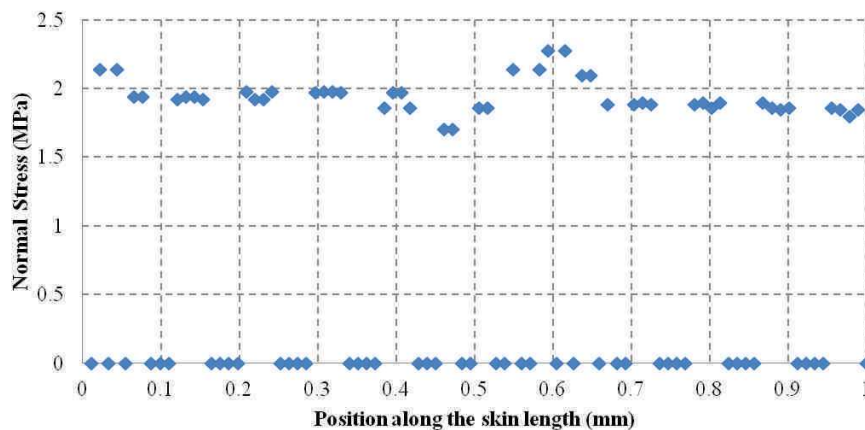


Figure 7-58: Distribution of normal stresses along the outer skin of the blade section

For the in-plane stresses it can be seen from the Figure 7-59 that the value of stress reaches 2.7 MPa which is also very much under the 25 MPa limit for the initiation of Mode II type failure of the cohesive zones. Therefore it can be inferred that the blade at this level of load does not risk any severe damage.

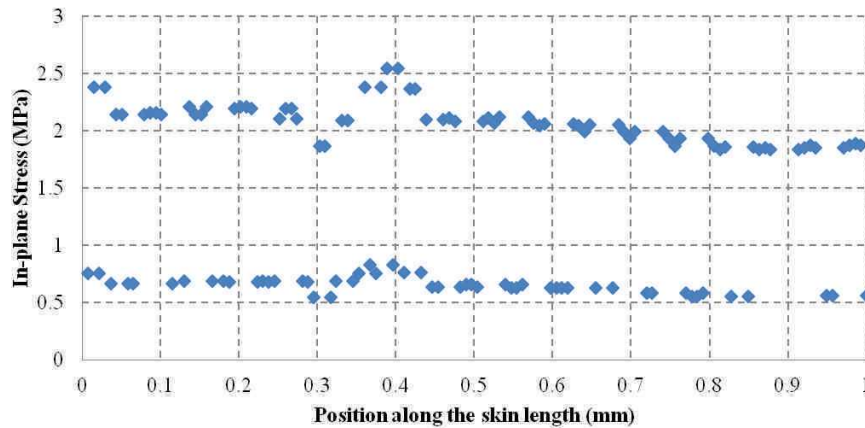


Figure 7-59: Distribution of in-plane principal stresses along the outer skin of the blade section

In essence the limiting factor for the design of this blade is the delamination resistance in the outer skin of the blade. The resistance of the in-plane crack propagation is sufficiently high hence will not pose a problem to the overall strength of the blade.

Since it is seen in the Figure 7-57 a that the unidirectional layer just under the outer skin is highly stressed hence we have modeled in this second phase the interlaminar cohesive zones for the first 5 layers of this region. Each cohesive zone layer is modeled with the interlaminar properties of the layups.

When loaded at the specified level of bending moments of 1350 kN-m we can see that the interlaminar stresses in the normal direction do not exceed 0.4 MPa which is safely under the level of 2.5 MPa required to initiate the delamination of this region.

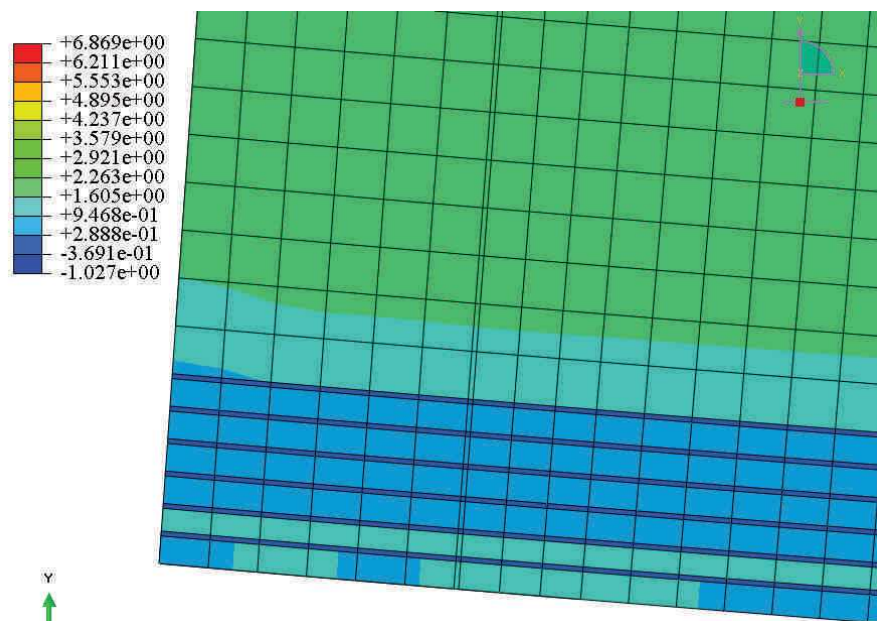


Figure 7-60: Zoom on the outer skin where it is the highest stressed and the first interlaminar cohesive zones.

To see the regions of interest when the blades starts to fail at very high loads, though not expected to be experienced. The blade section is loaded to a very high bending moment.

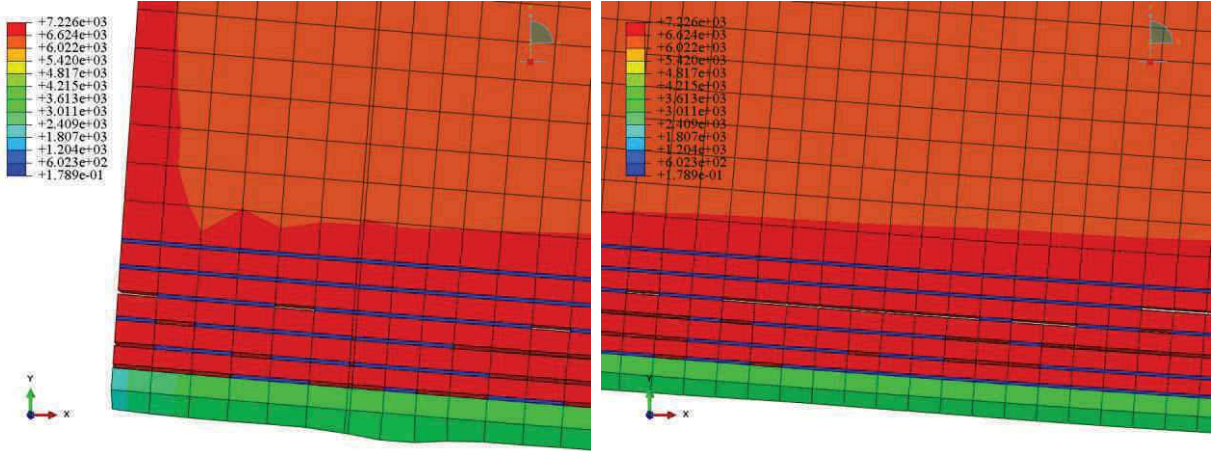


Figure 7-61: Delaminations start to appear all along the length of the outer skin and the adjacent uni-directional plies.

Notice here the missing cohesive elements (blue). This signifies the elements have started to fail at the outer skin and within the first 4 modeled interlaminar cohesive zones. This is however a very extreme case never to be expected in real service except in case of shocks and accidents where the dynamic properties would also be important.

For determining the limits of operation of this wind turbine blade the loads are increased incrementally in increments of 3 or 4 or up to N times the prescribed load levels to see at which instance the blade starts to show signs of failure or the damage starts to initiate. It is seen that at about 7 times the prescribed load levels the blade starts to show failure at the interlaminar level at the shear web blade surface interface. At this location the cohesive elements between the foam core and their skin reach the damage initiation stress levels of 2.5 MPa.

The same procedure has been adopted to check the design under STP type loading. The stress analysis shows no evidence of crack initiating at the outer highly stressed layer.

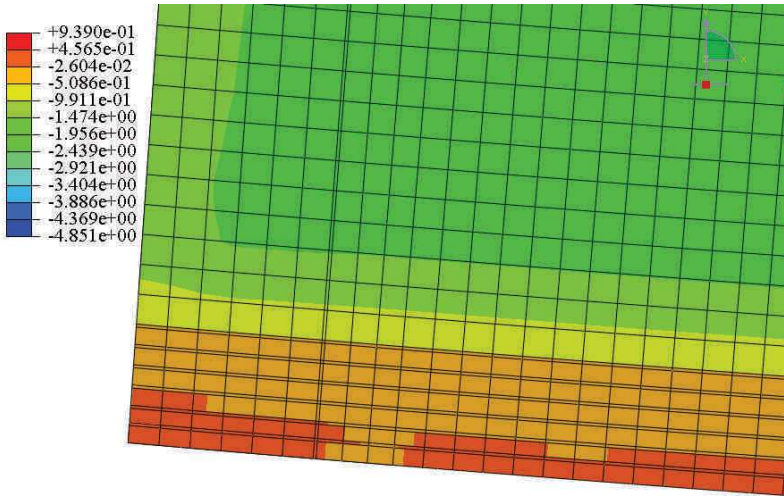


Figure 7-62: Cohesive zones in the outer skin layers show no evidence of crack initiating.

Upon closer inspection it is seen that the highest value of normal stress in these interlaminar cohesive layers do not exceed 1.4 MPa.

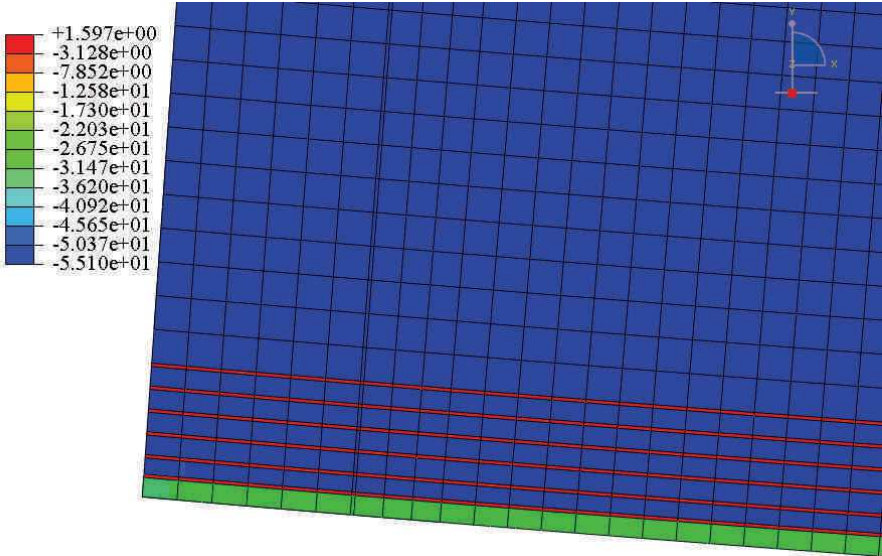


Figure 7-63: Maximum in-plane principal stresses in the cohesive interlaminar cohesive zones.

The interlaminar in-plane principal stresses at this load are fairly high reaching a maximum value of 1.0 MPa. Although this is still under the 25 MPa initiation limit, it can be inferred that the blade will start failing at its compression side during extreme conditions.

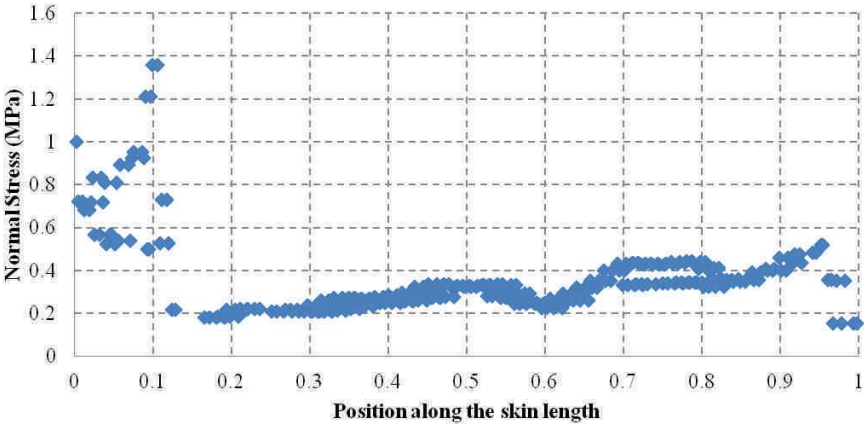


Figure 7-64: Distribution of normal stresses along the outer skin of the blade section

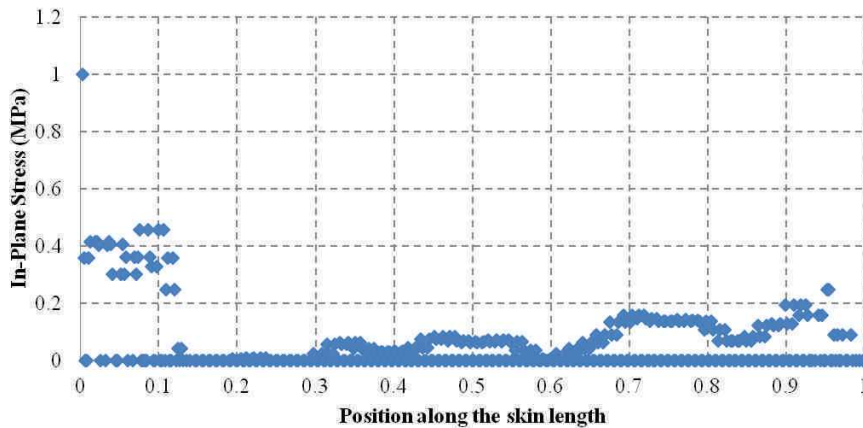


Figure 7-65: Distribution of in-plane principal stresses along the outer skin of the blade section.

7.5 Conclusions and Discussion

The modeling of the different specimen, substructure and the global structure level components has shown good correlation with the experimental data. The modeling has been used to ascertain the validity of the design and to validate if there is a risk of damage taking place during service. The other important feature of this modeling was to ascertain the safety of the wind turbine blade when faced to fatigue type loadings. It is seen as given in the chapter 6 on fatigue analysis that the in-fiber direction principal stresses should not exceed the limit of 160MPa approximately to keep the structure from fatigue induced strength and stiffness degradation.

However since the loads applied to the global model of the complete wind turbine blade were based on laboratory experiments on full scale blades, there is need to simulate the loadings according to the time history of the wind conditions at the site where the turbines are intended to be used.

This approach of modeling shows that the use of sub models can give a detailed overview as to what are the weak points within the structure that may need to be reinforced or modified. Either using thicker composite layups or by using a different scheme of fiber orientations.

In this analysis the non-linear elastic behavior of the composite polymer matrix has not been considered which can underestimate the blade tip deflection. The loads applied are not high enough to cause a remarkable effect in deflection due to non linearity so for the moment we can ignore these effects. During optimization of the blade the effects of non-linearity will be taken into account

Conclusions and Perspectives

The problem of design of wind turbine blades has been addressed in this research work. From the basic design using the commonly used aerodynamic design theories a design method has been developed. The materials used for the fabrication of wind turbines have been studied. The materials like epoxy resins which are expensive have been replaced with polyester to reduce costs. In the mechanical tests done on these materials it has been seen that the materials are sufficiently resistant to the mechanical loads being applied during the service of the blades.

In this PhD work, a new approach to the experimental characterization of composite materials under fatigue loads type was developed. This new approach allows performing tests that normally take days / weeks in a few hours / days. Some high speed fatigue testing techniques have been developed in order to reduce the time taken during testing. Modes of failure in fatigue have been identified and the fatigue analyses have been done in order to ascertain the life of the materials under cyclic loadings subjected to in fiber direction and out of fiber direction tensile loadings.

Finite element models have been used all through the design and development process to model and to validate the proposed designs. The use of cohesive zone elements with Hashin's damage criteria has given an insight into what goes on with the materials during failure. How the materials will behave under their strength limits. The behavior of simple overlap assembled joints has also been studied to validate the large scale finite element models.

Conclusions

The design methodology developed taking into account the aerodynamic loads at the service conditions of the blade using BEM theory gives a good initial design capable of being refined in later iterations. The strength of the blades is an important factor. The finite element modeling of the proposed designs show that from a strength point of view the blades would perform adequately. However the use of Hashin's damage criteria as shown in later sections, in some cases over estimate the strength or damage resistance of the blades, hence such designs should only be used as a starting point.

The strength of materials that were determined experimentally showed good repeatability even when taken from random places in the same batch. This shows a good quality control on the part of the manufacturer and the manufacturing process being used. It has however been seen that the use of higher ply thicknesses cause dimensional variations which affects the material characterization process. However the use of dimensionless constants or unit constants such variations can be reduced but the size effects always remain.

The resistance to delaminations and the resistance of interfaces was studied and seen to be effected especially in the case of sandwich composites, in relation to the material thicknesses. In general different thicknesses of materials caused some variations in the failure modes as well as in the strength of these materials. Size and scaling effects are expected in the case of composites. In sandwich

structures although closed cell cores were used but there is always a slight penetration of resin into the foam core causing it to affect the material properties.

The modeling of the specimens and sub assemblies using finite element models and cohesive zone elements showed good correspondence to the experimental results. These models further allowed the use of finite elements for the modeling of the complete blade model. The blade model was then disintegrated to smaller sub models using the properties defined in the complete blade model to keep the modeling accuracy. The blade is seen to perform without risk of failure as shown in the full scale experiments.

Perspectives

The design of the blades is often limited to by the maximum deflection at the tip of the blade. A design methodology needs to be developed which basis the blade design on tip deflection instead of the strength of the materials.

The phenomena of fatigue in composites and polymer based matrices are of vital importance. It has been seen that even at the in fiber direction loaded specimens there was fatigue failure. In addition the most dominant mode of failure was that of delamination. Hence the matrix resistance to fatigue needs to be studied in depth, its visco-plastic effects. DMA studies should be done to analyze the energy absorbed during fatigue tests and also to characterize the material properties when loaded at high frequencies.

The modeling of the blade is one of the most important aspects of the design process. Finite element models as they grow in detail they also grow in complexity. However detailed models are required for accurate results. Furthermore the models present for the moment although can use different damage criterion at a sub model level to ascertain the mode of failure however the use of multiple criterion at the global model level makes it too heavy computationally.

More realistic pressure loads based on CFD calculations should be applied to the blade surface to get an in-depth view of which zones are the most susceptible to damage during their service.

An optimization algorithm should also be developed which would take into account the different loading conditions and material properties, their resistance to damage and their stiffness to get a light and economical blade design. Genetic algorithms have been used in the past to treat such multi parameter problems, and should be developed to match the needs of this blade design study.

The crack propagation was seen not to rest always in the interlaminar region, especially where the adhesive is thick. Due to fiber bridging and resin inclusions into the foam core the crack can propagate into the layers as well. There is a need to use a model which can take into account this deviation of the crack path during propagation, for example XFEM can be used to predict crack growing in an adhesive layer.

Presently the blade has been loaded in physical tests under monotonic static loads. This is an essential step in figuring the global stiffness and strength of the blade under extreme wind conditions. However for optimizing the blade based on the expected life, full scale fatigue tests should also be carried out.

This project has been run as a prototyping project as a proof of concept that floating wind turbines are a viable source renewable energy. But to exploit fully their potential in an efficient fashion extremely large scale turbines are proposed capable of producing an upwards of 20 MW energy. For this purpose blade lengths of 100m would be normal. Such large blades would require a rethink of the design and manufacturing incorporating carbon fiber composites in the highly stressed regions to limit the blade tip deflections and to keep the blade weight under check.

Finally the ultimate goal would of course be able to fabricate turbines which are recyclable. For the moment turbine blades are fabricated using thermosets plastic composites. Thermosets are not reclaimable and the process to reclaim fiber reinforcements from thermoset polymer composites is costly and environmentally unfriendly. There are certain challenges in the use of thermoplastic in the fabrication phase for the moment but they shall be overcome to produce a truly “Green” energy source.

Bibliography

- Abedi, H., 2013. *Aerodynamic Loads on Rotor Blades*, Sweden: Chalmers University of Technology.
- Abouhnik, A. & Albarbar, A., 2012. Wind turbine blades condition assessment based on vibration measurements and the level of an empirically decomposed feature. *Energy Conversion and Management*, Volume 64, pp. 606-613.
- Advanced Materials, 2011. *Advanced Materials : S-2 Glass® Fiber*. [Online].
- Allix, O., Ladevèze, P. & Corigliano, A., 1995. Damage analysis of interlaminar fracture specimens.. *Composite Structures*, Issue 31, pp. 61-74.
- Andersen, S. I. et al., . *Fatigue of materials and components for wind turbine rotor blades*. ISSN 1018-5593.
- Andersons, J., Hojo, M. & Ochiai, S., 2004. Empirical model for stress ratio effect on fatigue délamination growth rate in composite laminates. *International Journal of Fatigue*, p. 597–604.
- Argüelles, A. et al., 2013. Using a statistical model for the analysis of the influence of the type of matrix carbon–epoxy composites on the fatigue delamination under modes I and II of fracture. *International Journal of fatigue*, pp. 54-59.
- Available at:
http://www.ewea.org/fileadmin/files/library/publications/statistics/European_offshore_statistics_1st-half_2014.pdf
- Available at:
http://www.siemens.com/innovation/en/publikationen/publications_pof/pof_fall_2007/materials_for_the_environment/wind_turbines.htm
- Available at:
Théorie de HELICIEL; <http://www.heliciel.com/helice/calcul-helice-aile/Theorie%20element%20de%20pale%20relative%20aux%20helices%20captrice%20motrices.htm>
- Avilés, F. & Carlsson, L., 2008. Analysis of the sandwich DCB specimen for debond characterization. *Engineering Fracture Mechanics*, 75(2), pp. 153-168.
- Bechly, M. & Clausen, P., 1997. Structural design of a composite wind turbine blade using finite element analysis. *Computers & Structures*, Volume 63.
- Beltz, G. E. a. R. J. R., 1991. *Dislocation Nucleation Versus Cleavage Decohesion at Crack Tips*, The Minerals, Metals & Materials Society, Harvard University, Cambridge.
- Berggreen, C., Branner, K., Jensen, J. F. & Schultz, J. P., 2007. Application and Analysis of Sandwich Elements in the Primary Structure of Large Wind Turbine Blades. *Journal of Sandwich Structures and Materials*, Issue 9, p. 525 – 551.
- Bizeul, M., Bouvet, C., Barrau, J. & Cuenca, R., 2011. Fatigue crack growth in thin notched woven glass composites under tensile loading. Part I: Experimental. *Composites Science and Technology*, p. 289–296 .

- Bizeul, M., Bouvet, C., Barrau, J. & Cuenca, R., 2011. Fatigue crack growth in thin notched woven glass composites under tensile loading. Part II: Modelling. *Composites Science and Technology*, p. 297–305.
- Botelho, E. C. et al., 2009. Fatigue behaviour study on repaired aramid fiber/epoxy composites. *Journal of Aerospace Technology and Management*, 1(2).
- Camacho, G. T. a. O. M., 1996. Computational Modelling of Impact Damage in Brittle Materials. *Int. J. Solids Struct*, Issue 33(20–22), p. 2899–2938..
- Camanho, P. et al., 2014. Three-dimensional invariant-based failure criteria for fiber-reinforced composites.. *International Journal of Solids and Structures*.
- Carvalho, N. D., Pinho, S. & Robinson, P., 2011. An experimental study of failure initiation and propagation in 2D woven composites under compression. *Composites Science and Technology*, 71(10), p. 1316–1325.
- Chamis, C. C., 1984. Simplified composites micromechanics equations for hygal, thermal and mechanical properties.. *SAMPE Qtrly*.
- Chazly, N. E., 1993. Static and dynamic analysis of wind turbine blades using the finite element method. *Renewable Energy*, 3(6–7), pp. 705-724.
- Choi, H. S., Achenbach, J. D. & Kim, C., 2001. Micromechanical Bilinear Behavior of Composite Lamina Subjected to Combined Thermal and Mechanical Loadings. *Mechanics of Composite Materials and Structures*, 8(2), pp. 135-155.
- Chr., T. L., Overgaard & Erik, L., 2005. *Structural Design Sensitivity Analysis and Optimization of Vestas V52 Wind Turbine Blade, DK-9220 Aalborg East, Denmark.*: Institute of Mechanical Engineering, Aalborg University.
- Christensen, R. M., 2014. *Failure Criteria for Anisotropic Fiber Composite Materials.*
- Clausen & Epaarachchi, J., 2003. A Model for Fatigue Behavior Prediction of Glass Fibre-Reinforced Plastic (GFRP) Composites for Various Stress Ratios and Test Frequencies. *Composite A: Applied Science and Manufacturing*, Issue 34, pp. 313-326.
- Colombo, C. & Vergani, L., 2014. Influence of delamination on fatigue properties of a fibreglass composite. *Composite Structures*, p. 325–333.
- Curà, F., Curti, G. & Sesana, R., 2005. A new iteration method for the thermographic determination of fatigue limit in steels. *International Journal of Fatigue*, 27(4), pp. 453-459.
- Damghani, M., Kennedy, D. & Featherston, C., 2014. Global buckling of composite plates containing rectangular delaminations using exact stiffness analysis and smearing method. *Computers & Structures*, Volume 134, pp. 32-47.
- Davidson, B. D. & Sundararaman, V., 1996. A single leg bending test for interracial fracture toughness determination. *International Journal of fracture*, Issue 78, pp. 193 - 210.
- Davidson, B. D. & Sunderaman, V., 1996. A single leg bending test for interracial fracture toughness determination. *International Journal of fracture*, Issue 78, pp. 193 - 210.
- Decolon & Christian, 2000. *Criteria of Failure*. In: *Structures Composites calcul des plaques et des poutres multicouches*. Paris: HERMES Science Publications, pp. 70 - 76.

Department of Trade and Industry, 2006. The Energy Challenge: Energy Review Report 2006, Department of Trade and Industry, UK Government.

Dubouloz, K. S. F., 2009. Adhesives for bonding wind turbine blades.

Elsam Engineering A/S., 2004. Life Cycle Assessment of Offshore and Onshore Sited Wind Farms, Elsam Engineering A/S.

Emery, T. & Dulieu-Barton, J., 2010. Thermoelastic Stress Analysis of damage mechanisms in composite materials. *Composites: Part A*, p. 1729–1742.

Esfahanian, V. et al., 2013. Numerical analysis of flow field around NREL PhaseII wind turbine by a hybrid CFD/BEM method. *Journal of Wind Engineering and Industrial Aerodynamics*, pp. 29 - 36.

European Wind Energy Association (EWEA), 2013. Deep water: The next step for offshore wind energy, European Wind Energy Association (EWEA)..

EWEA, 2013. The European offshore wind industry -key trends and statistics 1st half 2013.

Fargione, G., Geraci, A., Rosa, G. L. & Risitano, A., 2002. Rapid determination of the fatigue curve by the thermographic method. *International Journal of Fatigue*, p. 11–19.

Fern, N., Alam, P., Touaiti, F. & Toivakka, M., 2012. Fatigue life predictions of porous composite paper coatings. *Journal of Fatigue*, p. 181–187.

Freebury, G. & Musial, W., 2000. Determining Equivalent Damage Loading for Full-Scale Wind Turbine Blade Fatigue Tests. Nevada, 19th American Society of Mechanical Engineers (ASME) Wind Energy Symposium.

Freed, Y. a. B.-S. L., 2008. A New Cohesive Zone Model for Mixed Mode Interface Fracture in Bimaterials. *Eng. Fract. Mech.*, Issue 75(15), p. 4583–4593.

Gao, Y. F. & Bower, A. F., 2004. A simple technique for avoiding convergence problems in finite element simulations of crack nucleation and growth on cohesive interfaces.. *Modelling and simulation in materials science and engineering*, Issue 12, pp. 453-463.

Gebhardt, C. & Rocca, B., 2014. Non-linear aeroelasticity: An approach to compute the response of three-blade large-scale horizontal-axis wind turbines. *Renewable Energy*, Volume 66, pp. 495-514.

Geubelle, P. H. a. B. J. S., 1998. Impact-Induced Delamination of Composites: A 2D Simulation. *Compos. Part B: Eng.*, Issue 29(5), p. 589–602.

Global Wind Energy Council, 2005. Global Statistics 2005., .: Global Wind Energy Council (GWEC).

Griffin & Dayton., 2002. Blade System Design Studies Volume I: Composite Technologies for Large Wind Turbine, .: SAND2002-1879, Global Energy Concepts, LLC.

Griffin, D. A. & Zuteck, M. D., 2001. Scaling of Composite Wind Turbine Blades for Rotor of 80 to 120 Meter Diameter. *Journal of Solar Energy Engineering*, Issue 123, p. 310–318.

Griffin, D. A., 2002. Blade System Design Studies Volume I: Composite Technologies for Large Wind Turbine, .: SAND2002-1879, Global Energy Concepts, LLC.

- Griffin, D. A., 2002. Manufacturing Process and Structural Design for Large Wind Turbine Blades.. Nevada, USA, .
- Gunderson, J. D., Brueck, J. F. & Paris, A. J., 2007. Alternative test method for interlaminar fracture toughness of composites. *Int J Fract*, Issue 143, pp. 273 - 276.
- Hachemane, B. & Bezzazi, B., 2009. Comportement en fatigue de matériau composite. Toulouse, France, .
- Haj-Ali, R., Wei, B.-S., Johnson, S. & El-Hajjar, R., 2008. Thermoelastic and infrared-thermography methods for surface strains in cracked orthotropic composite materials. *Engineering Fracture Mechanics*, p. 58–75.
- Halpin, J. & Kardos, J., 1976. The Halpin–Tsai equations: a review. *Polym Engng Sci*, Volume 16, p. 344–352.
- Hamdi, H., Mrad, C., Hamdi, A. & Nasri, R., 2014. Dynamic response of a horizontal axis wind turbine blade under aerodynamic, gravity and gyroscopic effects. *Applied Acoustics*.
- Hamitouche, L., Tarfaoui, M. & Vautrin, A., 2008. An interface debonding law subject to viscous regularization for avoiding instability: Application to the delamination problems. *Engineering Fracture Mechanics*, 75(10), pp. 3084-3100.
- Hansen, P., Giannis, S. & Martin, a. R., 2008. Testing And Analysis Of Advanced Composite Materials And Structures In Wind Turbine Applications, MERL Ltd. Wilbury Way, Hitchin, Hertfordshire, SG4 0TW, UK.
- Hansen, P., Giannis, S. & Martin, R., 2008. Testing And Analysis Of Advanced Composite Materials And Structures In Wind Turbine Applications, .: MERL Ltd. Wilbury Way, Hitchin, Hertfordshire, SG4 0TW, UK.
- Harris, B., 2003. *Fatigue in Composites*. Woodhead Publishing ISBN 1 85573 608 X.
- HELICIEL, 2013. Théorie de HELICIEL. [Online]
- Hillmer, B., Borstelmann, T., Schaffarczyk, P. & Dannenberg, L., 2007. Aerodynamic and Structural Design of Multi MW Wind Turbine Blades beyond 5 MW. *The Science of Making Torque from Wind*.
- Holmes, J. W. & Brøndsted, B. F. S. a. P., 2007. *Reliability of Wind Turbine Blades: An Overview of Materials Testing*.
- Holmes, J. W., Sørensen, B. F. & Brøndsted, P., 2007. *Reliability of Wind Turbine Blades: An Overview of Materials Testing*. Wind Power Shanghai.
- Huang, Z.-M., 2002. Micromechanical modeling of fatigue strength of unidirectional fibrous composites. *International Journal of Fatigue*, p. 659–670.
- Ingram, G., Dec, 2005. *Wind Turbine Blade Analysis using the Blade Element Momentum Method*.
- International Energy Agency, 2005. “Key World Energy Statistics 2005., International Energy Agency (IEA).

- Janajreh, S. L. a. I., 2012. Development and application of an improved blade element momentum method model on horizontal axis wind turbines. *International Journal of Energy and Environmental Engineering*, 3(30).
- Ji, Y. & Han, K., 2014. Fracture mechanics approach for failure of adhesive joints in wind turbine blades. *Renewable Energy*, Volume 65, pp. 23-28.
- Joncas, S., De Ruiter, M. J. & Van Keulen, F., 2004. Preliminary Design of Large Wind Turbine Blades Using Layout Optimization Techniques. New York, USA, .
- Jørgensen, E. R. et al., 2004. Full scale testing of wind turbine blade to failure - flapwise loading, Roskilde : Risø National Laboratory.
- Kensche, C. W., 2004. Fatigue of composites for wind turbines.
- Kim, T., Hansen, A. M. & Branne, K., 2013. Development of an anisotropic beam finite element for composite wind turbine blades in multibody system. *Renewable Energy*, Volume 59, pp. 172-183.
- Knill, T. J., 2005. The Application of Aeroelastic Analysis Output Load Distributions to Finite Element Models of Wind. *Wind Engineering*, 2(29), p. 153 – 168.
- Kordatos, E., Dassiosa, K., Aggelisa, D. & Matikasa, T., 2013. Rapid evaluation of the fatigue limit in composites using infrared lock-in thermography and acoustic emission. *Mechanics Research Communications*, pp. 14 - 20.
- Kregting, R., 2005. Cohesive zone models towards a robust implementation of irreversible behaviour, MT05.11.
- Krstulovic-Opara, L., Klarin, B., Neves, P. & Domazet, Z., 2011. Thermal imaging and Thermoelastic Stress Analysis of impact damage of composite materials. *Engineering Failure Analysis*, p. 713–719..
- Krueger, R., Minguet, P. J. & O'Brien, T. K., 2000. A Method For Calculating Strain Energy Release Rates In Preliminary Design Of Composite Skin/Stringer Debonding Under Multi-Axial Loading. In: *Composite Structures: Theory and Practice*, ASTM STP 1383, pp. 105 - 128.
- Lekou, D., 2013. 10 - Probabilistic design of wind turbine blades. In: Woodhead Publishing, pp. 325-329.
- Li, D., Liu, Y. & Zhang, X., 2014. Low-velocity impact responses of the stiffened composite laminated plates based on the progressive failure model and the layerwise/solid-elements method. *Composite Structures*, Issue 110, p. 249–275.
- LLorca, J., 2000. Fatigue of particle and whisker reinforced metal matrix composites. *Progress in Materials Science*, pp. 283-353.
- Madsen & Krogsgaard, 2010. *Offshore Wind Power*, 2010 BTM Consult.
- Manca, M., Quispitupa, A., Berggreen, C. & Carlsson, L. A., 2012. Face/core debond fatigue crack growth characterization using the sandwich mixed mode bending specimen. *Composites: Part A*, Issue 43, pp. 2120-2127.
- Mason, K., 2004. Carbon/glass hybrids used in composite wind turbine rotor blade design, *Composites Technology*.

- McCartney, L., 2008. Energy methods for fatigue damage modelling of laminates. *Composites Science and Technology*, p. 2601–2615.
- Mckittrick, L. R. et al., 2001. Wind Turbine Using a Finite Element Model, SAND2001-1441, Sandia National Laboratories.
- Montesanoa, J., Fawaz, Z. & Bougherara, H., 2013. Use of infrared thermography to investigate the fatigue behavior of a carbon fiber reinforced polymer composite. *Composite Structures*, p. 76–83.
- Murri, G. B., 2011. Effect of Data Reduction and Fiber-Bridging on Mode I Delamination Characterization of Unidirectional Composites.
- Musial, L. S. a., 2000. Comprehensive Testing of Nedwind 12 - Meter Wind Turbine Blade at NERL, NREL/CP-500-27497.
- Nass & Wind, Cross Section Drawings of SPM 1 MW Wind Blade.
- Needleman, A., 1987. A Continuum Model for Void Nucleation by Inclusion Debonding. *ASME J. Appl. Mech*, Issue 54(3), p. 525–531.
- Needleman, A., 1990. An Analysis of Tensile Decohesion Along an Interface. *J. Mech. Phys. Solids*, p. 289–324.
- Ortiz, M. a. P. A., 1999. “Finite-Deformation Irreversible Cohesive Elements for Three Dimensional Crack-Propagation Analysis, . *Int. J. Numer. Methods Eng.*, Issue 44(9), p. 1267–1282.
- Paquette, Ashwill, T. D. & A., J., 2011. Composite Materials For Innovative Wind Turbine Blades, .: Wind Energy Technology Department Sandia National Laboratories..
- Paquette, T. D. A. a. J. A., 2011. Composite Materials For Innovative Wind Turbine Blades, .: Wind Energy Technology Department Sandia National Laboratories..
- Parida, S. & Pradhan, A., 2014. Influence of curvature geometry of laminated FRP composite panels on delamination damage in adhesively bonded lap shear joints. *International Journal of Adhesion and Adhesives*, Volume 54, pp. 57-66.
- Park, B., An, Y.-K. & Sohn, H., 2014. Visualization of hidden delamination and debonding in composites through noncontact laser ultrasonic scanning. *Composites Science and Technology*, Volume 100, pp. 10-18.
- Park, K. & Paulino, G. H., 2011. Cohesive Zone Models: A critical review of traction separation relationships across fracture surfaces. *Applied Mechanics Reviews*.
- Parlevliet, P. P. & Beukers, H. E. B. a. A., 2006. Residual stresses in thermoplastic composites—A study of the literature—Part I: Formation of residual stresses, .: Faculty of Aerospace Engineering, Delft University of Technology.
- Petersson, P. E., 1981. Crack Growth and Development of Fracture Zones in Plain Concrete and Similar Materials, .: LUTVDG/TVBM-1006 Lund Institute of Technology, Sweden.
- Reinoso, J. et al., 2012. Experimental and three-dimensional global-local finite element analysis of a composite component including degradation process at the interfaces. *Composites Part B: Engineering*, 43(4).

- REN21, 2011. Renewables 2011: Global Status Report., Paris: Renewable Energy Policy Network for the 21st Century.
- Rosa, G. L. & Risitano, A., 2000. Thermographic methodology for rapid determination of the fatigue limit of materials and mechanical components. *International Journal of Fatigue*, p. 65–73.
- Roth-Johnson, P., Wirz, R. E. & Lin, E., 2014. Structural design of spars for 100-m biplane wind turbine blades. *Renewable Energy*, Volume 71, pp. 133-155.
- Roylance, D., 2000. Laminated Composite Plates, Department of Materials Science and Engineering Massachusetts Institute of Technology.
- Russel, B. P., Liu, T., Fleck, N. A. & Deshpande, V. S., 2011. Quasi-Static Three-Point bending of carbon sandwich beams with square honeycomb cores.. *Journal of applied mechanics*, Volume 78.
- Scheider, I. & Brocks, W., 2003. Simulation of Cup-Cone Fracture Using the Cohesive Model. *Eng. Fract. Mech.*, Issue 70(14), p. 1943–1961..
- Shokrieh, M. M. & Rafiee, R., 2006. Simulation of fatigue failure in a full composite wind turbine blade. *Composite Structures*, 74(3), pp. 332-342.
- Siemens, 2008. Siemens Global Website. [Online]
- Smaïli, A. & Masson, C., 2010. Numerical modelling of flow around wind turbines using a hybrid method based on the Navier-Stokes solver and the generalized actuator disc concept. *Revue des Energies Renouvelables SMEE'10 Bou Ismail Tipaza*, pp. 301 - 309.
- Song, F., Ni, Y. & Tan, Z., 2011. Optimization Design. *Procedia Engineering*, Volume 16, pp. 369-37.
- Stanely, P., 1997. Application and potential of thermoelastic stress analysis. *Journal of material processing technology*, pp. 359-370.
- Sutherland, J., 1999. On The Fatigue Analysis of Wind Turbines, Sandia National Laboratories, SAND99-0089.
- Talreja, R., 2008. Damage and fatigue in composites – A personal account. *Composites Science and Technology*, p. 2585–2591.
- Tvergaard, V. & Hutchinson, J. W., 1993. The Influence of Plasticity on Mixed Mode Interface Toughness. *J. Mech. Phys. Solids*, Issue 41(6), p. 1119–1135.
- Tvergaard, V., 1990. Effect of Fibre Debonding in a Whisker-Reinforced Metal. *Mater. Sci. Eng.*, Issue A125(2), p. 203–213..
- Tyndall Centre, 2005. Decarbonising the UK: Energy for a Climate Conscious Future., Norwich: Tyndall Centre for Climate Change Research.
- U.S. Department of Energy (DOE)., 2011. Levelized Cost of New Generation Resources in the Annual Energy , US Energy Information Administration (EIA) of the U.S.
- Upitis, Z. T., Builis, I. V., Krauya, U. E. & Kulik, V. I., 1979. Initial Stages Of Failure Of An Orthogonally Reinforced Composite Material. *Fracture of Composite Materials*.
- Valencia, Locke, J. & Ulyses, 2004. Design Studies For Twist-Coupled Wind Turbine Blades, .: SAND2004-0522, Wichita State University National Institute for Aviation Research.

- Van Rijswijk, K. et al., 2005. Sustainable Vacuum-Infused Thermoplastic Composites for MW-Size Wind Turbine Blades - Preliminary Design and Manufacturing Issues. *Journal of Solar Energy Engineering*, Issue 127, p. 570–580.
- Vasconcellos, D. S. d., Touchard, F. & Chocinski-Arnault, L., 2013. Tension–tension fatigue behaviour of woven hemp fibre reinforced epoxy composite: A multi-instrumented damage analysis. *International Journal of Fatigue*.
- Veers, P. et al., 2003. Trends in the Design, Manufacture and Evaluation of Wind Turbine Blades. *Wind Energy*, Issue 6, p. 245–259.
- Verelst, D., 2009. Flexible wind turbine blades, .: Delft University of Technology.
- Wang, J. & Qiao, P., 2003. Novel beam analysis of end notched flexure specimen for mode-II fracture. *Engineering fracture mechanics*, Issue 71, pp. 219-231.
- Wang, L. et al., 2014. A mathematical model for calculating cross-sectional properties of modern wind turbine composite blades. *Renewable Energy*, Volume 64, pp. 52-60.
- Wang, L. et al., 2014. A mathematical model for calculating cross-sectional properties of modern wind turbine composite blades. *Renewable Energy*, Volume 64, pp. 52-60.
- Wang, Y., Liang, M. & Xiang, J., 2014. Yanfeng Wang, Ming Liang, Jiawei Xiang, Damage detection method for wind turbine blades based on dynamics analysis and mode shape difference curvature information, *Mechanical Systems and Signal Processing*, Volume 48, Issues 1–2, 3 October 2014, pp. 351-360.
- Williams, K. L. R. a. R. S., 1974. Determination of Fatigue-related Heat Emission in Composite Materials. *Experimental Mechanics*, pp. 479-485.
- Wu, F. & Yao, W., 2010. A fatigue damage model of composite materials. *International Journal of Fatigue*, p. 134–138 .
- Xiang, Y., Liu, R., Peng, T. & Liu, Y., 2014. A novel subcycle composite delamination growth model under fatigue cyclic loadings. *Composite Structures*, p. 31–40.
- Xu, X. -P. & Needleman, A., 1993. Void Nucleation by Inclusion Debonding in a Crystal Matrix. *Model. Simul. Mater. Sci. Eng.*, Issue 1(2), p. 111–132.
- Zhang, J. et al., 2014. The influence of wind shear on vibration of geometrically nonlinear wind turbine blade under fluid–structure interaction. *Ocean Engineering*, Volume 84, pp. 14-19.
- Zhou, H. et al., 2014. A review of full-scale structural testing of wind turbine blades. *Renewable and Sustainable Energy Reviews*, Volume 33, pp. 177-187.
- Zhuang, L. & Talreja, R., 2014. Effects of voids on postbuckling delamination growth in unidirectional composites. *International Journal of Solids and Structures*, 51(5), pp. 936-944.

Appendix A A Detail of composite layup for initial blade design

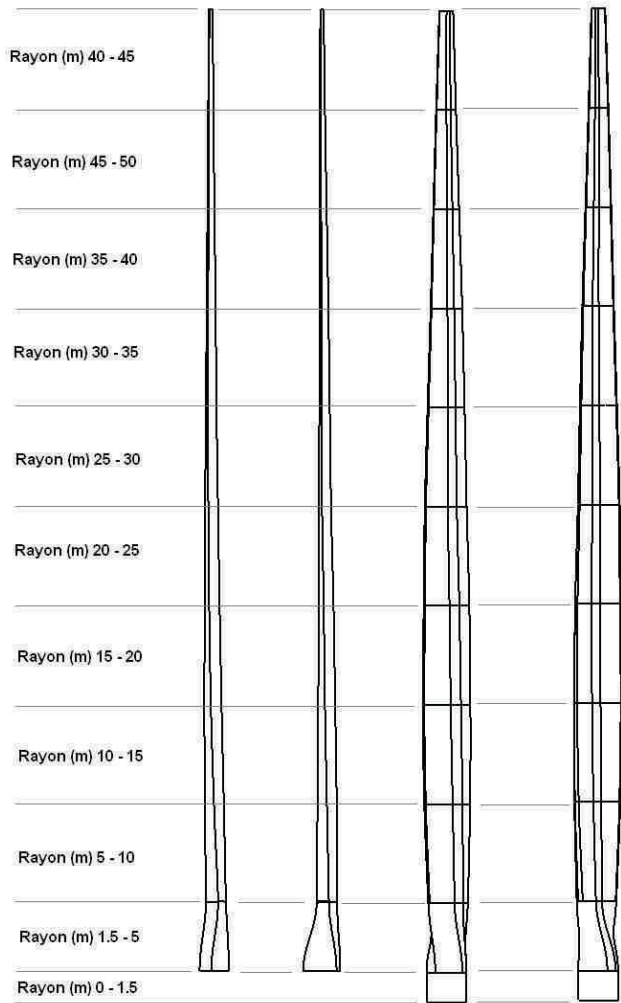


Figure A-1: Partitions of the blade in terms of radius from the root.

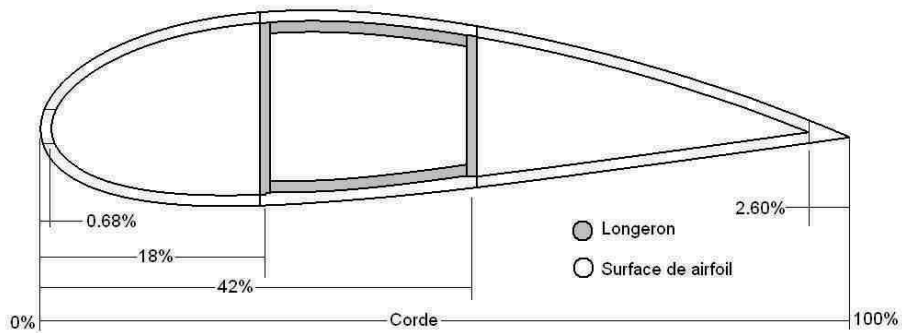
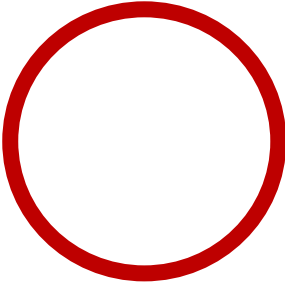
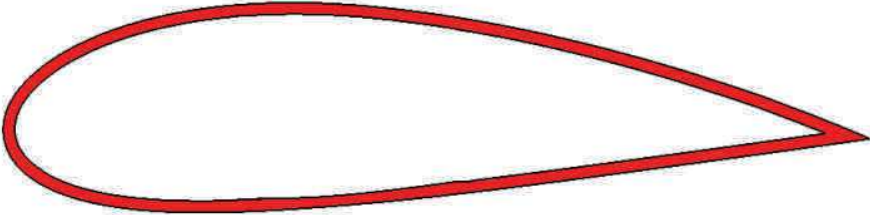
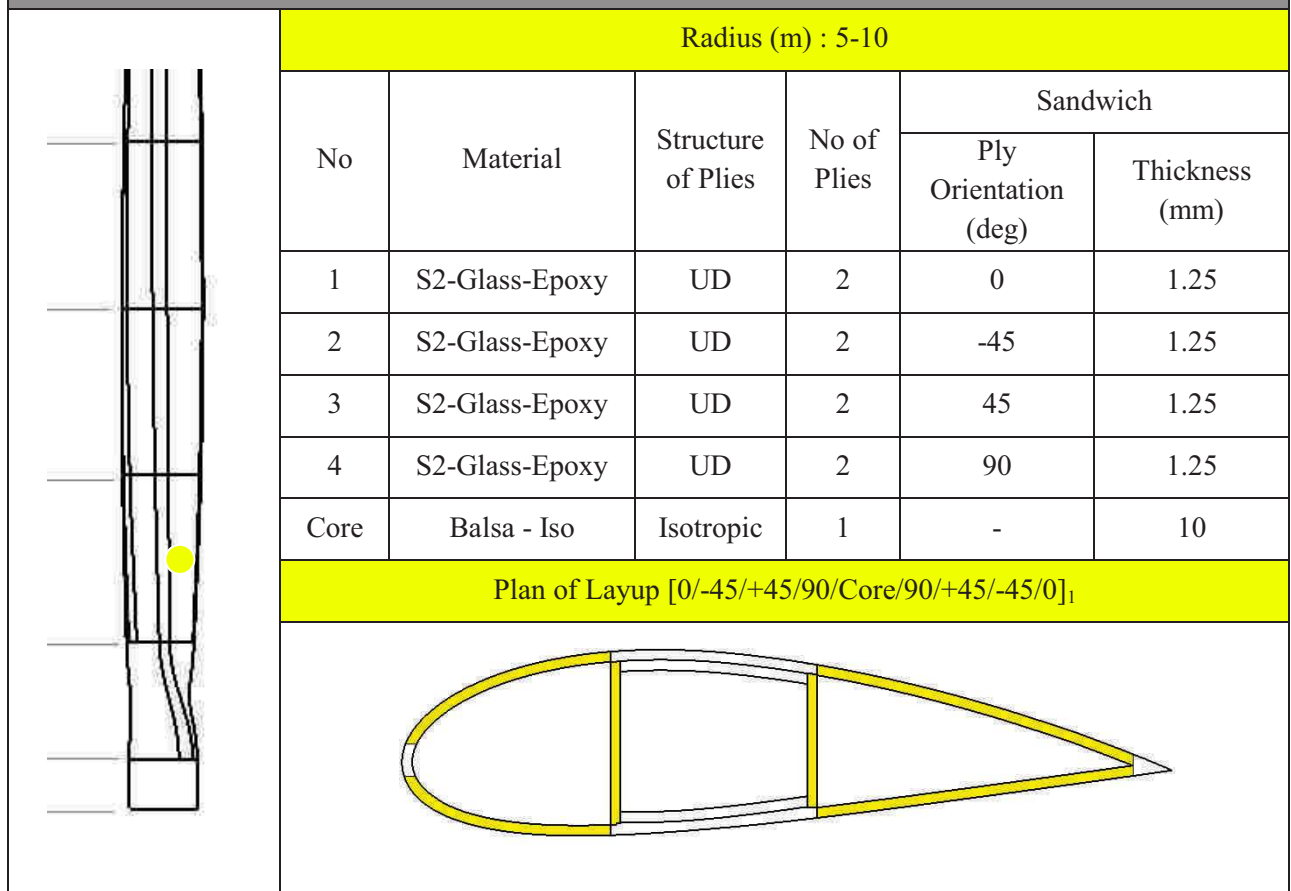
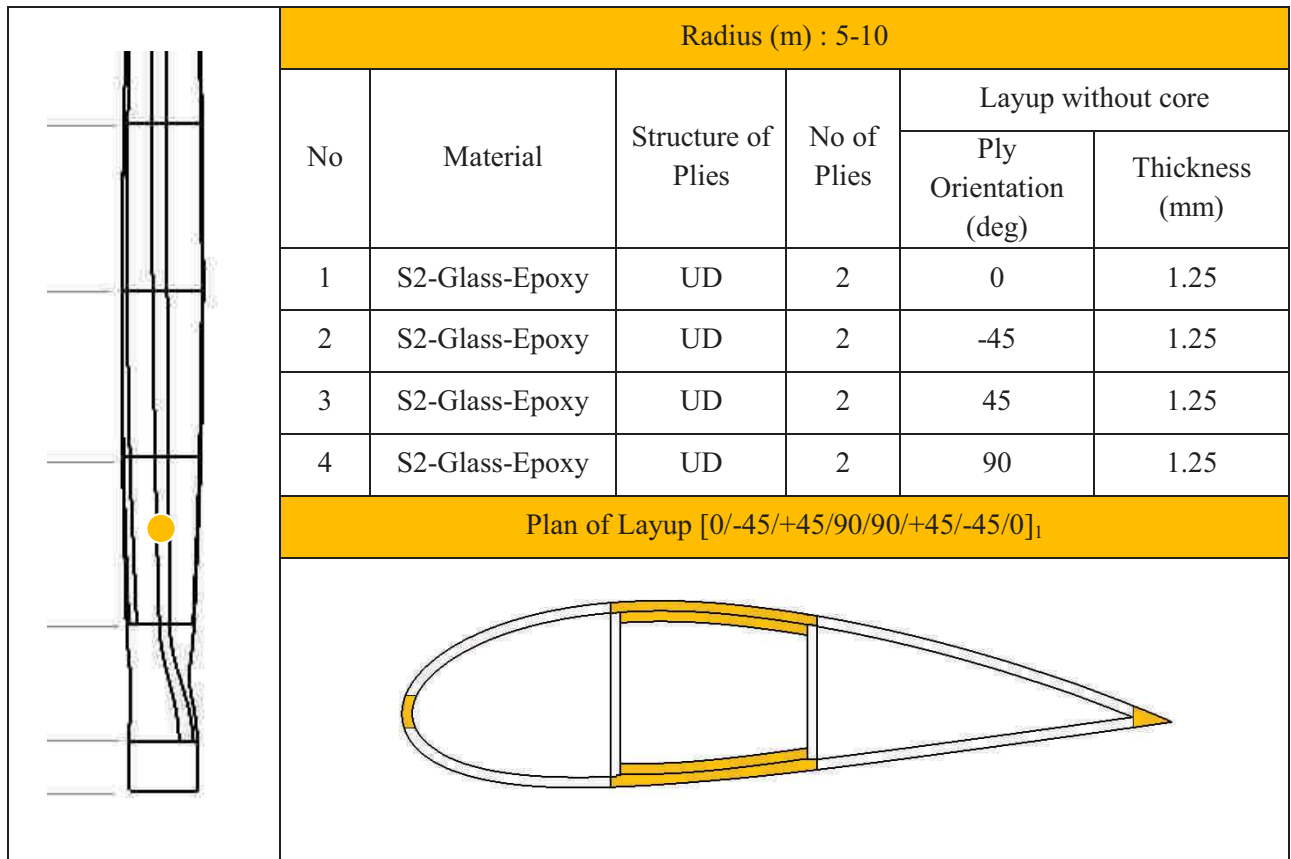


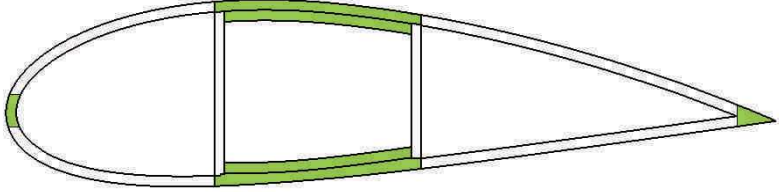
Figure A-2: Distribution of Material in the Section.

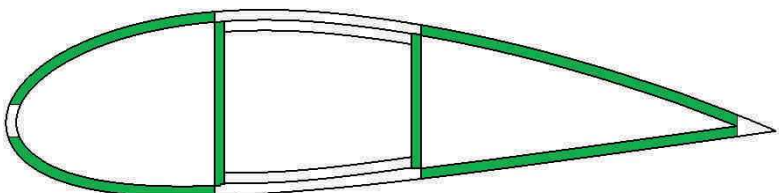
| Radius (m): 0 – 1.5 | | | | | |
|---|----------------|--------------------|-------------|-----------------------|----------------|
| No | Material | Structure of Plies | No of Plies | Layup without core | |
| | | | | Ply Orientation (deg) | Thickness (mm) |
| 1 | S2-Glass-Epoxy | UD | 16 | 0 | 2 |
| 2 | S2-Glass-Epoxy | UD | 16 | -45 | 2 |
| 3 | S2-Glass-Epoxy | UD | 16 | 45 | 2 |
| 4 | S2-Glass-Epoxy | UD | 16 | 90 | 2 |
| Plan of Layup [0/-45/+45/90/90/+45/-45/0] ₈ | | | | | |
|  | | | | | |

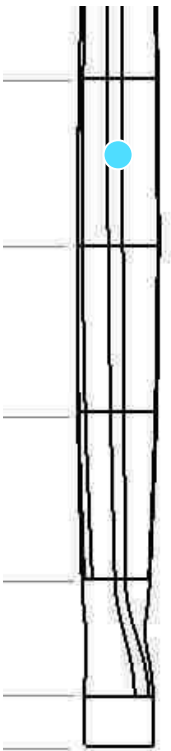
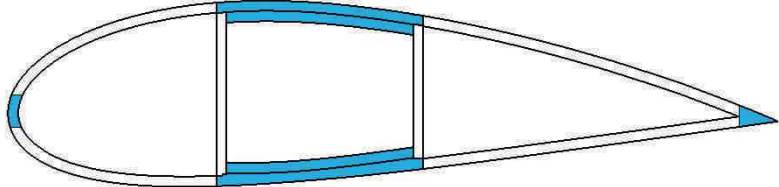
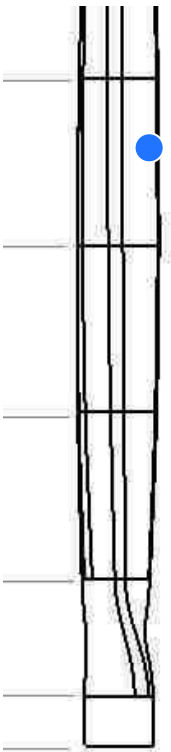
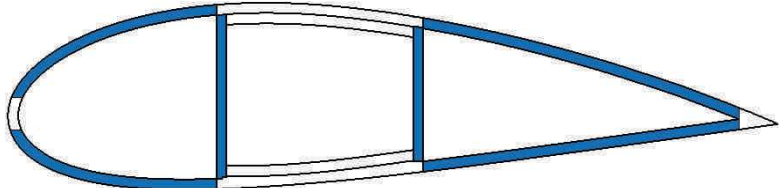


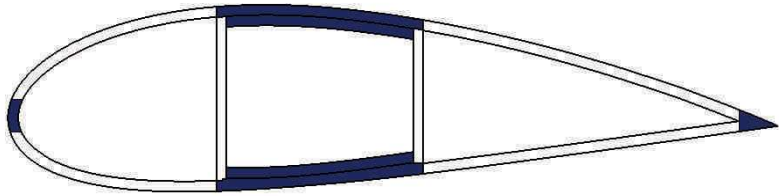
| Radius (m): 1.5 - 5 | | | | | |
|--|----------------|--------------------|-------------|-----------------------|----------------|
| No | Material | Structure of Plies | No of Plies | Layup without core | |
| | | | | Ply Orientation (deg) | Thickness (mm) |
| 1 | S2-Glass-Epoxy | UD | 6 | 0 | 2 |
| 2 | S2-Glass-Epoxy | UD | 6 | -45 | 2 |
| 3 | S2-Glass-Epoxy | UD | 6 | 45 | 2 |
| 4 | S2-Glass-Epoxy | UD | 6 | 90 | 2 |
| Plan of Layup [0/-45/+45/90/90/+45/-45/0] ₃ | | | | | |
|  | | | | | |

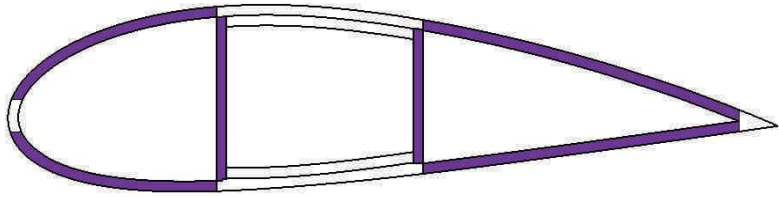


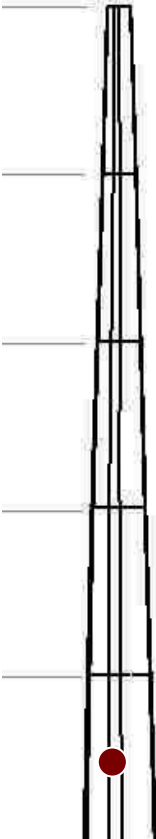
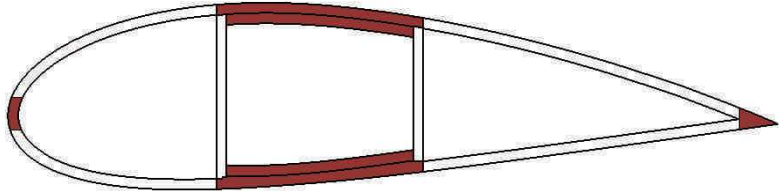
| Radius (m) : 10-15 | | | | | |
|--|----------------|--------------------|-------------|-----------------------|----------------|
| No | Material | Structure of Plies | No of Plies | Layup without core | |
| | | | | Ply Orientation (deg) | Thickness (mm) |
| 1 | S2-Glass-Epoxy | UD | 2 | 0 | 1.25 |
| 2 | S2-Glass-Epoxy | UD | 2 | -45 | 1.25 |
| 3 | S2-Glass-Epoxy | UD | 2 | 45 | 1.25 |
| 4 | S2-Glass-Epoxy | UD | 2 | 90 | 1.25 |
| Plan of Layup [0/-45/+45/90/90/+45/-45/0] ₁ | | | | | |
|  | | | | | |

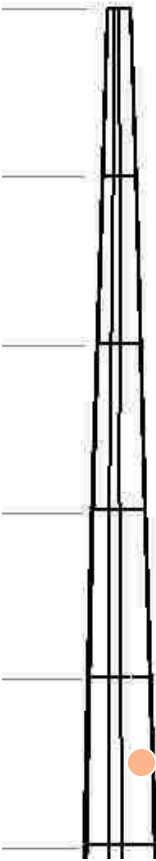
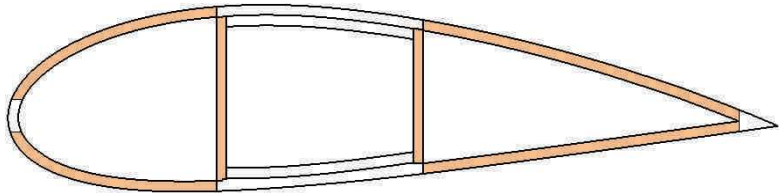
| Radius (m) : 10-15 | | | | | |
|--|----------------|--------------------|-------------|-----------------------|----------------|
| No | Material | Structure of Plies | No of Plies | Sandwich | |
| | | | | Ply Orientation (deg) | Thickness (mm) |
| 1 | S2-Glass-Epoxy | UD | 2 | 0 | 1.25 |
| 2 | S2-Glass-Epoxy | UD | 2 | -45 | 1.25 |
| 3 | S2-Glass-Epoxy | UD | 2 | 45 | 1.25 |
| 4 | S2-Glass-Epoxy | UD | 2 | 90 | 1.25 |
| Core | Balsa - Iso | Isotropic | 1 | - | 10 |
| Plan de Stratification [0/-45/+45/90/Core/90/+45/-45/0] ₁ | | | | | |
|  | | | | | |

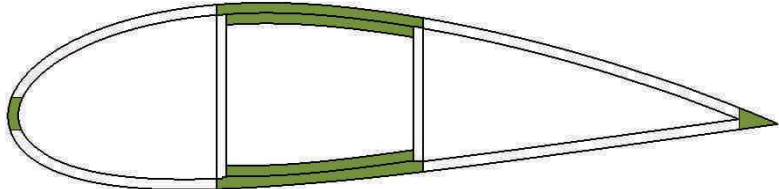
| | | | | | | |
|--|--------------------|----------------|--------------------|-------------|-----------------------|----------------|
|  | Rayon (m) : 15-20 | | | | | |
| | No | Material | Structure of Plies | No of Plies | Layup without core | |
| | | | | | Ply Orientation (deg) | Thickness (mm) |
| | 1 | S2-Glass-Epoxy | UD | 2 | 0 | 1.125 |
| | 2 | S2-Glass-Epoxy | UD | 2 | -45 | 1.125 |
| 3 | S2-Glass-Epoxy | UD | 2 | 45 | 1.125 | |
| 4 | S2-Glass-Epoxy | UD | 2 | 90 | 1.125 | |
| Plan de Stratification [0/-45/+45/90 /90/+45/-45/0] ₁ | | | | | | |
|  | | | | | | |
| | | | | | | |
|  | Radius (m) : 15-20 | | | | | |
| | No | Material | Structure of Plies | No of Plies | Sandwich | |
| | | | | | Ply Orientation (deg) | Thickness (mm) |
| | 1 | S2-Glass-Epoxy | UD | 2 | 0 | 1.125 |
| | 2 | S2-Glass-Epoxy | UD | 2 | -45 | 1.125 |
| 3 | S2-Glass-Epoxy | UD | 2 | 45 | 1.125 | |
| 4 | S2-Glass-Epoxy | UD | 2 | 90 | 1.125 | |
| Core | Balsa - Iso | Isotropic | 1 | - | 9 | |
| Plan de Stratification [0/-45/+45/90/Core/90/+45/-45/0] ₁ | | | | | | |
|  | | | | | | |

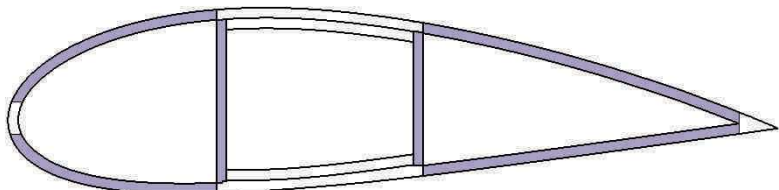
| Radius (m) : 20-25 | | | | | |
|--|----------------|--------------------|-------------|-----------------------|----------------|
| No | Material | Structure of Plies | No of Plies | Layup without core | |
| | | | | Ply Orientation (deg) | Thickness (mm) |
| 1 | S2-Glass-Epoxy | UD | 2 | 0 | 1.125 |
| 2 | S2-Glass-Epoxy | UD | 2 | -45 | 1.125 |
| 3 | S2-Glass-Epoxy | UD | 2 | 45 | 1.125 |
| 4 | S2-Glass-Epoxy | UD | 2 | 90 | 1.125 |
| Plan de Stratification [0/-45/+45/90 /90/+45/-45/0] ₁ | | | | | |
|  | | | | | |

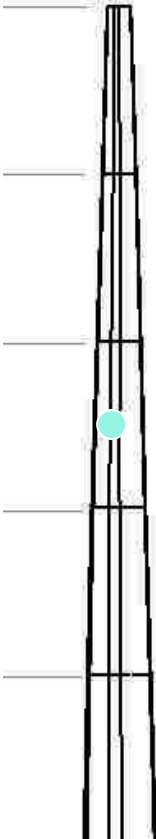
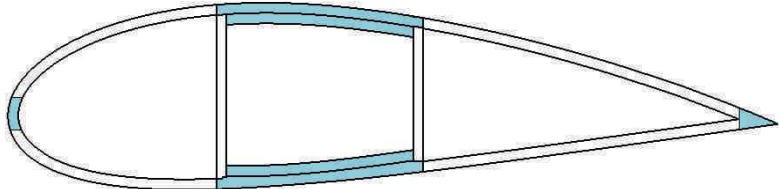
| Radius (m) : 20-25 | | | | | |
|--|----------------|--------------------|-------------|-----------------------|----------------|
| No | Material | Structure of Plies | No of Plies | Sandwich | |
| | | | | Ply Orientation (deg) | Thickness (mm) |
| 1 | S2-Glass-Epoxy | UD | 2 | 0 | 1.125 |
| 2 | S2-Glass-Epoxy | UD | 2 | -45 | 1.125 |
| 3 | S2-Glass-Epoxy | UD | 2 | 45 | 1.125 |
| 4 | S2-Glass-Epoxy | UD | 2 | 90 | 1.125 |
| Core | Balsa - Iso | Isotropic | 1 | - | 9 |
| Plan de Stratification [0/-45/+45/90/Core/90/+45/-45/0] ₁ | | | | | |
|  | | | | | |

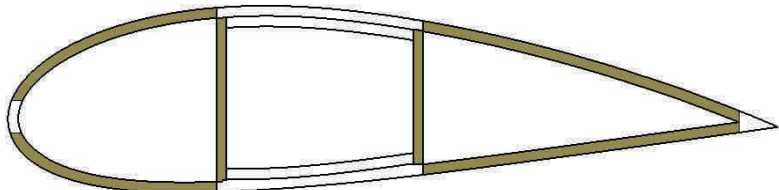
| Radius (m) : 25-30 | | | | | |
|---|----------------|--------------------|-------------|-----------------------|----------------|
| No | Material | Structure of Plies | No of Plies | Layup without core | |
| | | | | Ply Orientation (deg) | Thickness (mm) |
| 1 | S2-Glass-Epoxy | UD | 2 | 0 | 1 |
| 2 | S2-Glass-Epoxy | UD | 2 | -45 | 1 |
| 3 | S2-Glass-Epoxy | UD | 2 | 45 | 1 |
| 4 | S2-Glass-Epoxy | UD | 2 | 90 | 1 |
| Plan de Stratification [0/-45/+45/90/90/+45/-45/0] | | | | | |
|   | | | | | |

| Radius (m) : 25-30 | | | | | |
|--|----------------|--------------------|-------------|-----------------------|----------------|
| No | Material | Structure of Plies | No of Plies | Sandwich | |
| | | | | Ply Orientation (deg) | Thickness (mm) |
| 1 | S2-Glass-Epoxy | UD | 2 | 0 | 1 |
| 2 | S2-Glass-Epoxy | UD | 2 | -45 | 1 |
| 3 | S2-Glass-Epoxy | UD | 2 | 45 | 1 |
| 4 | S2-Glass-Epoxy | UD | 2 | 90 | 1 |
| Core | Balsa-Iso | Isotropic | 1 | - | 8 |
| Plan de Stratification [0/-45/+45/90/Core/90/+45/-45/0] ₁ | | | | | |
|   | | | | | |

| Radius (m) : 30-35 | | | | | |
|--|----------------|--------------------|-------------|-----------------------|----------------|
| No | Material | Structure of Plies | No of Plies | Layup without core | |
| | | | | Ply Orientation (deg) | Thickness (mm) |
| 1 | S2-Glass-Epoxy | UD | 2 | 0 | 0.875 |
| 2 | S2-Glass-Epoxy | UD | 2 | -45 | 0.875 |
| 3 | S2-Glass-Epoxy | UD | 2 | 45 | 0.875 |
| 4 | S2-Glass-Epoxy | UD | 2 | 90 | 0.875 |
| Plan de Stratification [0/-45/+45/90/90/+45/-45/0] ₁ | | | | | |
|  | | | | | |

| Radius (m) : 30-35 | | | | | |
|--|----------------|--------------------|-------------|-----------------------|----------------|
| No | Material | Structure of Plies | No of Plies | Sandwich | |
| | | | | Ply Orientation (deg) | Thickness (mm) |
| 1 | S2-Glass-Epoxy | UD | 2 | 0 | 0.875 |
| 2 | S2-Glass-Epoxy | UD | 2 | -45 | 0.875 |
| 3 | S2-Glass-Epoxy | UD | 2 | 45 | 0.875 |
| 4 | S2-Glass-Epoxy | UD | 2 | 90 | 0.875 |
| Core | Balsa-Iso | Isotropic | 1 | - | 7 |
| Plan de Stratification [0/-45/+45/90/Core/90/+45/-45/0] ₁ | | | | | |
|  | | | | | |

|  | Radius (m) : 35-40 | | | | | |
|--|--------------------|----------------|--------------------|-------------|-----------------------|----------------|
| | No | Material | Structure of Plies | No of Plies | Layup without core | |
| | | | | | Ply Orientation (deg) | Thickness (mm) |
| | 1 | S2-Glass-Epoxy | UD | 2 | 0 | 0.75 |
| | 2 | S2-Glass-Epoxy | UD | 2 | -45 | 0.75 |
| | 3 | S2-Glass-Epoxy | UD | 2 | 45 | 0.75 |
| 4 | S2-Glass-Epoxy | UD | 2 | 90 | 0.75 | |
| Plan of Layup [0/-45/+45/90/90/+45/-45/0] ₁ | | | | | | |
|  | | | | | | |

|  | Radius (m) : 35-40 | | | | | |
|--|--------------------|----------------|--------------------|-------------|-----------------------|----------------|
| | No | Material | Structure of Plies | No of Plies | Sandwich | |
| | | | | | Ply Orientation (deg) | Thickness (mm) |
| | 1 | S2-Glass-Epoxy | UD | 2 | 0 | 0.75 |
| | 2 | S2-Glass-Epoxy | UD | 2 | -45 | 0.75 |
| | 3 | S2-Glass-Epoxy | UD | 2 | 45 | 0.75 |
| 4 | S2-Glass-Epoxy | UD | 2 | 90 | 0.75 | |
| Core | Balsa-Iso | Isotropic | 1 | - | 6 | |
| Plan of Layup [0/-45/+45/90/Core/90/+45/-45/0] ₁ | | | | | | |
|  | | | | | | |

| | Radius (m) : 40-45 | | | | | |
|--|--------------------|----------------|--------------------|-------------|-----------------------|----------------|
| | No | Material | Structure of Plies | No of Plies | Layup without core | |
| | | | | | Ply Orientation (deg) | Thickness (mm) |
| | 1 | S2-Glass-Epoxy | UD | 2 | 0 | 0.5 |
| | 2 | S2-Glass-Epoxy | UD | 2 | -45 | 0.5 |
| | 3 | S2-Glass-Epoxy | UD | 2 | 45 | 0.5 |
| 4 | S2-Glass-Epoxy | UD | 2 | 90 | 0.5 | |
| Plan of Layup [0/-45/+45/90/90/+45/-45/0] ₁ | | | | | | |
| | | | | | | |

| | Radius (m) : 40-45 | | | | | |
|--|--------------------|----------------|--------------------|-------------|-----------------------|----------------|
| | No | Material | Structure of Plies | No of Plies | Sandwich | |
| | | | | | Ply Orientation (deg) | Thickness (mm) |
| | 1 | S2-Glass-Epoxy | UD | 2 | 0 | 0.5 |
| | 2 | S2-Glass-Epoxy | UD | 2 | -45 | 0.5 |
| | 3 | S2-Glass-Epoxy | UD | 2 | 45 | 0.5 |
| 4 | S2-Glass-Epoxy | UD | 2 | 90 | 0.5 | |
| Core | Balsa-Iso | Isotropic | 1 | - | 4 | |
| Plan de Stratification [0/-45/+45/90/Core/90/+45/-45/0] ₁ | | | | | | |
| | | | | | | |

| | Radius (m) : 45-50 | | | | | |
|---|--------------------|----------------|--------------------|-------------|-----------------------|----------------|
| | No | Material | Structure of Plies | No of Plies | Layup without core | |
| | | | | | Ply Orientation (deg) | Thickness (mm) |
| | 1 | S2-Glass-Epoxy | UD | 2 | 0 | 0.25 |
| | 2 | S2-Glass-Epoxy | UD | 2 | -45 | 0.25 |
| | 3 | S2-Glass-Epoxy | UD | 2 | 45 | 0.25 |
| 4 | S2-Glass-Epoxy | UD | 2 | 90 | 0.25 | |
| Plan de Stratification [0/-45/+45/90/90/+45/-45/0] ₁ | | | | | | |
| | | | | | | |

| | Radius (m) : 45-50 | | | | | |
|--|--------------------|----------------|--------------------|-------------|-----------------------|----------------|
| | No | Material | Structure of Plies | No of Plies | Sandwich | |
| | | | | | Ply Orientation (deg) | Thickness (mm) |
| | 1 | S2-Glass-Epoxy | UD | 2 | 0 | 0.25 |
| | 2 | S2-Glass-Epoxy | UD | 2 | -45 | 0.25 |
| | 3 | S2-Glass-Epoxy | UD | 2 | 45 | 0.25 |
| 4 | S2-Glass-Epoxy | UD | 2 | 90 | 0.25 | |
| Core | Balsa-Iso | Isotropic | 1 | - | 4 | |
| Plan de Stratification [0/-45/+45/90/Core/90/+45/-45/0] ₁ | | | | | | |
| | | | | | | |

A.1 Material definition

| Properties | Values |
|--------------------------------|-------------|
| Physical properties | |
| Fiber volume ratio (%) | 57 – 63 |
| Density(kg/m ³) | 1960 – 2020 |
| Engineering constants | |
| Longitudinal modulus (GPa) | 53 – 59 |
| Transverse modulus (GPa) | 16 – 20 |
| Shearing modulus (GPa) | 6 – 9 |
| Poisson's ratio | 0.26 – 0.28 |
| Strength properties | |
| Longitudinal Tensile (MPa) | 1540 – 2000 |
| Longitudinal Compression (MPa) | 690 – 1240 |
| Transverse Tensile (MPa) | 41 – 82 |
| Transverse Compression (MPa) | 110 – 200 |
| Plain Shear (MPa) | 62 – 165 |
| Inter-Laminar Shear (MPa) | 55 – 103 |
| Longitudinal Flexural (MPa) | 1240 – 1720 |
| Longitudinal Crushing (MPa) | 464 – 552 |
| Strain at failure | |
| Longitudinal Tensile (%) | 2.7 – 3.5 |
| Longitudinal Compression (%) | 1.1 – 1.8 |
| Transversal Tensile (%) | 0.25 – 0.50 |
| Transversal Compression (%) | 1.1 – 2 |
| Plain Shearing (%) | 1.6 – 2.5 |

Table A-1: Properties of Fiberglass/Epoxy Composite.

| Properties | Values |
|--------------------------------|---------------|
| Physical Properties | |
| Fiber volume fraction (%) | 70 |
| Density (kg/m ³) | 1600 |
| Engineering constants | |
| Longitudinal modulus (GPa) | 181 |
| Transverse modulus (GPa) | 10.22 |
| Shearing modulus (GPa) | 7.17 |
| Poisson's ratio | 0.28 |
| Strength Properties | |
| Longitudinal Tensile (MPa) | 1500 |
| Longitudinal Compression (MPa) | 1500 |
| Transverse Tensile (MPa) | 40 |
| Transverse Compression (MPa) | 246 |
| Plain Shear (MPa) | 68 |

Table A-2: Properties of T300/5208 Carbon/Epoxy Unidirectional Prepreg

| Properties | Values |
|--------------------------------|---------------|
| Physical Properties | |
| Fiber volume fraction (%) | 50 |
| Density (kg/m ³) | 1400 |
| Engineering constants | |
| Longitudinal modulus (GPa) | 76 |
| Transverse modulus (GPa) | 5.5 |
| Shearing modulus (GPa) | 2.3 |
| Poisson's ratio | 0.196 |
| Strength Properties | |
| Longitudinal Tensile (MPa) | 1400 |
| Longitudinal Compression (MPa) | 235 |
| Transverse Tensile (MPa) | 12 |
| Transverse Compression (MPa) | 53 |
| Plain Shear (MPa) | 34 |

Table A-3 : Propriétés du composite Kevlar/époxy

A.2 Stratifications des sections standards.

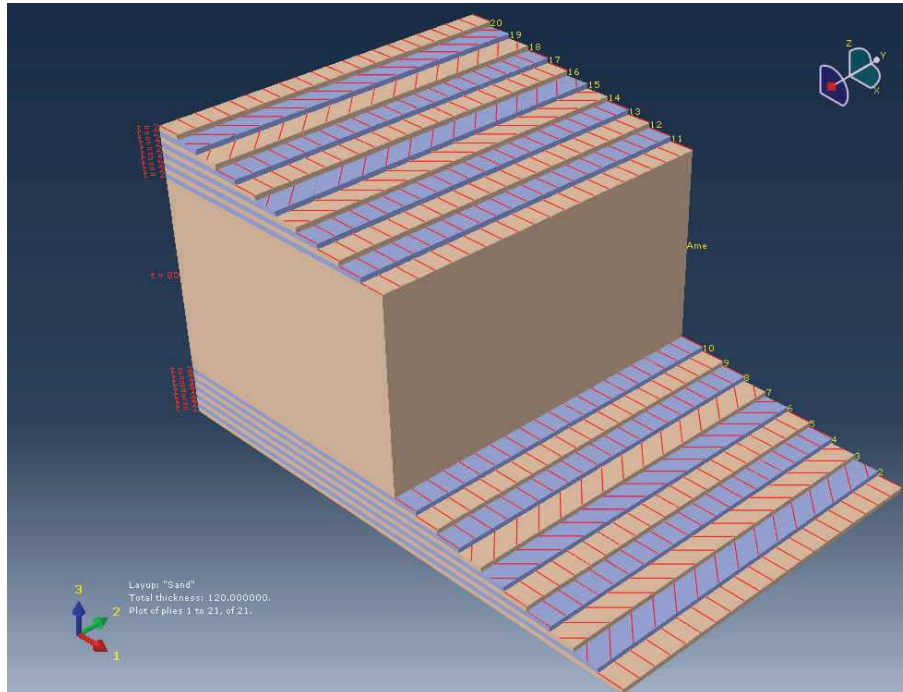


Figure A-3: Sandwich with wooden core (balsa)

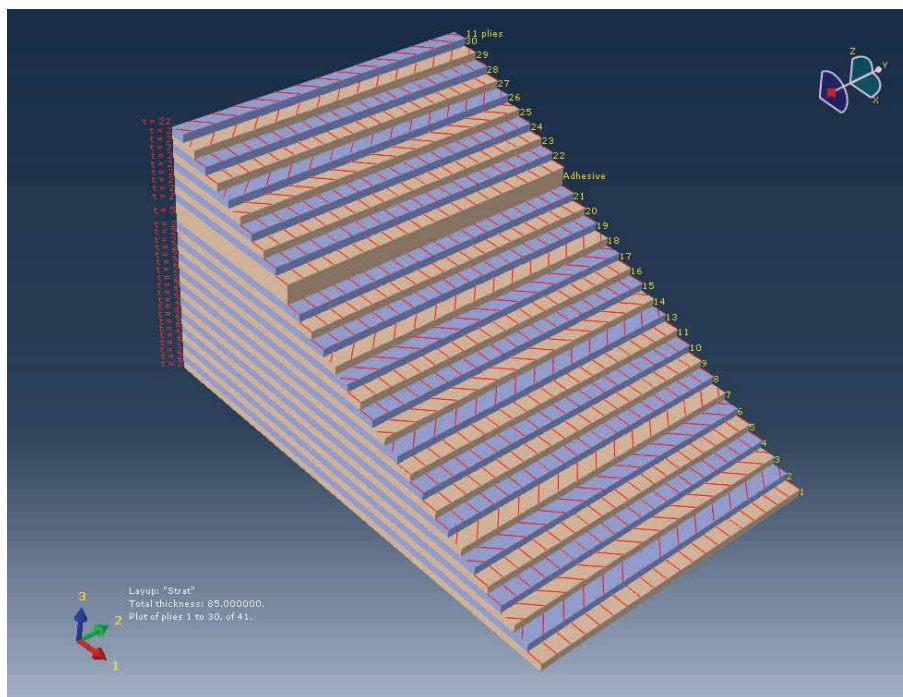


Figure A-4 : Structure stratifiée simple avec adhésif

A.3 Detail of the blade form.

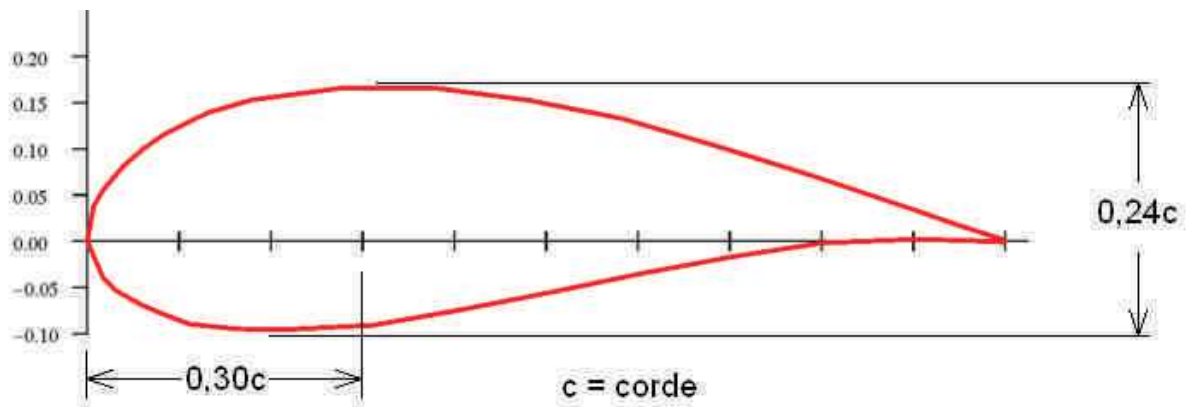


Figure A-5: Airfoil form used

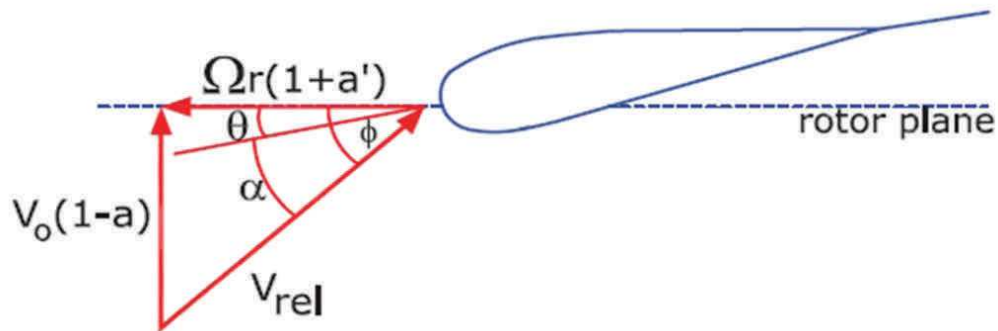


Figure A-6 : The coordinate system to determine the twist angle “ θ ”

| Element No. | Section Profile | Distance from the root (m) | Cord (m) | Angle of Twist Θ (deg) |
|-------------|-----------------|----------------------------|----------|-------------------------------|
| Root | Circle | 0.00-1.50 | 5.00 | - |
| 1 | NACA 4424 | 2.75 | 5.00 | 30.56 |
| 2 | NACA 4424 | 8.25 | 5.50 | 16.34 |
| 3 | NACA 4424 | 13.75 | 6.00 | 8.07 |
| 4 | NACA 4424 | 19.25 | 5.50 | 4.35 |
| 5 | NACA 4424 | 24.75 | 4.50 | 2.44 |
| 6 | NACA 4424 | 30.25 | 3.80 | 1.48 |
| 7 | NACA 4424 | 35.75 | 3.50 | 0.21 |
| 8 | NACA 4424 | 41.25 | 3.20 | -0.71 |
| 9 | NACA 4424 | 46.75 | 2.75 | -0.66 |
| 10 | NACA 4424 | 52.25 | 2.50 | -1.27 |
| Tip | NACA 4424 | 55.00 | 2.30 | -1.49 |

Table A-4 : Distribution of cords and twist angles along the length of the blade.

A.4 Définitions des sections avec plan de stratification.

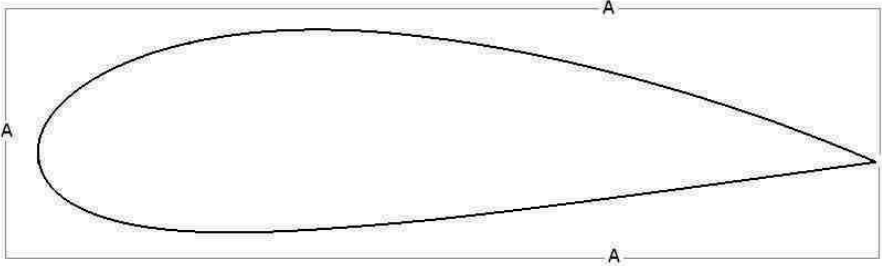
| | | | |
|-------|--|--|--|
| Shell |  | | |
| Layup | | | |
| Zones | A | | |
| Plan | 1 | | |

Figure A-7: Layup of the section Shell

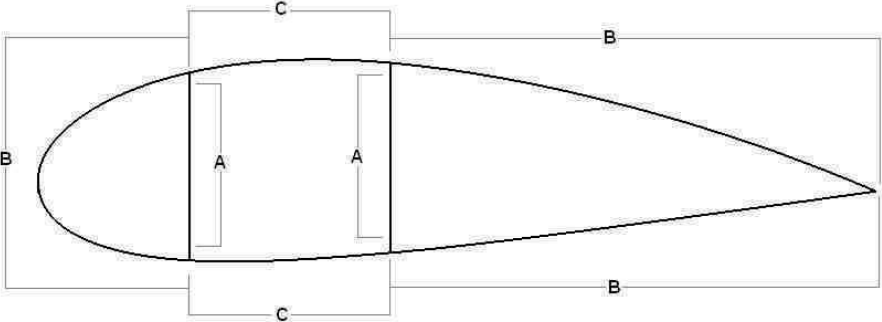
| | | | |
|-------|---|---|---|
| Box |  | | |
| Layup | | | |
| Zones | A | B | C |
| Plan | 1 | 1 | 2 |

Figure A-8 : Layup of the section Box

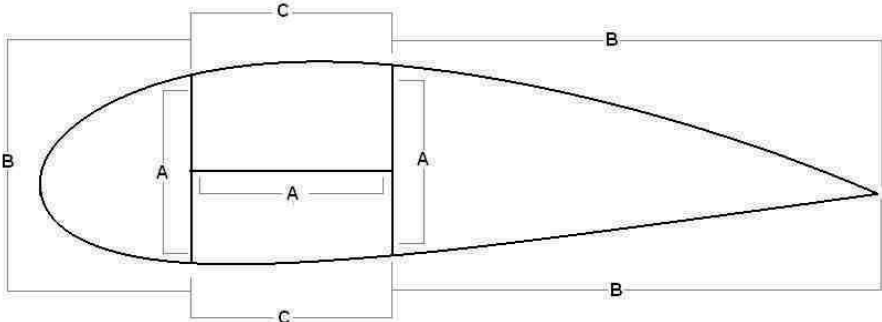
| | | | |
|-------|--|---|---|
| Box-H |  | | |
| Layup | | | |
| Zones | A | B | C |
| Plan | 1 | 1 | 2 |

Figure A-9 : Layup of the section Box-H

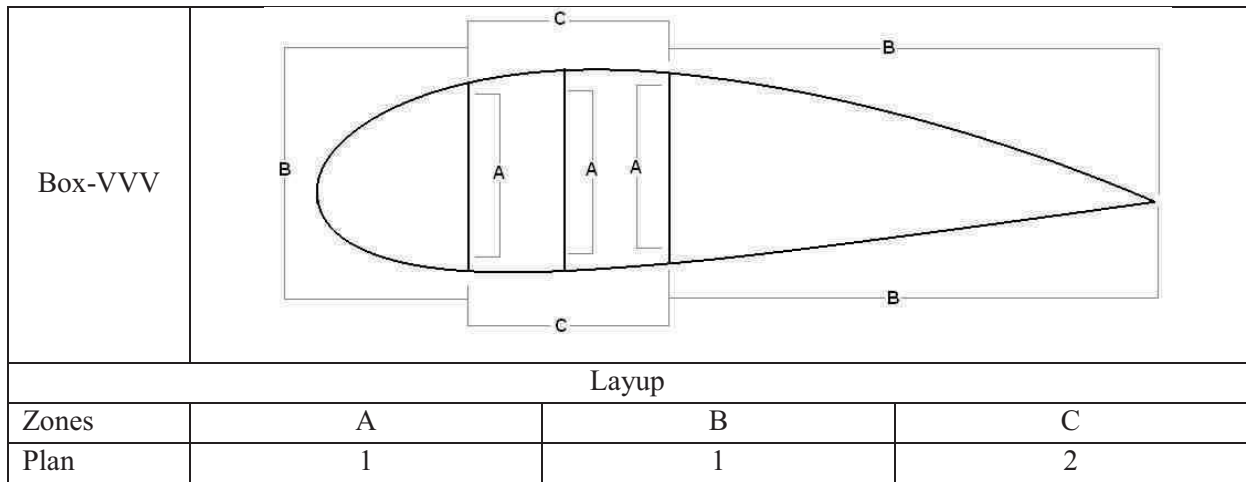


Figure A-10 : Layup of the section Box-VVV

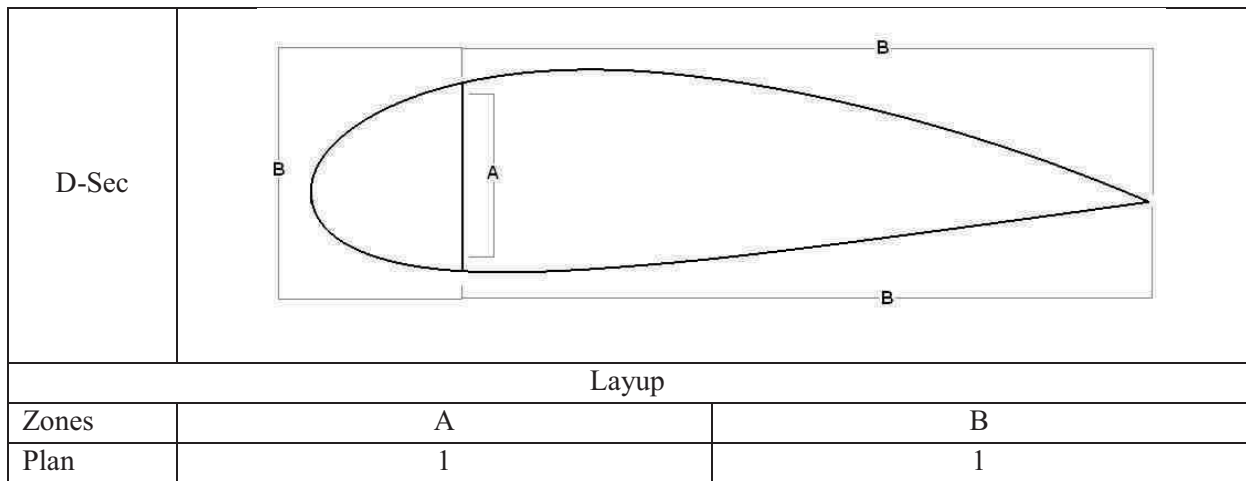


Figure A-11 : Layup of the section D-Sec

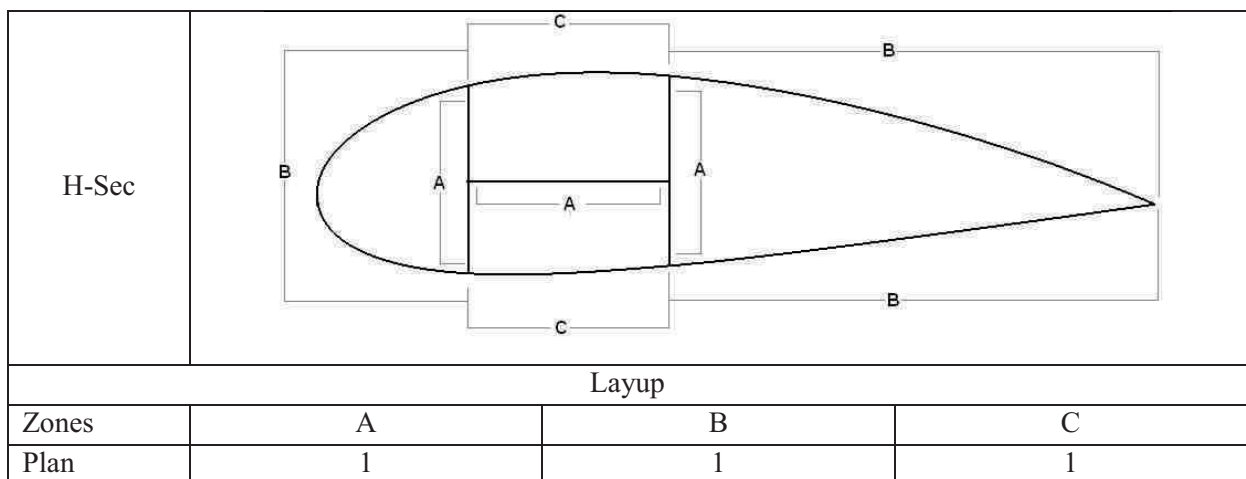


Figure A-12 : Layup of the section H-Sec

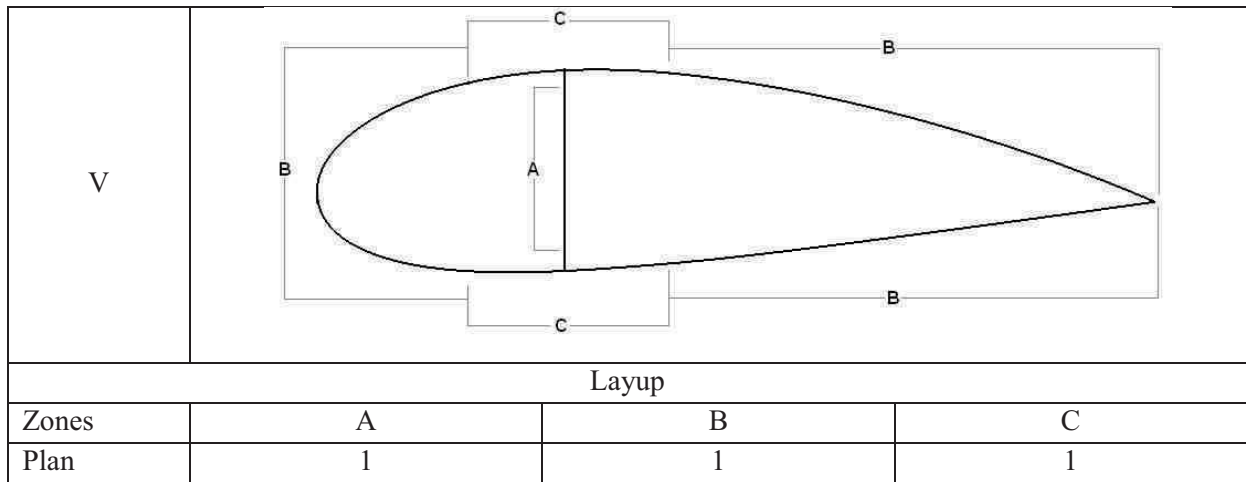


Figure A-13 : Layup of the section V

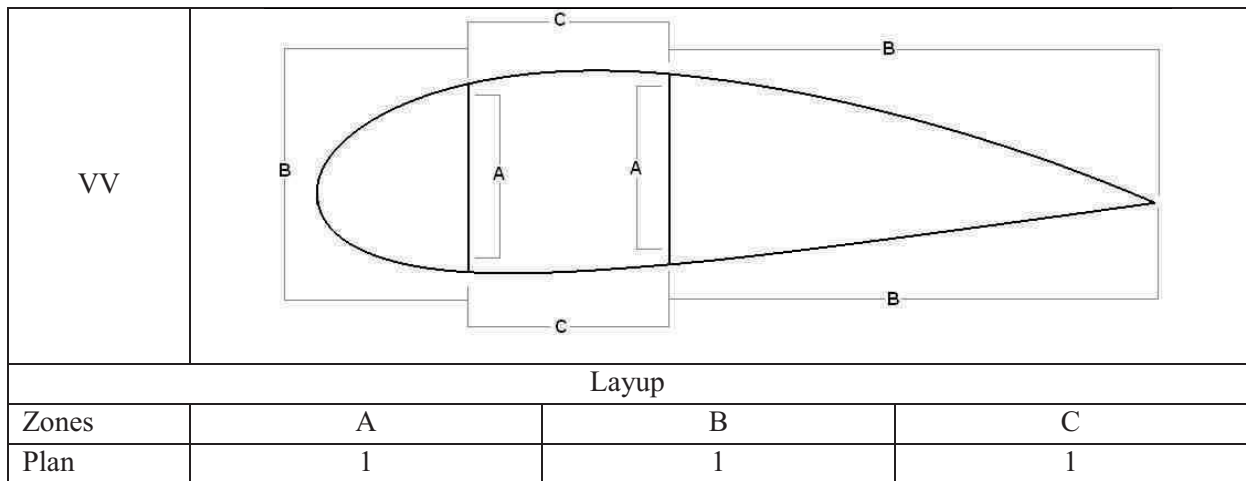


Figure A-14: Layup of the section VV

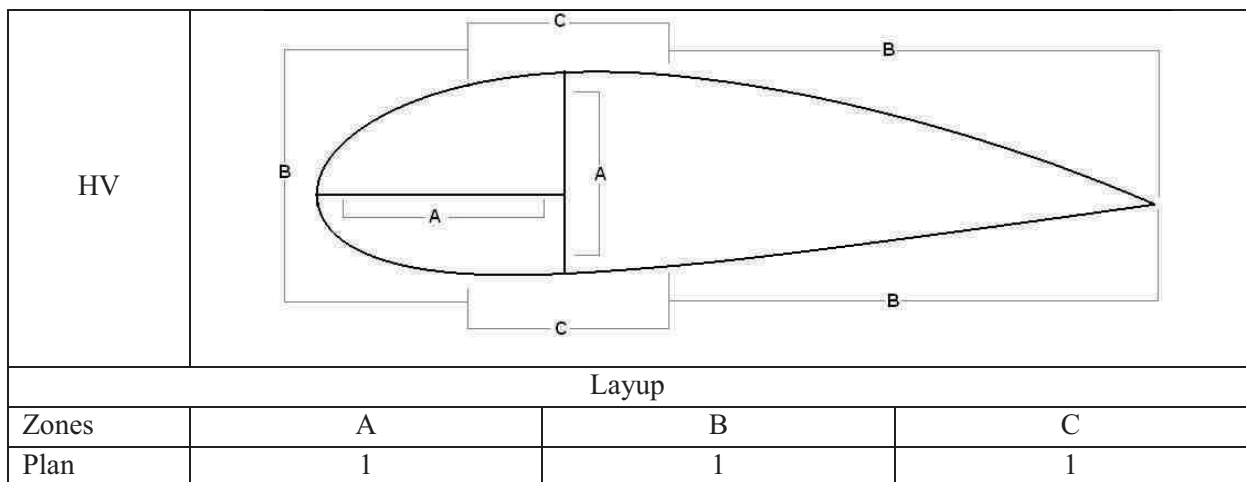


Figure A-15 : Layup of the section HV

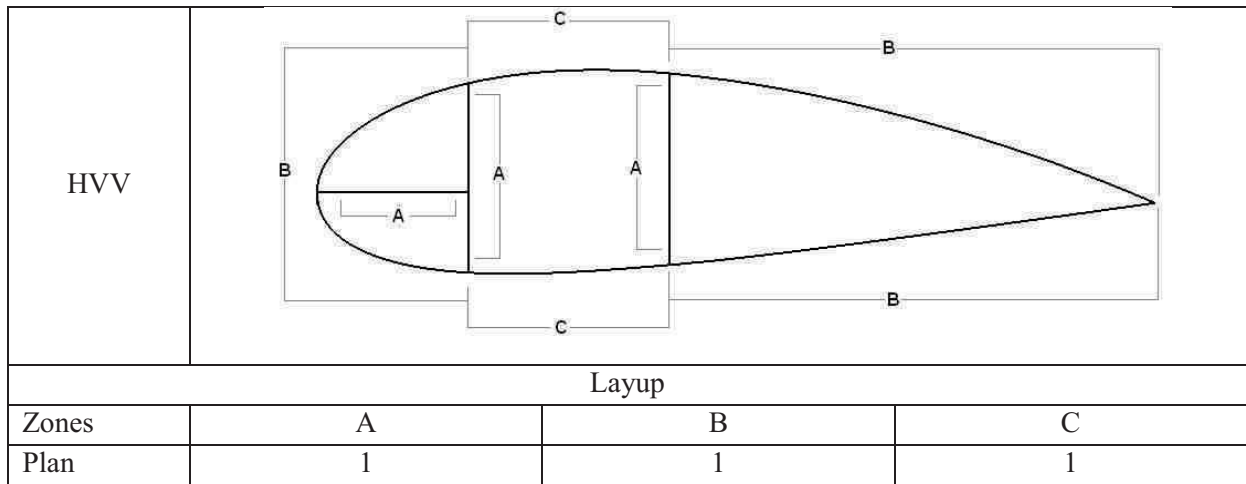


Figure A-16 : Layup of the section HVV

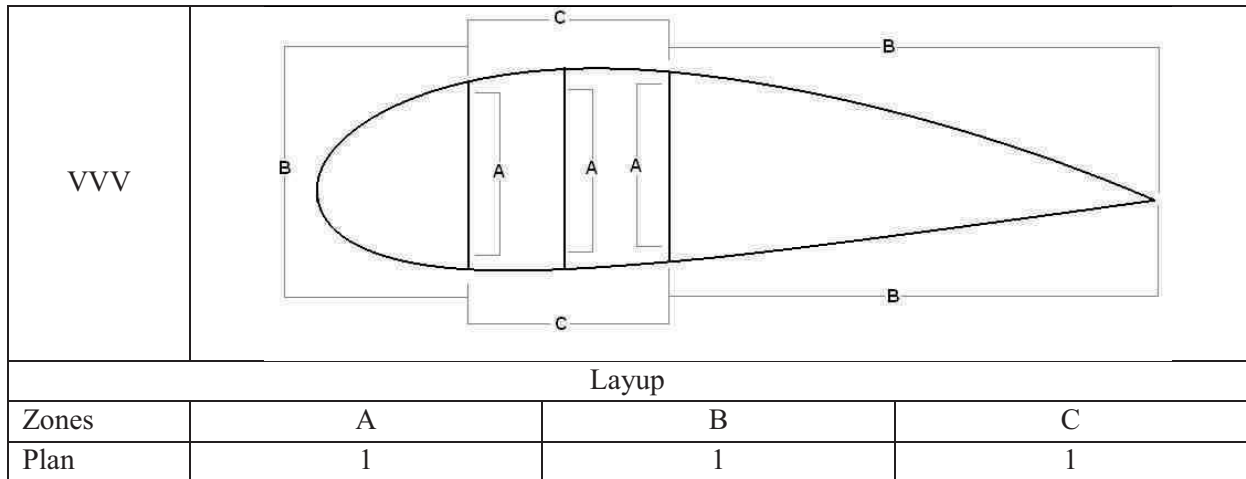


Figure A-17 : Layup of the section VVV

A.5 Layups and the distribution of materials for the designed blades

For each case the following general plan of layup is used.

| Component | Shell | | Spar |
|----------------|---|---|---|
| Zone | Zone A | Shell | Spar V |
| Stratification | $\pm 45 / 0_2 / \text{adhesive} / 0_2 / \pm 45$ | $\pm 45 / 0_2 / \text{core} / 0_2 / \pm 45$ | $\pm 45 / 0_2 / \text{core} / 0_2 / \pm 45$ |

Table A-5: Zones de stratification

The thicknesses and composition of materials is unique for each case and will be explained in the corresponding sections.

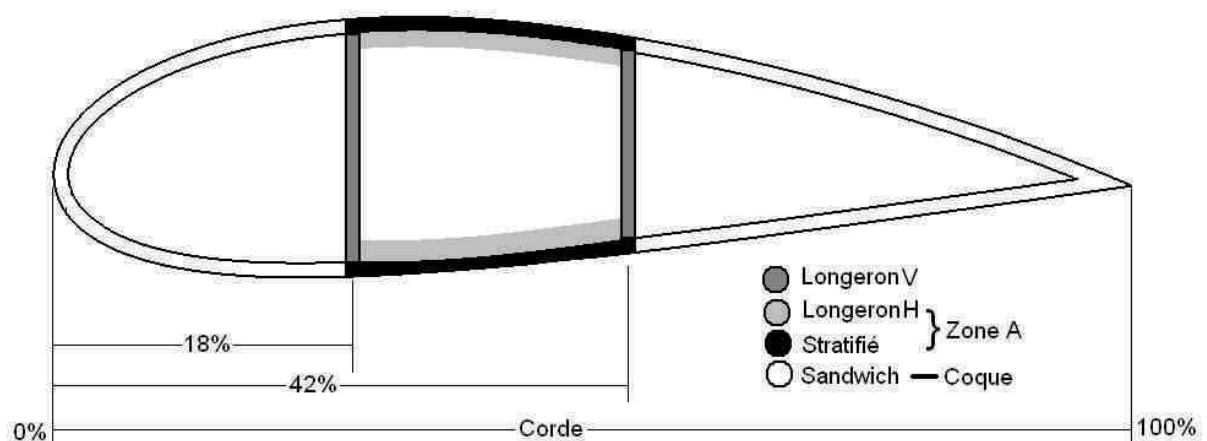


Figure A-18 : Partitions of the blade cross section.

1. NACA-4424-60m-200MPa

Materials : Fiberglass/Epoxy for the blade shell and spar

Weigth of the blade : 18.950

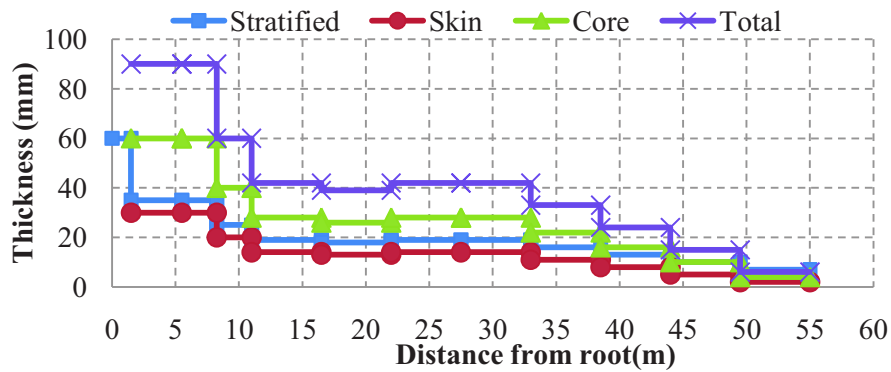


Figure A-19 : Distribution of materials for the blade surface shell

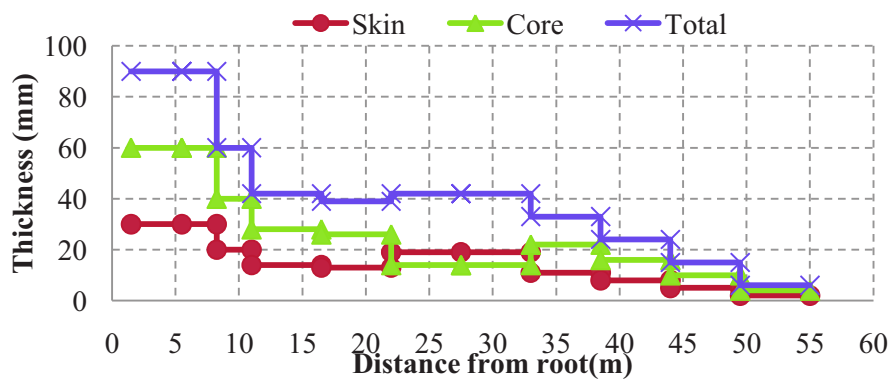


Figure A-20 : Distribution of materials for the spar

| Position (m) | Section | Shell (mm) | Sandwich (mm) | | | Spar V (mm) | | |
|--------------|------------|------------|---------------|------|-------|-------------|------|-------|
| | | Zone A | Skin | Core | Total | Skin | Core | Total |
| 0-1,5 | Root | 60 | | | | | | |
| 1,5-5,5 | Transition | 35 | 30 | 60 | 90 | 30 | 60 | 90 |
| 5,5-8,25 | 1 | 35 | 30 | 60 | 90 | 30 | 60 | 90 |
| 8,25-11,0 | 2 | 25 | 20 | 40 | 60 | 20 | 40 | 60 |
| 11,0-16,5 | 3 | 19 | 14 | 28 | 42 | 14 | 28 | 42 |
| 16,5-22,0 | 4 | 18 | 13 | 26 | 39 | 13 | 26 | 39 |
| 22,0-27,5 | 5 | 19 | 14 | 28 | 42 | 19 | 14 | 42 |
| 27,5-33,0 | 6 | 19 | 14 | 28 | 42 | 19 | 14 | 42 |
| 33,0-38,5 | 7 | 16 | 11 | 22 | 33 | 11 | 22 | 33 |
| 38,5-44,0 | 8 | 13 | 8 | 16 | 24 | 8 | 16 | 24 |
| 44,0-49,5 | 9 | 10 | 5 | 10 | 15 | 5 | 10 | 15 |
| 49,5-55,0 | 10 | 7 | 2 | 4 | 6 | 2 | 4 | 6 |

Table A-6 : Détail des épaisseurs des matériaux pour la pale

2. NACA-4424-60m-CL-200MPa

Materials: Fiberglass/Epoxy for the blade shell and carbon/epoxy for the spar
 Weight of the blade: 18.840

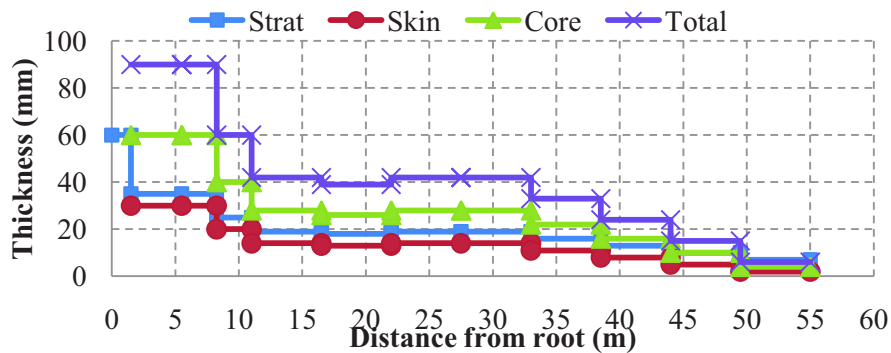


Figure A-21 : Distribution of materials for the blade surface shell

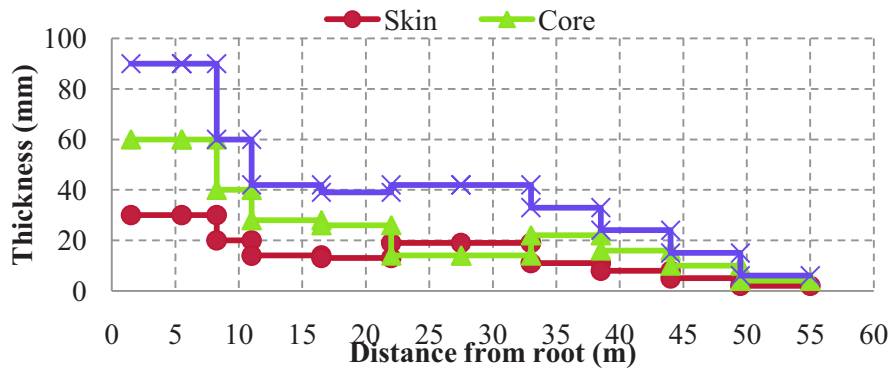


Figure A-22 : Distribution of materials for the spar.

| Position (m) | Section | Shell (mm) | Sandwich (mm) | | | Spar V (mm) | | |
|--------------|------------|------------|---------------|------|-------|-------------|------|-------|
| | | Zone A | Skin | Core | Total | Skin | Core | Total |
| 0-1,5 | Root | 60 | | | | | | |
| 1,5-5,5 | Transition | 35 | 30 | 60 | 90 | 30 | 60 | 90 |
| 5,5-8,25 | 1 | 35 | 30 | 60 | 90 | 60 | 120 | 180 |
| 8,25-11,0 | 2 | 25 | 20 | 40 | 60 | 40 | 80 | 120 |
| 11,0-16,5 | 3 | 19 | 14 | 28 | 42 | 28 | 56 | 84 |
| 16,5-22,0 | 4 | 18 | 13 | 26 | 39 | 26 | 52 | 78 |
| 22,0-27,5 | 5 | 19 | 14 | 28 | 42 | 28 | 56 | 84 |
| 27,5-33,0 | 6 | 19 | 14 | 28 | 42 | 14 | 28 | 42 |
| 33,0-38,5 | 7 | 16 | 11 | 22 | 33 | 11 | 22 | 33 |
| 38,5-44,0 | 8 | 13 | 8 | 16 | 24 | 8 | 16 | 24 |
| 44,0-49,5 | 9 | 10 | 5 | 10 | 15 | 5 | 10 | 15 |
| 49,5-55,0 | 10 | 7 | 2 | 4 | 6 | 2 | 4 | 6 |

Table A-7 : Details of material thicknesses for the blade.

2. NACA-4424-60m-CLE-200MPa

Material : Glassfiber/Epoxy for the blade shell, carbon/epoxy for the spar
 Weight of the blade (tons) : 20.580

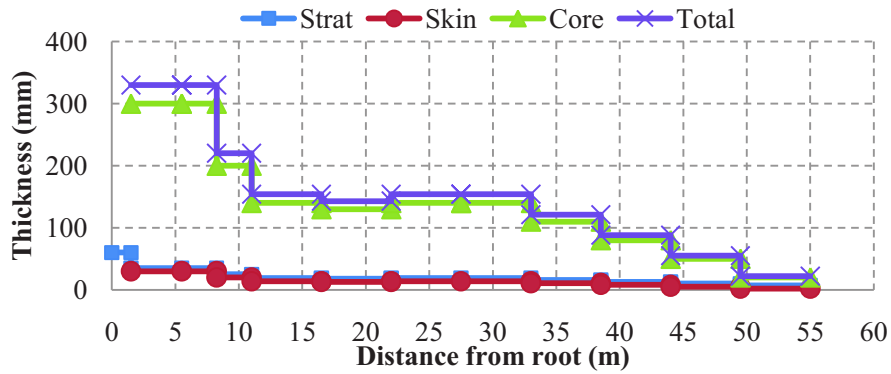


Figure A-23 : Distribution of materials for the blade surface shell.

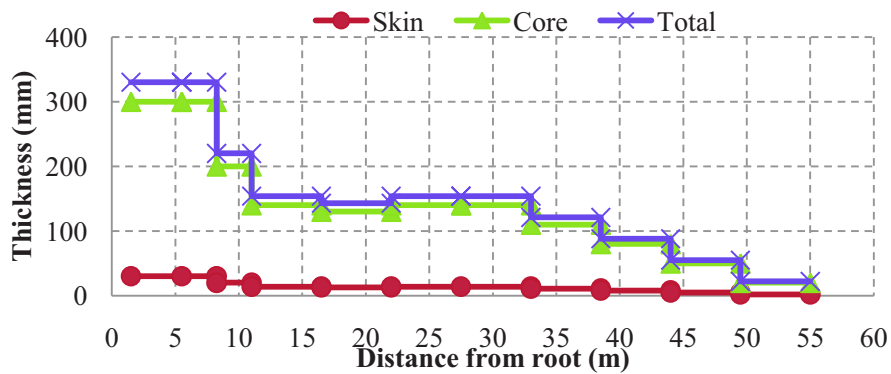


Figure A-24 : Distribution of materials for the spar.

| Position (m) | Section | Shell (mm) | Sandwich (mm) | | | Spar V (mm) | | |
|--------------|------------|------------|---------------|------|-------|-------------|------|-------|
| | | Zone A | Skin | Core | Total | Skin | Core | Total |
| 0-1,5 | Root | 60 | | | | | | |
| 1,5-5,5 | Transition | 35 | 30 | 300 | 330 | 30 | 300 | 330 |
| 8,25-11,0 | 2 | 25 | 20 | 200 | 220 | 20 | 200 | 220 |
| 11,0-16,5 | 3 | 19 | 14 | 140 | 154 | 14 | 140 | 154 |
| 16,5-22,0 | 4 | 18 | 13 | 130 | 143 | 13 | 130 | 143 |
| 22,0-27,5 | 5 | 19 | 14 | 140 | 154 | 14 | 140 | 154 |
| 27,5-33,0 | 6 | 19 | 14 | 140 | 154 | 14 | 140 | 154 |
| 33,0-38,5 | 7 | 16 | 11 | 110 | 121 | 11 | 110 | 121 |
| 44,0-49,5 | 9 | 10 | 5 | 50 | 55 | 5 | 50 | 55 |
| 49,5-55,0 | 10 | 7 | 2 | 20 | 22 | 2 | 20 | 22 |

Table A-8 : Detail of thicknesses for the blade.

4. NACA-4424-60m-AE-200MPa

Material: Fiberglass/Epoxy composite for the blade surface and spar
 Weight of the blade (tons): 28.580

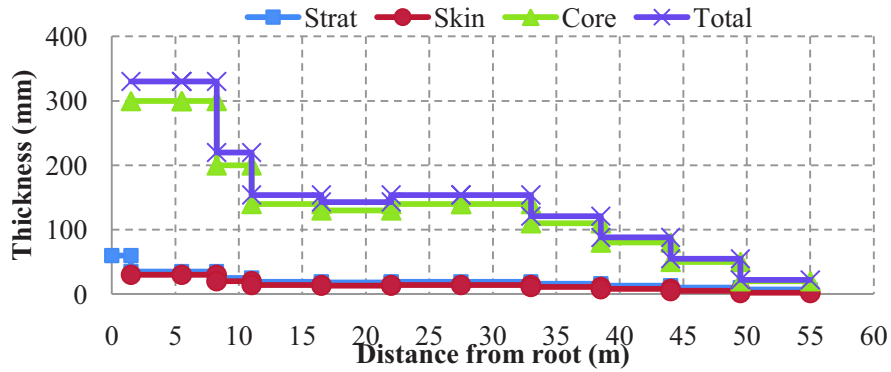


Figure A-25 : Distribution of materials for the blade surface shell

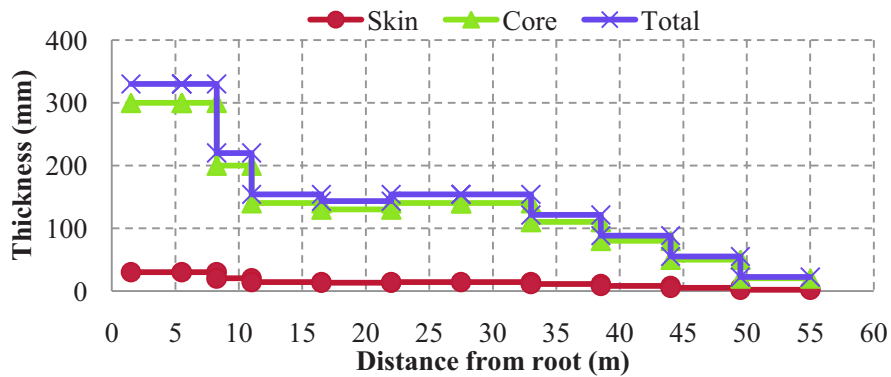


Figure A-26 : Distribution of materials for the spar.

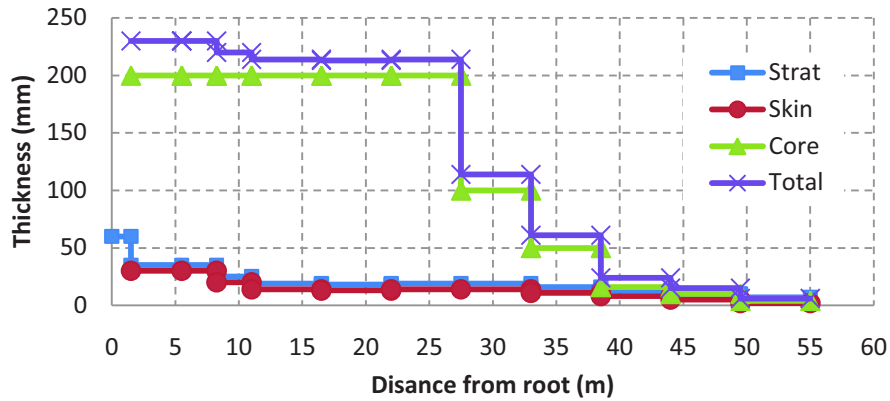
| Position (m) | Section | Shell (mm) | Sandwich (mm) | | | Spar V (mm) | | |
|--------------|------------|------------|---------------|------|-------|-------------|------|-------|
| | | Zone A | Skin | Core | Total | Skin | Core | Total |
| 0-1,5 | Root | 60 | | | | | | |
| 1,5-5,5 | Transition | 35 | 30 | 300 | 330 | 30 | 300 | 330 |
| 5,5-8,25 | 1 | 35 | 30 | 300 | 330 | 30 | 300 | 330 |
| 8,25-11,0 | 2 | 25 | 20 | 200 | 220 | 20 | 200 | 220 |
| 11-16,5 | 3 | 19 | 14 | 140 | 154 | 14 | 140 | 154 |
| 16,5-22,0 | 4 | 18 | 13 | 130 | 143 | 13 | 130 | 143 |
| 22,0-27,5 | 5 | 19 | 14 | 140 | 154 | 14 | 140 | 154 |
| 27,5-33,0 | 6 | 19 | 14 | 140 | 154 | 14 | 140 | 154 |
| 33,0-38,5 | 7 | 16 | 11 | 110 | 121 | 11 | 110 | 121 |
| 38,5-44,0 | 8 | 13 | 8 | 80 | 88 | 8 | 80 | 88 |
| 44,0-49,5 | 9 | 10 | 5 | 50 | 55 | 5 | 50 | 55 |
| 49,5-55,0 | 10 | 7 | 2 | 20 | 22 | 2 | 20 | 22 |

Table A-9 : Detail of thicknesses for the blade.

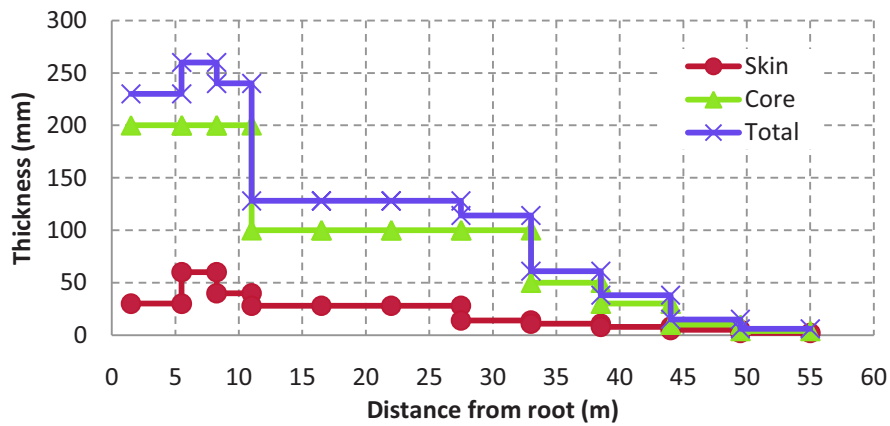
5. NACA-4424-60m-CLE-200MPa-SEC

Material : Fiberlass/Epoxy for the Shell, Carbon/Epoxy for the Spar

Weight of the Blade (tons) : 27.960



Distribution of materials for the Blade shell



Distribution of material for the spar

| Position (m) | Section | Shell (mm) | Sandwich (mm) | | | Spar V (mm) | | |
|--------------|------------|------------|---------------|------|-------|-------------|------|-------|
| | | Zone A | Skin | Core | Total | Skin | Core | Total |
| 0-1,5 | Root | 60 | | | | | | |
| 1,5-5,5 | Transition | 35 | 30 | 200 | 230 | 30 | 200 | 230 |
| 5,5-8,25 | 1 | 35 | 30 | 200 | 230 | 60 | 200 | 260 |
| 8,25-11,0 | 2 | 25 | 20 | 200 | 220 | 40 | 200 | 240 |
| 11,0-16,5 | 3 | 19 | 14 | 200 | 214 | 28 | 100 | 128 |
| 16,5-22,0 | 4 | 18 | 13 | 200 | 213 | 28 | 100 | 128 |
| 22,0-27,5 | 5 | 19 | 14 | 200 | 214 | 28 | 100 | 128 |
| 27,5-33,0 | 6 | 19 | 14 | 100 | 114 | 14 | 100 | 114 |
| 33,0-38,5 | 7 | 16 | 11 | 50 | 61 | 11 | 50 | 61 |
| 38,5-44,0 | 8 | 13 | 8 | 16 | 24 | 8 | 30 | 38 |
| 44,0-49,5 | 9 | 10 | 5 | 10 | 15 | 5 | 10 | 15 |
| 49,5-55,0 | 10 | 7 | 2 | 4 | 6 | 2 | 4 | 6 |

Detail of material thickness for the blade

A.6 Distribution of Blade weights

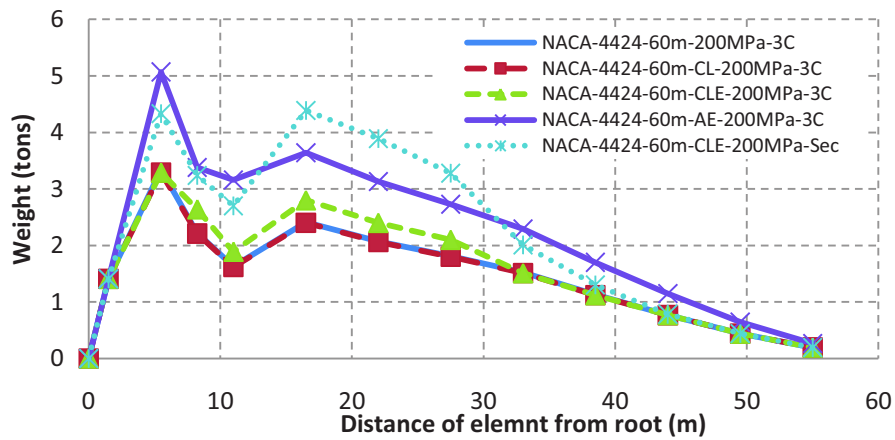


Figure A-27 : Weight distribution along the blade length

| Distance from the blade root (m) | Weight (ton) | | | | |
|----------------------------------|----------------------|-------------------------|--------------------------|-------------------------|------------------------------|
| | NACA-4424-60m-200MPa | NACA-4424-60m-CL-200MPa | NACA-4424-60m-CLE-200MPa | NACA-4424-60m-AE-200MPa | NACA-4424-60m-CLE-200MPa-Sec |
| 0 | 0 | 0 | 0 | 0 | 0 |
| 1.5 | 1.41 | 1.41 | 1.41 | 1.41 | 1.41 |
| 5.5 | 3.34 | 3.29 | 3.29 | 5.07 | 4.33 |
| 8.25 | 2.22 | 2.21 | 2.64 | 3.38 | 3.24 |
| 11 | 1.63 | 1.62 | 1.89 | 3.16 | 2.7 |
| 16.5 | 2.41 | 2.4 | 2.8 | 3.64 | 4.39 |
| 22 | 2.07 | 2.06 | 2.4 | 3.13 | 3.89 |
| 27.5 | 1.81 | 1.8 | 2.1 | 2.73 | 3.28 |
| 33 | 1.52 | 1.51 | 1.51 | 2.29 | 2.01 |
| 38.5 | 1.13 | 1.12 | 1.12 | 1.7 | 1.3 |
| 44 | 0.77 | 0.767 | 0.767 | 1.15 | 0.784 |
| 49.5 | 0.442 | 0.44 | 0.44 | 0.645 | 0.44 |
| 55 | 0.194 | 0.194 | 0.194 | 0.267 | 0.194 |
| Total weight (Tons) | 18.946 | 18.821 | 20.561 | 28.572 | 27.968 |

Table A-10 : Weight distribution along the length of the blade

A.7 Reactions at the blade root.

| Reaction at the root in the direction (kN) | NACA-4424-60m-200MPa | NACA-4424-60m-CL-200MPa | NACA-4424-60m-CLE-200MPa | NACA-4424-60m-AE-200MPa | NACA-4424-60m-CLE-200MPa-Sec |
|---|-----------------------------|--------------------------------|---------------------------------|--------------------------------|-------------------------------------|
| Axial | 1152.51 | 1146.42 | 1241.36 | 1745.35 | 1678.41 |
| Flapwise | 910.55 | 909.51 | 926.55 | 1005.17 | 999.08 |
| Edgewise | 21.13 | 21.13 | 21.23 | 2.99 | 1.50 |

Table A-11 : Reaction at the blade root under load case 1.

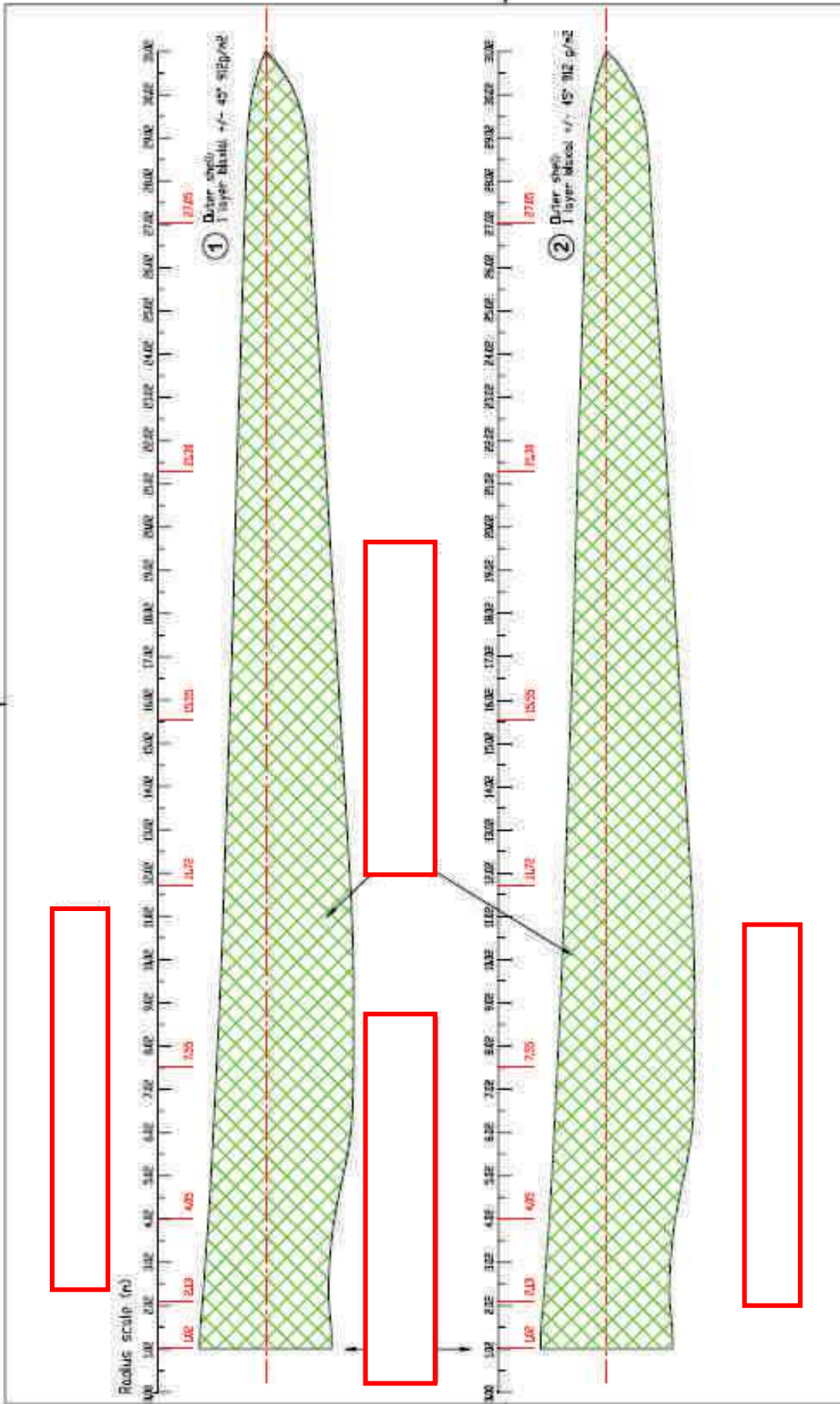
| Reaction at the root in the direction (kN) | All the blade types |
|---|----------------------------|
| Axial | 6.42 |
| Flapwise | 302.71 |
| Edgewise | 49.14 |

Table A-12 : Reaction at the root under aerodynamic loading.

Appendix **B** --- Layup plans and cross sections: GEV HP SPM184f 30m

The stratification plans of the wind turbine blade are shown in the following 10 sheets. The plans are used to cut the composite mats and to be laid in the blade mould before resin infusion with the layup 1 being the one closest to the mould and the layup being developed until the 10th plan.

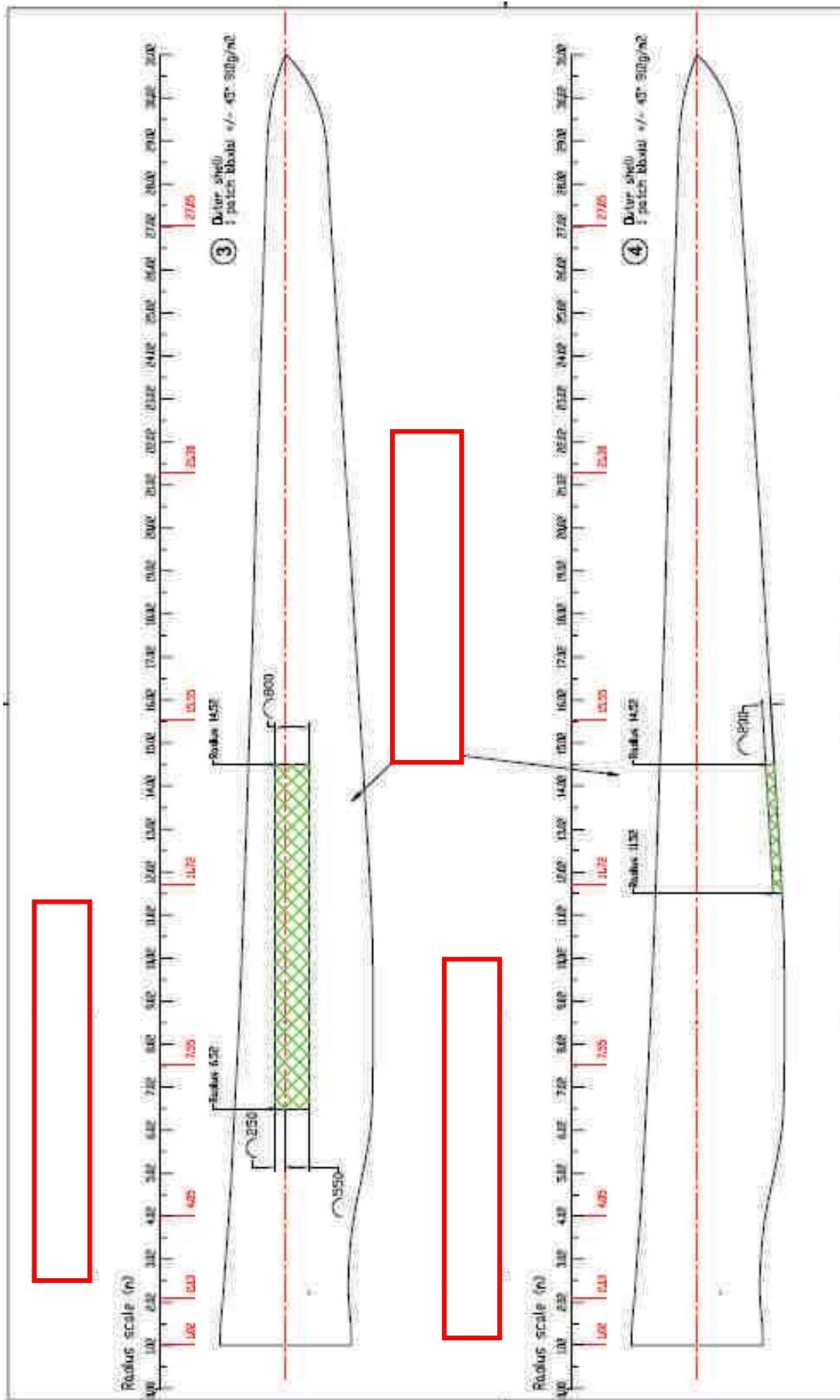
The second part of this annex shows the details of the blade cross sections.



| REV | DESCRIPTION | DATE | BY |
|-----|--|------------|--------|
| 01 | Creation | 02/12/2009 | 499003 |
| 02 | Additional comments | 11/02/2009 | |
| 03 | Revision between step 4 and 5 | 25/07/2009 | |
| 04 | Additional comments | 07/07/2009 | |
| 05 | Core material cut for block cabin outlet | 10/12/2009 | |

| | |
|---|--|
| ATTENTION: | |
| This drawing serves as illustration for the final design assessment discussion and is not provided for use in production. Additional information regarding materials, production conditions and requirements, tolerances, quality assurance, test instructions and approval conditions in the current version of the blade specification have to be considered. | |

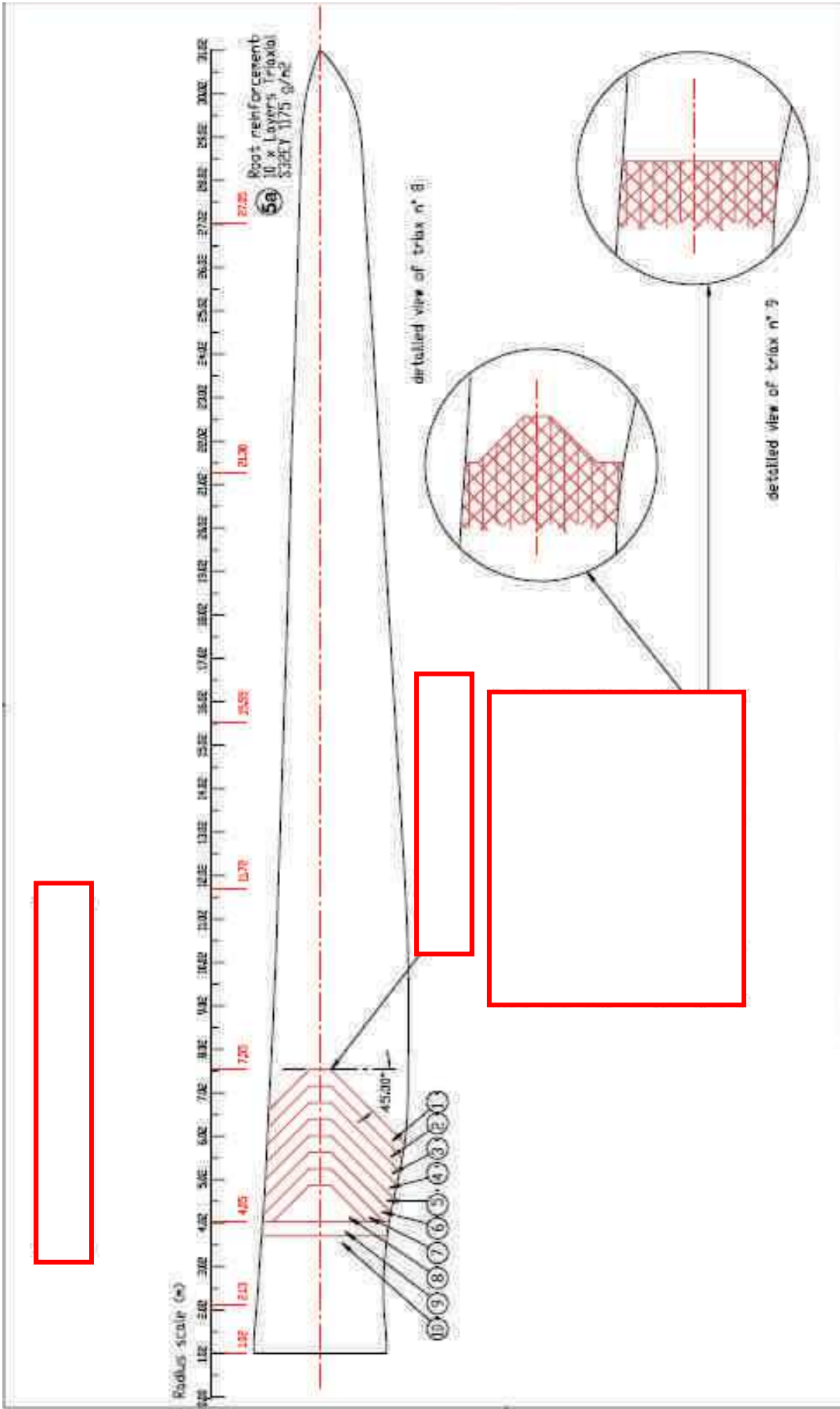
| | |
|--|-------------|
| ACC - GEV HP SPM184F 30m blade | |
| Drawing Laminate Plan | |
| FILE CONSOLE C:\p\dev\Archives 34560 GEV\BILIX 2004 07 23 43 42 | |
| DATE / TIME | DATE / TIME |
| 07/07/2009 | 18/12/2009 |
| BY: 49 | BY: 101 |
| SCALE: 1:1 | SHEET: 101 |



| REV | DESCRIPTION | DATE | APPROVED |
|-----|--|------------|----------|
| 01 | Creation | 02/12/2009 | |
| 02 | Additional comments | 11/02/2009 | |
| 03 | Inversion between step 4 and 3 | 25/02/2009 | |
| 04 | Additional comments | 07/07/2009 | |
| 05 | Core material cut for blade cable outlet | 18/10/2009 | |

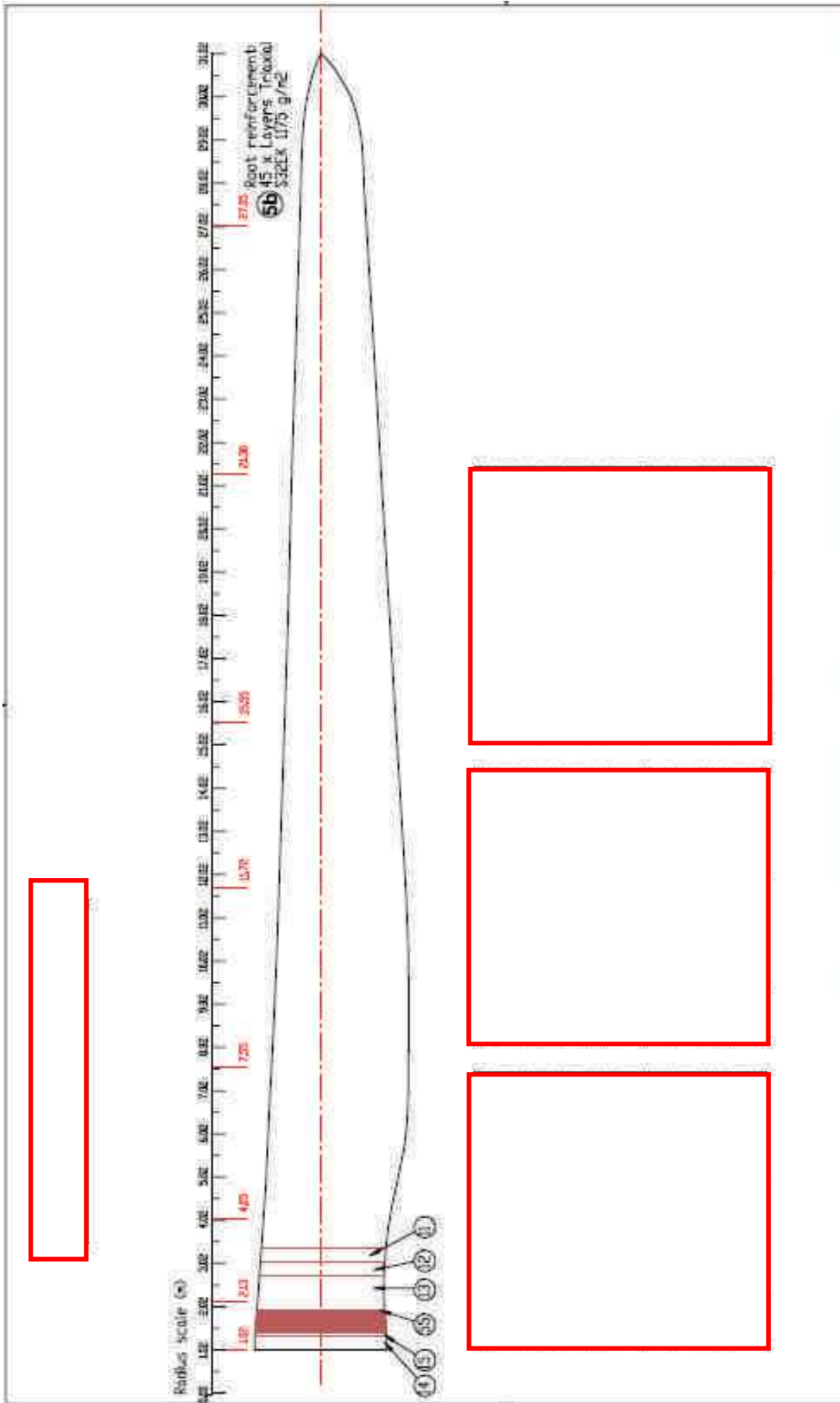
| | |
|---|--|
| ATTENTION: | |
| This drawing serves as (basis) for the final design assessment documentation and is not provided for use in production. Additional information regarding materials, production readiness and requirements, tolerances, quality assurance, test instructions and preparatory conditions in the current version of the blade specification have to be considered. | |

| | |
|--------------------------------|-----|
| ACC - GEV HP SPM184F 30m blade | |
| Drawing Laminate Plan | |
| DATE | REV |
| 18/12/2009 | 5.0 |
| SCALE | 001 |



| REV | DESCRIPTION | DATE | APPROVED |
|-----|--|------------|----------|
| 01 | Creation | 05/12/2008 | |
| 02 | Additional comments | 11/02/2009 | |
| 03 | Inversion between step 4 and 5 | 25/02/2009 | |
| 04 | Additional comments | 07/07/2009 | |
| 05 | Core material cut for blade cable outlet | 18/12/2009 | |

| | | |
|---|--|--|
| ATTENTION This drawing serves as (blueprint) for the final design assessment documentation and is not provided for use in production. Additional information regarding materials, production conditions and requirements, references, quality assurance, test procedures and acceptance conditions in the current version of the blade specification have to be considered. | | ACC - GEV HP SPM184f 30m blade Drawing Laminate Plan ACC 1328 MD 305 MD EC.SPM184.03.00-03 18/12/2009 003 |
|---|--|--|

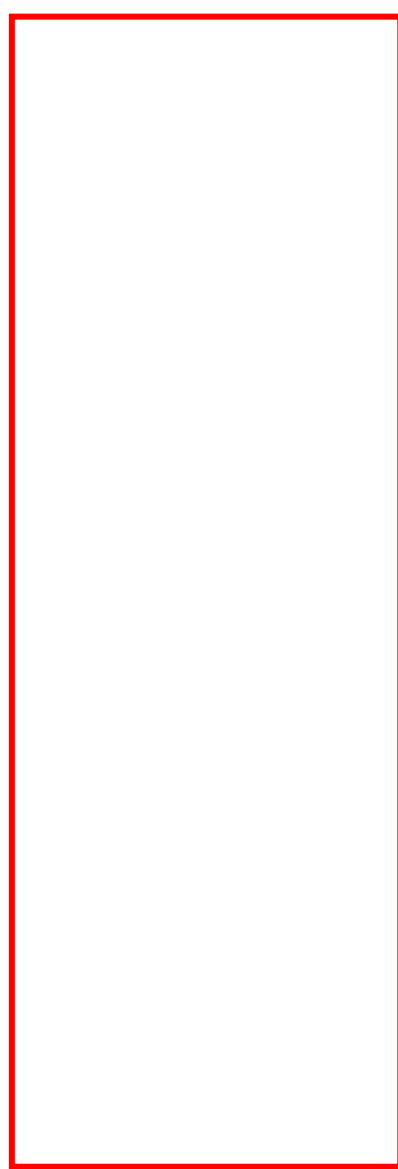
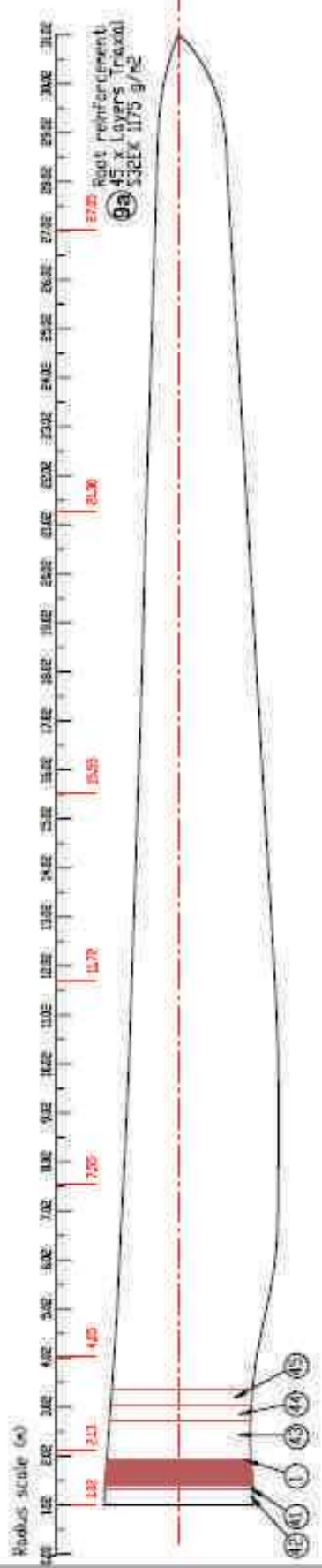


| REV | DESCRIPTION | DATE | APPROVED |
|-----|--|------------|----------|
| 01 | Creation | 02/12/2008 | |
| 02 | Additional comments | 11/02/2009 | |
| 03 | Revision between step 4 and 3 | 25/02/2009 | |
| 04 | Additional comments | 07/07/2009 | |
| 05 | Core material cut for blade cable outlet | 10/12/2009 | |

| | |
|--------------------------------|-----------------|
| ACD - GEV HP SPM184F 30m blade | |
| Drawing Laminate Plan | |
| SUB ITEM NO | 506 NO |
| AI | EC:SPM184F30-05 |
| REV | 5/0 |
| | |
| SCALE | Schematic |
| DATE | 10/12/2009 |
| REV | 004 |

Attention:
 This drawing serves as illustration for the local designer assessment discussion and is not provided for use in production. Additional information regarding materials, production conditions and requirements, tolerances, quality assurance, test procedures and approvals/modifications in the current version of the blade specification have to be considered.

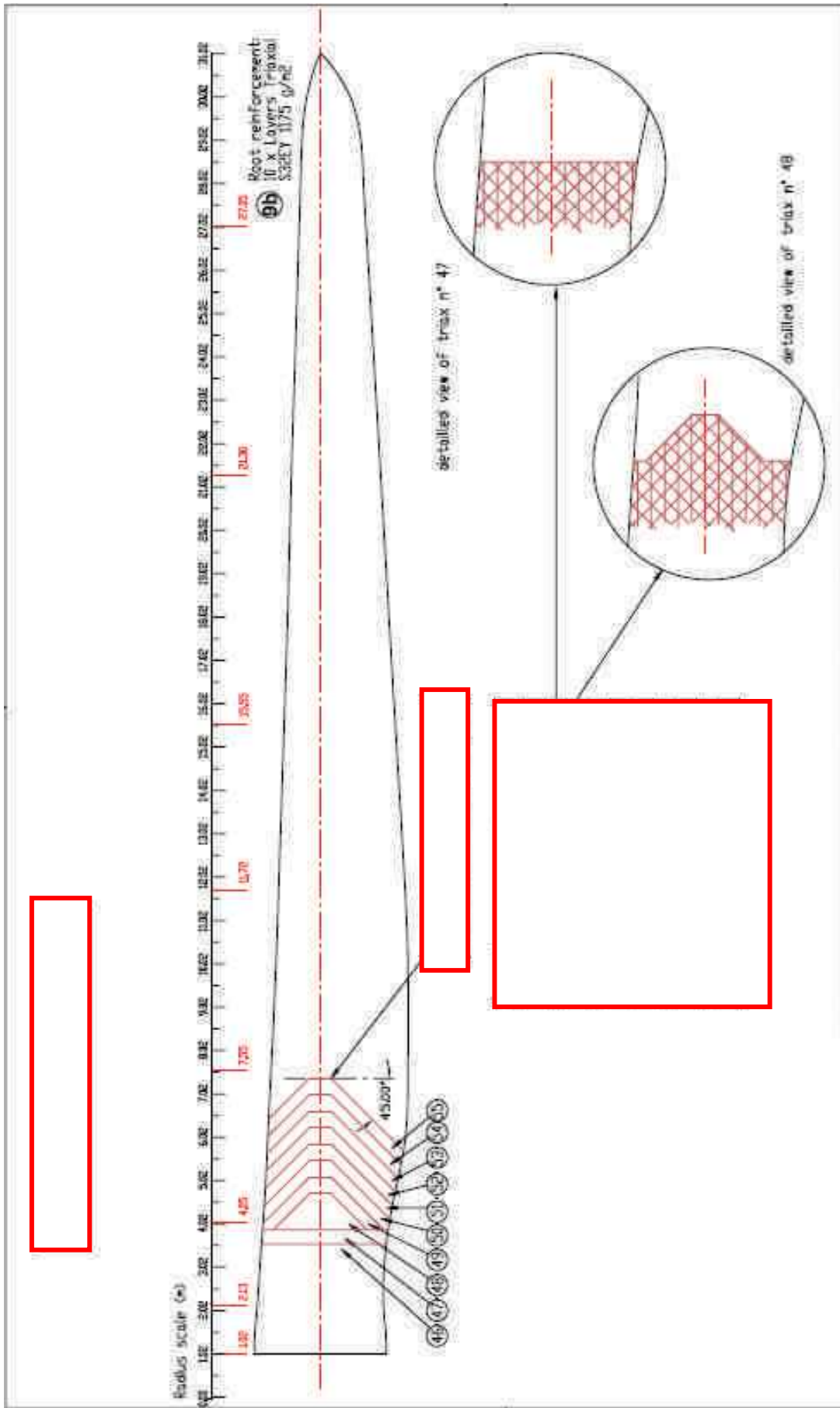
The laminate and core material lay-up is identical for suction and pressure side.



| REV | DESCRIPTION | DATE | APPROVED |
|-----|--|------------|----------|
| 01 | Creation | 02/12/2008 | |
| 02 | Additional comments | 11/02/2009 | |
| 03 | Inversion between step 4 and 3 | 25/02/2009 | |
| 04 | Additional comments | 07/07/2009 | |
| 05 | Core material cut for blade cable outlet | 01/12/2009 | |

| | | | |
|--|-------|--------------------------------|----------|
| SOLE CONSOLE 20, rue de la République 33500 BORDEAUX 3334 57 23 43 42 | | AEO - GEV HP SPM184F 30m blade | |
| JOHN B. RIEHER | | Drawing Laminate Plan | |
| SCALE | DATE | REV | REV |
| X3 | 06.01 | EC-SPM184.03.00-03 | 5.0 |
| SNEC Schematic | | 18/12/2009 | SNEC 007 |

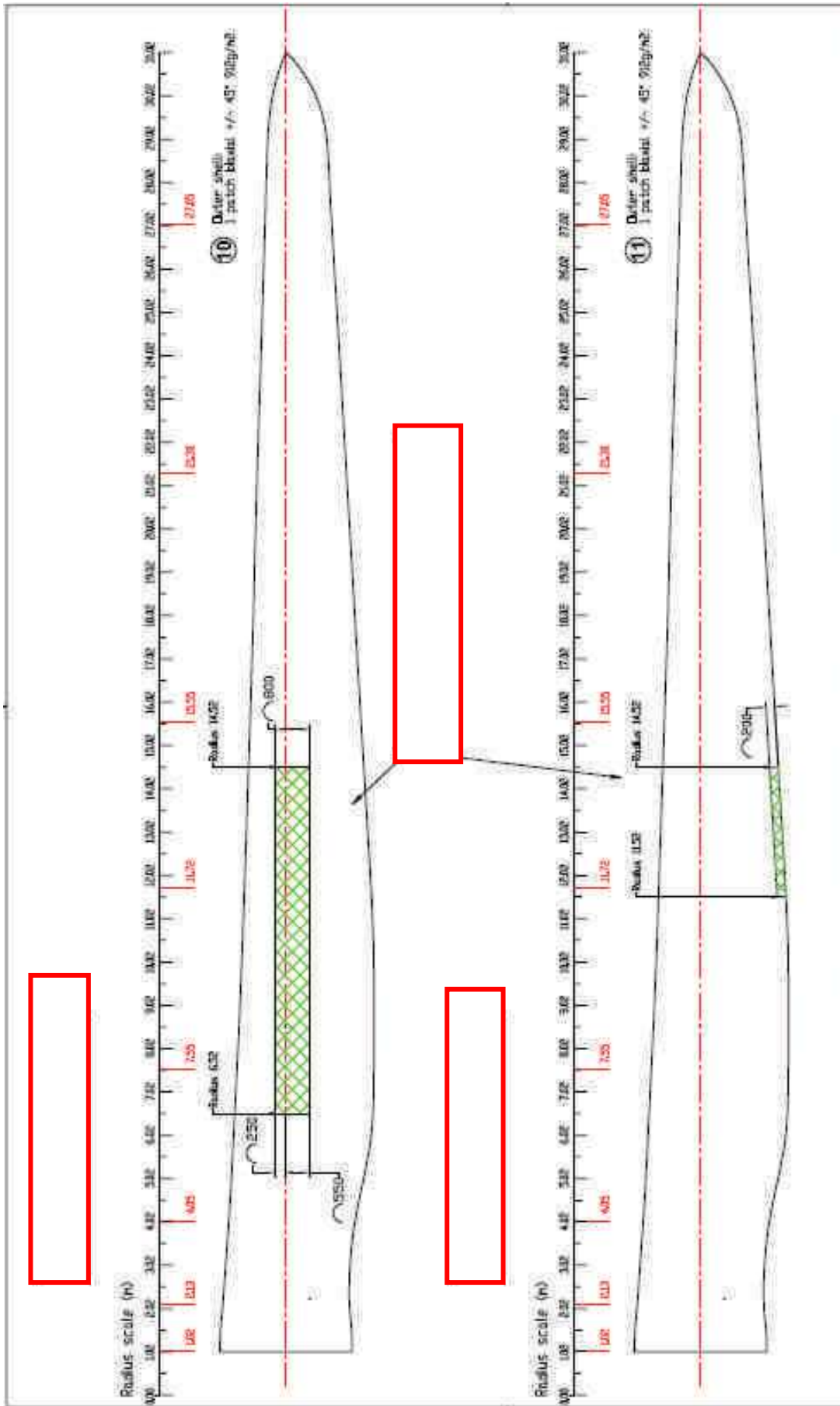
Attention:
This drawing serves as illustration for the 4and design assessment documentation and is not provided for use in production. Additional information regarding material, production conditions and requirements, tolerances, quality assurance, test procedures and equipment conditions in the current version of the blade specification have to be considered.



| REV | DESCRIPTION | DATE | APPROVED |
|-----|--|------------|----------|
| 01 | Creation | 08/12/2008 | |
| 02 | Additional comments | 11/02/2009 | |
| 03 | Inversion between step 4 and 5 | 25/02/2009 | |
| 04 | Additional comments | 07/07/2009 | |
| 05 | Core material cut for blade cable outlet | 18/12/2009 | |

| | | | |
|--|--|--------------------------------|--|
| FILE: CD\SEIL 14500_30m Blade 2314_27_23_43_42 | | ACC - GEV HP SPM184F 30m blade | |
| DRAWN BY: S. Richter DATE: 16/12/2009 | | Drawing Laminate Plan | |
| SCALE: Scientific | | REV: 5.0 | |

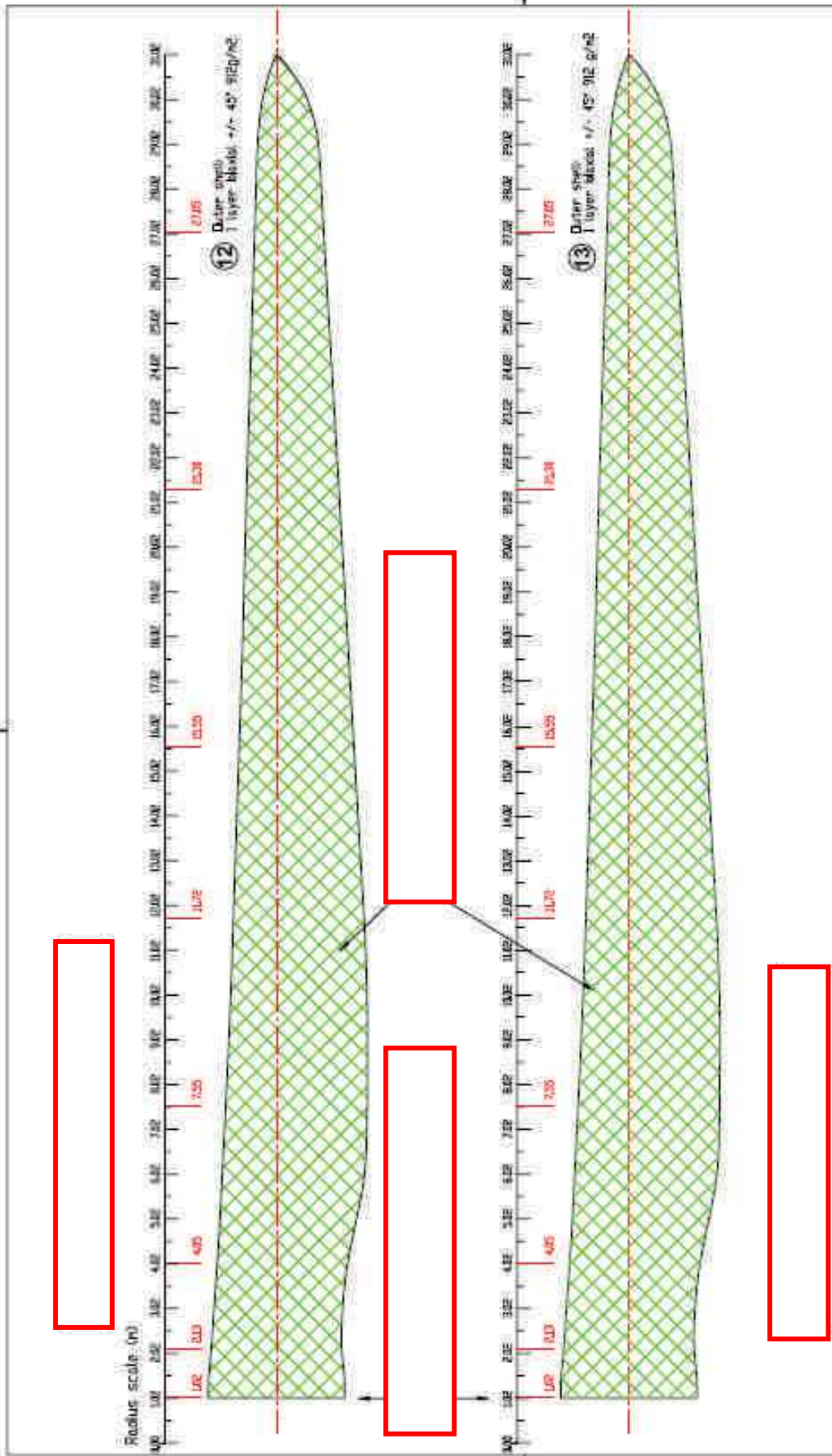
Attention:
 This drawing serves as illustration for the 4eclé design assessment phase and is not provided for use in production. Additional information regarding material, production conditions and requirements, tolerances, quality assurance, test instructions and approval conditions in the current version of the blade specification have to be considered.



| REV | DESCRIPTION | DATE | APPROVED |
|-----|---|------------|----------|
| 01 | Creation | 02/12/2008 | |
| 02 | Add burial comments | 11/02/2009 | |
| 03 | Inversion between step 4 and 5 | 25/02/2009 | |
| 04 | Add burial comments | 07/07/2009 | |
| 05 | Core material cut for blade cobble outlet | 10/12/2009 | |

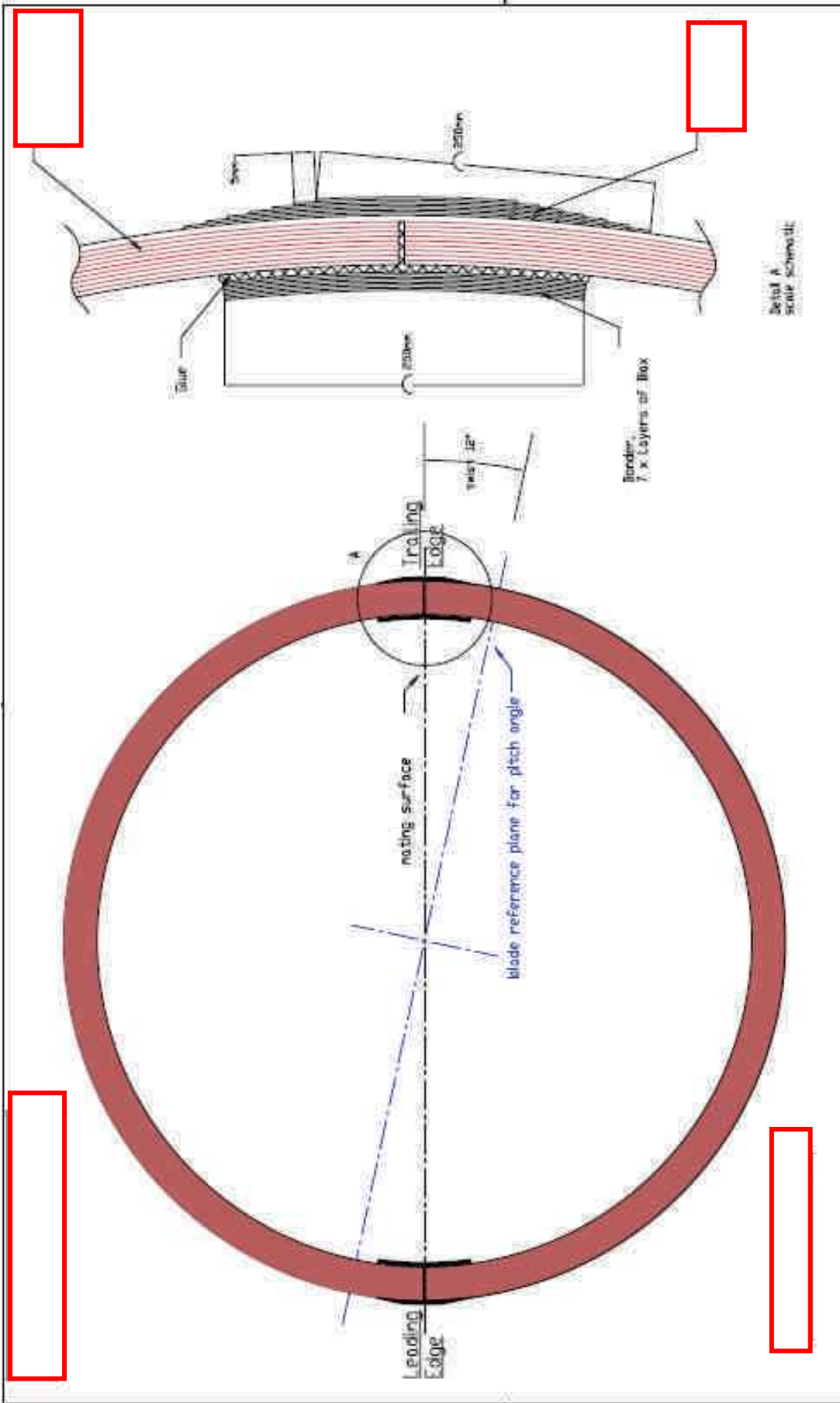
| | | | |
|--|--------|--------------------------------|----------|
| EDLE EDSEIL 20 Fair Ave 25500 Brackley 5314 57 23 43 42 | | ACC - GEV HP SPM184F 30m blade | |
| Drawing Laminate Plan | | | |
| MAN BY | CHK BY | DATE | REV |
| M. Richter | | 18/12/2009 | 5.0 |
| SCALE: Schematic | | | 9MET 009 |

Attention:
This drawing serves as illustration for the final design assessment discussion and is not provided for use in production. Additional information regarding material, production conditions and requirements, tolerances, quality assurance, test protocols and appropriate conditions in the current version of the blade specification have to be considered.



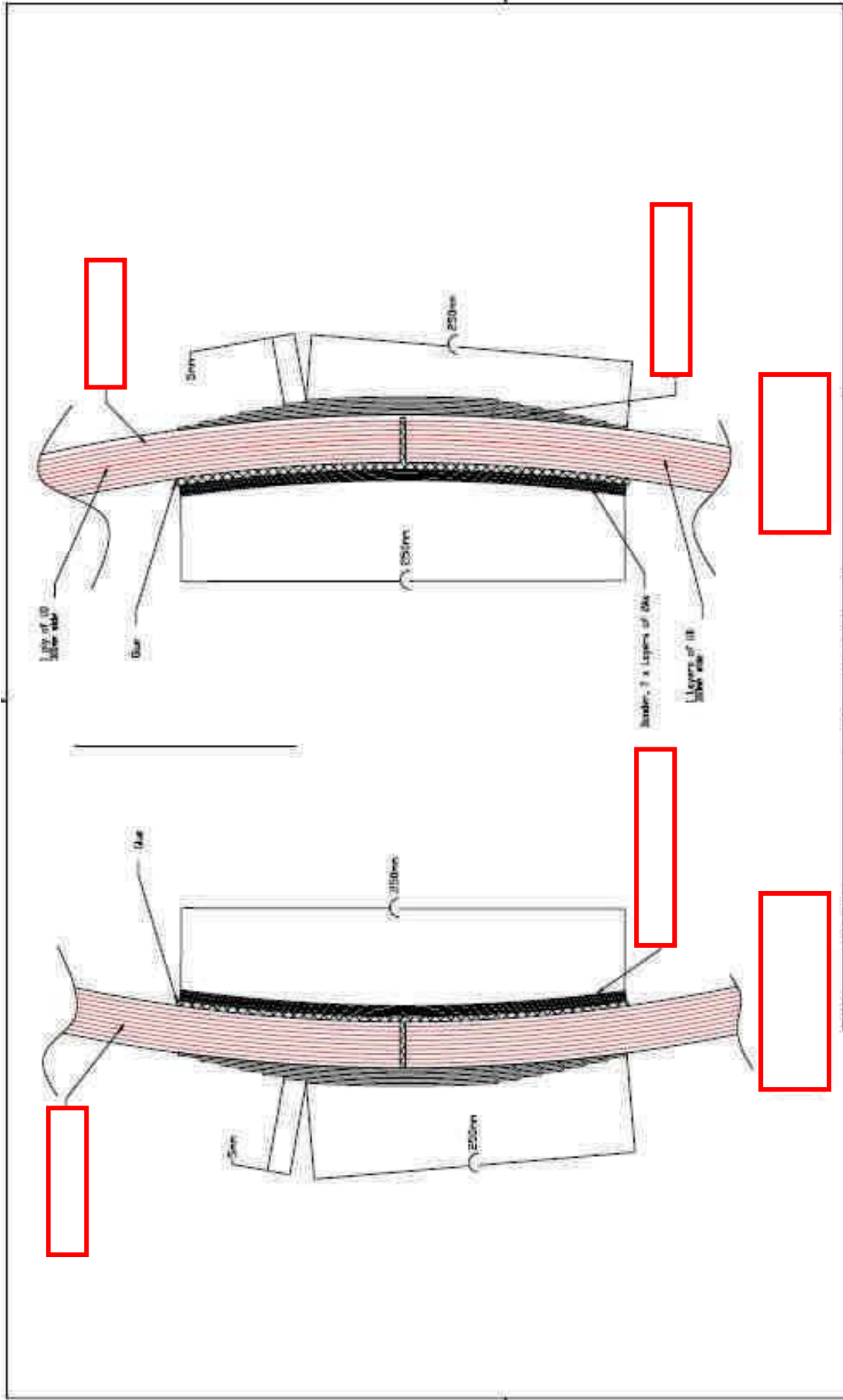
| REV | DESCRIPTION | DATE | APPROVED |
|-----|--|------------|----------|
| 01 | Creation | 08/12/2008 | |
| 02 | Additional comments | 11/02/2009 | |
| 03 | Inversion between step 4 and 5. | 05/02/2009 | |
| 04 | Additional comments. | 07/07/2009 | |
| 05 | Core material cut for blade cable outlet | 10/12/2009 | |

| | | | |
|--|------------|--|------------|
| ATTENTION: This drawing serves as illustration for the final knowledge assessment documentation and is not provided for use in production. Additional information regarding materials, production conditions and requirements, tolerances, quality assurance, test procedures and operational conditions in the current version of the blade specification have to be considered. | | FILE CONSOLE: R:\P\proj\div\Archives 24560\BIBL\EX 2008_07_23_43_42 | |
| ACC - GEV HP SPM184f 30m blade | | Drawing Laminate Plan | |
| MAN BY | E. Richter | DATE | 18/12/2009 |
| SCALE | Schematic | REV | 5.0 |
| | | SHEET | 0011 |

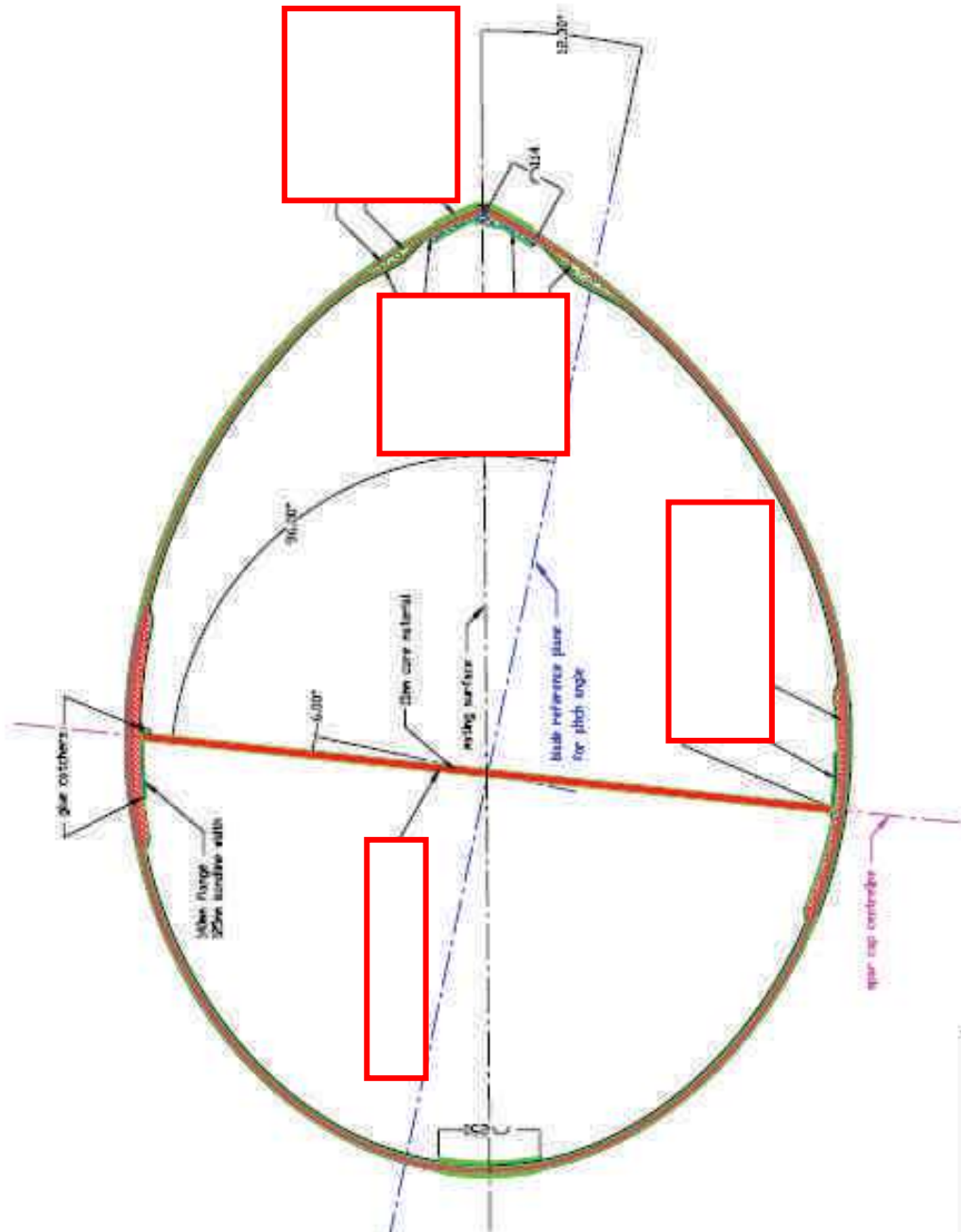


Detail A
Scale schematic

| | | | | | | | |
|---|--|---|--------------------|---|--------------------------|--|---------------------------------------|
| <p>Attention This drawing serves as illustration for the scope & design assessment documents and is not provided for use in production. Additional information regarding materials, production conditions and requirements, tolerances, quality assurance, test instructions and approval conditions in the current version of the blade specifications have to be considered.</p> | | <p>REV</p> <p>01 Creation</p> <p>02 Additional comments</p> <p>03 Additional comments</p> | <p>DESCRIPTION</p> | <p>DATE</p> <p>02/10/2006</p> <p>11/02/2009</p> <p>07/07/2009</p> | <p>BY</p> <p>4198/VD</p> | <p>FILE CONSOLE</p> <p>20 Purdes Attach</p> <p>24600 BEARER.DWG</p> <p>(334 67 23 43 42)</p> | <p>ACC - GEV HP SPM184F 30m blade</p> |
| | | <p>DRAWN BY: D. Richter</p> <p>SCALE: 1:10</p> | | | | <p>Drawing Cross-Section</p> <p>RJ.02</p> | |
| | | | | | | <p>SIZE FOR A4</p> <p>REV 3.0</p> | |
| | | | | | | <p>DATE: 07/07/2009</p> <p>SHEET: 001</p> | |



| | | | | |
|--|--|--|--|---|
| <p>Attention: This drawing serves as illustration for the Asent R&D design assessment documentation and is not provided for use in production. Additional information regarding materials, production conditions and requirements, tolerances, quality assurance, test instructions and approved conditions is the current version of the blade specification have to be considered.</p> | | <p>REV: 01</p> <p>DESCRIPTION: Cross-Section</p> <p>DATE: 07/25/2008</p> <p>BY: 02</p> <p>ADDITIONAL COMMENTS: Additional comments</p> <p>DATE: 11/02/2009</p> <p>BY: 03</p> <p>ADDITIONAL COMMENTS: Additional comments</p> <p>DATE: 07/07/2009</p> | <p>FILE: CONSEIL</p> <p>24630 BEBARD ELYX</p> <p>(33) 4 67 23 43 42</p> <p>NAME: J. Richer</p> <p>SCALE: Schematic</p> | <p>ACC - DEV HP SPM184F 30h blade</p> <p>Drawing Cross-Section R2.13</p> <p>REV: 3.0</p> <p>DATE: 07/07/2009</p> <p>SHEET: 0076</p> |
|--|--|--|--|---|



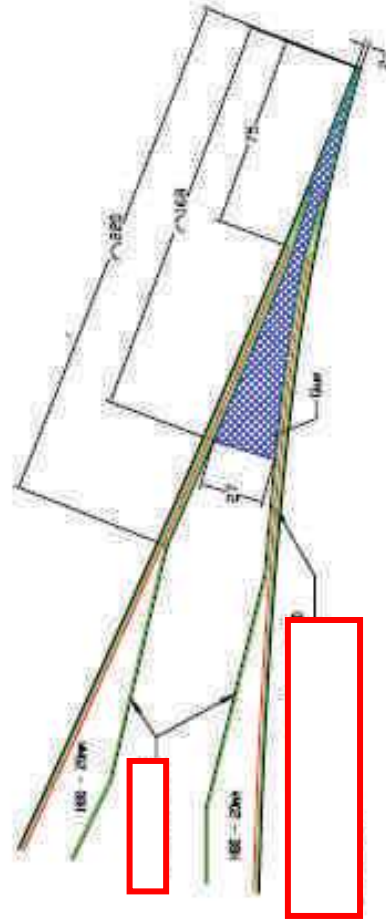
View From Root to Tip

Attention
 This drawing serves as illustration for the client for design assessment, discussion and is not provided for use in production. Additional information regarding materials, production conditions and requirements, tolerances, quality assurance, test instructions and approval conditions is the current version of the blade specification have to be considered.

| REV | DESCRIPTION | DATE | APP'D |
|-----|---------------------|------------|-------|
| 01 | Creation | 02/22/2008 | |
| 02 | Additional comments | 11/02/2009 | |
| 03 | Additional comments | 07/07/2009 | |

ELE CONSEIL
 20 Rue des Arches
 334 67 23 43 42
 NAIN Y. & Richer
 SCALE 1 : 10

| | |
|--------------------------------|-------|
| ACD - GEV HP SPM184f 30h blade | |
| Drawing Cross-Section R4,05 | |
| SIZE FEM NO. | REV |
| A1 | 3.0 |
| DATE | SHEET |
| 07/07/2009 | 003 |

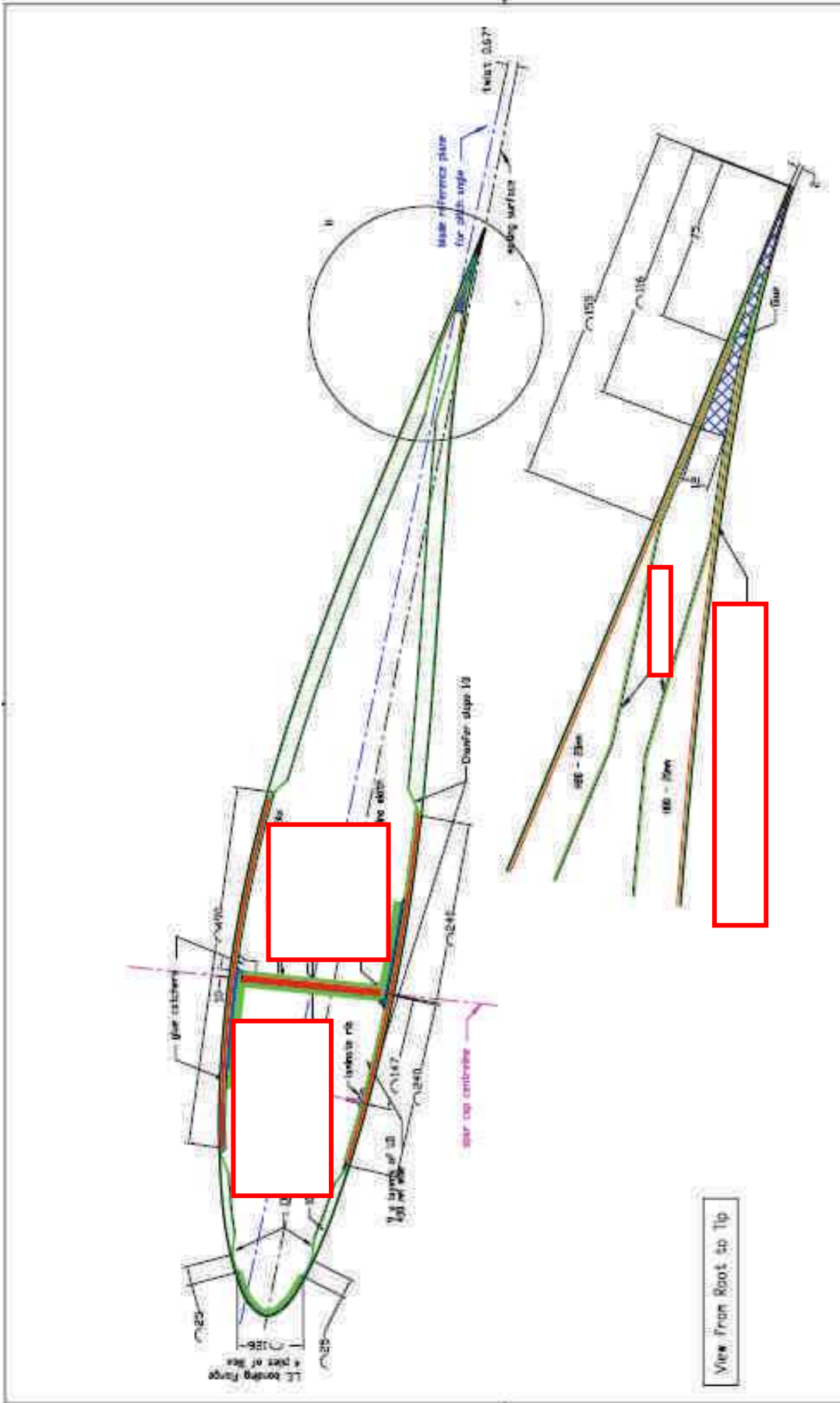


American
 This drawing serves as illustration for the lead foreign assessment documents and is not provided for use in production. Additional information regarding materials, production conditions and requirements, tolerances, quality assurance, test instructions and approval conditions in the current version of the blade specifications have to be considered.

| REV | DESCRIPTION | DATE | APPROVED |
|-----|---------------------|------------|----------|
| 01 | Creation | 12/12/2008 | |
| 02 | Additional comments | 11/02/2009 | |
| 03 | Additional comments | 07/07/2009 | |
| | | | |
| | | | |

EOLE CONSEIL
 20 rue des Archers
 34500 BEAUMÉDAN
 0334 67 23 43 42
 MAN BY B. Richter
 DATE 1 - 10
 07/07/2009
 DWG 007

ACC - GEV HP SPM184F 30m blade
 Drawing Cross-Section R21.30
 SIZE 10
 DWG NO. C.C.SPM184.03.02-03
 REV 3.0



| REV | DESCRIPTION | DATE | APPROVED |
|-----|---------------------|------------|----------|
| 01 | Creation | 02/12/2008 | |
| 02 | Additional comments | 11/02/2009 | |
| 03 | Additional comments | 07/07/2009 | |
| | | | |
| | | | |

| | | | |
|---|-----------------------------|---------------------------------|----------|
| EDLE CONSULT 20, rue des Arches 34500 BEZIERS 0334 67 23 43 42 | | ACCU - GEV HP SPM184F 30m blade | |
| DRAWN BY: R. Riecher | | Drawing Cross-Section R27.05 | |
| SIZE: A3 | DWG NO.: EC.SPM184.03.02-03 | DATE: 07/07/2009 | REV: 3.0 |
| SCALE: 1 : 5 | | DWG NO.: | DATE: |

Attention
 This drawing serves as illustration for the 4e and 5e design assessment documentation and is not provided for use in production. Additional information regarding materials, production conditions and requirements, tolerances, quality assurance, test instructions and approval conditions in the current version of the blade specifications have to be considered.

Appendix C GEV HP SPM184f 30m blade Static test results

C.1 PTS: Pressure to Suction side Flapwise bending test.

The blade positions and the loads applied at different locations is given by the table below. The loads are applied from the pressure side to the suction side.

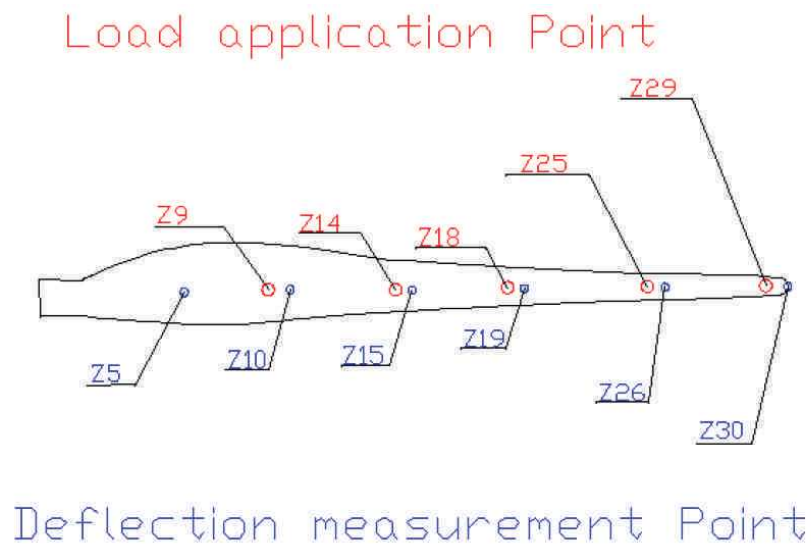


Figure C-1 : Load and deflection measurement locations.

| Blade side pointing up | Introduction point | Clamp position (m) | Applied load direction | Intended applied load (kN) |
|------------------------|--------------------|--------------------|------------------------|----------------------------|
| Pressure | A | 9.0 | PTS | 11.2 |
| | B | 14.0 | | 17.2 |
| | C | 18.0 | | 25.3 |
| | D | 25.0 | | 27.4 |
| | E | 29.0 | | 22.7 |

Table C-1: Loading point locations.

| Distance from the root (m) | Target moment (kN-m) | Test moment (kN-m) | Test moment of the target (%) |
|-----------------------------------|-----------------------------|---------------------------|--------------------------------------|
| 0 | 2138.5 | 2119.2 | 99.10% |
| 1 | 2034.8 | 2016.9 | 99.12% |
| 2 | 1931.1 | 1914.6 | 99.15% |
| 3 | 1827.4 | 1812.3 | 99.18% |
| 4 | 1723.7 | 1710 | 99.21% |
| 5 | 1620 | 1607.7 | 99.24% |
| 6 | 1516.3 | 1505.2 | 99.27% |
| 7 | 1412.6 | 1402.7 | 99.30% |
| 8 | 1308.9 | 1300.2 | 99.34% |
| 9 | 1205.2 | 1197.7 | 99.37% |
| 10 | 1112.7 | 1106.3 | 99.43% |
| 11 | 1020.2 | 1014.7 | 99.46% |
| 12 | 927.7 | 923 | 99.49% |
| 13 | 835.2 | 831.3 | 99.54% |
| 14 | 742.7 | 739.6 | 99.59% |
| 15 | 667.4 | 665.1 | 99.65% |
| 16 | 592.1 | 590.2 | 99.68% |
| 17 | 516.8 | 515.3 | 99.72% |
| 18 | 441.5 | 440.5 | 99.77% |
| 19 | 391.4 | 390.9 | 99.86% |
| 20 | 341.3 | 340.9 | 99.88% |
| 21 | 291.2 | 290.9 | 99.91% |
| 22 | 241.1 | 241 | 99.94% |
| 23 | 191 | 191 | 99.99% |
| 24 | 140.9 | 141 | 100.07% |
| 25 | 90.8 | 91 | 100.23% |
| 26 | 68.1 | 68.3 | 100.36% |
| 27 | 45.4 | 45.6 | 100.37% |
| 28 | 22.7 | 22.8 | 100.37% |

Table C-2: Applied bending moments.

C.2 STP: Suction to Pressure side Flapwise bending test.

The blade positions and the loads applied at different locations is given by the table below. The loads are applied from the suction side to the pressure side.

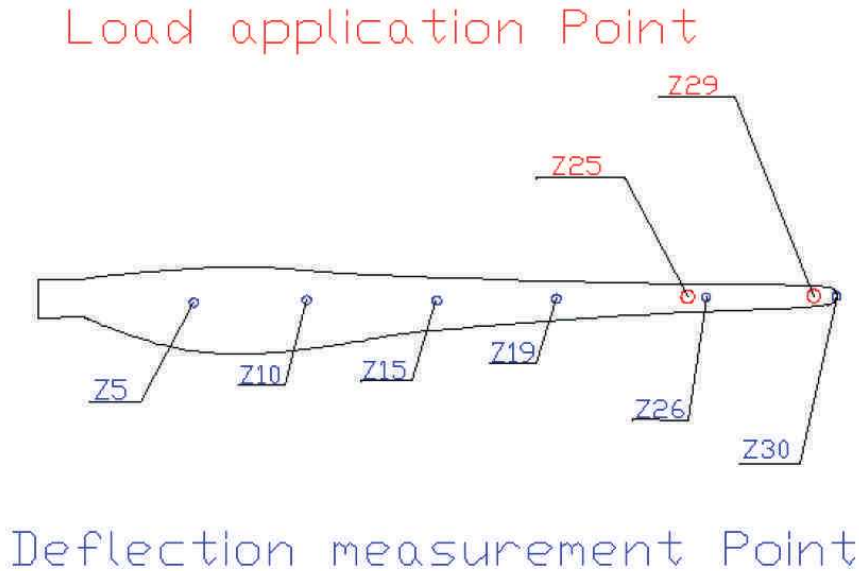


Figure C-2 : Load and deflection measurement locations.

| Blade side pointing up | Introduction point | Clamp position (m) | Applied load direction | Intended applied load (kN) |
|------------------------|--------------------|--------------------|------------------------|----------------------------|
| Suction | | | STP | |
| | | | | |
| | B | 14.0 | | 0.0 |
| | C | 18.0 | | 0.0 |
| | D | 25.0 | | 26.1 |
| | E | 29.0 | 26.9 | |

Table C-3: Loading point locations.

| Distance from the root (m) | Target moment (kN-m) | Test moment (kN-m) | Test moment of the target (%) |
|---------------------------------------|---------------------------------|-------------------------------|--|
| 0 | 1424.7 | 1402.5 | 98.44% |
| 1 | 1372 | 1351.3 | 98.49% |
| 2 | 1319.3 | 1300.1 | 98.54% |
| 3 | 1266.6 | 1248.9 | 98.60% |
| 4 | 1213.9 | 1197.7 | 98.66% |
| 5 | 1161.2 | 1146.4 | 98.73% |
| 6 | 1108.5 | 1095.1 | 98.79% |
| 7 | 1055.8 | 1043.7 | 98.85% |
| 8 | 1003.1 | 992.3 | 98.92% |
| 9 | 950.4 | 940.9 | 99.00% |
| 10 | 897.7 | 889.5 | 99.08% |
| 11 | 845 | 837.8 | 99.15% |
| 12 | 792.3 | 786.1 | 99.22% |
| 13 | 739.6 | 734.4 | 99.30% |
| 14 | 686.9 | 682.7 | 99.39% |
| 15 | 634.2 | 631 | 99.50% |
| 16 | 581.5 | 579 | 99.56% |
| 17 | 528.8 | 526.9 | 99.64% |
| 18 | 476.1 | 474.8 | 99.73% |
| 19 | 423.4 | 422.7 | 99.85% |
| 20 | 370.7 | 370.1 | 99.85% |
| 21 | 318 | 317.5 | 99.85% |
| 22 | 265.3 | 264.9 | 99.86% |
| 23 | 212.6 | 212.3 | 99.85% |
| 24 | 159.9 | 159.6 | 99.84% |
| 25 | 107.2 | 107 | 99.81% |
| 26 | 80.4 | 80.4 | 100.03% |
| 27 | 53.6 | 53.6 | 100.03% |
| 28 | 26.8 | 26.8 | 100.04% |

Table C-4: Applied bending moments.

C.3 TTL: Trailing to Leading edge Edgewise bending test.

The blade positions and the loads applied at different locations is given by the table below. The loads are applied from the suction side to the pressure side.

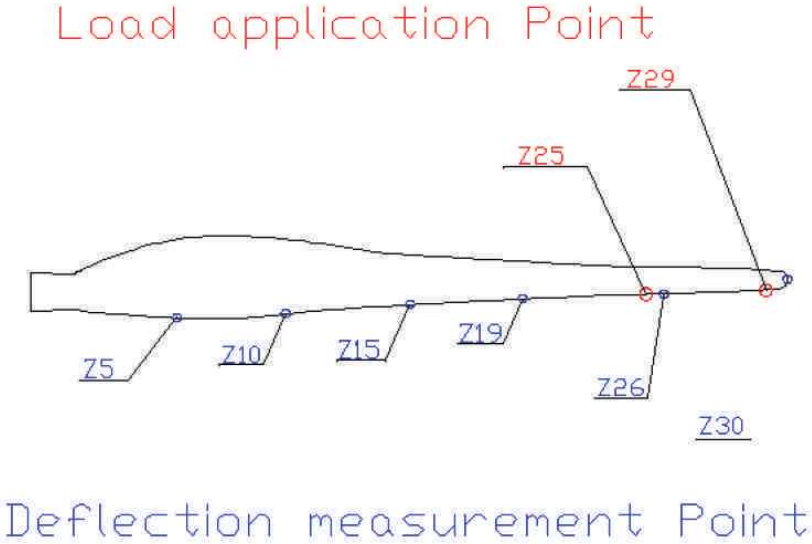


Figure C-3 : Load and deflection measurement locations.

| Blade side pointing up | Introduction point | Clamp position (m) | Applied load direction | Intended applied load (kN) |
|------------------------|--------------------|--------------------|------------------------|----------------------------|
| Suction | | | TTL | |
| | B | 14.0 | | 0.0 |
| | C | 18.0 | | 0.0 |
| | D | 25.0 | | 24.9 |
| | E | 29.0 | | 23.9 |

Table C-5: Loading point locations.

| Distance from the root (m) | Target moment (kN-m) | Test moment (kN-m) | Test moment of the target (%) |
|---------------------------------------|---------------------------------|-------------------------------|--|
| 0 | 1315.6 | 1324.6 | 100.69% |
| 1 | 1266.8 | 1275.5 | 100.69% |
| 2 | 1218 | 1226.5 | 100.70% |
| 3 | 1169.2 | 1177.4 | 100.70% |
| 4 | 1120.4 | 1128.3 | 100.71% |
| 5 | 1071.6 | 1079.2 | 100.71% |
| 6 | 1022.8 | 1030.2 | 100.72% |
| 7 | 974 | 981.1 | 100.72% |
| 8 | 925.2 | 932 | 100.73% |
| 9 | 876.4 | 882.9 | 100.74% |
| 10 | 827.6 | 833.8 | 100.74% |
| 11 | 778.8 | 784.6 | 100.75% |
| 12 | 730 | 735.5 | 100.76% |
| 13 | 681.2 | 686.4 | 100.77% |
| 14 | 632.4 | 637.3 | 100.77% |
| 15 | 583.6 | 588.2 | 100.79% |
| 16 | 534.8 | 539.1 | 100.80% |
| 17 | 486 | 489.9 | 100.81% |
| 18 | 437.2 | 440.8 | 100.82% |
| 19 | 388.4 | 391.7 | 100.84% |
| 20 | 339.6 | 342.5 | 100.86% |
| 21 | 290.8 | 293.4 | 100.89% |
| 22 | 242 | 244.3 | 100.93% |
| 23 | 193.2 | 195.1 | 100.99% |
| 24 | 144.4 | 146 | 101.09% |
| 25 | 95.6 | 96.8 | 101.30% |
| 26 | 71.7 | 72.6 | 101.30% |
| 27 | 47.8 | 48.4 | 101.30% |
| 28 | 23.9 | 24.2 | 101.30% |

Table C-6: Applied bending moments.

C.4 LTT: Leading to trailing edge edgewise bending test.

The blade positions and the loads applied at different locations is given by the table below. The loads are applied from the suction side to the pressure side.

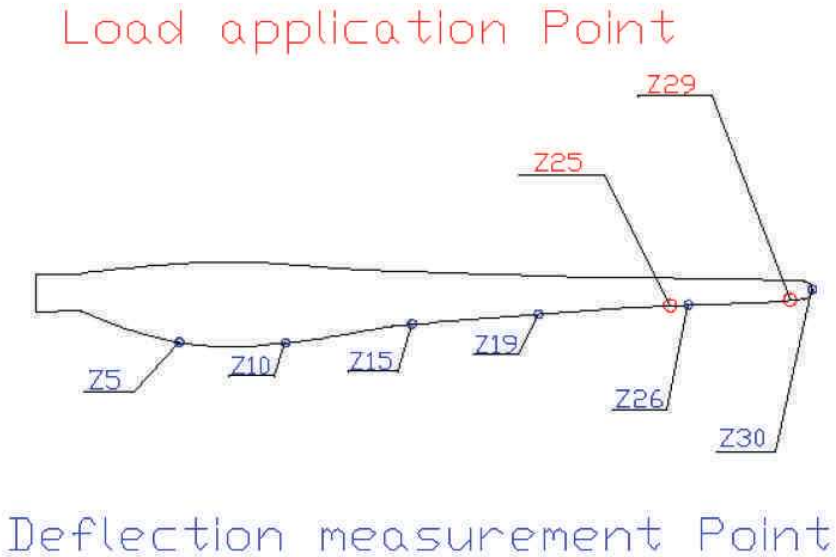


Figure C-4 : Load and deflection measurement locations.

| Blade side pointing up | Introduction point | Clamp position (m) | Applied load direction | Intended applied load (kN) |
|------------------------|--------------------|--------------------|------------------------|----------------------------|
| Leading edge | | | LTT | |
| | | | | |
| | B | 14.0 | | 0.0 |
| | C | 18.0 | | 0.0 |
| | D | 25.0 | | 17.2 |
| | E | 29.0 | 22.5 | |

Table C-7: Loading point locations.

| Distance from the root (m) | Target moment (kN-m) | Test moment (kN-m) | Test moment of the target (%) |
|---------------------------------------|---------------------------------|-------------------------------|--|
| 0 | 1315.6 | 1324.6 | 100.69% |
| 1 | 1266.8 | 1275.5 | 100.69% |
| 2 | 1218 | 1226.5 | 100.70% |
| 3 | 1169.2 | 1177.4 | 100.70% |
| 4 | 1120.4 | 1128.3 | 100.71% |
| 5 | 1071.6 | 1079.2 | 100.71% |
| 6 | 1022.8 | 1030.2 | 100.72% |
| 7 | 974 | 981.1 | 100.72% |
| 8 | 925.2 | 932 | 100.73% |
| 9 | 876.4 | 882.9 | 100.74% |
| 10 | 827.6 | 833.8 | 100.74% |
| 11 | 778.8 | 784.6 | 100.75% |
| 12 | 730 | 735.5 | 100.76% |
| 13 | 681.2 | 686.4 | 100.77% |
| 14 | 632.4 | 637.3 | 100.77% |
| 15 | 583.6 | 588.2 | 100.79% |
| 16 | 534.8 | 539.1 | 100.80% |
| 17 | 486 | 489.9 | 100.81% |
| 18 | 437.2 | 440.8 | 100.82% |
| 19 | 388.4 | 391.7 | 100.84% |
| 20 | 339.6 | 342.5 | 100.86% |
| 21 | 290.8 | 293.4 | 100.89% |
| 22 | 242 | 244.3 | 100.93% |
| 23 | 193.2 | 195.1 | 100.99% |
| 24 | 144.4 | 146 | 101.09% |
| 25 | 95.6 | 96.8 | 101.30% |
| 26 | 71.7 | 72.6 | 101.30% |
| 27 | 47.8 | 48.4 | 101.30% |
| 28 | 23.9 | 24.2 | 101.30% |

Table C-8: Applied bending moments.

Identification and characterization of mechanical and structural properties against static damage and fatigue of a composite floating wind turbine blade.

Abstract

Energy seems to be the world's one, the only and the most important problem at the moment. To be specific it's the production of energy in an ecological, economical and renewable manner, which is keeping the researchers very busy and up all night. Since more than half a century, researchers have been looking into ways of developing power with inexhaustible, replenishable and ecological means. To this end almost from the dawn of modern technology natural resources have been exploited. In the past nature was exploited in its modified state. That is by building dams and river wheels/turbine. Now though the emphasis on extracting energy from the nature while leaving it relatively unaffected. For having environmentally friendly renewable energy sources researchers have been looking to harness the power of the sun and the wind. There is a huge abundance of these two sources. However solar energy being available only a fraction of the time of the day, wind energy having chosen a suitable location can be continuous.

Once a location for wind energy convertors or wind turbines has been chosen the research then turns to convert the energy efficiently, cheaply and safely. Also the use of offshore wind resources where the turbines are placed in the seas are studied. It is seen that offshore units have their advantages the most important of which is the freeing up of space on land for agriculture, industry and housing. Once offshore, why stop near the coast? Why not go into deeper waters and capture the energy available in open seas also. Hence wind energy extraction technology is ever developing to find exploitable areas.

This PhD research work entitled "Identification and characterization of mechanical and structural properties under static damage and fatigue of a composite floating wind turbine blade" looks into the various aspects of the floating wind turbine blade design. Experimental and numerical techniques are developed to accelerate the design process and possible design optimization proposals are also given.